

THIS WEEK

EDITORIALS

FOR SALE Cash crisis threatens future of London's Royal Institution **p.452**

WORLD VIEW Poor world needs more than simple health solutions **p.453**



EARTH MOVE Marcia McNutt to leave the US Geological Survey **p.457**

Genetic privacy

The ability to identify an individual from their anonymous genome sequence, using a clever algorithm and data from public databases, threatens the principle of subject confidentiality.

How private is private? A study published on 17 January reveals vulnerabilities in the security of public databases that contain genetic data, the latest in a series of similar revelations. So far, research funders that host the databases have responded to such problems on a case-by-case basis, but it is now clear that the research community as a whole must devise a more comprehensive approach.

In the latest study, led by Yaniv Erlich at the Whitehead Institute for Biomedical Research in Cambridge, Massachusetts (M. Gymrek *et al.* *Science* **339**, 321–324; 2013), researchers showed that they could discover the identity of some men whose genomes had been sequenced as part of a genomics project (see *Nature* <http://dx.doi.org/10.1038/nature.2013.12237>; 2013). Erlich's team wrote an algorithm that infers an individual's pattern (a haplotype) of genetic markers called short tandem repeats from the nucleotide sequence of his Y chromosome. The team then searched genealogical databases for the names of men with corresponding Y-chromosome haplotypes. The team confirmed the correct names by cross-referencing the possible last names with public records of people of similar ages and locations.

Using this strategy, the team was able to confirm the identity of known individuals whose genomes have been sequenced, such as genomics entrepreneur Craig Venter, and to discover the identities of anonymous research subjects, including five men who participated in both the 1000 Genomes Project and a study of Utah Mormons initiated by the Centre for the Study of Human Polymorphism (CEPH) in Paris. Erlich's team was also able to discern the identity of some of the study subjects' family members, because family pedigrees were collected as part of the CEPH study.

It is important to note that the CEPH cohort is particularly suitable for this method of identification, because of the volume of informative data that has been collected and published about CEPH participants. Their family pedigrees, the places where they lived and their ages at the time of the data collection are all public information. Or at least they were until the US National Institute of General Medical Sciences, part of the National Institutes of Health (NIH), responded to Erlich's study by removing participants' ages from public view on the Human Genetic Cell Repository website that it funds.

It would probably be more difficult to use Erlich's method to identify participants in studies lacking extensive demographic information. And Erlich responded in an exemplary way to his team's findings by contacting the NIH and other genetics researchers with his findings before publishing them. This sets an important precedent for constructively dealing with newly discovered privacy loopholes, and other researchers should take note. Erlich's team is also not publishing the names of the anonymous study participants whose identities they uncovered.

How the genetics community addresses these issues is crucial to how large-scale genetic studies will proceed. Although research participants are already sometimes told that their data might not remain private — as the CEPH study participants were — the fact that their identities could

be revealed would seem a remote risk to them, as that has only recently become possible. It is now imperative that participants fully understand that it is unlikely that their identities can be kept hidden if their genetic data are revealed. Some participants might welcome this, such as those with an interest in genealogy. Others — perhaps those with stigmatized diseases, for instance — might not.

Moving data behind a controlled-access barrier lessens their utility to science and to society at large. But researchers need to show the

“Researchers need to show the public that they are acting as careful stewards of the data entrusted to them.”

public that they are acting as careful stewards of the data entrusted to them. Erlich argues that the solution is to make sure that participants understand what they're signing up for, and to adopt laws that adequately protect people against the misuse of their genetic information.

Geneticists are brainstorming other proposals for balancing data sharing with the need to protect the privacy of research subjects. One is to move more data behind a controlled-access barrier, but to authorize trusted users to access the data from many studies, rather than having to obtain it piecemeal from different studies, as researchers must do today. There are logistical barriers to this — for instance, ensuring compatibility across databases. And it is debatable whether such restrictions might do more harm than good.

But if controlled access is not the right solution, it is up to the research community, in consultation with the public, to devise a better one. A solution should come sooner, rather than later, because this latest revelation of a privacy loophole will be far from the last. ■

Vigilance needed

Experiments that make deadly pathogens more dangerous demand the utmost scrutiny.

The year-long voluntary moratorium on research to engineer strains of the H5N1 avian influenza virus that can transmit between mammals has already borne fruit. Claims of public-health benefits have received thorough scrutiny, and the researchers involved have better explained the biosafety and biosecurity precautions that they take. The debate has drawn attention to, and exposed gaps in, the rules that govern 'dual-use' research — work that can bring public benefit but might also be used for harmful purposes. The row has also, for example, prompted long-overdue national guidelines in the United States and made funders everywhere more aware of the need to assess

risky research proposals proactively. In short, the moratorium — the lifting of which is announced this week (see page 460) — has seen serious thought on the complex issues involved.

In the past year, the debate's focus has somewhat shifted from bioterrorism concerns — which, being classified, are difficult for outsiders to evaluate — towards biosafety issues. And it has concentrated attention more broadly on how best to regulate 'gain-of-function' research: work intended to increase the transmissibility, host range or virulence of pathogens. The United States is the main funder of such research, and what it decides is key to international thought. The proposed framework for assessing H5N1 gain-of-function research, outlined by the US National Institutes of Health at an international meeting in Bethesda, Maryland, in December, spells out several criteria that such research would need to meet before being funded.

One can quibble with some ambiguities in the wording of those proposals, but overall the framework should serve as an important checklist. The criteria include sensible questions, such as whether safer, alternative approaches exist that could address the same scientific points. Researchers already accept the need for regulations in areas such as animal welfare, and an extra layer of review for gain-of-function H5N1 research — which will affect only a few projects — is a small price to pay for improved public confidence in safety and oversight.

Flu researchers have been generous with their time over the past year. They have engaged in public debates and expressed their often-conflicting views in commentaries in scientific journals. The polarization of views between proponents and opponents of such research has, however, too often resulted in reiterations of entrenched viewpoints, rather than substantive discussions. Whether justified or not, there remains a perception among many critics that the debate has taken place largely behind closed doors, and has been dominated by flu scientists and research funders who have vested interests in the outcome.

As several critics point out, the assessments of the relative risks and benefits of such research remain restricted to largely qualitative arguments. The formal, quantitative risk assessment common in the nuclear power and other industries could have helped to nail down and quantify risks, and would have informed the debate better. One year on, an irreproachable, independent risk-benefit analysis of such research, perhaps convened by a body such as the World Health Organization (WHO), is still lacking.

"The lifting of the moratorium by researchers must not be seen as closure of the debate."

When it comes to mitigating risks, it is gratifying that the WHO guidelines on mammalian-transmissible H5N1 research, released last July, go beyond simply discussing the required level of biocontainment facility. They also recommend that labs doing such work should conform to international risk-management standards, thus encouraging a culture of safety in all procedures and practices.

The guidelines go on to state [original emphasis]: "Given the potential of these newly developed laboratory-modified H5N1 strains to start a pandemic, it is important that facilities that are NOT able to identify and appropriately control the risks associated with these agents REFRAIN from working with them." Those are sensible words, but unfortunately lack any means of enforcement.

The lifting of the moratorium by researchers must not be seen as closure of the debate. The potential risks of the work demand exceptional precautions in any future research. It is clear that the immediate practical applications of gain-of-function flu research remain largely hypothetical, and that its true value lies in long-term fundamental research to improve understanding of the transmissibility and pathogenicity of the virus. That makes it even more incumbent on researchers and authorities to exercise the greatest responsibility and prudence. ■

Science stakes

With the Royal Institution in trouble, Britain's crowded public-science scene must evolve.

Since 1799, the Royal Institution of Great Britain has occupied a grand building in London's Mayfair, surrounded today by luxury shops and private art galleries. For many years, the building was a central part of British science. Michael Faraday dazzled crowds there in the nineteenth century with pyrotechnic displays of chemistry.

In many respects, its address, 21 Albemarle Street, is the Royal Institution (RI) — hence the consternation in the United Kingdom and abroad when *The Times* newspaper last week reported that the RI building was up for sale. The news was no surprise. The RI has been on the financial ropes for years, lumbered with the costs of a misguided £22-million (US\$35-million) refurbishment.

Richard Sykes, the RI's current chairman, said last week that the charity was likely to be restructured. But the RI, whose property includes a remarkable collection of historic scientific equipment and documents, insists that it will continue its mission to educate and inform the public about science and will not fold.

In many ways, the RI is a victim of the trend it pioneered. When the charity started out in 1799, science itself was a novelty. What would now be deemed 'science outreach' was even more so. Albemarle Street became London's first one-way street, to deal with the crowds that headed there. Now, nearly every university encourages its academics to push their research to the public, and science communication itself has become a career.

Perhaps more importantly, people who wish to be informed about a topic no longer need to sit in an uncomfortable seat and listen to a

lecture by an *éminence grise*. While the RI resolutely championed this formal mode of engagement, the rest of the world has moved on. The vectors of knowledge are the Internet and mass media, not refined public meeting rooms. In its defence, the RI has made some attempt to modernize, but it is still known to most people as the place with the famous old (and very steep) lecture theatre.

Happily, there remains a market for science events. People flock to informal venues and to the type of flamboyant entertainment pioneered by Faraday. Cafés Scientifiques have taken off in many countries, and thousands of people attend science festivals in the United Kingdom, elsewhere in Europe and in the United States.

With the future of the RI in severe doubt, those who care about science communication in Britain should take this opportunity to discuss publicly how the landscape should change. And if such efforts fail to be self-sustaining, the RI's trustees should consider whom to favour with the charity's collection of historic equipment and other resources.

Here is *Nature's* brief guide to the runners and riders, should the RI withdraw from the race. The Royal Society does not have the corporate stomach or skills to take on a substantial increase in science communication and engagement activities. The British Science Association has appointed an ambitious new chief executive, and faces a tough challenge just to develop its annual public meeting into an event with national impact. The Wellcome Trust is strong in the crowded science-outreach field, at least in London, but is focused on biomedicine.

Alongside these, and with a lively pack of mass media, bloggers and tweeters snapping at its heels, the RI seems likely to emerge redundant, whatever happens to its lovely buildings. The institution best positioned to inherit its legacy is the Science Museum, which has invested well in showmanship and online facilities. It has yet to make its mark as a forum of national discussion, but has ambitions to do so. And its headquarters are always crowded with children and adults, and fun to visit, too. ■

➔ **NATURE.COM**
To comment online,
click on Editorials at:
go.nature.com/xhunq



Ensuring health in universal health coverage

Health systems must transcend clinical medicine and emphasize public-health approaches aimed at the drivers of disease, argues James D. Shelton.

Our planet's staggering ocean of death and disability — from backache to cancer — was painstakingly detailed in the Global Burden of Disease 2010 analysis, filling nearly an entire issue of *The Lancet* in December. One approach to this overwhelming disease burden is universal health coverage (UHC), which has been broadly defined as universal access to needed health services without financial hardship in paying for them. Indeed, *Lancet* editor Richard Horton declared the findings to be so far-reaching that “we should use them as a platform to advocate ever more vigorously for the growing consensus that universal health coverage could be the third great global health transition”. But faced with almost limitless need and finite resources, what form of UHC is best? Demand will only rise owing to ageing, growing populations and ever-more-sophisticated and expensive technologies. UHC must include all available options to improve health, but much of its language — coverage, access, payment — conveys clinical medical care, especially through insurance.

For UHC to have the impact it promises, we must approach it with a different mindset: one that is broader, is driven by impacts and goes beyond the conventional pay-per-procedure approach.

Look no farther than the United States to see huge sums spent on expensive medical services, yet little improvement in the key indicators of life expectancy and infant mortality. Clinical services clearly have benefits, but their cost-effectiveness and impact on population-level health are far from clear. That is partly because therapies are not always effective and some even harm. Also, many systems emphasize payment for procedures and not the overall health of the population. But most important is that medicine's curative arsenal tends to arrive too late to address the drivers of disease.

The Global Burden of Disease analysis is compelling. Of the top ten risk factors, only high blood pressure (which accounts for 7.0% of the overall burden) and high blood glucose (3.6%) can be readily addressed by the clinical, curative approaches that dominate medical services. The others almost entirely elude clinical intervention. And even blood pressure and glucose level are highly affected by lifestyle factors that the analysis couldn't completely tease out. Moreover, 29 of the remaining 33 risk factors listed, which include many dietary factors, are equally resistant to clinical tools. For developing countries, the balance shifts even more towards non-clinical causes, as conditions such as suboptimal breastfeeding and sanitation rise in importance.

Developing countries face particular challenges. They tend to have weak public-sector services, poor private-sector organization and large expenditures. Rapid economic advancement can offer a way to shift towards more-efficient,

equitable systems and avoid financial hardship, but the pitfall is preoccupation with clinical services. For example, Ghana's health-insurance programme follows the familiar pattern: reimbursement for mainly curative procedures (especially provision of drugs). Family planning and immunization are not covered, despite their substantial health benefits and major downstream cost savings, under the assumption that they are addressed by overburdened government clinics.

UHC will best serve developing countries if five approaches are used.

First, promoting healthy behaviours, such as exclusive breastfeeding and hand washing. Building overall health literacy is a good foundation.

Second, introducing structural and regulatory approaches such as tobacco taxation, clean-air requirements and speed bumps.

Third, prioritizing the clinical services that have the most impact: immunization, family planning and antenatal care. And programmes should be oriented towards the overall health of the population, rather than just paying for procedures. Health reform in the United States in the past few years has moved in these directions by making high-priority services free, and promoting organizations that take overall responsibility for their clients' health.

Fourth, deploying community-based services for high-impact health interventions. Ethiopia's Health Extension Worker cadre, which effectively provides key services, including sanitation and family planning, is a good example.

Finally, directing research and development less towards sophisticated technologies and more towards the strongest drivers such as nutrition and behaviour and towards low-cost, high-impact innovations, such as less-polluting cooking stoves.

Is it feasible? Yes. The economic extremes of Niger and New York City have shown this to be the case. Niger reduced child mortality by almost half between 2000 and 2009, emphasizing high-impact community-based and behavioural interventions. Almost half of the decline is attributed to improved nutrition and insecticide-treated bednets. New York City has seen life expectancy rise by 3.8 years and infant mortality fall by 23% in the past decade by emphasizing non-clinical approaches. Smoking has decreased markedly through increased taxes, decreased tobacco-product availability and hard-hitting public-health education programmes. Key community prevention-outreach programmes include HIV prevention and home visits to families with newborns. For true universal impact, other countries must follow suit. ■

James D. Shelton is science adviser, Bureau for Global Health, US Agency for International Development, Washington DC, USA. The views expressed are not necessarily those of the agency. e-mail: jshelton@usaid.gov

THE BULK OF
RISK FACTORS
IN THE GLOBAL
BURDEN OF
DISEASE
ANALYSIS ALMOST
ENTIRELY ELUDE
CLINICAL
INTERVENTION.

➔ **NATURE.COM**
Discuss this article
online at:
go.nature.com/zlmrak

RESEARCH HIGHLIGHTS

Selections from the
scientific literature

CLIMATE CHANGE

Black carbon a warming culprit

The soot that is emitted into the atmosphere from activities such as burning of diesel and biomass is making a bigger contribution to global warming than previously thought. This finding puts 'black carbon' second only to carbon dioxide in terms of its warming impact.

Tami Bond at the University of Illinois at Urbana-Champaign and her colleagues analysed data from a ground-based network of aerosol sensors, run by NASA, as well as satellite observations and global-emissions inventories. The authors found that the amount of warming from black carbon — which absorbs solar radiation and heats the atmosphere, as well as melting snow and ice — is roughly double most earlier estimates.

Lowering black-carbon emissions could be a quick way to cool the climate, but the overall effect of atmospheric aerosols on climate is still uncertain, the authors caution. *J. Geophys. Res.* <http://dx.doi.org/10.1002/jgrd.50171> (2013)

For more on this research, see go.nature.com/ztocgf

MATERIALS

Ceramics make water unwelcome

Water-repellent materials have a wide range of applications, but many hydrophobic coatings cannot withstand harsh conditions. Now, researchers at the Massachusetts Institute of Technology, Cambridge, report the production, from rare-earth

oxides, of ceramic materials that remain hydrophobic even after exposure to harsh environments.

Kripa Varanasi and his colleagues synthesized ceramics from the lanthanide oxide series, including cerium oxide. In analysing the surface chemistry of the ceramics, the researchers found that the oxides' electronic structure inhibits hydrogen bonding with water molecules. They show that water droplets bounce off a cerium oxide surface

(pictured), leaving the surface dry. Moreover, the ceramics maintain their hydrophobic nature even after abrasion and exposure to high temperatures. *Nature Mater.* <http://dx.doi.org/10.1038/nmat3545> (2013)

GENOMICS

Gene linked to Alzheimer's

Two studies have identified a rare genetic mutation that boosts the risk of

Alzheimer's disease.

Kári Stefánsson of deCODE Genetics in Reykjavik and his group analysed the genomes of 2,261 Icelanders and uncovered a mutation in the *TREM2* gene that increased the risk of Alzheimer's disease roughly threefold. A separate research team, led by John Hardy at University College London, discovered the same mutation, along with several others in the same gene, when analysing the genomes of more than 1,000 people with the disease.

The protein encoded by *TREM2* is expressed in brain immune cells called microglia, and regulates the process by which these cells engulf cell debris. The findings suggest



P. G. LOVELL ET AL. CURR. BIOL.

ANIMAL BEHAVIOUR

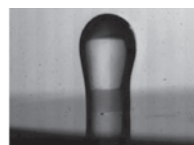
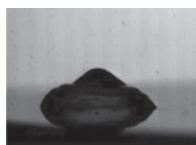
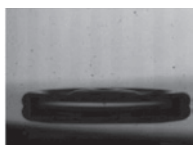
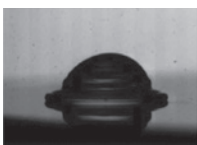
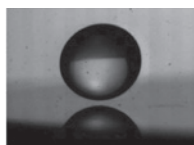
Quail pick nests that best hide eggs

Individuals of a bird species may nest in different areas according to which best camouflages the patterns on their eggs, report George Lovell at Abertay University in Dundee, UK, and his colleagues.

Japanese quail (*Coturnix japonica*) lay speckled eggs that vary greatly in appearance between mothers. The authors offered 15 females four different colours of sand in which to lay their eggs. Using photographic analysis, the team

found that females with more highly spotted eggs typically chose darker sand that matched the colour of the spots. By contrast, quail that laid lightly spotted eggs selected paler sand that matched the background colour of the eggs.

The authors suggest that individual female quail select egg-laying strategies best suited to hiding their eggs from detection by predators. *Curr. Biol.* <http://dx.doi.org/10.1016/j.cub.2012.12.031> (2013)



that, in the brains of people with the neurodegenerative disorder, immune cells are unable to clear away the plaques that are hallmarks of the disease.

N. Engl. J. Med. 368, 107–116; 117–127 (2013)

MICROBIOLOGY

Leprosy bacteria reprogram cells

The bacterium that causes leprosy spreads through the body by reprogramming infected cells to become stem-cell-like cells that can form other cell types.

Leprosy is caused by the bacterium *Mycobacterium leprae*, which infects Schwann cells that insulate nerve cells. When Anura Rambukkana at the University of Edinburgh, UK, and his colleagues infected mouse Schwann cells with the bacterium, they found that the cells expressed genes typical of an earlier developmental stage. After they were injected into mouse muscle, these stem-cell-like cells turned into muscle cells, and the bacteria spread to neighbouring muscle tissue. The stem-cell-like cells also transferred bacteria to immune cells called macrophages, which spread the infection further.

Understanding how *M. leprae* reprograms cells could inform treatment strategies, as well as provide tools for regenerative medicine, the authors say.

Cell 152, 51–67 (2013)

For a longer story on this research, see go.nature.com/fbkksy

IMAGING

Compressed picture-taking

Digital cameras take images as arrays of pixels that are compressed by algorithms into a smaller file. But a system designed by John Hunt and his colleagues at Duke University, Durham, North Carolina, can generate a compressed picture without the need for a post-processing stage.

The device uses an approach that samples image data at random, but still includes enough information to generate a good-quality image. The authors used an aperture made of a strip of metamaterial — an artificial structure that interacts with light in ways not found in nature — that guides microwaves to a single-pixel sensor. The patterns in the material are ‘transparent’ to certain wavelengths, so the signal ‘leaks’ information as it moves down the strip, allowing for the random data sampling.

Using this system, the researchers created a video of a moving object’s path in one dimension. The technology could one day be used in airport scanners, radar systems and infrared imaging, the authors say.

Science 339, 310–313 (2013)

HYDROLOGY

Irrigation brings more rain

Agricultural irrigation in the Central Valley of California doubles the amount of water vapour in the atmosphere, leading to increased rainfall throughout the southwestern United States.

James Famiglietti and Min-Hui Lo of the University of California, Irvine, analysed the impact of irrigation on climate using a global climate model. They found that irrigation adds so much water to the region’s hydrological cycle through evaporation and transpiration (whereby plants release water into the atmosphere) that summer precipitation is increased by 15%. As a result, summer run-off is raised by 56% across the region and by 28% in the Colorado River Basin, which is a source of fresh water for southern California.

A better understanding of the impact of irrigation on regional climate and water availability can improve resource management, the authors say.

Geophys. Res. Lett. <http://dx.doi.org/10.1002/grl.50108> (2013)

COMMUNITY CHOICE

The most viewed papers in science

BIOTECHNOLOGY

Cancer drugs from algae



Algae could be used to make complex, targeted cancer drugs, thanks to their photosynthetic organelles, the chloroplasts.

Immunotoxins are drugs that combine a toxin with an antibody; the antibody targets the toxin to specific cells, such as cancer cells. However, the drugs have proved difficult and expensive to produce. Stephen Mayfield and his colleagues at the University of California, San Diego, reasoned that the green alga *Chlamydomonas reinhardtii* could be used to produce immunotoxins. The chloroplasts of this alga contain the machinery to properly fold complex proteins — such as antibodies — and can tolerate some toxins.

The team used the alga to produce an antibody to CD22 — a protein found on a type of immune cell called a B cell — coupled to a bacterial toxin. The immunotoxin killed B cells in culture, and inhibited the growth of human B-cell tumours that had been implanted in mice.

Proc. Natl Acad. Sci. USA 110, E15–E22 (2013)



BRAGE BREMSET HANSEN

ECOLOGY

Arctic rain brings animal pain

Winter rain, an unusual event in the high north, drives animal numbers on a Norwegian Arctic island into decline, showing that extreme climate events can affect an entire community of vertebrates.

Brage Hansen at the Norwegian University of Science and Technology, Trondheim, and his team found that populations of Svalbard reindeer (*Rangifer tarandus platyrhynchus*), rock ptarmigan (*Lagopus muta hyperborea*) and sibling voles (*Microtus levis*) on the island of Spitsbergen crash during especially rainy winters — when the animals’ food is

coated in layers of ice. The extreme weather synchronizes fluctuations in the population numbers of these herbivores. This, in turn, causes numbers of the Arctic fox (*Vulpes lagopus*; pictured) — which preys on ptarmigans and voles, and feeds on reindeer carrion — to oscillate, but with a one-year lag.

The overwintering vertebrate community could represent a bellwether for the influence of global warming on Arctic ecosystems, if climate change raises the prevalence of warmer and wetter winters.

Science 339, 313–315 (2013)

► **NATURE.COM**

For the latest research published by Nature visit:

www.nature.com/latestresearch

SEVEN DAYS

The news in brief

POLICY

US climate agenda

Barack Obama has vowed to put climate change onto the nation's political agenda in his second term as president of the United States. He delivered his second inaugural address on 21 January before a crowd of thousands on the National Mall in Washington DC, stating that Americans "will respond to the threat of climate change, knowing that the failure to do so would betray our children and future generations". Environmental groups criticized Obama for not implementing climate policies in his first term.

Yes to flu vaccine

The US Food and Drug Administration on 16 January approved Flublok, the first seasonal flu vaccine made from recombinant proteins, which is produced in insect cells grown in culture. The standard vaccine-production method uses inactivated or weakened viruses grown in chicken eggs. Limited supplies of Flublok will be available this winter, providing some relief for vaccine shortages in the United States, which is suffering from a severe flu season. Development of Flublok by Protein Sciences in Meriden, Connecticut, was supported by the US Biomedical Advanced

NUMBER CRUNCH

13.2 GW

Wind-energy capacity installed by the United States last year — an annual record — with 5.5 gigawatts (GW) in December alone. US wind capacity is now 60 GW, 6% of the country's electricity-generating total.



HERIBERT PROEPER/AP/PRESS ASSOCIATION IMAGES

Insecticides linked to poor bee health

The European Food Safety Authority (EFSA) in Parma, Italy, has warned that three widely used neonicotinoid insecticides could pose a risk to honeybee health. It recommends their use be restricted to crops that are not attractive to the insects, amid concerns about declining bee populations. Syngenta, the Swiss company that

manufactures one of the chemicals investigated, described the EFSA's work as "hurried and inadequate", and suggested that the agency had succumbed to political pressure to reach quick conclusions. The EFSA had not responded to this allegation when *Nature* went to press. See go.nature.com/v3zdne for more.

Research and Development Authority. See go.nature.com/2cpzzy for more.

Gun research

US President Barack Obama has ordered the US Centers for Disease Control and Prevention (CDC) in Atlanta, Georgia, to conduct or fund research into the causes of gun violence. Obama announced the move on 16 January after a shooting at an elementary school in Newtown, Connecticut, in December killed 26 adults and children. The work ends a 17-year hiatus in the CDC's gun-research activities. See go.nature.com/xn75ly for more.

Mercury capped

A legally binding treaty to cap environmental emissions of the toxic metal mercury was agreed

by 140 nations on 19 January. The treaty has taken four years to negotiate and will be open for signatures at a meeting in Minamata, Japan, in October. It is expected to come into force within 3–5 years and requires countries with artisanal and small-scale gold-mining operations to draw up national plans to reduce and, if possible, eliminate the use of mercury. See go.nature.com/vqch6y for more.

RESEARCH

Flu work resumes

Flu scientists have partially lifted a year-long moratorium on research aimed at re-engineering highly pathogenic H5N1 avian influenza viruses to transmit efficiently between mammals. In a letter published on

23 January in *Nature* and *Science*, 40 flu scientists said that authorities have now reviewed the biosafety and biosecurity conditions under which the research can be done safely, and scientists with national approval should resume their work. See pages 451 and 460 for more.

India Moon mission

India's second mission to the Moon, scheduled for 2015, will be a solo affair and not the joint venture with Russia that was originally proposed, a top scientist at the Indian space agency told *Nature* on 22 January. Russia had agreed in 2007 to provide a lander and rover for the mission, but withdrew after a Russian mission to Mars's moon Phobos failed in November 2011, leading to a review of

USGS its lander technology. See go.nature.com/izhskf for more.

FUNDING

Disaster relief

The US House of Representatives on 15 January approved some US\$50 billion in emergency-relief funding to help the east coast recover from the destruction caused by Hurricane Sandy last year. The package includes roughly \$194.5 million for the National Oceanic and Atmospheric Administration to improve weather prediction and monitoring, and \$15 million for NASA to repair damaged facilities. The Senate is expected to consider the bill in the week of 21 January.

PEOPLE

Space chief quits

The president of the Canadian Space Agency, former astronaut Steve MacLean, announced that he is to leave the agency on 1 February after five years in the job. He is moving on to lead a research team in quantum physics at a new venture to be created by Mike Lazaridis, former co-chief executive and co-founder of the Research in Motion company, which makes BlackBerry smartphones. See go.nature.com/bxeq7 for more.



USGS departure

Marcia McNutt (pictured), director of the US Geological Survey (USGS), has announced that she will resign on 15 February. McNutt, a geophysicist, will stay to oversee the launch of the Landsat 8 Earth-observation satellite scheduled for 11 February. Her resignation is one of several leadership changes at national agencies as Barack Obama heads into his second term as US president. On 16 January, Ken Salazar announced his resignation as head of the Department of the Interior, the parent agency of the USGS.

FACILITIES

Fusion home

The European Union has awarded a €300-million (US\$399-million) contract to build the housing for ITER, the international experimental fusion reactor, to a consortium of French and Spanish construction

companies. Completion of the building is slated for mid-2018, and ITER is scheduled to conduct its first experiments in November 2020. The total cost of the project, located at Cadarache in the south of France, is estimated at roughly €15 billion. See go.nature.com/uvjx7 for more.

Reef lab saved

A beleaguered underwater research laboratory in Florida was thrown a lifeline on 15 January after Florida International University in Miami agreed to take over the running of the facility in 2013. The Aquarius Reef Base, owned by the US National Oceanic and Atmospheric Administration (NOAA), was set to close because of federal budget cuts. The university has received US\$600,000 from NOAA towards maintaining the lab this year, but the base's long-term future remains uncertain. See go.nature.com/4wup3y for more.

Institution for sale?

The luxurious west London headquarters of the esteemed Royal Institution, where electrical pioneer Michael Faraday made many of his discoveries and established the prestigious Christmas lectures, could be put on sale for upwards of £60 million (US\$95 million). In a statement on 17 January,

COMING UP

29 JANUARY

NASA is scheduled to launch the first in a new generation of communications satellites to transfer data from the International Space Station and agency satellites, craft and balloons. Its most recent data-relay satellite was launched a decade ago.

tdrs.gsfc.nasa.gov

30 JAN–2 FEB

ScienceOnline — a conference for writers and researchers to discuss science and science communication on the Internet — takes place in Raleigh, North Carolina.

scienceonline.com

chairman Richard Sykes said that the 200-year-old institution would consider subletting or selling the building. The move follows years of financial turmoil and internal strife at the institution, which in 2005–08 spent £22 million on a controversial refurbishment that left it short of funds. See go.nature.com/xoeldp and page 452 for more.

Slashed budget

A troubled cancer-research agency in Texas faces a massive budget cut announced in the state's preliminary spending plans on 14 January. The Cancer Prevention and Research Institute of Texas in Austin is set to receive only US\$5 million per year for 2014 and 2015, down from nearly \$300 million per year. The cut reflects criticisms last year that some grants awarded had not gone through the institute's peer-review system. See go.nature.com/sjyomo for more.

► NATURE.COM

For daily news updates see:

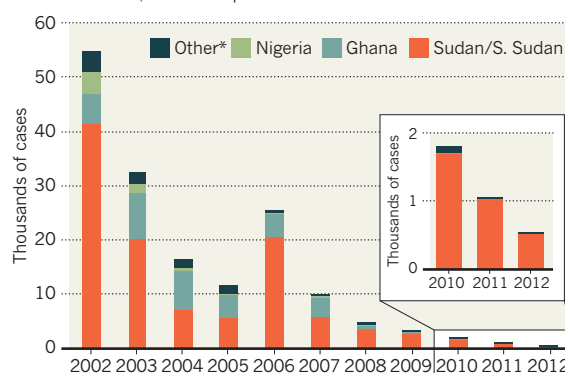
www.nature.com/news

TREND WATCH

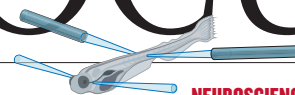
The Carter Center in Atlanta, Georgia, says that it is in the final stages of wiping out Guinea worm disease (dracunculiasis), which is carried by larvae in contaminated water. The disease was once endemic in 21 countries in Africa and Asia, but just 542 cases were reported in 2012, most of them in South Sudan (see chart). There are no medicines to treat dracunculiasis, but with health education and by teaching people to filter drinking water, the centre aims to eradicate it in the next few years.

GUINEA WORM ALMOST WIPED OUT

Dracunculiasis would be the second human disease to be eradicated, after smallpox.



NEWS IN FOCUS



ENVIRONMENT Oil-spill researchers wrangle over chemical remedy **p.461**

ASTRONOMY Masking a telescope so it can see an exo-Earth **p.464**

JAPAN Economic stimulus bets big on stem cells, space and materials **p.465**

NEUROSCIENCE Fish swimming in virtual world illuminate the brain **p.466**

CHRISTIAN MOREL



Isotopes in this ice core reveal how glaciers responded to climate change more than 100,000 years ago.

CLIMATOLOGY

Greenland defied ancient warming

But Antarctic glaciers may be more vulnerable than thought.

BY QUIRIN SCHIERMEIER

Over a few exceptionally warm days last July, Greenland's frozen surface turned into a colossal puddle. Even the coldest parts of the world's largest island saw ice thaw and rain fall, fuelling concerns over the future of glaciers that hold enough water to raise global sea levels by around 7 metres.

A record of the past written in an ancient ice core now reveals that Greenland's ice sheet is not melted as easily as some fear. But the message is not entirely reassuring: it also implies that Antarctica has much greater potential to raise sea levels than previously thought.

The 2,540-metre-long core comes from a site in northwestern Greenland that hosts some of the island's oldest ice, dating back to the Eemian

interglacial: the Earth's most recent warm period before temperate conditions returned once more some 12,000 years ago. Lasting from about 130,000 to 115,000 years ago, the Eemian warming was triggered by increases in summer sunshine, resulting from variations in Earth's orbit and axis of rotation. But it may be a good model of the man-made climate change expected over the coming centuries. "We are in a similar climate regime as the world was in the early Eemian," says Eric Steig, who studies ice cores at the University of Washington in Seattle.

The North Greenland Eemian Ice Drilling (NEEM) project, a 14-nation research team, has spent the past four years drilling and analysing the core, and its results are published in *Nature* this week¹. Extracting a record of the Eemian was a challenge: the core's lowest layers

had been deformed and folded by the constant movement of the ice sheet. "Of course we had hoped for a purer record," says Dorthe Dahl-Jensen, a palaeoclimatologist at the University of Copenhagen who led the NEEM project. "But it is a fantastic record even so, and it does have all the information we needed to reliably reconstruct the Eemian climate and ice-sheet history."

She and her colleagues painstakingly compared and synchronized the disturbed parts of their core, layer by layer, with other well-dated ice cores from Greenland and Antarctica to tease out the story. "I am very sure that we have got the picture right," says Dahl-Jensen.

The results confirm the warmth of the Eemian climate: ratios of oxygen and nitrogen isotopes in the core show that some 6,000 years after the onset of the Eemian, local temperatures reached about 8°C above the present-day annual average of roughly -25°C.

But the ice sheet at the NEEM site did not get much thinner than its present 2.5 kilometres, according to the air content in the core that the team correlated with elevation. Before the Eemian, the Greenland ice sheet was some 200 metres thicker than it is today, and after six millennia of strong warming the ice sheet lost just over one-tenth of its thickness, dropping to 130 metres below its present height. It then remained steady until the end of the Eemian (see 'Warm spell'). "It's illuminating to see just how strongly Greenland had warmed at the time," says Steig. "That the warming seemingly caused only relatively modest melting is of course also remarkable."

There is a small possibility that the reconstruction is incomplete because it reflects conditions at only one site, which may provoke debate about the results, says Steig. Until the past few years, most researchers had thought that Greenland contributed at least half of the 6–8 metres of Eemian sea-level rise that has been deduced from records of ancient corals and other markers². Yet the NEEM core implies that Greenland's ice sheet lost at most one-quarter of its volume, and contributed no more than 2 metres of sea-level rise. "The good news is that Greenland is not as sensitive to climate warming as we thought," says Dahl-Jensen.

"The bad news is that if Greenland's ice sheet did not disappear during the Eemian, Antarctica must have been responsible for a significant part ▶

➔ **NATURE.COM**
Read more about
the melting Arctic in
Nature's special at
go.nature.com/s5w2pr

► of the sea-level rise," she adds. These two ice sheets, the world's biggest, have been stable for most of the current interglacial period. But since temperatures began to soar a couple of decades ago, Greenland and Antarctica have been shedding ice fast. Between 1992 and 2011, they lost around 2,700 billion and 1,350 billion tonnes of ice, respectively — enough to raise sea levels by about 0.6 millimetres per year³. Scientists think that by 2100, the global sea level may have risen by 0.5–1.2 metres above current levels.

Although ice loss is currently greatest in Greenland, that could change: some parts of Antarctica are warming almost twice as fast as previously believed⁴, and glaciers in western Antarctica have retreated at a worrying rate in the past few decades⁵. Furthermore, Eemian sea-level rise seems to have proceeded in drastic jumps, rather than gradually⁶, suggesting that the ongoing sea-level rise could accelerate.

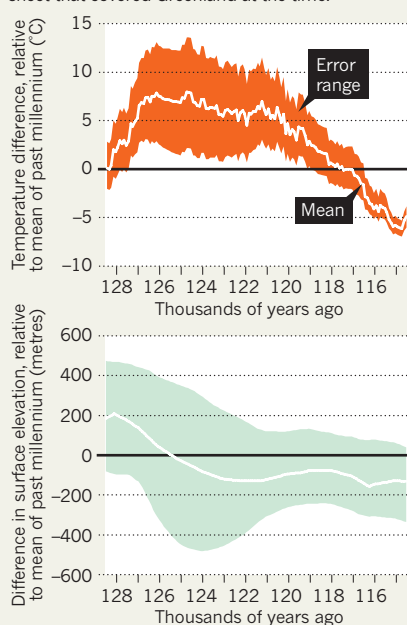
That may not be a menace to civilization yet. But, says Dahl-Jensen, if Antarctica's massive ice sheets do disintegrate — as the NEEM core suggests they did before — we could face an extremely rapid sea-level rise around the world. NEEM's message is that the Eemian is distant only in years, not in consequence. ■

1. NEEM community members *Nature* **493**, 489–494 (2013).
2. Cuffey, K. M. & Marshall, S. J. *Nature* **404**, 591–594 (2000).
3. Shepherd, A. *et al.* *Science* **338**, 1183–1189 (2012).
4. Bromwich, D. H. *et al.* *Nature Geosci.* <http://dx.doi.org/10.1038/ngeo1671> (2012).
5. Hillenbrand, C.-D. *et al.* *Geology* **41**, 35–38 (2013).
6. Blanchon, P., Eisenhauer, A., Fietzke, J. & Liebetrau, V. *Nature* **458**, 881–884 (2009).

SOURCE: NEEM

WARM SPELL

The Eemian interglacial period (130,000–115,000 years ago) began with a burst of climate warming — but this caused only a modest shrinkage of the ice sheet that covered Greenland at the time.



VIROLOGY

Work resumes on lethal flu strains

Study of lab-made viruses a 'public-health responsibility'.

BY DECLAN BUTLER

An international group of scientists this week ended a year-long moratorium on controversial work to engineer potentially deadly strains of the H5N1 avian flu virus in the lab.

Researchers agreed to temporarily halt the work in January 2012, after a fierce row erupted over whether it was safe to publish two papers reporting that the introduction of a handful of mutations enabled the H5N1 virus to spread efficiently between ferrets, a model of flu in mammals (see *Nature* <http://doi.org/fxv55r>; 2012). Both papers were eventually published, one in *Nature*¹ and one in *Science*².

Now, in a letter simultaneously published on 23 January by *Nature*³ and *Science*, the 40 scientists involved say that the moratorium has served its purpose: allowing time for authorities to review the conditions under which the research could be safely conducted and for scientists to explain the public-health benefits of the work. Scientists who now have official approval in their countries to conduct such research "have a public-health responsibility to resume this important work", the letter states, "because the risk exists in nature that an H5N1 virus capable of transmission in mammals may emerge".

The move follows a large international workshop convened on 17–18 December by the US National Institutes of Health in Bethesda, Maryland, to discuss 'gain-of-function research' — that intended to increase the transmissibility, host range or virulence — in H5N1 viruses, and the development of US rules for stricter oversight of research in this area. The proposed rules require an assessment of, for example, whether the scientific aims of such studies could be addressed using alternative, less-risky approaches, and whether biosafety and biosecurity risks can be adequately mitigated. They are expected to enter into force soon, allowing scientists working in the United States or on US-funded grants to restart such research.

The groups that published the original research have outlined a suite of possible follow-up experiments, including a search for other combinations of mutations that would allow H5N1 to transmit between mammals — which could answer basic-science

questions and, they argue, aid efforts to watch for dangerous mutations in the wild. The researchers also suggest extending the studies in ferrets to other mammals, such as guinea pigs, because further evidence of transmission within mammalian species would increase confidence that the mutated virus would transmit between humans.

But the scientific community remains divided on whether the practical benefits of the research outweigh the risks of an accidental or deliberate release of a lab-created flu strain. Ian Lipkin, a specialist on emerging infectious diseases at Columbia University in New York, believes that the risks are high and, worse, that such research may end up being done in labs with insufficient biosafety standards.

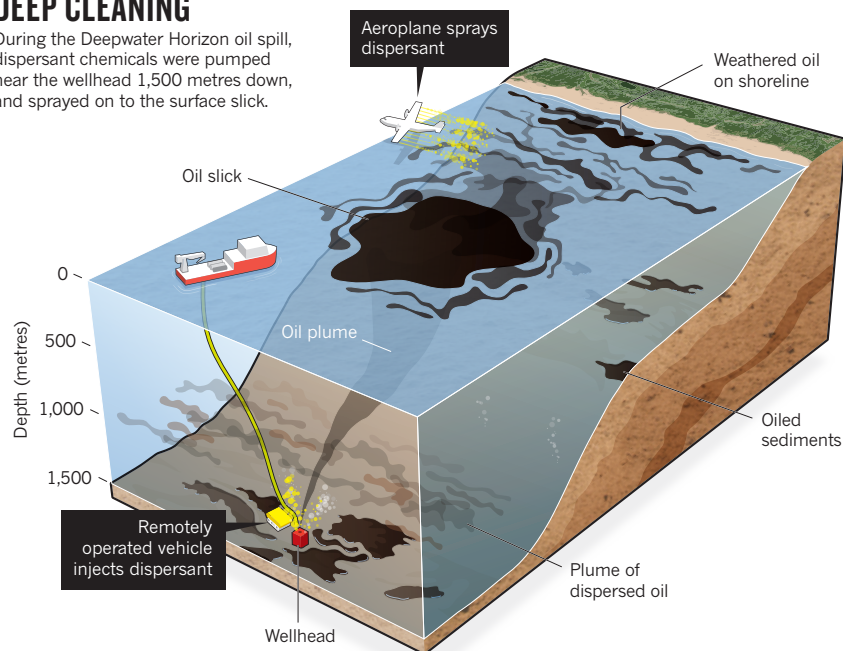
The World Health Organization (WHO) posted general biosafety guidelines for such work on its website last July (go.nature.com/4z4yzg), but Lipkin says such guidelines need to be extended and given more teeth before work restarts. He suggests that this could be done by including them in the WHO's international legally binding treaty on global threats to health — the 2005 International Health Regulations. Ron Fouchier at Erasmus Medical Centre in Rotterdam, the Netherlands, who led the research behind last year's *Science* paper, disagrees. He says that national and institutional procedures have long proved adequate. "If we have to wait until all national governments in the world agree on terms and conditions, we can wait for years if not forever," he says. "That is unacceptable."

But even some who support the lifting of the moratorium have misgivings about the future. Ilaria Capua, a flu researcher at the Veterinary Public Health Institute in Legnaro, Italy, who signed the letter, says that she is less concerned about current work, which is limited to a handful of labs with high biosafety standards, than about the risk of proliferation of such research in the longer term. "This is not a decision for scientists," she says, "it's a decision for policy-makers; do we want to continue to invest public funds in this type of work?" ■ **SEE EDITORIAL P.251**

1. Imai, M. *et al.* *Nature* **486**, 420–428 (2012).
2. Herfst, S. *et al.* *Science* **336**, 1534–1541 (2012).
3. Fouchier, R. A. M. *et al.* *Nature* <http://dx.doi.org/10.1038/nature11858> (2013).

DEEP CLEANING

During the Deepwater Horizon oil spill, dispersant chemicals were pumped near the wellhead 1,500 metres down, and sprayed on to the surface slick.



ENVIRONMENT

Researchers debate oil-spill remedy

Oil industry maintains that dispersants should be part of routine response to deep-water blowouts.

BY MARK SCHROPE

No aspect of the 2010 Deepwater Horizon oil spill in the Gulf of Mexico was more controversial than the decision to pump massive doses of chemical dispersant into the oil gushing from 1,500 metres down (see 'Deep cleaning'). Advocates said that the mixture of solvents and detergent would separate the deep oil plume into finer droplets, speeding its breakdown. Critics feared damage to deep-water ecosystems.

This week, researchers at the Gulf of Mexico Oil Spill and Ecosystem Science Conference in New Orleans, Louisiana, are assessing the outcome — and sometimes drawing markedly different conclusions from the scant data. Industry scientists argue that the nearly three million litres of subsea dispersant worked as expected and caused minimal ecological damage. Dispersant, they say, should be a standard option for fighting future sea-floor blowouts. But other researchers say that applying dispersants at depth has not yet been proved to be effective, let alone safe.

Both the US National Oceanographic and Atmospheric Administration and industry

representatives have touted aerial photos showing that the surface oil plume in the Gulf of Mexico diminished after dispersant was applied. And oil company BP, which owns the well, reported improvements in the air quality measured from work ships, suggesting that less oil was floating to the surface.

Seawater samples collected at depth during the spill for monitoring by the US Environmental Protection Agency also suggest that the dispersants worked, according to data presented by Kenneth Lee, a marine biologist at Fisheries and Oceans Canada in Dartmouth. He and his team documented droplet sizes that are consistent with lab experiments in which dispersant and oil are mixed in a wave tank.

Some post-spill results described at the conference this week offer support. Eric Adams, an engineer at the Massachusetts Institute of Technology in Cambridge, and his colleagues used glass beads as a proxy for oil in tank experiments simulating the spill. Based on their results, he says, "If your goal is to spread the oil out, then dispersant appears to help."

With an eye to the future, the American Petroleum Institute, an industry group in Washington DC, is studying the most

efficient means of injecting dispersant into a deep oil plume, as well as considering designs for dispersant applicators that could be installed at the wellhead in case of a spill. Study-group members are presenting their early findings at the conference. "We think subsurface dispersant played a critical role and that that response effort had a positive outcome," says Emily Kennedy, a policy analyst at the institute.

The oil industry's confidence leaves some researchers wary. "I think it's incredibly premature," says Sean Anderson, an ecologist at California State University Channel Islands in Camarillo, who is part of a group studying the spill¹. "We're in no way saying dispersants should never be used or didn't work at all; it's a question of, 'Show us the data to show it was actually effective,'" he says.

He and others cite hints that turbulence at the wellhead could have caused substantial dispersal on its own. And Claire Paris-Limouzy, an oceanographer at the University of Miami in Florida, questions some of the positive conclusions. Using a computer model, she and her colleagues concluded that dispersants may have had little effect on the amount of oil that ultimately surfaced².

The data are even thinner when it comes to the ecosystem effects of the chemicals, or of the oil they might have helped to disperse through the depths. Biologists conducting the government assessment of effects on deep-sea fish, for instance, concluded that they couldn't quantify any impacts because of a lack of baseline data on these populations.

In 2010, however, researchers found soft corals that had apparently been killed by dispersed oil from the spill³. At the conference, Charles Fisher, a deep-sea biologist at Pennsylvania State University in University Park, reported that the spill damaged at least one deep coral stand and possibly two more. His collaborators are also reporting substantial losses of sea-floor animals, such as worms, downstream of the spill. And in shipboard tests, Erik Cordes of Temple University in Philadelphia, Pennsylvania, who collaborates with Fisher, showed that an oil-dispersant mixture is highly toxic to deep-sea soft corals, which can take hundreds of years to grow.

Cordes admits that dispersant use presents a difficult choice: the possibility of faster breakdown of spilled oil against what could be a greater environmental impact from the finely dispersed oil. "I don't know where the trade-off lies," he says. "But my gut and what I've seen in these experiments tells me I would rather the oil just go a little further and last a little longer than have the oil and dispersant causing that kind of damage." ■

- Peterson, C. H. *et al. BioScience* **62**, 461–469 (2012).
- Paris, C. B. *et al. Environ. Sci. Technol.* **46**, 13293–13302 (2012).
- White, H. K. *et al. Proc. Natl Acad. Sci. USA* **109**, 20303–20308 (2012).

International aid projects come under the microscope

Clinical-research techniques deployed to assess effectiveness of aid initiatives.

BY NATASHA GILBERT

Not long ago, 'research' was a dirty word in international-development circles. The prevailing view was that the time and money available should be spent implementing aid projects rather than analysing their effects in detail. For most projects, assessment was limited to tracking how much they spent and whether they reached their end points.

That is now beginning to change. In recent months, studies have rigorously assessed aid projects such as farmer-training efforts and intestinal-worm-treatment programmes. These studies reflect a more analytical mindset that has emerged in the development community over the past decade, spurred by the need to assure weary donors that their investments are paying off. Drawing on methods used in clinical studies, the analyses could help to guide policy — but they are also raising fears that programmes could be axed prematurely if initial results are disappointing.

"As the larger and more careful impact studies come out, we will see more and more negative results," says Macartan Humphreys, an international-development economist at Columbia University in New York.

The Millennium Challenge Corporation (MCC), a US foreign-aid agency, has taken the lead in self assessment, committing to using scientific methods to analyse the success of 40% of its projects. Its first assessments — of farmer-training activities in five countries including Armenia, El Salvador and Ghana — delivered a mixed verdict.

Published in October 2012, the evaluations showed that in three of the countries, efforts to train farmers in business and agricultural skills helped them to sell more produce, boosting farm incomes. But, contrary to the assumption



In Bangladesh, women received nutrition advice through an aid programme, but few were able to use it.

that greater agricultural production reduces poverty, there was no evidence that the extra cash flowed to the farmers' households — an effect that the MCC cannot readily explain. "We are pushing back the boundaries of ignorance by doing these studies," says William Savedoff, an economic and social-development researcher at the Center for Global Development in Washington DC, who was not involved in the evaluation. "They are forcing us to grapple with what we do and don't know about the links between agricultural extension and poverty."

Some of the MCC's farmer-training assessments relied on randomized controlled trials (RCTs), a mainstay of clinical research. In development research, RCTs randomly enrol people in aid projects — equipping

households with bed nets to protect against disease-carrying mosquitoes, for example — and then track them along with an equal number of people not benefitting from that aid. This protocol allows researchers to evaluate whether a given development strategy makes a measurable difference to people's lives. "We think RCTs are very effective but still underused," says development economist Rachel Glennerster, a director of the Abdul Latif Jameel Poverty Action Lab (J-PAL) at the Massachusetts Institute of Technology in Cambridge.

Glennerster says that J-PAL researchers rely heavily on RCTs in assessing aid projects, but that not everyone regards them as a gold standard. Jeffrey Sachs, a sustainable-development


**MORE
ONLINE**

TOP STORY



Mathematicians launch Episciences in bid to take publishers out of publishing
go.nature.com/fdrnk1

MORE NEWS

- Faecal transplant beats antibiotics in some gut infections go.nature.com/xnez9
- International row lingers over coronavirus found in Saudi Arabia go.nature.com/vzlg9y
- South Korea makes billion-dollar bet on fusion power go.nature.com/y1ryj2

PODCAST



Genes that make you burrow; experimental archaeologists; and scientists' insider trading
go.nature.com/mzu7it

economist at Columbia University, worries that RCTs are not an ethical way to assess development projects, because they withhold aid intervention from control groups. Still, enough RCTs have been done for researchers to begin systematic reviews of particular interventions — but these meta-analyses are also attracting criticism.

Last year, for example, a systematic review of programmes to treat children in developing countries for intestinal worms found little evidence of nutritional, cognitive or educational benefit (D. C. Taylor-Robinson *et al.* *Cochrane DB Syst. Rev.* CD000371; 2012). The study was conducted by the Cochrane Collaboration, based in Oxford, UK, which is best known for its systematic reviews of medical treatments.

A group of prominent development researchers — some of whom, including Glennerster, are involved in deworming projects — argued that the review omitted or discounted key studies that showed benefits to school performance. “We were critical of the review because it just takes a bunch of studies, averages them and then finds there is no effect, when actually if you look at high-quality [primary] studies you do see an impact,” says Glennerster.

David Taylor-Robinson, a population-health scientist at the University of Liverpool, UK, and lead author of the review, stands by its

findings. “Our analysis was limited to [RCTs] comparing mass administration with placebo or no treatment,” he says, adding that three studies showing positive outcomes did not meet these criteria.

To aid such reviews, the International Initiative for Impact Evaluation (3ie), a non-profit organization based in Washington DC that funds and conducts aid-assessment research, is setting up a database in which researchers can register studies. Expected to launch later this year, the initiative aims eventually to provide a complete listing of assessments for various types of aid interventions, says Howard White, executive director of 3ie.

The goal is to help researchers avoid bias when conducting systematic reviews of development projects — by selectively reporting positive results or excluding negative ones. It is not yet clear whether development researchers will be required to register studies before publishing results in academic journals — as is the case for clinical trials in some countries.

Meanwhile, international-development researchers are increasingly applying ‘theory of change’, an analytical method that seeks to understand how a series of events leads to a particular result. “Philosophically, you don’t

need to understand the causal mechanisms to say there is a link between a treatment and an outcome,” explains White. “But we would like to understand more about the causal chain to help inform analysis and understand why programmes work in some places and not others.”

In 2005, the World Bank carried out one such analysis, of its programme to reduce malnutrition in Bangladesh. Between 1995 and 2002, the project taught mothers about nutrition — for themselves during pregnancy and for young children. Falling malnutrition rates in programme areas were initially hailed as a success, but an evaluation showed that similar trends had occurred in control areas, suggesting that the programme was not the driving factor.

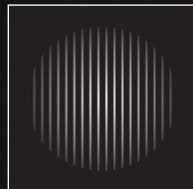
The analysis found that one of the main reasons the programme failed to make a difference was that fathers tended to be in charge of what food entered their homes — so mothers were unable to implement the nutritional education they received in the programme.

Depressing as such discoveries might be, they are part of an important culture change in development circles, says Humphreys. Negative results are integral to the research process, he argues, and it is important for researchers and donors to become more tolerant of them. If they do not, “there is a fear that when people see negative results, they will stop funding and pull out of research altogether”. ■

➔ NATURE.COM
Read *Nature's*
special on
science in Africa:
go.nature.com/ylnyfw

BLOT OUT THE LIGHT

Seeing an Earth-like planet orbiting a star 10 billion times brighter has been likened to trying to see a firefly next to a lantern from 10 kilometres away. To block the starlight, astronomers are developing five types of coronagraph:

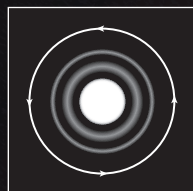


BAND LIMITED

Using a mask that resembles a barcode, this coronagraph suppresses starlight along the telescope's optical axis while transmitting light from off-axis planets.

Key challenge:

Precision manufacture of the barcode-like mask.

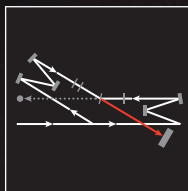


VECTOR VORTEX

A circular mask rotates the angle of polarization of photons from the star, so they cancel each other out.

Key challenge:

The need to manufacture the fine circular pattern of the mask, made from liquid-crystal polymers, to a precision of micrometres.



VISIBLE NULLING

Akin to flying several telescopes in formation, a device installed in a single spacecraft generates an interference pattern that suppresses starlight.

Key challenge:

Extending the technique to a broad band of wavelengths.

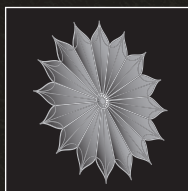


PHASE-INDUCED AMPLITUDE APODIZATION

Two asymmetrical mirrors reshape the incoming light beam to shunt starlight off to the side and preserve planetary light.

Key challenge:

The manufacture of correctly shaped optics.



STARSHADE

A petal-shaped structure carried into space on a separate spacecraft shades the telescope optics from the glare of the star.

Key challenge:

Telescope and shade must fly in formation, separated by tens of thousands of kilometres.

ASTRONOMY

Fresh bid to see exo-Earths

Improved instruments and a telescope windfall could aid the search for extrasolar life.

BY RON COWEN

As NASA's Kepler spacecraft finds signs that the Galaxy is teeming with Earth-sized planets, astronomers are renewing a stalled quest: to gather light directly from an Earth twin and tease it apart for the chemical signatures of life. That is not possible with current techniques, which find planets indirectly; and in 2006, NASA cancelled a mission that might have had a chance at doing so. The Terrestrial Planet Finder (TPF) would have used either an array of small telescopes or one giant, 8-metre mirror to capture planetary light. Now a new generation of instruments is raising hopes that a smaller, cheaper space telescope could do the job.

The TPF cancellation was "a big blow," says Olivier Guyon, an astronomer at the University of Arizona in Tucson who also works on Japan's Subaru Telescope in Hawaii, "but it also felt like a challenge to see what we could do with smaller telescopes". Guyon and others are hoping to meet that challenge with advanced coronagraphs: telescope devices that mask starlight like an artificial eclipse, allowing nearby planets that would otherwise be obscured by the star's glare to be seen (see 'Blot out the light'). NASA is exploring the idea of putting a coronagraph on one of a pair of 2.4-metre space telescopes donated to the agency by the National Reconnaissance Office, which operates the US fleet

of spy satellites (see *Nature* **490**, 16–17; 2012). Although a telescope that size — the same as the Hubble Space Telescope — would be hard-pressed to gather light from Earth-sized planets, it could image and take chemical spectra from planets the size of Jupiter and possibly even smaller than Neptune.

The impetus for such a mission is growing. This month, at a meeting of the American Astronomical Society in Long Beach, California, astronomers estimated the number of planets in the Milky Way, extrapolated from the number and types of planet that Kepler has already found in one small part of the Galaxy. The result: at least 100 billion extrasolar planets, one for every star. Even more tantalizingly, a potentially habitable Earth-sized orb is likely to reside within 6 parsecs (20 light years) of the Solar System.

Yet NASA, strapped for funds and burdened with the US\$8-billion James Webb Space Telescope project, is not about to resurrect the TPF. Planet hunters know that a smaller, pathfinder mission is their best chance. "This is the only show in town," says Alan Boss, an astronomer at the Carnegie Institution for Science in Washington DC.

A NASA-appointed team of astronomers, the Astrophysics Focused Telescope Assets

committee, will on 30 April deliver a report on the feasibility of using the donated telescopes for several types of observation, including planet imaging. Any planet hunting would have to be squeezed into a jam-packed operations schedule: astrophysicists are also eager to use the telescopes to study the mysterious phenomenon known as dark energy, which is accelerating the expansion of the Universe.

The structure of the instruments could also be a problem. The 2.4-metre telescopes contain two mirrors; the secondary one is held by six struts that cause light scattering, says Wes Traub, chief scientist for NASA's exoplanet exploration programme at the Jet Propulsion Laboratory in Pasadena, California. "The struts couldn't be in a worse place for imaging planets," he says.

Even so, exoplanet astronomers are enthusiastic. Coronagraphs have improved vastly in recent years: just a decade ago, says Guyon, they were good at blotting out most of the star's central light, but also threw away about 90% of the light reflected from the planet. One problem was caused by the sharp edges of the telescope mirror, which created a ring-like diffraction pattern in the region of the image where the planet resides.

NATURE.COM
For more about
exoplanets, see:
go.nature.com/pxgbbt

Guyon's coronagraph uses two asymmetrically polished mirrors to reshape the distribution of light gathered by the

telescope's main mirror and eliminate the diffraction pattern. The design, which in 2012 won him a 'genius' grant from the MacArthur Foundation, allows the starlight to be thrown away without sacrificing light from the planet. Guyon says that his device could enable a 4-metre telescope, half the diameter of the TPE, to see an Earth twin — but whether it could enable a 2.4-metre telescope to find Earths remains to be seen. "We're still in the grey zone," he says.

Dust adds to the uncertainty. Asteroid collisions have filled the inner Solar System with a haze of dust that reflects sunlight, creating what is known as zodiacal light. The worst nightmare of planet hunters is the possibility that the dust in other solar systems could generate so much 'exozodiacal' light that Earth-sized orbs would be lost within it. "This is the main non-technological risk for an exo-Earth imaging mission," says Ruslan Belikov, an astrophysicist at the

NASA Ames Research Center in Moffett Field, California. Measuring the levels of exozodiacal light around Sun-like stars is a key goal for a pathfinder mission, he adds.

Even if NASA decides against putting a coronagraph on one of the donated telescopes, says Guyon, he is not about to give up. Finding out if there are other habitable planets in the Galaxy, he says, "is the most interesting question in all of science". ■

FUNDING

Japan's stimulus package showers science with cash

But new leadership's largesse brings expectations of fast commercial pay-offs.

BY DAVID CYRANOSKI IN TOKYO

Three years ago, the picture for research funding in Japan looked bleak. As part of efforts to slash the national budget by ¥3 trillion (US\$33.5 billion), the government, led by the Democratic Party of Japan, had proposed sweeping cuts to science, sparking protests from the country's most eminent researchers. Japan's flagship K supercomputer project narrowly escaped being shut down after auditors questioned whether Japan needed to host the world's fastest computer.

Fast-forward to 2013, and Shinzo Abe, head of the newly elected Liberal Democratic Party-led government, seems to have no such doubts. "Of course we must aim for number one," he told reporters after a tour of the supercomputer facility on 11 January.

Science is a big winner in the government's massive ¥10.3-trillion economic stimulus package, approved by the cabinet on 15 January. The stimulus flags up the new leadership's determination that research should pull its weight in dragging Japan's economy out of recession. The supplementary budget provides billions of yen for key fields and significant boosts for many big scientific facilities (see 'Big winners') — including ¥8.4 billion for data links between the K supercomputer and Japan's universities.

Among the many other winners is the SPring-8 synchrotron, which will get ¥2.9 billion to spruce up its ageing beamlines, used for structural studies of materials and proteins. There is also ¥16.6 billion for the international fusion energy project ITER, which has been beset by budgetary difficulties since its inception (see *Nature* 487, 420; 2012). Meanwhile, the Japanese space agency JAXA will get ¥22.9 billion to refurbish its facilities and to speed up development of ALOS-2, a satellite

that will monitor natural disasters and measure atmospheric carbon dioxide levels. The extra cash will keep it on schedule for launch before April next year.

But the biggest beneficiary of the Abe government's stimulus is stem-cell research, especially that geared towards clinical applications. The science ministry alone has earmarked ¥21.4 billion for research on stem cells, mainly focused on induced pluripotent stem (iPS) cells — reprogrammed adult cells, first developed in Japan.

Yoshiki Sasai, who has been wowing biologists and non-scientists alike by growing rudimentary retinas, brain parts and other tissues from stem cells (see *Nature* 488, 444–446; 2012), has long been negotiating with the government for facilities to link basic research at the Center for Developmental Biology in Kobe, where he works, with clinics and industry. The

stimulus package, nonetheless, came "like thunder, out of the blue", he says. The budget includes ¥3.8 billion for a new building at Sasai's centre, with planned projects being largely collaborative ventures with Japanese businesses.

An even bigger windfall will benefit work by Shinya Yamanaka, a Nobel laureate who developed the first recipe for iPS cells. The Center for iPS Cell Research and Application at Kyoto University, which he directs, is to receive ¥4 billion for a building to house research on reprogramming mechanisms and clinical applications of iPS cells. Another ¥700 million will pay to create a cell-processing centre at the Foundation for Biomedical Research and Innovation in Kobe, mainly to support Masayo Takahashi, who works next door at the Center for Developmental Biology. Takahashi is planning the first trial of iPS cells in humans, in a clinical study set to start this year on the eye condition known as macular degeneration.

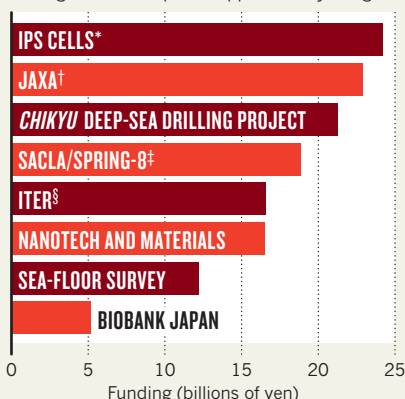
Other ministries have also jumped on the iPS-cell bandwagon. For example, with ¥2.2 billion the health ministry plans to build two centres to provide training on deriving and cultivating iPS cells.

The stimulus cash could be just the start of the good times for Japan's stem-cell researchers. The government is expected to announce a ten-year, ¥90-billion iPS-cell initiative in next year's budget, beginning in April.

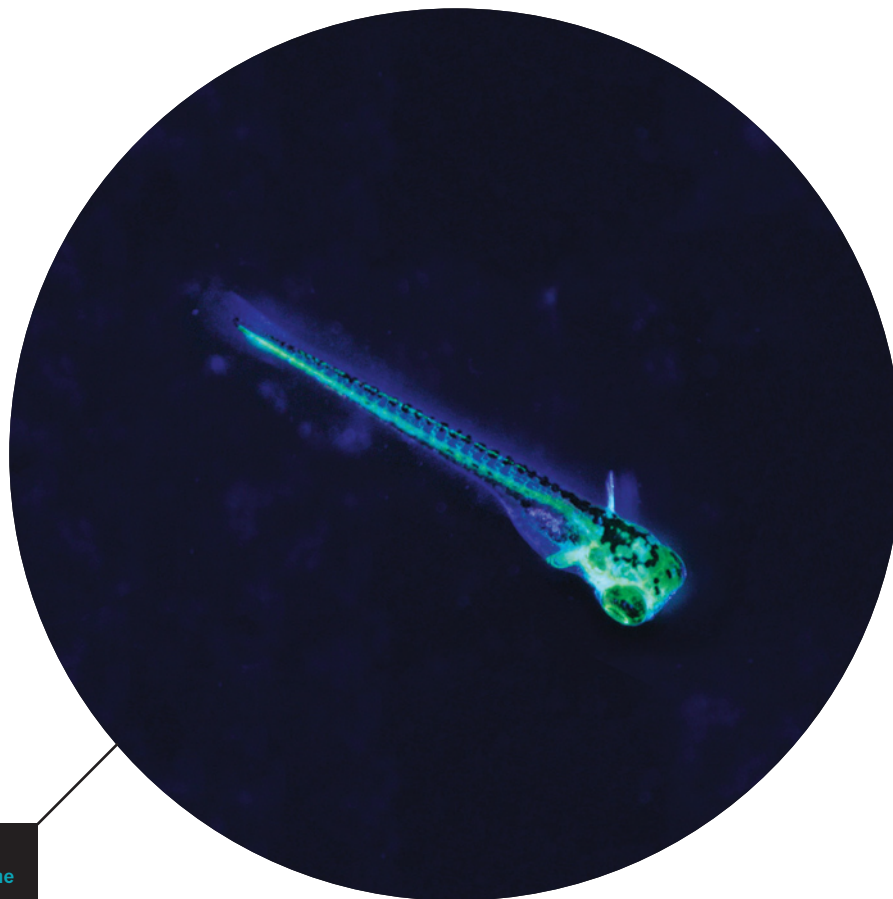
But the largesse comes with expectations. Of the ¥721 billion earmarked for science and technology by the science ministry, ¥180 billion will go towards translating university research into commercial applications, and most other projects are framed around clinical or industrial applications. With the stimulus, says Yamanaka, the government is "telling us to rush iPS-cell-related technologies to patients as quickly as possible". ■

BIG WINNERS

Some of the facilities or fields that receive big funding boosts in Japan's supplementary budget.



*Induced pluripotent stem cells; †Japanese space agency; ‡SACLA X-ray free electron laser/SPRING-8 synchrotron; §International fusion project



The transparency of zebrafish larvae makes the animals ideal models for seeing deep into tissues.

FISH-BOWL NEUROSCIENCE

Tiny fish trapped in a virtual world provide a window into complex brain connections.

BY VIRGINIA HUGHES



recently hatched zebrafish is swimming upriver for the first time. Its big round eyes, bulging on the front of its eyelash-sized body, scan the surroundings. Suddenly, it sees the scenery flying forwards as a gentle current pushes it backwards. The fish flicks its tail to try to stay in place. Or so it thinks.

In reality, the baby fish is paralysed and suspended in a water-filled Petri dish by glass pipettes. The dish sits on the stage of a US\$100,000 microscope in the corner of a darkened, cluttered laboratory. A film, projected from below, has transported the fish to a virtual world in which moving bands of light and dark simulate passing underwater scenery.

Although the fish doesn't move, the motor neurons that control its tail are firing away, just as if it were swimming. And when fed into a computer, those signals can control the video display, giving the fish nearly every sign that it is swimming normally. All the while, Florian Engert's microscope peers deep into the fish's tiny, translucent brain to watch

➔ **NATURE.COM**

Watch a video of a zebrafish in 'the matrix' at.

go.nature.com/lghpmp

CHARLES MAZEL/VISUALS UNLIMITED/CORBIS

neurons glow green as they fire.

Engert, the neuroscientist who developed the set-up, often jokes that the fish is just like Neo, a leading character from the 1999 sci-fi thriller *The Matrix*, in which humans have been enslaved by machines but are fed a virtual reality that leads them to believe that they are free. Engert's team at Harvard University in Cambridge, Massachusetts, hopes that the fish in this aquatic matrix will help to answer the biggest question in neuroscience: how a doughy mass of neurons in the brain gives rise to an exquisite suite of behaviours, absorbing information from the outside world and generating responses.

Since the late nineteenth century, when Spanish anatomist Santiago Ramón y Cajal pinpointed the neuron as the fundamental unit of the brain, most neuroscientists have focused on recording the electrical buzzing of individual cells. That has tended to mean sticking electrodes into the brains of cats, rabbits, rats, mice, sea slugs, squid, monkeys and even people. The approach reveals a lot about how neurons respond to inputs — such as a chemical messenger, a sound or a colour — and produce individual firing patterns, which the brain decodes to drive behaviour. But how these cells work together to translate and integrate complex, real-world sensory inputs — such as moving scenery, smells, sounds or an approaching predator — “is something that's still a big mystery”, Engert says. “That's probably the main challenge for the next decade.”

Larval zebrafish (*Danio rerio*) have been a workhorse model organism in developmental biology labs for about 30 years because they are cheap and relatively amenable to genetic manipulation, and have transparent tissues, allowing researchers to see inside them. Engert and a small group of neuroscientists have been looking to capitalize on these qualities to study how the brain encodes vision, hearing, movement and even fear, things that are impossible to do in the brains of more complex model organisms. And techniques such as Engert's matrix are allowing them to monitor the zebrafish's 300,000 or so neurons and to track activity in vast swathes of them simultaneously in living brains. Such innovations mean that grant reviewers and top-tier journals — which overwhelmingly favour neuroscience research in mammals — are now giving fish a chance.

“There is a sort of perfect convergence of model and methodology with zebrafish that is peaking right about now,” says Joseph Fetcho, a neurobiologist at Cornell University in Ithaca, New York, who pioneered brain-circuit research in the fish. This impressive array of tools, he adds, makes him wonder “why one would use any other model for basic questions about circuits and behaviour”.

SPOTLIGHT AQUARIUM

During his early career at Stony Brook University in New York, Fetcho worked on goldfish brains until he got frustrated recording from only a couple of cells at a time. He switched to zebrafish in the mid-1990s, after two strikes of serendipity.

First, at a zoology conference, Fetcho stumbled into a workshop on

using zebrafish in high-school biology classes. He realized how easy it was to watch their translucent embryonic cells divide and, over the course of just a few days, develop into organs and limbs.

Second, he came across a paper describing how to fill neurons with a green dye that is sensitive to calcium¹. Because neuronal firing requires an influx of calcium ions, this method provided a way to view cells in action. The paper used cells isolated from chick spinal cords, but Fetcho thought the same approach could light up the neurons of live zebrafish. He went to a local pet shop and bought a mating pair. The next day, he had fertilized eggs to experiment with.

In Fetcho's first zebrafish paper², published in 1995, he and his colleague Donald O'Malley used the calcium-sensitive green dye to track the activity of motor neurons during a predator-escape reflex, which is triggered by poking the fish in the head. His team went on to show that neurons in different segments of the hindbrain encode how the fish turns its body to escape from a predator³. The researchers then

created the first transgenic line of fish to express a calcium indicator, similar to the green dye, in all neurons, so that the dye no longer had to be injected⁴.

Neuroscientists also started to use calcium indicators to label neural circuits in other animals. In a landmark study in 2001, for example, researchers mounted miniature two-photon microscopes — which can probe more than a millimetre deep into tissues — on the heads of scampering rats to reveal the firing patterns of many individual neurons at once⁵. Another group observed the brain of a fruitfly that was secured under a microscope while its legs walked freely on top of a polystyrene ball⁶.

But when using rodents or flies, researchers must first cut windows in the animals' heads to expose the part of the brain they want to image. And even then, the microscopes can probe only superficial layers of these opaque brain tissues.

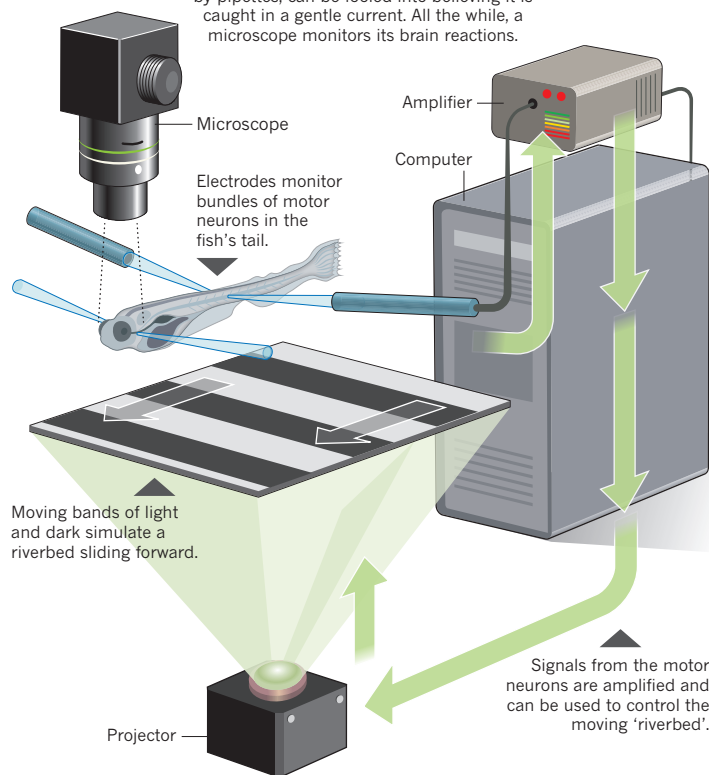
Only two popular model organisms have small, transparent brains and can be easily genetically engineered: the larval zebrafish and the soil nematode *Caenorhabditis elegans*, which has just 302 neurons. But to zebrafish researchers, *C. elegans* is too small and its circuits are too simple. Its brain is also covered in a tight cuticle and its neurons are tiny, making it difficult to make recordings with conventional electrodes. Besides, the worms don't show the same variety of behaviours — notably, those that require sophisticated vision — that a fish does. “We could probably do similar things in *C. elegans*,” says Engert, “but I'd be worried that the answers aren't as interesting.”

When Engert launched his Harvard lab in January 2002, he was determined to focus on the circuitry of larval zebrafish. His former adviser's father had been close friends with Nobel-prizewinning developmental biologist Christiane Nüsslein-Volhard, who helped to pioneer the zebrafish as a model for embryonic development. Still, Engert had never seen one in the flesh. “I was quite shocked when I saw one for the first time; they're so small,” he says.

It was an audacious choice, but it fit Engert's personality and penchant for risk. He's known around the Harvard biology building for never

A RIVER OF DECEIT

A zebrafish larva, paralysed and suspended by pipettes, can be fooled into believing it is caught in a gentle current. All the while, a microscope monitors its brain reactions.



wearing shirtsleeves, rollerblading into lectures and riding his motorbike without a helmet. A native German, he did his Harvard tenure talk in lederhosen (he earned tenure in 2009). Last year, he was nearly trapped under an avalanche while skiing off piste in Austria — shirtless.

At Harvard, it took Engert a couple of years to set up his lab experiments for zebrafish. At first, he tried imaging neurons while the fish were swimming freely. But “their whole brain wiggles”, he says, making imaging impossible. That’s when he started to build the virtual environment.

For a study published last May⁷, Engert’s postdocs Ruben Portugues and Misha Ahrens built a simple virtual world consisting of red and black stripes that moved under the fish. This visual stimulus, crude as it is, was enough to make the animals feel as though they were being swept backwards by a rushing river, and send out muscle commands to push forwards.

With the stroke of a few computer keys, the researchers can manipulate the scene, making the stripes go slower or faster. The tweaks make it seem, to the fish, that its movements have been either too weak or too strong, so it makes adjustments to stay in place. This behaviour is called motor adaptation, and it is akin to what people do when they’re walking and suddenly slide on a patch of ice, for instance. The brain takes in the new environmental information and adjusts movements to prevent a fall.

Studies in monkeys had revealed that specific neuronal populations were involved in motor adaptation. “If something happens that’s unexpected, it needs to get processed completely differently from if it’s expected,” Engert says. The processing “either tells me that something is happening in the world outside, independent of my motion, or it tells me there’s something wrong with my body”.

His fish study implicated the same populations of cells, but also showed something new. Certain neurons within these populations encode high-feedback gains — that is, visual feedback telling the fish that its muscles are stronger than expected — whereas others respond to feedback that its muscles are weaker than expected.

This is the sort of nitty-gritty detail that neuroscientists, hoping to look at the individual neurons within circuits, relish. In the past few years, other labs have revealed similar details. In 2010, for example, researchers in Japan pinpointed specific neurons in the habenula — a deep brain region that is difficult to study in mammals — as crucial players in the zebrafish’s response to fear⁸. In 2011, Fetcho showed that neurons in the fish’s hindbrain are neatly stacked during development in a way that allows the oldest cells to drive the fastest movements and younger cells to control more refined motions⁹.

But researchers are less excited by Engert’s results than by his technology, which allows them to view every neuron in an entire living, working brain. “You can’t do it in any other animal,” says Martin Meyer, a neuroscientist at King’s College London who used calcium imaging to show how different layers of cells in the zebrafish brain respond to objects moving in specific directions¹⁰. “There’s more or less endless scope, once you have that set up.”

Neuroscientists who work on other animals also applaud Engert’s technique, although they have some reservations. “It doesn’t give you everything that there is to know,” says Rex Kerr, who studies nematode brains at the Howard Hughes Medical Institute’s Janelia Farm

Research Campus in Ashburn, Virginia.

Kerr notes that the two-photon microscope can’t actually image all 300,000 neurons at once. Instead, Engert’s group systematically monitors 1,000 or so neurons in 300 subregions, from a total of 32 fish, and then uses a computer model to merge the activity onto a reference brain. For some behaviours, this averaged neural activity can mask interesting activity patterns in individual neurons, Kerr says. Still, a lot of interesting activity is determined by populations of many cells. Zebrafish are “extremely valuable” for looking at those ensembles, he says.

FISH FUTURES

There are practical reasons why more neuroscientists haven’t worked on zebrafish. Many sophisticated behaviours — such as communication, social interaction and complex emotions — aren’t displayed by the animal at all. And scientists have yet to develop ways to study even some basic reflexes in the fish.

That means it is not yet clear what other behaviours Engert’s technique will be able to test. Jason Rihel, who is setting up a lab at University College London, would like to use a similar approach to study neurons that produce hypocretin, which are involved in sleep and wakefulness.

“If we could watch the whole brain while we’re tickling the hypocretin neurons, or inhibiting them, then we might be able to map out every neuron in the brain that has altered activity,” Rihel says. He is a bit worried, however, that the immobilization will affect the fishes’ slumber.

Engert, in typical fashion, has ambitious plans. He’s got each of his five postdocs and about eight graduate students working on a different zebrafish experiment, from uncomfortably warm baths that test fear-learning to alcohol-rich waters to look at the effects of positive rewards.

He is also working on a “side project” that is likely to get a lot of attention later this year: the zebrafish connectome. Engert’s team is doing whole-brain func-

tional imaging of live, baby fish while they look at moving bars, and then passing those brains on to Harvard colleague Jeff Lichtman, who will use an electron microscope to trace the anatomical connections. “We’ll have a wiring diagram of the whole brain that can relate structure to function,” Engert says.

With these types of resource, Engert and his zebrafish might even find what neuroscientists have been searching for since Cajal: a fundamental principle that describes how circuits interact with one another. “My life will not be a failure if it doesn’t happen, but I’d love to find it,” Engert says. “And it’s ten times more likely to happen in fish than mice.” ■

Virginia Hughes is a freelance science writer in New York City.



“WE’LL HAVE A WIRING DIAGRAM OF THE WHOLE BRAIN THAT CAN RELATE STRUCTURE TO FUNCTION.”

FLORIAN ENGERT

1. O’Donovan, M. J., Ho, S., Sholomenko, G. & Yee, W. J. *Neurosci. Methods* **46**, 91–106 (1993).
2. Fetcho, J. R. & O’Malley, D. M. *J. Neurophysiol.* **73**, 399–406 (1995).
3. O’Malley, D. M., Kao, Y. H. & Fetcho, J. R. *Neuron* **17**, 1145–1155 (1996).
4. Higashijima, S., Masino, M. A., Mandel, G. & Fetcho, J. R. *J. Neurophysiol.* **90**, 3986–3997 (2003).
5. Helmchen, F., Fee, M. S., Tank, D. W. & Denk, W. *Neuron* **31**, 903–912 (2001).
6. Seelig, J. D. *et al. Nature Methods* **7**, 535–540 (2010).
7. Ahrens, M. B. *et al. Nature* **485**, 471–477 (2012).
8. Agetsuma, M. *et al. Nature Neurosci.* **13**, 1354–1356 (2010).
9. Kinkhabwala, A. *et al. Proc. Natl Acad. Sci. USA* **108**, 1164–1169 (2011).
10. Nikolau, N. *et al. Neuron* **76**, 317–324 (2012).



The ritual animal

Praying, fighting, dancing, chanting — human rituals could illuminate the growth of community and the origins of civilization.

By July 2011, when Brian McQuinn made the 18-hour boat trip from Malta to the Libyan port of Misrata, the bloody uprising against Libyan dictator Muammar Gaddafi had already been under way for five months.

“The whole city was under siege, with Gaddafi forces on all sides,” recalls Canadian-born McQuinn. He was no stranger to such situations, having spent the previous decade working for peace-building organizations in countries including Rwanda and Bosnia. But this time, as a doctoral student in anthropology at the University of Oxford, UK, he was taking the risk for the sake of research. His plan was to make contact with rebel groups and travel with them as they fought, studying how they used ritual to create solidarity and loyalty amid constant violence.

It worked: McQuinn stayed with the rebels for seven months, compiling a strikingly close and personal case study of how rituals evolved through combat and eventual victory. And his work was just one part of a much bigger project: a £3.2-million (US\$5-million)

BY DAN JONES

investigation into ritual, community and conflict, which is funded until 2016 by the UK Economic and Social Research Council (ESRC) and headed by McQuinn’s supervisor, Oxford anthropologist Harvey Whitehouse.

Rituals are a human universal — “the glue that holds social groups together”, explains Whitehouse, who leads the team of anthropologists, psychologists, historians, economists and archaeologists from 12 universities in the United Kingdom, the United States and Canada. Rituals can vary enormously, from the recitation of prayers in church, to the sometimes violent and humiliating initiations of US college fraternity pledges, to the bleeding of a young man’s penis with bamboo razors and pig incisors in purity rituals among the Iahita Arapesh of New Guinea. But beneath that diversity, Whitehouse believes, rituals are always about building community — which arguably makes them central to understanding how civilization itself began.

To explore these possibilities, and to

tease apart how this social glue works, Whitehouse’s project will combine fieldwork such as McQuinn’s with archaeological digs and laboratory studies around the world, from Vancouver, Canada, to the island archipelago of Vanuatu in the south Pacific Ocean. “This is the most wide-ranging scientific project on rituals attempted to date,” says Scott Atran, director of anthropological research at the CNRS, the French national research organization, in Paris, and an adviser to the project.

Human rites

A major aim of the investigation is to test Whitehouse’s theory that rituals come in two broad types, which have different effects on group bonding. Routine actions such as prayers at church, mosque or synagogue, or the daily pledge of allegiance recited in many US elementary schools, are rituals operating in what Whitehouse calls the ‘doctrinal mode’. He argues that these rituals, which are easily

NATURE.COM
For more on rituals
listen to the *Nature*
podcast.
go.nature.com/weyxwr

LIFE/PIXELS/GETTY IMAGES (LEFT)



FORGING LOYALTY

Members of large, stable groups such as religions, tribes and nations typically reinforce their commitment with routine rituals such as Buddhist prayers in Thailand (facing page). But members of small, committed groups such as the rebel cells that gathered in Benghazi, Libya, in March 2011 (this page) are often initiated by rituals or other experiences that are frightening and traumatic.

MADS NISSEN/BERLINGSKE/PANOS(RIGHT)

transmitted to children and strangers, are well suited to forging religions, tribes, cities and nations — broad-based communities that do not depend on face-to-face contact.

Rare, traumatic activities such as beating, scarring or self-mutilation, by contrast, are rituals operating in what Whitehouse calls the ‘imagistic mode’. “Traumatic rituals create strong bonds among those who experience them together,” he says, which makes them especially suited to creating small, intensely committed groups such as cults, military platoons or terrorist cells. “With the imagistic mode, we never find groups of the same kind of scale, uniformity, centralization or hierarchical structure that typifies the doctrinal mode,” he says.

Rebel yell

Whitehouse has been developing this theory of ‘divergent modes of ritual and religion’ since the late 1980s, based on his field work in Papua New Guinea and elsewhere¹. His ideas have attracted the attention of psychologists, archaeologists and historians.

Until recently, however, the theory was largely based on selected ethnographic and historical case studies, leaving it open to the charge of cherry-picking. The current rituals project is an effort by Whitehouse and his colleagues to answer that charge with deeper, more systematic data.

The pursuit of such data sent McQuinn to Libya. His strategy was to look at how the defining features of the imagistic and doctrinal modes — emotionally intense experiences

shared among a small number of people, compared with routine, daily practices that large numbers of people engage in — fed into the evolution of rebel fighting groups from small bands to large brigades.

At first, says McQuinn, neighbourhood friends formed small groups comprising “the number of people you could fit in a car”. Later, fighters began living together in groups of 25–40 in disused buildings and the mansions of rich supporters. Finally, after Gaddafi’s forces were pushed out of Misrata, much larger and hierarchically organized brigades emerged that patrolled long stretches of the defensive

“Rituals are the glue that holds social groups together.”

border of the city. There was even a Misratan Union of Revolutionaries, which by November 2011 had registered 236 rebel brigades.

McQuinn interviewed more than 300 fighters from 21 of these rebel groups, which varied in size from 12 to just over 1,000 members². He found that the early, smaller brigades tended to form around pre-existing personal ties, and became more cohesive and the members more committed to each other as they collectively experienced the fear and excitement of fighting a civil war on the streets of Misrata.

But six of the groups evolved into super-brigades of more than 750 fighters, becoming

“something more like a corporate entity with their own organizational rituals”, says McQuinn. A number of the group leaders had run successful businesses, and would bring everyone together each day for collective training, briefings and to reiterate their moral codes of conduct — the kinds of routine group activities characteristic of the doctrinal mode. “These daily practices moved people from being ‘our little group’ to ‘everyone training here is part of our group,’” says McQuinn.

McQuinn and Whitehouse’s work with Libyan fighters underscores how small groups can be tightly fused by the shared trauma of war, just as imagistic rituals induce terror to achieve the same effect. Whitehouse says that he is finding the same thing in as-yet-unpublished studies of the scary, painful and humiliating ‘hazing’ rituals of fraternity and sorority houses on US campuses, as well as in surveys of Vietnam veterans showing how shared trauma shaped loyalty to their fellow soldiers.

To gain a more global perspective on ritual practices, Whitehouse and Quentin Atkinson, a psychologist at the University of Auckland, New Zealand, and a member of the project, used a previously developed database containing information on world cultures to explore the connections between frequency, peak levels of emotional arousal, and average community size for 645 rituals across 74 cultures³. As predicted, the rituals fell into two clusters: low-frequency but high-arousal imagistic varieties that were more common in societies with a smaller average community size, and high-frequency, low-arousal doctrinal rituals that

were more established in societies in which communities are larger.

Given these data from contemporary cultures, it is hard not to speculate about ritual's role in history: did the transition from imagistic mode to doctrinal mode, with its emphasis on a common identity buttressed by daily activities and rituals, play a part in the emergence of large, complex societies 10,000 years ago?

The birth of civilization?

To address that question, Whitehouse, Atkinson and Camilla Mazzucato, also based at the University of Oxford, are looking at archaeological data from Çatalhöyük, one of the largest and best-preserved Neolithic towns known. Located in the Anatolian plains of northwestern Turkey, Çatalhöyük was founded during the dawn of agriculture roughly 9,500 years ago, and housed more than 8,000 people at its peak.

The town's early layers show that residents frequently buried their kin under the floors of their houses, sometimes with their heads severed. Wall paintings also depict the town's residents getting together to tease and kill enormous wild bulls for feasting. "The whole process of baiting and killing these animals would have been extremely intense, and have had a major emotional impact," says excavation director Ian Hodder, an archaeologist at Stanford University in California. These occasional feasts were also memorialized by mounting the skulls and horns of bulls inside houses, and burying the rest of the bones to commemorate the founding or abandonment of a house, which Hodder says were also highly ritualistic events.

Evidence for such imagistic-style rituals declines in the later layers of Çatalhöyük. Wild-bull rituals and bull-horn installations become less common as the herding of domesticated sheep, goats and cattle intensified, says Hodder. Human burials within houses fade out, and standardized symbolic artefacts, such as painted pottery and seal stamps, become more common. Whitehouse and Hodder believe that these changes represent a shift to a more doctrinal mode of ritual as people united into a larger, more cooperative community devoted to agriculture and animal herding. Although speculative, this interpretation is consistent with Whitehouse and Atkinson's cross-cultural survey, which found that in contemporary societies the doctrinal mode is more established where agriculture is practised most intensively.

Looking beyond Çatalhöyük, Whitehouse, Atkinson and Mazzucato are building a regional database chronicling similar changes in ritual at 60 other sites across the Middle East, from the end of the Palaeolithic around 10,000 years ago until the early Bronze Age around 7,000 years ago. This database will dovetail with another one that covers the entire world over the past 5,000 years⁴. That resource codifies information about the culture, religion and ritual

practices of people worldwide, and combines this with measures of social complexity — for example, how many levels of administration a society's government has, or the number of distinct professions — as well as data on the intensity of warfare. The plan is to use this database to explore the links between ritual and social life, as well as the roles of war and competition between societies in nurturing certain kinds of ritual and driving increases in social complexity.

Rituals could feed conflict by turning opinions into 'sacred values'.

Members of the ESRC project are also probing people's beliefs about how rituals work. For example, Cristine Legare at the University of Texas at Austin has studied Brazilian rituals called *simpatias*, which are used to solve everyday problems ranging from bad luck to asthma and depression⁵. A *simpatia* for getting a good job says that during the full Moon the jobseeker must take the jobs page out of a newspaper, fold it four times, and then place it on the floor with a small white candle surrounded by honey and cinnamon, imagining themselves in a new job with good pay. The candle stub and the paper should be buried with a plant and watered daily, and the dream job will soon emerge.

The ritual mind

Legare presented Brazilians with a variety of *simpatias*, and found that people judged them as more effective when they involved a large number of repetitive procedural steps that must be performed at a specific time and in the presence of religious icons. "We're built to learn from others," she says, which leads us to repeat actions that seemed to work for someone else — "even if we don't understand how they produce the desired outcomes".

Meanwhile, psychologist Ryan McKay at Royal Holloway, University of London, and Jonathan Lanman, a cognitive anthropologist at Queen's University, Belfast, are exploring how rituals can be broken down into their component parts and how each part influences behaviour. One such component is synchronized physical action — for example, the ritualized goose-stepping of military units — which social psychologists have shown⁶ promotes a sense of connection and trust between individuals.

This work builds on research by Richard Sosis, an anthropologist at the University of Connecticut, who has shown that immersion in collective rituals, such as communal prayer, in Israeli kibbutzim increases cooperative behaviour in economic games⁷ — but only with other kibbutz members⁸.

Ritual also has its darker side. Surveys by Ara Norenzayan, a psychologist at the University of British Columbia in Vancouver who has an advisory role on the project, suggest that support for suicide terrorism among Palestinians is more strongly tied to communal ritual attendance than to religious devotion, as measured by the frequency of private prayer⁹.

Atran thinks that rituals could also feed conflict by turning the opinions and preferences of groups into 'sacred values' — absolute and non-negotiable beliefs that cannot be traded against material benefits such as money. For many Israelis, for example, one such value is the right to occupy the West Bank, whereas for many Palestinians it is the right to return to the villages from which they were expelled. In fact, Atran has found that financial offers to compromise on these sacred values makes them even more entrenched¹⁰.

As an example of how rituals can cause values and preferences to become sacralized, Atran points to his studies showing that, in the United States, people who attend church more frequently are more likely to consider the right to bear arms a sacred value¹¹.

"Emotionally intense rituals have bound us together and pitted us against our enemies throughout the history of our species," says Whitehouse. "It was only when nomadic foragers began to settle down did we discover the possibilities for establishing much larger societies based on frequently repeated creeds and rituals."

The big question, he says, is whether this kind of unity can be extended to humanity at large. For Whitehouse, understanding the ways that rituals shape group behaviour is the first step towards finding out how they can be harnessed to dampen down conflict between groups. He hopes that such insights could help policy-makers to "establish new forms of peaceful cooperation, as well as bringing down dictators". ■

Dan Jones is a freelance writer in Brighton, UK.

1. Whitehouse, H. *Modes of Religiosity: A Cognitive Theory of Religious Transmission* (AltaMira Press, 2004).
2. McQuinn, B. *After the Fall: Libya's Evolving Armed Groups* Small Arms Survey Working Paper 12 (Small Arms Survey, 2012).
3. Atkinson, Q. D. & Whitehouse, H. *Evol. Hum. Behav.* **32**, 50–62 (2011).
4. Turchin, P., Whitehouse, H., Francois, P., Slingerland, E. & Collard, M. *Clodynamics* **3**, 271–293 (2012).
5. Legare, C. H. & Souza, A. L. *Cognition* **124**, 1–15 (2012).
6. Wiltermuth, S. S. & Heath, C. *Psychol. Sci.* **20**, 1–5 (2009).
7. Sosis, R. & Ruffle, B. J. *Curr. Anthropol.* **44**, 713–722 (2003).
8. Ruffle, B. J. & Sosis, R. J. *Econ. Behav. Org.* **60**, 147–163 (2006).
9. Ginges, J., Hansen, I. & Norenzayan, A. *Psychol. Sci.* **20**, 224–230 (2009).
10. Ginges, J., Atran, S., Medin, D. & Shikaki, K. *Proc. Natl Acad. Sci. USA* **104**, 7357–7360 (2007).
11. Sheikh, H., Ginges, J., Colman, A. & Atran, S. *Judgm. Decis. Mak.* **7**, 110–118 (2012).

COMMENT

ENERGY Critics of energy-efficiency policy overplay the rebound effect **p.475**

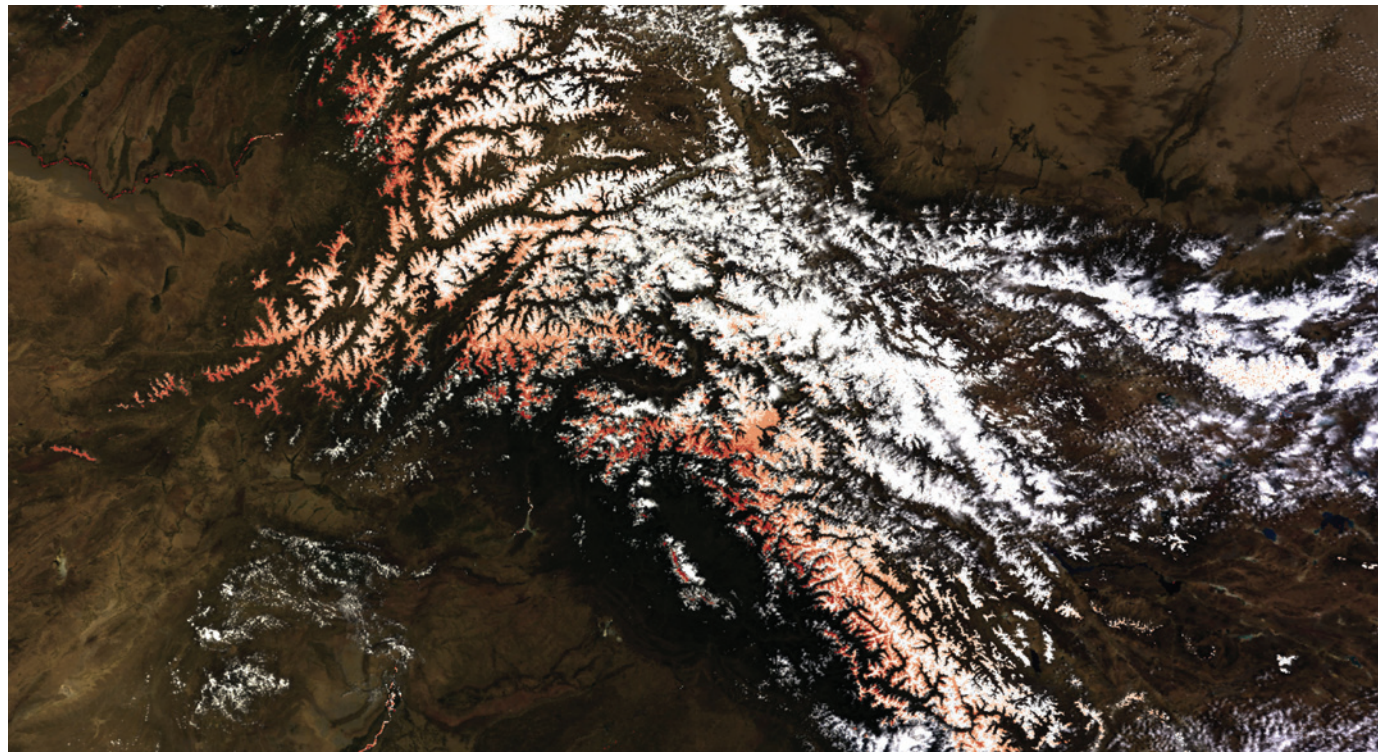
ANTHROPOLOGY Jared Diamond's paean to traditional societies, reviewed **p.477**

HISTORY Heroism, intrigue and posturing abound in a history of Antarctica **p.478**



PETITIONS Ganging up on research damages scientific discourse **p.480**

ANN C. BRYANT & THOMAS H. PAINTER, JPL/CALTECH SNOW OPTICS LAB.



A satellite image of snow on the Hindu Kush mountains in Asia, with regions of high absorption of sunlight by dust and black carbon shaded in red.

A vision for data science

To get the best out of big data, funding agencies should develop shared tools for optimizing discovery and train a new breed of researchers, says **Chris A. Mattmann**.

Two small words — ‘big data’ — are getting a lot of play across the sciences. Funding agencies, such as the National Science Foundation and the National Institutes of Health in the United States, have created million-dollar programmes around the challenges of storing and handling vast data streams. Although these are important, I believe that agencies should focus on developing shared tools for optimizing discovery.

Big data are big in three ways: the volume of information that systems must ingest, process and disseminate; the number and complexity of the types of information handled; and the rate at which information streams in or out. Terabyte-sized data sets

(10^{12} bytes) are now common in Earth and space sciences, physics and genomics (see ‘Data deluge’). But a lack of investment in services such as algorithm integration and file-format translation is limiting the ability to manipulate archival data to reveal new science.

At the Jet Propulsion Laboratory (JPL) in Pasadena, California, I am a principal investigator in a big-data initiative, pursuing projects on data archiving and mining, smart algorithms and low-power hardware for astronomy and Earth science. Rather than finding one system that can ‘do it all’ for any data set, my team aims to define a set of architectural patterns and collaboration models that can be adapted to a range of projects.

I believe that four advancements are necessary to achieve that aim. Methods for integrating diverse algorithms seamlessly into big-data architectures need to be found. Software development and archiving should be brought together under one roof. Data reading must become automated among formats. Ultimately, the interpretation of vast streams of scientific data will require a new breed of researcher equally familiar with science and advanced computing.

ALGORITHM INTEGRATION

A project by my team at the JPL illustrates the challenges of working with big data. In 2011, we were asked by the US National Climate Assessment to establish a ►

► computing facility to integrate a range of snow-related measurements — and to do so in a month. The data included observations from the western United States, Alaska and the Hindu Kush–Himalayan regions, as well as the entire Earth-observing record since 2000 and subsequent monitoring. The data products and maps would amount to several hundred terabytes.

The algorithms to be incorporated were varied, and included codes for estimating snow coverage, grain size and absorption of solar radiation by dust and black carbon¹. They had been written in IDL, a specialized programming language used by many researchers. Geographers, remote-sensing experts and software programmers contributed.

Most computer scientists would assume that such a system would take years, not weeks, to develop. The algorithms would presumably have to be rewritten in a standard language such as C++, Java or Python, or one that could run on a fast computer system or infrastructure, such as Google's MapReduce model.

But, in my experience, there is no need to rewrite scientific algorithms for big-data systems. Rewriting only increases the barriers to communication between scientists and computer engineers. Rewriting can also introduce costly errors.

Computer engineers should trust scientists to produce executable algorithms, which can be plugged into a larger processing framework. The skill is in tying the input and output files and relevant parameters unobtrusively into the big-data network, so that the algorithm can run seamlessly within it. With a modular approach, development can proceed quickly in parallel — we constructed our snow-science computing facility this way in less than a month.

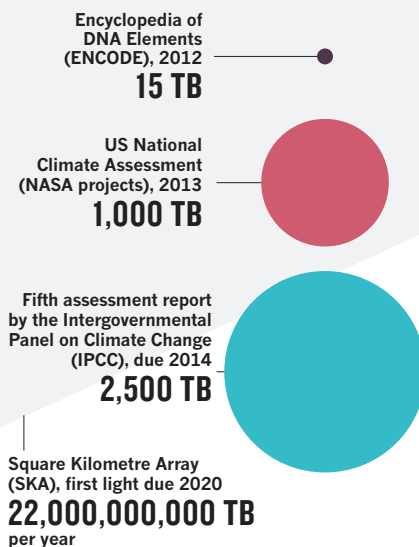
DEVELOPMENT AND STEWARDSHIP

Today, different big-data computing tasks are usually undertaken by different teams. The bulk of agency funding goes to building specific long-standing archives or data grids² — systems such as the NASA Earth science Distributed Active Archive Centers or the International Virtual Observatory Alliance in astronomy — that disseminate, preserve and steward³ data. Large archives have received an average of US\$100 million a year from US federal agencies over the past decade.

By contrast, the development, integration and updating of science algorithms receives only between \$1 million and \$5 million per year in the United States. These tasks are carried out in science-computing facilities, which are often small and transient. Because they must do more for less, such facilities largely use and generate community-based open-source software^{4–6}. Examples include

DATA DELUGE

The billions of terabytes (TB) produced in one year by the SKA telescope (grey) will dwarf today's data sets in genomics and climate science.



Apache Hadoop⁷ and Apache Tika⁸, used in Earth science, biomedicine and business.

Although data interpretation and archiving efforts have so far been funded separately and at strikingly dissimilar levels, their needs — such as workflow processing and file and resource management — are complementary and overlapping. As storage and computation costs fall, algorithm developers are moving into preservation, both to archive their own work and to open new research windows on large data sets that were previously closed.

In the next decade, I believe that archives and science-computing facilities must merge. The international radio-astronomy community is doing so in preparation for the Square Kilometre Array radio telescope, due to see first light in 2020. The enormous volume of data that the array will produce — 700 terabytes each second — will, after just a few days, eclipse the current size of the Internet. Archives in the United States such as those at the National Radio Astronomy Observatory's Expanded Very Large Array and the Atacama Large Millimeter/submillimeter Array are developing software to handle that deluge.

MANY FORMATS

Big-data systems must deal with thousands of file types and conventions. The communities that have formed around information modelling, ontology and semantic web software address this complexity of data and metadata (descriptive terms attached to files) to some extent. But they have so far relied on human intervention. None has delivered the silver bullet: automatic solutions that identify file types and extract meaningful data from them.

Comparisons of observational and model data are, for example, under construction for the US National Climate Assessment and the Coupled Model Intercomparison Project of the Intergovernmental Panel on Climate Change. NASA uses the Hierarchical Data Format version 5 (HDF-5) and the HDF-Earth Observing System metadata representation. The outputs of climate models are stored in the Network Common Data Form, typically with climate and forecast metadata conventions⁹. Automatic methods will be needed to match and analyse these data, which amount to petabytes (10^{15} bytes).

Some big-data fields are switching to formats like these that have better support. Astronomers, for instance, are turning to NASA's HDF-5 file format from the Flexible Image Transport System that has been their standard. But history shows that defining a single, unifying file format is not the answer, because proliferation of file types will continue. Instead, we need a toolkit of automatic ways to boil file formats down to their essence, and more formats that are amenable to those approaches. We need flexible systems that can perform multiple functions and deal with diverse data. Encouraging efforts are under way, including with Apache OODT¹⁰ and Apache Tika⁸.

PEOPLE POWER

To solve big-data challenges, researchers need skills in both science and computing — a combination that is still all too rare. A new breed of 'data scientist' is necessary.

As well as being data stewards, data scientists will develop bespoke algorithms for analysis and adapt file formats. They will understand the mathematics, statistics and physics necessary to integrate science algorithms into efficient architectures. They will find solutions beyond the fragmented community efforts that have dominated the past decade of development of big-data systems.

Funding agencies should support computing facilities that combine big-data stewardship and software development, employing data scientists to bridge the gap. Coordination between agencies is crucial to avoid duplication. The Big Data Senior Steering Group, linking efforts across the National Science Foundation, the National Institutes of Health, NASA and others, is a promising early example. More oversight will be needed to establish new working patterns.

Because big-data fields stretch across national as well as disciplinary boundaries, such facilities and panels must be international. In centres of excellence around the world, such as the JPL, data scientists will help astronomers and Earth scientists to share their approaches with bioinformaticians, and vice versa.

For the specialism to emerge and grow, data scientists will have to overcome barriers that are common to multidisciplinary research. As well as acquiring understanding of a range of science subjects, they must gain academic recognition. Journals such as the *Data Science Journal* should become more prominent within the computing community. Software products and technologies should be valued more by academic committees.

New interdisciplinary courses will be needed. The University of California, Berkeley, and Stanford University in California have set up introductory courses for computer scientists on big-data techniques — more universities should follow suit. Natural scientists, too, should become familiar with computing and format issues.

In my lectures for computer-science graduates, I have brought together students at the University of Southern California in Los Angeles with researchers at the JPL. Using real projects, my students see the challenges awaiting them in their future careers. I hope to employ some of them on the projects that will flow from the JPL's big-data initiative. The technologies and approaches that they develop will spread beyond NASA through contributions to the open-source community.

Empowering students with knowledge of big-data infrastructures and open-source systems now will allow them to make steps towards addressing the major challenges that big data pose. ■

Chris A. Mattmann is a senior computer scientist at the Jet Propulsion Laboratory, California Institute of Technology, Pasadena, California 91109, USA, and adjunct assistant professor in computer science at the University of Southern California, Los Angeles, California 90089, USA.
e-mail: chris.a.mattmann@nasa.gov

1. Painter, T. H., Bryant, A. C. & Skiles, S. M. *Geophys. Res. Lett.* **39**, L17502 (2012).
2. Foster, I., Kesselman, C. & Tuecke, S. *Int. J. High Perform. Comput. Appl.* **15**, 200–222 (2001).
3. Lynch, C. *Nature* **455**, 28–29 (2008).
4. Morin, A. et al. *Science* **336**, 159–160 (2012).
5. Spinellis, D. & Giannikas, V. J. *Syst. Softw.* **85**, 666–682 (2012).
6. Ven, K., Verelst, J. & Mannaert, H. *IEEE Software* **25**, 54–59 (2008).
7. White, T. *Hadoop: The Definitive Guide* 2nd edn (O'Reilly Media/Yahoo Press, 2010).
8. Mattmann, C. A. & Zitting, J. L. *Tika in Action* (Manning, 2011).
9. Cinquini, L. et al. *Proc. 2012 IEEE 8th Int. Conf. E-Science* Chicago, Illinois, 8–12 October 2012 (in the press).
10. Mattmann, C. A., Crichton, D. J., Medvidovic, N. & Hughes, S. in *Proc. 28th Int. Conf. Software Engineering (ICSE06), Software Engineering Achievements Track* 721–730 (2006).



ZHANG JUN/XINHUA PRESS/CORBIS

Fuel-efficient cars cost less to run, so people might use them a little more.

The rebound effect is overplayed

Increasing energy efficiency brings emissions savings. Claims that it backfires are a distraction, say **Kenneth Gillingham** and colleagues.

Buy a more fuel-efficient car and you will spend more time behind the wheel. That argument, termed the rebound effect, has earned critics of energy-efficiency programmes a voice in the climate-policy debate, for example with an article in *The New York Times* entitled 'When energy efficiency sullies the environment'¹.

The rebound effect idea — and its extreme variant the 'backfire' effect, in which

supposed energy savings turn into greater energy use — stems from nineteenth-century economist Stanley Jevons. In his 1865 book *The Coal Question*, Jevons hypothesized that energy use rises as industry becomes more efficient because people produce and consume more goods as a result².

The rebound effect is real and should be considered in strategic energy planning. But it has become a distraction. A vast ►



Villagers in Blanche Bay, New Guinea, in the 1890s.

ANTHROPOLOGY

Power of the past

Monique Borgerhoff Mulder assesses an exploration of how modern industrial and traditional societies differ.

When outsiders come into a discipline and publish a popular book that becomes a classic, insiders may not be pleased. Typically, there is territoriality (those ideas aren't yours); pedantry (so much inaccuracy); and jealousy (I should have done it myself).

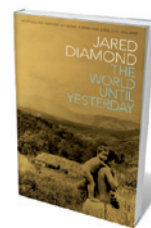
Jared Diamond — once ecologist, now ornithologist and geographer by trade — has ventured into anthropology twice before. In *Guns, Germs and Steel* (Norton, 1997) he offered distinct and powerful hypotheses for why different parts of the globe developed at such different rates, attracting a wide readership to big questions in anthropology that few had dared to tackle. In *Collapse* (Viking, 2005), he provided a loosely synthesized catalogue of the factors associated with the downfall of civilizations. Now we have *The World Until Yesterday*, offering the personal reflections of a Westerner who has visited communities still peripheral to the globalized world — thoughts that anthropologists rarely divulge.

Diamond uses his 50-odd years' worth of visits to remote New Guinea in the pursuit of birding fieldwork to meditate, as the prologue details, on "how all of our ancestors lived for tens of thousands of years, until virtually yesterday". He aims to identify what we can learn from the foraging and simple farming societies that preceded modern (and indeed ancient) states. In chapters on warfare, child rearing, the care of the elderly and health, we are treated to engaging stories from New Guinea and samplings from ethnographic texts on other traditional populations. The result — which reads in some places like a cultural-anthropology textbook from the 1970s, in others like a mesmerizing thriller — reveals a world in which some people strangle their elders rather than book them into retirement homes, and resolve conflicts with strangers over a ceremonial feast rather than an affidavit.

► **NATURE.COM**

For a review of Jared Diamond's *Collapse*, see: go.nature.com/8ug879

Diamond's central objective is to determine whether 'we' or 'they' do it better, be it in conflict resolution, child rearing or how we eat. He looks for what we can learn from them: co-sleeping with infants, multilingualism, restorative justice and enriched lives for the elderly, with no retirement age, are some highlights.



The World Until Yesterday: What Can We Learn from Traditional Societies?

JARED DIAMOND
Viking: 2012. 512 pp.
\$36

Many anthropologists will undoubtedly object to this us-versus-them framing, although for a popular readership it is clearly thought-provoking. Human diversity in social organization cannot be dichotomized as traditional versus modern. Diamond recognizes this in his preface, but thereafter chooses to ignore it. Instead, he compares foraging and hoe-cultivating societies in Africa, South America and New Guinea with communities typical of modern industrial states, primarily the United States. However, he does not address the intriguing question of how power, status and resources are distributed among individuals across the diverse kinds of societies that have existed in human history, or the implications of these distributions for human welfare.

Later chapters on danger, language, religion and health revert more to the style of argument Diamond used in *Guns, Germs and Steel*, with appeals to evolutionary and ecological explanations.

Apropos of danger, Diamond tells a ripping yarn of his canoe-wreck at dusk in the Indonesian archipelago. This ordeal suggested to him the concept of "constructive paranoia", an alertness to risk that he believes might be adaptive for traditional peoples living in dangerous environments. With regard to language, he follows others in noting that linguistic diversity maps onto high net primary productivity, low seasonality and low human-population mobility — in other words, languages diversify where there is plentiful food available all year and human settlements are not forced to move. And, in the theme of earlier chapters, he promotes language diversity as something to strive for, citing the cognitive benefits associated with bilingualism.

Evolution by natural selection appears only late in the book, in a well-balanced discussion of the multiple functions of religion and how these change in importance over time. Supernatural explanations for unforeseen events have declined as scientific thought gained ascendancy, whereas the provision of comfort, hope and meaning has become more prominent over time ►

▶ as inequalities among citizens have escalated. Again, the material draws on the work of other scholars, but Diamond suggests, interestingly, that US citizens may be more religious than those of other industrialized nations because of the high levels of economic inequality in their country (religion helps to rationalize prosperity for those at the top of the ladder and mitigate adversity for those at the bottom).

Finally, in a chapter on health, Diamond recapitulates arguments for the 'diseases of civilization' — that the fats and salts we consume do not suit physiologies designed for foraging, and cause the hypertension and diabetes crises that we see in populations transitioning to modern lifestyles. With reference to James Neel's 'thrifty gene' hypothesis, Diamond attributes the particularly high incidence of type 2 diabetes among Pima Native Americans and Nauruan Pacific Islanders to catastrophic recent famines in these populations, which may have favoured the survival of individuals who most efficiently converted sugars to fats. He also proposes that Europeans may have been through a gradual and largely undetectable diabetes crisis, starting in the fifteenth century, as food security increased with the development of state distribution systems — with Johann Sebastian Bach named as one possible victim.

Diamond has an engaging style, and has packed the book with grisly anecdotes and delightful detail from the jungles of New Guinea to the strip malls of Los Angeles, California, alerting us to grim realities of the industrial world. For example, a single pan-fried-noodle combo dish served in Los Angeles contains more than a year's worth of a Yanomami Indian's salt intake. The book brings anthropology alive for those who have never had the privilege of visiting, or reading deeply about, societies very different from their own. For those who have worked in the remote reaches of the world, it may tire or even annoy. Tire, because the book is long, and draws on overly familiar ethnographies; annoy, because the scale of comparison, us versus them, is conceptually limiting.

Diamond has previously described his writings on the cultures of New Guinea as journalism. Perhaps this is how we should read *The World Until Yesterday*, as a highly personal reflection on the virtues and vices of modern industrial civilization. ■

Monique Borgerhoff Mulder is a human behavioural ecologist at the University of California, Davis, USA.
e-mail: mborgerhoffmulder@ucdavis.edu



One of the vessels captured by US explorer Richard Byrd in Antarctica in the 1930s.

HISTORY

Frozen assets

Edmund Stump welcomes a history of Antarctica that covers the glory, the rivalries and the scientific legacy.

From James Cook's circumnavigation of Terra Australis Incognita in 1772–75 to today's shifting international population of researchers, Antarctica's history is stamped by the continent's remote isolation, extreme climate and scientific importance. Its strategic and economic potential have not escaped government attention. Behind the scenes, nations have long plotted to win sovereignty and control resources. And that is where David Day's *Antarctica: A Biography* takes us, into a two-faced world of public and covert intentions where personal and national rivalries abound.

Antarctica is the first comprehensive history of the continent, spanning the centuries since Cook's voyage. The heroic expeditions of Robert Falcon Scott, Roald Amundsen and other luminaries are all there, as are many that are less well known. Day couches these throughout in political contexts — how they served the motives of the colonial offices or state departments back home. The dramas, played out in secret memos and in published statements in newspapers, give the book a slow, even glacial, pace at times.

At every turn there is hesitancy on the part of diplomats and leaders: to claim or not to claim, to recognize others' claims or not, to offend trading partners or not, to respond to official memos or to let them go unanswered. In this way we have collectively backed into today's Antarctica, where all territorial claims are held in abeyance, a 50-year moratorium prohibits exploration for mineral and energy resources, and tourists flock in droves.

Day has done a remarkable job of collating information from rich and varied international sources.

Antarctica: A Biography

DAVID DAY

Oxford Univ. Press:
2013. 624 pp. £25

He draws from original accounts, newspaper articles, the recently released papers of US naval officer and polar explorer Richard Byrd, and numerous national archives with their copious committee reports and memos, some recently declassified.

The concealment of who made what claims where and when, and how different versions were presented to the public, dominate the book. One example is what Byrd told reporters in Dunedin, New Zealand, after his first Antarctic expedition (1928–30). Although he said he was "not the least concerned with claiming the land for America", he had recently photographed miles of mountains and coastline in Marie Byrd Land with just that intent. He had also instructed Laurence Gould, his second in command, to leave a note in a cairn claiming the territory for the United States when Gould's ground party traversed beyond the boundary of New Zealand's Ross Dependency.

Although I am familiar with the history of exploration in the Peninsula and Ross Sea sectors of Antarctica, Day expanded my horizons to the 'African' sector, the section of East Antarctica facing the tip of Africa. Here, between the world wars, Norwegians led the last great slaughter of Antarctic whales and mapped major sectors of the coastline, infringing on claims by the ever-vigilant

▶ as inequalities among citizens have escalated. Again, the material draws on the work of other scholars, but Diamond suggests, interestingly, that US citizens may be more religious than those of other industrialized nations because of the high levels of economic inequality in their country (religion helps to rationalize prosperity for those at the top of the ladder and mitigate adversity for those at the bottom).

Finally, in a chapter on health, Diamond recapitulates arguments for the 'diseases of civilization' — that the fats and salts we consume do not suit physiologies designed for foraging, and cause the hypertension and diabetes crises that we see in populations transitioning to modern lifestyles. With reference to James Neel's 'thrifty gene' hypothesis, Diamond attributes the particularly high incidence of type 2 diabetes among Pima Native Americans and Nauruan Pacific Islanders to catastrophic recent famines in these populations, which may have favoured the survival of individuals who most efficiently converted sugars to fats. He also proposes that Europeans may have been through a gradual and largely undetectable diabetes crisis, starting in the fifteenth century, as food security increased with the development of state distribution systems — with Johann Sebastian Bach named as one possible victim.

Diamond has an engaging style, and has packed the book with grisly anecdotes and delightful detail from the jungles of New Guinea to the strip malls of Los Angeles, California, alerting us to grim realities of the industrial world. For example, a single pan-fried-noodle combo dish served in Los Angeles contains more than a year's worth of a Yanomami Indian's salt intake. The book brings anthropology alive for those who have never had the privilege of visiting, or reading deeply about, societies very different from their own. For those who have worked in the remote reaches of the world, it may tire or even annoy. Tire, because the book is long, and draws on overly familiar ethnographies; annoy, because the scale of comparison, us versus them, is conceptually limiting.

Diamond has previously described his writings on the cultures of New Guinea as journalism. Perhaps this is how we should read *The World Until Yesterday*, as a highly personal reflection on the virtues and vices of modern industrial civilization. ■

Monique Borgerhoff Mulder is a human behavioural ecologist at the University of California, Davis, USA.
e-mail: mborgerhoffmulder@ucdavis.edu



CORBIS

One of the vessels captured by US explorer Richard Byrd in Antarctica in the 1930s.

HISTORY

Frozen assets

Edmund Stump welcomes a history of Antarctica that covers the glory, the rivalries and the scientific legacy.

From James Cook's circumnavigation of Terra Australis Incognita in 1772–75 to today's shifting international population of researchers, Antarctica's history is stamped by the continent's remote isolation, extreme climate and scientific importance. Its strategic and economic potential have not escaped government attention. Behind the scenes, nations have long plotted to win sovereignty and control resources. And that is where David Day's *Antarctica: A Biography* takes us, into a two-faced world of public and covert intentions where personal and national rivalries abound.

Antarctica is the first comprehensive history of the continent, spanning the centuries since Cook's voyage. The heroic expeditions of Robert Falcon Scott, Roald Amundsen and other luminaries are all there, as are many that are less well known. Day couches these throughout in political contexts — how they served the motives of the colonial offices or state departments back home. The dramas, played out in secret memos and in published statements in newspapers, give the book a slow, even glacial, pace at times.

At every turn there is hesitancy on the part of diplomats and leaders: to claim or not to claim, to recognize others' claims or not, to offend trading partners or not, to respond to official memos or to let them go unanswered. In this way we have collectively backed into today's Antarctica, where all territorial claims are held in abeyance, a 50-year moratorium prohibits exploration for mineral and energy resources, and tourists flock in droves.

Day has done a remarkable job of collating information from rich and varied international sources.

Antarctica: A Biography

DAVID DAY

Oxford Univ. Press:
2013. 624 pp. £25

He draws from original accounts, newspaper articles, the recently released papers of US naval officer and polar explorer Richard Byrd, and numerous national archives with their copious committee reports and memos, some recently declassified.

The concealment of who made what claims where and when, and how different versions were presented to the public, dominate the book. One example is what Byrd told reporters in Dunedin, New Zealand, after his first Antarctic expedition (1928–30). Although he said he was "not the least concerned with claiming the land for America", he had recently photographed miles of mountains and coastline in Marie Byrd Land with just that intent. He had also instructed Laurence Gould, his second in command, to leave a note in a cairn claiming the territory for the United States when Gould's ground party traversed beyond the boundary of New Zealand's Ross Dependency.

Although I am familiar with the history of exploration in the Peninsula and Ross Sea sectors of Antarctica, Day expanded my horizons to the 'African' sector, the section of East Antarctica facing the tip of Africa. Here, between the world wars, Norwegians led the last great slaughter of Antarctic whales and mapped major sectors of the coastline, infringing on claims by the ever-vigilant

Australians. During the 1929–30 summer season, for instance, the Norwegians and Australians converged on Enderby Land intent on extending their claims to the same territory and forestalling the other's.

I also enjoyed the account of the jostling at Deception Island during and immediately after the Second World War, when Argentina painted its colours on the abandoned British station. After the British removed them, subsequent claims were made by Chile and Argentina, ultimately leading to 'Operation Tabarin' — a secret UK mission charged with building and maintaining permanent British stations on the Peninsula. Following the war, scientific activity increased and responsibility was transferred to the Falkland Island Dependencies Survey, which in 1962 became the British Antarctic Survey.

Each chapter covers a specific period in dense detail. There is grist here for the ruminations of historians, although a more casual reader might find it hard to digest at times. But the final chapter, covering the period since the 1961 signing of the Antarctic Treaty, breezes through the turning points.

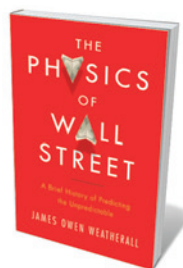
I was reminded of how, in June 1988, the Convention on the Regulation of Antarctic Mineral Resource Activities had been adopted and was poised for ratification by the treaty nations. Then, in January 1989, the Argentinian ship *Bahia Paraíso* ran aground off the Antarctic Peninsula, spilling oil into the surrounding waters. Two months later, the *Exxon Valdez* went down in Prince William Sound, Alaska, emptying 260,000 barrels of crude oil into similarly frigid waters. Countries that had quietly endorsed the convention scrambled to withdraw their support, and within two years the Protocol on Environmental Protection to the Antarctic Treaty (the Madrid Protocol), was in place, prohibiting the exploration and exploitation of mineral resources on the continent for 50 years.

But marine resources remain a contentious issue, as witnessed by the failure in Hobart last year of the Commission for the Conservation of Antarctic Marine Living Resources to establish proposed marine reserves in critical areas in the Southern Ocean.

Day ends by saying, "For centuries, the Antarctic defied man's approach. Now its dangers and its terrors have been largely conquered. Only its future remains unknown." I would add that, thanks to Day, the intrigues and posturing that saturate the history of this distant land have now been exposed. We are left to wonder what continues to be plotted behind the scenes. ■

Edmund Stump is a professor of exploration at Arizona State University who has led many Antarctic field projects. He is the author of *The Roof at the Bottom of the World: Discovering the Transantarctic Mountains*. e-mail: ed.stump@asu.edu

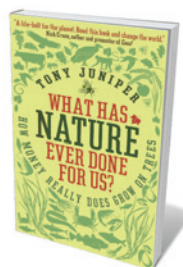
Books in brief



The Physics of Wall Street: A Brief History of Predicting the Unpredictable

James Owen Weatherall HOUGHTON MIFFLIN HARCOURT 304 pp. \$27 (2013)

Wall Street's 2008 meltdown is often pinned on 'quants', the physicists and mathematicians who invented financial instruments such as derivatives. Physicist James Owen Weatherall argues that it was less about the models than a catastrophic misuse of them. He bolsters his view with a concise history of scientific bravehearts out to tame the market, from Louis Bachelier, pioneer of the maths of financial markets, to recent risk-wrangers such as Didier Sornette.



What Has Nature Ever Done For Us? How Money Really Does Grow On Trees

Tony Juniper PROFILE BOOKS 256 pp. £9.99 (2013)

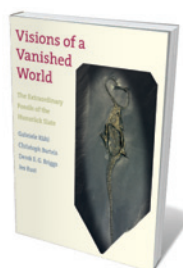
Microbes restore soils, trees oxygenate the atmosphere, vultures act as sanitation crews. And, says Tony Juniper in this crisp call to action, such 'ecosystem services' could back the currency of a new economics. The concept is hardly new, but Juniper — former head of Friends of the Earth — declares its time has come. As he trawls the biosphere and its rich array of services, his insights on environmental threats and solutions, backed by robust findings, form a pragmatic argument for a return to 'gardening the Earth'.



What's Wrong with Fat?

Abigail C. Saguy OXFORD UNIVERSITY PRESS 272 pp. \$29.95 (2013)

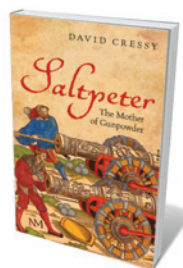
Obesity is an international epidemic. Or is it? Sociologist Abigail C. Saguy weighs in with an investigation of fatness that looks provocative, yet is thoughtful and thorough. By examining hefty through many lenses, from the ethical to the scientific, Saguy traces how labelling fat as a disease or as an indicator of immorality seeps into society. She argues that public-health diktats are issued despite scientific debate over the condition; and that factors in fatness, such as poverty, are often ignored. Ultimately, she avers, stigmatizing the condition serves to embed it further.



Visions of a Vanished World: The Extraordinary Fossils of the Hunsrück Slate

Gabriele Kühl, Christoph Bartels, Derek E. G. Briggs and Jes Rust YALE UNIVERSITY PRESS 128 pp. \$40 (2012)

Some 400 million years ago, catastrophic storms and seismic shifts may have triggered the release of a vast slick of sediment that buried thousands of soft-bodied marine organisms on the ocean floor. Germany's Hunsrück Slate is the result: a frozen slice of the Devonian, capturing trilobites, ammonites and more in their last second of life. Pyritization has left exquisitely detailed, golden-hued fossils, hauntingly displayed in this coffee-table volume.



Saltpeter: The Mother of Gunpowder

David Cressy OXFORD UNIVERSITY PRESS 356 pp. £16.99 (2013)

Gunpowder obsessed early-modern Europe and Islamic Asia. But its key ingredient — potassium nitrate, or saltpetre — had either to be extracted from excrement- and urine-drenched soils, or imported. The scramble to get enough is the focus for this science-tinged history of a Britain building up to empire and enlightenment. David Cressy tells the tale of this "crucial link in the chain of chemistry and power" with panache, from the unravelling of saltpetre's chemistry to the warmongering that fostered dependence on it.

Correspondence

Science petitions are a facade of numbers

Scientists and science organizations increasingly use petitions to influence public opinion and government decisions, and the practice is now spilling over into peer-reviewed journals. We question the effectiveness of public petitions, and suggest that ganging up against unpopular research risks damaging scientific discourse.

Petitioners recruit researchers as co-signatories to reinforce their argument, often for people who may not fully understand the debate. Last year, for example, 31,000 scientists signed a petition rejecting the idea of global warming (www.petitionproject.org) — but a counter-petition with 31,001 signatures won't resolve the debate. Numbers and scientific argument generally have little influence on public opinion or political decisions (D. Ding *et al.* *Nature Clim. Change* **1**, 462–466; 2011), partly because of the difficulty in assessing the authority of individual co-signatories.

'Gang science' is being used to quash unpopular ideas in peer-reviewed journals. For example, 141 scientists mounted an attack on proposals for managing introduced species (D. Simberloff *et al.* *Nature* **475**, 36; 2011), and 137 others challenged a paper written by three authors on the evolution of eusociality (P. Abbot *et al.* *Nature* **471**, E1–E4; 2011). In the absence of new data, such huge conglomerates contribute little more than intimidation.

We should judge the validity of scientific ideas on hard, replicable data and not on the number of authors. Otherwise, scientists risk being branded as another advocacy group with its own agenda.

Robert J. Warren *Buffalo State, State University of New York, Buffalo, New York, USA.*
warrenrj@buffalostate.edu
Mark A. Bradford *Yale*

University, New Haven, Connecticut, USA.

Small collections make a big impact

In an era in which support for natural-history collections is waning, we wish to point out how effective even a small, young collection can be.

We constructed a Google Scholar profile (called UAM Birds) of publications that used the bird collection we oversee at the University of Alaska Museum in Fairbanks. The collection is supported by 1.3 full-time-equivalent staff, and it served in whole or in part as research infrastructure for these publications, contributing and preserving specimens and associated information.

The body of work supported by the collection is diverse and well cited, with a profile *h*-index of 42, equivalent to an average Nobel laureate in physics (J. E. Hirsch *Proc. Acad. Natl Acad. Sci. USA* **102**, 16569–16572; 2005). This positively sings 'good investment' and should encourage other institutions to rediscover and reinvest in collections as important societal resources.

Kevin Winker, Jack J. Withrow *University of Alaska Museum, Fairbanks, Alaska, USA.*
kevin.winker@alaska.edu

Obesity: multiple factors contribute

The idea that obesity is mainly caused by a high intake of carbohydrate is only one of many possible explanations (G. Taubes *Nature* **492**, 155; 2012). The energy in–energy out hypothesis may also be valid, but it is likely to be an oversimplification.

It is important to consider the body's requirements for key nutrients such as the essential amino acids, as well as for energy. A high-energy diet deficient in these can lead to malnutrition

coupled to obesity.

Scientists need to take a closer look at the effects of dietary protein, lipid and carbohydrate on appetite and food intake. These should be assessed in the context of hormone regulation of intermediary metabolism and the large variation in basal metabolic rate among individuals.

We shall then have a more accurate basis for advising Western populations on how to avoid obesity.

Kristin Hamre *National Institute of Nutrition and Seafood Research, Bergen, Norway.*
kha@nifes.no

Obesity: appetite hormone weighs in

Gary Taubes suggests that obesity researchers are currently focusing on energy balance at the expense of hormonal factors (*Nature* **492**, 155; 2012), but hormonal factors have always been an important part of obesity research.

The German physician Bernard Mohr first described human obesity associated with abnormalities of the basal hypothalamus more than 170 years ago (*Wochenschr. Ges. Heilkunde* **6**, 565–571; 1840). In the second half of the twentieth century, a negative feedback loop gradually became evident between the hormone leptin (produced by fat cells) and the hypothalamus, which has turned out to be a crucial regulator of levels of body fat.

Since leptin's discovery in 1994, nearly 10,000 papers have appeared in PubMed on the involvement of leptin signalling in obesity.

Stephan J. Guyenet *University of Washington, Seattle, USA.*
guyenet@uw.edu

Undo NIH policy to ease effect of cuts

You say that a petition by US biomedical scientists against the one-retry limit on grant

applications to the National Institutes of Health (NIH) was "beside the point", despite acknowledging the validity of their arguments (*Nature* **492**, 7; 2012). As the petition's author, I disagree: trying to correct a poor policy decision is not the entire point, as we all recognize, but it is most certainly part of the point.

We believe that the petition — which has now been signed by more than 3,000 scientists (see go.nature.com/x5tik5) — outweighs the questionable arguments for retention of the policy put forth by the NIH (see go.nature.com/mwffql).

In our view, NIH study sections cannot distinguish the quality of proposals in the first quartile. Therefore, once the percentage of applications being funded falls significantly below the 25th percentile, those in the first quartile that go unfunded should be allowed to resubmit as many times as they wish because they are equal in merit to those that are funded.

We are not in the grip of an "unhealthy" obsession, as you suggest. The NIH's unfair decision could be undone with the stroke of a pen, which would help to ease these tough times for biomedical research. We urge scientists to continue working on all fronts to contain the damage caused by reduced federal spending on research.

Robert Benzeira *Memorial Sloan-Kettering Cancer Center, New York, USA.*
benzeira@mskcc.org

Chance thrown by inaccurate dice

The beauty of six-sided dice is that the spots on opposite sides add up to seven — a six and a one, five and two, and four and three. Your illustration wrongly depicts these pairs on adjacent sides (*Nature* **492**, 34–36; 2012).

Janet K. Burg *Eugene, Oregon, USA.*
bmeerkat@comcast.net

FORUM NEUROSCIENCE

Strength in numbers

A process called long-term potentiation mediates information storage — learning and memory — at the level of neurons. An *in vitro* study turns the molecular understanding of this process on its head. But researchers' opinions differ as to what can be inferred from these data. [SEE ARTICLE P.495](#)

THE PAPER IN BRIEF

- Information storage involves stimulation-induced strengthening of synaptic communication between neurons over a long time period.
- For some forms of memory, this phenomenon, called long-term potentiation (LTP), occurs in the brain's hippocampus region and involves AMPA receptors, which are activated by the neurotransmitter glutamate.
- It is widely believed that the cytoplasmic tail of GluA1, which is one of four isoforms that can constitute the four-subunit AMPA receptor, is essential for trafficking of

the receptor to synapses to mediate LTP (Fig. 1).

- Granger *et al.*¹ carried out a single-cell-based study to investigate the minimum amino-acid sequence of this tail that is required for LTP.
- They found that the GluA1 cytoplasmic tail was not required for LTP at all.
- In fact, the expression of a different glutamate receptor, the kainate receptor, was sufficient for LTP to occur.
- The only prerequisite for this process seemed to be a large reserve pool of glutamate receptors that could move to synapses to mediate LTP.

One step forward

MORGAN SHENG

The surprising findings of Granger *et al.*¹ invoke a possible shift in our view of how AMPA receptors are recruited to synapses.

The prevailing mechanistic view of LTP has focused on the GluA1 and GluA2 subunits of AMPA receptors, whose cytoplasmic tails (C-tails) dangle inside the cell. A variety of proteins bind differentially to the C-tails of GluA1 and GluA2, and disruption of these protein interactions affect AMPA-receptor distribution and trafficking in neurons². An appealing, albeit unproven, hypothesis is that protein interactions with the C-tails of GluA subunits — interactions that are somehow regulated by synaptic activity — would usher AMPA receptors into synapses to induce LTP.

Indeed, compelling studies from Malinow and co-workers concluded that specifically GluA1 and its C-tail are essential for the delivery of AMPA receptors to synapses during LTP (for a review, see ref. 3). However, these experiments relied largely on overexpression of GluA1 and/or GluA2 in hippocampal neurons in which normal endogenous AMPA receptors were still present and so possibly interfered with trafficking of the exogenous subunits.

In Granger and colleagues' experiments,

the genes encoding GluA1, GluA2 and GluA3 were deleted, and so endogenous AMPA receptors were absent. It was in this setting that the authors found that not only were the known protein interactions of the GluA1 C-tail unnecessary for LTP, but also GluA2 (previously thought not to support LTP³) and even kainate receptors were sufficient to mediate LTP.

This 'molecular replacement' of GluA subunits in neurons that are devoid of AMPA receptors can be rejected as being just as artificial as the experiments overexpressing them in the presence of endogenous AMPA receptors. Nonetheless, Granger and co-authors' data are intriguing because they show that, at least in the context of neurons lacking AMPA receptors, several different kinds of glutamate receptor can be recruited to synapses and are sufficient to support LTP — irrespective of their C-tails and presumably regardless of their associated proteins and accessory subunits.

This conclusion turns the mechanistic spotlight on the overall structural rearrangements that occur in the synapse during LTP — especially changes to a structure called the post-synaptic density, in which AMPA receptors are clustered⁴ — and how such rearrangements might lead to the capture of AMPA receptors. Indeed, the abundance of scaffolding proteins, such as PSD-95, capable of corraling AMPA receptors in the synapse, is regulated by phosphorylation, and such proteins may have an

underestimated role in synaptic plasticity^{5,6} — the process by which synapses grow stronger or weaker depending on their activity level.

Even if changes in synapse architecture are the main drivers for trapping AMPA receptors during LTP, it is still difficult to imagine how this mechanism could operate completely independently of the C-tails of the receptors or their accessory subunits. To resolve the roles of the different GluA subunits and their C-tails in LTP, it would be helpful to generate data from more subtle genetic experiments *in vivo* — in which, for example, the C-tail of endogenous GluA1 is replaced with the C-tail of GluA2, without otherwise altering the expression of the proteins.

Morgan Sheng is in the Department of Neuroscience, Genentech Inc., South San Francisco, California 94080, USA. e-mail: sheng.morgan@gene.com

Two steps back

ROBERTO MALINOW & RICHARD HUGANIR

In Granger and co-workers' experimental set-up, synapses can recruit any type of glutamate receptor to mediate LTP — a remarkable finding that suggests an incredible versatility for synapses. But does such behaviour occur when synapses contain their normal complement of proteins?

Genetically deleting all AMPA receptors, as the authors have done in their elegant system, may fundamentally change AMPA-receptor trafficking compared with that in normal synapses. Indeed, GluA1 subunits lacking their C-tail could reach synapses only when all AMPA receptors were deleted and not in the more normal situation, in which other AMPA-receptor subunits were present. Our interpretation of this observation is that the C-tail endows GluA1 with a competitive advantage to reach the synapse.

To address the mechanisms underlying LTP at normal synapses, more subtle experimental manipulations may be more informative;

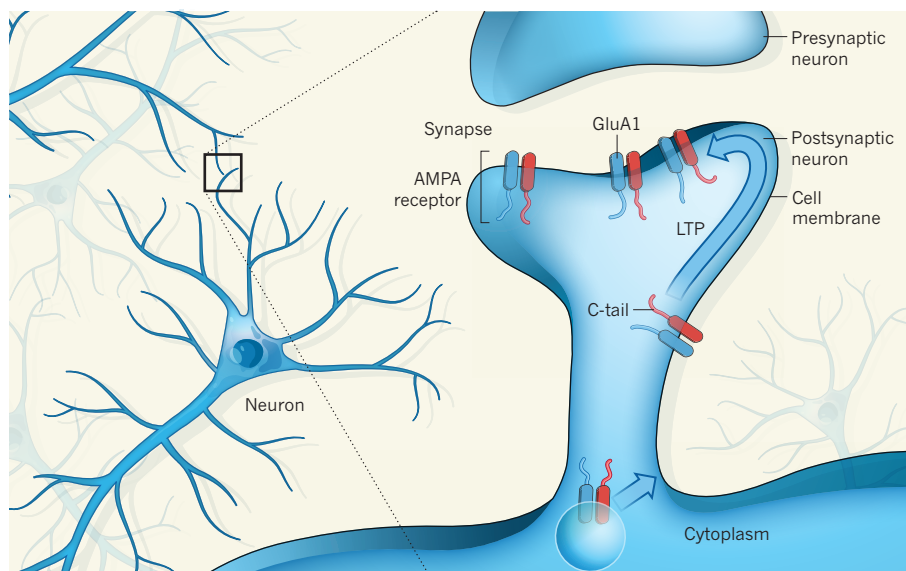


Figure 1 | AMPA receptors at the synapse. At the level of neurons, long-term potentiation (LTP) is mediated by AMPA receptors, which are transported from intracellular compartments and elsewhere in the cell membrane to the membrane of the postsynaptic neuron. Surprisingly, Granger *et al.*¹ report that the cytoplasmic tail of the GluA1 subunit of AMPA receptors is not required for this trafficking and thus for LTP. Instead, they propose that any type of glutamate receptor can support LTP, as long as enough of them reach the membrane.

these could include introducing mutations ('knock-in' mutations) into the genes encoding GluA1 and GluA2 to alter their C-tail structure without affecting their expression level. In fact, previous studies^{7,8} involving such mutations have shown that the C-tail phosphorylation sites and protein-interacting domains of these subunits are important for several forms of synaptic plasticity, including LTP.

Synapses lacking AMPA receptors may behave differently from normal synapses because loss of some essential regulatory proteins makes them less selective. Are AMPA-receptor subunits responsible for maintaining such crucial proteins at the synapse? It could be that synapses without AMPA receptors — such as those that are prevalent early in development⁹ — have lower selectivity for receptors during LTP than do more mature synapses containing AMPA receptors. Alternatively, there may be competition for entering the synapse between different receptors that have different interaction partners at the synapse to control their lifetime there. If that is the case, if a competitor with several such partners, say AMPA receptors, is removed, then other receptors with minimal numbers of partners and interactions could enter and remain in the synapse.

Granger and co-authors' study, therefore, may point to a novel view that synapses are sites of competition: how efficiently a receptor enters the synapse depends not only on its structural components, but also on those of its competitors. Such factors may determine how AMPA receptors get into and out of a synapse during conditions of synapse maintenance and plasticity.

But whatever the mechanism involved, the present study will focus future research on the

structural changes that occur at the synapse after LTP. Many scaffolding proteins regulate the complex structure of the postsynaptic density, and, according to Granger *et al.*, structural changes may occur that do not require specific glutamate receptor types. However, the identity of these common scaffolding proteins is not obvious, because most such proteins are known to be specific for AMPA or kainate receptors. In fact, some of the same authors have previously shown that AMPA-receptor-associated proteins known as TARPs are

crucial for LTP¹⁰. Yet the present study refutes those data and shows that even kainate receptors, which do not interact with TARPs, can completely rescue LTP in the absence of AMPA receptors.

So, one step forward, two steps back. The search for the mechanism underlying LTP is well into its third decade, and it looks as if it will continue to fascinate and elude neuroscientists for the next decade, too. ■

Roberto Malinow is in the Center for Neural Circuits and Behavior, Division of Biology, Neurobiology Section, and the Department of Neurosciences, University of California, San Diego, La Jolla, California 92093, USA.

Richard Huganir is in the Department of Neuroscience, Howard Hughes Medical Institute, Johns Hopkins University School of Medicine, Baltimore, Maryland 21205, USA. e-mails: rmalinow@ucsd.edu; rhuganir@jhmi.edu

1. Granger, A. J., Shi, Y., Lu, W., Cerpas, M. & Nicoll, R. A. *Nature* **493**, 495–500 (2013).
2. Anggono, V. & Huganir, R. L. *Curr. Opin. Neurobiol.* **22**, 461–469 (2012).
3. Malinow, R. *Phil. Trans. R. Soc. Lond. B* **358**, 707–714 (2003).
4. Sheng, M. & Kim, E. *Cold Spring Harb. Perspect. Biol.* <http://dx.doi.org/10.1101/cshperspect.a005678> (2011).
5. Opazo, P., Sainlos, M. & Choquet, D. *Curr. Opin. Neurobiol.* **22**, 453–460 (2012).
6. Kim, M. J. *et al. Neuron* **56**, 488–502 (2007).
7. Lee, H.-K. *et al. Cell* **112**, 631–643 (2003).
8. Steinberg, J. P. *et al. Neuron* **49**, 845–860 (2006).
9. Wu, G.-Y., Malinow, R. & Cline, H. T. *Science* **274**, 972–976 (1996).
10. Tomita, S., Stein, V., Stocker, T. J., Nicoll, R. A. & Brecht, D. S. *Neuron* **45**, 269–277 (2005).

M.S. declares competing financial interests. See go.nature.com/svmjy6 for details.

BIOENERGY

Biofuel production on the margins

An analysis shows that fuel made from wild, herbaceous vegetation grown on land currently unsuitable for cultivating field crops could contribute substantially to the United States' targets for biofuel production. SEE LETTER P.514

KLAUS BUTTERBACH-BAHL & RALF KIESE

The governments of more than 35 countries, including the United States, Brazil and members of the European Union, have established policies promoting the production and use of biofuels¹. This is driven by an interest in becoming more independent of fossil-fuel imports and reducing the climate footprint of their economies. However, the climate benefit of replacing fossil fuels with

biofuels is strongly disputed, because of the lack of compelling evidence to show that biofuels are indeed associated with much lower greenhouse-gas emissions than fossil fuels when the full life cycle of their production and use is taken into account. On page 514 of this issue, Gelfand *et al.*² report that certain wild, herbaceous vegetation, growing on 'marginal' lands currently unsuitable for arable farming, can be used as a biofuel crop, and does substantially mitigate greenhouse-gas emissions



50 Years Ago

International Tables for X-ray Crystallography. General Editor: Dame Kathleen Lonsdale — The fifty years which have elapsed since the discovery of X-ray diffraction by crystals have witnessed the development of X-ray crystallographic techniques as a structure-determining tool of unprecedented power and catholicity of application. By it the complexities of mineral structures have been rationalized ... and the elaborate architecture of the giant globular proteins mapped out. Fortunately, it was recognized early that this diversity would make discipline in the presentation of results, and uniformity of nomenclature and convention particularly desirable. The first attempt to provide such an authoritative basis was by the *Internationale Tabellen zur Bestimmung von Kristallstrukturen* of 1935. In 1946 the International Union of Crystallography decided on a complete revision and extension of these tables under the general editorship of Dame Kathleen Lonsdale. Two volumes ... have already appeared; Volume 3, dealing with physical and chemical tables, represents the completion of the 1946 project ... No X-ray crystallographical laboratory worthy of the name will fail to add this magnificently printed and luxuriously bound volume to the two they already should possess. **Struther Arnott**
From *Nature* 26 January 1963

100 Years Ago

It is not at all difficult to measure the ionisation produced by the radiation reflected by crystals, as indeed Prof. Barkla has already suggested. Using a sheet of mica and a pencil of a few millimetres diameter, I find it possible to follow with an ionisation chamber the movement of the reflected spot while the mirror is rotated. **W. H. Bragg**
From *Nature* 23 January 1913

compared with fossil-fuel use — even rivaling the benefits associated with growing traditional biofuel crops, such as maize (corn)*.

When assessing the potential climate benefits of biofuels, it is essential to consider the consequences of land-use change and of fertilization associated with growing biofuel crops^{3,4} — particularly any changes in the carbon stocks of affected ecosystems, and in the emissions of nitrous oxide, a potent greenhouse gas produced by soil bacteria. It is also crucial to determine whether the growing of biofuel crops poses local threats to biodiversity, or to water and nutrient cycling⁵.

Moreover, because biofuel feedstocks are currently produced mostly on fertile agricultural land, it has been questioned whether useful amounts of biofuels can be produced without threatening food production. The ensuing conflict of interest has been called the “food, energy and environment trilemma”⁶. To be acceptable to society, therefore, biofuel-production strategies must be shown to greatly mitigate greenhouse-gas emissions without jeopardizing food and animal-feed production through competition for land use, and to have a minimal effect on the environment.

Gelfand *et al.* compared the biofuel yields, greenhouse-gas emissions, changes in soil-carbon stocks, and energy consumption associated with field operations for six biofuel-cropping systems in the midwestern United States over a 20-year period. They then used these data in a rigorous life-cycle assessment of the climate benefits of the different systems. Because it is based on long-term data, this is the first convincing analysis of the impact of biofuel-production systems on global warming. By contrast, previous studies relied either on modelling or on short-term studies of a smaller number of systems.

The authors show that all the biofuel-cropping systems investigated are net sinks of atmospheric carbon dioxide if fossil-fuel offset credits are included in the analysis. These credits are the sum of all the CO₂ emissions potentially avoided when fossil fuels are replaced with biofuels, taking into account both the production and the combustion of the fossil fuels⁷. Surprisingly, the researchers found that the greenhouse-gas mitigation of wild, perennial, herbaceous vegetation (Fig. 1) — specifically, successional vegetation, which naturally regrows in marginal areas such as abandoned, low-productivity arable land — was markedly higher than that of intentionally grown crops, including maize, alfalfa, poplar and a maize-soya bean-wheat crop rotation, and that energy production was comparable. Moreover, Gelfand *et al.* show that moderate levels of nitrogen fertilization could further boost biofuel yields of the wild vegetation system by about 50%, with only a marginal increase in nitrous oxide emissions.

*This article and the paper under discussion² were published online on 16 January 2013.



Figure 1 | Wild biofuel crops. Gelfand *et al.*² report that wild, successional, herbaceous vegetation, such as that pictured, is an effective biofuel crop that has a greenhouse-gas-mitigation capacity rivalling that of traditional biofuel crops.

A big advantage of such native successional systems over other biofuel crops is that they can be productive despite the soil and climate restrictions typically found in marginal lands. This suggests that marginal lands could be a viable alternative to fertile cropland for biofuel production — which would be extremely useful, given the limited land resources^{8,9}.

To explore the regional implications of their study, Gelfand *et al.* used a computational approach to identify suitable marginal lands for biofuel production across ten states of the US Midwest. More specifically, they used information from a geographical database in a biogeochemical model to estimate the effects of soil and climate on biofuel yields.

One constraint on the production of biofuels is the need to minimize the energy consumed by the collection and transport of the crop. Gelfand and colleagues show that, given the distribution of marginal lands in the US Midwest, optimal biofuel production would be achieved if biomass is collected from within a region of 80-kilometre radius around refineries. Such a production strategy could yield approximately 21 billion litres of ethanol per year from 11 million hectares of marginal land. This is about 25% of the target mandated by the US Department of Energy's Biomass Program for cellulosic biofuel production in 2022 (cellulosic biofuel is that produced from lignocellulose, a major constituent of wood and grasses). It equates to an expected fossil-fuel offset of roughly 40 teragrams of CO₂ equivalents each year (1 teragram is 10¹² grams) — the same as the CO₂ emissions from 10 million medium-sized cars, each with an annual run of 20,000 km.

So would a native successional biofuel crop be all good? Perhaps not. Gelfand and

G. W. P. ROBERTSON, MICHIGAN STATE UNIV. W. K. KELLOGG BIOLOGICAL STATION

co-workers' study does not explicitly answer the question of whether all the marginal lands identified as suitable for biofuel production could be used without harming biodiversity and the environment. Moreover, land that is fallow today might be needed in the future for agricultural production, to offset the demands of the world's growing population.

Another question raised by the study concerns greenhouse-gas mitigation: for the biofuel-cropping systems under consideration, the authors found that, apart from fossil-fuel offset credits, increases in soil-carbon stocks are the major driver of climate benefits. But the rate of increase of soil-carbon stocks will slow down with time, so that the stocks reach

an equilibrium level within a few decades¹⁰. It therefore seems that comprehensive assessments of the long-term climate impacts of biofuels will require the quantification of spatially and temporally explicit soil-carbon sequestration potentials. ■

Klaus Butterbach-Bahl and Ralf Kiese are at the Institute of Meteorology and Climate Research, Atmospheric Environmental Research, Karlsruhe Institute of Technology, Garmisch-Partenkirchen 82467, Germany. **K.B.-B.** is also at the International Livestock Research Institute, Nairobi, Kenya. e-mails: klaus.butterbach-bahl@kit.edu; ralf.kiese@kit.edu

1. OECD-FAO *Agricultural Outlook 2011–2020*. Ch. 3 (OECD/FAO, 2012).
2. Gelfand, I. *et al. Nature* **493**, 514–517 (2013).
3. Fargione, J., Hill, J., Tilman, D., Polasky, S. & Hawthorne, P. *Science* **319**, 1235–1238 (2008).
4. Smith, K. A., Mosier, A. R., Crutzen, P. A. & Winiwarter, W. *Phil. Trans. R. Soc. B* **367**, 1169–1174 (2012).
5. Dominguez-Faus, R., Powers, S. E., Burken, J. G. & Alvarez, P. J. *Environ. Sci. Technol.* **43**, 3005–3010 (2009).
6. Tilman, D. *et al. Science* **325**, 270–271 (2009).
7. Gelfand, I. *et al. Proc. Natl Acad. Sci. USA* **108**, 13864–13869 (2011).
8. Kang, S. *et al. Land Use Policy* **30**, 106–113 (2013).
9. Werner, C. *et al. Glob. Change Biol. Bioenergy* **4**, 642–653 (2012).
10. Lal, R. *Science* **304**, 1623–1627 (2004).

SOLAR PHYSICS

Towards ever smaller length scales

Determining the real scale of structures in the Sun's corona has proved difficult because of limited spatial resolution. Now high-resolution imaging has allowed dynamic structures on scales of 150 kilometres to be observed. SEE LETTER P.501

PETER CARGILL

The origin of the Sun's outer atmosphere, the corona, is a long-standing scientific problem of great interest and complexity. Why does a star with a surface temperature of roughly 5,700 kelvin have an outer atmosphere with temperatures in excess of 1 megakelvin, and why does the corona exhibit phenomena such as flares? The answer lies in the energy contained in the Sun's magnetic field, which fills the corona, as inferred from coronal images at extreme ultraviolet and X-ray wavelengths. How the magnetic energy is dissipated in the corona and sustains its temperature is controversial, but comes down to a determination of the spatial scales of coronal structures. On page 501 of this issue, Cirtain *et al.*¹ identify dynamic structures on scales of 150 kilometres, which represents a major constraint that theories must now confront.

Before 2012, the best spatial resolution of the solar corona was obtained by NASA's Atmospheric Imaging Assembly (AIA) on the Solar Dynamics Observatory spacecraft, which was launched in 2010. The instrument resolves

scales of about 900 km and looks at several wavelength ranges corresponding to different temperatures. However, images of the visible solar surface at a resolution of 100 km show distinct magnetic and plasma structures,

and so the question arises as to whether structures with these scales are also present in the corona.

In their study, Cirtain *et al.* used the High-resolution Coronal Imager (Hi-C), a new extreme-ultraviolet instrument that was launched on a rocket on 11 July 2012 and obtained roughly 5 minutes of data before re-entering Earth's atmosphere. The instrument looks at coronal plasma with temperatures of around 1.5 MK, and is capable of spatial resolution at least five times better than the AIA: the Hi-C can resolve scales on the order of 150 km. To place this in context, it took more than 30 years to improve the spatial resolution from the few thousand kilometres obtained by instruments on NASA's Skylab observatory to that obtained with the AIA. The Hi-C instrumentation performed up to expectation, and images of the Sun show unambiguous structure at the desired resolution — a huge achievement.

A striking feature of Cirtain and colleagues' results is the dynamic structures visible at the limit of resolution, clearly evident by comparing images from the Hi-C and AIA in the paper's Supplementary Videos 1 and 2 (ref. 1). (The reader should also look at other aspects of the videos to note how much else is happening on these small scales, as is also evident in Fig. 1.) The dynamic behaviour of the observed structures is interpreted as evidence for 'magnetic braiding', an effect in which small bundles of magnetic field become wrapped around each other owing to plasma motions at the solar surface². Whether this is in fact the case is unclear, but there seems little doubt that magnetic-field dissipation on a fundamental scale is seen, with different field elements interacting with one another through magnetic

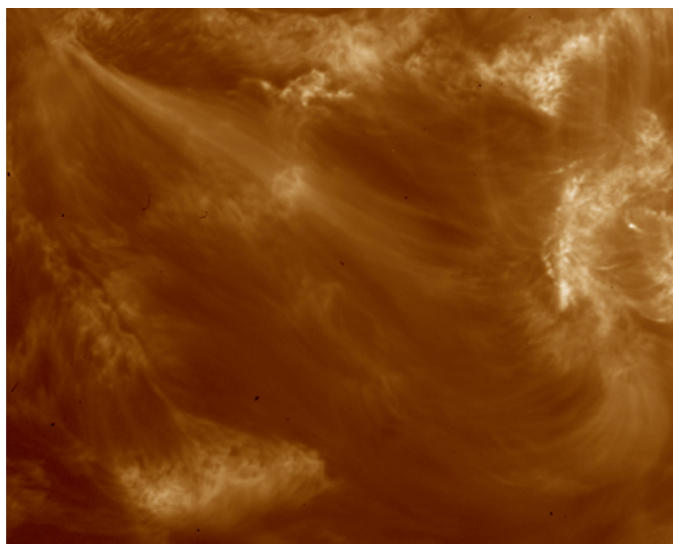


Figure 1 | Small structure in the corona. The image is a sub-field of the entire field of view observed by the High-resolution Coronal Imager (Hi-C) and analysed by Cirtain and colleagues¹. It shows the solar corona at a temperature of roughly 1.5 megakelvin over a dimension of 154.6×123.7 arcseconds, or $112,000 \times 90,000$ km. The strands running from top left to lower right are believed to outline the magnetic field in the corona, as are the other structures in the image. The remarkably fine structure is visible everywhere and constitutes the major advance achieved with the Hi-C. (Image prepared by J. Cirtain and A. Winebarger.)

reconnection³, a process that changes the magnetic-field topology through dissipation of electric currents. To me, the Hi-C images are reminiscent of computational models of the kink instability, a process known from plasma physics that is also thought to occur in the corona⁴. Although such processes have long been conjectured, *prima facie* evidence for coronal reconnection, as found by Hi-C, is an important result.

A more general point concerns the very presence of structures at this resolution. There has long been a debate about when coronal structures are resolved; that is, what is an elemental structure? In the past, some have stated that structures seen by earlier solar missions are resolved, or 'monolithic'. Others have argued from theory and interpretation of data^{5–7} that scales on the order of 100 km were to be expected, and that such high resolution was needed. Indirect evidence from the AIA had also begun to point the way to such scales⁸, but the Hi-C results show that any debate on the structure of the corona now needs to address scales of 100–200 km or smaller, as can be seen in Figure 1.

Clearly, even in 5 minutes of observations there is a wealth of data that need to be analysed. The next stage is securing Hi-C, or an instrument with similar or improved performance, on an orbiting spacecraft. This spacecraft must also carry a modern extreme-ultraviolet spectrometer⁹ — both to complement Hi-C and to provide fundamental plasma measurements of density, temperature, velocities and small-scale turbulence — as well as an instrument capable of measuring signatures of energetic particles, which are known to be a significant product of the magnetic-reconnection process¹⁰. Only with such complete instrumentation can a proper understanding of coronal structures be attained.

Has Hi-C really resolved the corona? To do this will require observation of a wider range of solar conditions than is feasible in a short rocket flight, and one should not bet against the existence of further fine structure within the scales detected by Hi-C. But for those who have wanted to see observations on such scales for decades, there is a feeling that things are getting interesting, and quantitative tests of competing theoretical ideas can be undertaken, as is evident from the above discussion of this short data set. ■

Peter Cargill is at the *Blackett Laboratory, Imperial College London, London SW7 2BZ, UK, and at the School of Mathematics and Statistics, University of St Andrews, UK.*
e-mail: p.cargill@imperial.ac.uk

1. Cirtain, J. W. *et al.* *Nature* **493**, 501–503 (2013).
2. Parker, E. N. *Astrophys. J.* **264**, 642–647 (1983).
3. Priest, E. R. & Forbes, T. G. *Magnetic Reconnection: MHD Theory and Applications* (Cambridge Univ. Press, 2000).
4. Botha, G. J. J., Arber, T. D. & Srivastava, A. K.

5. Cargill, P. J. & Klimchuk, J. A. *Astrophys. J.* **478**, 799–806 (1997).
6. Cargill, P. J. *Adv. Space Res.* **26**, 1759–1768 (2000).
7. Bookbinder, J. A. *et al.* *Proc. SPIE* **1177**, 1177 (1990).
8. Brooks, D., Warren, H. P. & Ugarte-Urra, I. *Astrophys. J. Lett.* **755**, L33 (2012).
9. Teriaca, L. *et al.* *Exp. Astron.* **34**, 273–309 (2012).
10. Cargill, P. J. *et al.* *Space Sci. Rev.* **173**, 223–245 (2012).

PALAEONTOLOGY

Gritting their teeth

A comparison of the wearing effect of plant-derived silica and desert dust on tooth enamel suggests that extreme wear on teeth might not be caused by food. The findings may change some thoughts about the diets of human ancestors.

BERNARD WOOD

Chewing is much like using a pestle and mortar, but upside down. Your jaw muscles supply the power and move your lower teeth (the pestle) up and across your upper teeth (the mortar). As long as any food caught between them is not especially hard or tough, it will be broken into smaller pieces and the teeth should remain intact. But, unlike the granite or marble pestle and mortar in your kitchen, teeth are gradually worn down. It has been widely assumed that interactions with food are the cause of this destructive damage. But, writing in the *Journal of the Royal Society Interface*, Lucas *et al.* suggest¹ that

the culprit may not be the food we chew, but the dust or grit we ingest along with it.

When teeth are newly erupted into the jaw, the enamel surface is relatively pristine. However, even though enamel is the hardest tissue in the body, once teeth have been used to chew on food, tiny grooves, scratches and pits soon pockmark the enamel. Living animals with different diets produce different patterns of dental microwear^{2,3}, so it was natural to assume that these patterns can be used to infer the types of food eaten by our ancestors and close evolutionary relatives⁴. However, a consideration of the physical processes that cause wear to hard surfaces calls some of these assumptions into question.



Figure 1 | Signs of wear. The fossilized palate and maxillary teeth, seen from below, of OH 5, the type specimen of *Paranthropus boisei*, an archaic hominin (human ancestors and close relatives) that lived approximately 2 million years ago. The species is referred to as a hypermegadont, meaning that it has large, broad cheek teeth and small front teeth. Although OH 5 was not yet an adult, the enamel on the grinding faces of both first molars (M1), the premolars (P4 and P3) and the canines (C) has been worn down to expose the softer dentine in the pulp cavities of the teeth (examples of wear are indicated by arrows). Lucas *et al.*¹ suggest that only grit, not food, is hard enough to have removed the exceptionally thick enamel covering of these teeth so quickly.

MUSEUM AND HOUSE OF CULTURE, DAR ES SALAAM

Materials scientists define wear as what happens when an object loses some of its volume. If you dance in high heels on your neighbour's softwood floor, you will annoy them by marking it, but marking merely deforms the surface of the floor — technically it is not worn. But if you were to dance in golf shoes, you will abrade the floor and eventually wear it away, because abrasion results in loss of volume. It seems unlikely that any food built primarily from either cellulose (deriving from plants) or collagen (from animal soft tissues) is going to abrade enamel, yet these are the foods we have in mind when we think about diet. Food acids can eventually dissolve enamel, but this is only a problem in some modern human populations. So what is it that wears teeth down? A basic understanding of wear in industrial processes suggests that it is probably something really hard, such as silica.

In the context of chewing, resistance to indentation — or hardness — is the crucial variable. In their experiments, Lucas *et al.* used an orang-utan molar tooth as a proxy for the thick-enamelled fossil teeth of our ancestors and close relatives. They measured its hardness (which ranged between 4.08 and 5.72 gigapascals), and compared it with the hardness of two sorts of phytolith, deriving from squash (which had a hardness range of 0.43–1.74 GPa) and grass (1.35–4.24 GPa), and of Kuwaiti desert dust (10.1–14.1 GPa). Phytoliths are silica particles produced by plants as a defence mechanism, but they are non-crystalline and, as can be seen from these hardness measurements, they are softer than both quartz grit and enamel.

The authors mounted individual microscopic particles of the phytoliths, quartz dust and chips of enamel from a tooth on a nanoin-denter (a device used for measuring wear effects on materials at the nanoscale) and then slid these across the surface of tooth enamel at a known force and angle. They found that neither the phytoliths nor the enamel chips resulted in any loss of volume of the tooth; the particles marked it, but they did not abrade it. Only the quartz dust resulted in the volume loss that would eventually accumulate to produce the type of wear on a tooth that is visible to the naked eye (Fig. 1).

The authors also found that the enamel was abraded only if the quartz particles have the right angle of 'attack'. The critical attack angle is set by the toughness of the tooth tissue; it is low for enamel, but higher for dentine, which is softer but tougher. Without the right geometry, even very hard particles will not abrade enamel.

All methods for reconstructing evolutionary history begin with observations about pattern, but what really matters are the processes that generate the pattern. Interpretations based on dental microwear are at the stage of shifting from questions about the patterns to more fundamental questions about the basic physics of the processes that determine them, and these findings suggest that dental wear results

from the dust and grit that is ingested along with food^{5,6}, rather than by factors intrinsic to the food.

So what do these results mean for attempts to reconstruct the diet of our ancestors and their close relatives? As well as dental microwear, the shape and size of the skull and teeth can be used to generate hypotheses about the types of food (hard versus soft, tough versus weak) that these primates were adapted to eat. The chemicals that accumulated in their bones and teeth also reflect the types of vegetation (dry tropical grass versus leaves) consumed⁷. And dental microwear can be used to interpret how quickly the enamel covering has been removed from the teeth. In many cases, these lines of evidence lead to similar conclusions, but in one of our close evolutionary relatives, *Paranthropus boisei*, the microwear on the teeth⁸ is not consistent with the extreme dental microwear seen in this taxon (Fig. 1). Lucas and colleagues suggest that this extreme microwear is not caused by diet,

but instead is most likely to be the result of these creatures literally 'gritting their teeth'. ■

Bernard Wood is in the Center for the Advanced Study of Hominid Paleobiology, Department of Anthropology, George Washington University, Washington DC 20052, USA.

e-mail: bernardawood@gmail.com

1. Lucas, P. W. *et al.* *J. R. Soc. Interface* **10**, 20120923 (2013).
2. Walker, A., Hoeck, H. & Perez, L. *Science* **201**, 908–910 (1978).
3. Teaford, M. F. *Scanning Microsc.* **2**, 1149–1166 (1988).
4. Scott, R. S. *et al.* *Nature* **436**, 693–695 (2005).
5. Ungar, P. S. *et al.* *Am. J. Phys. Anthropol.* **97**, 93–99 (1995).
6. Teaford, M. F. & Lytle, J. D. *Am. J. Phys. Anthropol.* **100**, 143–147 (1996).
7. Ungar, P. S. & Sponheimer, M. *Science* **334**, 190–193 (2011).
8. Ungar, P. S., Grine, F. E. & Teaford, M. F. *PLoS ONE* **3**, e2044 (2008).

CANCER

The to and fro of tumour spread

Two studies shed light on the role of cellular transitions between the epithelial and mesenchymal states during cancer metastasis, and provide food for thought as to which cellular processes should be targeted in cancer treatment.

**BRYCE J. W. VAN DENDEREN
& ERIK W. THOMPSON**

The spread of cells from the primary site of a solid tumour to distant sites remains the major cause of disease and death associated with these cancers. For tumour cells to spread, or metastasize, they must modify their 'anchored' state and detach from their neighbouring cells; migrate through tissues into the blood and lymph systems; survive in these circulation systems; and then leave the vessels at an appropriate site to form another tumour¹. Many of these events are favoured by conversions between two cellular states — the epithelial and mesenchymal phenotypes. But the role of these transitions in cancer metastasis is controversial. Writing in *Cancer Cell*, Tsai *et al.*² and Ocaña *et al.*³ help to clarify this issue.

Most cancers in adults are carcinomas, which arise from abnormal growth of epithelial cells that line the surfaces and cavities of organs such as the breasts, colon, lungs and liver. Epithelial cells are fully differentiated and non-mobile, whereas mesenchymal cells migrate easily. In the developing embryo, a process called the epithelial–mesenchymal

transition (EMT) allows epithelial cells to take on mesenchymal-cell characteristics and move sites, after which they revert back to an epithelial phenotype through the mesenchymal–epithelial transition (MET), and continue to form body structures. EMT is also involved in metastasis, but whether it is an absolute requirement is controversial, in part because metastatic tumours display an epithelial phenotype and lack mesenchymal markers⁴.

We have coined the term epithelial–mesenchymal plasticity for the dynamic interchange between epithelial and mesenchymal phenotypes⁵. Ten years ago, it was hypothesized that tumour cells that had undergone EMT and disseminated would then go through MET to successfully colonize a secondary site and form a metastatic tumour⁶; and preliminary evidence for MET has been reported in cancers of the colon, breast, bladder and prostate⁷. Although the abundance of studies on EMT still dwarfs those on MET, it is emerging as a crucial and possibly rate-limiting step in metastasis, and this is supported by the two new papers.

Previous work has shown that the EMT-inducing transcription-factor protein Twist1 is essential for spontaneous metastasis in a mouse model of mammary cancer⁸. Tsai and

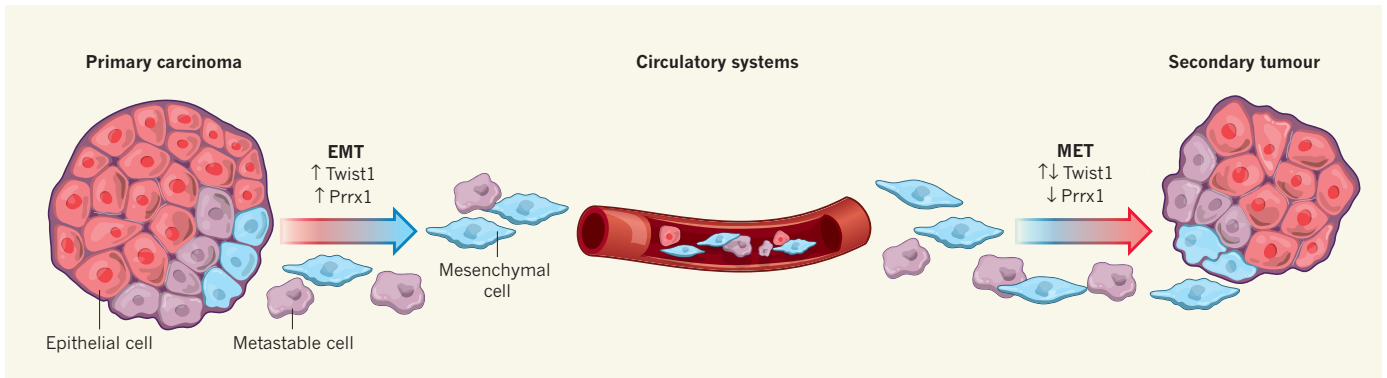


Figure 1 | Cellular transitions in cancer metastasis. Dissemination of cells from a primary solid tumour is facilitated by the epithelial–mesenchymal transition (EMT). This process allows epithelial tumour cells (carcinoma cells), which are fully differentiated and non-mobile, to acquire the more invasive characteristics of mesenchymal cells. Tsai *et al.*² show that EMT is induced by a transcription factor called Twist1, and that Twist1 expression also increases the number of metastable cells, which express both epithelial

and mesenchymal characteristics, in the bloodstream of mice. However, the authors found that sustained Twist1 expression prevents the formation of secondary tumours, possibly by preventing the cells from undergoing the mesenchymal–epithelial transition (MET) that is needed for them to revert to the epithelial state and form metastases. Ocaña *et al.*³ characterize another EMT-inducing transcription factor, Prrx1, and show that MET can be achieved with Prrx1 suppression, even during continued Twist1 expression.

co-workers have built on these findings using a mouse model of squamous-cell carcinoma in which Twist1 expression can be turned on and off. The authors found that Twist1 induces EMT and tumour-cell transit into the bloodstream (Fig. 1), but that metastases did not form if the cancer cells could not switch Twist1 off after disseminating. This suggests that halting EMT, and thereby allowing MET, is required for completion of the metastatic process.

Ocaña *et al.* have characterized a new EMT-inducing transcription factor, Prrx1, that they show drives EMT during embryonic development in chicks. The authors also show that, similarly to other embryonic EMT-driving factors, Prrx1 seems to play a part in the invasive, migratory phenotype of breast carcinoma cells undergoing metastasis. Moreover, the authors found that forced, continuous expression of Prrx1 blocked the capacity of otherwise metastasis-competent cells to produce metastatic tumours, and that Prrx1 suppression is needed for MET to proceed — consistent with Tsai and colleagues' observations for Twist1 (Fig. 1).

A notable advance in our appreciation of the role that EMT may have in solid-tumour biology came from observations that 'breast cancer stem cells' (cells isolated from clinical samples that have particularly strong cancerous properties and the ability to initiate new tumours from small numbers of cells) exhibit a mesenchymal profile⁹. Conversely, both normal and cancerous mammary epithelial cells that are induced to undergo EMT become more stem-cell-like⁸. This relationship was further refined when cells with progenitor-cell properties — those committed more towards differentiation than the mesenchymal-like stem cells — were seen to have higher cancerous potential^{9,10}.

Adding to this picture, Ocaña *et al.* show that the stem-cell-like features of carcinoma cells can be segregated from EMT by manipulating

the expression of Prrx1. Remarkably, they show that abrogation of Prrx1 in carcinoma-derived cells (called BT-549 cells) that would not normally form tumours when injected into a mouse makes them both tumorigenic and metastatic. Moreover, they show that reducing Prrx1 levels in cancer cells causes a reduction in EMT, but a gain of stem-cell activities. These findings are consistent with recent reports that pluripotency (the ability to differentiate into various cell types), which is associated with the epithelial phenotype more than the mesenchymal phenotype, is a major driver of both cancerous and metastatic potential^{10,11}. It is thus implicit that exhibiting the enhanced malignant properties associated with the mesenchymal stem-cell state requires an ability to spontaneously progress towards an epithelial state with pluripotent characteristics.

An additional twist to the tale comes from the fact that some tumour cells simultaneously show mesenchymal and epithelial characteristics^{12,13}. Also called the intermediate, or metastable, phenotype, it has long been recognized that co-expression of both phenotypes may offer cells a form of pluripotency, allowing them to dynamically adjust to the circumstances they encounter. Such plasticity seems to be key for the full spectrum of metastatic competence, because cells that are rigidly locked into one state or another are less capable of metastasis or even of primary-tumour growth, as seems to be the case with BT-549 cells. Furthermore, other studies^{10,14} have shown that cooperation between mesenchymal and epithelial variants of some cancer cells can allow the epithelial variants to escape their tumour site and metastasize. Thus, the combined evidence from these studies and the present papers suggests that both mesenchymal and epithelial phenotypes are required for metastatic competence, and that cancer cells must have sufficient plasticity between these phenotypes to spread.

The reports by Tsai *et al.* and Ocaña *et al.* leave little doubt as to the importance of MET and/or the epithelial phenotype for carcinoma metastasis. As stated by both sets of authors, this introduces the question of whether the therapies that many laboratories are chasing — treatments designed to inhibit cancer cells in the mesenchymal state — might in fact have a stimulatory effect on established metastases, or even activate dormant cancer cells. Models and experimental designs, such as those used for these studies, will be crucial to resolving this question, and they herald an exciting chapter in our understanding of metastasis. ■

Bryce J. W. van Denderen and **Erik W. Thompson** are at St Vincent's Institute, Fitzroy, Victoria 3065, Australia. **B.J.W.v. D.** is also in the Department of Medicine, University of Melbourne, and **E.W.T.** is in the Department of Surgery, University of Melbourne, St Vincent's Hospital, Fitzroy. e-mails: rik@svi.edu.au; bvanderenden@svi.edu.au

1. Fidler, I. J. *Semin. Cancer Biol.* **21**, 71 (2011).
2. Tsai, J. H., Donaher, J. L., Murphy, D. A., Chau, S. & Yang, J. *Cancer Cell* **22**, 725–736 (2012).
3. Ocaña, O. H. *et al. Cancer Cell* **22**, 709–724 (2012).
4. Tarin, D., Thompson, E. W. & Newgreen, D. F. *Cancer Res.* **65**, 5996–6000 (2005).
5. Thompson, E. W. & Haviv, I. *Nature Med.* **17**, 1048–1049 (2011).
6. Thiery, J. P. *Nature Rev. Cancer* **2**, 442–454 (2002).
7. Gunasinghe, N. P., Wells, A., Thompson, E. W. & Hugo, H. J. *Cancer Metastasis Rev.* **31**, 469–478 (2012).
8. Yang, J. *et al. Cell* **117**, 927–939 (2004).
9. Hollier, B. G., Evans, K. & Mani, S. A. *J. Mammary Gland Biol. Neoplasia* **14**, 29–43 (2009).
10. Celia-Terrassa, T. *et al. J. Clin. Invest.* **122**, 1849–1868 (2012).
11. Sarrio, D., Franklin, C. K., Mackay, A., Reis-Filho, J. S. & Isacke, C. M. *Stem Cells* **30**, 292–303 (2012).
12. Lee, J. M., Dedhar, S., Kalluri, R. & Thompson, E. W. *J. Cell Biol.* **172**, 973–981 (2006).
13. Klymkowsky, M. W. & Savagner, P. *Am. J. Pathol.* **174**, 1588–1593 (2009).
14. Tsuji, T. *et al. Cancer Res.* **68**, 10377–10386 (2008).

Eemian interglacial reconstructed from a Greenland folded ice core

NEEM community members*

Efforts to extract a Greenland ice core with a complete record of the Eemian interglacial (130,000 to 115,000 years ago) have until now been unsuccessful. The response of the Greenland ice sheet to the warmer-than-present climate of the Eemian has thus remained unclear. Here we present the new North Greenland Eemian Ice Drilling ('NEEM') ice core and show only a modest ice-sheet response to the strong warming in the early Eemian. We reconstructed the Eemian record from folded ice using globally homogeneous parameters known from dated Greenland and Antarctic ice-core records. On the basis of water stable isotopes, NEEM surface temperatures after the onset of the Eemian (126,000 years ago) peaked at 8 ± 4 degrees Celsius above the mean of the past millennium, followed by a gradual cooling that was probably driven by the decreasing summer insolation. Between 128,000 and 122,000 years ago, the thickness of the northwest Greenland ice sheet decreased by 400 ± 250 metres, reaching surface elevations 122,000 years ago of 130 ± 300 metres lower than the present. Extensive surface melt occurred at the NEEM site during the Eemian, a phenomenon witnessed when melt layers formed again at NEEM during the exceptional heat of July 2012. With additional warming, surface melt might become more common in the future.

A 2,540-m-long ice core was drilled during 2008–12 through the ice at the NEEM site, Greenland (77.45° N, 51.06° W, surface elevation 2,450 m, mean annual temperature -29°C , accumulation 0.22 m ice equivalent per year). The top 1,419 m is from the current interglacial, the Holocene, and together with the glacial ice below it can be matched to the NGRIP GICC05 extended timescale^{1,2} down to 2,206.7 m (108 thousand years before present, referred to as kyr BP, where 'present' is defined as AD 1950). Below this, the ice is disturbed and folded, but it contains zones with relatively high stable isotope values of H_2O ($\delta^{18}\text{O}_{\text{ice}}$, a proxy for condensation temperature), indicating that it stems from the last interglacial, the Eemian (130–115 kyr BP; Fig. 1). Near bedrock, low $\delta^{18}\text{O}_{\text{ice}}$ values suggest that the ice layers are most probably from the glacial period before the Eemian. The lowest 5 m of the ice core contain accreted ice, with dark layers 1–20 cm thick that contain high concentrations of basal material. In this study, information from the Eemian period of the NEEM ice core will be used to constrain the surface elevation of the ice sheet and the temperature of this warm climate period. Measurements of $\delta^{18}\text{O}_{\text{ice}}$ have been made, and air bubbles trapped within the ice have yielded concentrations of CH_4 and N_2O , stable isotope values $\delta^{15}\text{N}$ of N_2 and $\delta^{18}\text{O}$ of O_2 ($\delta^{18}\text{O}_{\text{atm}}$), and total air content (see details in Supplementary Information). In addition, the rheology of the ice, radio echo sounding (RES) images and surface temperatures and ice temperatures are used in the interpretation.

Reconstruction of the climate record

Stratigraphic disruptions are identified from discontinuities of $\delta^{18}\text{O}_{\text{ice}}$ at depths of 2,209.60 m, 2,262.15 m, 2,364.45 m and 2,432.19 m. Corresponding shifts in gas concentrations are found at these depths, so the bubble enclosure process has not caused the expected depth offset for stratigraphic undisturbed ice (Fig. 1). Possible discontinuities below 2,432.19 m have not been investigated. The records of CH_4 concentrations and $\delta^{18}\text{O}_{\text{atm}}$ are also disturbed and are not identical with the globally-homogeneous signals documented at the nearby NGRIP ice core (which contains undisturbed stratigraphy

back to 123 kyr BP) or with the EDML Antarctic ice core (which reaches back more than 135 kyr BP)^{3–6}. Measurements of N_2O , $\delta^{15}\text{N}$ and air content in the NEEM ice below 2,200 m further confirm these discontinuities.

NEEM data reveal spikes in CH_4 and N_2O records between depths of 2,370 m and 2,418 m, which are too rapid to be explained by climatic variability and coincide with lower air content in the ice (Figs 1b, 2, 4, shaded areas, and Supplementary Fig. 6). These characteristics point to surface melting or wet surface conditions. Indeed, surface melting or percolating rain reduces the firn air content and allows *in situ* production of CH_4 and N_2O . This hypothesis is supported by results in the near-surface ice from the warmer south Greenland Dye3 ice core (Supplementary Fig. 9, mean annual temperature -21°C) and by measurements of noble gases over the NEEM spikes, which also support the hypothesis of melting surface layers (Supplementary Fig. 8). The lack of parallel variability in $\delta^{18}\text{O}_{\text{ice}}$, $\delta^{15}\text{N}$ or $\delta^{18}\text{O}_{\text{atm}}$ suggests that these parameters are uninfluenced by surface melting. The spikes occur in the warmest interval at the depositional location indicated by water isotopes ($\delta^{18}\text{O}_{\text{ice}} > -33\text{‰}$). The mean water isotope value over the past millennium is -33.6‰ at NEEM, and very few melt layers are found in the ice core before 1995⁷. During our NEEM field campaigns (2007–12), the mean surface air temperature in July reached -5.4°C (with annual mean values of $\delta^{18}\text{O}_{\text{firn}} > -33\text{‰}$; ref. 8), and studies with ice cores and snow pits show that episodic melt events occurred. Over the period 12–15 July 2012, an exceptional heat wave produced significant surface melt over 97% of the Greenland ice sheet, leaving a strong fingerprint at the NEEM site in the form of melt layers 5–6 cm thick at 50–70 cm below the surface.

For depths of 2,201.10–2,432.19 m, the NEEM records of $\delta^{18}\text{O}_{\text{atm}}$ and the subset of CH_4 values not corrupted by surface melting are matched with globally-homogeneous signals of these values observed from other ice cores^{6,9,10} (Supplementary Figs 4 and 5). For younger ice, the nearby NGRIP $\delta^{18}\text{O}_{\text{ice}}$ record is used as a reference temperature target for synchronization by assuming simultaneous abrupt

*Lists of participants and their affiliations appear at the end of the paper.

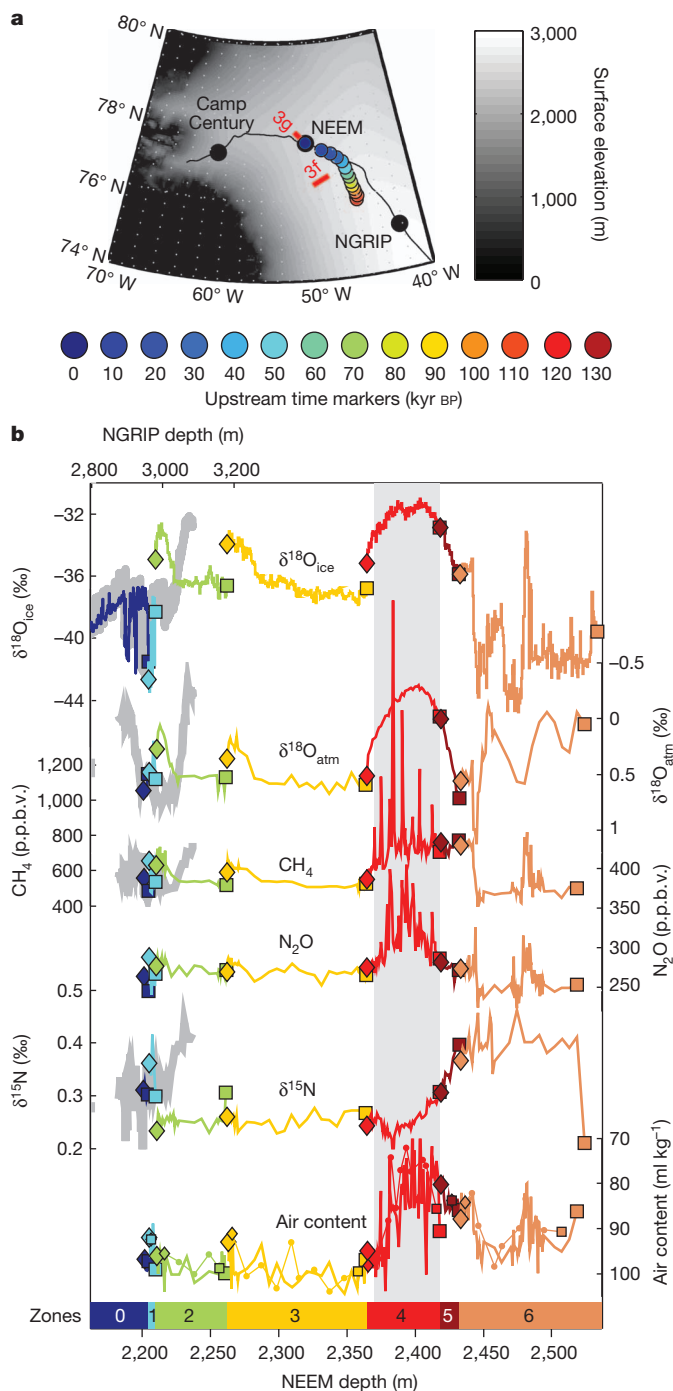


Figure 1 | Observed NEEM records. **a**, A surface elevation map (scale to the right) of the position of the NEEM camp, including coloured upstream depositional positions (upstream time marker scale below) of the ice found in the NEEM ice core. The deep ice-core sites NGRIP, NEEM and Camp Century and the tracks of the RES images shown in Fig. 3f and g (red lines) are shown on the map. **b**, The observed records of $\delta^{18}\text{O}_{\text{ice}}$, $\delta^{18}\text{O}_{\text{atm}}$ (reversed scale), CH_4 , N_2O , $\delta^{15}\text{N}$ and air content (reversed scale) from 2,162 m and deeper are plotted on the NEEM depth scale (bottom x axis). The air content measurements from LGGE and from University of Bern (thin curve, small symbols) are both included. Zones 0–6 (blue, 0–2,206.5 m; cyan, 2,206.5–2,209.6 m; green, 2,209.6–2,262.2 m; orange, 2,262.2–2,364.5 m; red, 2,364.5–2,418.0 m; dark red, 2,418.0–2,432.2 m; and brown, 2,432.2–2,537 m) represent the sections of the NEEM ice-core records with symbols marking the start (diamond) and end (square) of each zone. There is no discontinuity between zones 4 and 5 but spikes of CH_4 , N_2O and air content occur in zone 4 (shaded grey). For comparison, the NGRIP data are plotted as light grey curves on the NGRIP depth scale on top of the plot. The NEEM and NGRIP depth scale are synchronized between 2,162 and 2,207.6 m NEEM depths.

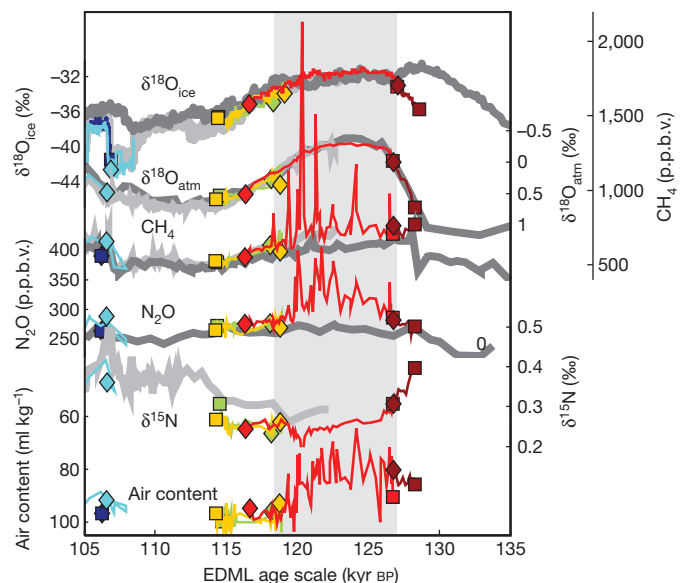


Figure 2 | Reconstructed records from the NEEM ice core. The reconstructed records of $\delta^{18}\text{O}_{\text{ice}}$, $\delta^{18}\text{O}_{\text{atm}}$ (reversed scale), CH_4 , N_2O , $\delta^{15}\text{N}$ and air content (reversed scale) on the EDML1 timescale¹². Zone 1 (cyan) is seen to contain a fold while zone 2 (green) and zone 3 (orange) are reversed and cover identical time periods. NGRIP records (light grey) and EDML records (dark grey) are included where they are available. The CH_4 , N_2O and air content records contain spikes from 127 to 118.3 kyr BP (shaded grey).

climate changes at the transitions between stadials and interstadials¹¹ (Supplementary Fig. 3).

In Fig. 2, the reconstructed NEEM records are shown on the EDML1 timescale¹² and compared to the NGRIP (light grey) and EDML (dark grey) records. Zones 1 to 5, identified in Fig. 1, map onto the timescale as coherent pieces. Zone 1 is folded such that the records are mirrored and repeated, zone 2 and zone 3 cover identical time periods, both inverted, while zone 4 (with melt-related spikes) and zone 5 are undisturbed and contain the major part of the ice from the Eemian (128.5–115 kyr BP) (Figs 2 and 3a, b). It cannot be ruled out that small disruptions or folds are present within the individual zones. The reconstructed records, however, show no unexpected discontinuities in either zones 1–5 or in all other measured parameters, such as $\delta^{15}\text{N}$ (Fig. 2), dust or electrical properties. As the timescale is transferred from the EDML ice core by matching it to the globally-homogeneous signals, small undetectable disruptions will not influence the conclusions based on the parameters presented here. The reconstruction is unambiguous and no other solution exists to match the NEEM $\delta^{18}\text{O}_{\text{atm}}$ and the uncorrupted CH_4 values simultaneously to the undisturbed EDML and NGRIP records. No ice from 114–108 kyr BP can be found in the NEEM ice core, while the ice layer from 118–115 kyr BP is found three times (zones 2, 3 and 4), two of which are inverted.

Northern Hemisphere temperatures are known to vary in parallel with the atmospheric CH_4 concentration^{13,14}, which is seen to increase abruptly into the warm Eemian period at 128 kyr BP at EDML. This is evidence that no substantial warm phases of the NEEM Eemian record are missing before 128.5 kyr BP. Ice from below 2,450 m (zone 6) appears to be too disturbed to reconstruct an age scale based on the data available at present. The very low (glacial) $\delta^{18}\text{O}_{\text{ice}}$ values (–44.9‰ at 2,476 m) are first found again in the record above 2,011 m. The ice layering at the NEEM site is undisturbed above 2,200 m (Fig. 3g), so the section below 2,476 m is believed to contain ice older than 128.5 kyr BP from Marine Isotopic Stage (MIS) 6, and we may speculate that the increased levels of $\delta^{18}\text{O}_{\text{ice}}$, CH_4 and N_2O at 2,480 m might be from MIS-7 interglacial.

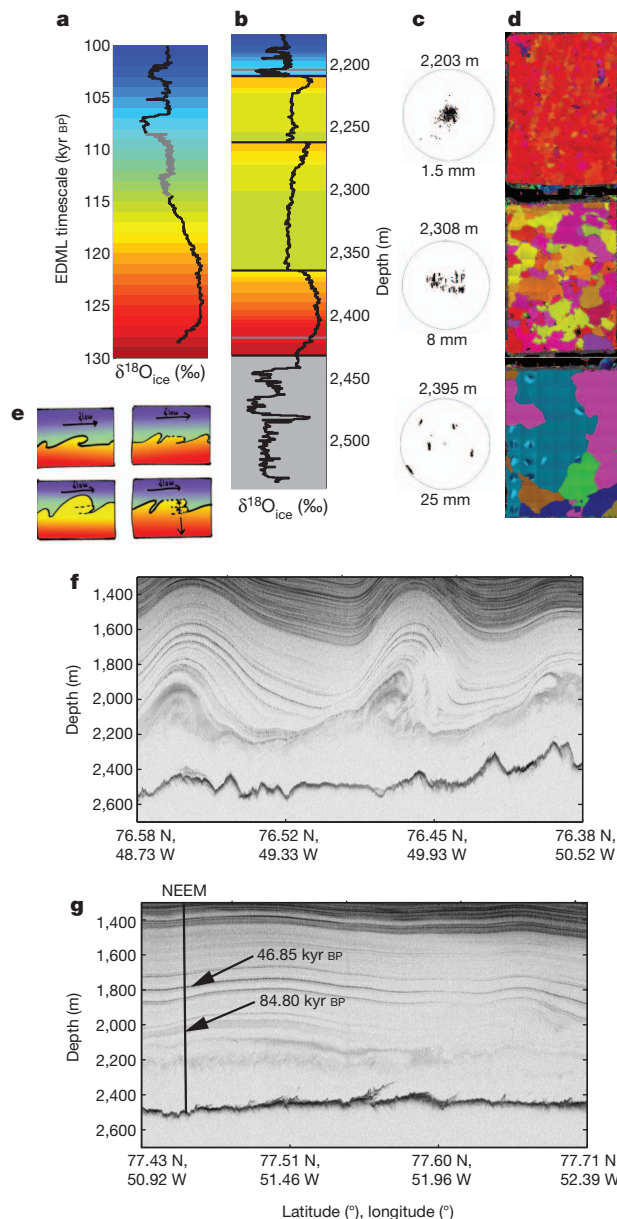


Figure 3 | Disturbances of the deep NEEM ice. **a**, The reconstructed NEEM water stable isotope record (black curve) including NGRIP data between 114–108 kyr BP (grey) on the EDML1 timescale that has been colour coded according to age. Below 2,432.19 m (grey shading) no dating has been attempted. **b**, The colour-coded data plotted with the original data on the NEEM depth scale visualizing the discontinuities and the reversed sections. **c**, **d**, *c*-Axis orientations on Schmidt diagrams for depths 2,203 m, 2,308 m and 2,395 m (**c**) and polarized light pictures of ice thin sections from the same three depths (**d**) demonstrate the very different ice rheology of the glacial and interglacial ice, leading to different flow properties. **e**, Cartoon of a possible history of the formation of two overturned folds at NEEM inspired by the observed undulations in the RES images (**f** and **g**). **f**, **g**, Center for Remote Sensing of Ice Sheets (CReSIS) ice-penetrating RES images from NASA Operation IceBridge campaign 2011. **f**, A 52-km-long line to the west that illustrates that overturning folds do occur (MCORDS: 20110329_02_020); **g**, a 48-km-long line crossing the deep drill site (MCORDS 20110329_02_028). The NEEM site is marked on the image, and two dated horizons are marked. More details can be found in Supplementary Information.

The disturbed and folded ice

RES data were collected in north Greenland during 2011 and 2012 with a multichannel coherent ice-penetrating radar depth sounder/imager^{15,16}. The RES images show continuous and undisturbed internal layers (isochrones) to a depth of about 2,200 m in the NEEM

region, which agrees with the ice-core observations¹⁷. Below 2,200 m, internal layers become fuzzy and less continuous: undulations and even overturned folds and shearing of basal material are observed (Fig. 3f, g, Supplementary Fig. 2b–e). The transition between clear and fuzzy layers often appears at the interface between ice from the glacial and Eemian periods. Very large differences in ice rheological properties are documented (Fig. 3c, d) between glacial ice (with crystal sizes of 1.5 mm and a strong preferred vertical *c*-axis orientation) and Eemian ice (with crystal sizes of 25 mm and multiple maxima fabrics). The viscosities of these two types of ice differ by a factor of 50–100 (refs 18–21), allowing glacial ice to deform very easily while the interglacial ice remains more rigid. The missing, folded and inverted parts of the ice are from the interface between the relatively rigid Eemian and the early glacial (118–106 kyr BP), supporting the idea that the glacial ice deforms over the harder Eemian ice. The broken record at 128.5 kyr BP can be explained by contrasting the deformation properties of the underlying ice from the previous glacial period and the Eemian ice. It should be noted that the discontinuous and folded structures of the GRIP and GISP2 ice cores also occur for ice older than 105 kyr (refs 9, 10). The consistency of the RES images and deep ice-core results at NEEM is a breakthrough result, and demonstrates that RES imaging can now be used to predict folded ice layering. This creates the potential for a systematic reconstruction of the Eemian Greenland ice-sheet layering from new RES imaging. Assimilation of such data in ice-sheet models may lead to much improved histories of the configuration of the ice sheet in the past, improving our ability to predict its future evolution.

Climate reconstruction from observed records

The reconstructed Eemian sequence (128.5–114 kyr BP, Fig. 2) allows for initial climate interpretations of this period. As mentioned above, the regular occurrence of melt features at 127–118.3 kyr BP is an indication of warmer temperatures at the depositional surface locations of the ice than the mean of the recent millennium at NEEM. This is independently confirmed by the decrease of $\delta^{15}\text{N}$ in this zone, which is indicative of $\sim 5^\circ\text{C}$ warmer mean annual firn temperatures at the depositional site^{22,23} (Supplementary Fig. 7). Between 128.5 kyr BP and 126.0 kyr BP, $\delta^{18}\text{O}_{\text{ice}}$ increases from -35‰ to -31.4‰ while EDML $\delta^{18}\text{O}_{\text{ice}}$ values slowly drop from those of the warm early Antarctic period²⁴. This bipolar see-saw behaviour suggests that inter-hemispheric heat redistribution by the Atlantic meridional overturning circulation²⁵ was taking place within the Eemian interglacial period; this has also been observed during the last Northern Hemisphere deglaciation 19–11 kyr BP^{24–27}. Before surface melt began between 128.5 and 126.7 kyr BP, the air content at the depositional site had a stable level of 85 ml kg^{-1} compared to the present level of 97.5 ml kg^{-1} . When corrected for changing local summer insolation^{28–30} (Supplementary Fig. 10), the air content difference suggests a surface elevation at the depositional site $540 \pm 300\text{ m}$ higher at the onset of the Eemian (128 kyr BP) than the surface elevation at NEEM today^{28,31–33}. The locations of the depositional sites of the Eemian ice found in the NEEM ice core are modelled using a nested three-dimensional flow model³⁴ (Fig. 1a and Supplementary Fig. 1). A second model used to date the NEEM ice core reaches similar locations³⁵ within 20 km. At present, the surface elevation at the depositional site of the 128-kyr-BP ice ($205 \pm 20\text{ km}$ upstream from NEEM) is $330 \pm 50\text{ m}$ higher than the present at NEEM^{33,34}. The surface elevation increase of $210 \pm 350\text{ m}$ at the 128-kyr-BP depositional site (Fig. 4c, blue) is the difference between the elevation at 128 kyr BP ($540 \pm 300\text{ m}$) and the present elevation ($330 \pm 50\text{ m}$), both related to the present elevation at NEEM. This surface elevation increase is expected at the onset of a warm climatic period due to increased precipitation and mass balance changes that occur before the central part of the ice sheet adjusts to the warmer climate by increasing the ice flow. This is also established at the onset of the present interglacial at 11.7 kyr BP³².

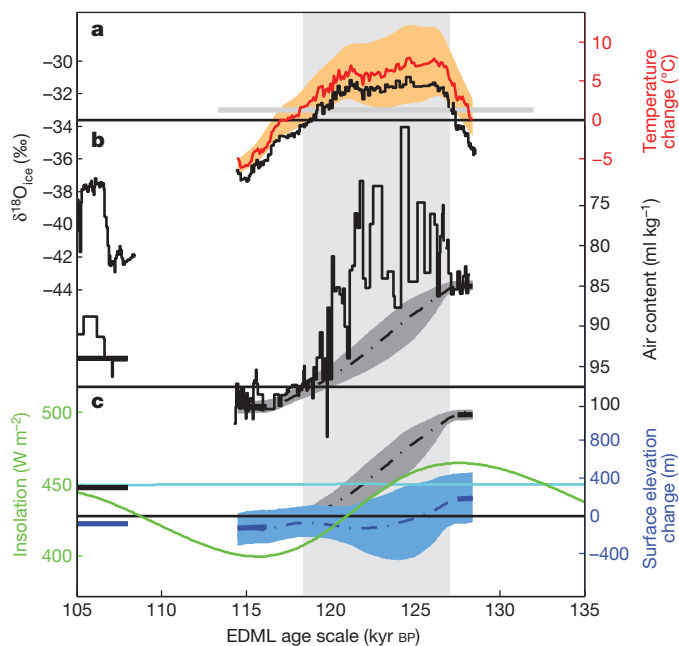


Figure 4 | Reconstruction of the temperature and elevation history.

Reconstruction of the temperature and elevation history through the Eemian based on the stable water isotopes ($\delta^{18}\text{O}_{\text{ice}}$) and the air content records. The zone with surface melt (127–118.3 kyr BP) is shaded in light grey. **a**, The measured $\delta^{18}\text{O}_{\text{ice}}$ record (black) on the constructed timescale. The average of the recent millennium (-33.6‰) is marked with a thin black line. It is seen that the $\delta^{18}\text{O}_{\text{ice}}$ values at the depositional locations in the melt zone are above -33.0‰ (grey horizontal line). The fixed-elevation change of temperature—constructed from the observed $\delta^{18}\text{O}_{\text{ice}}$, the elevation changes determined from the air content and the upstream corrections (curves below)—is shown as a red curve using the red axis. The standard error range (orange shading) is a sum of the error of the $\delta^{18}\text{O}_{\text{ice}}$ and the elevation change correction (Supplementary Information 1.1, equations (2) and (5) in Supplementary Information, Supplementary Table 2). **b**, Air content (black) is plotted and guided by the two stable levels on each side of the melt zone. A dot-dashed line connecting these levels has been suggested with an error range as the dark grey shaded area. The standard error range is a sum of the error assumed in the zone with surface melt (127–118.3 kyr BP) and the 1% error on the air content measurements (Supplementary Information section 1.4). In addition, the average level 107–105 kyr BP is marked with a horizontal black bar. The changes in the air content are caused by pressure changes due to changing surface elevation at the depositional sites and changes to the air trapping processes in the firm assumed to be controlled by the changing summer insolation^{28,32,49,50}. **c**, When corrected for upstream flow (cyan) and summer insolation changes (green), the air content curve can be ‘translated’ to elevation changes (blue, dashed) with the shaded zone indicating the uncertainty range introduced by this translation. Blue bars mark the air content of the ‘translated’ air content black bars. The standard error range is based on the error range of the air content (dark grey shaded area) and the additional standard errors from calculation of the elevation changes (equation (5) in Supplementary Information, and Supplementary Table 2).

In the period 127–118.3 kyr BP, the air content in the ice where surface melt occurred was highly variable and cannot directly be used for ice elevation reconstructions (Fig. 2, shaded zone). We can tentatively estimate elevation changes through the Eemian climate period by connecting the two air content levels before and after the melt zone (Fig. 4b) after correcting for summer insolation, which accounts for 50% of the observed change (Fig. 4c, Supplementary Information). At 126 kyr BP the surface elevation was 45 ± 350 m higher than at present. The $\delta^{18}\text{O}_{\text{ice}}$ increased to -31.4‰ at 126 kyr BP, exceeding the current mean value of the recent millennium of -33.6‰ (at the NEEM site) and the current mean value of -35.0‰ at the depositional site^{32,33} (Supplementary Information, section 2). Using the temperature–isotope relation of $2.1 \pm 0.5 \text{ K } \text{‰}^{-1}$ (calibrated using data from the present interglacial³²), the 3.6‰ anomaly at 126 kyr

BP implies that precipitation-weighted surface temperatures were $7.5 \pm 1.8 \text{ °C}$ warmer at the depositional site compared to the last millennium. Note that the modelled location of the depositional site is the only modelled parameter required to compare the 126-kyr-BP data to the present-day data at the depositional site. When further correcting for the more uncertain elevation change of 45 ± 350 m at the 126-kyr-BP depositional site using a lapse rate of $7.5 \pm 0.5 \text{ K km}^{-1}$, the fixed-elevation temperature increase here is $8 \pm 4 \text{ °C}$ (Fig. 4a, red). Our data depict a gradual cooling until 110 kyr BP (Fig. 4a, red curve).

The reconstructed precipitation-weighted annual temperature changes are remarkably high. In general, warmer summer temperatures are reported from palaeorecords^{36,37}, and a few find temperatures at 126 kyr BP on high Arctic latitudes as high as those reported from NEEM^{38–40}. Climate models equipped with water stable isotopes point to a limited (1 °C) seasonality bias caused by a stronger enhancement of temperature and precipitation in summer than in winter^{41–43}. A large spread in temperature has been reported among simulations of the last interglacial climate, which appear to systematically underestimate North Atlantic/Arctic warming, possibly due to missing vegetation and ice-sheet feedback^{37,42,43}.

Within 6,000 yr, from 128 to 122 kyr BP, the surface elevation is estimated to have decreased from 210 ± 350 m above to 130 ± 300 m below the present surface elevation, which translates to a moderate ice thickness change of 400 ± 350 m after accounting for isostatic rebound. Based on this estimate, the ice thickness at NEEM decreased by an average of 7 ± 4 cm per year between 128 and 122 kyr BP and stayed at this level until 117–114 kyr BP, long after surface melt stopped and temperatures fell below modern levels.

Even with minimum ice thickness of only about 10% less than the present ice thickness at the NEEM site, as reported here, substantial melting can cause significant reduction of ice thickness near the margins; this in turn reduces the volume of the Greenland ice sheet. Although the documentation of ice thickness at one location on the Greenland ice sheet cannot constrain the overall ice-sheet changes during the last interglacial period, the NEEM data can only be reconciled with Greenland ice-sheet simulations³⁰ that point to a modest contribution (2 m) to the observed 4–8 m Eemian sea level high stand^{44,45}. For comparison, no continuing elevation change has so far been detected in areas with elevations above 2,000 m in north Greenland during the past few decades⁴⁶. These findings strongly imply that Antarctica must have contributed significantly to the Eemian sea level rise⁴⁷.

Despite the complex ice flow, the disturbed record of the deep ice in the NEEM ice core can be unambiguously reconstructed. The anatomy of the last interglacial shows that Greenland temperatures peaked after the onset of the Eemian, 126 kyr BP, with temperatures (at fixed elevations) $8 \pm 4 \text{ °C}$ warmer than the average of the recent millennium and multiple indications of summer melt. Temperatures gradually decreased during the interglacial, very probably owing to the strong local summer insolation decreasing trend. The surface elevation first increased due to increased mass balance to 210 ± 350 m above the present at 128 kyr BP, then decreased to 130 ± 300 m below the present elevation around 122 kyr BP. Our results provide multiple new targets to constrain coupled climate/ice-sheet models. Our record, together with recent observations of rainfall and strong surface melting in July 2012 at NEEM, show that conditions are conducive to the start of melt layer formation at NEEM, with the 2010–12 mean annual surface temperatures $1\text{--}2 \text{ °C}$ above the 1950–80 average.

Our results have implications for both ice deformation near the bedrock and the response of the Greenland ice sheet to climate change. The combination of high-resolution RES data and NEEM glacial–interglacial ice layers brings new knowledge of the near-bed deformation of ice. We believe that the folding and disturbances we observe near the bed are strongly related to the rigid deformation properties of the interglacial ice. This offers an alternative explanation

for the large anomalies in RES profiles recently observed under both the Antarctic and Greenland ice sheets, which were previously attributed to refrozen basal water⁴⁸.

METHODS SUMMARY

Measurements of stable water isotopes in the ice ($\delta^{18}\text{O}_{\text{ice}}$) and CH_4 , N_2O concentrations and the isotopes $\delta^{15}\text{N}$ of N_2 and $\delta^{18}\text{O}_{\text{atm}}$ of O_2 , noble gases and the air content have been measured in the air extracted from the air bubbles in the ice, all using well-described methods. These measurements are presented in Supplementary Information section 1. Models calculating temperatures from water isotopes, elevation changes from air content, and temperature changes from $\delta^{15}\text{N}$ values have been calibrated using observations from the present interglacial.

Received 31 July; accepted 13 November 2012.

- Wolff, E. W., Chappellaz, J., Blunier, T., Rasmussen, S. O. & Svensson, A. Millennial-scale variability during the last glacial: the ice core record. *Quat. Sci. Rev.* **29**, 2828–2838 (2010).
- Svensson, A. *et al.* A 60 000 year Greenland stratigraphic ice core chronology. *Clim. Past* **4**, 47–57 (2008).
- Andersen, K. K. *et al.* High-resolution record of Northern Hemisphere climate extending into the last interglacial period. *Nature* **431**, 147–151 (2004).
- Barbante, C. *et al.* One-to-one coupling of glacial climate variability in Greenland and Antarctica. *Nature* **444**, 195–198 (2006).
- Schilt, A. *et al.* Glacial–interglacial and millennial-scale variations in the atmospheric nitrous oxide concentration during the last 800,000 years. *Quat. Sci. Rev.* **29**, 182–192 (2010).
- Capron, E. *et al.* Synchronising EDML and NorthGRIP ice cores using $\delta^{18}\text{O}$ of atmospheric oxygen ($\delta^{18}\text{O}_{\text{atm}}$) and CH_4 measurements over MIS5 (80–123 kyr). *Quat. Sci. Rev.* **29**, 222–234 (2010).
- Steen-Larsen, H. C. *et al.* Understanding the climatic signal in the water stable isotope records from the NEM shallow firn/ice cores in northwest Greenland. *J. Geophys. Res.* **116**, D06108, doi:10.1029/2010JD014311 (2011).
- Buchardt, S. L., Clausen, H. B., Vinther, B. M. & Dahl-Jensen, D. Investigating the past and recent $\delta^{18}\text{O}$ -accumulation relationship seen in Greenland ice cores. *Clim. Past* **8**, 2053–2059 (2012).
- Landais, A. *et al.* A tentative reconstruction of the last interglacial and glacial inception in Greenland based on new gas measurements in the Greenland Ice Core Project (GRIP) ice core. *J. Geophys. Res.* **108**, 4563, doi:10.1029/2002jd003147 (2003).
- Suwa, M., von Fischer, J. C., Bender, M. L., Landais, A. & Brook, E. J. Chronology reconstruction for the disturbed bottom section of the GISP2 and the GRIP ice cores: implications for Termination II in Greenland. *J. Geophys. Res.* **111**, D02101, doi:10.1029/2005JD006032 (2006).
- Johnsen, S. J. *et al.* Oxygen isotope and palaeotemperature records from six Greenland ice-core stations: Camp Century, Dye-3, GRIP, GISP2, Renland and NorthGRIP. *J. Quat. Sci.* **16**, 299–307 (2001).
- Ruth, U. *et al.* “EDML1”: a chronology for the EPICA deep ice core from Dronning Maud Land, Antarctica, over the last 150 000 years. *Clim. Past* **3**, 475–484 (2007).
- Caillon, N., Jouzel, J., Severinghaus, J. P., Chappellaz, J. & Blunier, T. A novel method to study the phase relationship between Antarctic and Greenland climate. *Geophys. Res. Lett.* **30**, 1899, doi:10.1029/2003GL017838 (2003).
- Chappellaz, J. *et al.* Synchronous changes in atmospheric CH_4 and Greenland climate between 40 and 8 kyr BP. *Nature* **366**, 443–445 (1993).
- Rodriguez-Morales, F. *et al.* Advanced multi-frequency radar instrumentation for polar research. *IEEE Trans. Geosci. Rem. Sens.* (in the press).
- Leuschen, C. *et al.* The CReSIS radar suite for measurements of the ice sheets and sea ice during Operation Ice Bridge. *Am. Geophys. Un. Fall Meet.*, abstr. C44A-02 (2010).
- Buchardt, S. L. & Dahl-Jensen, D. At what depth is the Eemian layer expected to be found at NEM? *Ann. Glaciol.* **48**, 100–102 (2008).
- Dahl-Jensen, D. & Gundestrup, N. in *The Physical Basis of Ice Sheet Modelling* (ed. Waddington, E.) 31–43 (Proc. Vancouver Symp., August 1987, IAHS Publ. No. 170, 1987).
- Dahl-Jensen, D. & Gundestrup, N. S. Derivation of flow-law properties from borehole tilt data: discussion of the Dye 3, Camp Century, and Byrd Station bore-hole results. *Ann. Glaciol.* **12**, 200–201 (1989).
- Azuma, N. & Higashi, A. Mechanical properties of Dye 3 Greenland deep ice cores. *Ann. Glaciol.* **5**, 1–8 (1984).
- Jacka, T. H. Laboratory studies on relationships between ice crystal size and flow rate. *Cold Reg. Sci. Technol.* **10**, 31–42 (1984).
- Goujon, C., Barnola, J.-M. & Ritz, C. Modeling the densification of polar firn including heat diffusion: application to close-off characteristics and gas isotopic fractionation for Antarctica and Greenland sites. *J. Geophys. Res.* **108**, 4792, doi:10.1029/2002JD003319 (2003).
- Severinghaus, J. P., Grachev, A. & Battle, M. Thermal fractionation of air in polar firn by seasonal temperature gradients. *Geochem. Geophys. Geosyst.* **2**, 1048, doi:10.1029/2000GC000146 (2001).
- Masson-Delmotte, V. *et al.* Abrupt change of Antarctic moisture origin at the end of Termination II. *Proc. Natl Acad. Sci. USA* **107**, 12091–12094 (2010).
- Stocker, T. F. & Johnsen, S. J. A minimum thermodynamic model for the bipolar seesaw. *Paleoceanography* **18**, 1087, doi:10.1029/2003PA000920 (2003).
- Pedro, J. B. *et al.* The last deglaciation: timing the bipolar seesaw. *Clim. Past* **7**, 671–683 (2011).
- Stenni, B. *et al.* Expression of the bipolar see-saw in Antarctic climate records during the last deglaciation. *Nature Geosci.* **4**, 46–49 (2011).
- Raynaud, D. *et al.* The local insolation signature of air content in Antarctic ice. A new step toward an absolute dating of ice records. *Earth Planet. Sci. Lett.* **261**, 337–349 (2007).
- Berger, A., Loutre, M. F. & Laskar, J. Stability of the astronomical frequencies over the Earth's history for paleoclimate studies. *Science* **255**, 560–566 (1992).
- van de Berg, W. J., van den Broeke, M., Ettema, J., van Meijgaard, E. & Kaspar, F. Significant contribution of insolation to Eemian melting of the Greenland ice sheet. *Nature Geosci.* **4**, 679–683 (2011).
- Raynaud, D., Chappellaz, J., Ritz, C. & Martinier, P. Air content along the Greenland Ice Core Project core: a record of surface climatic parameters and elevation in central Greenland. *J. Geophys. Res.* **102**, 26607–26613 (1997).
- Vinther, B. M. *et al.* Holocene thinning of the Greenland ice sheet. *Nature* **461**, 385–388 (2009).
- Bamber, J. L., Layberry, R. L. & Gogineni, S. A new ice thickness and bed data set for the Greenland ice sheet 1. Measurement, data reduction, and errors. *J. Geophys. Res.* **106**, 33773–33780 (2001).
- Huybrechts, P., Rybak, O., Pattyn, F., Ruth, U. & Steinhage, D. Ice thinning, upstream advection, and non-climatic biases for the upper 89% of the EDML ice core from a nested model of the Antarctic ice sheet. *Clim. Past* **3**, 577–589 (2007).
- Buchardt, S. L. *Basal Melting and Eemian Ice Along the Main Ice Ridge in Northern Greenland*. Thesis, Univ. Copenhagen (2009); available at http://www.iceandclimate.nbi.ku.dk/publications/theses/PhD_Buchardt.pdf/.
- Otto-Bliesner, B. L. *et al.* Simulating arctic climate warmth and icefield retreat in the last interglaciation. *Science* **311**, 1751–1753 (2006).
- Lunt, D. J. *et al.* A multi-model assessment of last interglacial temperatures. *Clim. Past Discuss.* **8**, 3657–3691 (2012).
- Axford, Y. *et al.* Chironomids record terrestrial temperature changes throughout Arctic interglacials of the past 200,000 yr. *Geol. Soc. Am. Bull.* **123**, 1275–1287 (2011).
- Francis, D. R., Wolfe, A. P., Walker, I. R. & Miller, G. F. Interglacial and Holocene temperature reconstructions based on midge remains in sediments of two lakes from Baffin Island, Nunavut, Arctic Canada. *Palaeogeogr. Palaeoclimatol. Palaeoecol.* **236**, 107–124 (2006).
- Turney, C. S. M. & Jones, R. T. Does the Agulhas Current amplify global temperatures during super-interglacials? *J. Quat. Sci.* **25**, 839–843 (2010).
- Born, A. & Nisancioglu, K. H. Melting of Northern Greenland during the last interglacial. *Cryosphere Discuss.* **5**, 3517–3539 (2011).
- Masson-Delmotte, V. *et al.* Sensitivity of interglacial Greenland temperature and $\delta^{18}\text{O}$: ice core data, orbital and increased CO_2 climate simulations. *Clim. Past* **7**, 1041–1059 (2011).
- Masson-Delmotte, V. *et al.* EPICA Dome C record of glacial and interglacial intensities. *Quat. Sci. Rev.* **29**, 113–128 (2010).
- Kopp, R. E., Simons, F. J., Mitrovica, J. X., Maloof, A. C. & Oppenheimer, M. Probabilistic assessment of sea level during the last interglacial stage. *Nature* **462**, 863–867 (2009).
- Dutton, A. & Lambeck, K. Ice volume and sea level during the last interglacial. *Science* **337**, 216–219 (2012).
- Dahl-Jensen, D. *et al.* in *Snow, Water, Ice and Permafrost in the Arctic (SWIPA): Climate Change and the Cryosphere* (ed. AMAP) Ch. 8 (Arctic Monitoring and Assessment Programme (AMAP), Oslo, 2011).
- Bradley, S. L., Siddall, M., Milne, G. A., Masson-Delmotte, V. & Wolff, E. Where might we find evidence of a Last Interglacial West Antarctic Ice Sheet collapse in Antarctic ice core records? *Glob. Planet. Change* **88–89**, 64–75 (2012).
- Bell, R. E. *et al.* Widespread persistent thickening of the East Antarctic Ice Sheet by freezing from the base. *Science* **331**, 1592–1595 (2011).
- Raynaud, D. & Lebel, B. Total gas content and surface elevation of polar ice sheets. *Nature* **281**, 289–291 (1979).
- Martinier, P. *et al.* Air content paleo record in the Vostok ice core (Antarctica): a mixed record of climatic and glaciological parameters. *J. Geophys. Res.* **99**, 10565–10576 (1994).

Supplementary Information is available in the online version of the paper.

Acknowledgements We thank the many persons involved in logistics, drill developments and drilling, and ice-core processing and analysis in the field and in our laboratories. NEM is directed and organized by the Centre of Ice and Climate at the Niels Bohr Institute and US NSF, Office of Polar Programs. It is supported by funding agencies and institutions in Belgium (FNRS-CFB and FWO), Canada (NRC/GSC), China (CAS), Denmark (FIST), France (IPEV, CNRS/INSU, CEA and ANR), Germany (AWI), Iceland (Rannls), Japan (NIPR), South Korea (KOPRI), The Netherlands (NWO/ALW), Sweden (VR), Switzerland (SNF), the United Kingdom (NERC) and the USA (US NSF, Office of Polar Programs) and the EU Seventh Framework programmes Past4Future and Waterunderthelce. NASA is acknowledged for the OIB 2011 programme.

Author Contributions All authors contributed to the discussions that led to the results presented in the paper. M.R.A., A.-M.B., C.B., K. Keegan, P.M., S.B.S. and E.W. performed analysis and interpretation of the firm processes; A.A., D.B.-C., M. Baumgartner, M. Bigler, T. Blunier, E.J.B., E.C., J. Chappellaz, J. Chung, O.E., H.F., L.G.F., G.G., V.G., K.G.-A., M.H., Y.I., T.J., T.R.J., J.J., K. Kawamura, E.K., H.A.K., T.K., A.L., D.L., V.L., O.J.M., V.M.-D.,

J.R.M., O.M., R. Muscheler, J.-R.P., K.P., G.P., T.P., M.P., D.R., C.R., T.R., J.L.R., M.R., C.J.S., A.S., J.S., S. Schüpbach, J. P. Severinghaus, T.S., P.S., T.F.S., C.S., W.T.S., A.S.S., A. Sveinbjörnsdóttir, A. Svensson, J.U., P.V., G.v.d.W., B.H.V., B.V., A.W. and F.W. were involved in the data measurements described in detail in Supplementary Information; N.A., T. Binder, S.K., A.M., M.M.-R., D.S., E.W. and I.W. contributed to the understanding of ice rheology; J.C.B. and A.M.Z.S. investigated the biology of the ice cores; S.L.B., P.H., M.K., F.P., A.Q., C.R., O.R., A.M.S. and R.S.W.v.d.W. produced ice-sheet models; H.B.C., S.M.D., D.A.F., A.G., H.G., M.G., S.J.J., P.K., A.L., T.L., M.L., S.O.R., I.S., J. P. Steffensen and M.W. participated in the dating of the NEEM ice core; I.C., P.D., P.L.L. and J.S. produced atmosphere models; D.D.-J. analysed the data; J.W.C.W. and E.W.W. put the discussion into the text; S.G., N.B.K., C.L., J.L., J.P., C. P. and D.S. participated in obtaining and interpreting the RES images; S.B.H. and S.S. were the chief mechanic and electronic engineer on the deep ice-core drill; M.G., S.H., S.D.H., H.M., R. Mulvaney, J.R. and C.X. participated in the planning of the NEEM project; L.B.L. and C.S.H. used a GPS net to determine the surface velocities; E.C., A.L., A.J.O., F.P., H.C.S.-L., K.S. and J.Z. participated in measuring temperatures and isotopes in the firn and air; J.-L.T. was involved in the interpretation of the basal ice.

Author Information Reprints and permissions information is available at www.nature.com/reprints. The authors declare no competing financial interests. Readers are welcome to comment on the online version of the paper. Correspondence and requests for materials should be addressed to D.D.-J. (ddj@gfy.ku.dk).

NEEM community members

D. Dahl-Jensen¹, M. R. Albert², A. Aldahan^{3†}, N. Azuma⁴, D. Balslev-Clausen¹, M. Baumgartner⁵, A.-M. Berggren⁶, M. Bigler⁷, T. Binder⁸, T. Blunier¹, J. C. Bourgeois⁷, E. J. Brook⁸, S. L. Buchardt¹, C. Buizert^{1,8}, E. Capron^{9,10}, J. Chappellaz¹¹, J. Chung¹², H. B. Clausen¹, I. Cvijanovic¹, S. M. Davies¹³, P. Ditlevsen¹, O. Eicher⁵, H. Fischer⁵, D. A. Fisher⁷, L. G. Fleet¹⁰, G. Gfeller⁵, V. Gkinis¹⁴, S. Gogineni¹⁵, K. Goto-Azuma¹⁶, A. Grinsted¹, H. Gudlaugsdóttir¹⁷, M. Guillemin¹⁸, S. B. Hansen¹, M. Hansson¹⁸, M. Hirabayashi¹⁹, S. Hong¹⁹, S. D. Hur¹², P. Huybrechts²⁰, C. S. Hvidberg¹, Y. Iizuka^{18,26}, T. Jenk^{1†}, S. J. Johnsen¹, T. R. Jones¹⁴, J. Jouzel⁹, N. B. Karlsson¹, K. Kawamura¹⁶, K. Keegan², E. Kettner¹, S. Kipfstuhl²², H. A. Kjær¹, M. Koutnik²³, T. Kuramoto^{16,21}, P. Köhler²², T. Laepple²², A. Landais⁹, P. L. Langen¹, L. B. Larsen¹, D. Leuenberger⁵, M. Leuenberger⁵, C. Leuschen¹⁵, J. Li¹⁵, V. Lipenkov²⁴, P. Martinerie¹¹, O. J. Maselli²⁵, V. Masson-Delmotte⁹, J. R. McConnell²⁵, H. Miller²², O. Mini⁵, A. Miyamoto²⁶, M. Montagnat-Rentier¹, R. Mulvaney¹⁰, R. Muscheler²⁷, A. J. Orsi²⁸, J. Paden¹⁵, C. Pantoni¹, F. Pattyn²⁹, J.-R. Petit¹¹, K. Pol^{9,10}, T. Popp¹, G. Possnert³⁰, F. Prié⁹, M. Prokopiou³¹, A. Quiquet¹¹, S. O. Rasmussen¹, D. Raynaud¹¹, J. Ren³², C. Reutenauer¹, C. Ritz¹¹, T. Röckmann³¹, J. L. Rosen⁸, M. Rubino^{1,33}, O. Rybak²⁰, D. Samyn³⁴, C. J. Sapart³¹, A. Schilt^{5,8}, A. M. Z. Schmidt¹, J. Schwander⁵, S. Schüpbach⁵, I. Seierstad¹, J. P. Severinghaus²⁸, S. Sheldon¹, S. B. Simonsen¹, J. Sjolte^{1,27}, A. M. Solgaard¹, T. Sowers³⁴, P. Sperlich^{1†}, H. C. Steen-Larsen¹⁹, K. Steffen^{35†}, J. P. Steffensen¹, D. Steinhage²², T. F. Stocker⁵, C. Stowasser¹, A. S. Sturevik³, W. T. Sturges³⁶, A. Sveinbjörnsdóttir¹⁷, A. Svensson¹, J.-L. Tison²⁹, J. Uetake¹⁶, P. Vallelonga¹, R. S. W. van de Wal³¹, G. van der Wel⁵, B. H. Vaughn¹⁴, B. Vinther¹, E. Waddington²³, A. Wegner²², I. Weikusat²², J. W. C. White¹⁴, F. Wilhelms²², M. Winstrup¹, E. Witrant³⁷, E. W. Wolff¹⁰, C. Xiao^{32,38} & J. Zheng⁷

¹Centre for Ice and Climate, Niels Bohr Institute, University of Copenhagen, Juliane Maries Vej 30, 2100 Copenhagen K, Denmark. ²Thayer School of Engineering, Dartmouth University, Hanover, New Hampshire 03755, USA. ³Department of Earth Sciences, Uppsala University, Villavägen 16, 752 36 Uppsala, Sweden. ⁴Department of Mechanical

Engineering, Nagaoka University of Technology, 1603-1 Kamitomioka-machi, Nagaoka 940-2188, Japan. ⁵Climate and Environmental Physics, Physics Institute and Oeschger Centre for Climate Change Research, University of Bern, Sidlerstrasse 5, 3012 Bern, Switzerland. ⁶IWR, University of Heidelberg, Speyerer Straße 6, D-69115 Heidelberg, Germany. ⁷Natural Resources Canada, Geological Survey of Canada, 601 Booth Street, Ottawa K1A 0E8, Canada. ⁸College of Earth, Ocean, and Atmospheric Sciences, Oregon State University, 104 CEOAS Administration Building, Corvallis, Oregon 97331-5503, USA. ⁹Laboratoire des Sciences du Climat et de l'Environnement, CEA-CNRS-UVSQ, IPSL, Bâtiment 701 L'Orme des Merisiers, CEA Saclay, 91 191 Gif sur Yvette, France. ¹⁰British Antarctic Survey, Madingley Road, Cambridge CB3 0ET, UK. ¹¹LGGE, UJF-Grenoble 1, CNRS, 64 rue Molière, BP 96, 38402 St Martin d'Hères, France. ¹²Korea Polar Research Institute, Songdo Techno Park, 7-50, Songdo-dong, Yeonsu-gu, Incheon 406-840, South Korea. ¹³Department of Geography, College of Science, Swansea University, Singleton Park, Swansea SA2 8PP, UK. ¹⁴INSTAAR, University of Colorado, Boulder, Colorado 80309, USA. ¹⁵CRISIS, University of Kansas, Nichols Hall, 2335 Irving Hill Road, Lawrence, Kansas 66045, USA. ¹⁶National Institute of Polar Research, 10-3 Midori-cho, Tachikawa, Tokyo 190-8518, Japan. ¹⁷Institute of Earth and Sciences, University of Iceland, Sturlugata 7, IS-107, Reykjavik, Iceland. ¹⁸Department of Physical Geography and Quaternary Geology, Stockholm University, S-106 91 Stockholm, Sweden. ¹⁹Department of Ocean Sciences, Inha University, 100 Inha-ro, Nam-gu, Incheon 402-751, South Korea. ²⁰Earth System Sciences and Department of Geography, Vrije Universiteit Brussel, Pleinlaan 2, B-1050 Brussels, Belgium. ²¹Institute of Mountain Science, Shinshu University, 3-1-1, Asahi, Matsumoto City 390-8621, Japan. ²²Alfred Wegener Institute for Polar and Marine Research, PO Box 12 01 61, D-27515 Bremerhaven, Germany. ²³Department of Earth and Space Sciences, University of Washington, Seattle, Washington 98195-1310, USA. ²⁴Arctic and Antarctic Research Institute, St Petersburg 199397, Russia. ²⁵Desert Research Institute, Nevada System of Higher Education, Reno, Nevada 89512, USA. ²⁶Institute of Low Temperature Science, Hokkaido University, Sapporo 060-0819, Japan. ²⁷Department of Geology, Lund University, Sölvegatan 12, SE-22362 Lund, Sweden. ²⁸Scripps Institution of Oceanography, UC San Diego, La Jolla, California 92093, USA. ²⁹Laboratoire de Glaciologie, Université Libre de Bruxelles, CP160/03, Avenue F.D. Roosevelt 50, B-1050 Brussels, Belgium. ³⁰Tandem Laboratory, Uppsala University, Lagerhyddsvägen 1, 751 20 Uppsala, Sweden. ³¹Institute for Marine and Atmospheric Research Utrecht (IMAU), Utrecht University, Princetonplein 5, 3584 CC Utrecht, The Netherlands. ³²State Key Laboratory of Cryospheric Sciences, Cold and Arid Regions Environmental and Engineering Research Institute, Chinese Academy of Sciences, Lanzhou 730000, China. ³³Centre for Australian Weather and Climate Research, CSIRO Marine and Atmospheric Research, Aspendale, 3195 Victoria, Australia. ³⁴Earth and Environment Systems Institute, Penn State University, 2217 EES Building, University Park, Pennsylvania 16802, USA. ³⁵CIRES, University of Colorado, 216 UCB Boulder, Colorado 80309-0216, USA. ³⁶University of East Anglia, Norwich, Norfolk NR4 7TJ, UK. ³⁷UJF – Grenoble 1/CNRS, Grenoble Image Parole Signal Automatique (GIPSA-lab), UMR 5216, BP 46, 38402 St Martin d'Hères, France. ³⁸China Institute of Climate System, Chinese Academy of Meteorological Sciences, Beijing 100081, China.

†Present addresses: Department of Geology, United Arab Emirates University, Al Ain, United Arab Emirates (A.A.); Paul Scherrer Institute, OFLB/109, 5232 Villigen – PSI, Switzerland (T.J.); Max-Planck-Institute for Biogeochemistry, Hans-Knöll-Strasse 10, 07745 Jena, Germany (P.S.); Swiss Federal Research Institute WSL, Zuercherstrasse 111, CH-8903 Birmensdorf, Switzerland; Institute for Atmosphere and Climate Science (IAC), Swiss Federal Institute of Technology (ETH), Universitaetstrasse 16, CH-8092 Zurich, Switzerland; School of Architecture, Civil and Environmental Engineering (ENAC), Ecole polytechnique fédérale de Lausanne (EPFL), Station 2, CH-1015 Lausanne, Switzerland (K.S.).

LTP requires a reserve pool of glutamate receptors independent of subunit type

Adam J. Granger¹, Yun Shi², Wei Lu^{2†}, Manuel Cerpas² & Roger A. Nicoll²

Long-term potentiation (LTP) of synaptic transmission is thought to be an important cellular mechanism underlying memory formation. A widely accepted model posits that LTP requires the cytoplasmic carboxyl tail (C-tail) of the AMPA (α -amino-3-hydroxy-5-methyl-4-isoxazole propionic acid) receptor subunit GluA1. To find the minimum necessary requirement of the GluA1 C-tail for LTP in mouse CA1 hippocampal pyramidal neurons, we used a single-cell molecular replacement strategy to replace all endogenous AMPA receptors with transfected subunits. In contrast to the prevailing model, we found no requirement of the GluA1 C-tail for LTP. In fact, replacement with the GluA2 subunit showed normal LTP, as did an artificially expressed kainate receptor not normally found at these synapses. The only conditions under which LTP was impaired were those with markedly decreased AMPA receptor surface expression, indicating a requirement for a reserve pool of receptors. These results demonstrate the synapse's remarkable flexibility to potentiate with a variety of glutamate receptor subtypes, requiring a fundamental change in our thinking with regard to the core molecular events underlying synaptic plasticity.

Information storage in the brain is widely accepted to involve the rapid increase in synaptic strength between two neurons that can persist over long periods of time. This phenomenon, known as long-term potentiation (LTP), has been well described at glutamatergic synapses in the hippocampus, a region of the brain that is required for the formation of new memories. At these CA1 synapses, LTP is expressed by the immediate increase in postsynaptic AMPA-type glutamate receptors (AMPA receptors) after coincident activation of pre- and postsynaptic neurons. However, the exact mechanism of rapid AMPAR insertion during LTP is not fully understood.

AMPA receptors mediate most fast, excitatory synaptic transmission in the brain. A functional AMPAR is a tetramer of individual subunit proteins, of which there are four unique isoforms, GluA1, GluA2, GluA3 and GluA4 (refs 1, 2). In CA1 pyramidal neurons, which serve as a model for understanding LTP, most receptors exist as GluA1–GluA2 heteromers, with a minor contribution from GluA2–GluA3 receptors^{3,4}. Over the past decade, a large body of research has focused on how individual AMPAR subunits are trafficked. A widely held model posits that GluA1–GluA2 receptors are excluded from synapses unless an LTP stimulus is provided, whereas GluA2–GluA3 receptors traffic to the synapse constitutively. This difference in trafficking behaviour is mediated by the C-tails of the individual subunit proteins^{5–7}. Supporting this model is the finding that LTP is impaired in GluA1 knockout mice⁸ but is normal in GluA2–GluA3 double knockouts⁹. On the basis of these findings, a broad consensus has emerged that LTP is mediated by synaptic insertion of GluA1-containing receptors via its C-tail interactions^{10–17}.

Despite the consensus that GluA1 is required for LTP, no single phosphorylation site or protein–protein interaction in the GluA1 C-tail has been shown to be absolutely necessary. Our goal was to find the minimum requirement of the GluA1 C-tail for LTP, and, if found, use that region to identify crucial protein interactions that mediate synaptic AMPAR potentiation. To accomplish this, we used a single-cell molecular replacement strategy to replace all endogenous AMPARs with transfected subunits^{18,19}. Using this approach, we

systematically mutated the GluA1 C-tail and examined the effects on three stages of AMPAR trafficking in mice: surface expression, synaptic transmission and LTP. Surprisingly, we failed to identify any region in the GluA1 C-tail that was essential either for basal synaptic incorporation or for LTP. In fact, homomeric GluA2 receptors exhibited normal LTP. Most surprisingly, hippocampal synapses in which AMPARs had been replaced with kainate-type glutamate receptors (KARs) also expressed normal LTP. Only manipulations that severely compromised the extrasynaptic surface pool of receptors showed defects in potentiation.

The role of the GluA1 C-tail in surface expression

AMPA trafficking can be broken down into three distinct steps: surface expression, basal synaptic targeting, and activity-dependent synaptic insertion. Because GluA1 is normally abundantly expressed on the neuronal surface^{3,20}, we first screened for surface expression of various GluA1 C-tail truncations in wild-type neurons using somatic outside-out patches in organotypic slice culture. Because overexpressed receptors form inwardly rectifying homomers⁷, whereas endogenous heteromeric receptors show linear current–voltage (*I*–*V*) relationships²¹, we can detect surface expression of the expressed subunits as an increase in surface rectification (Fig. 1a). Overexpression of full-length GluA1 by biolistic transfection into CA1 pyramidal neurons increased the rectification by approximately 40% compared to wild-type controls (Fig. 1b), indicating the presence of surface homomers. In contrast, overexpressing a GluA1 subunit with a full C-tail truncation (Δ C) showed rectification similar to wild-type neurons (Fig. 1b), indicating an impairment in trafficking to the surface. However, a less severe truncation up to amino acid 824 (GluA1(Δ 824)), which removes two serine phosphorylation sites and the PDZ-binding domain, increased rectification to a similar degree as full-length GluA1. Selective excision of the remaining membrane proximal region (Δ MPR), which contains a well-characterized binding site of the protein 4.1N^{22,23}, also significantly increased rectification (Fig. 1b). Combined, these two modified subunits represent complementary

¹Neuroscience Graduate Program, University of California San Francisco, California 94158, USA. ²Department of Cellular and Molecular Pharmacology, University of California San Francisco, California 94143, USA. [†]Present address: Synapse and Neural Circuit Research Unit, National Institute of Neurological Disorders and Stroke, National Institutes of Health, Bethesda, Maryland 20892, USA.

truncations of the entire C-tail, ruling out a necessary role for any single part of the C-tail for steady-state surface expression.

Because competition with endogenous receptors may have hindered GluA1(Δ C) trafficking, we next studied surface expression in the absence of native AMPARs. To accomplish this, we used mice in which the genes coding for GluA1, GluA2 and GluA3 were flanked by *loxP* sites (*Gria1^{fl/fl} Gria2^{fl/fl} Gria3^{fl/fl}*; hereafter referred to as *Gria1-3^{fl/fl}*). A previous study has shown that expression of Cre into *Gria1-3^{fl/fl}* neurons results in a complete absence of AMPARs within 12–15 days³, providing an effective AMPAR-null background onto which mutant GluA1 subunits can be expressed. We confirmed that Cre expression eliminated all glutamate-evoked current from somatic outside-out patches of *Gria1-3^{fl/fl}* CA1 neurons, which can be rescued to control amplitudes by co-expression with full-length GluA1 (Fig. 1c, d), indicating full rescue of surface expression. Consistent with overexpression, molecular replacement with GluA1(Δ C) showed significantly decreased glutamate-evoked currents (Fig. 1c, d). This trafficking defect was not due to decreased association with TARPs (that is, auxiliary subunits important for AMPAR trafficking^{24,25}), as both full-length and GluA1(Δ C) subunits had KA/Glu ratios similar to control (Supplementary Fig. 1a). Also, both GluA1 and GluA1(Δ C) replacement subunits showed strong inward rectification, confirming the absence of endogenous receptors (Supplementary Fig. 1b). Because both GluA1(Δ MPR) and GluA1(Δ S24) showed normal surface trafficking, the GluA1(Δ C) subunit may be impaired owing to its severe truncation so close to the transmembrane region, which may inhibit proper protein folding.

Synaptic transmission doesn't require the GluA1 C-tail

Given the decreased surface expression caused by complete truncation of the GluA1 C-tail, we next examined whether it would also

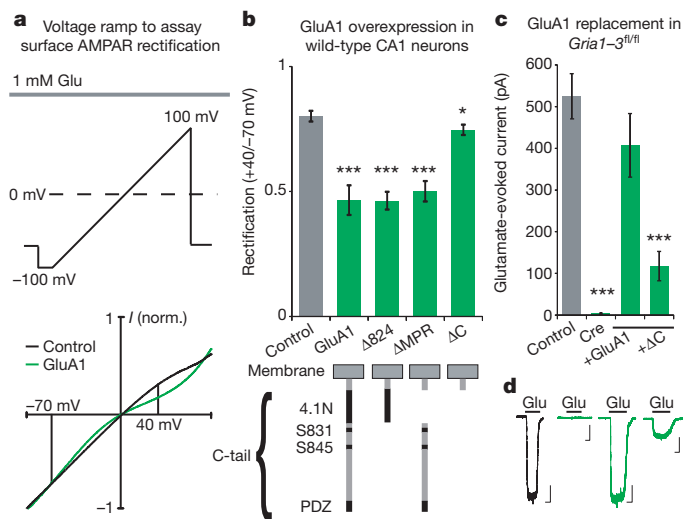


Figure 1 | The role of the GluA1 C-tail in surface trafficking. **a**, Experimental protocol and example trace showing voltage ramps applied to outside-out patches of control (black) and GluA1-overexpressing (green) CA1 neurons. Rectification was measured as the normalized glutamate-evoked current at +40 mV over -70 mV. **b**, Full-length GluA1, GluA1(Δ S24) and GluA1(Δ MPR) significantly increased rectification of surface currents compared to control. Overexpression of GluA1(Δ C) slightly increased rectification (control, $n = 47$; GluA1, $n = 10$, $P < 0.001$; GluA1(Δ S24), $n = 13$, $P < 0.001$; GluA1(Δ MPR), $n = 18$, $P < 0.001$; GluA1(Δ C), $n = 8$, $P < 0.05$). **c**, Cre expression eliminates glutamate-evoked currents in *Gria1-3^{fl/fl}* CA1 neuron outside-out patches, which is rescued to control levels by co-expression with full-length GluA1, but not GluA1(Δ C) (control, $n = 28$; Cre, $n = 9$, $P < 0.001$; GluA1, $n = 11$, $P > 0.05$; GluA1(Δ C), $n = 15$, $P < 0.001$). **d**, Example traces of glutamate-evoked current from (left to right) *Gria1-3^{fl/fl}* control neurons, Cre-expressing neurons, GluA1, and GluA1(Δ C) replacement neurons. Scale bars: 1 s, 100 pA. Error bars represent mean \pm s.e.m. * P < 0.05; *** P < 0.001 in b, c.

impair basal synaptic targeting. Similar to surface currents, we assessed baseline synaptic transmission by transfecting *Gria1-3^{fl/fl}* organotypic slice cultures with Cre and a replacement GluA1 subunit. After 17 days, we recorded evoked AMPAR excitatory postsynaptic currents (EPSCs) simultaneously from control and neighbouring GluA1-replacement CA1 neurons. Similar to previously described results¹⁹, full-length GluA1 rescued AMPAR EPSC amplitudes to ~68% of control cells, while leaving NMDAR EPSCs unchanged (Fig. 2a, c). However, these results contrast with previous studies showing that GluA1 only traffics to synapses after an LTP stimulus^{5,7}. For experimental exploration of this discrepancy, please refer to

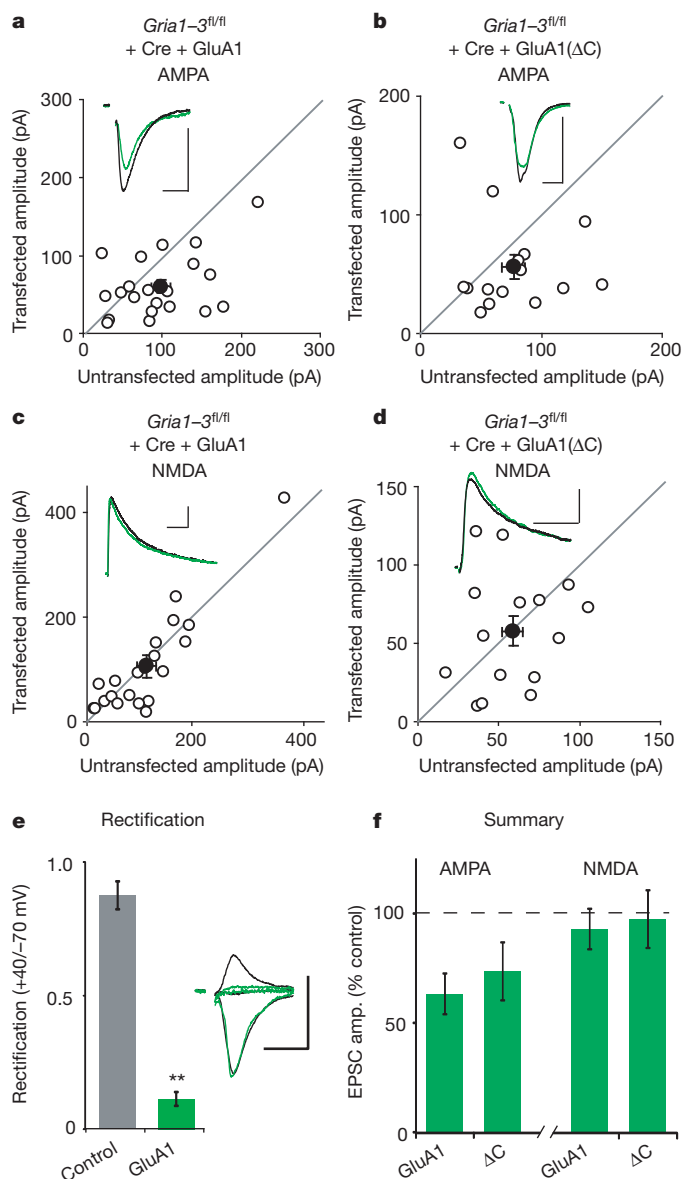


Figure 2 | GluA1(Δ C) has normal synaptic targeting. Paired whole-cell recordings from control and Cre plus GluA1 or Cre plus GluA1(Δ C)-expressing CA1 neurons in *Gria1-3^{fl/fl}* organotypic slice cultures. **a**, **c**, Full-length GluA1 rescued synaptic AMPAR EPSCs to 68% of control cells ($n = 13$, $P > 0.05$), whereas NMDA EPSCs remained unchanged between control and transfected cells ($P > 0.05$). **b**, **d**, Replacement with GluA1(Δ C) results in 73% rescue of AMPA EPSCs without a change in the NMDA EPSC ($n = 15$, both $P > 0.05$). **e**, Replacement with GluA1 showed inwardly rectifying EPSCs ($n = 8$, $P < 0.01$). **f**, Summary graph of AMPA and NMDA EPSC rescue between GluA1 and GluA1(Δ C). Example traces show average EPSCs for paired control (black) and replacement (green) neurons. Scale bars: 20 ms (AMPA), 100 ms (NMDA), 50 pA. Error bars represent mean \pm s.e.m. ** P < 0.01 in e.

Supplementary Fig. 2. We also observed no change in paired-pulse ratio, indicating that GluA1 molecular replacement did not affect presynaptic release probability (Supplementary Fig. 3a). Synaptic EPSCs from GluA1-replacement CA1 neurons were strongly inwardly rectifying compared to control, confirming the absence of endogenous receptors (Fig. 2e and Supplementary Fig. 3b). Replacement with GluA1(Δ C) rescued AMPAR EPSCs to the same degree as full-length GluA1, and also had no effect on the NMDA EPSCs (Fig. 2b, d). Replacement with GluA1(Δ 824) produced similar results (Supplementary Fig. 3c–e). This demonstrates that despite having markedly decreased somatic expression owing to its severe truncation, GluA1(Δ C) manages to rescue basal synaptic transmission effectively.

GluA1 C-tail domains are not required for LTP

To assess how GluA1 C-tail truncations affect LTP, we transfected Cre and GluA1 into the hippocampus of embryonic day \sim E15.5 *Gria1*-3^{fl/fl} mouse embryos by electroporation. Like biolistic transfection, this results in sparse expression of transfected cells. Electroporation of Cre alone resulted in complete absence of an AMPAR EPSC by post-natal day 10 (P10) with no effect on NMDAR EPSCs, and no AMPAR EPSCs appeared after an LTP stimulus (Supplementary Fig. 4a–c). In P17–20 acute hippocampal slices, we induced LTP after recording stable (3–5 min) baseline AMPAR EPSCs simultaneously from control and GluA1-replacement neurons. We found that replacement with full-length GluA1 exhibited normal LTP (Fig. 3a), confirming that the GluA1 subunit is sufficient. To avoid the confounding effect of decreased surface expression seen by GluA1(Δ C), we next assessed the competence of GluA1(Δ 824) and GluA1(Δ MPR) subunits, which represent overlapping truncations of the entire C-tail. Both truncated subunits expressed LTP comparable to control (Fig. 3b, c), as did neurons replaced with a truncated GluA1(Δ 824) subunit with S816A and S818A mutations (GluA1(Δ 824-AA)) to specifically prevent 4.1N binding²⁶ (Supplementary Fig. 5a, b). We also found that expressing GluA1(Δ C) with GluA2 to produce more natural GluA1–GluA2 heteromers was able to rescue the surface trafficking defect of GluA1(Δ C) (Supplementary Fig. 6a–d), and show synaptic responses similar to controls (Supplementary Fig. 6e–h). Finally, LTP was fully rescued by replacement with GluA1(Δ C)–GluA2 (Fig. 3d). Combined, these data show that the GluA1 C-tail is not required for LTP.

GluA2 is sufficient for LTP

Given that no individual portion of the GluA1 C-tail was necessary for LTP, we hypothesized that expression of an alternative AMPAR subunit might also rescue LTP. GluA2 is another such subunit with limited C-tail homology to GluA1 (ref. 15) that is normally highly expressed in CA1 neurons, but is ineffective at forming homomers and trafficking to the cell surface^{3,20}. This is attributable to Q/R RNA editing in the pore of the receptor, which severely limits channel permeability and may make formation of homomers energetically unfavourable²⁷. Expression of unedited GluA2 with an R586Q mutation (GluA2(Q)) resulted in abundant appearance of homomers on the neuronal surface, as observed by increased rectification (Fig. 4a). Like GluA1(Δ C), GluA2((Q) Δ C) also showed impaired surface expression (Supplementary Fig. 7d). Similarly, both full-length GluA2(Q) (Fig. 4b) and GluA2((Q) Δ C) (Supplementary Fig. 7b) trafficked to the synapse, arguing against any necessary role for the GluA2 C-tail in synaptic targeting, in agreement with previous experiments²¹. NMDA EPSCs and paired-pulse ratio remain unchanged in these replacement neurons, and complete replacement of endogenous receptors was confirmed by synaptic rectification (Supplementary Fig. 7a, b). Moreover, LTP in *Gria1*-3^{fl/fl} neurons that expressed only GluA2(Q) was indistinguishable from control cells (Fig. 4c), despite lacking any of the intracellular phosphorylation sites and protein–protein binding sites of GluA1. Similarly intact synaptic targeting and

LTP was seen in a GluA2(Q) truncation that lacks most of its C-tail and known protein–interaction sites (Supplementary Fig. 7c–e).

LTP requires a reserve pool of AMPARs

Previous studies have shown that LTP is impaired in mice with constitutive deletion of GluA1 (ref. 8), but not GluA2 or GluA3 (ref. 9), demonstrating that GluA1 is both necessary and sufficient for LTP. These findings seem to contradict our data showing that GluA2(Q) homomers readily express LTP. We therefore re-examined the requirement for GluA1 in single-cell conditional knockouts and

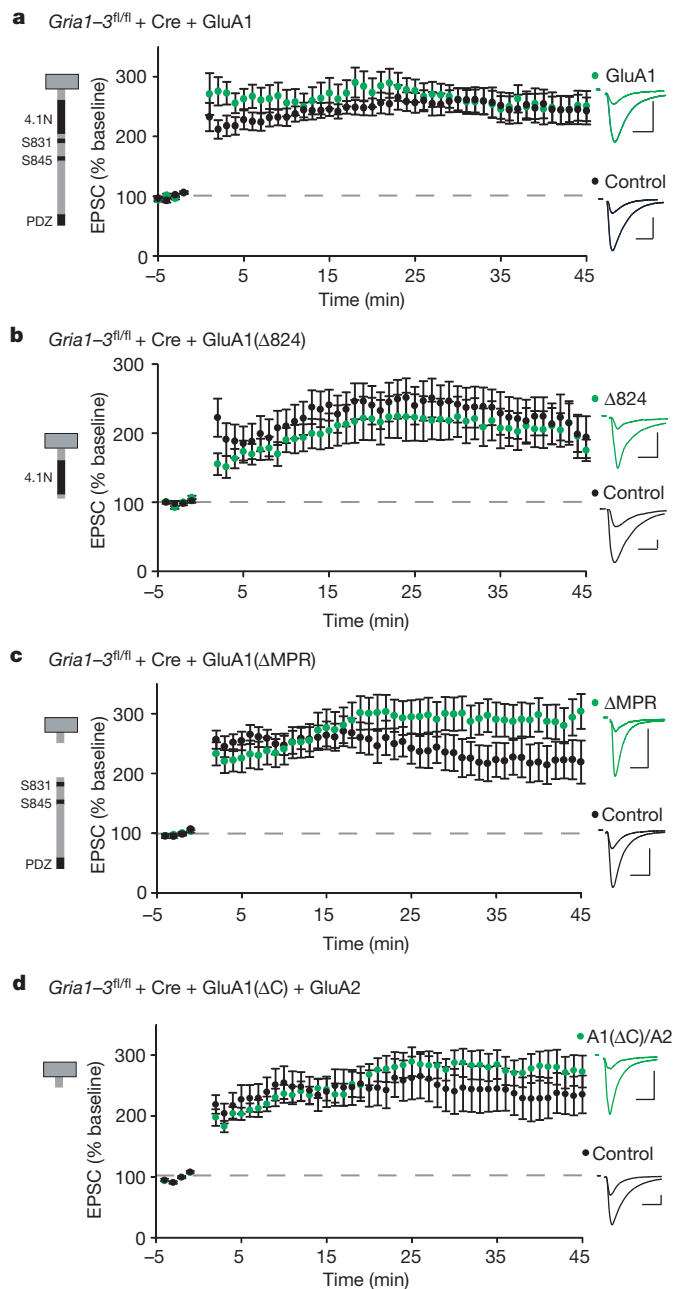


Figure 3 | LTP requires no single portion of the GluA1 C-tail. Paired whole-cell recordings from control CA1 neurons and neighbouring Cre plus GluA1-expressing neurons in P17–20 *Gria1*-3^{fl/fl} acute slices. **a–d**, LTP is similar to control in GluA1 (**a**), GluA1(Δ 824) (**b**), GluA1(Δ MPR) (**c**) and GluA1(Δ C) plus GluA2 (**d**) replacement neurons (GluA1, $n = 11$; GluA1(Δ 824), $n = 11$; GluA1(Δ MPR), $n = 20$; GluA1(Δ C) plus GluA2, $n = 11$; all $P > 0.05$). Example traces show EPSCs before and 45 min after LTP induction in paired control (black) and GluA1-replacement neurons (green). Scale bars: 20 ms, 100 pA. Error bars represent mean \pm s.e.m.

found that conditional deletion of GluA1 alone did indeed impair LTP (Fig. 5a). Furthermore, deletion of GluA2 or GluA3 separately (Supplementary Fig. 8a, b) or in combination (Fig. 5b) had no effect. How can these data be reconciled with our previous experiments? One profound difference between deleting GluA1 and deleting GluA2 and/or GluA3 is that in the former condition there is an absence of extrasynaptic receptors^{3,8,20}, whereas in the latter condition this pool remains entirely intact³. Also, unlike endogenous GluA2, our replacement GluA2(Q) showed abundant surface expression. We reasoned that perhaps it is the depletion of this pool that accounts for the loss of LTP in the GluA1 knockout. To test this possibility, we again used the extreme C-tail truncations of both GluA1 and GluA2(Q), in which surface expression is impaired but synaptic targeting is maintained (Fig. 1b, c and Supplementary Fig. 7d). Indeed, LTP was substantially impaired in both GluA1(Δ C) and GluA2((Q) Δ C) replacement neurons (Fig. 5c, d). These findings suggest that the minimum requirement for LTP is a reserve pool of extrasynaptic AMPARs, regardless of the subunit type.

GluK1 is sufficient for mediating LTP

Having failed to identify any specific domains in the C-tails that are important for LTP, we wondered whether other domains in the AMPAR are required. In search of a null condition to conduct domain-swapping experiments, we turned to KARs, a separate class of fast, ionotropic glutamate receptor which differs in fundamental ways from AMPARs. KARs bind to different auxiliary subunits and have no sequence homology in their C-tails²⁸. We therefore set out to replace all endogenous AMPARs with KARs at CA1 synapses. CA1 pyramidal neurons do not express synaptic KARs, as shown by the

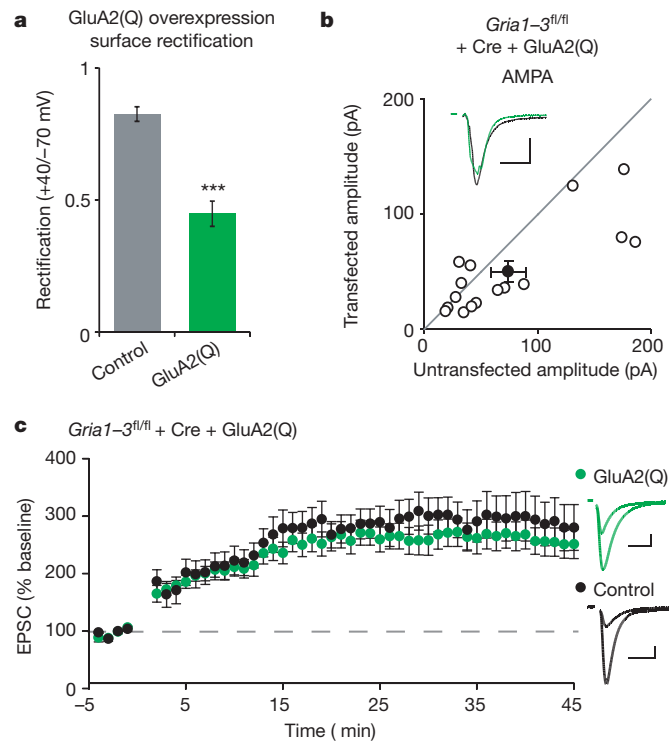


Figure 4 | GluA2(Q) is sufficient to express LTP. **a**, Overexpression of GluA2(Q) caused significantly increased surface rectification compared to control (control, $n = 8$; GluA2(Q), $n = 14$, $P < 0.001$). **b**, Paired whole-cell recordings between control and Cre plus GluA2(Q)-expressing *Gria1-3^{fl/fl}* CA1 neurons show rescue of AMPA EPSCs (GluA2(Q), $n = 16$, $P < 0.05$). Average AMPA EPSC example traces are shown for paired control (black) and GluA2-replacement neurons (green). **c**, Expression of Cre plus GluA2(Q) shows LTP similar to control ($n = 14$, $P > 0.05$, minute 45). Example traces show average AMPA EPSCs before and 45 min after LTP induction. Scale bars: 20 ms and 50 pA. Error bars represent mean \pm s.e.m. *** $P < 0.001$ in **a**.

absence of synaptic currents in the presence of the AMPAR-selective antagonist GYKI (4-(8-methyl-9H-1,3-dioxol[4,5-*h*][2,3]benzodiazepine-5-yl)-benzamine dihydrochloride) (Supplementary Fig. 9a). However, co-expression of the KAR subunit GluK1 with the auxiliary

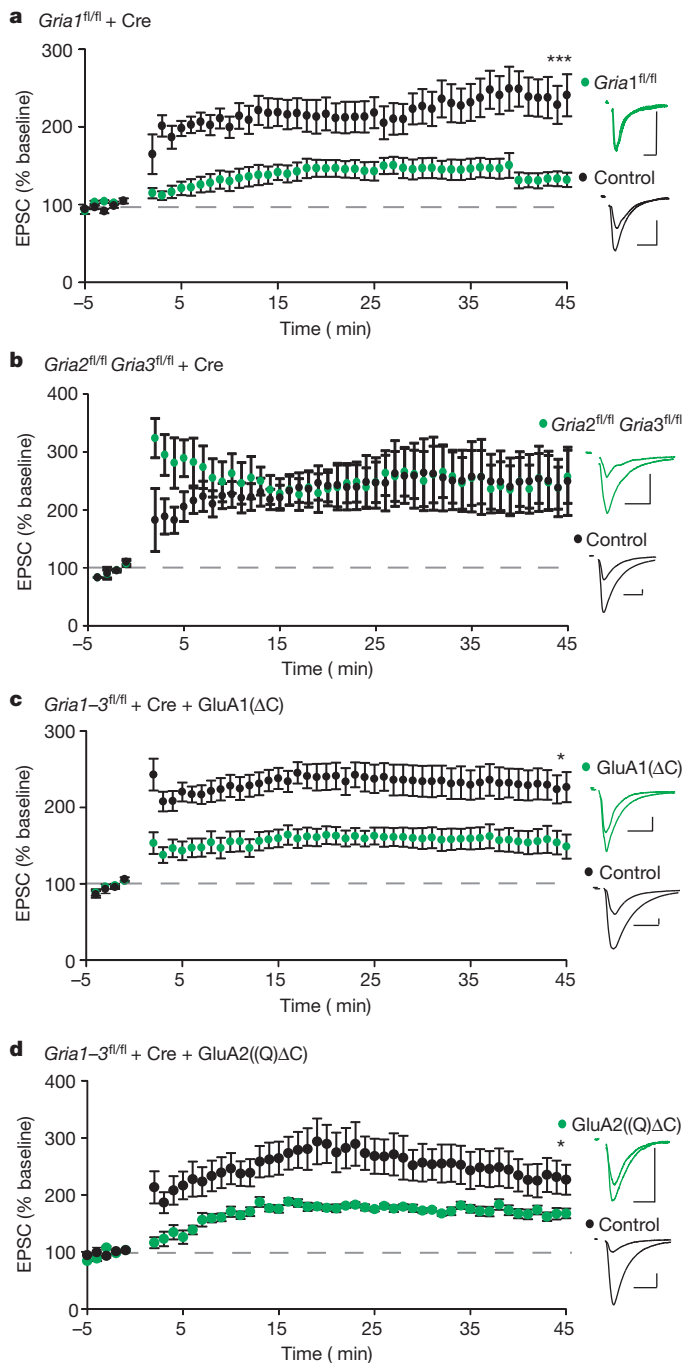


Figure 5 | Lack of surface expression corresponds with loss of LTP in GluA1 conditional knockouts, and GluA1(Δ C) and GluA2((Q) Δ C) replacement neurons. **a**, Conditional GluA1 knockout cells (*Gria1^{fl/fl}* plus Cre) demonstrate impaired LTP compared to control ($n = 13$, $P < 0.001$, 45 min). **b**, GluA2 and GluA3 knockout cells (*Gria2^{fl/fl} Gria3^{fl/fl}* plus Cre) demonstrate comparable LTP to control ($n = 6$, $P > 0.05$, 45 min). **c**, **d**, Molecular replacement with either GluA1(Δ C) or GluA2((Q) Δ C) results in reduced expression of LTP (GluA1(Δ C), $n = 16$, $P < 0.05$; GluA2((Q) Δ C), $n = 10$, $P < 0.05$, both at 45 min). Example traces show averaged AMPA EPSCs before and 45 min after induction of LTP in paired experimental neurons (green) and control cells (black). Scale bars: 20 ms, 50 pA. Error bars represent mean \pm s.e.m. *** $P < 0.001$ in **a**; * $P < 0.05$ in **c**, **d**.

subunit Neto2^{29,30} in wild-type CA1 neurons generated a GYKI-resistant current that was blocked by NBQX (2,3-dioxo-6-nitro-1,2,3,4-tetrahydrobenzo(f)quinoxaline-7-sulfonamide), an antagonist that blocks both KARs and AMPARs (Supplementary Fig. 9a). This indicates that overexpressed KARs are capable of being targeted to the synapse and contribute to EPSCs. To examine KAR currents in isolation, we co-expressed Cre with GluK1 and Neto2 in *Gria1-3^{fl/fl}* CA1 neurons. In this case, we recorded a population of pure KARs on the surface that desensitize to glutamate even in the presence of cyclothiazide and are completely blocked by ACET, a highly specific GluK1 antagonist³¹ (Fig. 6a). Furthermore, in this AMPAR-null background, these neurons exhibit EPSCs that are entirely blocked by ACET, whereas the EPSCs in neighbouring control neurons are unaffected (Fig. 6b), further demonstrating that exogenously expressed KARs are capable of being targeted to synapses. As with AMPAR replacement, NMDA EPSCs were unaffected (Supplementary Fig. 9b). Finally, we tested whether neurons expressing only KARs could express LTP. Unexpectedly, we found that the KAR EPSCs showed potentiation indistinguishable from that recorded simultaneously from neighbouring control neurons (Fig. 6c). To ensure that the EPSC in the KAR-expressing neuron was mediated entirely by KARs, we applied ACET at the end of the experiments and found that it abolished the EPSC, but had no effect on neighbouring control neurons (Fig. 6c). We also wanted to confirm that LTP mediated by KARs, which are also Ca²⁺-permeable, was not induced by a fundamentally different mechanism than wild-type LTP. We therefore tried inducing LTP in the presence of the NMDAR antagonist AP5 (D(-)-2-amino-5-phosphonopivalic acid), and saw no significant potentiation (Supplementary Fig. 9d, e). These experiments demonstrate that even neurons completely lacking AMPARs can undergo LTP, as long as they are provided with an alternative fast, ionotropic glutamate receptor.

Discussion

Using a single-cell molecular replacement approach that gave us complete control over the complement of expressed AMPA receptors, we found no requirement for the GluA1 C-tail for basal synaptic transmission or for LTP. In fact, we found no requirement for the GluA1 subunit generally, as both GluA2(Q), another AMPAR subunit, and GluK1, an entirely separate class of glutamate receptor, exhibited normal levels of LTP. Previous studies that have implicated the GluA1 C-tail in LTP demonstrated phenotypes with a largely normal initial stage of potentiation, followed by a gradual decrease in EPSC amplitude towards baseline^{5,6,28,32}. The most compelling of these studies demonstrates impaired LTP in mice with phospho-null knock-in mutations of two key phosphorylation sites, and complete absence of long-term depression (LTD)³². Another study with phospho-mimetic knock-in mutations also demonstrated a decreased threshold for LTP induction³³. Given these findings, we cannot rule out the possibility that the C-tails have some modulatory effect on synaptic plasticity. In the present experiments, however, we saw immediately impaired potentiation in GluA1 conditional knockout cells and cells with GluA1(Δ) and GluA2(Δ) replacement, which more closely mimics the absence of LTP seen with pharmacological blockade of NMDA receptors. With all three of these manipulations, there was a profound decrease in the pool of extrasynaptic receptors, indicating that the main requirement for LTP is an adequate reserve pool of glutamate receptors. Another equally plausible model is that AMPAR-containing recycling endosomes are required for LTP, and conditions that deplete the surface receptor pool also deplete this pool³⁴ (see Supplementary Discussion).

Fundamentally, our results suggest that synapses can accumulate a broad variety of receptors after LTP, shifting the focus of LTP expression from the receptor subunits to the synapse itself and specifically the postsynaptic density (PSD). Our data suggest a model in which AMPARs freely diffuse on the neuronal surface, and are trapped at the PSD for use in synaptic transmission³⁵. LTP, then, can be understood as an immediate increase in the ability of the PSD to trap receptors

that relies on a reserve pool of freely diffusing surface receptors. This model is consistent with evidence from two-photon glutamate uncaging experiments, which show an immediate increase in the volume of postsynaptic spines after LTP induction^{36–38}, suggesting significant alterations to the synapse and PSD. Despite this shift of focus, research

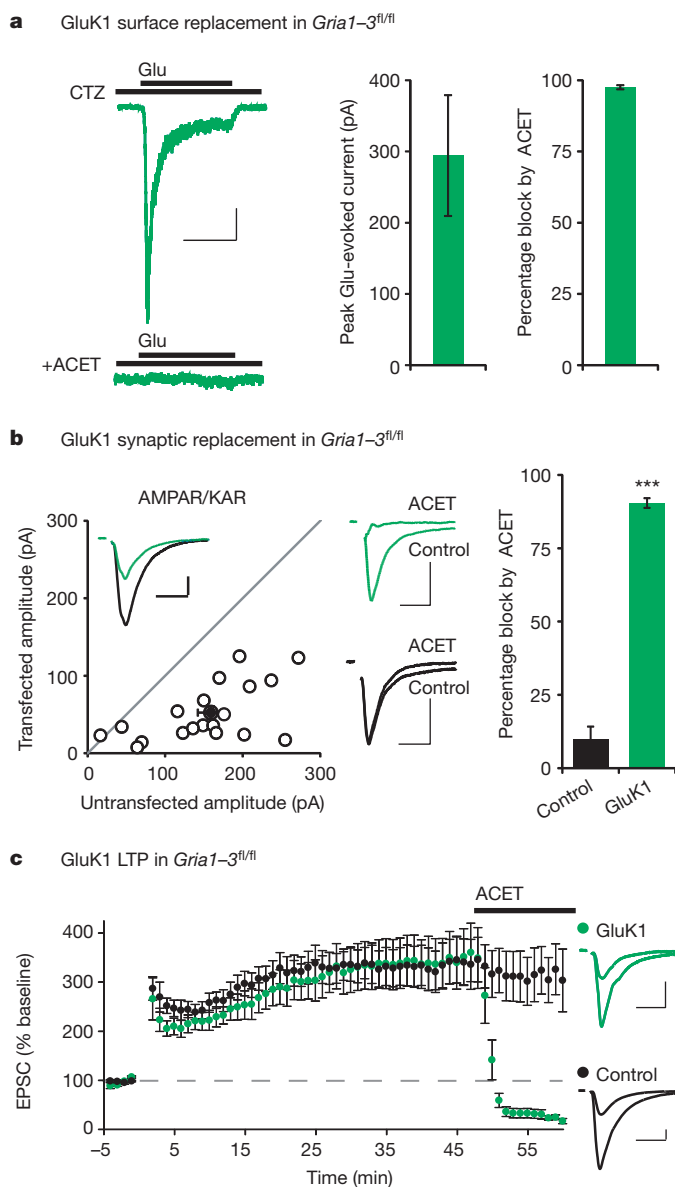


Figure 6 | GluK1 expresses on the neuronal surface, targets to synapses and mediates LTP. **a**, Co-expression of Cre, GluK1 and Neto2 in *Gria1-3^{fl/fl}* neurons results in robust glutamate-evoked currents from somatic outside-out patches ($n = 10$). The current desensitizes in the presence of 100 μ M cyclothiazide (CTZ), and is completely blocked by 1 μ M ACET. **b**, Paired recordings from Cre/GluK1/Neto2-expressing and neighbouring control CA1 neurons resulted in a 33% rescue of synaptic EPSCs ($n = 20$, $P < 0.001$). Example trace (inset) shows paired control (black) and GluK1-replacement (green) EPSCs. 1 μ M ACET completely blocks the GluK1 replacement EPSCs (green example traces, upper middle), with no block of control cell EPSCs (black example traces, lower middle) ($n = 14$, $P < 0.001$). **c**, Paired whole-cell recording from control and Cre/GluK1/Neto2-expressing *Gria1-3^{fl/fl}* CA1 neurons shows similar levels of LTP ($n = 12$, $P > 0.05$, minute 45). 1 μ M ACET completely blocks the GluK1-replacement EPSC, but not control ($n = 11$, $P < 0.001$, minute 60). Example traces show average EPSCs before and 45 min after LTP induction in control (black) and GluK1-replacement neurons (green). Scale bars: 1 s (**a**), 20 ms (**b**, **c**) and 50 pA (**a–c**). Error bars represent mean \pm s.e.m. *** $P < 0.001$ in **b**.

on AMPARs and their auxiliary subunits, such as TARPs, remain important for identifying LTP-related PSD proteins. In the absence of a role for the GluA1 C-tail, the question remains exactly which specific interactions cluster AMPARs at the synapse both basally and during plasticity. Identification of these interactions may be crucial to understanding the synaptic modifications that underlie learning in the brain.

METHODS SUMMARY

Electrophysiology and neuronal transfection. Whole-cell and outside-out patch recordings were performed as previously described³. Slice cultures were prepared on P6–8 as previously described³⁹ and recorded on day *in vitro* (DIV) 9–24 depending on the experiment. Acute slices for LTP experiments were prepared between P17–23. All slices were maintained during recording in artificial cerebral spinal fluid (aCSF) containing (in mM): 119 NaCl, 2.5 KCl, 1 NaH₂PO₄, 26.2 NaHCO₃ and 11 glucose. For acute slices, 2.5 mM CaCl₂ and 1.3 mM MgSO₄ were added to the aCSF, and 4 mM CaCl₂ and MgSO₄ were added for organotypic slice cultures. The internal whole-cell recording solution contained (in mM): 135 CsMeSO₄, 8 NaCl, 10 HEPES, 0.3 EGTA, 5 QX-314, 4 Mg-ATP, 0.3 Na-GTP and 0.1 spermine. Osmolarity was adjusted to 290–295 mOsm, and pH buffered at 7.3–7.4. Synaptic responses were evoked by stimulating with a monopolar glass electrode filled with aCSF in stratum radiatum of CA1. Biolistic transfections and ~E15.5 electroporations were carried out as previously described^{40–42}.

Full Methods and any associated references are available in the online version of the paper.

Received 11 June; accepted 9 November 2012.

Published online 12 December 2012.

- Hollmann, M. & Heinemann, S. Cloned glutamate receptors. *Annu. Rev. Neurosci.* **17**, 31–108 (1994).
- Wisden, W. & Seeburg, P. H. Mammalian ionotropic glutamate receptors. *Curr. Opin. Neurobiol.* **3**, 291–298 (1993).
- Lu, W. *et al.* Subunit composition of synaptic AMPA receptors revealed by a single-cell genetic approach. *Neuron* **62**, 254–268 (2009).
- Wenthold, R. J., Petralia, R. S., Blahos, J. II & Niedzielski, A. S. Evidence for multiple AMPA receptor complexes in hippocampal CA1/CA2 neurons. *J. Neurosci.* **16**, 1982–1989 (1996).
- Shi, S., Hayashi, Y., Esteban, J. A. & Malinow, R. Subunit-specific rules governing AMPA receptor trafficking to synapses in hippocampal pyramidal neurons. *Cell* **105**, 331–343 (2001).
- Boehm, J. *et al.* Synaptic incorporation of AMPA receptors during LTP is controlled by a PKC phosphorylation site on GluR1. *Neuron* **51**, 213–225 (2006).
- Hayashi, Y. *et al.* Driving AMPA receptors into synapses by LTP and CaMKII: requirement for GluR1 and PDZ domain interaction. *Science* **287**, 2262–2267 (2000).
- Zamanillo, D. *et al.* Importance of AMPA receptors for hippocampal synaptic plasticity but not for spatial learning. *Science* **284**, 1805–1811 (1999).
- Meng, Y., Zhang, Y. & Jia, Z. Synaptic transmission and plasticity in the absence of AMPA glutamate receptor GluR2 and GluR3. *Neuron* **39**, 163–176 (2003).
- Kessels, H. W. & Malinow, R. Synaptic AMPA receptor plasticity and behavior. *Neuron* **61**, 340–350 (2009).
- Anggono, V. & Huganir, R. L. Regulation of AMPA receptor trafficking and synaptic plasticity. *Curr. Opin. Neurobiol.* **22**, 461–469 (2012).
- Collingridge, G. L., Isaac, J. T. & Wang, Y. T. Receptor trafficking and synaptic plasticity. *Nature Rev. Neurosci.* **5**, 952–962 (2004).
- Malenka, R. C. & Bear, M. F. LTP and LTD: an embarrassment of riches. *Neuron* **44**, 5–21 (2004).
- Malenka, R. C. Synaptic plasticity and AMPA receptor trafficking. *Ann. NY Acad. Sci.* **1003**, 1–11 (2003).
- Malinow, R. & Malenka, R. C. AMPA receptor trafficking and synaptic plasticity. *Annu. Rev. Neurosci.* **25**, 103–126 (2002).
- Bredt, D. S. & Nicoll, R. A. AMPA receptor trafficking at excitatory synapses. *Neuron* **40**, 361–379 (2003).
- Shepherd, J. D. & Huganir, R. L. The cell biology of synaptic plasticity: AMPA receptor trafficking. *Annu. Rev. Cell Dev. Biol.* **23**, 613–643 (2007).
- Granger, A. J., Gray, J. A., Lu, W. & Nicoll, R. A. Genetic analysis of neuronal ionotropic glutamate receptor subunits. *J. Physiol. (Lond.)* **589**, 4095–4101 (2011).
- Lu, W., Isozaki, K., Roche, K. W. & Nicoll, R. A. Synaptic targeting of AMPA receptors is regulated by a CaMKII site in the first intracellular loop of GluA1. *Proc. Natl Acad. Sci. USA* **107**, 22266–22271 (2010).
- Andrasfalvy, B. K., Smith, M. A., Borchardt, T., Sprengel, R. & Magee, J. C. Impaired regulation of synaptic strength in hippocampal neurons from GluR1-deficient mice. *J. Physiol. (Lond.)* **552**, 35–45 (2003).
- Panicker, S., Brown, K. & Nicoll, R. A. Synaptic AMPA receptor subunit trafficking is independent of the C terminus in the GluR2-lacking mouse. *Proc. Natl Acad. Sci. USA* **105**, 1032–1037 (2008).
- Shen, L., Liang, F., Walensky, L. D. & Huganir, R. L. Regulation of AMPA receptor GluR1 subunit surface expression by a 4.1N-linked actin cytoskeletal association. *J. Neurosci.* **20**, 7932–7940 (2000).
- Coleman, S. K., Cai, C., Mottershead, D. G., Haapalahti, J. P. & Keinänen, K. Surface expression of GluR-D AMPA receptor is dependent on an interaction between its C-terminal domain and a 4.1 protein. *J. Neurosci.* **23**, 798–806 (2003).
- Jackson, A. C. & Nicoll, R. A. The expanding social network of ionotropic glutamate receptors: TARPs and other transmembrane auxiliary subunits. *Neuron* **70**, 178–199 (2011).
- Tomita, S. *et al.* Stargazin modulates AMPA receptor gating and trafficking by distinct domains. *Nature* **435**, 1052–1058 (2005).
- Lin, D. T. *et al.* Regulation of AMPA receptor extrasynaptic insertion by 4.1N, phosphorylation and palmitoylation. *Nature Neurosci.* **12**, 879–887 (2009).
- Greger, I. H., Ziff, E. B. & Penn, A. C. Molecular determinants of AMPA receptor subunit assembly. *Trends Neurosci.* **30**, 407–416 (2007).
- Contractor, A., Mulle, C. & Swanson, G. T. Kainate receptors coming of age: milestones of two decades of research. *Trends Neurosci.* **34**, 154–163 (2011).
- Zhang, W. *et al.* A transmembrane accessory subunit that modulates kainate-type glutamate receptors. *Neuron* **61**, 385–396 (2009).
- Copits, B. A., Robbins, J. S., Frausto, S. & Swanson, G. T. Synaptic targeting and functional modulation of GluK1 kainate receptors by the auxiliary neuropilin and tollid-like (NETO) proteins. *J. Neurosci.* **31**, 7334–7340 (2011).
- Dargan, S. L. *et al.* ACET is a highly potent and specific kainate receptor antagonist: characterisation and effects on hippocampal mossy fibre function. *Neuropharmacology* **56**, 121–130 (2009).
- Lee, H. K. *et al.* Phosphorylation of the AMPA receptor GluR1 subunit is required for synaptic plasticity and retention of spatial memory. *Cell* **112**, 631–643 (2003).
- Makino, Y., Johnson, R. C., Yu, Y., Takamiya, K. & Huganir, R. L. Enhanced synaptic plasticity in mice with phosphomimetic mutation of the GluA1 AMPA receptor. *Proc. Natl Acad. Sci. USA* **108**, 8450–8455 (2011).
- Lisman, J., Yasuda, R. & Raghavachari, S. Mechanisms of CaMKII action in long-term potentiation. *Nature Rev. Neurosci.* **13**, 169–182 (2012).
- Opazo, P. & Choquet, D. A three-step model for the synaptic recruitment of AMPA receptors. *Mol. Cell. Neurosci.* **46**, 1–8 (2011).
- Matsuzaki, M., Honkura, N., Ellis-Davies, G. C. & Kasai, H. Structural basis of long-term potentiation in single dendritic spines. *Nature* **429**, 761–766 (2004).
- Murakoshi, H. & Yasuda, R. Postsynaptic signaling during plasticity of dendritic spines. *Trends Neurosci.* **35**, 135–143 (2012).
- Patterson, M. & Yasuda, R. Signalling pathways underlying structural plasticity of dendritic spines. *Br. J. Pharmacol.* **163**, 1626–1638 (2011).
- Stoppini, L., Buchs, P. A. & Muller, D. A simple method for organotypic cultures of nervous tissue. *J. Neurosci. Methods* **37**, 173–182 (1991).
- Schnell, E. *et al.* Direct interactions between PSD-95 and stargazin control synaptic AMPA receptor number. *Proc. Natl Acad. Sci. USA* **99**, 13902–13907 (2002).
- Elias, G. M., Elias, L. A., Apostolides, P. F., Kriegstein, A. R. & Nicoll, R. A. Differential trafficking of AMPA and NMDA receptors by SAP102 and PSD-95 underlies synapse development. *Proc. Natl Acad. Sci. USA* **105**, 20953–20958 (2008).
- Navarro-Quiroga, I., Chittajallu, R., Gallo, V. & Haydar, T. F. Long-term, selective gene expression in developing and adult hippocampal pyramidal neurons using focal *in utero* electroporation. *J. Neurosci.* **27**, 5007–5011 (2007).

Supplementary Information is available in the online version of the paper.

Acknowledgements We thank A. Jackson, J. Levy, S. Fischbach, K. Lovero, N. Sheng, S. Shipman and M. Younger for critical discussions and reading of the manuscript; K. Bjorgen for technical help with organotypic slice cultures; and L. Subramanian from the Kriegstein laboratory for technical help with *in utero* electroporations. We thank P. Seeburg and R. Sprengel for the *Gria1*–3^{fl/fl} mice. A.J.G. was supported by the National Science Foundation Graduate Research Fellowship. R.A.N. is supported by the National Institute of Health.

Author Contributions M.C. carried out electroporations and maintained *Gria1*–3^{fl/fl} mice. Y.S. collected GluK1 overexpression data. W.L. was involved in study design and cloned several constructs. A.J.G. designed the study, collected and analysed data, and wrote the paper. R.A.N. conceived the study, contributed to the design of experiments and wrote the paper. All authors discussed the results and commented on the manuscript.

Author Information Reprints and permissions information is available at www.nature.com/reprints. The authors declare no competing financial interests. Readers are welcome to comment on the online version of the paper. Correspondence and requests for materials should be addressed to R.A.N. (nicoll@cmp.uscf.edu).

METHODS

Mouse genetics. Animals were housed according to the IACUC guidelines at the University of California, San Francisco. *Gria1*^{-3^{fl/fl}} mice were generated and genotyped as previously described³.

Experimental constructs. Flip-isoform GluA1, GluA2(Q) and Cre:mCherry were cloned into the pFUGW expression plasmid by PCR and In-Fusion HD Cloning System (Invitrogen). pFUGW-GluA1 and GluA2(Q) co-expressed with GFP behind an internal ribosomal entry site (IRES). GluA1 and GluA2(Q) truncations were generated by overlapping extension PCR. GluA1(Δ C) ended in amino acid 812, with the last four amino acids being EFCY. GluA1(Δ 824) ended in amino acid 824, with the sequence MKGF. GluA(Δ 824-AA) contained the C-tail sequence EFCYKSRRAEAKRMKGK. GluA1(Δ MPR) had the following amino acids excised from the C-tail: KRSSESKRMKGFC, with the rest of the C-tail intact. GluA2((Q) Δ C) also truncated to amino acids EFCY, and GluA2((Q) Δ 847) ended in amino acids MKGF. GluK1 and Neto2 were cloned into the pCAGGs expression plasmid with GFP and mCherry, respectively, co-expressed behind an IRES.

Neuronal transfection. Sparse biolistic transfections of organotypic slice cultures were performed as previously described^{3,40}. Briefly, 80 μ g total of mixed plasmid DNA was coated on 1 μ m-diameter gold particles in 0.5 mM spermidine, precipitated with 0.1 mM CaCl₂, and washed four times in pure ethanol. The gold particles were coated onto PVC tubing, dried using ultra-pure N₂ gas, and stored at 4 °C in desiccant. DNA-coated gold particles were delivered with a Helios Gene Gun (BioRad). Cre expression was confirmed by mCherry epifluorescence, and replacement AMPA/KAR subunits confirmed by GFP epifluorescence.

For *in utero* electroporations, ~E15.5 pregnant *Gria1*^{-3^{fl/fl}} mice were anaesthetized with 2.5% isoflurane in O₂ and injected with buprenorphine for analgesic. Embryos within the uterus were temporarily removed from the abdomen and injected with 2 μ l of mixed plasmid DNA into the left ventricle via a bevelled micropipette. pFUGW-Cre:mCherry was typically diluted to approximately 0.5 μ g μ l⁻¹ in 2–3 μ g μ l⁻¹ of the replacement pFUGW AMPAR or pCAGGS GluK1 plasmid. Each embryo was electroporated with 5 \times 50 ms, 35 V pulses. The positive electrode was placed in the lower right hemisphere and the negative electrode placed in the upper left hemisphere⁴¹. After electroporation, the embryos were sutured into the abdomen, and killed on P17–20 for LTP recording. For further detail on electroporation, please see ref. 42.

Electrophysiology. Voltage-clamp recordings were taken from CA1 pyramidal neurons in either acute hippocampal slices or organotypic slice cultures. For acute slices, 300 μ m transverse slices were cut using a Microslicer DTK-Zero1 (Ted Pella) in chilled high sucrose cutting solution containing (in mM): 2.5 KCl, 7 MgSO₄, 1.25 NaH₂PO₄, 25 NaHCO₃, 7 glucose, 210 sucrose, 1.3 ascorbic acid, 3 sodium pyruvate. The slices were then incubated for 30 min at 34 °C in artificial cerebral spinal fluid (aCSF) containing (in mM): 119 NaCl, 2.5 KCl, 1 NaH₂PO₄, 26.2 NaHCO₃ and 11 glucose. For acute slices, 2.5 mM CaCl₂ and 1.3 mM MgSO₄ were added to the aCSF, and for organotypic slice cultures 4 mM CaCl₂ and MgSO₄ were added. The aCSF was bubbled with 95% O₂ and 5% CO₂ to maintain pH, and the acute slices allowed to recover at room temperature for 45 min to 1 h. Cultured slices were prepared as previously described³⁹, and recorded between 7–24 days *in vitro* (DIV) depending on the experiment. During recording, slices were transferred to a perfusion stage on an Olympus BX51WI upright microscope

and perfused at 2.5 ml min⁻¹ with aCSF containing 0.1 mM picrotoxin for acute slices experiments, and 0.01 mM gabazine, and 2–5 μ M 2-Cl⁻ adenosine for organotypic slice cultures. Synaptic responses were evoked by stimulating with a monopolar glass electrode filled with aCSF in stratum radiatum of CA1. To ensure stable recording, membrane holding current, input resistance, and pipette series resistance were monitored throughout recording. Data were gathered through a MultiClamp 700B amplifier (Axon Instruments), filtered at 2 kHz, and digitized at 10 kHz.

Whole-cell synaptic recordings and LTP. Simultaneous dual whole-cell recordings were made between GFP and/or mCherry positive experimental cells as identified by epifluorescence, and neighbouring non-transfected control cells. Internal recording solution contained (in mM): 135 CsMeSO₄, 8 NaCl, 10 HEPES, 0.3 EGTA, 5 QX-314, 4 Mg-ATP, 0.3 Na-GTP, and 0.1 spermine. Osmolarity was adjusted to 290–295 mOsm, and pH buffered at 7.3–7.4. AMPAR- and KAR-mediated responses were isolated by voltage-clamping the cell at -70 mV, whereas NMDA responses were recorded at +40 mV, with amplitudes taken 100 ms after stimulation to avoid contamination by AMPA receptor current. Paired-pulse ratios of AMPAR EPSCs were taken by stimulating twice at a 40-ms interval. To examine AMPA receptor rectification, 0.1 mM AP5 (D(-)-2-amino-5-phosphonopivalic acid) was washed in to block NMDA receptors. LTP was induced by stimulating at 2 Hz for 90 s while clamping the cell at 0 mV, after recording a stable 3–5 min baseline, but not more than 6 min after breaking into the cell. To minimize run-up of baseline responses during LTP, slices were stimulated for ~10 min before breaking in, and both cells held cell-attached for 2–5 min before breaking into the whole cell. Before breaking in, stimulation intensity was calibrated just below the threshold required to elicit an action potential from the wild-type control neuron. Rectification was calculated as the ratio of the slopes of the lines connecting AMPA EPSC amplitude from 0 to +40 mV and from -70 mV to 0 mV. This calculation can be taken as follows: $RI = 7(I_{40} - I_0)/(I_0 - I_{70})$ where I_x represent EPSC amplitude at x mV.

Outside-out patches. Outside-out patches were taken from CA1 cells by obtaining whole-cell access to CA1 pyramidal neurons at -70 mV with a 4–5 M Ω patch pipette, then slowly pulling the pipette away from the soma until a high-resistance seal reformed. HEPES-aCSF containing (in mM) 150 NaCl, 2.5 KCl, 10 HEPES, 10 glucose, 1 MgCl₂, 2 CaCl₂, 0.1 AP5, 0.1 picrotoxin, 0.1 cyclothiazide and 0.5 μ M TTX was then perfused over the tip of the pipette. Glutamate and kainate currents were evoked by perfusion of HEPES-ACSF containing 1 mM L-glutamic acid and 1 mM kainic acid, respectively. A ValveLink 8 (AutoMate Scientific Inc.) was used for fast perfusion of control, glutamate and kainate containing HEPES-aCSF. During outside-out patch experiments, experimental cells were interleaved with non-transfected control cells. Rectification was calculated as in synaptic experiments.

Statistics. For all experiments involving unpaired data, including all outside-out patch data, a Mann–Whitney *U*-test with Bonferroni correction for multiple comparisons was used. For all experiments using paired whole-cell data, including all synaptic replacement and synaptic overexpression, a two-tailed Wilcoxon signed-rank test was used. LTP data were gathered as pairs of control and experimental neurons, but occasionally during experiments one of the cells would be lost. Comparisons were therefore made using the Mann–Whitney *U*-test, and the reported *n* values represent the number of cells at the end of each experiment. Data analysis was carried out in Igor Pro (Wavemetrics), Excel (Microsoft), and R (The R Project for Statistical Computing, <http://www.r-project.org/>).

Energy release in the solar corona from spatially resolved magnetic braids

J. W. Cirtain¹, L. Golub², A. R. Winebarger¹, B. De Pontieu³, K. Kobayashi⁴, R. L. Moore¹, R. W. Walsh⁵, K. E. Korreck², M. Weber², P. McCauley², A. Title³, S. Kuzin⁶ & C. E. DeForest⁷

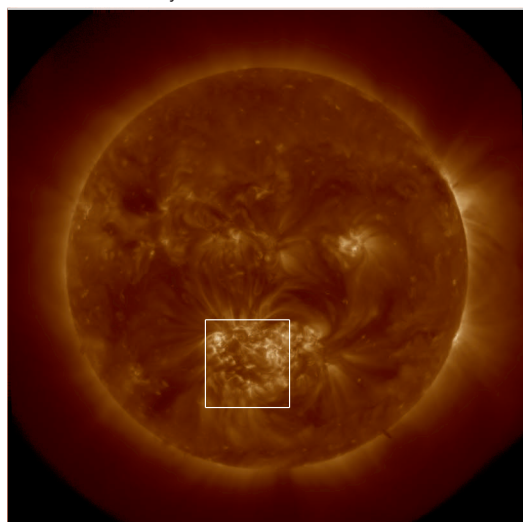
It is now apparent that there are at least two heating mechanisms in the Sun's outer atmosphere, or corona^{1–5}. Wave heating may be the prevalent mechanism in quiet solar periods and may contribute to heating the corona to 1,500,000 K (refs 1–3). The active corona needs additional heating to reach 2,000,000–4,000,000 K; this heat has been theoretically proposed^{6–12} to come from the reconnection and unravelling of magnetic 'braids'. Evidence favouring that process has been inferred^{13,14}, but has not been generally accepted because observations are sparse and, in general, the braided magnetic strands that are thought^{1–3,15–17} to have an angular width of about 0.2 arc seconds have not been resolved^{10,18–20}. Fine-scale braiding has been seen^{21,22} in the chromosphere but not, until now, in the corona. Here we report observations, at a resolution of 0.2 arc seconds, of magnetic braids in a coronal active region that are reconnecting, relaxing and dissipating sufficient energy to heat the structures to about 4,000,000 K. Although our 5-minute observations cannot unambiguously identify the field reconnection and subsequent relaxation as the dominant heating mechanism throughout active regions, the energy available from the observed field relaxation in our example is ample for the observed heating.

Observations of the solar atmosphere in the visible and infrared spectral ranges have been made from ground-based instruments on ~0.2-arcsec spatial scales, in particular in H α emission, and these show coherent structures 0.2 arcsec in diameter²¹. But for the ultraviolet and

X-ray emission corresponding to temperatures in excess of 100,000 K, there is a paucity of data. Detecting these wavelengths requires the use of instruments outside Earth's atmosphere, and observations so far, including those of the NASA Atmospheric Imaging Assembly²³ (AIA) instrument at present operating on the Solar Dynamics Observatory (SDO), have been limited to a resolution of about 1.0 arcsec. The High-resolution Coronal Imager (Hi-C; see Supplementary Fig. 1) was launched on a sounding rocket on 11 July 2012 and took images of the 1,500,000-Kelvin (1.5-MK) corona with a resolution of 0.2 arcsec (roughly 150 km). The Hi-C passband isolates a very narrow window in the extreme ultraviolet, centred at 193 Å. It is dominated by emission lines of Fe XII with a peak temperature of formation of 1.5 MK. AIA has an identical channel that images the full solar disk (Fig. 1; see also Supplementary Video 1).

The data from Hi-C show evidence of magnetic field braiding and axial twist in loops along their length, reconnection and consequent heating in the low corona, whereas the simultaneous images from AIA/SDO at a resolution of 1.2 arcsec (900 km) do not resolve the braiding. We have studied the intensity of emission in a loop at several AIA wavelengths covering more than two orders of magnitude in temperature (Fig. 2), and found that the twist in the structures increases during the observations (Supplementary Fig. 2 and Supplementary Video 2). After the end of the Hi-C observations, a small flare observed by AIA peaks at the intersection of the converging strands (indicated

a AIA 193 Å: 11 July 2012 18:55:07



b Hi-C 193 Å: 11 July 2012 18:55:20

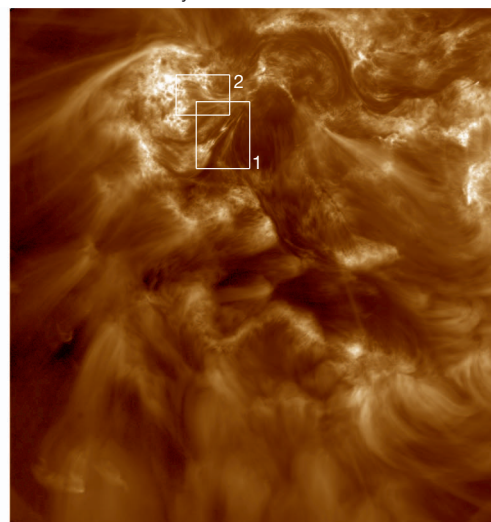


Figure 1 | The 1.5-MK sun. **a**, The co-temporal 1-arcsec-resolution AIA full-sun image (11 July 2012, 18:55 UT) using the 193 Å passband. The field of view for the Hi-C rocket flight is indicated by the box. **b**, The full Hi-C field-of-view

image. The two boxes show the locations of the examples that are discussed in the text and shown in Fig. 2 (box 1) and Fig. 3 (box 2). The Hi-C experiment is described in Supplementary Fig. 1.

¹Marshall Space Flight Center, NASA, Mail Code ZP13, MSFC, Alabama 36812, USA. ²Harvard-Smithsonian Center for Astrophysics, 60 Garden Street, Cambridge, Massachusetts 02138, USA. ³Lockheed Martin Solar and Astrophysics Laboratory, 3251 Hanover Street, Palo Alto, California 94304, USA. ⁴Center for Space and Aeronautics Research, University of Alabama-Huntsville, 320 Sparkman Avenue, Huntsville, Alabama 35812, USA. ⁵University of Central Lancashire, Preston, Lancashire PR1 2HE, UK. ⁶Lebedev Physical Institute, 53 Leninski Prospekt, 119991 Moscow, Russia. ⁷Southwest Research Institute, Instrumentation and Space Research Division, 1050 Walnut Street, Suite 300, Boulder, Colorado 80302, USA.

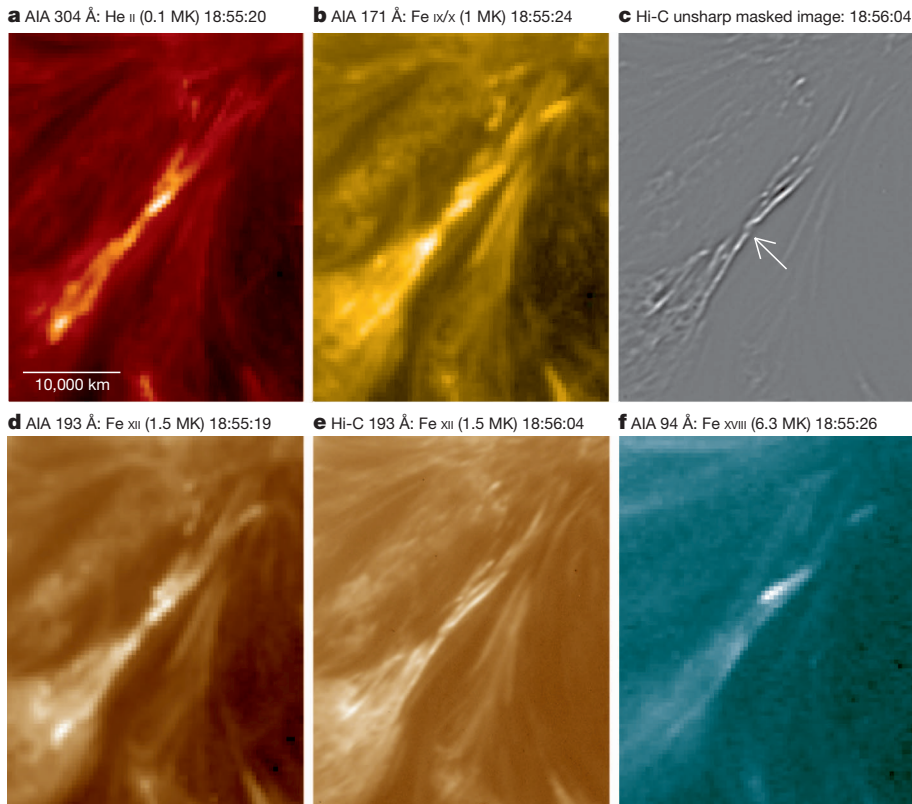


Figure 2 | A coronal loop seen at several different coronal temperatures by AIA and Hi-C. Labels indicate the passbands, the dominant emitting ion and the peak formation temperature of the ion. The image in **c** was constructed by smoothing the original image (**e**) and subtracting the processed image from the original. This ‘unsharp mask’ version of the Hi-C data enhances the shapes of fine-scale structures in the image relative to the image background. All panels show a narrow magnetic arch that Hi-C resolves to be twisted along its length. The twisted loops converge and appear to intersect (arrow in **c**). A C1.7 flare centred on this intersection is seen in the AIA images about 3 min after the Hi-C flight (Supplementary Video 1).

by an arrow in Fig. 2c, Supplementary Fig. 2 and Supplementary Video 2). At the location of the flare, strong (150 km s^{-1}) outflows of plasma from the reconnection region are observed. These twisting loops are sheared across a polarity inversion line in magnetic field in the photosphere (field

strength, 10^3 G ; see magnetogram in Supplementary Fig. 3), along which strong shearing flows are present (Supplementary Video 3). Using the Extreme-ultraviolet Imaging Spectrometer²⁴ observations from the Japan Aerospace Exploration Agency’s Hinode spacecraft, we have determined

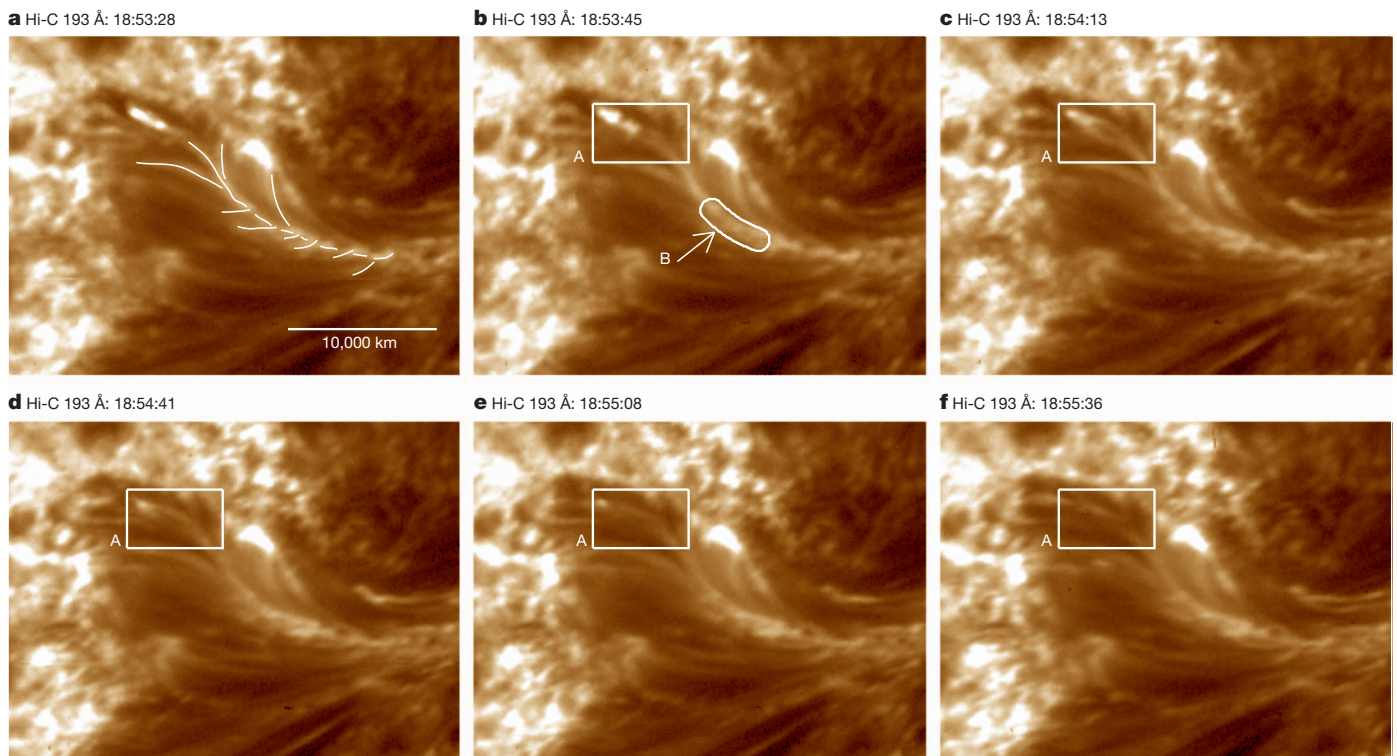


Figure 3 | A time series from Hi-C data. Box A is centred on a location in the braided structure where multiple loops converge and wind about each other. In **a**, we trace along several of the features to guide the eye. As the time sequence proceeds, the loops unwind, as evidenced by the structural changes shown in

box A, discernible by comparing **c** with **f** (see also Supplementary Video 2). Area B in **b** highlights a section of the loop ensemble that is found to unwind or simplify during the observation period.

the density of the loops to be $10^{10} e^- \text{ cm}^{-3}$ (where e is electrons) and the peak temperature to be ~ 7 MK. The structure heats to this peak temperature in 42 s, and then cools in roughly the radiative cooling time, 13 min. The example shown in Fig. 2 is found to generate many such transient events near the location indicated with the arrow (Fig. 2c). AIA data in several passbands show repeated impulsive events, but at the lower resolution of AIA only the increases in intensity are observable—the structural changes in the loops remain unresolved.

In a second example, Hi-C observed a small bundle of loops that are wrapped or braided about each other along their length (Fig. 3). The AIA telescopes also observed this bundle of loops, but saw it as a single structure. The braided loop ensemble is visible over the temperature range 0.1–3 MK. Higher-temperature loops are rooted close to the footpoints of the braided loops, that is, the points at which the loops intersect the photosphere, and are observed in the soft-X-ray range at 4–6 MK. In box A at the end of the braided structure (Fig. 3b), the twist in the loops simplifies and eastward high-speed outflows at 100–150 km s^{-1} along this fan of loops persist throughout the observations (Supplementary Video 3). The bundle's axial field strength estimated from observations is 500 G. We can determine the pitch angle of the twist of the bundle by estimating the number of braids along the length of the bundle (Fig. 3a) and, hence, the strength of the azimuthal component (B_ϕ) of the magnetic field. We count roughly five braids, giving an azimuthal field of order 100 G. The amount of free energy is of order $(B_\phi)^2 V / 8\pi$, where V is the volume of the bundle, which we have estimated to be approximately 10^{11} km^3 . This yields a total free energy of order 10^{29} erg .

At plasma temperatures of 1 MK, the speed of sound is $\sim 100 \text{ km s}^{-1}$ and the observed outflows at $\sim 100 \text{ km s}^{-1}$ are therefore indicative of plasma pressure driving mass motion along the field as the plasma is heated locally and expands at the speed of sound into lower-pressure locations along the braided loops. As is the case for the first example, this braided bundle seems to be heated as the free energy stored in the twisting or braiding of the magnetic field is dissipated by means of reconnection. We have summed the emission observed by AIA from the bundle in area B in Fig. 3e to form light curves (Fig. 4; see also Supplementary Video 4). These curves show the duration of the heating and the initial sharp increase in emission and subsequent decay. The event lasts for about 12 min, for the return from the peak to the basal emission level. The radiated energy from this event can be calculated from the light curves and density and is found to be $\sim 10^{26} \text{ erg}$; about $\sim 0.1\%$ of the stored energy in the braided ensemble is converted into

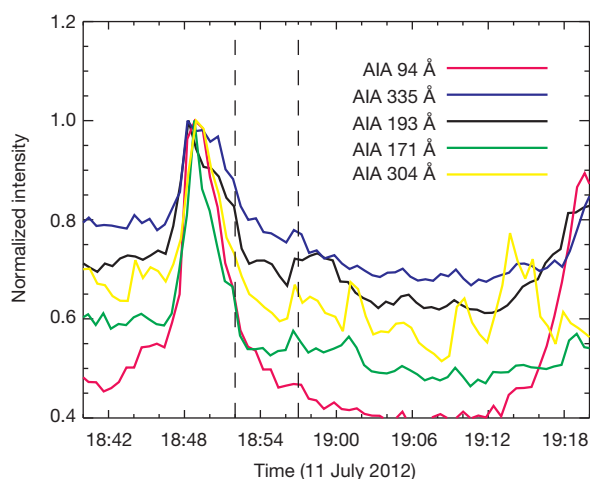


Figure 4 | The light curves for example two. The light curves from multiple AIA channels for area B in Fig. 3b show the increase in intensity for the braided ensemble of loops just before the Hi-C flight. The start and end of the Hi-C flight are indicated by the vertical dashed lines in the plot. The intensities for all passbands decrease over a 10-min period. The heating process shown here repeats several times per hour over the 12 or more hours the structure is present in the AIA data.

thermal energy to power the observed radiation. This braided bundle of loops, seen in the AIA data as a single broader loop, is observed for over 12 h and brightens repeatedly over the AIA observation period.

Several instances of braiding and loop-to-loop interaction were visible to Hi-C during its brief flight: the two examples seen here are the clearest. These observations demonstrate that the active region corona, at a spatial scale of approximately 150 km, is replete with current-laden locations that provide sites for the dissipation of magnetic free energy. The observations show magnetic fields that are braided, and not simply twisted. By reconnecting, presumably at current sheets between entwined flux strands, the braided loops release energy into the corona. The braiding is driven by the ubiquitous small-scale, convection-driven motion of the photospheric feet of the magnetic field, and thus provides a d.c. (that is, non-wavelike) energy source for the corona.

Received 27 August; accepted 1 November 2012.

1. Wedemeyer-Böhm, S. *et al.* Magnetic tornadoes as energy channels into the solar corona. *Nature* **486**, 505–508 (2012).
2. McIntosh, S. *et al.* Alfvénic waves with sufficient energy to power the quiet solar corona and fast solar wind. *Nature* **475**, 477–480 (2011).
3. De Pontieu, B. *et al.* Chromospheric Alfvénic waves strong enough to power the solar wind. *Science* **318**, 1574–1577 (2007).
4. Cirtain, J. *et al.* Evidence for Alfvén waves in solar X-ray jets. *Science* **318**, 1580–1582 (2007).
5. Priest, E. *et al.* Nature of the heating mechanism for the diffuse solar corona. *Nature* **393**, 545–547 (1998).
6. Parker, E. Magnetic neutral sheets in evolving fields. I. General Theory. *Astrophys. J.* **264**, 635–641 (1983).
7. Parker, E. Magnetic neutral sheets in evolving fields. II. Formation of the solar corona. *Astrophys. J.* **264**, 642–647 (1983).
8. Schrijver, K. Braiding-induced interchange reconnection of the magnetic field and the width of solar coronal loops. *Astrophys. J.* **662**, L119–L122 (2007).
9. Gudiksen, B. V. & Nordlund, Å. An ab initio approach to the solar coronal heating problem. *Astrophys. J.* **618**, 1020–1030 (2005).
10. Klimchuk, J. On solving the coronal heating problem. *Sol. Phys.* **234**, 41–77 (2006).
11. Gold, T. in *Stellar and Solar Magnetic Fields* (ed. Lüst, R.) 390–398 (Proc. IAU Symp. 22, International Astronomical Union, 1965).
12. Warren, H. P., Winebarger, A. R. & Hamilton, P. S. Hydrodynamic modeling of active region loops. *Astrophys. J.* **579**, L41–L44 (2002).
13. Schrijver, K. *et al.* Large-scale coronal heating by the small-scale magnetic field of the Sun. *Nature* **394**, 152–154 (1998).
14. Lee, J. *et al.* Coronal currents, magnetic fields, and heating in a solar active region. *Astrophys. J.* **501**, 853–865 (1998).
15. De Pontieu, B. *et al.* Observing solar coronal heating in the chromosphere. *Astrophys. J.* **701**, L1–L6 (2009).
16. De Pontieu, B. *et al.* The origins of hot plasma in the solar corona. *Science* **331**, 55–58 (2011).
17. DeForest, C. E. On the size of structures in the corona. *Astrophys. J.* **661**, 532–542 (2007).
18. Berger, M. & Asgari-Targhi, M. Self-organized braiding and the structure of coronal loops. *Astrophys. J.* **705**, 347–355 (2009).
19. van Ballegoijen, A. Heating of the solar chromosphere and corona by Alfvén wave turbulence. *Astrophys. J.* **736**, 3–9 (2011).
20. Malanushenko, A., Yusuf, M. H. & Longcope, D. Direct measurements of magnetic twist in the solar corona. *Astrophys. J.* **736**, 97–109 (2011).
21. Rutten, R. H α as chromospheric diagnostic. *ASP Conf. Ser.* **397**, 54–58 (2008).
22. Martin, S. Conditions for the formation and maintenance of filaments. *Sol. Phys.* **182**, 107–137 (1998).
23. Lemen, J. R. *et al.* The Atmospheric Imaging Assembly (AIA) on the Solar Dynamics Observatory (SDO). *Sol. Phys.* **275**, 17–40 (2012).
24. Culhane, J. *et al.* The EUV imaging spectrometer for Hinode. *Sol. Phys.* **243**, 19–61 (2007).

Supplementary Information is available in the online version of the paper.

Acknowledgements We thank the NASA Low-Cost Access to Space programme for supporting the development of the Hi-C instrument, the NASA Sounding Rocket Office for the launch of the instrument and the NASA Marshall Space Flight Center for instrument development support. This LPI work was supported in part by the Russian Foundation for Basic Research (project 11–02–01079-a), Program No. 22 of the Presidium of the Russian Academy of Sciences.

Author Contributions J.W.C., A.R.W., B.D.P., P.M. and C.E.D. performed image processing and analysis of observations. M.W., K.K., B.D.P., C.E.D. and A.R.W. all contributed to the calibration and alignment of the instrument and science data. J.W.C., L.G., K.K. and K.E.K. managed the design, construction and testing of the experiment. J.W.C. and A.R.W. determined velocities and J.W.C. and R.L.M. calculated the stored energy. A.T., R.W.W. and S.K. contributed to the instrumentation.

Author Information Reprints and permissions information is available at www.nature.com/reprints. The authors declare no competing financial interests. Readers are welcome to comment on the online version of the paper. Correspondence and requests for materials should be addressed to J.W.C. (jonathan.w.cirtain@nasa.gov).

Laser cooling of a semiconductor by 40 kelvin

Jun Zhang^{1*}, Dehui Li^{1*}, Renjie Chen¹ & Qihua Xiong^{1,2}

Optical irradiation accompanied by spontaneous anti-Stokes emission can lead to cooling of matter, in a phenomenon known as laser cooling, or optical refrigeration, which was proposed by Pringsheim in 1929¹. In gaseous matter, an extremely low temperature can be obtained in diluted atomic gases by Doppler cooling², and laser cooling of ultradense gas has been demonstrated by collisional redistribution of radiation³. In solid-state materials, laser cooling is achieved by the annihilation of phonons, which are quanta of lattice vibrations, during anti-Stokes luminescence. Since the first experimental demonstration in glasses doped with rare-earth metals⁴, considerable progress has been made, particularly in ytterbium-doped glasses or crystals: recently a record was set of cooling to about 110 kelvin from the ambient temperature, surpassing the thermoelectric Peltier cooler^{5,6}. It would be interesting to realize laser cooling in semiconductors, in which excitonic resonances dominate^{7–9}, rather than in systems doped with rare-earth metals, where atomic resonances dominate. However, so far no net cooling in semiconductors has been achieved despite much experimental^{10–12} and theoretical^{7–9,13,14} work, mainly on group-III–V gallium arsenide quantum wells. Here we report a net cooling by about 40 kelvin in a semiconductor using group-II–VI cadmium sulphide nanoribbons, or nanobelts, starting from 290 kelvin. We use a pump laser with a wavelength of 514 nanometres, and obtain an estimated cooling efficiency of about 1.3 per cent and an estimated cooling power of 180 microwatts. At 100 kelvin, 532-nm pumping leads to a net cooling of about 15 kelvin with a cooling efficiency of about 2.0 per cent. We attribute the net laser cooling in cadmium sulphide nanobelts to strong coupling between excitons and longitudinal optical phonons (LOPs), which allows the resonant annihilation of multiple LOPs in luminescence up-conversion processes, high external quantum efficiency and negligible background absorption. Our findings suggest that, alternatively, group-II–VI semiconductors with strong exciton–LOP coupling could be harnessed to achieve laser cooling and open the way to optical refrigeration based on semiconductors.

Optical refrigeration has the advantages of compactness, freedom from vibration and the need for cryogen, high reliability¹⁵, and could have applications in all-solid-state cryocoolers¹⁶ and athermal or self-cooling lasers¹⁵. Although net cooling has primarily been demonstrated in a variety of rare-earth metal (REM)-doped glasses and crystals^{4,5,15–17}, the laser cooling of direct-bandgap semiconductors, for example gallium arsenide (GaAs), is more appealing because semiconductors allow more efficient pump light absorption, much lower achievable cooling temperatures and direct integrability into electronic and photonic devices^{10–12,18}. Nevertheless, the net cooling of a GaAs-based semiconductor has inherent impediments due to high background absorption and low luminescence extraction efficiency, although anti-Stokes up-conversion can be readily achieved^{9,11,12,18}.

According to Sheik-Bahae/Epstein (SBE) theory^{9,19}, the cooling efficiency, $\eta_c(h\nu, T)$, of optical refrigeration in semiconductors is given by

$$\eta_c(h\nu, T) = \eta_{\text{exe}} \eta_{\text{abs}} \frac{\bar{\nu}_f(T)}{\nu} - 1 \quad (1)$$

Here ν is the pump laser frequency, T is the absolute temperature of the sample, $\bar{\nu}_f(T)$ is the mean emission frequency and h is Planck's constant; η_{exe} is the external quantum efficiency, written as $\eta_{\text{exe}} = \eta_e W_{\text{rad}} / (\eta_e W_{\text{rad}} + W_{\text{nr}})$, where η_e is the luminescence extraction efficiency and W_{rad} and W_{nr} are respectively the radiative and non-radiative recombination rates; and $\eta_{\text{abs}} = [1 + \alpha_b / \alpha(\nu, T)]^{-1}$ is the absorption efficiency, quantifying the percentage of photons absorbed that are engaged in cooling, where α_b is the background absorption coefficient and $\alpha(\nu, T)$ is the semiconductor absorption coefficient. Net laser cooling requires $\eta_c(h\nu, T) > 0$, which might be achieved in three related ways: having a large energy difference $\Delta E = h\bar{\nu}_f(T) - h\nu$; having η_{exe} approach unity; and having η_{abs} approach unity through the minimization of the background absorption, α_b .

In the classical Pringsheim picture applied to solids, each cooling cycle removes $\Delta E = h\bar{\nu}_f(T) - h\nu \approx k_B T$ during the thermalization of cold electrons and holes, owing to absorption of various phonons. In GaAs, single LOP-assisted transitions in band-tail absorption (Urbach tail) have been proposed to facilitate laser cooling^{20,21}. It has also been proposed that the band structure can be engineered, for example by introducing donor–acceptor pairs, which modifies the density of states and could lead to a larger ΔE , making the dependence on the other two factors (η_{exe} and η_{abs}) less important. However, experimentally that is difficult to achieve because the doping density and binding energies of both donors and acceptors have to be simultaneously optimized. We find that strong exciton–LOP coupling in II–VI semiconductors such as cadmium sulphide (CdS) can be harnessed to facilitate laser cooling by the annihilation of one or more LOPs, leading to the removal of several $k_B T$ units of heat in each cooling cycle.

Figure 1a shows the anti-Stokes photoluminescence spectra of a CdS nanobelt excited by a 532-nm laser (bottom) and a 514-nm laser (top) at 294 K at three different pumping powers. Strong anti-Stokes photoluminescence with a peak position of ~ 506 nm is identified, facilitated by resonant annihilation of multiple LOPs (one for the 514-nm laser and three for the 532-nm laser; $h\nu_{\text{LO}} \approx 37$ meV, or 300 cm^{-1}). We note that 514-nm pumping led to much stronger up-conversion, owing to stronger band-tail absorption. Systematic study of the anti-Stokes photoluminescence intensity as a function of laser power (Fig. 1b) indicates that two-photon absorption can be excluded at low-to-moderate power (below ~ 12 mW), at which our laser cooling experiments are conducted. Further analysis of the Stokes and anti-Stokes Raman spectra reveals that both the LOP anti-Stokes component and the 2LOP anti-Stokes component are stronger than their Stokes counterparts, suggesting that multiple-LOP annihilation dominates over the LOP creation process. This dominance of the anti-Stokes component can be readily achieved in CdS under resonant conditions, that is, when the laser energy is red-detuned from the exciton energy by roughly an integer multiple of $h\nu_{\text{LO}}$ (Supplementary Fig. 3a). Following the theory in ref. 22, we evaluate the Huang–Rhys factor, S , which quantifies the exciton–LOP coupling strength (Supplementary Information, part 2). As shown in Supplementary Fig. 3b, we find that S is considerably enhanced in CdS on the nanoscale, in good agreement with a recent report on ZnTe nanorods²³. Therefore, we speculate that the resonant

¹Division of Physics and Applied Physics, School of Physical and Mathematical Sciences, Nanyang Technological University, 637371, Singapore. ²Division of Microelectronics, School of Electrical and Electronic Engineering, Nanyang Technological University, 639798, Singapore.

*These authors contributed equally to this work.

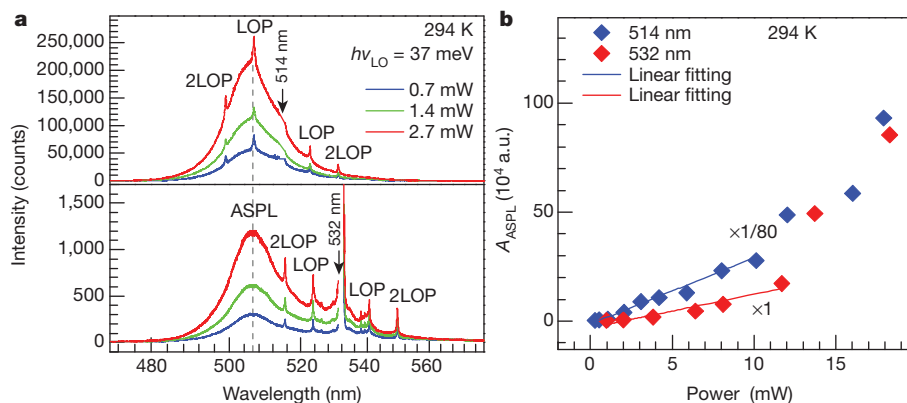


Figure 1 | Multiple-LOP-assisted up-conversion spectra of CdS nanobelts. **a**, Room temperature anti-Stokes photoluminescence (ASPL) spectra of a single, 100-nm-thick CdS nanobelt excited by a 514-nm (top) and a 532-nm (bottom) laser at three power levels. **b**, Power dependence of anti-Stokes

photoluminescence pumped at 532 and 514 nm and at 294 K. Below ~ 12 mW, the intensity scales linearly with power. Two-photon-absorption-induced photoluminescence starts to take effect only at high power. A_{ASPL} , integrated peak area of anti-Stokes photoluminescence. a.u., arbitrary units.

annihilation of one or more LOPs facilitates the up-conversion in CdS nanobelts owing to the resulting increase in the exciton–LOP coupling, leading to the removal of multiple $k_B T$ units of heat in each cooling cycle. The microscopic mechanism by which multiple LO phonons are actually involved in the up-conversion still remains to be addressed within the framework of higher-order exciton–LOP coupling.

Next we systematically evaluate the dependence of ΔE on pump power and temperature (between 77 and 340 K) when pumped by 514- and 532-nm lasers (Methods Summary). Cooling is possible only if ΔE is positive. Therefore, the sign and magnitude of ΔE at a defined temperature have important implications for the cooling potential. Figure 2a and Fig. 2b show the temperature evolution of anti-Stokes

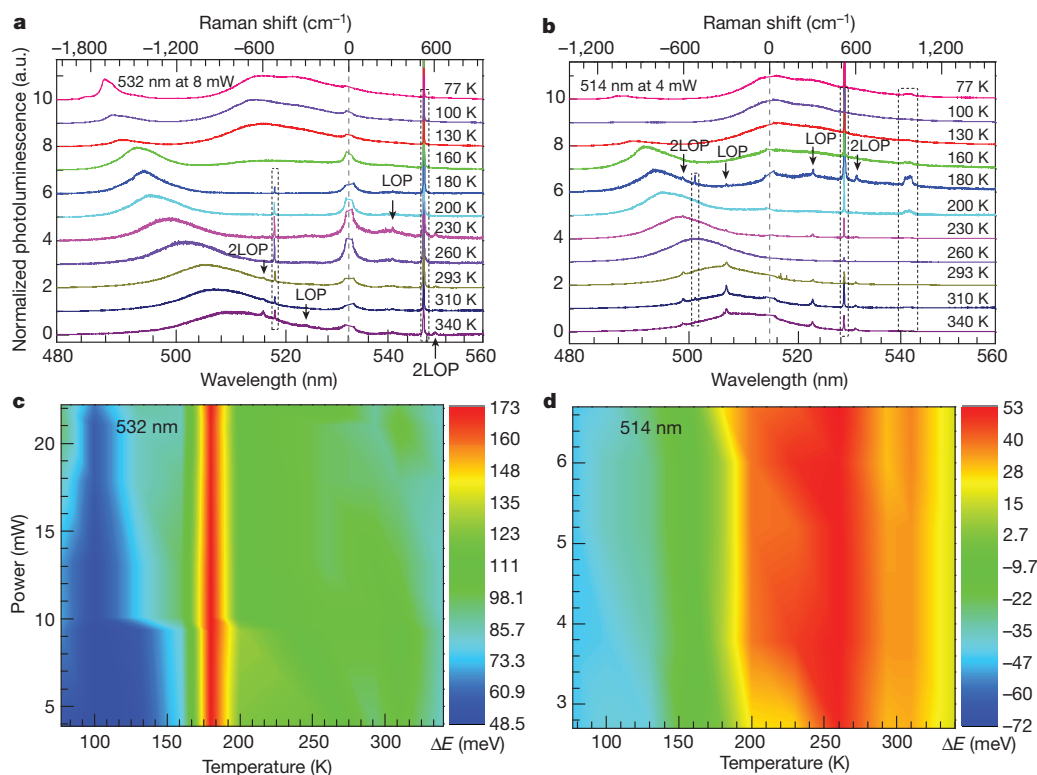


Figure 2 | Surface plot of ΔE as a function of temperature and pump power. **a**, Anti-Stokes photoluminescence spectra taken from 77 to 340 K using an 8.0-mW, 532-nm laser. As the temperature is decreased from 340 to 180 K, the photoluminescence peak gradually blueshifts. Below ~ 180 K, donor–acceptor pair (DAP) emission becomes pronounced. Both DAP and exciton emissions blueshift marginally. **b**, Anti-Stokes photoluminescence spectra of the same nanobelt excited by a 4.0-mW, 514-nm laser. Below 200 K, DAP emission peaks appear and dominate the spectra. The spectra are offset vertically for clarity, with vertical dashed lines indicating the wavelengths of the pump lasers and dashed boxes indicating the first-order anti-Stokes (-520 cm^{-1}), first-order Stokes (520 cm^{-1}) and second-order (980 cm^{-1}) Raman features from the silicon substrate in **a** and

b, ΔE as a function of temperature and power for 532-nm pumping. The maximum energy difference, of ~ 173 meV, is obtained at around 180 K. Below 180 K, DAP emission peaks (**a**) appear and lead to pronounced redshifts of the mean wavelength of luminescence. **d**, ΔE surface plot for 514-nm pumping. The maximum ΔE , of ~ 52.5 meV, is achieved at around 200 K. Below 200 K, the DAP emission peaks (**b**) appear and dominate the spectra, leading to the redshift of the mean wavelength of luminescence. Because the DAP energy levels resonate approximately with the pump laser, the DAP emission is much stronger than the exciton emission, which causes ΔE to be negative below 180 K, suggesting that no net cooling is achievable using 514-nm pumping. In both **c** and **d**, Si Raman features are excluded before the mean emission wavelength is evaluated.

photoluminescence spectra for laser excitation at 532 nm (8.0 mW) and 514 nm (4.0 mW), respectively. Detailed peak assignment to the excitons and donor–acceptor pairs (DAP) is referred to in Supplementary Information, parts 2–3. By extracting the mean emission frequency, we can obtain surface plots of $\Delta E = h\nu_f(T) - h\nu$ (Fig. 2c, d). For the 532-nm pumping, a maximum ΔE of ~ 173 meV is reached at around 180 K. With a further decrease in temperature, DAP emission begins and leads to a reduction in ΔE . Over the whole temperature range we investigate (77–340 K), ΔE remains positive, indicating that net cooling is possible. For the 514-nm pumping, a maximum ΔE of ~ 53 meV is reached at around 200 K, below which DAP emission begins, leading to a transition from a positive to a negative ΔE at around 180 K. Therefore, it is impossible to achieve net cooling below 180 K when pumping at 514 nm, in good agreement with our cooling experiments to be discussed (see below). Over the power range we investigate, no strong dependence of ΔE on power is observed, as manifested by the vertically striped bands in the surface plots (Fig. 2c, d). However, net laser cooling is possible only below 12 mW, because the two-photon process will dominate the luminescence up-conversion when a higher power is used (Supplementary Information, part 3.2).

We use a pump–probe luminescence thermometry (PPLT) technique to measure the laser cooling with the sample image, set-up and time sequence as shown in Fig. 3. The main idea is to use the temperature dependence of the Stokes photoluminescence peak position for non-contact local thermometry, essentially similar to differential luminescence thermometry¹⁹ (Supplementary Information, part 3.1). Nevertheless, in our laser cooling experiments the change in temperature is sufficient for our high-resolution spectrometer to detect cooling from the shifting of the luminescence peak to shorter

wavelengths. We use a solid-state, 532-nm laser and an argon ion laser (variously 514, 502 and 488 nm) as pump lasers, and use a solid-state, 473-nm laser as a probe beam to measure the cooling or heating. The CdS nanobelts are suspended to decrease the thermal conduction through substrates and to improve the luminescence extraction efficiency on hole-patterned SiO₂/Si substrates (Methods Summary).

We first measure and evaluate the temperature calibration curves by monitoring the peak shift of the photoluminescence spectrum of the CdS nanobelt excited by the probe beam around the starting temperatures, 290 and 100 K, respectively (Supplementary Fig. 5b, d). Then we use these calibration curves to deduce the temperature change caused by the laser cooling, ΔT . Figure 4a and Fig. 4d respectively show the Stokes photoluminescence evolution on continuous 6.3-mW, 514-nm laser pumping starting from 290 K and continuous 6.5-mW, 532-nm laser pumping starting from 100 K. After every ~ 5 min of pumping, the pump laser was momentarily blocked while each spectrum was recorded. We observe a pronounced systematic blueshift on laser pumping until a steady state is reached in ~ 30 –40 min, suggesting that a maximum net cooling is established for the given device structure and geometry. After the cooling is stopped (by switching off the pump laser), the Stokes photoluminescence shifts to longer wavelengths, indicating a temperature increase (dashed curves in Fig. 4a, d, shifted vertically for clarity). On the basis of the calibration curves, ΔT is plotted in Fig. 4b and Fig. 4e, showing respective net laser coolings of ~ 40 K for 514-nm pumping and ~ 20 K for 532-nm pumping, both at 290 K. At 100 K, only 532-nm pumping can lead to a net laser cooling of 15 K; 514-nm pumping cannot, owing to redshifting of the mean emission wavelength at 100 K, in agreement with Fig. 2b, d. Pumping at 488 and 502 nm leads to heating of the sample at all temperatures in the range investigated. Complete data for all wavelengths and temperatures are shown in Supplementary Fig. 7.

Knowledge of the absorption at the band tail is crucial to evaluating the up-conversion and laser cooling. At the single-nanobelt level, the direct measurement of optical absorption remains elusive. We have devised a photoconductivity measurement to provide a direct quantification of the absorption²⁴, which agrees well with the absorption coefficient extracted from the photoluminescence spectra based on the van Roosbroeck/Shockley equation²⁵ (Supplementary Fig. 2b). Figure 4c shows the Stokes photoluminescence (black curve) and the corresponding photoconductivity gain spectra (blue curve and, on a logarithmic scale, red curve) at 290 K. We find that at 532 nm, there is about 6% absorption compared with the maximum absorption at around 480 nm, whereas at 514 nm, the corresponding absorption is $\sim 36\%$. Figure 4f shows the normalized temperature change as a function of pump laser wavelength at 290 K (blue curve), calculated on the basis of the SBE model and an analysis of cooling power (Supplementary Information, parts 4–6). The discrete data points provide values of experimental temperature change, ΔT , pumped by four different laser lines, that are in good agreement with theoretical analysis except for that corresponding to 488 nm, which underestimates the actual heating considerably (Supplementary Information, part 6). The final cooling power depends on both ΔE and band-tail absorption. In CdS nanobelts at 290 K, 514 nm seems to be the optimal cooling wavelength with the highest cooling power. The red regions in Fig. 4c, f correspond to the laser cooling tail.

Two underlying factors make net cooling impractical in GaAs-based semiconductors. These factors are high parasitic background absorption and low luminescence extraction efficiency, both of which lead to heating and so represent the existing challenges not only in fundamental materials science but also in device engineering in laser cooling^{15,16,19}. In CdS nanobelts, each cooling cycle can remove more heat than in GaAs, as indicated by the ΔE analysis, because of the extremely strong exciton–LOP coupling (the Fröhlich coupling constant in bulk is 0.51 for CdS and 0.07 for GaAs²⁶, and is even higher on the nanoscale, as shown in Supplementary Fig. 3b) and resonant anti-Stokes up-conversion. When the pump laser (at, for example, 514 or

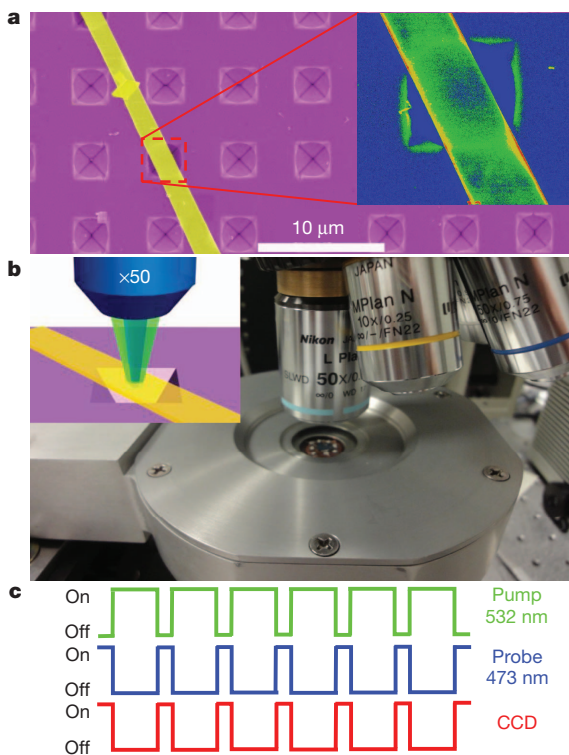


Figure 3 | Laser cooling pump–probe luminescence thermometry. **a**, False-colour scanning electron microscope image of a single CdS nanobelt suspended on a SiO₂/Si substrate. The laser cooling demonstration was conducted on the suspended segment as shown in the inset. **b**, Measurement set-up with two laser beams (pump and probe) aligned on the same spot. **c**, Time sequence of the PPLT. After every 5 min of pumping (for example, using a 532-nm laser), the pump laser was blocked momentarily and the probe Stokes photoluminescence spectrum was acquired immediately, excited by a 20- μ W, 473-nm laser. CCD, charge-coupled device.

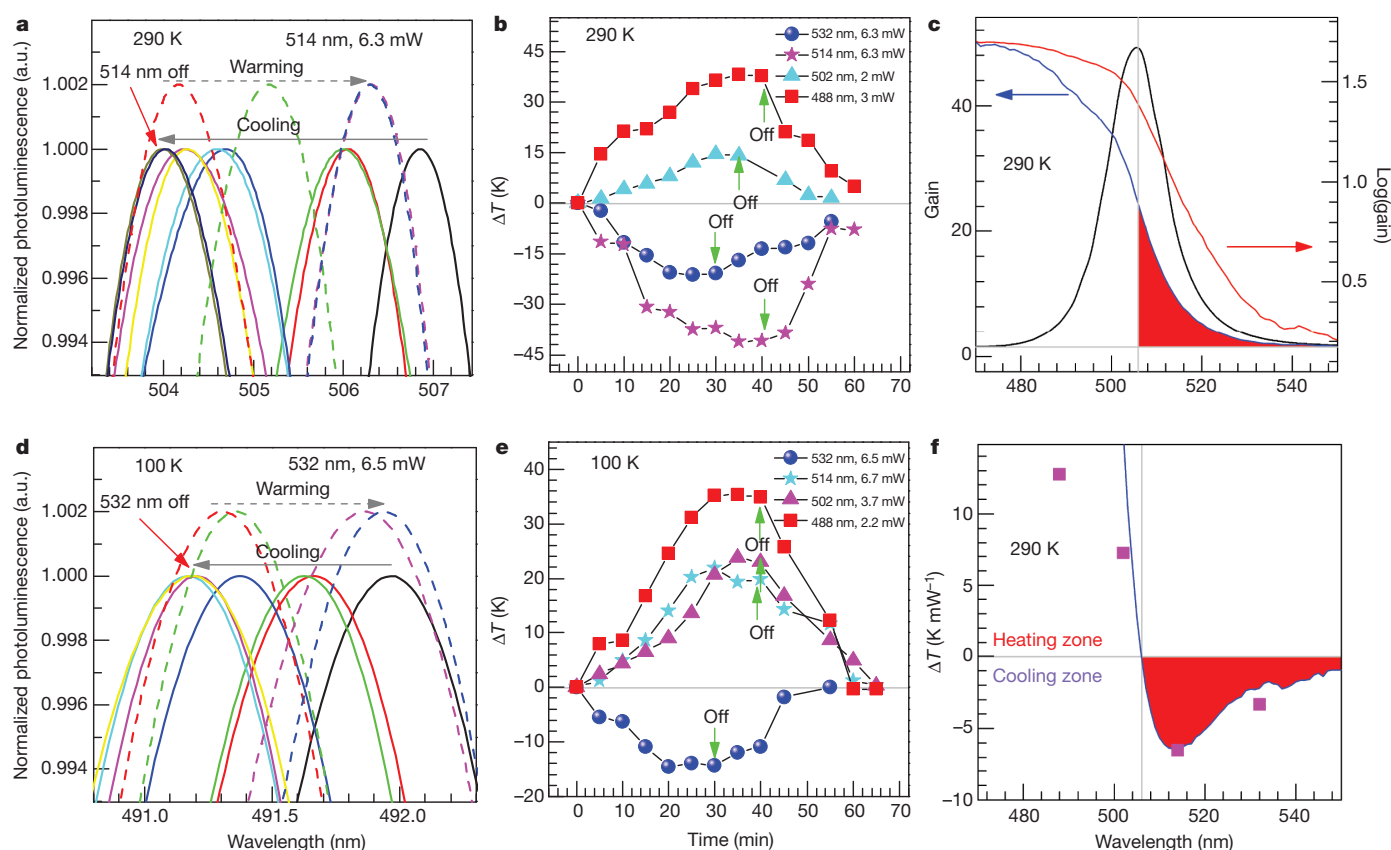


Figure 4 | Net laser cooling of CdS nanobelts. **a**, Evolution of PPLT spectra starting from 290 K, pumped by a 514-nm laser with a power of ~ 6.3 mW. Solid curves represent the cooling cycle, and the dashed curves represent the warming up after the pump laser is switched off. Dashed curves are shifted vertically for clarity. **b**, Temperature change, ΔT , versus time pumped by four laser lines (532, 514, 502 and 488 nm), using data extracted from the PPLT spectra (shown in **a** for 514-nm pumping; complete data are shown in Supplementary Fig. 7) and corresponding calibration curve around 290 K (Supplementary Fig. 5b). **c**, Photocurrent gain spectrum (linear scale, blue; logarithmic scale, red) and Stokes photoluminescence spectrum (black) of a single CdS nanobelt at 290 K. **d**, Evolution of PPLT spectra for another nanobelt

pumped by a 6.5-mW, 532-nm laser starting from 100 K (complete data are shown in Supplementary Fig. 7). We observe cooling and warming cycles similar to those in **a**. **e**, Temperature change, ΔT , versus time pumped by four laser lines (532, 514, 502 and 488 nm), using data extracted from the PPLT spectra (shown in **d** for 532-nm pumping; complete data are shown in Supplementary Fig. 7) and the corresponding calibration curve around 100 K (Supplementary Fig. 5d). **f**, Summary of measured maximum ΔT (pink squares) and theoretically calculated temperature change (blue curve) normalized to pump power for different pump wavelengths at 290 K. In **c** and **f**, the red regions correspond to the cooling zone.

532 nm) moves to the Urbach tail of CdS, the background absorption due to free carriers can no longer be ignored. Nonetheless, our analysis shows that the free-carrier absorption in a CdS nanobelt is negligible. The luminescence extraction efficiency approaches unity as a result of the subwavelength thickness of the nanobelt (Supplementary Information, part 4). We did not observe any emission at the longer-wavelength side of the pump laser wavelength (532 nm), suggesting no background absorption contribution due to defects or surface recombination.

Compared with GaAs, CdS has a much smaller surface recombination velocity²⁷ and a much lower Auger non-radiative recombination coefficient, owing to the larger bandgap²⁸. Our previous data²⁹ and more in-depth analysis have indeed revealed that the radiative recombination decay lifetime is of the order of tens to hundreds of picoseconds, whereas the non-radiative decay lifetime is three orders of magnitude larger than this at room temperature and is even greater at low temperatures, justifying the near-unity external quantum efficiency ($>99\%$) in CdS nanobelts. Cooling efficiencies of $\sim 4.8\%$ at 290 K and $\sim 2.0\%$ at 100 K are estimated from the above analysis for 532-nm pumping, and a cooling efficiency of 1.3% at 290 K is estimated for 514-nm pumping (Supplementary Information, part 5). The cooling powers are estimated to be ~ 97 and $180 \mu\text{W}$ for 532- and 514-nm pumping at 290 K, respectively, with corresponding thermal conductive loads of about 80 and $160 \mu\text{W}$, in good agreement

with the cooling power. The radiative load is negligible according to a black-body model for both wavelengths, suggesting that the thermal conductive load dominates the heat dissipation (Supplementary Information, part 6).

Our work demonstrates a substantial net laser cooling of a semiconductor CdS nanobelt by ~ 40 K from room temperature when pumped by a 514-nm laser, and a net cooling by ~ 15 K from 100 K when pumped by a 532-nm laser. In principle, the thermal conductive load can be further minimized by device engineering to facilitate the laser cooling of CdS nanobelts from ambient temperature to that of liquid nitrogen. Our work opens the way to the design of materials for the laser cooling of semiconductors with strong electron-LOP coupling. It would be an immediate advance to test other II-VI materials in the single-crystal, thin-film or nanomaterial morphology for laser cooling.

METHODS SUMMARY

The CdS nanobelts were synthesized in a home-built, vapour-transport chemical-vapour-deposition system. Synthesis and characterization details have been published elsewhere²⁹. The CdS nanobelt was deposited on indium foil substrates or silicon substrates with a 100-nm oxide layer to evaluate the Raman spectrum (Fig. 1) and the mean emission wavelength (Fig. 2), respectively. The thickness of the nanobelt was measured by atomic force microscopy (Nanoscope III, Veeco Instruments). We conducted experiments using six different laser powers, at every ~ 20 -K interval between 77 and 340 K, to generate the ΔE surface plot. The laser

cooling was performed on nanobelts suspended across inverted-pyramid-shaped holes ($\sim 3\ \mu\text{m}$ wide) on a SiO_2/Si substrate etched using a potassium hydroxide solution. The sample was mounted on the cold finger of a continuous-flow microscopy cryostat. A PPLT technique was used to cool and measure the local temperature variation of the nanobelts. The power of probe beam of wavelength 473 nm was kept as low as $20\ \mu\text{W}$ to eliminate the laser heating effect. Both the pump beam (Ar ion laser, 488, 502 and 514 nm; Nd:YAG solid-state laser, 532 nm) and the probe beam (solid-state laser, 473 nm) were collimated and focused thorough a $\times 50$ objective onto the single CdS nanobelt that crossed an etched hole. All the spectra were collected using a confocal triple-grating spectrometer (Horiba-JY T64000) in a backscattering configuration. With a 640-mm focal length and $1,800\text{-mm}^{-1}$ grating, the spectrometer has a spectral resolution of $\sim 0.5\text{ cm}^{-1}$, corresponding to a resolution of $\sim 0.01\text{ nm}$ at a wavelength of $\sim 500\text{ nm}$. Full methods and more details about PPLT and the calibration can be found in the Supplementary Information.

Received 21 September; accepted 25 October 2012.

- Pringsheim, P. Zwei Bemerkungen über den Unterschied von Lumineszenz- und Temperaturstrahlung. *Z. Phys. A* **57**, 739–746 (1929).
- Phillips, W. D. Nobel Lecture: Laser cooling and trapping of neutral atoms. *Rev. Mod. Phys.* **70**, 721–741 (1998).
- Vogl, U. & Weitz, M. Laser cooling by collisional redistribution of radiation. *Nature* **461**, 70–73 (2009).
- Epstein, R. I., Buchwald, M. I., Edwards, B. C., Gosnell, T. R. & Mungan, C. E. Observation of laser-induced fluorescent cooling of solid. *Nature* **377**, 500–503 (1995).
- Seletskiy, D. V. *et al.* Laser cooling of solids to cryogenic temperatures. *Nature Photon.* **4**, 161–164 (2010).
- Seletskiy, D. V. *et al.* Local laser cooling of Yb:YLF to 110 K. *Opt. Express* **19**, 18229–18236 (2011).
- Rivlin, L. A. & Zadernovsky, A. A. Laser cooling of semiconductors. *Opt. Commun.* **139**, 219–222 (1997).
- Rupper, G., Kwong, N. H. & Binder, R. Large excitonic enhancement of optical refrigeration in semiconductors. *Phys. Rev. Lett.* **97**, 117401 (2006).
- Sheik-Bahae, M. & Epstein, R. I. Can laser light cool semiconductors? *Phys. Rev. Lett.* **92**, 247403 (2004).
- Finkeiß, E., Potemski, M., Wyder, P., Vina, L. & Weimann, G. Cooling of a semiconductor by luminescence up-conversion. *Appl. Phys. Lett.* **75**, 1258–1260 (1999).
- Gauck, H., Gfroerer, T. H., Renn, M. J., Corneli, E. A. & Bertness, K. A. External radiative quantum efficiency of 96% from a GaAs/GaN heterostructure. *Appl. Phys. A* **64**, 143–147 (1997).
- Imangholi, B., Hasselbeck, M. P., Sheik-Bahae, M., Epstein, R. I. & Kurtz, S. Effects of epitaxial lift-off on interface recombination and laser cooling in GaInP/GaAs heterostructures. *Appl. Phys. Lett.* **86**, 081104 (2005).
- Rupper, G., Kwong, N. H. & Binder, R. Optical refrigeration of GaAs: theoretical study. *Phys. Rev. B* **76**, 245203 (2007).
- Khurgin, J. B. Surface plasmon-assisted laser cooling of solids. *Phys. Rev. Lett.* **98**, 177401 (2007).
- Nemova, G. & Kashyap, R. Laser cooling of solids. *Rep. Prog. Phys.* **73**, 086501 (2010).
- Epstein, R. I. & Sheik-Bahae, M. *Optical Refrigeration* (Wiley-VCH, 2009).
- Sheik-Bahae, M. & Epstein, R. I. Optical refrigeration. *Nature Photon.* **1**, 693–699 (2007).
- Eshlaghi, S., Worthoff, W., Wieck, A. D. & Suter, D. Luminescence upconversion in GaAs quantum wells. *Phys. Rev. B* **77**, 245317 (2008).
- Sheik-Bahae, M. & Epstein, R. I. Laser cooling of solids. *Laser Photon. Rev.* **3**, 67–84 (2009).
- Khurgin, J. B. Band gap engineering for laser cooling of semiconductors. *J. Appl. Phys.* **100**, 113116 (2006).
- Khurgin, J. B. Role of bandtail states in laser cooling of semiconductors. *Phys. Rev. B* **77**, 235206 (2008).
- Merlin, R. *et al.* Multiphonon processes in YbS. *Phys. Rev. B* **17**, 4951–4958 (1978).
- Zhang, Q. *et al.* Exciton-phonon coupling in individual ZnTe nanorods studied by resonant Raman spectroscopy. *Phys. Rev. B* **85**, 085148 (2012).
- Li, D. H., Zhang, J., Zhang, Q. & Xiong, Q. H. Electric field-dependent photoconductivity in CdS nanowires and nanobelts: exciton ionization, Franz-Keldysh and Stark effects. *Nano Lett.* **12**, 2993–2999 (2012).
- Basu, P. K. *Theory of Optical Processes in Semiconductors: Bulk and Microstructures* 209–210 (Oxford Univ. Press, 2003).
- Sadao, A., Peter, C., Safa, K. & Arthur, W. *Properties of Semiconductor Alloys: Group-IV, III-V and II-VI Semiconductors* 103 (Wiley, 2009).
- Huppert, D., Evenor, M. & Shapira, Y. Measurements of surface recombination velocity on CdS surfaces and Au interfaces. *J. Vac. Sci. Technol. A* **2**, 532–533 (1984).
- Imangholi, B. *Investigation of Laser Cooling in Semiconductors* 46–49. PhD thesis, Univ. New Mexico (2006).
- Xu, X. *et al.* Dynamics of bound exciton complexes in CdS nanobelts. *ACS Nano* **5**, 3660–3669 (2011).

Supplementary Information is available in the online version of the paper.

Acknowledgements We thank M. Sheik-Bahae and R. Merlin for helpful discussions. Q.X. acknowledges the support from the Singapore National Research Foundation through a fellowship grant (NRF-RF2009-06). This work was also supported in part by the Singapore Ministry of Education via a Tier 2 grant (MOE2011-T2-2-051) and start-up grant support (M58113004) from Nanyang Technological University.

Author Contributions J.Z., D.L. and Q.X. had the idea for this work; J.Z., D.L. and Q.X. designed the experiments; J.Z. and D.L. performed the experiments; R.C. patterned the substrates; and J.Z., D.L. and Q.X. analysed the data and wrote the manuscript.

Author Information Reprints and permissions information is available at www.nature.com/reprints. The authors declare no competing financial interests. Readers are welcome to comment on the online version of the paper. Correspondence and requests for materials should be addressed to Q.X. (qihua@ntu.edu.sg).

Interface-engineered templates for molecular spin memory devices

Karthik V. Raman^{1,2†*}, Alexander M. Kamerbeek^{1†*}, Arup Mukherjee³, Nicolae Atodiresel⁴, Tamal K. Sen³, Predrag Lazić⁵, Vasile Caciuc⁴, Reent Michel⁶, Dietmar Stalke⁶, Swadhin K. Mandal³, Stefan Blügel⁴, Markus Münzenberg⁷ & Jagadeesh S. Moodera^{1,8}

The use of molecular spin state as a quantum of information for storage, sensing and computing has generated considerable interest in the context of next-generation data storage and communication devices^{1,2}, opening avenues for developing multifunctional molecular spintronics³. Such ideas have been researched extensively, using single-molecule magnets^{4,5} and molecules with a metal ion⁶ or nitrogen vacancy⁷ as localized spin-carrying centres for storage and for realizing logic operations⁸. However, the electronic coupling between the spin centres of these molecules is rather weak, which makes construction of quantum memory registers a challenging task⁹. In this regard, delocalized carbon-based radical species with unpaired spin, such as phenalenyl¹⁰, have shown promise. These phenalenyl moieties, which can be regarded as graphene fragments, are formed by the fusion of three benzene rings and belong to the class of open-shell systems. The spin structure of these molecules responds to external stimuli^{11,12} (such as light, and electric and magnetic fields), which provides novel schemes for performing spin memory and logic operations. Here we construct a molecular device using such molecules as templates to engineer interfacial spin transfer resulting from hybridization and magnetic exchange interaction with the surface of a ferromagnet; the device shows an unexpected interfacial magnetoresistance of more than 20 per cent near room temperature. Moreover, we successfully demonstrate the formation of a nanoscale magnetic molecule with a well-defined magnetic hysteresis on ferromagnetic surfaces. Owing to strong magnetic coupling with the ferromagnet, such independent switching of an adsorbed magnetic molecule has been unsuccessful with single-molecule magnets¹³. Our findings suggest the use of chemically amenable phenalenyl-based molecules as a viable and scalable platform for building molecular-scale quantum spin memory and processors for technological development.

The diversity and flexibility of molecular synthesis has given researchers ample freedom to design functional molecules for spintronics. These include molecular magnets¹⁴, spin-filter molecules¹⁵, spin-crossover molecules¹⁶, molecular batteries¹⁷, molecular conductors¹⁰, molecular switches¹², and spacer layers for organic spin valves¹⁸ and magnetic tunnel junctions^{19,20}. Using such synthetic techniques, we have designed a neutral planar phenalenyl-based molecule, zinc methyl phenalenyl (ZMP, $C_{14}H_{10}O_2Zn$; see Fig. 1a and Methods), that has no net spin. When these molecules are grown on a ferromagnetic surface, interface spin transfer causes a hybridized organometallic supramolecular magnetic layer to develop, which shows a large magnetic anisotropy and spin-filter properties²¹. This interface layer creates a spin-dependent resistance and gives rise to an interface magnetoresistance (IMR) effect.

We demonstrate IMR response in a vertical-junction molecular device consisting of a ZMP thin film grown on a (111) textured f.c.c. cobalt (Co) film surface (see Methods). Figure 1b shows a magnetotransport measurement on such a device with copper (Cu) as the top contact electrode over a 40-nm ZMP spacer layer. The device is cooled down to 4.2 K in a magnetic field of -550 Oe. The nonlinear current–voltage (I – V) characteristics of the device (see Supplementary Information) suggest tunnelling as the dominant transport mechanism. A large magnetoresistance signal, close to 25%, is observed when the Co magnetization switches at its coercive field. Here we only show the minor loop corresponding to the switching of one ferromagnetic electrode, while the second electrode is non-magnetic Cu. Furthermore, when the bottom Co electrode is replaced by Cu, there is no magnetoresistance signal. These observations imply that the magnetoresistance effect arises due to the switching of the Co electrode with respect to a hard magnetic layer, either at the interface or within the bulk of the ZMP film. Bulk magnetism in ZMP can be ruled out (see Supplementary Information), clearly pointing to an interfacial phenomenon as being responsible for the IMR effect.

The IMR response is confirmed by performing magnetoresistance measurements on a standard magnetic junction structure, replacing Cu with Permalloy (Py): Co/ZMP (35 nm)/Py (Fig. 2a). Instead of seeing a ‘standard’ magnetoresistance signal, a large IMR of 42% with sharp switching at the coercivity (H_c) of Co (± 38 Oe) is observed. A low-field scan showed a second independent IMR loop corresponding to the H_c of the Py electrode (± 3 Oe). The H_c of the ferromagnetic electrodes is confirmed from the anisotropic magnetoresistance (AMR) measurements of the electrodes. These results suggest that the magnetoresistance does not arise from conventional spin-conserved tunnelling/transport through the organic barrier between the two ferromagnetic electrodes²⁰. This is further confirmed by inserting an ultrathin layer of Al_2O_3 , 0.7 nm thick, at the bottom interface to create an interface-modified junction—Co/ Al_2O_3 /ZMP/Py—that showed a resistance change only when the Py magnetization was switched (Fig. 2b). Clearly, the ZMP has to be in direct contact with the ferromagnetic surface to observe IMR. The switching response of the interface layer was characterized in larger magnetic fields (Fig. 3a and b, and Supplementary Information). For Co/ZMP/Py at 4.2 K, the bottom Co/ZMP interface layer switches at about ± 600 Oe to the low-resistance state (the switching field varied from device to device). After warming up to near room temperature (~ 250 K), the device showed a large IMR of 22% with a lower switching field (~ 100 Oe) of the interface layer.

A similar two-step switching magnetoresistance response has been reported in devices using one ferromagnetic electrode: (Ga,Mn)As/

¹Francis Bitter Magnet Laboratory, Massachusetts Institute of Technology, Massachusetts 02139, USA. ²Department of Materials Science and Engineering, Massachusetts Institute of Technology, Massachusetts 02139, USA. ³Department of Chemical Sciences, Indian Institute of Science Education and Research (IISER)-Kolkata, Mohanpur 741252, India. ⁴Peter Grünberg Institut and Institute for Advanced Simulation, Forschungszentrum Jülich and JARA, 52425 Jülich, Germany. ⁵Theoretical Physics Division, Rudjer Boskovic Institute, PO Box 180, HR-10002 Zagreb, Croatia. ⁶Institut für Anorganische Chemie, Universität Göttingen, Göttingen 37077, Germany. ⁷Physikalisches Institut, Georg-August-Universität Göttingen, Göttingen 37077, Germany. ⁸Physics Department, Massachusetts Institute of Technology, Massachusetts 02139, USA. [†]Present address: IBM India Research Laboratory, Bangalore 560045, India (K.V.R.); Institute for Advanced Materials, University of Groningen, Nijenborgh 4, 9747 AG, Groningen, The Netherlands (A.M.K.).

*These authors contributed equally to this work.

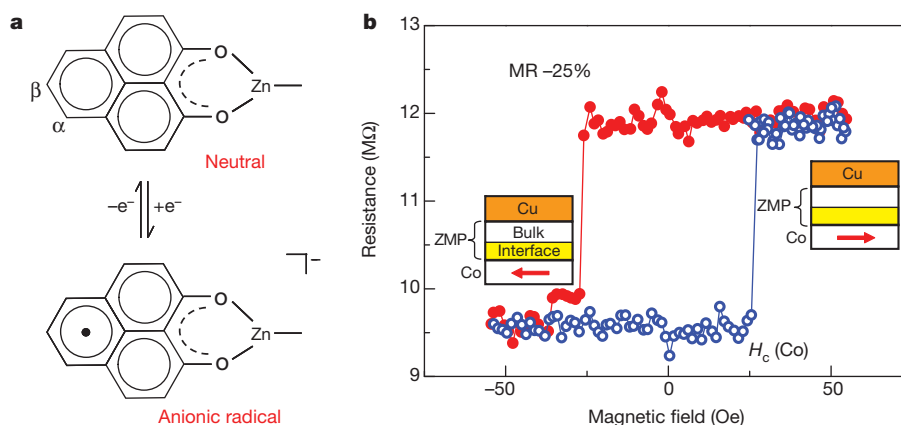


Figure 1 | Interface magnetoresistance effect. **a**, Molecular structure of zinc methyl phenalenyl (ZMP) in a neutral state with no net spin (top). Charge transfer processes through hybridization on the ferromagnet surface can change the chemical state of the phenalenyl moiety from neutral to an anionic radical (bottom) with net moment. **b**, Magnetoresistance measurements (data points) of a device with a single ferromagnetic electrode (Co (8 nm)/ZMP (40 nm)/Cu(12 nm)), measured at 15 mV after cooling the device to 4.2 K in a

$\text{Al}_2\text{O}_3/\text{Al}$ tunnel junctions²². The magnetoresistance in such tunnel devices is referred to as tunnelling anisotropy magnetoresistance (TAMR), which arises from the magnetization-dependent total density of states of the tunnelling electrons at the surface. The observation of TAMR has also been reported in organic spin-valve structures using epitaxial lanthanum strontium manganese oxide electrodes²³. However, our above experimental observations suggest the origin of IMR in our device to be interfacial and different to that of TAMR. Though the details of the interface phenomenon need further study, we suggest an interface model strengthened by *ab initio* calculations that reasonably explain our experimental observations. Figure 3c and d shows the model: the interface magnetic layer comprises the hybridized Co surface layer with an adsorbed ZMP dimer. The adsorbed dimer forms a pair of magnetic and spin-filter molecules. The Co electrode with spin polarized *s-p* electrons serves as the spin-polarizer, and the interface magnetic layer with spin-dependent interface resistance serves as the spin analyser, giving rise to IMR.

Chemical modification of the ferromagnet/ZMP molecule interface arises owing to charge transfer and hybridization of the molecular orbitals with the *d*-orbitals of the ferromagnet, creating new hybrid

magnetic field (about -550 Oe). Blue and red data points refer to positive and negative field sweeps respectively. The solid lines are guides to the eye. The magnetoresistance loop corresponds to the switching of the Co magnetization, as shown in the two insets, with respect to the hard magnetic layer forming at the interface (yellow). Left and right insets show the Co magnetization pointing in the negative and positive direction, respectively.

metal–organic interface states that directly affect the electronic and magnetic properties of the adsorbed molecule²⁴. These interactions strongly depend on the specific molecular structure and morphology^{25,26}, influencing the efficiency of spin polarization and spin injection at the interface. In the case of ZMP, the planar geometry of the molecule provides an ideal situation for strong orbital overlap leading to *d-p* hybridization effects. Spin-polarized first-principles calculations using density-functional theory (DFT) were carried out in zero magnetic field on such a hybrid metal–organic interface, comprising five Co(111) layers and either one or two molecular layers of ZMP on top (see Methods and Supplementary Information).

The p_z atomic-type orbitals of the planar ZMP molecule hybridize strongly with the *d*-states (mainly with d_{z^2} , d_{xz} and d_{yz} orbitals) of the Co atoms, forming hybrid molecule–metal p_z -*d* interface states with bonding and anti-bonding characters²⁴. The calculated spin-resolved projected density-of-states (PDOS) is shown in Fig. 4a and b. The molecular energy levels of the first adsorbed ZMP molecule are broadened, becoming a component of the metallic hybrid molecule–surface states. In addition, the molecular layer acquires a net moment of $0.11\mu_B$ oriented anti-parallel to the moment of the hybridized

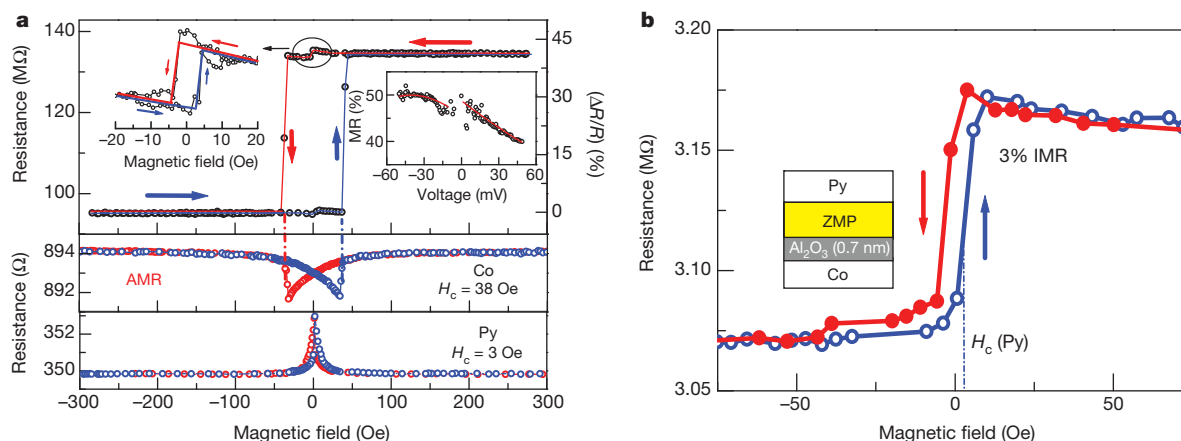


Figure 2 | Confirmation of IMR. **a**, Top panel, magnetoresistance measurements (black data points) on a Co (8 nm)/ZMP (35 nm)/Py (12 nm) device (at 25 mV) show independent IMR response of both the bottom Co/ZMP interface and the top ZMP/Py interface around zero field. Left inset, zoomed-in view showing low field scan. Right inset, IMR of bottom Co/ZMP interface versus applied bias shows a flat response under low bias conditions

with a maximum of 50% in negative bias. Middle and bottom panels show AMR measurements of Co and Py electrode, respectively. **b**, Magnetoresistance measurements on an interface-modified junction, Co (8 nm)/ Al_2O_3 (0.7 nm)/ZMP (30 nm)/Py (12 nm), show 3% IMR (at 50 mV) due only to Py switching (data points). The blue and red curves refer to positive and negative field sweeps, respectively, and arrows show sweep direction.

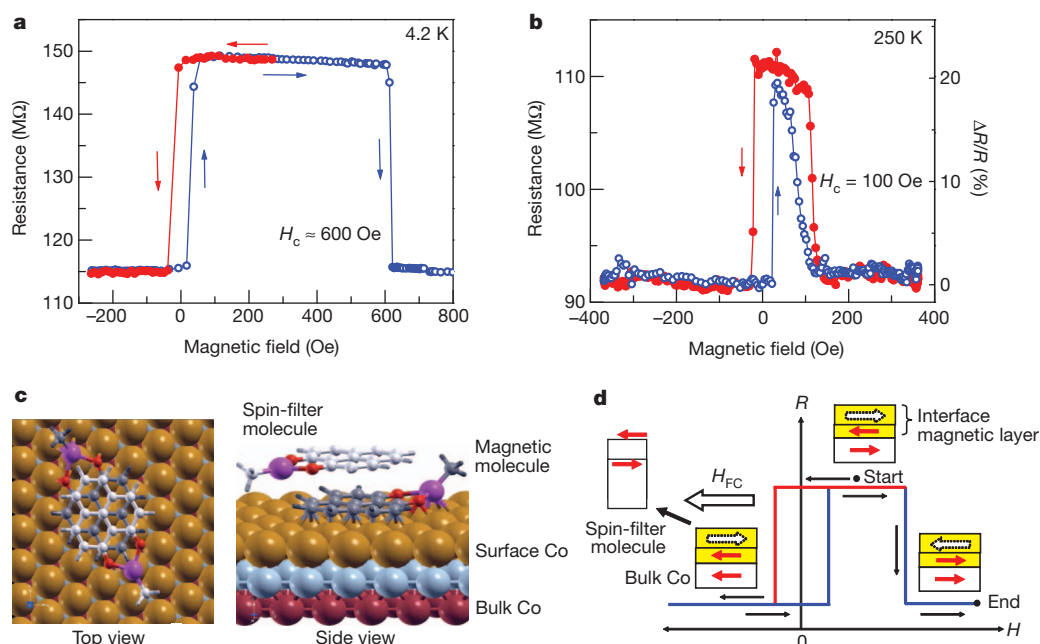


Figure 3 | Interface switching response and interface model. **a**, IMR measurements under high magnetic field on the device Co (8 nm)/ZMP (35 nm)/Py (12 nm): **a**, at 4.2 K showing large switching field ($H_c \approx 600$ Oe) of the interface layer; **b**, at 250 K, showing large IMR of 22% with reduction in switching field (~ 100 Oe). **c**, *Ab initio* model: top view (left) and side view (right) of the relaxed molecules' configuration on a Co(111) surface; grey, carbon; red, oxygen; purple, zinc. The first-layer ZMP molecule ('magnetic molecule') adsorbs flat, with six α -carbons and the central carbon of the phenalenyl sitting directly on top of Co atoms, while the β -carbons of the phenalenyl sit in a bridge position between Co atoms. The molecular plane is

~ 2.1 – 2.2 Å above the Co(111) surface (the C atoms are ~ 2.1 Å above, the O and Zn atoms are ~ 2.2 Å above). The second molecule ('spin filter molecule') sits in a staggered configuration over the first adsorbed molecule with a spacing of ~ 3.26 Å, forming a molecular π -dimer. **d**, Device model: an interface magnetic layer comprises the surface hybridized Co atoms with the molecular dimer on top, forming a magnetic molecule and a tunnel spin-filter molecule. Shown are relative magnetization directions of the interface magnetic layer and the bottom bulk Co at various field values (R , resistance; H , magnetic field; arrow labelled H_{FC} shows direction of field cooling). Arrows in the spin-filter molecule represent the two electron-spin energy levels.

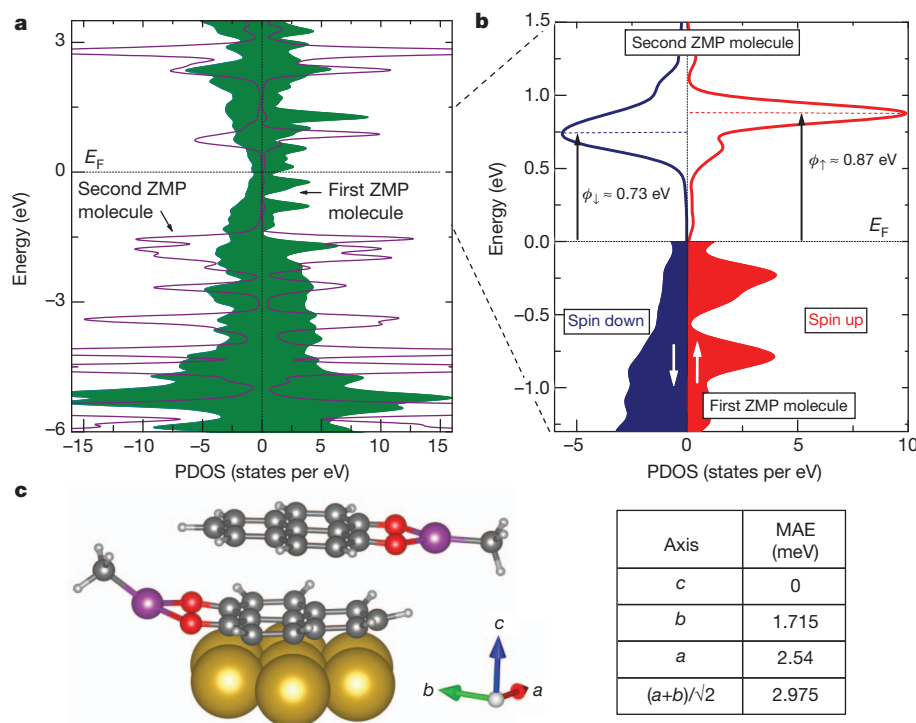


Figure 4 | Spin-filter effect and interface MAE. **a**, Spin-resolved PDOS of the p -states for the first-layer (green) and second-layer (purple) ZMP molecule of the relaxed interface system. Interface p_z - d hybridization creates spin-unbalanced electronic structure in the two molecules. **b**, Zoomed-in view of the PDOS in **a** in the energy interval $[-1.5, 1.5]$ eV. The LUMO of the second ZMP molecule is spin-split by 0.14 eV, leading to a difference in the barrier height for

the two spin channels. **c**, Calculation of MAE due to surface magnetocrystalline anisotropy for the organometallic supramolecule comprising seven hybridized Co atoms (gold) with the ZMP molecular dimer as a model system. The MAE of the supramolecule is calculated (table) for three different in-plane magnetization orientations with respect to the out-of plane magnetization defined here as the c axis.

surface layer of Co atoms giving an anti-ferromagnetic (AFM) coupling ($J_{\text{Co-ZMP}} < 0$). The moment of the surface Co atoms is lowered to $\sim 1.7 \mu_B$ per atom (bulk moment $\sim 1.9 \mu_B$ per atom).

Our calculations show that the distance between the phenalenyl rings in the magnetic molecule and the molecule above is $\sim 3.26 \text{ \AA}$, which is smaller than the sum of the van der Waals radii of the carbon atoms¹¹. This suggests a weak chemical bonding of the molecular π -dimer. The PDOS of the second-layer ZMP molecule resembles the molecular-type discrete energy levels above and below the Fermi level (E_F). Although the calculations show that the second ZMP molecule has no magnetic moment, the π - π interaction with the magnetic molecule creates a spin-unbalanced electronic structure. The first energy level above E_F (the lowest unoccupied molecular orbital (LUMO) level) is observed to be spin-split by $\sim 0.14 \text{ eV}$ (Fig. 4b), defining two different barrier heights for spin tunnelling injection: a lower one for spin-down electrons (ϕ_{\downarrow}) of 0.73 eV and a higher one for spin-up electrons (ϕ_{\uparrow}) of 0.87 eV , leading to a spin-dependent interface resistance. It is well known that conventional spin-filter tunnelling of this type (using magnetic semiconductors such as EuS, EuO, and so on) can be highly efficient²¹.

The independent switching of the interface magnetic layer close to room temperature implies a significantly large surface magnetic anisotropy energy (MAE $\sim > 10 kT$). Because the molecule is composed of low-atomic-number elements that show weak spin-orbit coupling, the magnetic molecule alone cannot account for such large MAE. DFT study shows that the induced magnetic moment in the adsorbed ZMP molecule depends directly on the magnetic interaction with the surface Co layer. Therefore, the observation of IMR response suggests interface hybridization as the source of MAE. We expect an enhancement in MAE^{5,27} of the Co surface (K_{sur} , in units of per surface atom) and significant weakening of the magnetic exchange interaction between the surface Co layer and the layers below it (J_{\perp}). Calculations of MAE were performed on a model organometallic supramolecule, comprising seven Co atoms with the molecular dimer on top. The calculated MAE for different in-plane magnetization orientations is listed in Fig. 4c, showing a large enhancement of in-plane K_{sur} , $\sim 180 \mu\text{eV}$ per surface Co atom as compared to bulk anisotropy energy of $19 \mu\text{eV}$ per atom²⁸. This enhancement in K_{sur} is in line with our experimental observations. Further, the anisotropy tends to be uniaxial, with the easy axis along the field cooled orientation (see Supplementary Information).

Magnetic exchange interactions at the ferromagnet surface can be weaker than within the bulk. Owing to reduction in the moment and fewer magnetic neighbours at the interface, the interatomic magnetic exchange coupling (J) can reduce considerably, and become comparable to or even lower than the surface anisotropy^{29,30}: that is, $J/K_{\text{sur}} \sim < 1$. In such cases, the bulk magnetization can switch before the surface magnetization²⁸. For bulk f.c.c. Co, J is computed to be $\sim 8.54 \text{ meV}$ per atom, consistent with the values reported by others²⁸ (see Supplementary Information). For a hybridized Co surface this value is reduced to 1.34 meV per Co atom, corresponding to a 70% reduction in J_{\perp} compared to a clean Co surface (see Supplementary Information for J_{\perp} calculation). The strong effect of interface hybridization on the properties of the Co surface layer is clearly evident from these studies, signifying a large increase in the ratio K_{sur}/J_{\perp} compared to the bulk ($K/J \approx 0.002$)²⁸. This phenomenon explains the switching response of the interface magnetic layer responsible for the observed IMR. Deeper understanding of the interface mechanisms responsible for magnetic switching and the occurrence of IMR is a subject for future studies.

In order to use the adsorbed magnetic molecule as a source of information or a magnetic 'bit', one needs to be able to independently switch the moment of the adsorbed molecule. The use of phenalenyl-derived molecules provides a unique advantage in this regard. Using chemical synthesis, one could tune the chemical state (that is, cation, radical or anion) as well as the topological state of the phenalenyl

moiety in the molecule, and control the charge transfer and hybridization effects with the ferromagnet surface. In the case of ZMP, the observation of an asymmetric magnetoresistance behaviour near room temperature (Fig. 3b) suggests a weakening of magnetic exchange coupling $J_{\text{Co-ZMP}}$, leading to independent magnetization switching of the magnetic molecular dimer from parallel to anti-parallel alignment and vice-versa with respect to the hybridized surface Co layer. The above results demonstrate the potential for engineering the interface magnetic exchange interaction at the molecular level to control the independent hysteretic response of the adsorbed magnetic molecule. In addition, the IMR response provides a robust mechanism to probe and manipulate the spin state of the magnetic molecule, paving way to the development of room temperature molecular memory devices. Furthermore, the spin structure of the phenalenyl ligands can take the role of bus qubits⁹ in tailor-made molecular networks for realizing future molecular quantum information processing systems.

METHODS SUMMARY

Synthesis of ZMP. (ZMP has CCDC structure no. 859902.) As a starting material 9-hydroxy-1-oxophenylene was synthesized and dissolved (0.196 g, 1.0 mmol) in tetrahydrofuran (20 ml) and ZnMe_2 (1.2 M in toluene; 1.0 ml, 1.2 mmol) was added. The resulting solution was concentrated under reduced pressure and kept at -20°C for a day to develop suitable crystals (see Supplementary Information for details).

Device preparation. The thin film devices were fabricated on pre-cleaned glass substrates in a high vacuum thermal deposition chamber (10^{-7} torr) with *in situ* shadow masking. The Co bottom electrode was grown on cooled substrates (80 K) using electron-beam evaporation. The ZMP organic layer and top electrodes were subsequently grown at room temperature. The junction area was $200 \mu\text{m} \times 200 \mu\text{m}$. The device was covered by a 10-nm-thick Al_2O_3 capping layer. In each pump-down 72 junctions were made, and about 15 such junction sets were investigated by varying the organic layer thickness and the interface as well as the type of top and bottom electrodes.

DFT method. Spin-polarized first-principles calculations were performed using density-functional theory (DFT) by employing the generalized gradient approximation (PBE, for Co atom PBE+U, with $U_{\text{eff}} = 3.0 \text{ eV}$; see Supplementary Information for details) in a projector augmented plane-wave formulation as implemented in VASP code. The structural relaxations included the van der Waals forces in a semi-empirical approach.

Received 11 May; accepted 23 October 2012.

- Verdaguer, M. Molecular electronics emerges from molecular magnetism. *Science* **272**, 698–699 (1996).
- Miyamachi, T. *et al.* Robust spin crossover and memristance across a single molecule. *Nature Commun.* **3**, 938 (2012).
- Rocha, A. R. *et al.* Towards molecular spintronics. *Nature Mater.* **4**, 335–339 (2005).
- Leuenberger, M. N. & Loss, D. Quantum computing in molecular magnets. *Nature* **410**, 789–793 (2001).
- Mannini, M. *et al.* Magnetic memory of a single-molecule quantum magnet wired to a gold surface. *Nature Mater.* **8**, 194–197 (2009).
- Sessoli, R., Gatteschi, D., Caneschi, A. & Novak, M. A. Magnetic bistability in a metal-ion cluster. *Nature* **365**, 141–143 (1993).
- Fuchs, G. D., Burkard, G., Klimov, P. V. & Awschalom, D. D. A quantum memory intrinsic to single nitrogen–vacancy centres in diamond. *Nature Phys.* **7**, 789–793 (2011).
- Ardavan, A. *et al.* Will spin-relaxation times in molecular magnets permit quantum information processing? *Phys. Rev. Lett.* **98**, 057201 (2007).
- Morita, Y., Suzuki, S., Sato, K. & Takui, T. Synthetic organic spin chemistry for structurally well-defined open-shell graphene fragments. *Nature Chem.* **3**, 197–204 (2011).
- Haddon, R. C. Design of organic metals and superconductors. *Nature* **256**, 394–396 (1975).
- Hicks, R. G. What's new in stable radical chemistry? *Org. Biomol. Chem.* **5**, 1321–1338 (2007).
- Itkis, M. E. *et al.* Magneto-opto-electronic bistability in a phenalenyl-based neutral radical. *Science* **296**, 1443–1445 (2002).
- Wende, H. *et al.* Substrate-induced magnetic ordering and switching of iron porphyrin molecules. *Nature Mater.* **6**, 516–520 (2007).
- Manriquez, J. M., Yee, G. T., Mclean, R. S., Epstein, A. J. & Miller, J. S. A room-temperature molecular/organic-based magnet. *Science* **252**, 1415–1417 (1991).
- Herrmann, C., Solomon, G. C. & Ratner, M. A. Organic radicals as spin filters. *J. Am. Chem. Soc.* **132**, 3682–3684 (2010).
- Gütlich, P. & Goodwin, H. A. *Spin Crossover in Transition Metal Compounds I* (Springer, 2004).
- Morita, Y. *et al.* Organic tailored batteries materials using stable open-shell molecules with degenerate frontier orbitals. *Nature Mater.* **10**, 947–951 (2011).

18. Xiong, Z. H., Wu, D., Vardeny, Z. V. & Shi, J. Giant magnetoresistance in organic spin-valves. *Nature* **427**, 821–824 (2004).
19. Santos, T. S. *et al.* Room-temperature tunnel magnetoresistance and spin-polarized tunneling through an organic semiconductor barrier. *Phys. Rev. Lett.* **98**, 016601 (2007).
20. Shim, J. H. *et al.* Large spin diffusion length in an amorphous organic semiconductor. *Phys. Rev. Lett.* **100**, 226603 (2008).
21. Moodera, J. S., Santos, T. S. & Nagahama, T. The phenomena of spin-filter tunneling. *J. Phys. Condens. Matter* **19**, 165202 (2007).
22. Gould, C. *et al.* Tunneling anisotropic magnetoresistance: a spin-valve-like tunnel magnetoresistance using a single magnetic layer. *Phys. Rev. Lett.* **93**, 117203 (2004).
23. Grünewald, M. *et al.* Tunneling anisotropic magnetoresistance in organic spin valves. *Phys. Rev. B* **84**, 125208 (2011).
24. Atodiresei, N. *et al.* Design of the local spin polarization at the organic-ferromagnetic interface. *Phys. Rev. Lett.* **105**, 066601 (2010).
25. Raman, K. V. *et al.* Effect of molecular ordering on spin and charge injection in rubrene. *Phys. Rev. B* **80**, 195212 (2009).
26. Sanvito, S. Molecular spintronics: The rise of spinterface science. *Nature Phys.* **6**, 562–564 (2010).
27. Gambardella, P. *et al.* Supramolecular control of the magnetic anisotropy in two-dimensional high-spin Fe arrays at a metal interface. *Nature Mater.* **8**, 189–193 (2009).
28. Dimitrov, D. A. & Wysin, G. M. Magnetic properties of spherical fcc clusters with radial surface anisotropy. *Phys. Rev. B* **51**, 11947–11950 (1995).
29. Siegmann, H. C. Surface and 2D magnetism. *J. Phys. Condens. Matter* **4**, 8395–8434 (1992).
30. Miller, J. S. & Drillon, M. *Magnetism: Molecules to Materials* Vol. 3, *Magnetism: Nanosized Magnetic Materials* (Wiley-VCH, 2002).

Supplementary Information is available in the online version of the paper.

Acknowledgements We thank J. M. D. Coey of Trinity College, Ireland, for discussions. K.V.R. and J.S.M. were supported by the Office of Naval Research (ONR grant N00014-09-1-0177) and the National Science Foundation (grants DMR 0504158 and

ULFR 09-0532-01). A.M.K. thanks the University of Groningen for partial financial support during his stay at MIT. N.A. and V.C. thank the Julich Supercomputing Centre, Forschungszentrum Julich (Germany), for performing calculations on JUROPA and JUGENE supercomputers. A.M. and T.K.S. thank IISER-Kolkata and CSIR, India, respectively, for research fellowships. S.K.M. thanks CSIR (sanction no. 01(2369)/10/EMR-II), India, for financial support. M.M. thanks the German Science foundation for support within SFB 602 and SPP 1538, and S. Demeshko for SQUID measurements. D.S. and R.M. thank the Deutsche Forschungsgemeinschaft (DFG) Priority Programme 1178 and the Danish National Research Foundation (DNRF) funded Center for Materials Crystallography (CMC) for support, and the Land Niedersachsen for providing a fellowship in the Catalysis for Sustainable Synthesis (CaSuS) Ph.D. program. J.S.M., M.M., S.K.M. and D.S. thank the Göttingen-Kolkata 'Open shell systems (G-KOSS)' initiative for supporting the collaboration.

Author Contributions S.K.M., M.M. and J.S.M. designed the original research approach; A.M. and S.K.M. developed molecule synthesis; A.M.K., A.M., T.K.S., S.K.M., R.M. and D.S. performed material characterization; K.V.R. and A.M.K. prepared devices, performed transport experiments and analysed transport and magnetic characterization; N.A., P.L. and V.C. performed DFT calculations; K.V.R., A.M.K., N.A. and J.S.M. developed the organic spin-filter model; K.V.R., N.A. and J.S.M. developed the interface magnetic anisotropy model; K.V.R. coordinated collaboration; K.V.R., J.S.M. and M.M. wrote the manuscript; N.A., A.M.K., A.M. and S.K.M. provided the discussion and contributed to manuscript preparation. All authors discussed the experiments and commented on the manuscript.

Author Information Reprints and permissions information is available at www.nature.com/reprints. The authors declare no competing financial interests. Readers are welcome to comment on the online version of the paper. Correspondence and requests for materials should be addressed to K.V.R. (vkarthik@mit.edu, for experimental work and modelling), J.S.M. (moodera@mit.edu, for experimental work and modelling), N.A. (n.atodiresei@fz-juelich.de, for DFT) or S.K.M. (swadhin.mandal@iiserkol.ac.in, for materials).

Sustainable bioenergy production from marginal lands in the US Midwest

Ilya Gelfand^{1,2}, Ritvik Sahajpal^{1,3,4}, Xuesong Zhang^{1,3}, R. César Izaurralde^{1,3,4}, Katherine L. Gross^{1,2,5} & G. Philip Robertson^{1,2,6}

Legislation on biofuels production in the USA¹ and Europe^{2,3} is directing food crops towards the production of grain-based ethanol^{2,3}, which can have detrimental consequences for soil carbon sequestration⁴, nitrous oxide emissions⁵, nitrate pollution⁶, biodiversity⁷ and human health⁸. An alternative is to grow lignocellulosic (cellulosic) crops on 'marginal' lands⁹. Cellulosic feedstocks can have positive environmental outcomes^{10,11} and could make up a substantial proportion of future energy portfolios^{12,13}. However, the availability of marginal lands for cellulosic feedstock production, and the resulting greenhouse gas (GHG) emissions, remains uncertain. Here we evaluate the potential for marginal lands in ten Midwestern US states to produce sizeable amounts of biomass and concurrently mitigate GHG emissions. In a comparative assessment of six alternative cropping systems over 20 years, we found that successional herbaceous vegetation, once well established, has a direct GHG emissions mitigation capacity that rivals that of purpose-grown crops (-851 ± 46 grams of CO₂ equivalent emissions per square metre per year ($\text{gCO}_2\text{e m}^{-2}\text{yr}^{-1}$)). If fertilized, these communities have the capacity to produce about 63 ± 5 gigajoules of ethanol energy per hectare per year. By contrast, an adjacent, no-till corn-soybean-wheat rotation produces on average 41 ± 1 gigajoules of biofuel energy per hectare per year and has a net direct mitigation capacity of $-397 \pm 32 \text{ gCO}_2\text{e m}^{-2}\text{yr}^{-1}$; a continuous corn rotation would probably produce about 62 ± 7 gigajoules of biofuel energy per hectare per year, with 13% less mitigation. We also perform quantitative modelling of successional vegetation on marginal lands in the region at a resolution of 0.4 hectares, constrained by the requirement that each modelled location be within 80 kilometres of a potential biorefinery. Our results suggest that such vegetation could produce about 21 giga litres of ethanol per year from around 11 million hectares, or approximately 25 per cent of the 2022 target for cellulosic biofuel mandated by the US Energy Independence and Security Act of 2007, with no initial carbon debt nor the indirect land-use costs associated with food-based biofuels. Other regional-scale aspects of biofuel sustainability², such as water quality^{11,14} and biodiversity¹⁵, await future study.

US legislation mandates the annual production of 80 GJ of ethanol from non-grain sources by 2022¹, which will represent ~25% of projected best-case liquid transportation fuel needs by 2050. Although much of the land need could be satisfied by growing high-productivity feedstocks on fertile land now used for grain production¹⁶, this strategy fails to consider the long-term need for fertile land to meet future food demands and the need to abate the indirect GHG impacts created when land now in grain ethanol production was originally diverted to biofuel use^{4,17,18}.

An alternative is to grow cellulosic crops on marginal lands⁹. Marginal lands are those poorly suited to field crops because of low crop productivity due to inherent edaphic or climatic limitations or because they are located in areas that are vulnerable to erosion or other

environmental risks when cultivated. Often such lands are suitable for grasses, short-rotation tree crops or other perennial vegetation with persistent roots that are better adapted to low-nutrient, erodible or droughty soils. As long as the conversion of these lands to biofuel production avoids local carbon debt^{4,19} and the replacement crop removes from the atmosphere more CO₂ than the pre-existing vegetation would have stored^{17,19}, cellulosic crops on marginal lands might provide substantial GHG emissions mitigation without the risk of indirect carbon costs due to displaced food and feed production¹⁷. Recent estimates place the indirect carbon costs for corn grain ethanol at $25\text{--}200 \text{ gCO}_2\text{e MJ}^{-1}$ (ref. 18), putting at risk much of the fossil fuel offset benefit of biofuels grown on arable land.

Still uncertain, however, are the availability of non-arable marginal lands for cellulosic feedstock production and the resulting implications for GHG emissions. First, not all marginal lands are sufficiently close to a potential biorefinery to make transportation economical. Second, the productivity of marginal lands can vary because of low-fertility soils and location-specific interactions between soils and climate. Third, not all cellulosic feedstocks deliver equivalent climate benefits: soil carbon sequestration, N₂O fluxes and other sources of global warming can differ widely among different feedstocks²⁰. Of available cellulosic feedstocks, only existing herbaceous vegetation—or purpose-grown feedstocks such as switchgrass seeded into existing vegetation—avoids local carbon debt associated with land conversion and planting^{4,9,17,19}, but the potential productivity of this vegetation has been questioned¹² and there have been no long-term comparative analyses of its potential GHG benefits.

Here we provide a 20-yr comparative assessment of direct GHG benefits, or GHG balances, for six alternative biofuel cropping systems, including native successional vegetation, replicated at the Kellogg Biological Station (KBS) Long-term Ecological Research (LTER) site in southwest Michigan, USA. We compare GHG emissions and the productivity of established successional vegetation with those of both annual and perennial crops at a single, moderate-fertility location, without consideration of indirect carbon costs. We then project the potential for early successional vegetation to produce biofuel on marginal lands across a ten-state region of the US Midwest using a well-established quantitative crop productivity model calibrated at KBS for successional vegetation and tested elsewhere (Methods Summary). Our intent is to provide a conservative and realistic estimate of the capacity of marginal lands in the US Midwest to produce cellulosic biofuel without carbon debt¹⁹ and without the added carbon cost of indirect land-use change¹⁷.

Twenty-year patterns of GHG balances for the annual cropping systems (Table 1) show that without fossil fuel offsets, the conventionally managed system had a net release of GHG equivalents, whereas the no-till system accumulated enough soil carbon to offset the GHG costs of farming inputs and N₂O losses. In contrast to earlier results²⁰, the poplar system was also a net source of GHG, owing mainly to soil

¹Great Lakes Bioenergy Research Center, Michigan State University, East Lansing, Michigan 48824, USA. ²W.K. Kellogg Biological Station, Michigan State University, Hickory Corners, Michigan 49060, USA. ³Joint Global Change Research Institute, Pacific Northwest National Laboratory and University of Maryland, College Park, Maryland 20740, USA. ⁴Department of Geographical Sciences, University of Maryland, College Park, Maryland 20740, USA. ⁵Department of Plant Biology, Michigan State University, East Lansing, Michigan 48824, USA. ⁶Department of Plant, Soil, and Microbial Sciences, Michigan State University, East Lansing, Michigan 48824, USA.

Table 1 | Average annual GHG emissions for each candidate feedstock cropping system

| Cropping system | Soil carbon* | N ₂ O† | CH ₄ ‡ | Farming inputs‡ | | | | | | Net GHG balance |
|------------------|--------------|-------------------|-------------------|-----------------|-----|---|------|------|-------|-----------------|
| | | | | N | P | K | Lime | Fuel | Seeds | |
| Conventional CSW | 0 ± 31 | 34 ± 6 | -0.8 ± 0.1 | 32.7 | 0.4 | 1 | 3 | 13 | 7 | 98 ± 31 |
| No-till CSW | -122 ± 31 | 35 ± 4 | -0.8 ± 0.1 | 32.7 | 0.3 | 1 | 4 | 9 | 7 | -20 ± 31 |
| Alfalfa | -122 ± 92 | 33 ± 3 | -1.0 ± 0.1 | 0 | 0.3 | 4 | 14 | 11 | 6 | -52 ± 92 |
| Poplar | 61 ± 153 | 17 ± 3 | -0.8 ± 0.0 | 3.3 | 0 | 0 | 0 | 1 | 0 | 84 ± 153 |
| Successional | -397 ± 31 | 11 ± 1 | -1.1 ± 0.1 | 0 | 0 | 0 | 0 | 0 | 0 | -383 ± 31 |
| Successional + N | -397 ± 31 | 27 ± 5 | -1.2 ± 0.5 | 55.5 | 0 | 0 | 0 | 8 | 0 | -308 ± 31 |

Values shown are means ± s.e. ($n = 4-6$; $\text{gCO}_2\text{e m}^{-2}\text{ yr}^{-1}$), calculated without consideration of fossil fuel offset credits (Table 2) or the cost of indirect land use change for the period 1989–2009. For detailed information, see Supplementary Tables 1 and 6–10. CSW, corn–soybean–wheat rotation.

* A/A₀ horizon (surface soil to plow depth), from ref. 21; there were no significant soil carbon changes in lower horizons to 1 m. For calculation see Supplementary Information, equation (2).

† $n = 4$.

‡ Rotational average.

carbon loss following harvest²¹. This is probably due to microbial activity stimulated by warmer and wetter soil conditions caused by the absence of shade and by lower transpiration by resprouting trees before canopy closure²². Conversely, alfalfa provided significant mitigation despite high N₂O fluxes. In the successional system, high rates of soil carbon accumulation and low N₂O emissions provided substantial mitigation under both unfertilized and fertilized conditions (Table 1).

Including fossil fuel offset credits makes all six systems net direct sinks of atmospheric CO₂. Biorefinery yields of 0.43 l of bioethanol per

kilogram of dry corn grain and 0.38 l of cellulosic ethanol per kilogram of biomass^{19,23,24} provide offsets of 280 ± 16 and $309 \pm 10 \text{ gCO}_2\text{e m}^{-2}\text{ yr}^{-1}$ for conventional and no-till annual crops; 319 ± 35 and $514 \pm 14 \text{ gCO}_2\text{e m}^{-2}\text{ yr}^{-1}$ for the perennial poplar and alfalfa; and 463 ± 34 and $624 \pm 46 \text{ gCO}_2\text{e m}^{-2}\text{ yr}^{-1}$ for unfertilized and fertilized successional systems (Fig. 1a and Table 2). Including these offsets in the GHG balance (Fig. 1b) results in net direct mitigation that ranges from -247 ± 35 to $-397 \pm 32 \text{ gCO}_2\text{e m}^{-2}\text{ yr}^{-1}$ for the annual crops, from -241 ± 157 to $-605 \pm 93 \text{ gCO}_2\text{e m}^{-2}\text{ yr}^{-1}$ for the perennial crops and from -851 ± 46 to $-932 \pm 55 \text{ gCO}_2\text{e m}^{-2}\text{ yr}^{-1}$ for the successional communities (Table 2).

In absolute terms, energy production was highest for the fertilized successional system ($63 \pm 5 \text{ GJ ha}^{-1}\text{ yr}^{-1}$) and lowest for poplar ($30 \pm 3 \text{ GJ ha}^{-1}\text{ yr}^{-1}$); other systems had intermediate values of energy production (Table 2). Had the annual no-till crop rotation been continuous corn with county-average yields rather than being corn–soybean–wheat at KBS, we estimate that the energy yield would have been $\sim 60\%$ higher ($62 \pm 7 \text{ GJ ha}^{-1}\text{ yr}^{-1}$) with a direct GHG balance $\sim 13\%$ less negative (Table 2). Although the GHG emission intensity of the fertilized successional system was higher than that of an unfertilized system (-147 ± 14 versus $-197 \pm 18 \text{ gCO}_2\text{e MJ}^{-1}$ for a 90% harvest efficiency), it remains substantially lower than that of most other systems examined, with a direct GHG emission reduction of 105% relative to fossil fuels (Table 2). In contrast, the wheat and corn portions of the annual rotations had GHG emission reductions of only 23 and 28%, respectively, although the equivalent soybean reduction was 240% owing to the allocation of emissions to co-products (Table 2).

The low mitigation potential of the poplar system is due to its relatively low productivity in addition to the soil carbon loss noted above. Additional fertilization²⁵ and protection from a 2-yr defoliation by

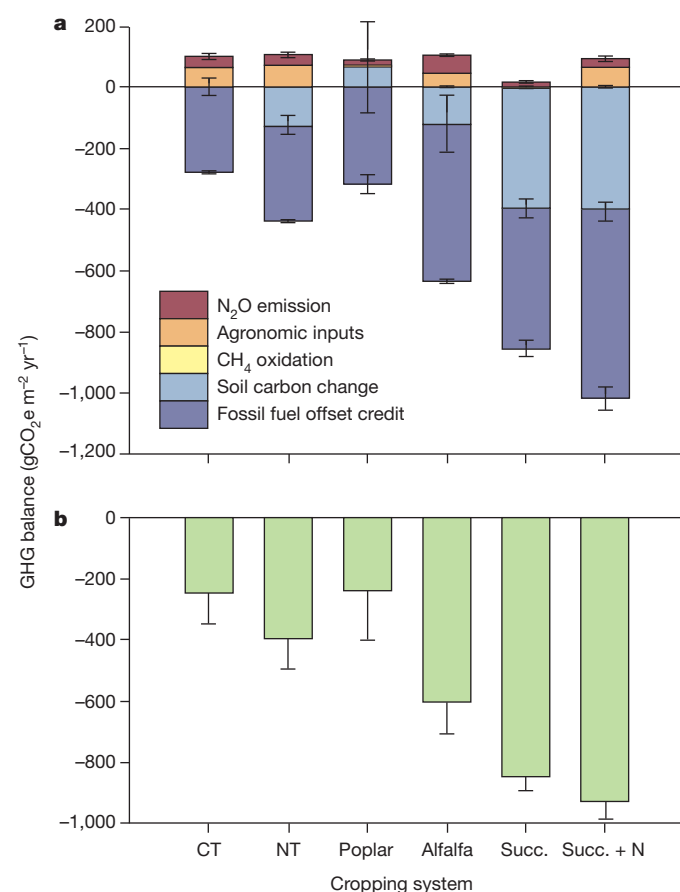


Figure 1 | GHG balances of alternative cropping systems in southwest Michigan for biofuel feedstock production. a, Detailed GHG balance; b, net GHG balance. Bars represent different components of the GHG balance for a given system and were measured as soil emissions of N₂O and CH₄ (1989–2010), changes in soil carbon (1989–2001), and agronomic inputs and yields (used to calculate fossil fuel credits) from 1989 to 2009. Agricultural inputs include GHG emissions from farm machinery, agricultural chemicals and crop seed production. Fluxes of CH₄ are insignificant and are too small to be visible in the figure. Errors, s.e. ($n = 4-6$ replicates). CT, conventionally tilled system; NT, no-till system.

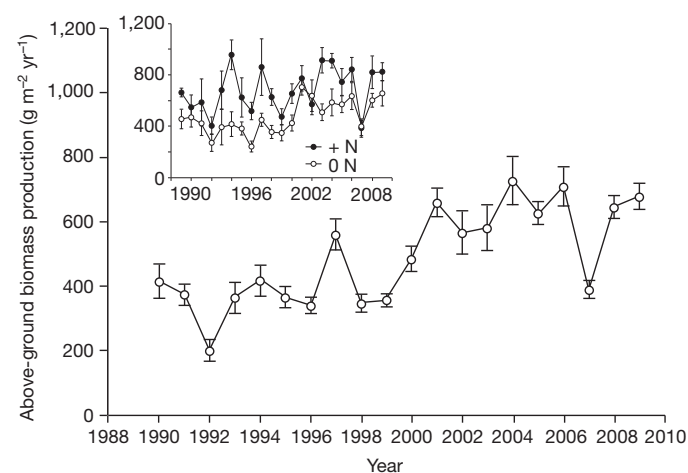


Figure 2 | Above-ground biomass production of the successional system between 1989 and 2009 in 1-ha treatment plots. Inset, effects of nitrogen fertilizer (+N; $124 \text{ kgN ha}^{-1}\text{ yr}^{-1}$) and no fertilizer (0N) in subplots. Errors, s.e. ($n = 6$).

Table 2 | Energy production, GHG emission intensity, GHG emission reduction, fossil fuel offset credit and net GHG balance for the cropping systems in Table 1

| Cropping system | GHG emission intensity (gCO ₂ e MJ ⁻¹) | Energy production (GJ ha ⁻¹ yr ⁻¹) | GHG emissions reduction (%) | Fossil fuel offset credit (gCO ₂ e m ⁻² yr ⁻¹) | Net GHG balance (gCO ₂ e m ⁻² yr ⁻¹) |
|-------------------|---|---|-----------------------------|--|--|
| Conventional CSW* | -65 ± 11 | 38 ± 4 | 28 (C), 240 (S), 23 (W) | 280 ± 16 | -247 ± 35 |
| No-till CSW | -97 ± 9 | 41 ± 2 | 31 (C), 240 (S), 25 (W) | 309 ± 10 | -397 ± 32 |
| No-till CC† | -56 ± 12 | 62 ± 7 | 40 (C), 40 (C) | 256 ± 52 | -344 ± 60 |
| Alfalfa | -119 ± 19 | 51 ± 1 | 111 | 514 ± 14 | -605 ± 93 |
| Poplar | -80 ± 52 | 30 ± 3 | 112 | 319 ± 35 | -241 ± 157 |
| Successional‡ | -260 ± 24 to -197 ± 18 | 24 ± 2 to 43 ± 3 | 114 | 463 ± 34 | -851 ± 46 |
| Successional + N‡ | -208 ± 19 to -147 ± 14 | 35 ± 3 to 63 ± 5 | 105 | 624 ± 46 | -932 ± 55 |

Values shown are means ± s.e. (n = 6), except for GHG emissions reductions, which are given as per cent relative to gasoline (94 gCO₂e MJ⁻¹) for each grain crop in rotation (C, corn; S, soybean; W, wheat), the numbers are for grain based biofuels. For wheat straw, the GHG emissions reduction is 107%. Energy production was calculated from biomass yields (Supplementary Table 1). No corn or soybean stover was harvested for bioenergy production, owing to site-specific limitations to protect soil carbon, whereas wheat straw was harvested.

*Use of average corn yields for Kalamazoo county instead of KBS (Supplementary Methods) would increase fossil fuel offset credit for the rotation by 8% (303 ± 10 gCO₂e m⁻² yr⁻¹) and the overall net GHG balance by 9% (-270 ± 33 gCO₂e m⁻² yr⁻¹).

†Estimated values for a no-till corn-corn (CC) rotation with all grain and 17% of stover removed for bioethanol production, including a 10% continuous-corn-rotation yield penalty (Supplementary Table 1). Fossil fuel offset credits are from ref. 19; for calculation of the GHG emissions reduction, we used relative contributions of corn grain and corn stover ethanol to total GHG reduction. For net GHG balance, we assumed that soil emissions of N₂O and CH₄ and soil carbon sequestration rates were similar to measured rates in the no-till CSW rotation.

‡The range for the successional system reflects a 55% contemporary and 90% potential harvest efficiency.

gypsy moths²⁶ might have improved poplar yield in its first rotation. On average, nitrogen fertilization boosted yields by 47% in the successional system (Fig. 2, inset, and Supplementary Table 1) and provided a fossil fuel offset credit greater by 35% (Table 2). Although the carbon cost of additional fertilizer and the N₂O flux it induced (Table 1) negate part of the net GHG gain in the fertilized successional system (Fig. 1), the higher productivity with fertilization allows for greater land-use intensity from these systems with little additional carbon cost.

We used the Environmental Policy Integrated Climate (EPIC) model^{27–29} to estimate the productivity of fertilized and unfertilized successional systems (Table 1 and Fig. 1) across a ten-state region of the US Midwest. The model was run on a fine-grained spatial scale (0.4-ha resolution) to capture interactions between local soils and climates and to allow modelled cells within an explicit geographic area to be aggregated by distance. Simulated annual yields for unfertilized marginal lands in the region averaged 6 ± 3 Mg ha⁻¹ yr⁻¹ (Supplementary Table 2). Simulated fertilization at 68 kgN ha⁻¹ yr⁻¹ (kgN, kilograms of nitrogen) increased average yields by 36% to 8 ± 3 Mg ha⁻¹ yr⁻¹ (Supplementary Table 2), which is consistent with measured fertilization response over grasslands in North America³⁰ and with measured estimates of on-farm switchgrass production within the region³¹. Our modelled estimates of switchgrass productivity correlate well with those of successional vegetation (Pearson correlation coefficient, $R^2 = 0.94$; Supplementary Fig. 1).

For the region, total modelled yield sums to 262 Tg yr⁻¹ (Supplementary Table 3). Of this, about 58%, or 152 Tg yr⁻¹, are produced within 80 km of 35 potential biorefineries, each with a minimum feedstock requirement of 653 × 10³ Mg yr⁻¹ (Supplementary Information, equation (1)). This provides a total fossil fuel offset of up to

44 TgCO₂e yr⁻¹ (Fig. 3, Supplementary Fig. 2 and Supplementary Table 3). Total ethanol production for all biorefineries sums to 20.8 GJ yr⁻¹ and represents ~27% of the cellulosic ethanol mandated by the US Energy Independence and Security Act of 2007¹. The 80-km collection radius is optimal for the current distribution of marginal lands in the region. With no biorefinery minimum feedstock requirement, maximum production would decline by ~5% were the collection radius increased to 120 km (19.2 GJ yr⁻¹) or decreased to 40 km (19.3 GJ yr⁻¹) (Supplementary Fig. 3). A fine-scale distributed network of smaller processing facilities²⁴ would relax the constraint imposed by the 80-km collection radius and increase collectable biomass from the 42% now excluded.

Not all lands classified as marginal for crop production are idle; on average about 8% of our biomass production areas are grazed (with a range of 0–71%), which reduces our estimate of available biomass from marginal lands by as much as 10% (Supplementary Table 3). Depending on collection radii and biorefinery size restrictions, excluding grazed areas from our analysis lowers our estimated biomass production to 136 Tg yr⁻¹, for a fossil fuel offset of 39 TgCO₂e yr⁻¹ and an ethanol yield of 18.6 GJ yr⁻¹ (Supplementary Table 4).

In contrast to earlier estimates of potential cellulosic feedstock availability in ref. 12, our analysis limits production to marginal lands and uses a process-based crop model operating on a fine-grained scale to estimate biomass yields, rather than estimating yields by statistical extrapolation to both marginal and cropped land. A state-by-state yield comparison reveals little relationship between the average yields predicted by the two approaches ($R^2 = 0.008$; Supplementary Table 5). Overall, our approach predicts average yields that are 20% lower than those projected by ref. 12.

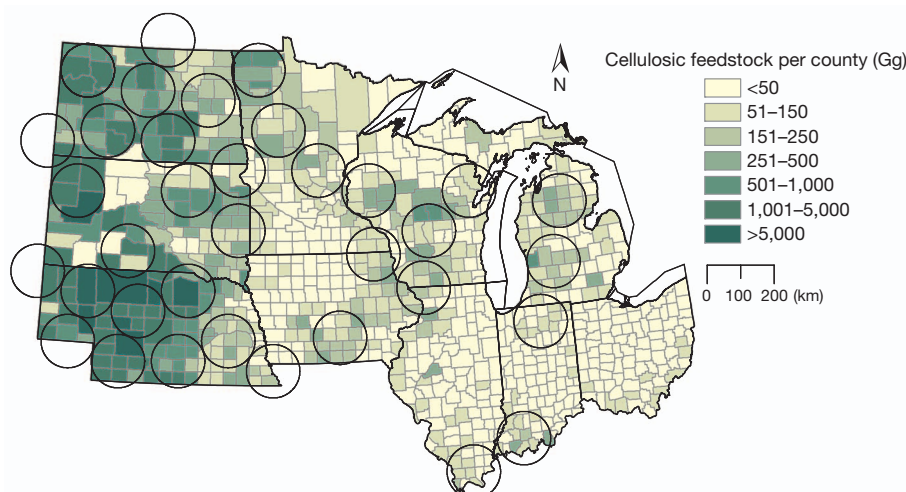


Figure 3 | Potential biomass collection areas for cellulosic biorefineries within ten US midwest states. Each circle represents an area of 80-km radius with sufficient biomass resources to produce at least 89 Ml of cellulosic ethanol per year, according to quantitative simulation of yields from fertilized successional vegetation on non-forested marginal lands at a resolution of 60 m × 60 m. County-scale totals of marginal lands biomass production are shown in green.

Restoring or improving the productivity of marginal lands while using them as biofuel cropping systems might allow them to contribute even more to US energy and GHG mitigation goals in addition to providing greater conservation benefits. Many marginal lands are degraded and not managed, others simply have low productivity, and still others are environmentally sensitive and perhaps in set-aside programs such as the US Department of Agriculture's Conservation Reserve Program. Our results show that management allowing the continued growth of perennial herbaceous species on these lands, undisturbed but for harvest and fertilization, could avoid the carbon costs of conversion, forgone sequestration and indirect land-use change. Furthermore, management could promote the establishment and growth of highly productive species such as future switchgrass cultivars with high nitrogen-use efficiency. This would provide additional GHG benefits in the form of increased energy yields, nitrogen fertilizer savings and greater soil carbon sequestration¹⁷, and might concomitantly improve site fertility³². Other aspects of biofuel sustainability² not considered here, such as landscape-scale water quality^{11,14} and biodiversity benefits¹⁵, might be readily co-managed.

METHODS SUMMARY

GHG emissions quantification. We studied six ecosystems established in south-west Michigan²⁰ in 1989 at the KBS LTER site (<http://lter.kbs.msu.edu>). We compared two 3-yr rotations of corn (*Zea mays* L.), soybean (*Glycine max* (L.) Merrill) and wheat (*Triticum aestivum* L.) with all grain biomass and wheat straw used for biofuel production (Supplementary Table 1). One system was chisel-plowed (conventional tillage) and the other was permanent no-till. We also analysed three perennial systems: alfalfa (*Medicago sativa* L.), short-rotation poplar trees (*Populus × canadensis* Moench var. *eugenei*) and a successional old-field system that has been burned biannually since 1997 and annually since 2002. In the successional system, we compared biomass production with and without nitrogen fertilization. For each system, we constructed total net GHG (CO₂e) budgets that include the carbon costs of all farming operations and inputs from 1989 to 2009 (Supplementary Tables 6–8) and measured fluxes of N₂O and CH₄ for the period 1991–2010 (Supplementary Table 9), the annual accumulation of soil carbon to 1 m for the period 1989–2001 (Supplementary Table 10) and fossil fuel offset credits calculated from the biomass produced weighted by ethanol and biodiesel life cycle impacts (Supplementary Table 11). None of our GHG budgets include estimates of indirect GHG impact associated with diverting food crops to biofuel production^{17,18}. The total net GHG budget for an equivalent no-till, continuous corn rotation was calculated using average corn yields of Kalamazoo County, Michigan and fossil fuel offset credits from ref. 19, together with the net GHG balance of the no-till system.

Regional productivity modelling. The EPIC model was evaluated for successional vegetation growing on former agricultural fields with above-ground net primary production data from the KBS and Cedar Creek, Minnesota LTER sites (Supplementary Materials). Yields for biofuel feedstock production were then simulated across a ten-state region at a resolution of 60 m × 60 m (Supplementary Table 3).

Full Methods and any associated references are available in the online version of the paper.

Received 29 March; accepted 20 November 2012.

Published online 16 January 2013.

1. US 110th Congress. *Energy Independence and Security Act of 2007*. Public Law 110–140; <http://www.gpo.gov/fdsys/pkg/PLAW-110publ140/pdf/PLAW-110publ140.pdf> (2007).
2. Robertson, G. P. *et al.* Sustainable biofuels redux. *Science* **322**, 49–50 (2008).
3. Fischer, G. *et al.* Biofuel production potentials in Europe: sustainable use of cultivated land and pastures, part II. Land use scenarios. *Biomass Bioenergy* **34**, 173–187 (2010).
4. Fargione, J., Hill, J., Tilman, D., Polasky, S. & Hawthorne, P. Land clearing and the biofuel carbon debt. *Science* **319**, 1235–1238 (2008).
5. Crutzen, P. J., Mosier, A. R., Smith, K. A. & Winiwarter, W. N₂O release from agro-biofuel production negates global warming reduction by replacing fossil fuels. *Atmos. Chem. Phys.* **8**, 389–395 (2008).
6. Donner, S. D. & Kucharik, C. J. Corn-based ethanol production compromises goal of reducing nitrogen export by the Mississippi River. *Proc. Natl Acad. Sci. USA* **105**, 4513–4518 (2008).
7. Landis, D. A., Gardiner, M. M., van der Werf, W. & Swinton, S. M. Increasing corn for biofuel production reduces biocontrol services in agricultural landscapes. *Proc. Natl Acad. Sci. USA* **105**, 20552–20557 (2008).

8. Hill, J., Polasky, S., Nelson, E., Tilman, D. & Huo, H. Climate change and health costs of air emissions from biofuels and gasoline. *Proc. Natl Acad. Sci. USA* **106**, 2077–2082 (2009).
9. Tilman, D., Hill, J. & Lehman, C. Carbon-negative biofuels from low-input high-diversity grassland biomass. *Science* **314**, 1598–1600 (2006).
10. Meehan, T. D., Hurlbert, A. H. & Gratton, C. Bird communities in future bioenergy landscapes of the upper midwest. *Proc. Natl Acad. Sci. USA* **107**, 18533–18538 (2010).
11. Robertson, G. P., Hamilton, S. K., Del Grosso, S. J. & Parton, W. J. The biogeochemistry of bioenergy landscapes: carbon, nitrogen, and water considerations. *Ecol. Appl.* **21**, 1055–1067 (2011).
12. Perlack, R. D. *et al.* *US Billion-Ton Update: Biomass Supply for a Bioenergy and Bioproducts Industry*. Report No. ORNL/TM-2011/224 (US DOE, 2011).
13. Ohlrogge, J. *et al.* Driving on biomass. *Science* **324**, 1019–1020 (2009).
14. Dominguez-Faus, R., Powers, S. E., Burken, J. G. & Alvarez, P. J. The water footprint of biofuels: a drink or drive issue? *Environ. Sci. Technol.* **43**, 3005–3010 (2009).
15. Webster, C. R., Flaspohler, D. J., Jackson, R. D., Meehan, T. D. & Gratton, C. Diversity, productivity and landscape-level effects in North American grasslands managed for biomass production. *Biofuels* **1**, 451–461 (2010).
16. Somerville, C., Youngs, H., Taylor, C., Davis, S. C. & Long, S. P. Feedstocks for lignocellulosic biofuels. *Science* **329**, 790–792 (2010).
17. Searchinger, T. D. *et al.* Fixing a critical climate accounting error. *Science* **326**, 527–528 (2009).
18. Plevin, R. J. & Kammen, D. M. in *Encyclopedia of Biodiversity* (ed. Levin, S. A.) (Elsevier, in the press).
19. Gelfand, I. *et al.* Carbon debt of Conservation Reserve Program (CRP) grasslands converted to bioenergy production. *Proc. Natl Acad. Sci. USA* **108**, 13864–13869 (2011).
20. Robertson, G. P., Paul, E. A. & Harwood, R. R. Greenhouse gases in intensive agriculture: contributions of individual gases to the radiative forcing of the atmosphere. *Science* **289**, 1922–1925 (2000).
21. Syswerda, S. P., Corbin, A. T., Mokma, D. L., Kravchenko, A. N. & Robertson, G. P. Agricultural management and soil carbon storage in surface vs. deep layers. *Soil Sci. Soc. Am. J.* **75**, 92–101 (2011).
22. Stoffel, J. L., Gower, S. T., Forrester, J. A. & Mladenoff, D. J. Effects of winter selective tree harvest on soil microclimate and surface CO₂ flux of a northern hardwood forest. *For. Ecol. Manage.* **259**, 257–265 (2010).
23. Kim, S. & Dale, B. E. Life cycle assessment of various cropping systems utilized for producing biofuels: bioethanol and biodiesel. *Biomass Bioenergy* **29**, 426–439 (2005).
24. Eranki, P. L. & Dale, B. E. Comparative life cycle assessment of centralized and distributed biomass processing systems combined with mixed feedstock landscapes. *GCB Bioenergy* **3**, 427–438 (2011).
25. Coleman, M. *et al.* Post-establishment fertilization of Minnesota hybrid poplar plantations. *Biomass Bioenergy* **30**, 740–749 (2006).
26. Kosola, K., Dickmann, D., Paul, E. & Parry, D. Repeated insect defoliation effects on growth, nitrogen acquisition, carbohydrates, and root demography of poplars. *Oecologia* **129**, 65–74 (2001).
27. Izaurralde, R. C., Williams, J. R., McGill, W. B., Rosenberg, N. J. & Jakas, M. C. Q. Simulating soil C dynamics with EPIC: model description and testing against long-term data. *Ecol. Modell.* **192**, 362–384 (2006).
28. Zhang, X. *et al.* An integrative modeling framework to evaluate the productivity and sustainability of biofuel crop production systems. *GCB Bioenergy* **2**, 258–277 (2010).
29. Soil Survey Staff. Soil Survey Geographic Database. *National Resources Conservation Service* <http://soildatamart.nrcs.usda.gov> (USDA, 2011).
30. Clark, C. M. *et al.* Environmental and plant community determinants of species loss following nitrogen enrichment. *Ecol. Lett.* **10**, 596–607 (2007).
31. Schmer, M. R., Vogel, K. P., Mitchell, R. B. & Perrin, R. K. Net energy of cellulosic ethanol from switchgrass. *Proc. Natl Acad. Sci. USA* **105**, 464–469 (2008).
32. Fornara, D. A. & Tilman, D. Ecological mechanisms associated with the positive diversity productivity relationship in an N-limited grassland. *Ecology* **90**, 408–418 (2009).

Supplementary Information is available in the online version of the paper.

Acknowledgements We thank S. Bohm, K. A. Kahmark, I. Shcherbak, and S. VanderWulp for help with data assembly; C. McMinn, J. Simmons and many others for field and laboratory assistance; J. R. Williams for EPIC model advice; and D. H. Manowitz for programming and computational assistance. We are additionally indebted to B. Bond-Lamberty, B. E. Dale, V. H. Dale, J. D. Hill, W. M. Post and T. O. West for comments on an earlier version of the manuscript. Financial support for this work was provided by the US DOE Office of Science (DE-FC02-07ER64494, KP1601050) and Office of Energy Efficiency and Renewable Energy (DE-AC05-76RL01830, OBP 20469-19145), the US National Science Foundation LTER program (DEB 1027253), NASA (NNH08ZDA001N), and MSU AgBioResearch. EPIC simulations were performed on the PNNL Evergreen computer cluster, which is supported by the US DOE Office of Science (DE-AC05-76RL01830).

Author Contributions G.P.R., I.G. and R.C.I. designed the study. I.G., R.C.I., R.S. and X.Z. analysed data and wrote initial drafts of the manuscript. R.C.I., R.S. and X.Z. performed simulations. X.Z. designed the spatially explicit modelling system. K.L.G. designed and performed the fertilization study. I.G. and G.P.R. wrote the final version of the manuscript.

Author Information Reprints and permissions information is available at www.nature.com/reprints. The authors declare no competing financial interests. Readers are welcome to comment on the online version of the paper. Correspondence and requests for materials should be addressed to I.G. (igelfand@msu.edu) or G.P.R. (robert30@msu.edu).

METHODS

GHG sampling and calculation of CO₂ equivalents. The CO₂ equivalents (gCO₂e m⁻² yr⁻¹) for N₂O and CH₄ emissions were calculated using IPCC 100-yr horizon factors³³ (Supplementary Information, equations (3) and (4)). Measurements of soil GHG fluxes (Supplementary Table 9) were performed bi-weekly using a static-chamber method²⁰. Cumulative emissions of N₂O (grams per hectare of nitrogen from N₂O) and CH₄ (grams per hectare of carbon from CH₄) for each plot were determined by interpolating daily fluxes between sampling days over the course of the entire growing season from first thaw in late winter until soils froze in late autumn during 1989–2010.

Farming CO₂e calculation. Total GHG emissions associated with farming (Supplementary Tables 6–8) were calculated as the sum of CO₂e emissions from the production of fertilizers and herbicides and from farm agricultural machinery fuel use. Calculations (Supplementary Information, equation (5)) were based on actual field practice at the study sites, with average fuel use and production costs from published tables^{20,34–37} and the LTER Narrative Agronomic Field Log (<http://lter.kbs.msu.edu/datatables/16>). For perennial and successional systems, GHG emissions were calculated on a yearly basis.

Calculation of fossil fuel displacement due to the use of renewable fuels. We used results of published analyses for the calculation of fossil fuel displacement due to the use of renewable fuels and their co-products, or fossil fuel offset credits, similar to the procedure explained in ref. 19.

For carbon offsets due to biodiesel production, we used published results for the GREET life cycle analysis model³⁸, which compares five different approaches for crediting GHG emissions allocations to co-products: a displacement approach, an allocation approach based on the energy value of co-products, an allocation approach based on the market value of co-products and two hybrid approaches that integrate the displacement and allocation methods. We used the approach based on the energy value of co-products, which sums to 7.6 kgCO₂e per kilogram of soybean diesel, or 193.9 gCO₂e MJ⁻¹ using a biodiesel energy yield of 34.5 MJ l⁻¹ and a diesel volumetric density of 0.88 g ml⁻¹ (refs 39, 40). Of this sum, 1.16 kgCO₂e per kilogram of biodiesel is allocated to soy meal, 1.29 kgCO₂e kg⁻¹ to glycerin, 1.08 kgCO₂e kg⁻¹ to fuel gas (displacing natural gas), 0.76 kgCO₂e kg⁻¹ to heavy oil, 0.20 kgCO₂e kg⁻¹ to propane fuel mix, 0.96 kgCO₂e kg⁻¹ to product gas, 0.99 kgCO₂e kg⁻¹ to light cycle gas and 1.15 kgCO₂e kg⁻¹ to clarified slurry oil³⁸.

Further, we substituted our measured emissions from agricultural inputs for the 39.4 gCO₂e MJ⁻¹ estimated by the GREET model, which are based on emissions of 278 gCO₂e kg⁻¹ for produced soybean grain (GREET, version 1.8d.1). More specifically, GREET assumes farm energy use of 825.9 kJ per kilogram of soybean grain produced (21,310 BTU per bushel); additionally, GREET assumes the following farming inputs (per kilogram of soybean grain): 1.9 g N fertilizer, 5.6 g P₂O₅, 11.2 g K₂O, 157.0 g CaCO₃, 0.5 g herbicides and 0.001 g insecticide. One kilogram of soybean grain can produce 0.2051 of biodiesel (using conversion factors as above), which will contain 7.1 MJ of energy. For conversion of GREET assumptions to an areal basis, we assume an average production of 2.5 Mg ha⁻¹ (average soybean grain yield in Kalamazoo county, Michigan¹⁸). Thus, using our site soybean yields and GREET assumptions, we calculate, for our site, emissions of 69.2 gCO₂e m⁻² during soybean farming (278 gCO₂e per kilogram of soybeans × 2,489 kg soybeans per hectare).

Using measured farming activities (Supplementary Tables 6–8), we calculate that overall emissions from farming during the average soybean rotational year in KBS LTER fields were lower than assumed in the GREET and summed to 10.2 and 11.1 gCO₂e m⁻² yr⁻¹ for conventionally tilled and no-till systems, respectively (Supplementary Table 11). Using a similar procedure to calculate GHG emissions per energy unit (gCO₂e MJ⁻¹; see above), we estimate that KBS LTER emissions sum to 7.1 and 6.8 gCO₂e MJ⁻¹ of biodiesel energy for conventionally tilled and no-till systems, respectively. Thus, we added the difference between emissions from agricultural inputs in both cases (32.3 and 32.6 gCO₂e MJ⁻¹) to the carbon offset of biodiesel, calculated by the GREET model. This makes our fossil fuel offset value greater than those estimated by GREET, that is, 225.6 and 225.9 gCO₂e MJ⁻¹ of biodiesel energy produced for conventionally tilled and no-till systems, respectively (Supplementary Table 11). Average soybean yields for our sites were between 2.0 and 2.3 Mg ha⁻¹ yr⁻¹ or ~217 g m⁻² yr⁻¹ (Supplementary Table 1), which could produce ~39 g of biodiesel per square metre, or ~1.5 MJ m⁻², and thus could offset ~339 gCO₂e m⁻² yr⁻¹.

For carbon offsets associated with the production of corn grain ethanol, we used a comparison between results of life cycle analysis by the EBAMM and GREET models, with the latter using dry milling for corn ethanol production^{38,41,42}. We estimate the CO₂e cost of producing, distributing and combusting fossil gasoline at 94.0 gCO₂e per megajoule of gasoline energy, calculated from the EBAMM model as reported in ref. 41. For estimation of the CO₂e costs of production and distribution of corn ethanol, we used management data from our site for the agricultural phase and the corn ethanol scenario from GREET (version 1.8d.1).

Using measured farming activities (Supplementary Tables 6 and 7), we calculate that overall emissions from farming during the average corn rotational year at KBS LTER fields are between 72.9 and 73.0 gCO₂e m⁻² yr⁻¹ for conventionally tilled and no-till systems, respectively (Supplementary Table 8) or 37.7 and 34.7 gCO₂e MJ⁻¹, respectively, on the basis of KBS yields (Supplementary Table 1) and agricultural inputs used for the Fuel_Prod_TS module of the GREET model. In GREET, the emissions associated with the agricultural part of corn ethanol production sum to 36.1 gCO₂e MJ⁻¹ (GREET, version 1.8d.1); the differences between GREET and measured emissions are associated with differences in agricultural inputs such as fertilizers and energy and assumed crop yield. For example, GREET assumes 15.3 gN fertilizer per kilogram of corn, whereas our measured values are 21.4 gN per kilogram of corn. Assumed P and K use, on the other hand, was larger in the GREET model than at KBS: 5.8 versus 6.8 gP per kilogram of corn and 0.3 versus 1.4 gK per kilogram of corn (GREET versus KBS). Agricultural lime usage also was higher in GREET than at KBS: 45.3 versus 1.3 g per kilogram of corn. Energy-use assumptions in GREET were similar to measured values: ~0.4 and ~0.5 MJ per kilogram of corn, respectively. Finally, the actual yields at KBS were lower than assumed in the GREET (9.9 versus 6.1 Mg of corn per hectare for GREET and KBS, respectively), owing to rainfall variability over the period examined; irrigated yields at KBS are ~13 Mg of corn per hectare (Supplementary Materials). We assumed no emissions associated with land-use change for our long-cropped, well-equilibrated KBS soils. All emissions associated with the ethanol production phase in GREET were accounted for without adjustments (except yield differences).

We used these estimates for calculations of overall emissions from corn grain ethanol production, and adjusted CO₂e offsets generated by the GREET model accordingly, similar to estimates of CO₂e emissions from the production of soybeans (above). We thus estimate that overall emissions from corn-based ethanol for KBS are 68.1 and 65.1 gCO₂e per megajoule of ethanol energy for conventionally tilled and no-till systems, respectively (37.7 and 34.7 gCO₂e MJ⁻¹ for the agricultural part and 30.4 gCO₂e MJ⁻¹ for the biorefinery part), after adjustment of assumed GREET inputs to measured KBS inputs. In comparison, overall emissions calculated by GREET (version 1.8d.1) were 66.5 gCO₂e MJ⁻¹: 36.1 and 30.4 gCO₂e MJ⁻¹ for the agricultural and biorefinery parts of the cycle, respectively. This makes the estimated fossil fuel offset credits for KBS very similar to that estimated by GREET for average corn grain ethanol production across the United States. This analysis accounts for CO₂e emissions from farm operations, transportation and biorefinery operations. Thus, we estimate the net reduction in CO₂e emissions as the difference between emissions from the production, distribution and combustion of fossil gasoline (94.0 gCO₂e MJ⁻¹; EBAMM, release 1.1^{42,43}) and the distribution and production of corn ethanol, for net savings of 25.9 and 28.9 gCO₂e per megajoule of corn ethanol energy produced by KBS fields under conventional and no-till management, respectively.

For ethanol produced from wheat grain, we adjusted GREET model inputs to those actually measured at KBS for wheat farming, and estimated overall emissions from the agricultural phase in GREET to be 37.8 and 35.6 gCO₂e per megajoule of ethanol energy for conventionally tilled and no-till systems, respectively. Although the GREET model has no wheat scenario, we assumed that the use of measured agricultural inputs and wheat yields provides a good approximation of the emissions associated with wheat production, especially because other farming activities (travel of workers to farm fields, labour input, machinery production and so on) are similar in wheat and corn farming. Furthermore, we assumed that the ethanol distillation phase of corn ethanol does not differ significantly from that of wheat ethanol.

We used GREET-generated CO₂e emissions per megajoule of energy to estimate potential fossil fuel offset credits when wheat grain is used for bioethanol production, that is, 25.8 and 28.0 gCO₂e MJ⁻¹ for conventionally tilled and no-till systems, respectively. Although we assumed that the biorefinery part of wheat ethanol production is similar to that of corn ethanol production, the energy value of wheat ethanol co-products, dried distillers grains with solubles, is on average 17% lower than that of corn dried distillers grains with solubles⁴³. Thus, we reduced the fossil fuel offset calculated from GREET for wheat grain ethanol further by 17%, with offset final values of 21.4 and 23.2 gCO₂e MJ⁻¹ for conventionally tilled and no-till systems, respectively. For cellulosic ethanol from wheat straw, we estimated net CO₂e offsets of 108.3 gCO₂e per megajoule of ethanol energy for both types of management, after allocation of all agricultural emissions to wheat grain production.

For the estimation of fossil fuel offsets for scenarios with cellulosic ethanol production from poplar, alfalfa and herbaceous vegetation (successional and successional + N), we similarly used comparisons of emissions assumed in GREET with those measured at our site. Emissions associated with agricultural inputs assumed in GREET, 6.6 and 18.6 gCO₂e MJ⁻¹ for the production of tree and herbaceous vegetation, respectively, were different from those measured at

our sites: 2.3, 8.0, 1.0 and 9.9 gCO₂e MJ⁻¹ for poplar, alfalfa, successional and successional + N systems, respectively (Supplementary Table 8). Furthermore, we adjusted GREET-generated fossil fuel carbon offset values for measured emissions. We estimate that production of 1 MJ of energy from cellulosic feedstock in the alfalfa scenario would save 103.3 gCO₂e and that the savings would be 105.0 gCO₂e MJ⁻¹ in the poplar scenario and 107.3 and 98.4 gCO₂e MJ⁻¹ in the successional and successional + N scenarios, respectively (Supplementary Table 8). Under the original GREET assumptions, ethanol production would save 89.7 gCO₂e MJ⁻¹ from herbaceous vegetation and 100.7 gCO₂e MJ⁻¹ from the farmed woody biomass.

To calculate the potential energy produced from biofuels, we used average KBS LTER yields, harvestable biomass from the successional treatment (Supplementary Table 1) and ethanol energy content (lower heating value assumed to be 21.1 MJ per litre of ethanol). We assumed a biorefinery yield of 0.43 l of bioethanol per kilogram of dry corn and wheat grain; 0.38 l of bioethanol per kilogram of dry wheat straw, corn stover and cellulosic biomass^{19,44}; and 0.21 l of biodiesel per kilogram of soybean grain^{39,40}. The energy-equivalent amounts of fossil fuel use avoided due to the use of biofuels were calculated (Supplementary Information, equation (6)) using lower-heating-value energy contents (34.5 and 21.1 MJ l⁻¹ for biodiesel and ethanol, respectively) and the specific densities of each fuel^{19,40,45}.

To compare the sustainability of biofuel production between different scenarios, we estimated the GHG emission intensity (gCO₂e MJ⁻¹), defined here as the net CO₂e balance per unit of biofuel energy produced in the system (Supplementary Information, equations (7)–(8)).

Model simulations of plant biomass yields at regional scales. We used the EPIC model^{46–48} to simulate plant biomass yields on regional scales (for site-specific simulations and sensitivity analysis, see Supplementary Methods and Supplementary Figs 4 and 5). EPIC is a comprehensive biophysical process model capable of simulating plant yield and net primary productivity for diverse types of vegetation using weather, terrain, soil and management data. To simulate plant growth, EPIC uses radiation-use efficiency⁴⁹ to calculate the potential daily photosynthetic biomass production. Calculated daily potential growth is decreased proportionately by the most severe stress due to non-optimal conditions of water, nutrients (N and P), air and soil temperatures, soil acidity and soil salinity. EPIC has undergone comprehensive validation for a wide range of soils, management practices and climates in the United States⁵⁰ and across the world⁵¹.

Regional EPIC simulations. We implemented an EPIC-based, spatially explicit integrative modelling framework⁴⁸ to simulate yields of perennial species grown on marginal lands across the ten-state study area in the US north-central region (Supplementary Fig. 6). This region extends from North Dakota in the northwest corner to Nebraska in the southwest corner, Ohio in the southeast corner, and Michigan in the northeast corner. The Canadian–US border defines the northern border of the study region. A spatially explicit geospatial database containing soil, terrain, weather, land-use/land-cover and management data was used to obtain relevant parameters for running the EPIC model. Details of the geospatial database follow.

Soils. Soil Survey Geographic data from the US Department of Agriculture Geospatial Data Gateway (<http://datagateway.nrcs.usda.gov>) were used to create a continuous-scale soil property database at ~30-m scale. Properties included the number of soil layers; layer depth; slope gradient and length; bulk density; pH; per cent sand, silt, clay and coarse fragments; and per cent organic carbon and total nitrogen. To define marginal lands, we also extracted the land capability class (LCC) variable, which describes land classes on the basis of use limitation such as erosion risk, soil depth, wetness and slope⁵². There are eight LCCs, ranging from class I (lands without any limitations for agricultural use) to class VIII (lands with severe limitations). Classes I–IV can support cropland agriculture, whereas classes V–VIII contain non-arable land.

Topography. To derive topographical information, we used data from NASA's Shuttle Radar Topography Mission, which produced a digital elevation model for the region at a resolution of 30 m (ref. 53). Geospatial analysis was used to derive slope length and gradient for each spatial modelling unit.

Climate data. EPIC requires daily weather information including daily temperature (maximum and minimum), precipitation, solar radiation, wind speed and relative humidity. The North America Regional Reanalysis database (<http://www.esrl.noaa.gov/psd/data/gridded/data.narr.html>) was used to derive daily weather files at 32-km resolution⁵⁴.

Land use and land cover. The US National Agricultural Statistical Service's cropland data layer for 2008⁵⁵ and the Soil Survey Geographic database (ref. 29, accessed 26 August 2011) were combined to define land use, land cover and soil type at a spatial resolution of 60 m for the simulation domain. We excluded vegetation that has been planted in recreational areas such as parks or golf courses, vegetation for erosion control in developed areas and vegetation on federal lands.

Marginal lands. Marginal lands were identified as rural lands falling into LCCs V–VII with slope gradients of <20% (Supplementary Table 12) under non-forested vegetation. Available data sets do not allow us to distinguish between marginal lands readily available for biofuel feedstocks production and areas currently grazed. We use the cropland data layer estimate for grazed land to provide a maximum worst-case estimate, recognizing that only a portion of this estimate will fall into LCCs V–VII with slope gradients of <20%.

We gave special consideration to the Sandhills region of Nebraska, where unique grass-stabilized sand dune topography distinguishes the dunes from the surrounding prairies⁵⁶. The sand dunes can be 100 m tall and several kilometres long. To exclude the highly erodible dune ridges and slopes from the analysis, we used the topographic position index algorithm in ArcGIS⁵⁷. This index is a classification scheme based on the difference in elevation value between a cell in a digital elevation model raster and its neighbours. The extent to which a cell is higher or lower than its neighbours, combined with its slope, can be used to assign it a landform classification such as valley, slope or ridge. Removing the dune ridges and slopes from the analysis reduced the area available for consideration as marginal lands by more than 200,000 ha. The interdune valleys falling into LCCs V–VII and with slope gradients of <20% were then used for further analysis.

EPIC simulations and identification of biorefinery locations. For each grid of marginal land, we simulated above-ground net primary productivity using the calibrated EPIC model with three levels of nitrogen fertilization: 0, 68 and 123 kgN ha⁻¹ yr⁻¹. Modelled field size for the estimation of potential productivity varied substantially, with a minimum size of 0.36 ha and a maximum of >650 × 10³ ha. Overall, we simulated 78,184 fields having unique combinations of soil type, land use and LCC. The connectivity between each field and nearby fields was not assessed. The maximum potential overlap of our defined marginal lands with grazing lands within each potential biorefinery circle ranges from 0 to 71%, with a regional maximum average of ~8% (Supplementary Table 3).

The values of above-ground net primary productivity obtained from EPIC (Supplementary Tables 2 and 3) were used to identify the location of potential biorefineries that could process the cellulosic feedstocks to ethanol production (Supplementary Information, equation (1)). We limited potential biorefineries to areas where potential feedstock production in fertilized (68 kgN ha⁻¹ yr⁻¹) simulations were at least 653 Ggyr⁻¹ of cellulosic biomass on marginal lands from within an economically feasible transportation distance of 80 km (ref. 58). For this, we used a moving-window algorithm over the ten-state US midwest region and aggregated biomass yields from marginal lands falling within an 80-km-radius circle. Subsequently, non-overlapping circles with the highest biomass yields were selected for potential biorefinery locations. Actual locations of circles are partly dependent on geographic starting points for the moving-window analysis.

33. Forster, P. et al. in *Climate Change 2007: The Physical Science Basis* (eds Solomon, S. et al.) 129–234 (Cambridge Univ. Press, 2007).
34. West, T. O. & Marland, G. A synthesis of carbon sequestration, carbon emissions, and net carbon flux in agriculture: comparing tillage practices in the United States. *Agric. Ecosyst. Environ.* **91**, 217–232 (2002).
35. Lal, R. Carbon emission from farm operations. *Environ. Int.* **30**, 981–990 (2004).
36. Stein, D. 2008–2009 Custom Machine and Work Rate Estimates. *MSUE District Farm Business Management* <https://www.msu.edu/user/steind/> (2009).
37. Syswerda, S. P., Basso, B., Hamilton, S. K., Tausig, J. B. & Robertson, G. P. Long-term nitrate loss along an agricultural intensity gradient in the Upper Midwest USA. *Agric. Ecosyst. Environ.* **149**, 10–19 (2012).
38. Huo, H., Wang, M., Bloyd, C. & Putsche, V. Life-cycle assessment of energy use and greenhouse gas emissions of soybean-derived biodiesel and renewable fuels. *Environ. Sci. Technol.* **43**, 750–756 (2009).
39. Sheehan, J. et al. *Life Cycle Inventory of Biodiesel and Petroleum Diesel for Use in an Urban Bus*. Report No. NREL/SR-580-24089 (USDA, 1998).
40. Patzek, T. W. A first law thermodynamic analysis of biodiesel production from soybean. *Bull. Sci. Technol.* **29**, 194–204 (2009).
41. Farrell, A. E. et al. Ethanol can contribute to energy and environmental goals. *Science* **311**, 506–508 (2006).
42. Plevin, R. J. Modeling corn ethanol and climate: a critical comparison of the BESS and GREET models. *J. Ind. Ecol.* **13**, 495–507 (2009).
43. Nuez Ortin, W. G. & Yu, P. Nutrient variation and availability of wheat DDGS, corn DDGS and blend DDGS from bioethanol plants. *J. Sci. Food Agric.* **89**, 1754–1761 (2009).
44. Kim, S. & Dale, B. E. Life cycle assessment of various cropping systems utilized for producing biofuels: bioethanol and biodiesel. *Biomass Bioenergy* **29**, 426–439 (2005).
45. Oak Ridge National Laboratory. Bioenergy conversion factors. <http://www.localenergy.org/pdfs/Document Library/Bioenergy conversion factorspdf> (2011).
46. Williams, J. R. in *Computer Models of Watershed Hydrology* (ed. Singh, V. P.) 909–1000 (Water Research Publications, 1995).
47. Izaurre, R. C. et al. Simulating soil C dynamics with EPIC: model description and testing against long-term data. *Ecol. Modell.* **192**, 362–384 (2006).

48. Zhang, X. *et al.* An integrative modeling framework to evaluate the productivity and sustainability of biofuel crop production systems. *GCB Bioenergy* **2**, 258–277 (2010).
49. Sinclair, T. R., Muchow, R. C. & Donald, L. S. Radiation use efficiency. *Adv. Agron.* **65**, 215–265 (1999).
50. Izaurralde, R. C., Rosenberg, N. J., Brown, R. A. & Thomson, A. M. Integrated assessment of Hadley Center (HadCM2) climate-change impacts on agricultural productivity and irrigation water supply in the conterminous United States: Part II. Regional agricultural production in 2030 and 2095. *Agric. For. Meteorol.* **117**, 97–122 (2003).
51. Tan, G. & Shibasaki, R. Global estimation of crop productivity and the impacts of global warming by GIS and EPIC integration. *Ecol. Modell.* **168**, 357–370 (2003).
52. Klingebiel, A. A. & Montgomery, P. H. *Land-Capability Classification* (USDA, 1961).
53. Farr, T. G. *et al.* The shuttle radar topography mission. *Rev. Geophys.* **45**, RG2004 (2007).
54. Mesinger, F. *et al.* North American regional reanalysis. *Bull. Am. Meteorol. Soc.* **87**, 343–360 (2006).
55. Johnson, D. M. & Mueller, R. The 2009 cropland data layer. *Photogramm. Eng. Remote Sensing* **76**, 1201–1205 (2010).
56. Eggemeyer, K. D. *et al.* Ecophysiology of two native invasive woody species and two dominant warm-season grasses in the semiarid grasslands of the Nebraska sandhills. *Int. J. Plant Sci.* **167**, 991–999 (2006).
57. Tagil, S. & Jenness, J. GIS-Based automated landform classification and topographic, landcover and geologic attributes of landforms around the Yazoren Polje, Turkey. *J. Appl. Sci.* **8**, 910–921 (2008).
58. Bailey, C., Dyer, J. F. & Teeter, L. Assessing the rural development potential of lignocellulosic biofuels in Alabama. *Biomass Bioenergy* **35**, 1408–1417 (2011).

Stable creeping fault segments can become destructive as a result of dynamic weakening

Hiroyuki Noda¹ & Nadia Lapusta^{2,3}

Faults in Earth's crust accommodate slow relative motion between tectonic plates through either similarly slow slip or fast, seismic-wave-producing rupture events perceived as earthquakes^{1–3}. These types of behaviour are often assumed to be separated in space and to occur on two different types of fault segment: one with stable, rate-strengthening friction and the other with rate-weakening friction that leads to stick-slip^{2–5}. The 2011 Tohoku-Oki earthquake with moment magnitude $M_w = 9.0$ challenged such assumptions by accumulating its largest seismic slip in the area that had been assumed to be creeping^{6–10}. Here we propose a model in which stable, rate-strengthening behaviour at low slip rates^{11,12} is combined with coseismic weakening due to rapid shear heating of pore fluids^{13–16}, allowing unstable slip to occur in segments that can creep between events. The model parameters are based on laboratory measurements on samples from the fault of the M_w 7.6 1999 Chi-Chi earthquake¹⁷. The long-term slip behaviour of the model, which we examine using a unique numerical approach that includes all wave effects^{16,18}, reproduces and explains a number of both long-term and coseismic observations—some of them seemingly contradictory—about the faults at which the Tohoku-Oki and Chi-Chi earthquakes occurred, including there being more high-frequency radiation from areas of lower slip^{8,19–21}, the largest seismic slip in the Tohoku-Oki earthquake having occurred in a potentially creeping segment^{6,7}, the overall pattern of previous events in the area⁸ and the complexity of the Tohoku-Oki rupture⁹. The implication that earthquake rupture may break through large portions of creeping segments, which are at present considered to be barriers, requires a re-evaluation of seismic hazard in many areas.

Seismic and geodetic observations have revealed that faults in Earth's crust can accommodate slow tectonic motion in different ways. Some fault areas respond with stable, quasi-static motion, with slip rates comparable to tectonic rates of millimetres to tens of millimetres per year; other fault regions remain locked for years and then experience fast dynamic ruptures that we perceive as earthquakes, with average slip rates of the order of 1 m s^{-1} (refs 1–3). One way to account for such observations is to separate fault areas into two types—stable areas, which mostly creep, and unstable areas, which produce earthquakes—perhaps with some complexity related to their interaction^{1–5}. As a consequence, large creeping segments may be regarded as intrinsically 'stable' or 'decoupled', and, hence, as barriers to seismic rupture.

The 2011 M_w 9.0 Tohoku-Oki earthquake challenged such assumptions by accumulating its exceptionally large seismic slip, of as much as $\sim 50 \text{ m}$, in the shallower area of the megathrust, which had been considered creeping and, hence, stable^{6–10} (Fig. 1a). This unanticipated slip not only surprised the earthquake science community but resulted in the unexpectedly large magnitude of the earthquake and the extremely high tsunami that followed⁸. Previous large (M_w 7–8) events recorded in the area had occurred deeper on the megathrust⁸. The geodetic data cannot resolve whether the shallower area of large coseismic slip had been creeping or not^{7,10}. Another puzzling observation from the Tohoku-Oki earthquake is the fact that the lower-slip area produced

more high-frequency radiation^{8,21}. A similar observation has been previously made for the 1999 M_w 7.6 Chi-Chi earthquake^{19,20} (Fig. 1b).

The earthquake source model that we propose here—in which creeping segments can generate large seismic slips owing to rapid shear heating of pore fluids and the resulting coseismic weakening—can qualitatively explain these and other observations within a single physical framework. Our model includes two aspects of earthquake source physics that have been gaining acceptance and validation through laboratory experiments and comparison of earthquake models with observations.

The first is the 'rate-and-state' nature of fault friction at low, aseismic slip rates, which has been conclusively documented in laboratory experiments and used to reproduce, both qualitatively and quantitatively, a number of earthquake-source observations^{11,12}. In the rate-and-state friction laws (Methods), the steady-state frictional strength, τ_{ss} , depends on the slip rate, V , and the effective normal stress, $\sigma - p$, and is given by

$$\tau_{ss}(V) \approx (\sigma - p)[f_0 + (a - b) \ln(V/V_0)] \quad (1)$$

Here σ is the fault normal stress, p is the pore pressure of fluids that permeate the fault, f_0 is the steady-state friction coefficient at a reference slip rate V_0 and $a - b$ is the rate-and-state parameter, which can be used to model both stable, rate-strengthening fault segments ($a - b > 0$) and potentially seismic, rate-weakening fault segments ($a - b < 0$).

The second emerging property of the earthquake source is additional substantial fault weakening at seismic slip rates. Although theories of such weakening have a long history¹³, relatively recent laboratory confirmations of this phenomenon^{23,24} have lent further credence to this notion in earthquake science. One of the physical mechanisms for coseismic weakening is the temperature increase due to rapid shear heating, which causes thermal expansion of pore fluids^{13–16}. If the rock surrounding the fault shear zone has sufficiently low permeability, the resulting increase in p lowers $\sigma - p$ and, hence, the friction resistance in equation (1). Such thermal pressurization has been suggested as an important source mechanism for the 1999 Chi-Chi earthquake^{18,22}. Several other mechanisms of coseismic weakening have been proposed and used to simulate fault-slip phenomena, including in the Tohoku-Oki area^{15,24,25}.

Our fault model (Fig. 1c, d) incorporates a patch that combines stable, rate-strengthening properties at low slip rates with substantial coseismic weakening due to thermal pressurization of pore fluids. Such a set of properties is motivated by laboratory measurements¹⁷ on samples from the Chelungpu fault, Taiwan, which hosted the 1999 M_w 7.6 Chi-Chi earthquake, one of the most well-studied seismic events^{17,19,20}. Chi-Chi's fault rupture nucleated in the southern region of the Chelungpu fault and propagated mainly to the north, where it accumulated its largest coseismic slip, of about 8 m (Fig. 1b). However, the southern region, of substantially lower slip, generated more high-frequency radiation²⁰, just as observed for the Tohoku-Oki earthquake²¹. Laboratory measurements¹⁷ on rock samples from two shallow boreholes that penetrated the Chelungpu fault indicate that, at low slip rates, the southern fault region has earthquake-prone

¹Institute for Research on Earth Evolution, Japan Agency for Marine-Earth Science and Technology, Yokohama, Kanagawa, 236-0001, Japan. ²Division of Geological and Planetary Sciences and ³Division of Engineering and Applied Science, California Institute of Technology, Pasadena, California 91125, USA.

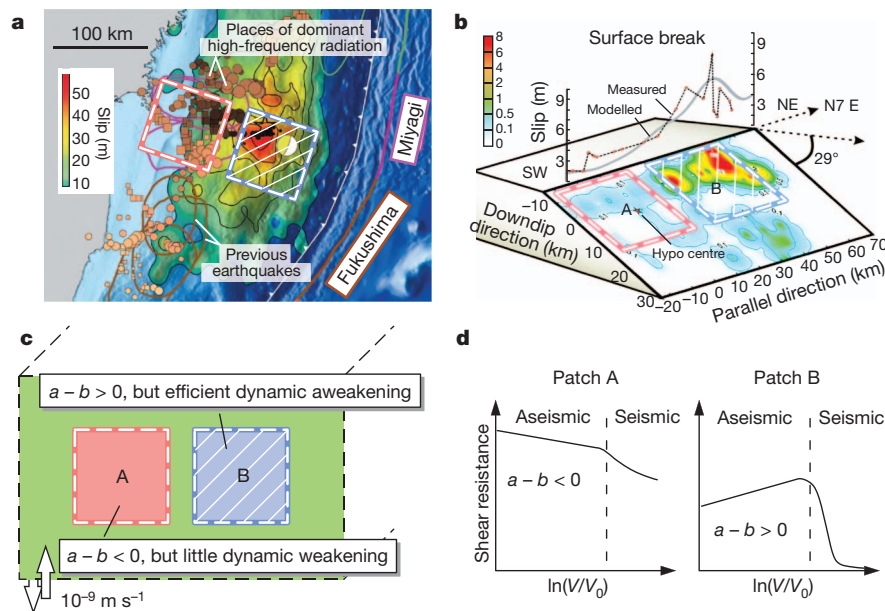


Figure 1 | Schematics of the fault model and its correspondence to great earthquakes. **a, b**, Slip distributions in the 2011 Tohoku-Oki earthquake (**a**; adapted from ref. 8) and the 1999 Chi-Chi earthquake (**b**; adapted from ref. 20). They featured a higher-slip patch producing less high-frequency radiation than the neighbouring lower-slip patch. The two squares outline the patches of our model. **c**, Fault model motivated by experimental studies¹⁷ for the

Chelungpu fault, which hosted the Chi-Chi earthquake. At aseismic slip rates, patch A has instability-prone, rate-weakening friction whereas patch B has stable, rate-strengthening friction. However, patch B is more susceptible to coseismic weakening. **d**, Schematic plots of how shear resistance in the patches depends on their respective slip rates.

rate-weakening friction ($a - b < 0$) whereas the northern region has stable, rate-strengthening friction ($a - b > 0$). However, the rock permeability is lower in the north by about two orders of magnitude¹⁷, indicating that the northern part of the fault is more susceptible to coseismic weakening by thermal pressurization of pore fluids. Motivated by these measurements, our model considers the interaction of two patches, A and B, with the corresponding laboratory-measured properties (Fig. 1, section 1 of Supplementary Information, Supplementary Fig. 1 and Supplementary Table 1). To the best of our knowledge, this is the first study of long-term fault behaviour motivated by laboratory studies of materials from an actual fault zone.

We study the implications of this rich fault rheology in a simplified model of a planar fault embedded into a homogeneous, elastic space. This set-up allows us to investigate the qualitative consequences of the rheology without additional complexity associated with fault geometry and bulk properties. It also enables us to use a unique and highly efficient computational methodology^{16,18} for simulation of earthquake sequences and slow slip, which incorporates both slow tectonic loading and all inertial (wave) effects of dynamic ruptures but is at present restricted to relatively simple fault geometries. The numerical approach solves for the time evolution of fault slip and stress governed by a highly nonlinear coupled system of elastodynamic equations describing stress interactions, and includes rate-and-state friction on the fault that depends, in part, on the evolving slip rate and pore pressure, and explicit calculation of temperature and pore pressure evolution on the fault that incorporates fault-normal diffusion of heat and pore fluids (Methods). On the fault, the two interacting patches are surrounded by a rate-strengthening region with no coseismic weakening, which, in turn, is surrounded by areas steadily moving at a representative plate rate of 10^{-9} m s^{-1} .

The resulting model response in terms of earthquake sequences and slow slip qualitatively reproduces a range of observations for both the Chi-Chi and the Tohoku-Oki earthquake on scales ranging from that of a single seismic event to several earthquake cycles (Figs 2 and 3).

The produced earthquake sequences consist of two types of event: smaller, more-frequent events that rupture only patch A, and larger,

model-spanning events that spread over both patches (Fig. 2a). All seismic events initiate in patch A, which is susceptible to earthquake nucleation owing to its rate-weakening properties at low slip rates, and many of them arrest without rupturing patch B. However, occasional events manage to penetrate into patch B and activate coseismic weakening there, essentially changing the patch from being (interseismically) stable to (coseismically) unstable. In such model-spanning events, the slip is largest in patch B, owing to larger pore-pressure-induced weakening and the associated larger stress drop (Supplementary Fig. 2a). Whether dynamic rupture is successful in activating coseismic weakening in patch B depends on a number of factors (Supplementary Information, section 3).

Such an overall pattern of seismic slip is consistent with observations and inferences for the areas of both the Tohoku-Oki and the Chi-Chi earthquake. In the Tohoku subduction zone, many M_w 7–8 events have occurred on the deeper part of the subduction interface, which experienced lower slip in the Tohoku-Oki earthquake⁸ (Fig. 1a). Similarly, a series of trench surveys along the Chelungpu fault has revealed that earthquakes occur more often in the southern part of the Chi-Chi earthquake source region, which experienced less slip, than in the northern part²⁶. The model dimensions are tailored to the size of the Chi-Chi source, and many model-spanning events indeed have peak slip comparable to the 8 m observed in the northern part of the Chi-Chi rupture.

Patch B, which combines laboratory-measured properties that allow for both interseismic creep and rapid coseismic slip, produces a rich variety of behaviours in a single model (Fig. 2), from creeping with the long-term convergence rate (that is, being fully decoupled), to occasionally participating in large seismic events, to being locked (that is, fully coupled) (section 2 of Supplementary Information, Supplementary Figs 2b and 3, and Supplementary Videos 1 and 2). Such behaviour provides a new physical interpretation of the conceptual notion of ‘conditionally stable’ fault behaviour¹². Importantly, immediately before a seismic event manages to propagate through it, patch B can be creeping (decoupled), in contrast to the notion that large earthquakes rupture mostly locked patches or asperities^{2–4}. This richness of

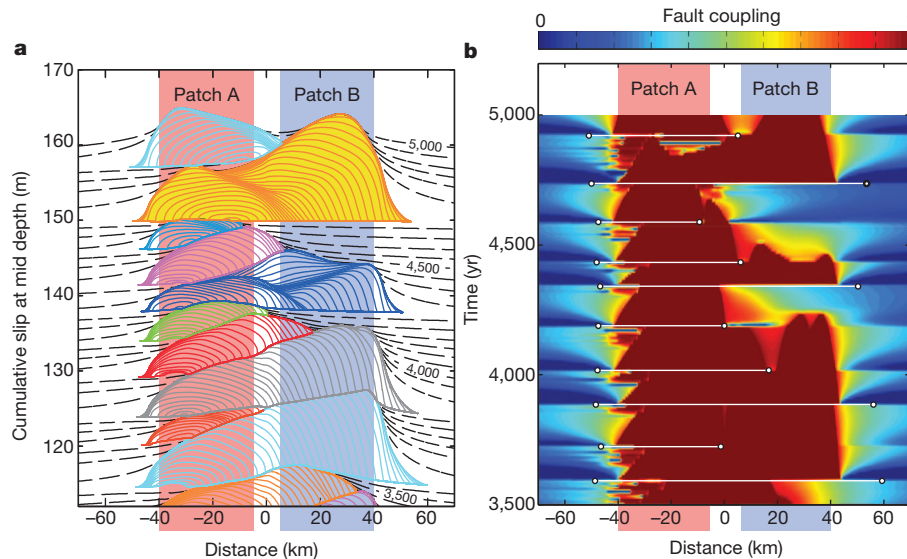


Figure 2 | Long-term behaviour of the model in terms of earthquake sequences and aseismic slip. **a**, Cumulative slip distribution along the fault at mid depth. Earthquakes are shown by the solid lines, which are plotted with a time step of 1 s. Dashed lines represent slow slip every 50 yr, with the numbers indicating the simulated time in years. Patch A experiences stick-slip. Patch B

behaviour stands in contrast to patch A, which has relatively simpler stick-slip response.

In addition to capturing the long-term behaviour, our model simultaneously reproduces the coseismic observations on less-pronounced high-frequency radiation from the area of the largest slip in both the Chi-Chi and the Tohoku-Oki earthquake^{20,21}. Patch B has higher slip but a smoother slip-rate history than does patch A (Fig. 3a, b), as a result of both more-gradual weakening through pore pressurization and the velocity-strengthening nature of the initial response at the rupture front. This is reflected in the power spectrum of the source time functions (Fig. 3c): in patch B, the low-frequency content is larger but the spectrum decays more rapidly.

The interaction of the two patches can also produce the complex rupture pattern (Fig. 3a and Supplementary Video 1, from 59 s to 1 min 2 s) inferred for the Tohoku-Oki earthquake⁹. After nucleating near the middle of the fault, the rupture first propagates mostly to the left, into patch A. As thermally induced weakening of patch B progresses, the rupture there accelerates and accumulates larger slip, creating stress concentration over patch A and causing re-rupturing of patch A. This re-rupturing would be more prominent in models with higher slip contrast between the two patches. The re-rupturing

can both creep and participate in earthquakes, accumulating large seismic slip. **b**, Evolution of fault coupling (Methods Summary), with locked segments corresponding to a coupling of 1. White lines indicate the extent of earthquake ruptures. Note that patch B can be either creeping or locked before model-spanning seismic events.

feature is also present in simulations with patches of identical frictional properties but different permeabilities; however, the behaviour of that model differs in other important respects (section 4 of Supplementary Information, Supplementary Figs 4 and 5, and Supplementary Table 1).

Our study shows that both long-term and coseismic observations from the areas of the Tohoku-Oki and Chi-Chi earthquakes can be explained and reconciled by the presence of fault patches that are stable at low slip rates but can experience shear-induced coseismic weakening. Our results demonstrate how fluids can cause stable fault behaviour to become destructive through thermal fluid pressurization during rapid slips. In fact, experimental studies have shown that wet, clay-rich sediments, which are likely to be present in shallow portions of subduction zones, are indeed susceptible to thermal pressurization²⁷. Other coseismic weakening processes^{15,23–25} may have similar effects. Our findings add to the accumulating evidence that earthquake source processes may be controlled by the interaction between rate- and state-dependent friction properties and effects of fluids that permeate Earth's crust; for example, fluid effects related to dilatancy have been shown to facilitate slow slip events²⁸. Combination of another coseismic weakening formulation with a mix of rate-strengthening or rate-weakening low-slip-rate properties has been

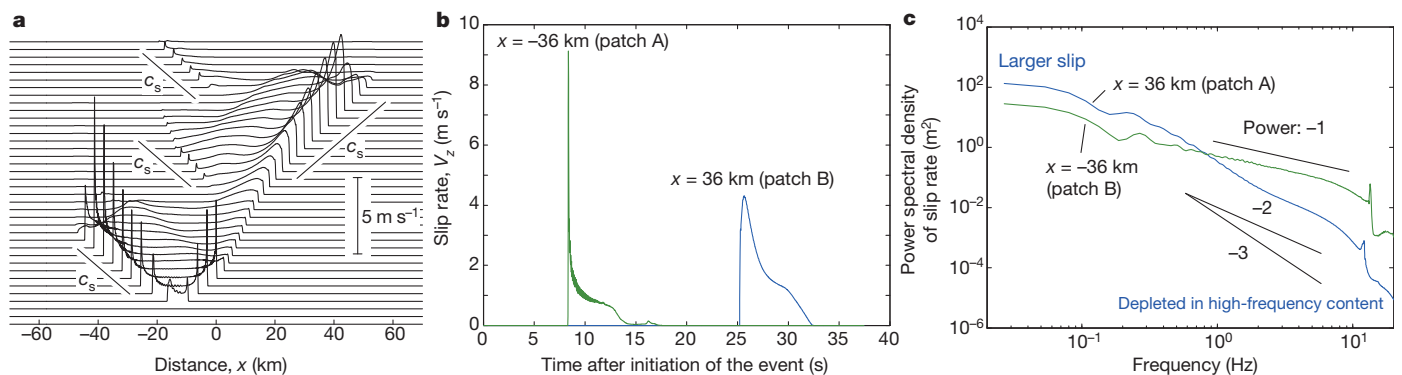


Figure 3 | Coseismic behaviour of a model-spanning event. The event is that shown in yellow in Fig. 2a. **a**, Snapshots of slip-rate distribution every 1 s along the fault at mid depth, displaced vertically for clarity. The event nucleates near the middle of the fault, ruptures patch A, ruptures patch B with larger slip and then re-ruptures patch A, as inferred for the Tohoku-Oki earthquake⁹. c_s ,

shear-wave speed. **b**, Slip-rate histories at representative points. The history of patch B is smoother than that of patch A, owing to initial rate-strengthening behaviour and subsequent more gradual weakening. **c**, Frequency structure of the slip-rate histories. Patch B produces larger slip but less high-frequency content, as observed in the Tohoku-Oki and Chi-Chi earthquakes^{20,21}.

shown to match the long-term slip pattern in a geometrically realistic model of the Tohoku-Oki area²⁵; however, coseismic properties of the resulting ruptures have not been explored and would be difficult to interpret owing to the quasi-dynamic approximation used in those studies.

Findings such as these have important implications for seismic hazard, because they suggest that currently creeping (decoupled) fault regions, which are thought to be stable and aseismic, may participate in destructive events and host large seismic slip. After large events, such regions would stay locked for a while, but would eventually accumulate enough stress to start creeping again, obscuring the evidence of their destructive past. Hence, using only the relatively short recorded seismic and geodetic history to estimate seismic hazard is inadequate, as demonstrated by the unexpected 2011 Tohoku-Oki earthquake. For example, on the basis of fewer than 100 years of recorded history²⁹, the creeping section of the San Andreas fault in California is thought to provide a barrier between the southern and northern locked parts of the fault, essentially preventing a massive earthquake that would involve all of California from San Diego and Los Angeles to San Francisco. However, our study provides a plausible physical mechanism by which that segment could join such a massive event. The possibility that dynamic rupture may penetrate into regions stable at low slip rates is important for the down-dip limit of large earthquakes.

To understand whether a creeping segment will participate in seismic events, it is important to assess whether it is susceptible to coseismic weakening. This can be achieved through palaeoseismic studies that look for evidence of past rapid slip³⁰. However, such studies are not feasible in many places. This highlights the importance of materials-science-based models, such as the one presented here, which can incorporate laboratory findings and explore a full range of potential fault behaviours. To be not only qualitatively but also quantitatively useful, the models need to be refined on the basis of more experimental studies on physical fault properties under realistic depth-dependent temperature–pressure conditions.

METHODS SUMMARY

Our simulation approach produces a sequence of spontaneous earthquakes and aseismic slip in a fault model, accounting for both inertial effects and long-term tectonic loading^{16,18}. In the model, a planar fault is embedded in a linear, elastic, infinite medium. Part of the fault is governed by rate- and state-dependent friction¹¹ coupled with fluctuation in the pore fluid pressure due to frictional heating and diffusion normal to the fault^{13–17}. The surrounding fault areas move with the assigned plate convergence rate, providing tectonic-like loading for the fault region of interest. The coupled problem of the elastodynamic equations in the bulk and the friction boundary condition on the fault is solved by a three-dimensional spectral boundary integral equation method that uses an adaptive time-stepping procedure^{16,18}. The fault-normal diffusion equations for temperature and pore pressure are solved by an unconditionally stable spectral method¹⁶. To investigate the combined effect of rate strengthening at low slip rates and efficient dynamic weakening at coseismic slip rates, we create a model with two fault patches of different properties (Fig. 1c). The seismogenic region that includes the two patches is comparable in size to the source region of the M_w 7.6 1999 Chi-Chi earthquake^{19,20}. The two patches have laboratory-measured frictional and hydraulic properties¹⁷ based on samples collected from boreholes penetrating the northern and southern part of the Chelungpu fault, Taiwan, which hosted the Chi-Chi earthquake. Specific values of the parameters used are given in Supplementary Information. The fault coupling plotted in Fig. 2b is defined as $1 - V/V_{pl}$ when $V \leq V_{pl}$ and as 0 when $V > V_{pl}$, where V is the slip rate and V_{pl} is the long-term plate rate.

Full Methods and any associated references are available in the online version of the paper.

Received 15 May; accepted 23 October 2012.

Published online 9 January 2013.

1. Bürgmann, R. *et al.* Earthquake potential along the northern Hayward fault, California. *Science* **289**, 1178–1182 (2000).
2. Chlieh, M., Avouac, J.-P., Sieh, K., Natawidjaja, D. H. & Galetzka, J. Heterogeneous coupling of the Sumatran megathrust constrained by geodetic and paleogeodetic measurements. *J. Geophys. Res.* **113**, B05305 (2008).

3. Perfettini, H. *et al.* Seismic and aseismic slip on the central Peru megathrust. *Nature* **465**, 78–81 (2010).
4. Lay, T., Kanamori, H. & Ruff, L. The asperity model and the nature of large subduction zone earthquakes. *Earthq. Predict. Res.* **1**, 3–71 (1982).
5. Kaneko, Y., Avouac, J.-P. & Lapusta, N. Towards inferring earthquake patterns from geodetic observations of interseismic coupling. *Nature Geosci.* **3**, 363–369 (2010).
6. Tsuru, T. *et al.* Tectonic features of the Japan Trench convergent margin off Sanriku, northeastern Japan, revealed by multichannel seismic reflection data. *J. Geophys. Res.* **105**, 16,403–16,413 (2000).
7. Loveless, J. P. & Meade, B. Geodetic imaging of plate motions, slip rates, and partitioning of deformation in Japan. *J. Geophys. Res.* **115**, B02410 (2010).
8. Simons, M. *et al.* The 2011 magnitude 9.0 Tohoku-Oki earthquake: mosaicking the megathrust from seconds to centuries. *Science* **332**, 1421–1425 (2011).
9. Ide, S., Baltay, A. & Beroza, G. C. Shallow dynamic overshoot and energetic deep rupture in the 2011 M_w 9.0 Tohoku-Oki earthquake. *Science* **332**, 1426–1429 (2011).
10. Wei, S., Graves, R., Helmberger, D., Avouac, J.-P. & Jiang, J. Sources of shaking and flooding during the Tohoku-Oki earthquake: a mixture of rupture styles. *Earth Planet. Sci. Lett.* **333–334**, 91–100 (2012).
11. Dieterich, J. H. in *Treatise on Geophysics* Vol. 4 (ed. Kanamori, H.) 107–129 (Elsevier, 2007).
12. Scholz, C. H. Earthquakes and friction laws. *Nature* **391**, 37–42 (1998).
13. Sibson, R. H. Interaction between temperature and pore-fluid pressure during earthquake faulting: a mechanism for partial or total stress relief. *Nature* **243**, 66–68 (1973).
14. Andrews, D. J. A fault constitutive relation accounting for thermal pressurization of pore fluid. *J. Geophys. Res.* **107**, 2363 (2002).
15. Rice, J. R. Heating and weakening of faults during earthquake slip. *J. Geophys. Res.* **111**, B05311 (2006).
16. Noda, H. & Lapusta, N. Three-dimensional earthquake sequence simulations with evolving temperature and pore pressure due to shear heating: effect of heterogeneous hydraulic diffusivity. *J. Geophys. Res.* **115**, B12314 (2010).
17. Tanikawa, W. & Shimamoto, T. Frictional and transport properties of the Chelungpu fault from shallow borehole data and their correlation with seismic behavior during the 1999 Chi-Chi earthquake. *J. Geophys. Res.* **114**, B01502 (2009).
18. Lapusta, N. & Liu, Y. Three-dimensional boundary integral modeling of spontaneous earthquake sequences and aseismic slip. *J. Geophys. Res.* **114**, B09303 (2009).
19. Ma, K. F. *et al.* Spatial slip distribution of the September 20, 1999, Shi-Shi, Taiwan, earthquake (M_w 7.6)–inverted from teleseismic data. *Geophys. Res. Lett.* **27**, 3417–3420 (2000).
20. Ma, K. F. *et al.* Evidence for fault lubrication during the 1999 Chi-Chi, Taiwan, earthquake (M_w 7.6). *Geophys. Res. Lett.* **30**, 1244 (2003).
21. Meng, L., Inbal, A. & Ampuero, J.-P. A window into the complexity of the dynamic rupture of the 2011 M_w 9 Tohoku-Oki earthquake. *Geophys. Res. Lett.* **38**, L00G07 (2011).
22. Ishikawa, T. *et al.* Coseismic fluid-rock interactions at high temperatures in the Chelungpu fault. *Nature Geosci.* **1**, 679–683 (2008).
23. Tsutsumi, A. & Shimamoto, T. High velocity frictional properties of gabbro. *Geophys. Res. Lett.* **24**, 699–702 (1997).
24. Tullis, T. E. in *Treatise on Geophysics* Vol. 4 (ed. Kanamori, H.) 131–152 (Elsevier, 2007).
25. Shibazaki, B. *et al.* 3D modeling of the cycle of a great Tohoku-Oki earthquake, considering frictional behavior at low to high slip velocities. *Geophys. Res. Lett.* **38**, L21305 (2011).
26. Ota, Y. *et al.* Low-angle reverse faulting during two earthquakes on the northern part of the Chelungpu fault, deduced from the Fengyuan trench, central Taiwan. *Terr. Atmos. Ocean. Sci.* **18**, 55–66 (2007).
27. Faulkner, D. R., Mitchell, T. M., Behn, J., Hirose, T. & Shimamoto, T. Stuck in the mud? Earthquake nucleation and propagation through accretionary forearcs. *Geophys. Res. Lett.* **38**, L18303 (2011).
28. Segall, P., Rubin, A. M., Bradley, A. M. & Rice, J. R. Dilatant strengthening as a mechanism for slow slip events. *J. Geophys. Res.* **115**, B12305 (2010).
29. Bakun, W. H. *et al.* Implications for prediction and hazard assessment from the 2004 Parkfield earthquake. *Nature* **437**, 969–974 (2005).
30. Sakaguchi, A. *et al.* Seismic slip propagation to the updip end of plate boundary subduction interface faults: vitrinite reflectance geothermometry on Integrated Ocean Drilling Program NanTro SEIZE cores. *Geology* **39**, 395–398 (2011).

Supplementary Information is available in the online version of the paper.

Acknowledgements This study was supported by the US National Science Foundation (NSF) (grant EAR 0548277), the Southern California Earthquake Center (SCEC) and the Gordon and Betty Moore Foundation. The SCEC is funded by NSF Cooperative Agreement EAR-0106924 and USGS Cooperative Agreement 02HQAG0008. This is SCEC contribution no. 1675 and Caltech Tectonics Observatory contribution no. 213. Numerical simulations for this study were performed on the CiTerra Dell cluster at the Division of Geological and Planetary Sciences of the California Institute of Technology.

Author Contributions Both authors contributed to developing the main ideas, interpreting the results and producing the manuscript. H.N. designed, carried out and analysed the numerical experiments described in the paper.

Author Information Reprints and permissions information is available at www.nature.com/reprints. The authors declare no competing financial interests. Readers are welcome to comment on the online version of the paper. Correspondence and requests for materials should be addressed to H.N. (hnoda@jamstec.go.jp).

METHODS

Our model is mathematically represented by a highly nonlinear coupled system of elastodynamic equations describing stress interactions, and includes rate-and-state friction on the fault that depends, in part, on the evolving slip rate and pore pressure, and explicit calculation of temperature and pore pressure evolution on the fault that incorporates fault-normal diffusion of heat and pore fluids. Here we summarize the set of partial differential equations solved and the distributions of parameters assumed in the present study. For the solution techniques and numerical implementation, see ref. 16.

The elastodynamics of a three-dimensional infinite body is treated by a spectral boundary integral equation method^{16,18}. Shear traction on a planar fault τ is expressed as

$$\tau(\mathbf{x}, t) = \tau_0 + \phi[\mathbf{x}, t; V] - \frac{\mu}{2c_s} V(\mathbf{x}, t)$$

where \mathbf{x} is the position vector spanning the fault, t is time, τ_0 is the shear traction that would act on the fault if it were prevented from slipping, V is the slip rate, μ is the shear modulus, c_s is the shear-wave speed and ϕ is the stress redistribution term, which depends on the previous spatiotemporal distribution of V . The spatial Fourier transform of ϕ , denoted by Φ , is expressed as

$$\Phi(\mathbf{k}, t) = C_S(\mathbf{k})D(\mathbf{k}, t) + \int_{-t_w}^0 C_D(\mathbf{k}, t - t')\dot{D}(\mathbf{k}, t') dt'$$

where \mathbf{k} is the wavenumber vector, C_S and C_D are matrices of functions¹⁸, D and \dot{D} are the spatial Fourier transforms of the slip and slip rate distributions, respectively, and t_w is the time window within which we consider dynamic propagation of elastic waves. We take this window to be long enough for the shear wave to propagate over the two patches.

Frictional resistance of the fault is given by

$$\tau = (\sigma - p)f(V, \theta) \frac{V}{V_0} \quad (4)$$

where σ is the elastodynamic normal stress, p is the pore pressure on the fault, $\sigma - p$ is the effective normal stress and f is the friction coefficient, which depends on the magnitude of slip rate, V , and a state variable, θ , that characterizes the evolving properties of contacts in the shearing layer. For the friction law, we use a regularized version³¹ of the experimentally derived rate-and-state laws^{32–34} with the ageing state evolution equation

$$\begin{aligned} f &= \text{arcsinh} \left[\frac{V}{2V_0} \exp \left(\frac{f_0 + b \log(V_0 \theta / L)}{a} \right) \right] \\ &\approx f_0 + a \log \left(\frac{V}{V_0} \right) + b \log \left(\frac{V_0 \theta}{L} \right) \\ \frac{d\theta}{dt} &= 1 - \frac{V\theta}{L} \end{aligned} \quad (5)$$

where f_0 is the steady-state friction coefficient at a reference slip rate V_0 , and a , b and L are the parameters that quantify variations in friction due to varying values of the slip rate and state variable. Note that the state variable evolves with slip, so that the friction law (equation (5)) combines the dependence of friction on both slip and slip rate. The steady-state value of friction, f_{ss} , that prevails at a constant slip rate is given by

$$\begin{aligned} f_{ss} &= \text{arcsinh} \left[\frac{V}{2V_0} \exp \left(\frac{f_0 - b \log(V/V_0)}{a} \right) \right] \\ &\approx f_0 + (a - b) \log \left(\frac{V}{V_0} \right) \end{aligned}$$

By varying the sign of the parameter $a - b$, the laws can be used to describe both stable, rate-strengthening fault segments ($a - b > 0$) and potentially seismic, rate-weakening fault segments ($a - b < 0$).

Motivated by the laboratory-measured properties of the rock samples from the Chelungpu fault¹⁷, we combine the rate-and-state formulation (equation (5)) with the coseismic weakening due to pore fluid pressurization. To that end, we explicitly track the evolution of temperature, T , due to frictional heating and the associated evolution in pore pressure, accounting for fault-normal diffusion of both heat and pore fluids^{16,35}:

$$\frac{\partial T(x, y, z, t)}{\partial t} = \alpha_{th} \frac{\partial^2 T(x, y, z, t)}{\partial y^2} + \frac{\omega}{\rho c}$$

$$\frac{\partial p(x, y, z, t)}{\partial t} = \alpha_{hy} \frac{\partial^2 p(x, y, z, t)}{\partial y^2} + A \frac{\partial T(x, y, z, t)}{\partial t}$$

Here y is the fault-normal direction, x and z parameterize the fault plane, $\omega(x, y, z, t)$ is the shear heating source caused by fault slip, α_{th} and α_{hy} are respectively the thermal and hydraulic diffusivities, ρc is the specific heat capacity and A is the pore pressure change per unit temperature change under undrained conditions. Note that permeability of near-fault materials affects the value of α_{hy} . In the simulated examples, it is assumed that V is accommodated by a fault layer of half-width w , with the resulting shear heating source in the form

$$\omega = \tau(x, z, t) \cdot V(x, z, t) \frac{\exp(-y^2/2w^2)}{\sqrt{2\pi}w}$$

The resulting evolution of pore pressure is then coupled with frictional resistance, because pore pressure enters the friction formulation (equation (4)).

Because we are interested in fault phenomena on a wide range of timescales, from the weakening process at the rupture front (order of milliseconds) to the recurrence of large earthquakes (order of 100 yr), we need an accurate and stable numerical procedure for the integration of the state variable, θ , the temperature, T , and the pore pressure, p . We use an algorithm¹⁶ in which the time integrations of θ and Fourier coefficients of T and p are explicit, unconditionally stable, second order in time and spectral in wavenumber, and that allows adaptively varying time steps on a logarithmic scale. We use the adaptive stepper developed in ref. 36. The details of numerical implementation are described in ref. 16.

The geometry of the model and the physical parameters used in the simulation presented in the main article are shown in Supplementary Fig. 1 and Supplementary Table 1. The spatial distribution of the parameters is infinitely differentiable because the boundaries between regions with different properties are represented by a smoothed boxcar function

$$\begin{aligned} B(x; W_1, W_2) &= \begin{cases} 1 & |x| \leq W_1 \\ \frac{1}{2} \left[1 + \tanh \left(\frac{W_2 - W_1}{|x| - W_2} + \frac{W_2 - W_1}{|x| - W_1} \right) \right] & W_1 < |x| < W_2 \\ 0 & W_2 \leq |x| \end{cases} \end{aligned}$$

where W_1 and W_2 are the half-lengths of the flat plateau and the support of the smoothed boxcar, respectively. The smoothed boxcar functions, which take the value of 1 inside patches A and B are given respectively by

$$B_A(x, z) = B(x + (W_1 + W_2)/2; W_1, W_2)B(z; W_1, W_2)$$

and

$$B_B(x, z) = B(x - (W_1 + W_2)/2; W_1, W_2)B(z; W_1, W_2)$$

The non-uniform parameters are distributed as

$$\begin{aligned} f_0 &= f_{0A} + (f_{0B} - f_{0A})B_B \\ b &= b_A B_A + b_B B_B \\ L &= 1 \text{ m} + (L_{AB} - 1 \text{ m})(B_A + B_B) \\ \log(\alpha_{hy}) &= \log(\alpha_{hyA}) + (\log(\alpha_{hyB}) - \log(\alpha_{hyA}))B_B \\ A &= A_A B_A + A_B B_B \\ w &= 1 \text{ m} + (w_{AB} - 1 \text{ m})(B_A + B_B) \end{aligned}$$

where subscripts A and B indicate the values inside patches A and B, respectively. The parameter values in the patches are listed in Supplementary Table 1, which also gives the parameters uniform over the model. We choose the value of L to be large (1 m) far from the patches to confine the ruptures better.

The fault coupling plotted in Fig. 2b is defined as $1 - V/V_{pl}$ when $V \leq V_{pl}$ and as 0 when $V > V_{pl}$, where V is the slip rate and V_{pl} is the long-term plate rate.

1. Rice, J. R., Lapusta, N. & Ranjith, K. Rate and state dependent friction and the stability of sliding between elastically deformable solids. *J. Mech. Phys. Solids* **49**, 1865–1898 (2001).
2. Dieterich, J. H. Modeling of rock friction: 1. Experimental results and constitutive equations. *J. Geophys. Res.* **84**, 2161–2168 (1979).
3. Dieterich, J. H. In *Mechanical Behavior of Crustal Rocks* (eds Carter, N. L., Logan, J. M. & Stearns, D. W.) 103–120 (Geophys. Monogr. Ser. 24, American Geophysical Union, 1981).

34. Ruina, A. L. Slip instability and state variable friction laws. *J. Geophys. Res.* **88**, 10359–10370 (1983).
35. Lachenbruch, A. H. Frictional heating, fluid pressure, and the resistance to fault motion. *J. Geophys. Res.* **85**, 6097–6112 (1980).
36. Lapusta, N., Rice, J. R., Ben-Zion, Y. & Zheng, G. Elastodynamic analysis for slow tectonic loading with spontaneous rupture episodes on faults with rate- and state-dependent friction. *J. Geophys. Res.* **105**, 23765–23789 (2000).

Earliest evidence for cheese making in the sixth millennium BC in northern Europe

Mélanie Salque¹, Peter I. Bogucki², Joanna Pyzel³, Iwona Sobkowiak-Tabaka⁴, Ryszard Grygiel⁵, Marzena Szmyt⁶ & Richard P. Evershed¹

The introduction of dairying was a critical step in early agriculture, with milk products being rapidly adopted as a major component of the diets of prehistoric farmers and pottery-using late hunter-gatherers^{1–5}. The processing of milk, particularly the production of cheese, would have been a critical development because it not only allowed the preservation of milk products in a non-perishable and transportable form, but also it made milk a more digestible commodity for early prehistoric farmers^{6–10}. The finding of abundant milk residues in pottery vessels from seventh millennium sites from north-western Anatolia provided the earliest evidence of milk processing, although the exact practice could not be explicitly defined¹. Notably, the discovery of potsherds pierced with small holes appear at early Neolithic sites in temperate Europe in the sixth millennium BC and have been interpreted typologically as ‘cheese-strainers’¹⁰, although a direct association with milk processing has not yet been demonstrated. Organic residues preserved in pottery vessels have provided direct evidence for early milk use in the Neolithic period in the Near East and south-eastern Europe, north Africa, Denmark and the British Isles, based on the $\delta^{13}\text{C}$ and $\Delta^{13}\text{C}$ values of the major fatty acids in milk^{1–4}. Here we apply the same approach to investigate the function of sieves/strainer vessels, providing direct chemical evidence for their use in milk processing. The presence of abundant milk fat in these specialized vessels, comparable in form to modern cheese strainers¹¹, provides compelling evidence for the vessels having been used to separate fat-rich milk curds from the lactose-containing whey. This new evidence emphasizes the importance of pottery vessels in processing dairy products, particularly in the manufacture of reduced-lactose milk products among lactose-intolerant prehistoric farming communities^{6,7}.

The emergence of dairying was a major innovation in prehistoric societies, enabling the supply of nutritious food without the slaughtering of precious livestock¹⁰. The processing of milk, particularly the production of cheese, would have been an important development; however, the origins of cheese making are currently unknown. Iconographic and written evidence from the mid-third-millennium BC weakly documents the history of cheese making^{12,13}, although its origins probably lie much earlier in prehistory.

The production of cheese is a technically complex process. It involves the coagulation of milk, either enzymatically or by acid treatment, yielding the semi-solid curds (a combination of the major milk nutrients—protein, mainly casein, and milk fat) and then removal of the water-soluble lactose by straining off the liquid whey. Today, the straining process is commonly achieved using a coarse textile, ‘cheese-cloth’, or plastic or metal sieves as the curds are sufficiently coarse to be strained effectively through^{11,14}.

Although straining of the curds through textile or even wicker containers would have been possible in prehistoric times, fragments of pottery pierced with small holes (2–3 mm in diameter, Fig. 1) recovered

from central European Linear Pottery (*Linearbandkeramik*) culture sites have attracted considerable attention. Critically, the Linear Pottery culture represents the first communities using cultivated plants and domestic animals in interior central Europe. By typological comparison with modern and ethnographic perforated vessels¹¹ (Supplementary Fig. 1), these sieve vessels have been interpreted as ‘cheese-strainers’^{10,15}. Indeed, the coexistence of such vessels with archaeozoological evidence for domestic ruminants led to the proposal of the emergence of milk exploitation at the beginnings of animal domestication, at least a millennium earlier than Sherratt’s secondary products revolution hypothesis predicted¹². However, other suggestions have been made concerning the use of sieve vessels, for example as flame covers, honey strainers or for beer making^{16–18}. Preliminary investigations of similar

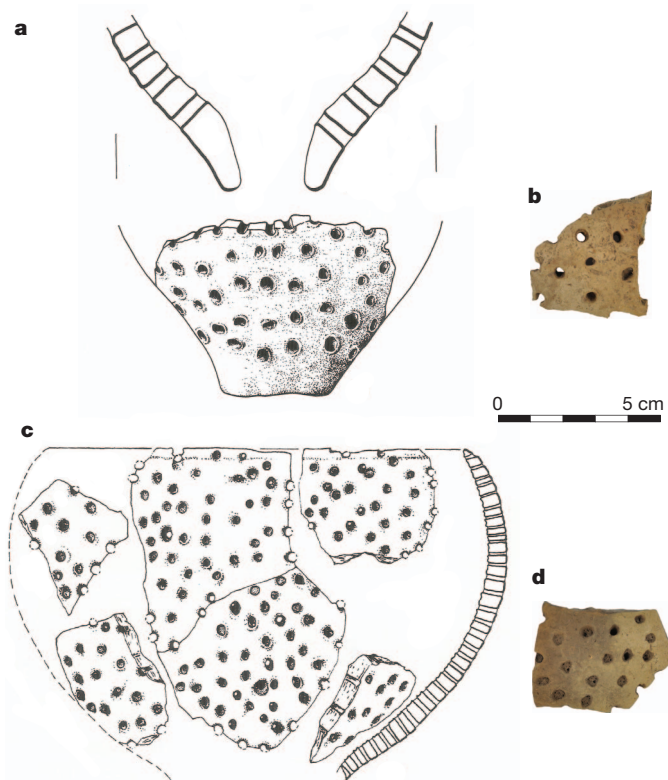


Figure 1 | Drawings of representative reconstructed sieve vessels and photographs of specific sieve fragments from the region of Kuyavia submitted to lipid residue analyses. a, b, KUY0750, from Brześć Kujawski site 3. c, d, KUY0757 from Smólsk site 4. The typology of the sieve vessels is comparable to those used by modern-day cheese producers (Supplementary Fig. 1). Drawings used with permission from ref. 20.

¹Organic Geochemistry Unit, School of Chemistry, University of Bristol, Cantock's Close, Bristol BS8 1TS, UK. ²School of Engineering and Applied Science, Princeton University, C-207 Engineering Quad, Princeton, New Jersey 08544, USA. ³Institute of Archaeology, University of Gdańsk, ul. Bielańska 5, 80-851 Gdańsk, Poland. ⁴Institute of Archaeology and Ethnology Polish Academy of Sciences, Centre for Prehistoric and Medieval Research, ul. Rubież 46, 61-612 Poznań, Poland. ⁵Museum of Archaeology and Ethnography in Łódź, Plac Wolności 14, 91-415 Łódź, Poland. ⁶Poznań Archaeological Museum, Pałac Górków, ul. Wodna 27, 61-781 Poznań, Poland.

Table 1 | List of sherds selected for lipid residue analyses

| | Early phase | Classic phase | Late phase | Unknown | Total |
|---|-------------|---------------|------------|---------|---------|
| Sieves from the region of Kuyavia | | | | | |
| Ludwinowo 6 | - | 2 (2) | - | - | 2 (2) |
| Ludwinowo 7 | - | 19 (12) | 16 (8) | 2 (1) | 37 (21) |
| Brześć Kujawski 3 | - | 2 (2) | - | - | 2 (2) |
| Brześć Kujawski 4 | - | - | 2 (2) | - | 2 (2) |
| Miechowice 4 | 1 (1) | 2 (2) | - | - | 3 (3) |
| Smólsk 4 | - | - | 2 (2) | - | 2 (2) |
| Wolica Nowa 1 | - | 1 (1) | - | - | 1 (1) |
| Stare Nakonowo 2 | - | 1 (1) | - | - | 1 (1) |
| Non-perforated vessels from Ludwinowo 7 | | | | | |
| Cooking pots | 6 | 19 | 19 | - | 44 |
| Bowls | 1 | 2 | 4 | - | 7 |
| Flasks | 2 | 6 | 7 | - | 15 |

Each non-perforated sherd corresponds to a single vessel. For the sieves, the total number of individual sieves is indicated in parenthesis. Early phase, 5,400/5,300–5,200 cal. bc; classic phase, 5,200–5000 cal. bc and late phase, 5,100/5,000–4,900/4,800 cal. bc^{20,21}.

strainer vessels from third millennium Haparan sites in Asia showed the presence of fatty acids, although this data alone is insufficient to ascribe an association with dairy product processing¹⁹. The development of lipid biomarker and stable isotope proxies that allow identification of lipid sources from absorbed organic residues in pottery vessels, offers a direct means of testing ideas related to specialized uses of vessels, the antiquity of dairying and related processing activities^{1–4}.

Here we investigate the function of Linear Pottery sieves using chromatographic (gas-chromatography), spectrometric (gas chromatography–mass spectrometry, GC–MS) and isotopic (GC–combustion–isotope ratio MS, GC–C–IRMS) analyses of organic residues in archaeological potsherds from settlements in the region of Kuyavia, Poland. Furthermore, we compare the contents of these vessels with other types of pottery to assess whether specialization existed in the use of vessels. Lipid residue analyses focused on 50 fragments of sieves from 34 vessels recovered from Linear Pottery settlements along the lower Vistula river (including Brześć Kujawski 3 and 4, Miechowice 4, Smólsk 4, Wolica Nowa 1, Stare Nakonowo 2, and Ludwinowo 6 and 7; Supplementary Fig. 2) and, for comparison, coarse ware potsherds from the

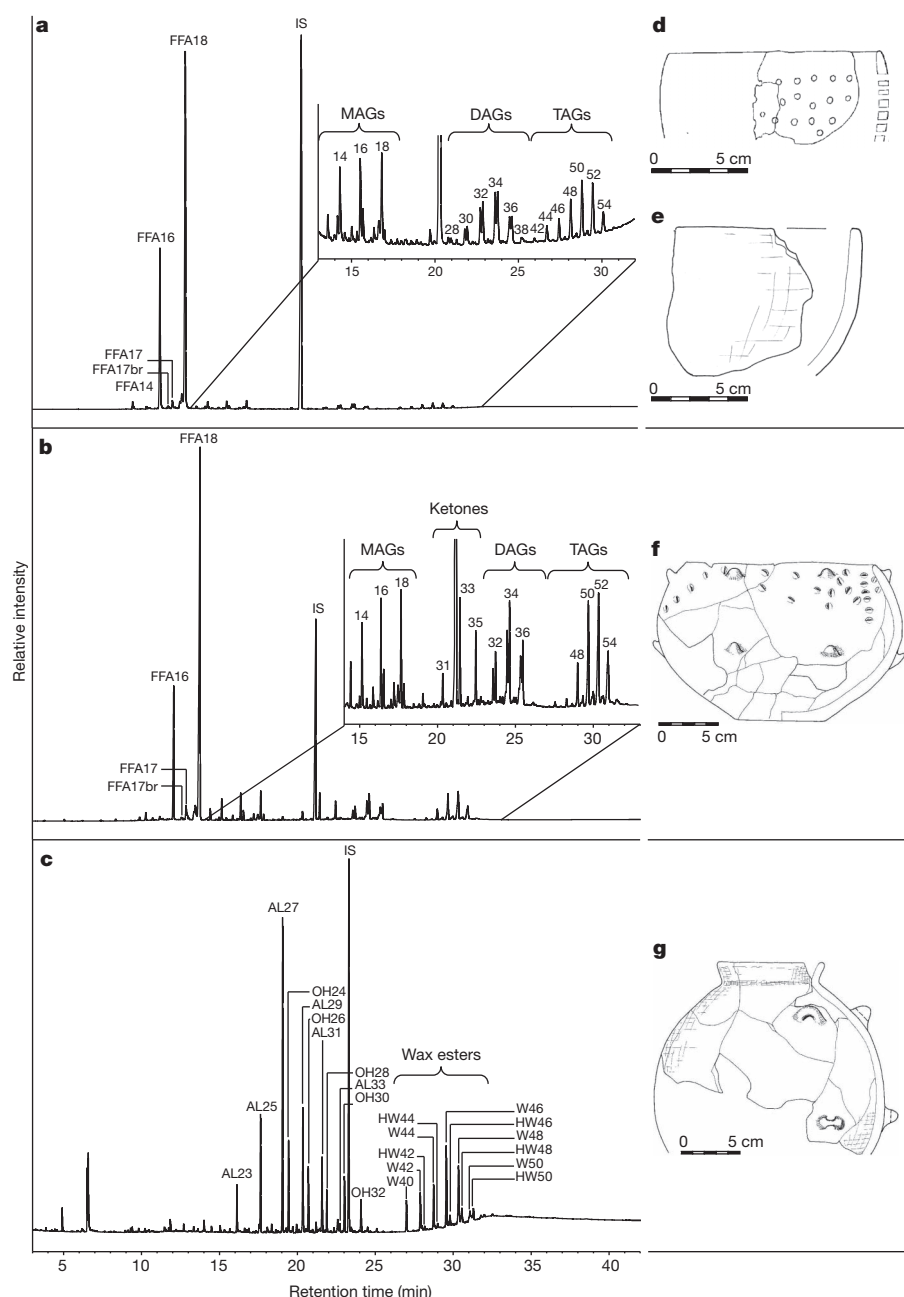


Figure 2 | Partial gas chromatograms of total lipid extracts from typical pottery from Ludwinowo 7 (Poland). **a**, Sieve and bowl: degraded animal fat with a wide distribution of triacylglycerols (sieve LDW0769). **b**, Cooking pot: degraded animal fat with a narrow distribution of triacylglycerols (LDW1020). **c**, Collared flask, beeswax (LDW1070) and associated shapes: **d**, Sieve LDW0769; **e**, bowl LDW1059; **f**, cooking pot LDW1039; **g**, collared flask LDW1074. AL, alkanes; DAG, diacylglycerols; FFA *n*, fatty acids with *n* carbon atoms and no double bonds; br, branched; HW, wax hydroxymonoesters; K, mid-chain ketones with 31, 33 and 35 carbon atoms; IS, internal standard (*n*-tetratriacontane); MAG, monoacylglycerols; OL, alcohols; TAG, triacylglycerols; with M, acyl carbon number; and W, wax monoesters.

three major vessel types from Ludwinowo 7 ('cooking' pots or *kümpfe*, $n = 44$; bowls, $n = 7$; and collared flasks, $n = 15$; Supplementary Tables 1 and 2) dating from the early (5,400/5,300–5,200 calibrated calendar years BC (cal. BC)), classic (5,200–5,000 cal. BC) and late (5,100/5,000–4,900/4,800 cal. BC) phases of the Linear Pottery in Kuyavia^{20,21} (Table 1 and Fig. 2d–g).

Lipids were extracted using well-established protocols^{1,4,22}. A high proportion of the sieve sherds, around 40%, contained lipid residues, with concentration up to $875 \mu\text{g g}^{-1}$ (mean $166 \mu\text{g g}^{-1}$, for the sherds containing lipids), consistent with observations from food processing vessels from other European archaeological sites^{22,23}. Likewise, lipid residues were extracted from around 59%, 29% and 33% of the cooking pots, bowls and collared flasks, respectively, with concentrations up to 2 mg g^{-1} (means for sherds with residues: 225, 13 and $15 \mu\text{g g}^{-1}$, respectively); the high concentrations of lipids in cooking pots suggests their extensive use in cooking fat-rich animal foodstuffs.

Most total lipid extracts were dominated by $\text{C}_{16:0}$ and $\text{C}_{18:0}$ fatty acids, accompanied by odd-number and branched-chain fatty acids ($\text{C}_{17:0}$ and $\text{C}_{17:0\text{br}}$) which are biomarkers of bacterial populations found in the rumen of milk-producing species as well as ruminant animal fats²⁴ (Fig. 2a, b). Triacylglycerols (TAGs) and their degradation products (diacylglycerols (DAGs) and monoacylglycerols (MAGs))²⁵ were observed in around 90% of the animal fats, indicating the high level of preservation of residues. As fresh dairy and adipose fats are characterized by wide and narrow distributions of TAGs, respectively²², the

contrasting distributions in sieves (C_{46} to C_{54}) and cooking pots (C_{42} to C_{54}) suggest specialization in the use of the two vessel types (Fig. 3a, b). This was confirmed through the determination of the $\delta^{13}\text{C}$ values of the individual n -alkanoic acids, palmitic ($\text{C}_{16:0}$) and stearic ($\text{C}_{18:0}$) acids. The use of the $\Delta^{13}\text{C}$ ($= \delta^{13}\text{C}_{18:0} - \delta^{13}\text{C}_{16:0}$) proxy removes the exogenous factors linked to the environment, thereby highlighting the metabolic and biosynthetic characteristics of the animal fat source and allowing the distinction between non-ruminant and ruminant fats, and adipose from dairy fats, to be drawn²⁴.

Comparison of the $\Delta^{13}\text{C}$ values obtained for the 16 animal fat residues preserved in sieve fragments and corresponding to 12 individual sieves with modern reference fats²⁴ showed that all the residues but one exhibited $\Delta^{13}\text{C}$ values expected for dairy fats (Fig. 3c, e). Likewise, the residues in bowls ($n = 2$) displayed the same range of values characteristic of dairy fats. Significantly, all the extracts from cooking pots ($n = 24$) show a very different signature plotting within, or on the edge of, the isotopic range expected for ruminant adipose fats (Fig. 3d, f). The presence of odd-carbon number ketones (C_{31} to C_{35}) in two cooking pots implies that they were heated to high temperatures²⁶ (Fig. 2b). All the biomarker and isotopic evidence indicate markedly different uses of the cooking and strainer vessels.

The presence of beeswax in 80% of the collared flasks with residues was confirmed by GC–MS through the identification of odd-carbon numbered alkanes (C_{21} to C_{33}), even-carbon numbered alcohols (C_{24}

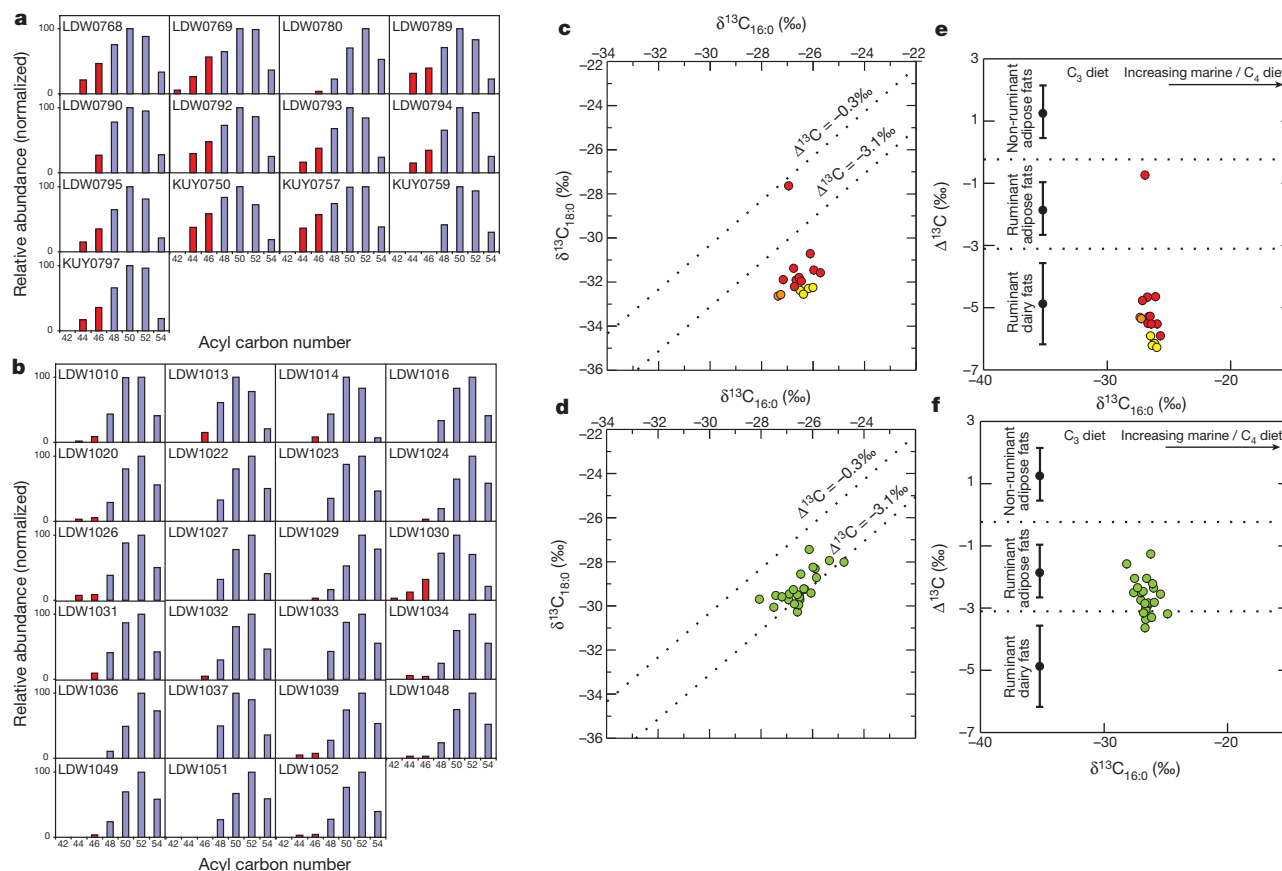


Figure 3 | Histograms of triacylglycerol distributions and fatty acid carbon isotope compositions of lipids extracted from Kuyavia pottery. TAG distributions of total lipid extracts of sieves from the region of Kuyavia (including Ludwinowo 7) (a), and cooking pots from Ludwinowo 7 (b). The blue bars denote TAGs present in both adipose and milk fats whereas those in red are only detectable in milk fat. c, d, Plots of the $\delta^{13}\text{C}$ values for the $\text{C}_{16:0}$ and $\text{C}_{18:0}$ fatty acids prepared from animal fat residues extracted from sieves and cooking pots (see Supplementary Tables 1 and 2). Each data point represents an individual vessel (the orange and yellow data points represent duplicates—of two and four fragments, respectively—of one sieve vessel each). The analytical error ($\pm 0.3\text{‰}$) is

approximately the size of the points on the graph. e, f, $\Delta^{13}\text{C}$ values ($= \delta^{13}\text{C}_{18:0} - \delta^{13}\text{C}_{16:0}$) of the extracts plotted against their $\delta^{13}\text{C}_{16:0}$ values from the same potsherds. Ranges show the mean ± 1 s.d. of the $\Delta^{13}\text{C}$ values for a global database comprising modern reference animal fats from United Kingdom (animals raised on a pure C_3 diet), Africa, Kazakhstan, Switzerland and the Near East². Significantly, the residues extracted from sieves (c and e) mostly contain dairy fats, whereas cooking pots (d and f) contain ruminant adipose fats. The difference in the $\Delta^{13}\text{C}$ means is $\sim 2.5\text{‰}$, which is highly significant (t -test; $P < 0.0005$). The figure clearly demonstrates the presence of dairy residues in sieves from the region of Kuyavia and specialization in pottery use at the Linear Pottery site of Ludwinowo 7.

to C₃₄), even-carbon numbered wax monoesters and hydroxymonoesters (C₄₀ to C₅₀), and in some cases diesters^{27,28} (Fig. 2c). Beeswax was also detected in one cooking pot.

These data provide evidence for the use of the Linear Pottery sieves to process milk, between around 5,200 and 4,900–4,800 cal. BC. The specific features of the potsherds, characterized by the presence of randomly distributed holes and the presence of high concentration dairy residues in the sieves support arguments in favour of the use of Linear Pottery sieves for cheese making, as butter making would not require such technology^{11,14}. Beeswax was present in three sieves, probably for waterproofing, helping to turn the cheese out of the mould or straining honey from the comb. Interestingly, the bowl-form vessels contained dairy fats and could have been used in combination with the sieves to collect filtered whey¹¹.

Hence, we demonstrate the first evidence for specialized use of vessels during the early Neolithic between approximately 5,400/5,300 and 4,900/4,800 cal. BC. No obvious evolution in use exists through the period studied, with vessels of different ages containing analogous lipids. In contrast to the sieves and the bowls, the cooking pots were largely used for processing ruminant carcass products, probably cattle or sheep and goats. Animal bone assemblages from Linear Pottery settlements in Kuyavia are characterized by high proportions of the bones of domestic cattle (from 68% to 80% of the overall number of identified specimens), relatively few sheep and goat bones (from 13% to 18% of the overall number of identified specimens), and very few pig or wild herbivore bones, indicating a high reliance on domestic ruminants, especially cattle²⁰ (M. Osypińska, unpublished observations). The high abundance of cattle at milk-yielding sites points to the importance of this ruminant in the intensification of milk use. The presence of beeswax in most of the collared flasks suggests either honey storage or, more probably, of the use of beeswax as a waterproofing agent²⁷, allowing their use in the storage or transport of water-based commodities. One collared flask appears to have been waterproofed with ruminant adipose fat rather than beeswax. The extensive recovery of beeswax in pottery from Ludwinowo 7 underlines the importance of bee products during the early Neolithic in Europe^{27–30}.

The evidence for the specialized use of Linear Pottery sieves in association with milk is important for three main reasons: (1) the typology of the sieves and the presence of dairy fats are consistent with milk processing, providing the earliest evidence of cheese making, which is notable because the manufacture of cheese increases the ease of handling of milk and allows the nutritional properties of milk to be readily available through the year; (2) the processing of milk to manufacture low-lactose-content cheese is consistent with the predicted low level of lactase persistence in northern Europe in the early Neolithic⁷; and (3) the evidence of milk use by the people of the Linear Pottery culture is consistent with the predicted increase in frequency of the –13,910*T allele associated with lactase persistence among prehistoric northern Europeans in this region⁶.

METHODS SUMMARY

Fifty fragments of sieves, representing 34 vessels, were sampled from the Kuyavia region (Poland), of which 37 fragments representing 21 sieves were excavated in Ludwinowo 7 (Supplementary Table 1). A further 66 potsherds from Ludwinowo 7 were analysed, of which 44 were cooking pots, the rest originating from collared flasks ($n = 15$) and bowls ($n = 7$, Supplementary Table 2). Lipid residue analyses and interpretations were based on established protocols^{1,2,4,22,23}. Briefly, ~1 to 3 g potsherds were sampled and their surfaces cleaned with a modelling drill to remove any exogenous lipids. The sherds were then ground to a powder, an internal standard added and solvent extracted by ultrasonication (chloroform/methanol, 2:1 v/v, 2 × 10 ml). Solvent was evaporated under a gentle stream of nitrogen to obtain the total lipid extract. Aliquots of the total lipid extract were trimethylsilylated (*N,O*-bis(trimethylsilyl)trifluoroacetamide, 40 µl, 70 °C, 1 h) and submitted to analysis by gas chromatography and GC–MS. Further aliquots of the total lipid extract were treated with NaOH/H₂O (9:1 w/v) in methanol (5% v/v, 70 °C, 1 h). Following neutralization, lipids were extracted into chloroform (3 × 3 ml) and excess solvent evaporated under a gentle stream of nitrogen. Fatty

acid methyl esters were prepared by reaction with BF₃-methanol (14% w/v, 70 °C, 1 h). Fatty acid methyl esters were extracted with chloroform (3 × 2 ml) and the solvent removed with a gentle stream of nitrogen. Fatty acid methyl esters were then re-dissolved into hexane for analysis by gas chromatography and GC–C–IRMS.

Received 26 July; accepted 23 October 2012.

Published online 12 December 2012.

1. Evershed, R. P. *et al.* Earliest date for milk use in the Near East and southeastern Europe linked to cattle herding. *Nature* **455**, 528–531 (2008).
2. Dunne, J. *et al.* First dairying in green Saharan Africa in the fifth millennium BC. *Nature* **486**, 390–394 (2012).
3. Craig, O. E. *et al.* Ancient lipids reveal continuity in culinary practices across the transition to agriculture in Northern Europe. *Proc. Natl Acad. Sci. USA* **108**, 17910–17915 (2011).
4. Copley, M. S. *et al.* Direct chemical evidence for widespread dairying in prehistoric Britain. *Proc. Natl Acad. Sci. USA* **100**, 1524–1529 (2003).
5. Craig, O. E. *et al.* Did the first farmers of central and eastern Europe produce dairy foods? *Antiquity* **79**, 882–894 (2005).
6. Itan, Y., Powell, A., Beaumont M. A., Burger J. & Thomas M. G. The origins of lactase persistence in Europe. *PLoS Comput. Biol.* **5**, e1000491 (2009).
7. Burger, J., Kirchner M., Bramanti B., Haak W. & Thomas M. G. Absence of the lactase-persistence-associated allele in early Neolithic Europeans. *Proc. Natl Acad. Sci. USA* **104**, 3736–3741 (2007).
8. Flatz, G. & Rothauwe, H. W. The human lactase polymorphism: physiology and genetics of lactose absorption and malabsorption. *Prog. Med. Genet.* **2**, 205–249 (1977).
9. McCracken, R. D. Lactase deficiency: an example of dietary evolution. *Curr. Anthropol.* **12**, 479–517 (1971).
10. Bogucki, P. I. Ceramic sieves of the Linear Pottery culture and their economic implications. *Oxf. J. Archaeol.* **3**, 15–30 (1984).
11. Gouin, P. Ancient oriental dairy techniques derived from archaeological evidence. *Food Foodways* **7**, 157–188 (1997).
12. Sherratt, A. in *Pattern of the Past: Studies in Honour of David Clarke* (eds Hodder, I., Isaac, G. & Hammond, N.) 261 (Cambridge Univ. Press, 1981).
13. Hallo, W. W. The house of Ur-Meme. *J. Near East. Stud.* **31**, 87–95 (1972).
14. Houdet, V. *Laiterie, Beurrerie, Fromagerie* 7th edn (Hachette, 1919).
15. Poplin, F. L'origine de la production laitière. *Initiation à l'Archéologie et à la Préhistoire* **17**, 13–17 (1980).
16. Wood, J. in *Fire as an Instrument: The Archaeology of Pyrotechnologies* (ed. Gheorghiu, D.) Vol. 1619, 53 (Archaeopress, 2007).
17. Clark, J. G. D. *Prehistoric Europe: the Economic Basis*. (Cambridge Univ. Press, 1952).
18. Kindstedt, P. S. *Cheese and Culture: a History of Cheese and its Place in Western Civilization* (Chelsea Green Publishing Company, 2012).
19. Bourgeois, G. & Gouin, P. Résultats d'une analyse de traces organiques fossiles dans une 'faisselle' harappéenne. *Paléorient* **21**, 125–128 (1995).
20. Grygiel, R. *Neoliti i Początki Epoki Brązu w Rejonie Brzeźcia Kujawskiego i Oslonek (The Neolithic and Early Bronze Age in the Brzeźcie Kujawski and Oslonki Region)*, Vol. 1 (Konrad Jazdzewski Foundation for Archaeological Research, Museum of Archaeology and Ethnography, 2004).
21. Pyzel, J. in *Creating Communities: New Advances in Central Europe Neolithic Research* (eds Hofmann, D. & Bickle, P.) 71 (Oxbow books, 2009).
22. Dudd, S. N. & Evershed, R. P. Direct demonstration of milk as an element of archaeological economies. *Science* **282**, 1478–1481 (1998).
23. Charters, S. *et al.* Quantification and distribution of lipid in archaeological ceramics: implications for sampling potsherds for organic residue analysis and the classification of vessel use. *Archaeometry* **35**, 211–223 (1993).
24. Keeney, M., Katz, I. & Allison, M. J. On the probable origin of some milk fat acids in rumen microbial lipids. *J. Am. Oil Chem. Soc.* **39**, 198–201 (1962).
25. Evershed, R. P. *et al.* Chemistry of archaeological animal fats. *Acc. Chem. Res.* **35**, 660–668 (2002).
26. Raven, A. M., van Bergen P. F., Stott A. W., Dudd S. N. & Evershed R. P. Formation of long-chain ketones in archaeological pottery vessels by pyrolysis of acyl lipids. *J. Anal. Appl. Pyrolysis* **40–41**, 267–285 (1997).
27. Heron, C., Nemchek, N., Bonfield K. M., Dixon D. & Ottaway B. S. The chemistry of neolithic beeswax. *Naturwissenschaften* **81**, 266–269 (1994).
28. Regert, M., Colinart, S., Degrand, L. & Decavallas, O. Chemical alteration and use of beeswax through time: accelerated ageing tests and analysis of archaeological samples from various environmental contexts. *Archaeometry* **43**, 549–569 (2001).
29. Clark, J. G. D. Bees in antiquity. *Antiquity* **16**, 208–215 (1942).
30. Crane, E. *The Archaeology of Beekeeping* (Cornell Univ. Press, 1983).

Supplementary Information is available in the online version of the paper.

Acknowledgements We thank the 7th EU framework Marie Curie Initial Training Networks (FP7-ITN-215362-2) for a Ph.D. studentship to M.Sa and the UK Natural Environment Research Council for mass spectrometry facilities.

Author Contributions M.Sa., R.P.E. and P.I.B. planned the project and wrote the paper. M.Sa. performed analytical work and data analysis. P.I.B., J.P., I.S.-T., R.G. and M.Sz. either directed sampling of archaeological material or directed excavations. All authors read and approved the final manuscript.

Author Information Reprints and permissions information is available at www.nature.com/reprints. The authors declare no competing financial interests. Readers are welcome to comment on the online version of the paper. Correspondence and requests for materials should be addressed to R.P.E. (r.p.evershed@bristol.ac.uk).

Insights into bilaterian evolution from three spiralian genomes

Oleg Simakov^{1,2}, Ferdinand Marletaz^{1†}, Sung-Jin Cho², Eric Edsinger-Gonzales², Paul Havlak³, Uffe Hellsten⁴, Dian-Han Kuo^{2†}, Tomas Larsson¹, Jie Lv³, Detlev Arendt¹, Robert Savage⁵, Kazutoyo Osoegawa⁶, Pieter de Jong⁶, Jane Grimwood^{4,7}, Jarrod A. Chapman⁴, Harris Shapiro⁴, Andrea Aerts⁴, Robert P. Otiillar⁴, Astrid Y. Terry⁴, Jeffrey L. Boore^{4†}, Igor V. Grigoriev⁴, David R. Lindberg⁸, Elaine C. Seaver^{9†}, David A. Weisblat², Nicholas H. Putnam^{3,10} & Daniel S. Rokhsar^{2,4,11}

Current genomic perspectives on animal diversity neglect two prominent phyla, the molluscs and annelids, that together account for nearly one-third of known marine species and are important both ecologically and as experimental systems in classical embryology^{1–3}. Here we describe the draft genomes of the owl limpet (*Lottia gigantea*), a marine polychaete (*Capitella teleta*) and a freshwater leech (*Helobdella robusta*), and compare them with other animal genomes to investigate the origin and diversification of bilaterians from a genomic perspective. We find that the genome organization, gene structure and functional content of these species are more similar to those of some invertebrate deuterostome genomes (for example, amphioxus and sea urchin) than those of other protostomes that have been sequenced to date (flies, nematodes and flatworms). The conservation of these genomic features enables us to expand the inventory of genes present in the last common bilaterian ancestor, establish the tripartite diversification of bilaterians using multiple genomic characteristics and identify ancient conserved long- and short-range genetic linkages across metazoans. Superimposed on this broadly conserved pan-bilaterian background we find examples of lineage-specific genome evolution, including varying rates of rearrangement, intron gain and loss, expansions and contractions of gene families, and the evolution of clade-specific genes that produce the unique content of each genome.

Molluscs, annelids and numerous smaller phyla typically share stereotyped spiral cleavage patterns, cell-fate assignments and characteristic ciliated trochophore larvae, features that originated in the Precambrian era^{3–5}. These spiralian phyla are included in the larger lophotrochozoan clade⁶ that is a sister group to the ecdysozoans (arthropods, nematodes and other related phyla) but whose internal branching remains controversial. However, so far the only deeply sequenced lophotrochozoan genomes are those of platyhelminth flatworms (two parasitic schistosomes^{7,8} and a free-living planarian⁹), whose comparatively rapid rates of genome evolution do not reflect a general condition of lophotrochozoans (see below). In this study, we explore spiralian diversity at the genomic level by comparative analysis of one mollusc and two annelid genomes (Supplementary Note 1).

We assembled the limpet, polychaete and leech genomes from approximately eight-fold random whole-genome shotgun coverage with Sanger dideoxy sequencing reads (Supplementary Note 2). No genetic or physical maps were available for these systems, so we reconstructed each genome as scaffolds (gap-containing sequences). The three genomes reported here each encode an estimated 23,000 to 33,000 protein-coding genes (Table 1,

Supplementary Table 2.2.2 and Supplementary Note 2.2. The repetitive landscape of these genomes is discussed in Supplementary Note 3.2).

Comparing the new genomes with other metazoan sequences, we characterized 8,756 modern bilaterian gene families as likely to have arisen from single progenitor genes in the last common bilaterian ancestor (Supplementary Note 3.4). As gene loss is common and highly diverged orthologues can be difficult to detect, this is a conservative lower bound on the number of genes encoded by the last common bilaterian ancestor. Of the 8,756 gene families, 763 were newly identified as being of bilaterian ancestry based on the new spiralian genomes (Supplementary Note 3.4). These newly identified bilaterian families belong to various functional categories (Supplementary Table 3.4.1), the most prominent being members of the G-protein-coupled receptor superfamily and epithelial sodium channels (see below) as well as various metabolic enzymes. Through subsequent gene duplication, the 8,756 ancestral bilaterian families conservatively account for 47 to 85% of genes in other bilaterian species (70% of human genes; Supplementary Note 3.4). Most of the remaining genes in extant bilaterian genomes share at least one domain with the bilaterian gene families, or have a significant BLAST (Basic Local Alignment Search Tool) hit when compared against sequences from bilaterian gene families, suggesting that they have arisen through descent with modification (Supplementary Note 3.5).

Exon–intron structures are highly conserved between spiralian and other animals; thus we infer that *cis*-splicing of intron-rich genes was the ancestral state of metazoans, bilaterians and protostomes (Supplementary Note 5.2). In most cases, exon boundaries in the newly sequenced spiralian genomes are precisely conserved between orthologous genes in sequenced deuterostomes (vertebrates, sea urchin and amphioxus) and non-bilaterians (*Trichoplax* and starlet sea anemone). For example, 75% of human introns are present in one or more of the spiralian genomes, whereas only 14% of the same introns are found in *Drosophila*^{10,11}. However, intron gain or loss rates vary markedly among the three spiralian genomes. In particular, *H. robusta* also has substantially more novel introns than do the other two sequenced spiralian genomes (Supplementary Notes 5.2 and 5.3, and Supplementary Fig. 5.2.1), the first of several indicators of a notably dynamic genome in this lineage.

Collectively and individually, the spiralian genomes reported here retain most of the inferred ancestral bilaterian gene families (8,203 out of 8,756, corresponding to a 94% retention rate, compared to 7,553 or 86% retention rate in human). In contrast, the collective retention rate of only 65% for sequenced flatworms (53% for schistosomes and 60% for *Schmidtea*) reflects the absence (and presumed

¹European Molecular Biology Laboratory, Meyerhofstraße 1, 69117 Heidelberg, Germany. ²Department of Molecular and Cell Biology, University of California, Berkeley, California 94720, USA. ³Department of Ecology & Evolutionary Biology, Rice University, P.O. Box 1892, Houston, Texas 77251-1892, USA. ⁴DOE Joint Genome Institute, 2800 Mitchell Drive, Walnut Creek, California 94598, USA. ⁵Department of Biology, Williams College, Thompson Biology Laboratory, 59 Lab Campus Drive, Williamstown, Massachusetts 01267, USA. ⁶Children's Hospital Oakland Research Institute, 5700 Martin Luther King Jr. Way, Oakland, California 94609, USA. ⁷Hudson Alpha Institute for Biotechnology, 601 Genome Way, Huntsville, Alabama 35806-2908, USA. ⁸Department of Integrative Biology, University of California, Berkeley, California 94720, USA. ⁹Kewalo Marine Laboratory, University of Hawaii at Manoa, 41 Ahui Street, Honolulu, Hawaii 96813, USA. ¹⁰Department of Biochemistry and Cell Biology, Rice University, Houston, Texas 77251, USA. ¹¹Okinawa Institute of Science and Technology, 1919-1 Tancha, Onna-son, Okinawa 904-0495, Japan. †Present addresses: Department of Zoology, University of Oxford, The Tinbergen Building, South Parks Road, Oxford OX1 3PS, UK (F.M.); Institute of Zoology, National Taiwan University, 1 Roosevelt Road, Taipei 10617, Taiwan (D.-H.K.); Genome Project Solutions, 1024 Promenade Street, Hercules, California 94547, USA (J.L.B.); The Whitney Laboratory for Marine Bioscience, 9505 Ocean Shore Boulevard, St. Augustine, Florida 32080-8610, USA (E.C.S.).

Table 1 | Genome sequencing and annotation summary

| Species | Size of genome assembly (Mbp) | Scaffold N50 (Mbp) | Repetitive content(%) | GC (%) | Predicted number of genes | Number of genes in orthologous clusters with other species | Number of genes in ancestral bilaterian gene families | Mean number of exons per gene (with ≥ 2 orthologues) | Mean exon length (bp) | Mean intron length (bp) |
|---------------------------|-------------------------------|--------------------|-----------------------|--------|---------------------------|--|---|---|-----------------------|-------------------------|
| <i>Lottia gigantea</i> | 348 | 1.87 | 21 | 33 | 23,800 | 16,183 | 10,681 | 8 | 213 | 787 |
| <i>Capitella teleta</i> | 324 | 0.19 | 31 | 40 | 32,389 | 20,537 | 11,911 | 7 | 221 | 291 |
| <i>Helobdella robusta</i> | 228 | 3.06 | 33 | 33 | 23,400 | 13,820 | 8,707 | 8 | 203 | 526 |

GC, fraction of guanine plus cytosine nucleobases; Scaffold N50, the length such that half of the assembled sequence is in scaffolds longer than this length; Mbp, megabase pairs.

loss) of more than 3,018 ancestral bilaterian gene families in these flatworms. Similar losses are observed for introns (Supplementary Note 5.3), as well as synteny (see below), which indicate a higher rate of genomic turnover in platyhelminths than in the mollusc and annelid genomes reported here.

Against this background of conserved gene content and structure, we find several significantly ($P < 0.05$) expanded gene families in specific spiralian clades (Supplementary Note 4.2). The sensory transduction and signalling genes of the G-protein-coupled receptor (GPCR) superfamily in *C. teleta* are a prime example. All six of the rhodopsin-like GPCRs represented in the KEGG (Kyoto Encyclopedia of Genes and Genomes) neuroactive ligand–receptor interaction pathway are expanded in *C. teleta* (but not in *H. robusta* or *L. gigantea*), as are several other GPCRs (Supplementary Figs 4.3.2 and 4.4.1). Moreover, the *C. teleta* genome encodes 372 putative GPCR receptors that are most similar to peptide-binding GPCR subfamilies according to the family classification in the GPCR database (<http://www.gpcr.org/7tm/proteinfamily/>). This number is considerably higher than that obtained for *H. robusta* (58), *L. gigantea* (113), *Drosophila* (32) or human (120) using the same methods (Supplementary Note 4.4). Most of these expansions occur as tandem duplicates. The *C. teleta* genome also shows an expansion of the calcium-signalling pathway downstream of GPCR (Supplementary Note 4.3). It is tempting to speculate that these expansions are related to the function of polychaete chemosensory structures such as antennae, palps and cirri (head sensory organs), and the nuchal organ¹². Another notable feature of all three genomes is the presence of several atypical GPCRs with weak similarity to both vertebrate rhodopsin-like GPCRs and chemosensory receptors described previously in nematodes (Supplementary Fig. 4.4.1). Further studies are needed to determine whether these receptors can be classified as divergent members of previously described GPCR classes or whether they constitute novel groupings as described recently in planarians¹³.

We also find changes in gene content associated with sensory processing in the leech. These changes include expansion of the epithelial sodium channel (ENaC) receptor gene family that functions in the taste-transduction pathway (Supplementary Fig. 4.3.5), and the gap-junction-forming innexin gene family, as well as gene families involved

in development (for example, homeobox genes (see below, and Supplementary Notes 4.5 and 4.6)). Both mollusc and annelid genomes are also enriched in specific metabolic enzymes and pathways of unknown relevance (for example, galactoside 2- α -L-fucosyltransferase; see Supplementary Notes 4.2 and 4.3). In general, lineage-specific gene family expansions seem to be the norm in the evolutionary diversification of modern taxa from the bilaterian ancestor, whereas the more ancient unicellular–metazoan¹⁴ and metazoan–bilaterian transitions are more notably marked by the acquisition of apparently novel (or highly divergent) gene families (Supplementary Table 3.5.1).

We identified 231 putative spiralian-specific gene families whose members are readily aligned across all three spiralian (indicating purifying selection), but which lack obvious orthologues by BLAST in non-spiralian genomes (Supplementary Note 3.6). However, nearly two-thirds of these (188 out of 231; 62%) showed residual similarity to non-spiralian genes using more sensitive Hidden Markov Model methods, which suggests that they belong to ancient bilaterian gene families (Supplementary Note 3.6) that diverged extensively on the stem lineage leading from the bilaterian ancestor to the mollusc–annelid ancestor ('type II' novelties¹⁵). The remaining 43 out of 231 novel gene families are without any significant (E values of less than 0.01) similarities outside of spiralian ('type I' novelties¹⁵). More than one-half of the 231 spiralian novelties are transcribed based on existing expressed sequence tag (EST) evidence, with enriched expression in adult rather than embryonic tissues (Supplementary Notes 2.4 and 3.7), hinting at roles in clade-specific adaptations beyond the early conserved stages of development.

The inference of deep phylogenetic relationships among animal phyla is controversial but has benefitted from the use of multiple orthologous genes as phylogenetic markers^{16,17}. Recent EST-based studies provide broad taxonomic representation but rely on a limited number of available genes or are forced to accommodate a substantial amount of missing data^{6,18}. In contrast, full genome sequences provide nearly complete sets of orthologues exempt from sampling bias, but can be more sensitive to long-branch attraction artefacts.

To strike a balance between the number of phylogenetically informative characters and possible long-branch artefacts we ranked 1,180

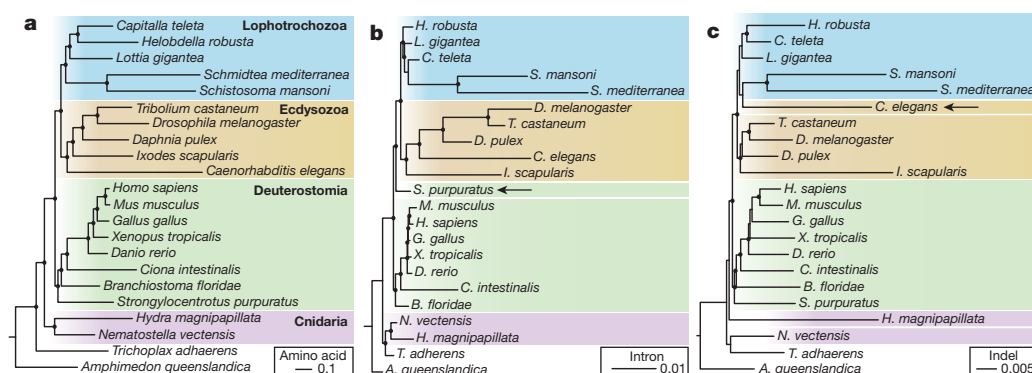


Figure 1 | Full-genome evidence resolves metazoan relationships and verifies the monophyly of lophotrochozoans and spiralian. a, A protein tree inferred from 299,129 amino acid positions gathered from 827 slow-evolving orthologues using RAXML and modelling heterogeneity of substitution processes using a LG + Γ_4 model with each gene partitioned. Strong support is obtained for the monophyly of lophotrochozoans. **b**, Intron tree obtained from

a matrix of 5,377 introns analysed using MrBayes and an asymmetric binary model (probability of gain: 0.01). **c**, Indel tree reconstructed from a matrix of 1,928 indel sites using a regular binary model. Circles at nodes indicate a bootstrap support of >0.90 (**a**) or a posterior probability of >0.95 (**b** and **c**). In **b** and **c**, arrows indicate species that do not follow the protein family tree topology.

clusters of orthologous genes (from 22 complete genomes) by their evolutionary rates (Supplementary Fig. 5.1.1) and identified a set of 827 slowly evolving genes that include 299,129 aligned amino acid positions suitable for deep phylogenetic analysis. These characters strongly support the tripartite view of bilaterians and the monophyly of available lophotrochozoans (annelids, molluscs and platyhelminths) (Fig. 1a)¹⁹; the progressive addition of characters representing more rapidly evolving genes monotonically erodes support for this view, as expected under long-branch attraction (Supplementary Fig. 5.1.2). Although taxon sampling is generally considered critical to resolving deep phylogeny, our analyses show the importance of gene sampling. The rate-stratification approach introduced here could be used to place problematic taxa (for example, acoels, ctenophores and chaetognaths) when appropriate genome data becomes available.

We also examined the phylogenetic signals in the gain and loss of introns, and insertions or deletions (indels) within coding sequences, incorporating spiralian sequences for the first time. Although few evolutionary reconstructions have been attempted with these characters, they have attractive properties for phylogenetic analysis as change is rare and generally irreversible^{20,21} (Supplementary Note 5.3). Phylogenetic reconstruction using binary matrices encoding intron and indel presence or absence recovered the backbone of metazoan phylogeny, and intron data provided strong support for grouping molluscs, annelids and platyhelminths (Fig. 1b). However, the analysis based on indels showed specific discrepancies relative to other data sets, notably the grouping of nematodes and platyhelminths (Fig. 1c). As this grouping is not consistent with either amino acid or intron analyses, we ascribe it to the accelerated genome evolution in these taxa and the low number of phylogenetically informative indel characters.

All three trees possess short internal branches near the base of bilateria (see ref. 22), which indicates that the diversification into separate lophotrochozoan, deuterostome and ecdysozoan lineages was relatively fast, taking perhaps 30 to 80 million years (Myr) (comparable to the diversification of mammals; Supplementary Note 5.5).

We also sought evidence for genome-wide functional diversification across metazoan genomes using principal component analysis (Supplementary Note 4.1). Remarkably, this phenetic approach grouped the newly sequenced mollusc and annelids with invertebrate deuterostomes (amphioxus, sea urchin and sea squirt) and non-bilateria metazoan phyla (cnidarian, placozoan and demosponge) (Fig. 2). Given that this grouping includes both bilaterians and non-bilateria metazoans, cladistic logic implies that these genomes approximate the ancestral bilateria (and metazoan) genomic repertoire. In contrast, vertebrate genomes form a distinct cluster, and are thus functionally derived relative to this ancestral bilateria state, partly owing to the diversification of genes related to the vertebrate innate and adaptive immune system that dominate the loadings of principal component 1 (PC1, Fig. 2) (Supplementary Table). The functional coherence of the genes that differentiate currently available ecdysozoan genomes through PC2 is unclear. Although this analysis may be skewed by the more complete functional annotation of vertebrates and classical model systems, other similar analyses less dependent on function confirm the clear separation of vertebrates from other metazoan genomes (Supplementary Note 4.1).

The *L. gigantea* and *C. teleta* genomes show extensively conserved macrosynteny with each other, with chordates (including human; see Fig. 3 and Supplementary Note 6) and with several other extant metazoan lineages (sea anemone¹⁵, placozoan²³ and demosponge¹⁴). In our analyses, conserved macrosynteny requires only conserved linkage between orthologous genes, and is independent of intra-chromosome rearrangements (that is, scrambling of gene order) that are typical in phylogenetically deep comparisons^{10,15,23}. Conserved macrosynteny in *L. gigantea* and *C. teleta* involves nearly one-half of the conserved protein coding genes in these species (Supplementary Note 6 and Supplementary Table 6.3.1). In contrast, we found no significant conservation of macrosynteny between *H. robusta* and other species, implying

extensive reorganization in the leech genome relative to the last common spiralian ancestor.

The observed conserved macro-synteny demonstrates the persistence of 17 ancient bilateria ancestral linkage groups (ALGs) in the common ancestor of *L. gigantea* and *C. teleta*. Independent fusions (two in *L. gigantea*, three in *C. teleta*) subsequently reduced the number of bilateria ALGs that remain distinct in these genomes. The conservation of 17 bilateria ALGs among *L. gigantea*, *C. teleta* and various deuterostomes implies that the last common protostome and deuterostome ancestors also had this organization. Some ecdysozoans like *Caenorhabditis elegans* (soil nematode), *Tribolium castaneum* (beetle) and *Bombyx mori* (moth) (Supplementary Note 6) also show clear evidence of conserved macrosynteny. However, the large number of chromosome fusions and rearrangement events make similar reconstruction of the ancestral ecdysozoan ALGs impossible with current data (Supplementary Note 6).

Remarkably, we can also use the *L. gigantea* and *C. teleta* genomes to infer ancient translocations between linkage groups (Supplementary Note 6). For example, *L. gigantea* and *C. teleta* share a translocation relative to the last common bilateria ancestor (Fig. 3), indicating that this genomic rearrangement occurred on the stem lineage leading from the bilateria to the mollusc–annelid node. As noted above, more recent translocations that are not shared between *L. gigantea* and *C. teleta* are also evident (Supplementary Note 6). It remains unclear whether these genome reorganizations were causally involved in the radiation of diverse bilateria lineages, or were simply neutral changes.

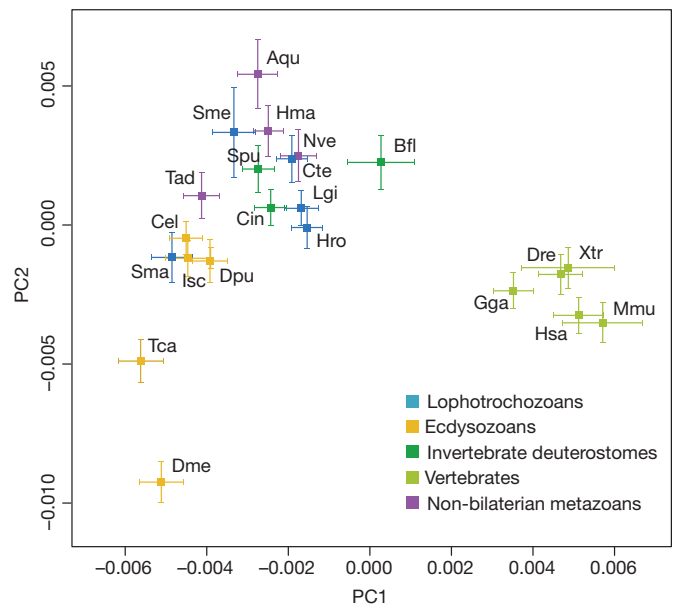


Figure 2 | Clustering of metazoan genomes in a multidimensional space of molecular functions. The first two principal components are displayed, accounting for 20% and 15% of variation, respectively. At least three clusters are evident, including a vertebrate cluster (far right), a non-bilateria metazoan, invertebrate deuterostome or spiralian cluster (centre, top), and an ecdysozoan group (lower left). *Drosophila* and *Tribolium* (lower left) are outliers. Aqu, *Amphimedon queenslandica* (demosponge); Bfl, *Branchiostoma floridae* (amphioxus); Cel, *Caenorhabditis elegans*; Cte, *Capitella teleta* (polychaete); Cin, *Ciona intestinalis* (sea squirt); Dme, *Drosophila melanogaster*; Dpu, *Daphnia pulex* (water flea); Dre, *Danio rerio* (zebrafish); Isc, *Ixodes scapularis* (tick); Gga, *Gallus gallus* (chicken); Hsa, *Homo sapiens* (human); Hma, *Hydra magnipapillata*; Hro, *Helobdella robusta* (leech); Lgi, *Lottia gigantea* (limpet); Mmu, *Mus musculus* (mouse); Nve, *Nematostella vectensis* (sea anemone); Sma, *Schistosoma mansoni*; Sme, *Schmidtea mediterranea* (planarian); Spu, *Strongylocentrotus purpuratus* (sea urchin); Tad, *Trichoplax adhaerens* (placozoan); Tca, *Tribolium castaneum* (flour beetle); Xtr, *Xenopus tropicalis* (clawed frog).

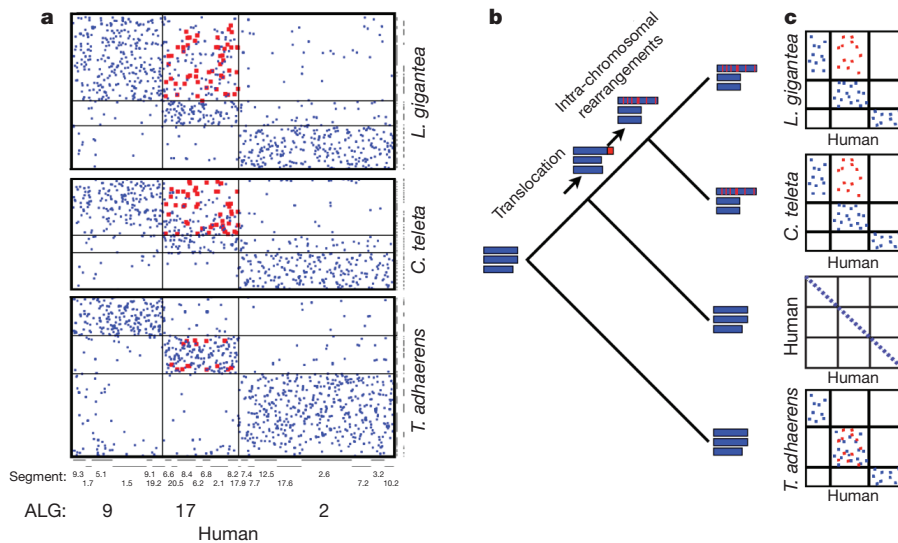


Figure 3 | Macrosynteny between spiralian, humans and *Trichoplax*.

a, The location of genes in scaffolds of *L. gigantea*, *C. teleta* and *Trichoplax* (a non-bilaterian outgroup that conserves synteny) relative to the position of their orthologues in the human genome. The human chromosome segments have been grouped according to their ancestral linkage group (ALG); chromosome segment identifiers are also shown (see ref. 10). Human genes in ALG 2 have their orthologues co-located on a limited set of scaffolds in *L. gigantea*, *C. teleta* and *Trichoplax*, indicating conserved linkage of this group of genes across eumetazoan lineages. In contrast, although ALG 17 and ALG 9 are preserved separately in *Trichoplax*, scaffolds of *L. gigantea* and *C. teleta* have homologous gene content either with ALG 9 or with both ALG 9 and ALG 17, indicating a

translocation of one or more chromosome segments from ALG 17 to ALG 9 in the common ancestor of molluscs and annelids, after the divergence of the spiralian and vertebrate lineages. Genes inferred to derive from this translocated segment are shown in red. Subsequent intra-chromosomal rearrangement has dispersed the translocated genes among the genes of ALG 9. **b**, The scenario in panel **a** represented schematically on a phylogenetic tree, with chromosomes of ancestral and living genomes represented as horizontal blue bars and the translocated segment represented in red. **c**, The positions of human genes and their *L. gigantea*, *C. teleta* and *Trichoplax adhaerens* orthologues compared in dot plots schematically (and in the real data; see panel **a**) for three ALGs.

The most famous example of conserved microsynteny—conserved tight linkages between orthologous genes—is the *Hox* complex, an ancient cluster of homeodomain-containing transcription factors with conserved roles in patterning the anteroposterior body axis of animals²⁴. In *L. gigantea*, 11 *Hox* genes occur as a single cluster that is structurally collinear with intact *Hox* clusters found in other genomes, and is the first intact cluster found in a lophotrochozoan (Fig. 4). *C. teleta* *Hox* genes occur in one-to-one correspondence with their *L. gigantea* counterparts but lie on three scaffolds, with the scaffold harbouring the posterior class gene *post1* clearly disconnected from the main cluster²⁵. We therefore infer that the last common mollusc–annelid ancestor had a single 11-gene *Hox* cluster (Supplementary Note 8) with 3 anterior- and 6 central-class genes, plus 2 posterior-class genes (*post1* and *post2*) that arose by duplication along the spiralian (or lophotrochozoan) stem lineage²⁶. In contrast, the *Hox* complex of *H. robusta* has fragmented extensively, consistent with the general loss of synteny conservation in

H. robusta, and there have been multiple duplications and loss of two mollusc–annelid paralogy groups (the orthologues of the anterior-class *proboscipedia* and *post1*). Intriguingly, although the gene rearrangements observed in *H. robusta* are as extreme as in *C. elegans*, the leech is not particularly derived with respect to other genomic characters. This lineage may therefore be an interesting model for focused studies on rapid evolution of gene order. We also find other tightly linked groups of anciently duplicated (that is, paralogous) genes, including clusters of deeply diverged gene superfamilies such as the homeodomain²⁵, forkhead box²⁷ and wingless²⁸ gene families that duplicated extensively before the bilaterian radiation but have remained linked (Supplementary Note 7.4).

Overall, we found hundreds of other examples of conserved microsyntentic blocks involving thousands of genes in *L. gigantea*, *C. teleta* and other metazoan genomes (Supplementary Note 7.1). We consider a microsyntentic block to be a group of three or more genes whose

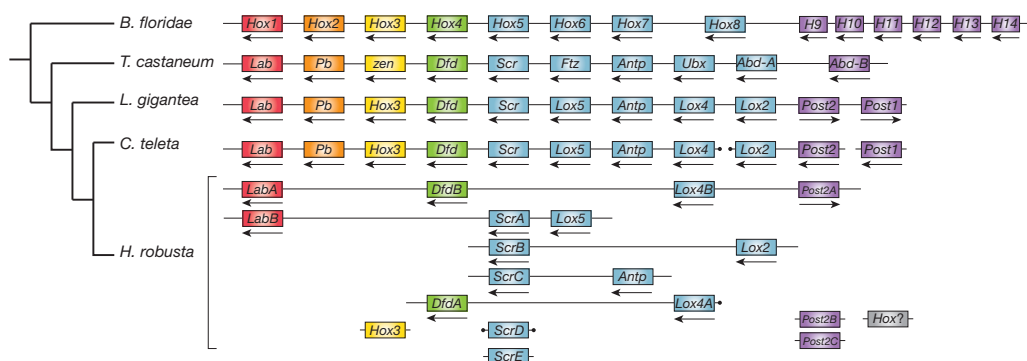


Figure 4 | The *Hox* gene complement and linkage in the three lophotrochozoan genomes and selected bilaterians. Arrows indicate direction of transcription (orientation between scaffolds is arbitrary). Scaffolds with ends marked by black dots may be part of a larger *Hox* complex because

the *Hox* gene is at the end of the scaffold. *B. floridae*, *Branchiostoma floridae*. Colours indicate unambiguously assigned paralogy groups (*Hox1*, *Hox2*, *Hox3*, *Hox4*, central class and posterior class).

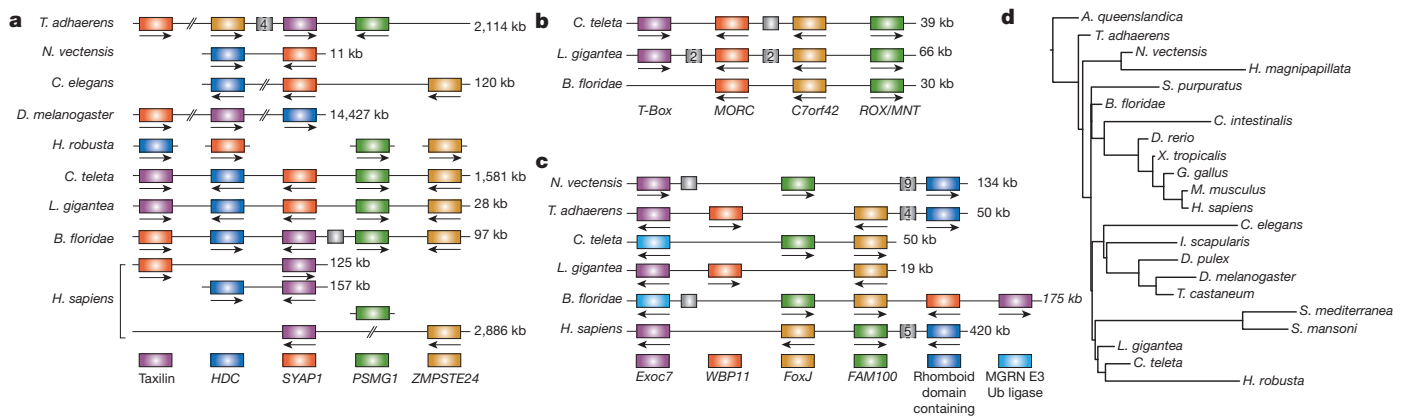


Figure 5 | Examples of conserved orthologous gene clusters. a–c, Clusters of linked genes across diverse species. Within each panel, genes in the same colour are members of the same orthologous group, with the gene identifiers of defining members of the group indicated: *C7orf42*, (human) chromosome 7 open reading frame 42; *Exoc7*, exocyst complex component 7; *FAM100*, family with sequence similarity 100; *FoxJ*, forkhead box protein J; *HDC*, histidine decarboxylase; *MGRN E3 Ub ligase*, mahogunin ring finger E3 ubiquitin ligase; *MORC*, MORC family CW-type zinc finger; *PSMG1*, proteasome (prosome, macropain) assembly chaperone 1; *ROX/MINT*, Max-binding protein family member; *SYAP1*, synapse-associated protein 1; *WBP11*, WW domain binding

orthologues are tightly linked (that is, separated by no more than ten intervening genes) in two or more genomes. Microsyntenic blocks are often, but not always, embedded in a conserved macrosyntentic context. The count of 469 microsyntenic blocks that are putatively preserved from the bilaterian ancestor in at least one protostome and one deuterostome genome is substantially greater than the 157 blocks that would persist by chance in a simple model of genome rearrangement in which gene order is randomized within the macrosyntentic blocks defined above (Supplementary Notes 6 and 7), implying either functional constraint on genome organization or intrinsically slow rates of rearrangement in some genomic regions. Considering the deeply diverged bilaterian lineages represented by *L. gigantea*, *C. teleta* and amphioxus (Supplementary Table), we found 77 conserved microsyntenic blocks (Supplementary Note 7.1), which in some cases are stably conserved across other metazoan genomes (Fig. 5). It is tempting to speculate that these conserved linkages are due to selection for preserving complex *cis*-regulatory landscapes (Supplementary Note 7.2).

Although molluscs and annelids are related to flies, nematodes and flatworms within the protostomes, we find that their genomes are in many ways more similar to those of invertebrate deuterostomes (such as amphioxus and sea urchin) as well as non-bilaterian metazoans (such as cnidarians, sponges and placozoans). These similarities reveal features of bilaterian and/or metazoan genomes that have been lost or diverged in many protostome genomes reported so far, and thus enable a more complete reconstruction of genomic features of the last common ancestors of protostomes, bilaterians and metazoans, including gene and chromosome structure and organization. Superimposed on these conserved features are evolutionary innovations—novel gene families and gene-family expansions and losses, as well as large- and small-scale genomic rearrangements—that make each clade unique. Nearly 20 other phylum-level taxa lack even a single genome sequence, and intra-phylum genomic variation can be extensive. Thus, for a comprehensive genomic understanding of the metazoan radiation a far larger sampling of genomes will be needed.

METHODS SUMMARY

Gene families and phylogeny. Orthology relationships were reconstructed for 22 metazoan genomes (Supplementary Fig. 3.3.1) using a phylogenetic clustering approach, which progressively examined reciprocal best scoring BLAST hits at decreasing phylogenetic nodes of a reference animal tree. We recovered 1,235 gene families with orthologous members in all genomes. To assess the effect of fast and

protein 11; *ZMPSTE24*, zinc metalloproteinase, STE24 homologue. Scaffold positions for all displayed linkages are listed in Supplementary Note 7.2. **d**, Cumulative rates of microsynteny change plotted on a fixed metazoan tree topology. Branch lengths are proportional to the number of inferred genomic rearrangements. *A. queenslandica*, *Amphimedon queenslandica*; *C. intestinalis*, *Ciona intestinalis*; *D. melanogaster*, *Drosophila melanogaster*; *D. pulex*, *Daphnia pulex*; *D. rerio*, *Danio rerio*; *G. gallus*, *Gallus gallus*; *H. magnipapillata*, *Hydra magnipapillata*; *I. scapularis*, *Ixodes scapularis*; *M. musculus*, *Mus musculus*; *N. vectensis*, *Nematostella vectensis*; *Ub*, ubiquitin; *X. tropicalis*, *Xenopus tropicalis*.

slow evolving characters on the tree topology, several phylogenetic approaches were taken (see Supplementary Note 5).

Identification of 8,756 ancestral bilaterian genes. Gene families were considered to be ancestral bilaterian gene families when an orthologous group had at least two protostome and two deuterostome representatives (in-group) or two sequences from either in-group and two from basal (that is, non-bilaterian) metazoans (out-group).

Macrosynteny. Draft genome scaffolds were clustered into ancestral linkage groups (ALGs) based on the locations of orthologous genes in other metazoan genomes, as described previously¹⁰. We iteratively constructed a parsimonious scenario of chromosome evolution, and ancestral genes were assigned to ancestral ALGs when any other assignment would imply more hops between ALGs in the history of that gene family (Supplementary Note 6).

Microsynteny. Chromosomal locations of orthologous genes in two different species were compared. If another set of orthologous genes is identified within a maximal distance of 10 genes of the previous set, both sets were merged together into a microsyntenic block. Only syntenic blocks with at least three orthologues per species were considered.

Intron and indel identification and phylogeny. Gene families with a maximum of 2 missing species (out of 22) were included. Intron and indel positions were detected using conserved flanking sites (3 out of 8 amino acids), no gaps were allowed to flank introns. For indels, the flanking amino acids had to be conserved. Phylogenetic inference based on presence or absence was computed with MrBayes as described in Supplementary Note 5.3.

Received 7 January; accepted 24 October 2012.

Published online 19 December 2012.

- Wilson, E. B. The cell-lineage of Nereis. A contribution to the cytogeny of the annelid body. *J. Morphol.* **6**, 361–480 (1892).
- Conklin, E. G. *The Embryology of Crepidula: a Contribution to the Cell Lineage and Early Development of Some Marine Gasteropods* (Ginn & Company, 1897).
- Henry, J. Q., Hejnal, A., Perry, K. J. & Martindale, M. Q. Homology of ciliary bands in spiralian trochophores. *Integr. Comp. Biol.* **47**, 865–871 (2007).
- Fedonkin, M. A. & Waggoner, B. M. The Late Precambrian fossil *Kimberella* is a mollusc-like bilaterian organism. *Nature* **388**, 868–871 (1997).
- Mallof, A. C. et al. The earliest Cambrian record of animals and ocean geochemical change. *Geol. Soc. Am. Bull.* **122**, 1731–1774 (2010).
- Dunn, C. W. et al. Broad phylogenomic sampling improves resolution of the animal tree of life. *Nature* **452**, 745–749 (2008).
- Berriman, M. et al. The genome of the blood fluke *Schistosoma mansoni*. *Nature* **460**, 352–358 (2009).
- The *Schistosoma japonicum* Genome Sequencing and Functional Analysis Consortium. The *Schistosoma japonicum* genome reveals features of host–parasite interplay. *Nature* **460**, 345–351 (2009).
- Robb, S. M., Ross, E. & Sanchez Alvarado, A. SmedGD: the *Schmidtea mediterranea* genome database. *Nucleic Acids Res.* **36**, D599–D606 (2008).
- Putnam, N. H. et al. The amphioxus genome and the evolution of the chordate karyotype. *Nature* **453**, 1064–1071 (2008).

11. Raible, F. *et al.* Vertebrate-type intron-rich genes in the marine annelid *Platynereis dumerilii*. *Science* **310**, 1325–1326 (2005).
12. Purschke, G. Sense organs in polychaetes (Annelida). *Dev. Hydrobiology* **179**, 53–78 (2005).
13. Zamanian, M. *et al.* The repertoire of G protein-coupled receptors in the human parasite *Schistosoma mansoni* and the model organism *Schmidtea mediterranea*. *BMC Genomics* **12**, 596 (2011).
14. Srivastava, M. *et al.* The *Amphimedon queenslandica* genome and the evolution of animal complexity. *Nature* **466**, 720–726 (2010).
15. Putnam, N. H. *et al.* Sea anemone genome reveals ancestral eumetazoan gene repertoire and genomic organization. *Science* **317**, 86–94 (2007).
16. Telford, M. J. & Copley, R. R. Improving animal phylogenies with genomic data. *Trends Genet.* **27**, 186–195 (2011).
17. Delsuc, F., Brinkmann, H. & Philippe, H. Phylogenomics and the reconstruction of the tree of life. *Nature Rev. Genet.* **6**, 361–375 (2005).
18. Philippe, H. *et al.* Phylogenomics revives traditional views on deep animal relationships. *Curr. Biol.* **19**, 706–712 (2009).
19. Adoutte, A. *et al.* The new animal phylogeny: reliability and implications. *Proc. Natl Acad. Sci. USA* **97**, 4453–4456 (2000).
20. Roy, S. W. & Gilbert, W. Resolution of a deep animal divergence by the patterns of intron conservation. *Proc. Natl Acad. Sci. USA* **102**, 4403–4408 (2000).
21. Roy, S. W. & Irimia, M. Rare genomic characters do not support Coelomata: intron loss/gain. *Mol. Biol. Evol.* **25**, 620–625 (2008).
22. Rokas, A., King, N., Finnerty, J. & Carroll, S. B. Conflicting phylogenetic signals at the base of the metazoan tree. *Evol. Dev.* **5**, 346–359 (2003).
23. Srivastava, M. *et al.* The *Trichoplax* genome and the nature of placozoans. *Nature* **454**, 955–960 (2008).
24. Duboule, D. The rise and fall of Hox gene clusters. *Development* **134**, 2549–2560 (2007).
25. Frobius, A. C. & Seaver, E. C. *Capitella* sp. I homeobrain-like, the first lophotrochozoan member of a novel paired-like homeobox gene family. *Gene Expr. Patterns* **6**, 985–991 (2006).
26. de Rosa, R. *et al.* Hox genes in brachiopods and priapulids and protostome evolution. *Nature* **399**, 772–776 (1999).
27. Shimeld, S. M., Boyle, M. J., Brunet, T., Luke, G. N. & Seaver, E. C. Clustered Fox genes in lophotrochozoans and the evolution of the bilaterian Fox gene cluster. *Dev. Biol.* **340**, 234–248 (2010).
28. Cho, S. J., Valles, Y., Giani, V. C. Jr, Seaver, E. C. & Weisblat, D. A. Evolutionary dynamics of the *wnt* gene family: a lophotrochozoan perspective. *Mol. Biol. Evol.* **27**, 1645–1658 (2010).

Supplementary Information is available in the online version of the paper.

Acknowledgements Work conducted by the US Department of Energy Joint Genome Institute is supported by the Office of Science of the US Department of Energy under contract no. DE-AC02-05CH11231. Early work on the analysis of these genomes was also supported by the Gordon and Betty Moore Foundation through a grant to the Center for Integrative Genomics at the University of California. D.S.R. thanks R. Melmon for a grant in support of this project. N.H.P. is supported by the National Science Foundation (NSF) under grant EF-0850294; D.A.W. is supported by the National Institutes of Health (NIH; RO1 GM 074619) and NSF (IOS-0922792); and O.S. is supported by Boehringer Ingelheim Fonds. E.E.-G. was supported by a training grant from the US National Human Genome Research Institute. We thank A. Meyer and J. Gerhart for helpful discussions.

Author Contributions This study was conceived by J.L.B., D.R.L., D.A.W., E.C.S. and D.S.R. The project was led by D.S.R. with N.H.P. and O.S. The three genomes were assembled by H.S. and annotated by A.Y.T., R.P.O., A.A. and I.V.G. Comparative analyses of gene complements were carried out by N.H.P., P.H. and O.S. Phylogenomic analyses were carried out by F.M. and O.S. Macro- and microsynteny was analysed by N.H.P., O.S. and J.L. GPCR complements were analysed by T.L., O.S. and D.A. Innexin analysis was carried out by O.S., D.A.W. and D.-H.K. *Hox* gene complements were analysed by D.A.W. and D.-H.K., S.-J.C. and E.C.S. Additional analyses, data and materials were contributed by U.H., J.A.C. J.G., P.d.J., K.O., R.S. and E.E.-G. The main paper was written by O.S., F.M., N.H.P., D.A.W., E.C.S. and D.S.R. with input from other authors. O.S. wrote the Supplementary Information with input from other authors.

Author Information The *Lottia gigantea* whole-genome shotgun project has been deposited in GenBank under the accession AMQ000000000. The sequence version described in this paper is deposited under accession AMQ001000000 (PRJNA175706). The *Helobdella robusta* whole-genome shotgun project has been deposited in GenBank under the accession AMQ000000000. The sequence version described in this paper is the first version, AMQ01000000 (PRJNA175704). The *Capitella teleta* whole-genome shotgun project has been deposited in GenBank under the accession AMQN000000000. The sequence version described in this paper is the first version, AMQN01000000 (PRJNA175705). Reprints and permissions information is available at www.nature.com/reprints. The authors declare no competing financial interests. Readers are welcome to comment on the online version of the paper. Correspondence and requests for materials should be addressed to N.H.P. (nputnam@gmail.com) or D.S.R. (dsrokhsar@gmail.com).



This work is licensed under a Creative Commons Attribution-NonCommercial-Share Alike 3.0 Unported licence. To view a copy of this licence, visit <http://creativecommons.org/licenses/by-nc-sa/3.0>

Rapid regulation of depression-related behaviours by control of midbrain dopamine neurons

Dipesh Chaudhury^{1*}, Jessica J. Walsh^{1,2*}, Allyson K. Friedman¹, Barbara Juarez^{1,2}, Stacy M. Ku^{1,2}, Ja Wook Koo², Deveroux Ferguson², Hsing-Chen Tsai³, Lisa Pomeranz⁴, Daniel J. Christoffel², Alexander R. Nectow⁴, Mats Ekstrand⁴, Ana Domingos⁴, Michelle S. Mazei-Robison², Ezekiell Mouzon², Mary Kay Lobo², Rachael L. Neve⁵, Jeffrey M. Friedman⁴, Scott J. Russo², Karl Deisseroth³, Eric J. Nestler^{1,2} & Ming-Hu Han^{1,2}

Ventral tegmental area (VTA) dopamine neurons in the brain's reward circuit have a crucial role in mediating stress responses^{1–4}, including determining susceptibility versus resilience to social-stress-induced behavioural abnormalities⁵. VTA dopamine neurons show two *in vivo* patterns of firing: low frequency tonic firing and high frequency phasic firing^{6–8}. Phasic firing of the neurons, which is well known to encode reward signals^{6,7,9}, is upregulated by repeated social-defeat stress, a highly validated mouse model of depression^{5,8,10–13}. Surprisingly, this pathophysiological effect is seen in susceptible mice only, with no apparent change in firing rate in resilient individuals^{5,8}. However, direct evidence—in real time—linking dopamine neuron phasic firing in promoting the susceptible (depression-like) phenotype is lacking. Here we took advantage of the temporal precision and cell-type and projection-pathway specificity of optogenetics to show that enhanced phasic firing of these neurons mediates susceptibility to social-defeat stress in freely behaving mice. We show that optogenetic induction of phasic, but not tonic, firing in VTA dopamine neurons of mice undergoing a subthreshold social-defeat paradigm rapidly induced a susceptible phenotype as measured by social avoidance and decreased sucrose preference. Optogenetic phasic stimulation of these neurons also quickly induced a susceptible phenotype in previously resilient mice that had been subjected to repeated social-defeat stress. Furthermore, we show differences in projection-pathway specificity in promoting stress susceptibility: phasic activation of VTA neurons projecting to the nucleus accumbens (NAc), but not to the medial prefrontal cortex (mPFC), induced susceptibility to social-defeat stress. Conversely, optogenetic inhibition of the VTA–NAc projection induced resilience, whereas inhibition of the VTA–mPFC projection promoted susceptibility. Overall, these studies reveal novel firing-pattern- and neural-circuit-specific mechanisms of depression.

To selectively target VTA dopamine neurons, we injected a double-floxed (DIO) Cre-dependent adeno-associated virus (AAV) vector expressing channelrhodopsin-2 (ChR2) fused with enhanced yellow fluorescent protein (eYFP) (AAV-DIO-ChR2–eYFP) into the VTA of tyrosine hydroxylase (TH)–Cre transgenic mice^{7,14}. We first validated the specificity and efficacy of AAV-DIO-ChR2–eYFP expression in VTA dopamine neurons of TH–Cre mice *in vivo* (Fig. 1a, b). Next, functional validation of ChR2–eYFP expression in VTA dopamine neurons using *in vitro* and *in vivo* electrophysiological recordings confirmed that optogenetic stimulation enables precise temporal control of these neurons (Supplementary Fig. 1a–c) and can be used to mimic the *in vivo* pathophysiological upregulation in phasic firing seen in the social-defeat-stress model of depression^{8,12}.

To investigate the functional consequence of the increase in phasic firing of VTA dopamine neurons observed after repeated (10-day) social-defeat stress, we examined the effect of optogenetically inducing

tonic (0.5-Hz) or phasic (20-Hz) firing (Fig. 1c; 5 spikes for each 10 s) in ChR2-expressing VTA dopamine neurons of TH–Cre mice while undergoing subthreshold exposure to social defeat (Fig. 1d). Mice that

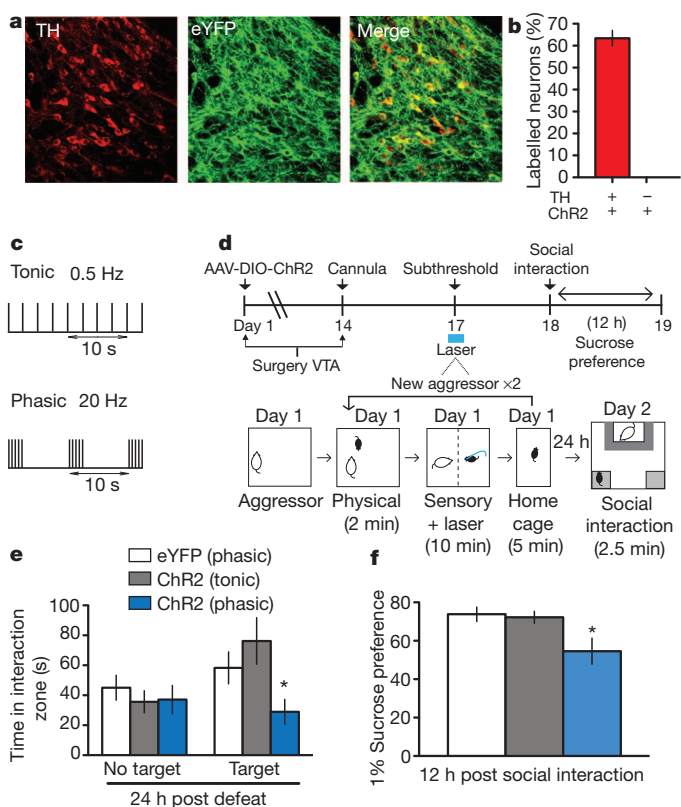


Figure 1 | Phasic, but not tonic, optical stimulation of VTA dopamine neurons during a subthreshold social defeat induces a susceptible phenotype. **a**, Confocal image showing co-expression of AAV-DIO-ChR2 in TH-positive dopamine cells from TH–Cre mice. **b**, Quantification shows that ChR2-expressing TH-positive cells are $62 \pm 4\%$ of total TH-positive neurons in the VTA. No expression of ChR2 was found in TH-negative neurons ($n = 2–3$ sections from $n = 4$ animals). **c**, Optical stimulation protocols for mimicking tonic (0.5-Hz) or phasic (20-Hz) firing. Note that for both stimulating protocols, 5 spikes are induced over each 10-s period. **d**, Top panel, experimental timeline. Bottom panel, detailed schematic of the subthreshold paradigm showing laser stimulation during social defeat. **e**, Social-interaction data from control, tonic and phasic groups. ($F_{2,30} = 4.70$, $P < 0.05$; post hoc test, $*P < 0.05$; $n = 7–14$). **f**, Sucrose preference measured over a 12-h period after the social-interaction test ($F_{2,22} = 5.22$, $P < 0.05$; post hoc test, $*P < 0.05$; $n = 7–10$). Error bars, \pm s.e.m.

¹Department of Pharmacology and Systems Therapeutics, Friedman Brain Institute, Mount Sinai School of Medicine, New York, New York 10029, USA. ²Fishberg Department of Neuroscience, Friedman Brain Institute, Mount Sinai School of Medicine, New York, New York 10029, USA. ³Departments of Bioengineering and Psychiatry and Behavioural Sciences, Stanford University, Stanford, California 94305, USA. ⁴Laboratory of Molecular Genetics, Howard Hughes Medical Institute, Rockefeller University, New York, New York 10056, USA. ⁵McGovern Institute for Brain Research, Massachusetts Institute of Technology, Cambridge, Massachusetts 02139, USA.

*These authors contributed equally to this work.

undergo this subthreshold paradigm do not exhibit social avoidance or other depression-like behaviours (Supplementary Fig. 1d), but they are more vulnerable to subsequent stress^{5,15}. We stimulated VTA dopamine neurons during the subthreshold defeat paradigm and measured social interaction and sucrose preference as two sequelae of defeat stress: social avoidance and reduced sucrose preference characterize the susceptible phenotype induced by our repeated (10-day) social-defeat paradigm^{5,8,10}. Mice that received phasic stimulation exhibited a robust increase in the depression-like phenotype as indicated by the significant decrease both in social interaction in the presence of a target mouse (Fig. 1e and Supplementary Fig. 1e–g) and in sucrose preference (Fig. 1f) compared to both tonic stimulated ChR2–eYFP mice and phasic stimulated eYFP control mice. These data confirm the functional importance of increased phasic, but not tonic, firing of VTA dopamine neurons during exposure to stress for promoting susceptibility for depression-like behavioural abnormalities.

To test directly the causal link between phasic dopamine-neuron firing and stress susceptibility, mice were exposed to subthreshold defeat and then to stimulation of VTA dopamine neurons during the social-interaction test (Supplementary Fig. 2a). Phasic stimulation of VTA dopamine neurons instantly induced a susceptible phenotype (increased social avoidance) during the social-interaction test in the presence of a target CD1 mouse (or a target C57 mouse, Supplementary Fig. 3), an effect not seen in tonic stimulated ChR2 mice or phasic stimulated eYFP control mice (Fig. 2a and Supplementary Fig. 2b–d). ChR2-expressing mice that received phasic stimulation during the brief 2.5-min social-interaction test also showed reduced sucrose preference compared to tonic-stimulated ChR2 mice or phasic-stimulated eYFP control mice (Fig. 2b). These findings are striking because they reveal the rapid induction of such depression-like behaviours that normally require repeated social-defeat stress.

In contrast to the ability of VTA dopamine-neuron stimulation to promote depression-like behaviours either during or after social-defeat stress, we found that phasic stimulation of these neurons in naive animals had no effect on social interaction, on sucrose preference or on baseline anxiety-related measures (Supplementary Fig. 4). These findings show that the pro-depression-like effects of VTA dopamine-neuron activation demonstrated here are context-specific, an important finding in light of the pro-reward consequences of such dopamine-neuron activation in other systems^{6,7,9}. Furthermore, chronic mild stressors or physically aversive stimuli inhibit the activity of VTA dopamine neurons, whereas more severe stressors increase this activity^{16,17}, as is the case with severe social stress. Also, chronic mild stress and chronic social-defeat stress have been shown recently to produce different changes in extracellular levels of several neurotransmitters in a number of brain areas¹⁸. These findings raise the possibility that, in addition to context, the severity of stress is another important determinant of stress regulation of dopamine-neuron firing.

We next investigated whether phasic firing of VTA dopamine neurons could convert resilient mice to susceptible mice. Using our standard repeated (10-day) social-defeat paradigm^{5,8,10}, we identified the subgroup of mice that remained resilient based on normal social-interaction scores, which we know are highly correlated with normal sucrose preference and other behavioural and biochemical endpoints⁵. Our previous work had shown that VTA dopamine neurons of resilient mice display normal firing rates and patterns due to unique adaptations within these neurons that prevent the stress-induced increase in their excitability^{5,8}. To test the effect of increased phasic stimulation of VTA dopamine neurons in resilient mice, we switched to herpes simplex virus (HSV)-ChR2 and control vectors with confirmed immunohistochemical and functional validation (Supplementary Fig. 5a–d).

HSV vectors have the advantage of expressing their transgenes very rapidly (within 24 h) compared to AAV vectors, which require 10–14 days for maximal expression^{5,10,14}. In this experiment, wild-type mice were subjected to the standard repeated social-defeat stress and then a social-interaction test on day 11 to identify the resilient mice as noted above. Resilient mice were injected with HSV–eYFP or

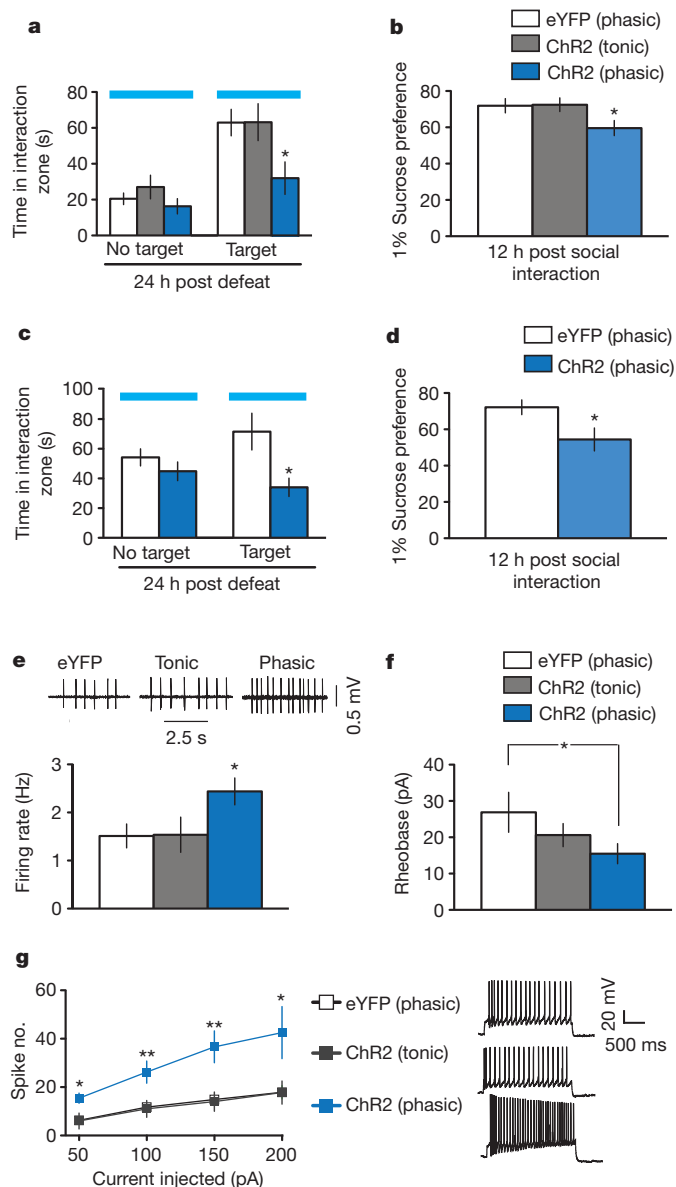


Figure 2 | Phasic optical stimulation of VTA dopamine neurons during the social-interaction test instantly induces a susceptible phenotype in two social-defeat paradigms. **a**, Social-interaction data in control, tonic and phasic groups ($F_{2,22} = 4.00$, $P < 0.05$; post hoc test, $*P < 0.05$; $n = 7–11$). Blue light stimulation was used during the tests (blue horizontal bars in **a** and **c**). **b**, Sucrose preference measured over a 12-h period after the social-interaction test ($F_{2,25} = 3.47$, $P < 0.05$; post hoc test, $*P < 0.05$; $n = 8–11$). **c**, Social-interaction data measured on day 17 ($t_{15} = 2.72$, $*P < 0.05$; two-tailed t -test, $n = 11–18$). **d**, Sucrose preference measured over a 12-h period after the social-interaction test ($t_{17} = 2.34$, $*P < 0.05$; two-tailed t -test, $n = 6–12$). **e**, Sample traces showing *in vitro* spontaneous activity of VTA dopamine neurons from TH–Cre mice that underwent tonic and phasic stimulation during the social-interaction test 24 h after subthreshold social defeat (see Supplementary Fig. 5j for the experimental timeline). Bar graph, comparison of spontaneous firing in VTA dopamine neurons from eYFP control, tonic and phasic-stimulated mice ($F_{2,50} = 3.19$, $P < 0.05$; post hoc test, $*P < 0.05$; $n = 17–19$). **f**, Significantly less current was required to evoke a single spike in phasic-stimulated mice compared to eYFP control mice ($t_{21} = 1.8$, $*P < 0.05$; one-tailed t -test, $n = 12–16$). **g**, VTA dopamine cells from phasic-stimulated mice display greater overall increased cell excitability in response to incrementally increased current injections (50, 100, 150 and 200 pA) than eYFP control and tonic-stimulated mice ($F_{2,140} = 16.13$, $P < 0.001$; post hoc test, $*P < 0.05$, $**P < 0.005$; $n = 5–17$). Error bars, \pm s.e.m.

HSV-ChR2-eYFP and subsequently analysed in a second social-interaction test during which time they underwent optogenetic phasic stimulation (Supplementary Fig. 5e, f). Although optogenetically stimulated HSV-eYFP-injected mice remained resilient, optically induced phasic firing of the VTA of HSV-ChR2-eYFP injected mice instantly converted their behavioural phenotype from resilient to susceptible as evidenced by the decrease in time spent in the interaction zone (Fig. 2c and Supplementary Fig. 5g–i). Furthermore, such phasic firing of the VTA induced anhedonic traits as evidenced by decreased sucrose preference compared to HSV-eYFP-injected mice (Fig. 2d).

Given the striking impairment in sucrose preference approximately 12 h after the optogenetic activation of VTA neurons, we proposed that such stimulation might induce lasting changes in VTA dopamine-neuron excitability. To investigate this hypothesis, we measured intrinsic membrane properties of these neurons of TH-Cre mice that had previously undergone the subthreshold social-defeat paradigm followed by *in vivo* optogenetic stimulation during the social-interaction test (Supplementary Fig. 5j). Phasic stimulation induced increased VTA dopamine-neuronal excitability compared to eYFP and tonic-stimulated mice as measured by increased spontaneous (Fig. 2e) and evoked (Fig. 2f, g) activity 8–12 h after optical stimulation. These findings suggest that subthreshold defeat followed by acute optogenetic activation leads to long-lasting neuroadaptations in VTA dopamine neurons that underlie the sustained decrease in sucrose preference observed.

VTA dopamine neurons project broadly throughout the brain. The role of the VTA–NAc pathway in reward is well known^{6,9,14}, but it has also been implicated in stress responses, as has the VTA–mPFC pathway^{1,2,4,5,10,19}. Therefore we were interested in investigating the role of these two distinct VTA projection pathways in promoting the susceptible and resilient phenotypes. We first investigated the VTA–NAc circuit by specifically labelling VTA neurons projecting to the NAc; this was accomplished by injecting the retrograde green fluorescent tracer lumafluor into the NAc and measuring the firing rate of dye-positive VTA–NAc neurons in control, susceptible and resilient mice after repeated (10-day) social-defeat stress (see Supplementary Fig. 6a, b for anatomical validation). We found that NAc-projecting VTA dopamine neurons in brain slices from susceptible mice showed a significantly higher firing rate compared to those of control and resilient mice (Fig. 3a, b), which is in agreement with increased phasic firing events from our previous work^{5,8}. Next we used optogenetic techniques to selectively stimulate this VTA–NAc pathway. To do this, we injected a replication-defective version of the retrograde travelling pseudorabies virus expressing Cre (PRV–Cre) into the NAc and the Cre-dependent AAV-DIO-ChR2-eYFP into the VTA of wild-type mice (Supplementary Fig. 6c). Immunohistochemical and electrophysiological validation confirmed the viability of using PRV–Cre to express functional ChR2 in VTA cells projecting to the NAc (Supplementary Fig. 6d–h). Mice were then subjected to the subthreshold social-defeat paradigm and 24 h later were optogenetically stimulated during the social-interaction test (Supplementary 6i). Optical induction of phasic, but not tonic, firing in VTA–NAc neurons induced the susceptible phenotype as measured by increased social avoidance and decreased sucrose preference (Fig. 3c, d and Supplementary 6j, k). Although the vast majority of dopamine neurons in this pathway were optically stimulated, only a small number of non-dopamine neurons were labelled with our approaches. Further work will be needed to study any potential influence of these non-dopamine cells on stress responses.

To investigate the effect of inhibiting the VTA–NAc pathway on the expression of the stress response, we injected AAV-DIO-halorhodopsin (NpHR)–eYFP (version 3.0 of NpHR) into the VTA followed by PRV–Cre in the NAc (Supplementary Fig. 7a, b). Functional validation confirmed that yellow light (563 nm) reliably inhibited VTA neuronal firing both *in vitro* and *in vivo* (Supplementary Fig. 7c, d) and, importantly, we did not observe any NpHR-activated rebound effect in these neurons as a result of the light protocol that we used during the behavioural experiments (Supplementary Fig. 7e). Furthermore, anatomical

quantification showed robust NpHR expression in VTA cells projecting to NAc (Supplementary Fig. 7f, g). Mice were first put through the standard repeated social-defeat stress paradigm followed by a social-interaction test on day 11 to identify the susceptible mice for eYFP control and NpHR groups (Supplementary Fig. 7h). Optogenetically stimulated DIO–eYFP injected mice remained susceptible in the second social-interaction test (both during target presence and absence), whereas inhibition of the VTA–NAc projection of DIO–NpHR–eYFP-injected mice instantly induced the resilient phenotype as evidenced by the increase in both the amount of time spent in the interaction zone and preference for sucrose (Fig. 3e, f and Supplementary Fig. 7i, j). These mice had undergone a chronic social-defeat paradigm and an earlier social-interaction test. It is therefore likely that the optogenetic attenuation of the increased activity of the VTA–NAc pathway that is typically seen in susceptible mice, combined with reactivation of the memory of the previous social-interaction test, resulted in those NpHR-injected mice spending longer times in the interaction zone, both in the absence and presence of a target mouse, during the second social-interaction test.

We also carried out experiments to investigate the functional importance of mPFC-projecting VTA dopamine neurons in promoting a susceptible phenotype (Fig. 4). We first labelled VTA neurons projecting to mPFC by injecting the retrograde red fluorescent tracer lumafluor into the mPFC (Supplementary Fig. 8a, b). Surprisingly, the firing rate of VTA–mPFC neurons was dramatically decreased in brain slices obtained from susceptible mice after repeated (10-day) social-defeat

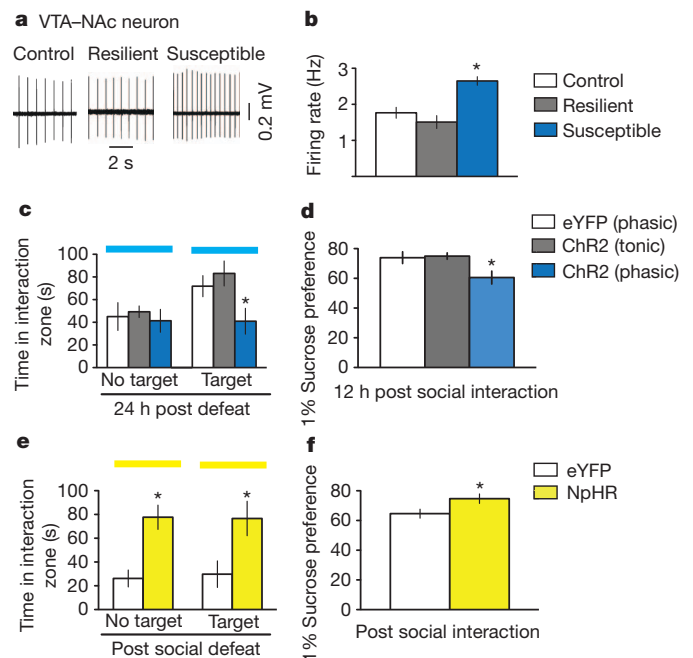


Figure 3 | Bidirectional effect of modulating the VTA–NAc pathway on susceptibility to social defeat. **a**, Sample traces recorded from VTA–NAc neurons in VTA slices. **b**, Firing rates of VTA–NAc neurons from control, resilient and susceptible mice ($F_{2,89} = 15.77$, $P < 0.001$; post hoc test, $*P < 0.001$; $n = 12–52$). **c**, Social-interaction data obtained during optical stimulation of VTA–NAc neurons in control, tonic and phasic groups ($F_{2,20} = 4.43$, $P < 0.05$; post hoc test, $*P < 0.05$; $n = 5–10$). Blue light stimulation was used during the tests (blue horizontal bars). **d**, Sucrose-preference data measured over a 12-h period after the social-interaction test ($F_{2,18} = 4.80$, $P < 0.05$; post hoc test, $*P < 0.05$; $n = 5–9$). **e**, Social interaction during optical inhibition of VTA–NAc neurons in previously susceptible mice (No target: $t_{15} = 4.2$, $*P < 0.001$; two-tailed t -test, $n = 8–9$; Target: $t_{15} = 2.6$, $*P < 0.05$; two-tailed t -test, $n = 8–9$). Yellow light stimulation was used during the tests (yellow horizontal bars). **f**, Sucrose preference measured over a 12-h period after the social-interaction test ($t_{14} = 2.3$, $*P < 0.05$; two-tailed t -test, $n = 8–9$). Error bars, \pm s.e.m.

stress, compared to that of control and resilient mice (Fig. 4a, b). This is consistent with a recent report of decreased extracellular dopamine levels in this region after repeated social-defeat stress¹⁸. We next used optogenetic techniques to selectively stimulate the VTA–mPFC pathway. To do this, we injected the retrograde PRV–Cre viral vector into the mPFC and the Cre-dependent AAV-DIO-ChR2-eYFP into the VTA of wild-type mice (Supplementary Fig. 8c), and confirmed the viability of using PRV–Cre to express functional ChR2 in VTA cells projecting to mPFC (Supplementary Fig. 8d–h). Optically induced phasic firing of these VTA–mPFC neurons, during the social-interaction test in mice that had previously undergone subthreshold social defeat, had no effect on social interaction and sucrose preference, compared to tonic stimulation and control viral vectors (Fig. 4c, d and Supplementary Fig. 8i, j). We next investigated the effect of inhibiting the VTA–mPFC pathway on the expression of the stress response by injecting DIO-NpHR–eYFP into the VTA followed by PRV–Cre into the mPFC (Supplementary Fig. 9a–d). *In vivo* optical inhibition of the VTA–mPFC pathway by activation of NpHR, during the social-interaction test in mice that had previously undergone subthreshold social defeat, induced the susceptible phenotype as measured by decreased social interaction, an effect that is not seen in control mice (Fig. 4e and Supplementary Fig. 9e, f). Interestingly, there was no difference in sucrose preference (Fig. 4f).

Our study establishes a direct link between VTA dopamine-neuronal firing patterns and susceptibility to a depression-related phenotype, in cases in which phasic firing of NAc-projecting VTA dopamine neurons encodes a signal for susceptibility. This finding is consistent with the proposed role of VTA–NAc (mesolimbic) dopamine-neuronal phasic firing in this stress model: we previously showed that the VTA–NAc

pathway is a key determinant of susceptibility versus resilience to repeated social-defeat stress⁵, and that the pathophysiological increase in phasic firing occurs selectively in susceptible mice⁸. The observation that VTA dopamine-neuron phasic firing has a functional role in encoding for both depression-like symptoms after social-defeat stress, and conditioned place preference⁷, suggests that firing patterns of these neurons and the subsequent encoding of the depressive or reward phenotype are highly context-dependent. Such encoding of stress versus reward is more complex still, because it is not only firing-pattern selective⁷ but also dependent on the severity of stress (as noted above) and shows clear projection-pathway specificity¹⁹.

In addition, our observation of the rapid onset of the susceptible phenotype in response to optical stimulation corresponds to the inferred function of mesolimbic dopamine neurons in mediating rapid antidepressant effects^{1,20}. Similarly, hyperpolarization-activated cation channels (I_h), a key channel responsible for the transition from tonic to phasic firing of VTA dopamine neurons^{21,22} that is highly expressed in VTA–NAc neurons¹⁹, is increased in susceptible mice, whereas I_h inhibitors display rapid and long-lasting antidepressant-like efficacy^{8,23}. Furthermore, the rapid antidepressant effects of ketamine^{24–26}, sleep deprivation²⁷ and deep brain stimulation^{28–30} support the existence of rapidly reversible brain mechanisms and support the idea of regulating neural circuits to treat depression. Consistent with these studies, we show a rapid ‘rescue’ effect of VTA–NAc pathway inhibition when it occurs in the context of repeated severe social stress. In marked contrast, our findings that the VTA–mPFC pathway serves the opposite function to the VTA–NAc pathway, are consistent with a recent study demonstrating the differential role of largely distinct VTA dopamine neuron populations in response to rewarding versus aversive stimuli¹⁹. In addition, our observation that modulation of the VTA–NAc pathway but not the VTA–mPFC pathway induces anhedonic-like effects suggests a functional role for the VTA–NAc pathway but not VTA–mPFC pathway in encoding reward-related information in the context of depression. Our projection-specific findings thus provide new insights into the complex role that VTA dopamine neurons have in an individual’s adaptations to repeated stress and the development of depression-like behavioural abnormalities.

METHODS SUMMARY

Viral-vector delivery to discrete brain regions. Viral vectors (0.5 μ l) were stereotactically and bilaterally injected at a rate of 0.1 μ l min^{−1}. AAV-DIO-ChR2-eYFP and AAV-eYFP (purchased from the University of North Carolina Vector Core Facility) were delivered into the VTA of TH–Cre mice. Retrograde PRV–Cre was injected into either NAc or mPFC and then AAV-DIO-ChR2-eYFP or AAV-DIO-eYFP was injected into the VTA. All viral vectors used were functionally validated with electrophysiological approaches in brain slices and/or intact animals. Retrograde pseudorabies virus (PRV)–Cre and PRV–GFP have a deletion in the viral thymidine kinase gene so that they do not replicate in non-dividing cells, cannot be transmitted trans-synaptically, and do not produce detectable effects on the health of infected neurons. Injected animals remained healthy when brain tissues were taken 7 to 10 days after surgery.

Social-defeat stress and social-interaction test. The subthreshold social-defeat paradigm involved placing the test C57BL/6J mouse into the home cage of a larger retired breeder mouse (CD1) for 2 min during which time the experimental mouse was physically attacked by the CD1 mouse. After two bouts of defeat the mouse was returned to its home cage. Mice underwent the social-interaction test 24 h after the defeat episodes. Mice received laser stimulation either during the subthreshold defeat encounters or during the subsequent social-interaction test. For some experiments in Figs 2 and 3, a repeated social-defeat paradigm (5–10 min defeat per day for 10 days) was used to separate out susceptible and resilient mice. The segregation of susceptible and resilient mice was based on the social-interaction test⁵. These subthreshold and repeated social-defeat paradigms have been extensively validated^{5,8,10}.

Light stimulation. For *in vivo* behavioural experiments using ChR2 mice (473 nm), these mice were given low-frequency tonic (0.5 Hz) or high-frequency phasic (20 Hz) light stimulations. In both tonic and phasic light-stimulation protocols, VTA dopamine neurons were exposed to 5 spikes over each 10-s period. For *in vivo* behavioural experiments using NpHR mice (563 nm), these mice were given 8 s light on and 2 s light off.

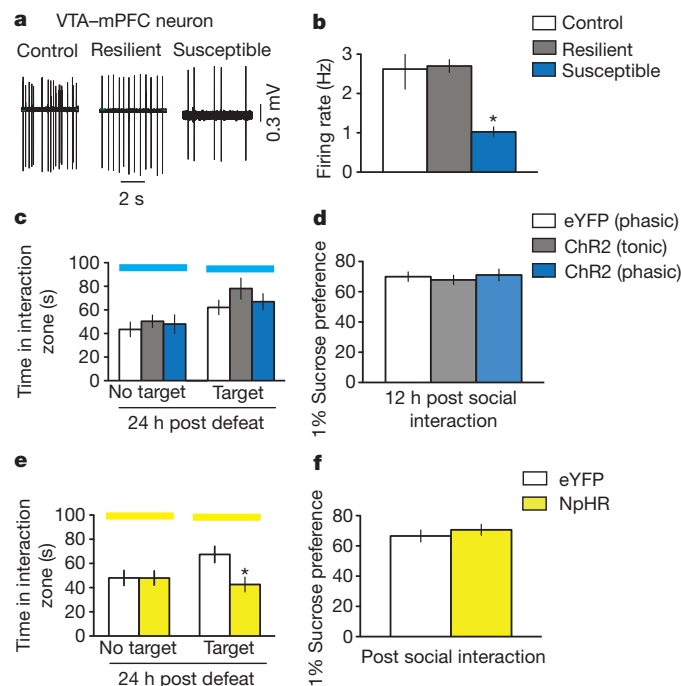


Figure 4 | Effect of modulating the VTA–mPFC pathway on susceptibility to social defeat. **a**, Sample traces recorded from VTA–mPFC neurons in VTA slices. **b**, Firing rates of VTA–mPFC neurons from control, resilient and susceptible mice ($F_{2,38} = 15.07$, $P = 0.0005$; post hoc test, $*P < 0.005$; $n = 11–15$). **c**, Social-interaction data obtained by optical stimulation of VTA–mPFC neurons in control, tonic and phasic groups ($F_{2,39} = 1.29$, $P = 0.29$; $n = 11–17$). **d**, Sucrose-preference data measured over a 12-h period after the social-interaction test ($F_{2,33} = 0.19$, $P = 0.82$; $n = 10–16$). **e**, Social-interaction data obtained during optical inhibition of VTA–mPFC neurons ($t_{29} = 2.5$, $*P < 0.05$; two-tailed t -test, $n = 12–19$). **f**, Sucrose preference measured over a 12-h period after the social-interaction test ($t_{29} = 0.38$, $P > 0.05$, $n = 12–19$). Error bars, \pm s.e.m.

Full Methods and any associated references are available in the online version of the paper.

Received 1 March; accepted 25 October 2012.

Published online 12 December 2012.

1. Willner, P., Hale, A. S. & Argyropoulos, S. Dopaminergic mechanism of antidepressant action in depressed patients. *J. Affect. Disord.* **86**, 37–45 (2005).
2. Nestler, E. J. & Carlezon, W. A. Jr. The mesolimbic dopamine reward circuit in depression. *Biol. Psychiatry* **59**, 1151–1159 (2006).
3. Berton, O. & Nestler, E. J. New approaches to antidepressant drug discovery: beyond monoamines. *Nature Rev. Neurosci.* **7**, 137–151 (2006).
4. Yadid, G. & Friedman, A. Dynamics of the dopaminergic system as a key component to the understanding of depression. *Prog. Brain Res.* **172**, 265–286 (2008).
5. Krishnan, V. *et al.* Molecular adaptations underlying susceptibility and resistance to social defeat in brain reward regions. *Cell* **131**, 391–404 (2007).
6. Grace, A. A., Floresco, S. B., Goto, Y. & Lodge, D. J. Regulation of firing of dopaminergic neurons and control of goal-directed behaviors. *Trends Neurosci.* **30**, 220–227 (2007).
7. Tsai, H. C. *et al.* Phasic firing in dopaminergic neurons is sufficient for behavioral conditioning. *Science* **324**, 1080–1084 (2009).
8. Cao, J. L. *et al.* Mesolimbic dopamine neurons in the brain reward circuit mediate susceptibility to social defeat and antidepressant action. *J. Neurosci.* **30**, 16453–16458 (2010).
9. Schultz, W. Dopamine signals for reward value and risk: basic and recent data. *Behav. Brain Funct.* **6**, 24 (2010).
10. Berton, O. *et al.* Essential role of BDNF in the mesolimbic dopamine pathway in social defeat stress. *Science* **311**, 864–868 (2006).
11. Anstrom, K. K., Miczek, K. A. & Budygin, E. A. Increased phasic dopamine signaling in the mesolimbic pathway during social defeat in rats. *Neuroscience* **161**, 3–12 (2009).
12. Razzoli, M., Andreoli, M., Michielin, F., Quarta, D. & Sokal, D. M. Increased phasic activity of VTA dopamine neurons in mice 3 weeks after repeated social defeat. *Behav. Brain Res.* **218**, 253–257 (2011).
13. Krishnan, V., Berton, O. & Nestler, E. The use of animal models in psychiatric research and treatment. *Am. J. Psychiatry* **165**, 1109 (2008).
14. Lobo, M. K. *et al.* Cell type-specific loss of BDNF signaling mimics optogenetic control of cocaine reward. *Science* **330**, 385–390 (2010).
15. Iñiguez, S. D. *et al.* Extracellular signal-regulated kinase-2 within the ventral tegmental area regulates responses to stress. *J. Neurosci.* **30**, 7652–7663 (2010).
16. Valenti, O., Gill, K. M. & Grace, A. A. Different stressors produce excitation or inhibition of mesolimbic dopamine neuron activity: response alteration by stress pre-exposure. *Eur. J. Neurosci.* **35**, 1312–1321 (2012).
17. Ungless, M. A., Magill, P. J. & Bolam, J. P. Uniform inhibition of dopamine neurons in the ventral tegmental area by aversive stimuli. *Science* **303**, 2040–2042 (2004).
18. Venzala, E., Garcia-Garcia, A. L., Elizalde, N. & Tordera, R. M. Social vs. environmental stress models of depression from a behavioural and neurochemical approach. *Eur. Neuropsychopharmacol.* advance online publication, <http://dx.doi.org/10.1016/j.euroneuro.2012.05.010> (June 27, 2012).
19. Lammel, S., Ion, D. I., Roeper, J. & Malenka, R. C. Projection-specific modulation of dopamine neuron synapses by aversive and rewarding stimuli. *Neuron* **70**, 855–862 (2011).
20. Willner, P. The mesolimbic dopamine system as a target for rapid antidepressant action. *Int. Clin. Psychopharmacol.* **12** (Suppl. 3), S7–S14 (1997).
21. Radulescu, A. R. Mechanisms explaining transitions between tonic and phasic firing in neuronal populations as predicted by a low dimensional firing rate model. *PLoS ONE* **5**, e12695 (2010).
22. Inyushin, M. U., Arencibia-Albite, F., Vazquez-Torres, R., Velez-Hernandez, M. E. & Jimenez-Rivera, C. A. Alpha-2 noradrenergic receptor activation inhibits the hyperpolarization-activated cation current (I_h) in neurons of the ventral tegmental area. *Neuroscience* **167**, 287–297 (2010).
23. Han, H. M. *et al.* Essential role of ventral tegmental area dopamine neurons in mediating the induction and rapid reversal of depression-like behaviours. Abstract, <http://www.acnp.org/annualmeeting/programbooks.aspx> (The 50th Anniversary Meeting of ACNP, 2011).
24. Berman, R. M. *et al.* Antidepressant effects of ketamine in depressed patients. *Biol. Psychiatry* **47**, 351–354 (2000).
25. Li, N. *et al.* mTOR-dependent synapse formation underlies the rapid antidepressant effects of NMDA antagonists. *Science* **329**, 959–964 (2010).
26. Autry, A. E. *et al.* NMDA receptor blockade at rest triggers rapid behavioural antidepressant responses. *Nature* **475**, 91–95 (2011).
27. Hemmeter, U. M., Hemmeter-Spernal, J. & Krieg, J. C. Sleep deprivation in depression. *Expert Rev. Neurother.* **10**, 1101–1115 (2010).
28. Giacobbe, P., Mayberg, H. S. & Lozano, A. M. Treatment resistant depression as a failure of brain homeostatic mechanisms: implications for deep brain stimulation. *Exp. Neurol.* **219**, 44–52 (2009).
29. Sartorius, A. *et al.* Remission of major depression under deep brain stimulation of the lateral habenula in a therapy-refractory patient. *Biol. Psychiatry* **67**, e9–e11 (2010).
30. Li, B. *et al.* Synaptic potentiation onto habenula neurons in the learned helplessness model of depression. *Nature* **470**, 535–539 (2011).

Supplementary Information is available in the online version of the paper.

Acknowledgements This work was supported by the National Institute of Mental Health (R01 MH092306 to D.C. and M.H.H.), Johnson & Johnson IMHRO Rising Star Translational Research Award (M.H.H.), the National Research Service Awards (F31 MH095425 to J.J.W. and F32 MH096464 to A.K.F.) and the Mount Sinai PREP R25 GM064118 (B.J.). We would like to thank K. Roy for help with some of the schematics in the figures, and we thank R. Cacho and J. Cheer for help with chronic fibre implantation techniques.

Author Contributions D.C., J.J.W., A.K.F., B.J., J.W.K., D.F., D.J.C., H.C.T., M.K.L., M.S.M.-R. and S.M.K. collected and analysed data. L.P., A.R.N. M.E., A.D., E.M., R.L.N., S.J.R., J.M.F., K.D. and E.J.N. generated and provided viral vectors and TH-Cre mice. D.C., J.J.W., E.J.N. and M.H.H. designed and wrote the paper.

Author Information Reprints and permissions information is available at www.nature.com/reprints. The authors declare no competing financial interests. Readers are welcome to comment on the online version of the paper. Correspondence and requests for materials should be addressed to M.H.H. (ming-hu.han@mssm.edu).

METHODS

Experimental subjects. CD1 male retired breeders (Charles River), C57BL/6J male mice (7–9 weeks; Jackson Laboratories) and tyrosine hydroxylase (TH)–Cre male transgenic mice (7–9 weeks; Charles Rivers) were used in these studies. TH–Cre transgenic mice (EM:00254) were obtained from the European Mutant Archive and mated with C57BL/7 wild-type mice^{7,31}. All TH–Cre subjects used in this study were backcrossed for at least 10 generations. Mice were singly housed and maintained on a 12-h light–dark cycle with food and water available *ad libitum*. All animal protocols were in accordance with the National Institutes of Health Guide for Care and Use of Laboratory Animals and approved by the Mount Sinai Institutional Animal Care and Use Committee.

Virus vectors. AAV-DIO-ChR2–eYFP, AAV-DIO-NpHR–eYFP and AAV-DIO–eYFP virus plasmids³² were initially generated using previous protocols³³ and then purchased from the University of North Carolina vector core facility (UNC). HSV-ChR2–eYFP and HSV–eYFP were provided by the laboratory of R.L.N. (MIT). Retrograde pseudorabies virus (PRV)–Cre was engineered by the laboratory of J.M.F. (Rockefeller University).

Stereotaxic surgery, viral mediated gene transfer, cannula placement and optic-fibre placement. Mice were anaesthetized with a ketamine (100 mg kg^{−1}) and xylazine (10 mg kg^{−1}) mixture, placed in a stereotaxic apparatus (Kopf Instruments) and their skull was exposed by scalpel incision. For ChR2 viruses, 33-gauge needles were placed either bilaterally or unilaterally at a 0° angle into the VTA (anterior–posterior, −3.3 mm; lateral–medial, +0.5 mm; dorsal–ventral, −4.4 mm) and 0.5–1 µl of virus was infused at a rate of 0.1 µl min^{−1}. NpHR virus was injected bilaterally into the VTA at a 7° angle (anterior–posterior, −3.3 mm; lateral–medial, +1.05 mm; dorsal–ventral, −4.6 mm) and 1 µl of virus was infused at a rate of 0.1 µl min^{−1}. For PRV–Cre viral injections 33-gauge needles were placed bilaterally at either a 10° angle into the NAc (anterior–posterior, +1.6 mm; lateral–medial, +1.5 mm; dorsal–ventral, −4.4 mm) or 15° angle into the mPFC (anterior–posterior, +1.7; lateral–medial, +0.75; dorsal–ventral, −2.5) and 0.5–1 µl of virus was infused at a rate of 0.1 µl min^{−1}. Bilateral (26-gauge) or unilateral (20-gauge) cannulae, with a length of 3.9 mm from the cannula base, were implanted over the VTA (anterior–posterior, −3.3 mm; lateral–medial, +0.5 mm; dorsal–ventral, −3.7 mm). For secure fixture of the cannula to the skull, instant adhesive (Loctite 454) was placed between the base of the cannula and the skull, and then dental cement (Ortho-Jet) was added around the cannula and the skull. For NpHR-expressing viral vectors, we used the chronically implantable optical-fibre system³⁴. Chronically implantable fibres were homemade with 200 µm core optic fibre and were implanted into the VTA at a 7° angle (anterior–posterior, −3.3 mm; lateral–medial, +1.05 mm; dorsal–ventral, −4.4 mm). For secure fixture of the implantable fibre to the skull, the skull was dried and then industrial-strength dental cement (Grip cement; Dentsply) was added between the base of the implantable fibre and the skull. For AAV surgeries on TH–Cre mice (cell-specific study), we carried out two surgeries in which we first injected the ChR2 virus then performed cannula surgery at least 2 weeks later when the AAV virus was expressed. Mice were allowed to recover for at least 3 days before starting the behavioural paradigm. For AAV surgeries on C57 mice (projection-specific study) we again undertook two surgeries, in which ChR2 virus surgery was carried out and then PRV–Cre and cannula or implantable-fibre surgery was carried out at least 2 weeks later. To enable the mice to recover and for PRV–Cre to retrograde back to the VTA we waited 5 days before starting the behavioural paradigm. For HSV surgeries both ChR2 virus and cannula placement were carried out on the same day and mice were allowed to recover for at least 3 days before starting the behavioural paradigm. Lumafluor tracing for retrograde labelling of VTA neurons projecting to NAc or mPFC, the retrobeads were injected into the NAc or mPFC at the coordinates mentioned previously. Lumafluor (1 µl) was injected into each hemisphere.

For *in vivo* optical control of VTA neuronal firing with ChR2 experiments, a 200-µm core optic fibre was modified for attachment to the cannula. When the fibre was secured to the cannula, the tip of the fibre extended approximately 0.5 mm beyond the cannula. This experimental set up was based on and slightly modified from previous studies^{14,35}. For NpHR experiments 200 µm fibre core was attached to an chronically implanted fibre. Optic fibres were only secured *in vivo* during the behavioural paradigm (during subthreshold social-defeat or social-interaction tests).

Blue light stimulation. Optical fibres (Thor Labs, BFL37-200) were connected using an FC/PC adaptor to a 473-nm blue laser diode (Crystal Laser, BCL-473-050-M), and a stimulator (Agilent Technologies, no. 33220A) was used to generate blue light pulses. For *in vitro* slice electrophysiological validation of ChR2 activation we tested 0.1–50-Hz stimulation protocols. For *in vivo* optrode recordings we tested similar stimulation protocols. For all *in vivo* behavioural experiments, mice were given either low-frequency tonic (0.5 Hz, 15 ms) or high-frequency phasic (20 Hz, 40 ms) light stimulations. In both tonic and phasic light stimulation protocols, VTA dopamine neurons were exposed to 5 spikes over each 10-s period

(Fig. 1c). For ChR2 activation during the subthreshold social defeat, mice received bilateral stimulation, whereas for all ChR2 activation during the social-interaction test mice received unilateral stimulations.

Yellow light stimulation. Optical fibres (Thor Labs, SFS200/220Y) were connected using an FC/PC adaptor to a 561-nm yellow laser diode (Crystal Laser, CL561-050-L), and a stimulator (Agilent Technologies, no. 33220A) was used to generate yellow light pulses. For *in vitro* slice electrophysiological validation of NpHR activation, we tested different durations of yellow light activation (1–60 s duration) to examine the duration-dependent inhibition of the firing rate (Supplementary Fig. 7d). For all *in vivo* behavioural experiments, mice was given a protocol of 8 s of yellow light on and then by 2 s light off during the social-interaction test. All NpHR experiments were performed using bilateral stimulations.

Social-defeat stress and social interaction. Mice underwent either a subthreshold social-defeat stress paradigm or a repeated social-defeat stress paradigm³⁶. The subthreshold paradigm involved placing the test mice (intruder) into the home cage of a larger, retired 'resident' breeder mouse (CD1) for 2 min during which time the experimental mouse was physically attacked (defeated) by the CD1 mouse. After 2 min of physical interaction, the experimental mice underwent 10 min of sensory stress. For this, a perforated plexiglass partition was placed in the middle of the CD1 mouse home cage, and the resident CD1 and intruder experimental mouse were physically separated but kept next to each other. After 10 min of sensory stress the experimental mouse was returned to its home cage for 5 min after which time it went through a second round of physical interaction and sensory stress in the home cage of a new CD1 mouse. After two bouts of defeats the experimental mouse was returned to its home cage and underwent social-interaction test the next day. In a subset of experiments the experimental mice underwent bilateral light stimulation (5 min per hemisphere), in order to stimulate VTA dopamine cells, during the sensory-stress period.

For the repeated social-defeat paradigm, an experimental mouse was placed into the home cage of a CD1 mouse for 10 min during which time it was physically defeated by the CD1 mouse. After 1 min of physical interaction, the CD1 and experimental mouse were maintained in sensory contact for 24 h using a perforated plexiglass partition dividing the resident home cage in two. The experimental mice were exposed to a new CD1 mouse home cage for 10 consecutive days and tested for social interaction on day 11. Both subthreshold and repeated social defeat were carried out between 13:00 and 15:00.

Social-avoidance behaviour towards a novel CD1 mouse was measured in a two-stage social-interaction test. In the first 2.5-min test (target absent), the experimental mouse was allowed to freely explore a square-shaped arena (44 × 44 cm) containing a wire mesh cage (10 × 6 cm) placed on one side of the arena. In the second 2.5 min test, the experimental mouse was reintroduced back into the arena with an unfamiliar CD1 mouse contained behind a wire mesh cage. Video tracking software (Ethovision 3.0, Noldus) was used to measure the amount of time the experimental mouse spent in the 'interaction zone' (14 × 26 cm), 'corner zone' (10 × 10 cm) and 'total travel' within the arena. In a subset of studies experimental mice underwent unilateral blue light stimulation to activate the VTA dopamine cells or yellow light stimulation to inhibit VTA dopamine cells, during both the target absent and target present sessions of the social-interaction test. The interaction ratio was measured as (interaction time, target present)/(interaction time, target absent) and normalized to 100. Susceptible and resilient mice were segregated based on the interaction ratio: mice with scores <100 were defined as 'susceptible' and those with scores ≥100 were defined as 'resilient'. To confirm that the optogenetic activation-induced depression-related avoidance is not a simple fear memory of a CD1 aggressor, a social-interaction test using a C57 mouse as a target was carried out. Mice that had undergone subthreshold social defeat and then phasic stimulation during the social-interaction test similarly avoided the non-aggressive C57 social target to the same degree as observed with a CD1 target (Supplementary Fig. 2). This is consistent with our previous work showing that a C57 social target induced social avoidance in the repeated social-defeat paradigm⁵.

Sucrose preference. Mice were initially habituated to 50-ml tubes with stoppers fitted with ball-point sipper tubes (a two-bottle choice) filled with drinking water 2 days before the sucrose-preference measurements. After completion of the social-interaction test mice were given access to a two-bottle choice of water or 1% sucrose solution. Bottles containing water and sucrose were weighed at several time points during the day at 15:00, 18:00 and 09:00 for 3 days. The position of the bottles was interchanged (left to right, right to left) after each weight measurement to ensure that the mice did not develop a side preference. Sucrose preference was calculated as a percentage (amount of sucrose consumed × 100 (bottle A)/total volume consumed (bottles A + B)). Total sucrose consumption during the first 12 h after the social-interaction test was measured and used to obtain sucrose preference in this study.

Elevated plus maze. Mice were placed in the centre of an elevated plus maze (arms are 33 × 5 cm, with 25-cm tall walls on the closed arms) and their behaviour was

digitally tracked for 5 min. Mice received VTA optical stimulation during the whole duration of the elevated plus maze. A video-tracking system (Ethovision 3.0, Noldus) was used to measure the amount of time spent in the closed and open arms.

Open field. Mice were tested for their activity during 15 min in an open field arena (44 × 44 cm). A video-tracking system (Ethovision 3.0, Noldus) was used to measure the locomotor activity of the animal, as well as the time spent in the centre (34 × 34 cm) and periphery of the test arena.

In vitro patch-clamp electrophysiology. Whole-cell optogenetic recordings were obtained from VTA dopamine neurons in acute brain slices from TH-Cre mice that had been stereotactically injected with AAV-DIO-ChR2-eYFP into the VTA, C57 mice that had been injected with HSV-ChR2-eYFP into the VTA or C57 mice that had been injected with the retrograde viral vector PRV-Cre in either the NAc or mPFC, and AAV-DIO-ChR2-eYFP or AAV-DIO-NpHR-eYFP into the VTA. Cell-attached recordings were obtained from VTA dopamine neurons in acute brain slices from wild type C57 mice that had been stereotactically injected with the retrograde dye lumafluor in either NAc or mPFC. To minimize stress and to obtain healthy VTA slices, mice were anaesthetized and perfused immediately for 40–60 s with ice-cold aCSF (artificial cerebrospinal fluid), which contained 128 mM NaCl, 3 mM KCl, 1.25 mM NaH₂PO₄, 10 mM D-glucose, 24 mM NaHCO₃, 2 mM CaCl₂ and 2 mM MgCl₂ (oxygenated with 95% O₂ and 5% CO₂, pH 7.4, 295–305 mOsm). Acute brain slices containing VTA dopamine neurons were cut using a microslicer (DTK-1000, Ted Pella) in cold sucrose aCSF, which was derived by fully replacing NaCl with 254 mM sucrose and saturated by 95% O₂ and 5% CO₂. Slices were maintained in holding chambers with aCSF for 1 h at 37 °C. Patch pipettes (3–5 mΩ) for whole-cell current-clamp, voltage-clamp and cell-attached recordings were filled with internal solution containing the following: 115 mM potassium gluconate, 20 mM KCl, 1.5 mM MgCl₂, 10 mM phosphocreatine, 10 mM HEPES, 2 mM magnesium ATP and 0.5 mM GTP (pH 7.2, 285 mOsm). Whole-cell and cell-attached recordings were carried out using aCSF at 34 °C (flow rate = 2.5 ml min⁻¹). For whole-cell recordings during optogenetic stimulation resting membrane potential and action potentials were recorded in current-clamp mode and inward current measurements were made in voltage-clamp mode using the Multiclamp 700B amplifier and data acquisition was done in pClamp 10 (Molecular Devices). Series resistance was monitored during the experiments and membrane currents and voltages were filtered at 3 kHz (Bessel filter). For ChR2 experiments, sustained and trains (0.1–50 Hz) of blue light were generated by a stimulator (mentioned above) and delivered to VTA dopamine neurons expressing ChR2 through a 200-mm optic fibre attached to a 473-nm laser. For NpHR experiments, different durations of yellow light were generated by a stimulator mentioned above and delivered to VTA dopamine neurons expressing NpHR through a 200-mm optic fibre attached to a 561-nm laser. For cell-attached action potential recordings, signals were band-pass filtered at 300 Hz–1 kHz to identify dopamine neurons and were then Bessel filtered at 10 kHz (gain 50) using a Multiclamp 700B amplifier and data acquisition was carried out using pClamp 10. For measurements of the spontaneous activity of VTA dopamine neurons, cell-attached recordings were performed. To measure the intrinsic membrane properties of VTA dopamine neurons, whole-cell recordings were carried out in current-clamp mode and spikes were induced by incremental increases of current injection (each step increase was 50 pA; range 50–200 pA).

In vivo optrode recording. Viral injection and *in vivo* optrode recordings were carried out as described previously^{7,37}. AAV-DIO-ChR2-eYFP was injected into VTA (anterior–posterior, –3.44 mm; lateral–medial, +0.48 mm; dorsal–ventral, –4.4 mm) of TH-Cre mice and left for at least 2 weeks to allow for viral expression. Prior to recordings mice were deeply anaesthetized with a ketamine and xylazine mixture, and placed on a stereotactic frame and attached to a temperature regulator.

The area of skull directly above the VTA was removed and an optrode consisting of a tungsten electrode (1 mΩ resistance; 125 μm length) tightly bundled with an optical fibre (200-μm core, 0.2 NA) was lowered to the boundary of the VTA (anterior–posterior, –3.44 mm; lateral–medial, +0.48 mm; dorsal–ventral, –4 mm). The tip of the electrode protruded about 0.4 mm beyond the optical fibre to ensure illumination of the recorded neurons. At the VTA boundary simultaneous optical stimulation and recordings of the electrical response of neurons expressing ChR2 was carried out as the optrodes were gradually lowered in 0.1-mm increments until a clear response to optical stimulation was measured. The optical fibre was coupled to a 473-nm solid-state laser diode with an approximately 20-mW output. Recorded signals were band-pass filtered at 300 Hz–5 kHz using an 1800 Microelectrode AC amplifier.

Immunohistochemistry. For double-immunofluorescence experiments, tissue sections were fixed in 4% (weight divided by volume; wt/vol) PBS-buffered paraformaldehyde. Tissues and cells were blocked in PBS-T (0.3% Triton X-100) including 2% (wt/vol) bovine serum albumin (BSA; Sigma) and then exposed overnight to these primary antibody mixtures: anti-GFP (Invitrogen, 1:2000) and anti-TH (Sigma, 1:10,000). Detection of primary antibodies was carried out with mixtures of the secondary antibodies Cy2-anti-mouse and Cy3-conjugated anti-rabbit (1:500; Jackson ImmunoResearch). Anti-NeuN (Aves Laboratories, NUN) raised from chicken was used at a dilution ratio of 1:1000 and was detected by Cy3-anti-chicken. For TH labelling, anti-TH (Sigma) from mouse at a dilution ratio of 1:5000 was used and detected with Cy5-anti-mouse. For GFP labelling, anti-GFP (Invitrogen) from rabbit was used at a dilution ratio of 1:2000 and was detected by Cy2-anti-rabbit. Tissues and cells were counterstained and mounted with anti-fade solution, including 4',6-diamidino-2-phenylindole (DAPI; VectaShield, Vector Laboratories). Sections were subsequently imaged (×20 magnification) on a LSM 710 confocal (Zeiss). Cell counting was carried out manually using ImageJ. For immuno-validation of PRV-Cre, animals were killed with a lethal dose of Isoflurane and then transcardially perfused with PBS then 10% formalin 5–10 days post PRV-Cre injections. After perfusion, brains were kept in 10% formalin at 4 °C for 18–24 h, at which point the brains were transferred to PBS and sliced into coronal sections using a vibrating blade microtome (Leica Microsystems, model VT1000S). For immunostaining, we processed the slices using antibodies against GFP (Abcam, chicken, 1:1000) and tyrosine hydroxylase (Pel-Freez, rabbit, 1:1000). The antibodies were labelled with goat anti-chicken Alexa 488 and goat anti-rabbit Alexa 633 (Invitrogen, 1:1000), respectively. mCherry expression from the AAV was sufficiently intense for confocal microscopy. Sections were imaged at ×20 magnification for analysis, which was performed manually.

31. Lindeberg, J. *et al.* Transgenic expression of Cre recombinase from the tyrosine hydroxylase locus. *Genesis* **40**, 67–73 (2004).
32. Cardin, J. A. *et al.* Targeted optogenetic stimulation and recording of neurons in vivo using cell-type-specific expression of Channelrhodopsin-2. *Nature Protocols* **5**, 247–254 (2010).
33. Hommel, J. D., Sears, R. M., Georgescu, D., Simmons, D. L. & DiLeone, R. J. Local gene knockdown in the brain using viral-mediated RNA interference. *Nature Med.* **9**, 1539–1544 (2003).
34. Sparta, D. R. *et al.* Construction of implantable optical fibers for long-term optogenetic manipulation of neural circuits. *Nature Protocols* **7**, 12–23 (2011).
35. Gradinaru, V. *et al.* Targeting and readout strategies for fast optical neural control *in vitro* and *in vivo*. *J. Neurosci.* **27**, 14231–14238 (2007).
36. Golden, S. A., Covington, H. E. III, Berton, O. & Russo, S. J. A standardized protocol for repeated social defeat stress in mice. *Nature Protocols* **6**, 1183–1191 (2011).
37. Stuber, G. D. *et al.* Excitatory transmission from the amygdala to nucleus accumbens facilitates reward seeking. *Nature* **475**, 377–380 (2011).

Dopamine neurons modulate neural encoding and expression of depression-related behaviour

Kay M. Tye^{1,2*}, Julie J. Mirzabekov^{2*}, Melissa R. Warden^{2*}, Emily A. Ferenczi^{2,3}, Hsing-Chen Tsai^{2,3}, Joel Finkelstein², Sung-Yon Kim^{2,3}, Avishek Adhikari², Kimberly R. Thompson², Aaron S. Andalman², Lisa A. Gunaydin², Ilana B. Witten² & Karl Deisseroth^{2,3,4,5,6}

Major depression is characterized by diverse debilitating symptoms that include hopelessness and anhedonia¹. Dopamine neurons involved in reward and motivation^{2–9} are among many neural populations that have been hypothesized to be relevant¹⁰, and certain antidepressant treatments, including medications and brain stimulation therapies, can influence the complex dopamine system. Until now it has not been possible to test this hypothesis directly, even in animal models, as existing therapeutic interventions are unable to specifically target dopamine neurons. Here we investigated directly the causal contributions of defined dopamine neurons to multi-dimensional depression-like phenotypes induced by chronic mild stress, by integrating behavioural, pharmacological, optogenetic and electrophysiological methods in freely moving rodents. We found that bidirectional control (inhibition or excitation) of specified midbrain dopamine neurons immediately and bidirectionally modulates (induces or relieves) multiple independent depression symptoms caused by chronic stress. By probing the circuit implementation of these effects, we observed that optogenetic recruitment of these dopamine neurons potently alters the neural encoding of depression-related behaviours in the downstream nucleus accumbens of freely moving rodents, suggesting that processes affecting depression symptoms may involve alterations in the neural encoding of action in limbic circuitry.

Major depressive disorder is a debilitating disease characterized by diverse symptoms that include depressed mood, suicidality, psychomotor retardation or agitation, reduced motivation or hopelessness, and anhedonia¹. Current medical therapies for depression take weeks to achieve full efficacy, and are ineffective in many patients or cause intolerable side effects, pointing to the need for deeper understanding of depression states and treatment. Given that there is strong evidence linking the mesolimbic dopamine system with reward-related^{2,3}, hedonic^{4–6} and motivated^{7–9} behaviours, we proposed to test whether midbrain dopamine neurons could have a causal role in both induction and relief of diverse stress-induced depression-related behaviours¹⁰, including reduced motivation and anhedonia^{4,8,10,11}. To test this, we developed and used an array of tools for real-time assessment and control of depression-related states in freely moving rodents.

We first tested whether selective inhibition of ventral tegmental area (VTA) dopamine neurons could acutely induce multiple depression-like behaviours. We expressed an enhanced halorhodopsin that hyperpolarizes neuronal membranes upon illumination (eNpHR version 3.0; eNpHR3.0) in VTA tyrosine hydroxylase (TH)-expressing dopamine neurons, by injecting a Cre-dependent adeno-associated virus (AAV) carrying this eNpHR3.0 into the VTA of TH::Cre mice⁶ (Fig. 1a and Supplementary Fig. 1). eNpHR3.0 was fused to the enhanced yellow fluorescent protein (eYFP) so that targeting specificity could be tracked by quantifying the proportion of VTA neurons expressing

eNpHR3.0–eYFP (or eYFP alone in age-matched controls) that were also TH-positive (Fig. 1b and Supplementary Fig. 2).

Primary categories of depression assays in rodents involve well-validated tests of motivation and anhedonia^{12–15} in which performance degrades with chronic stress and improves with chronic antidepressant-medication treatment^{13,15}. In the context of depressive phenotypes, motivation is assayed by presenting rodents with an inescapable stressor, such as those used in the tail-suspension test (TST) or forced-swim test (FST), and quantifying the proportion of time spent performing escape-related behaviour (struggling) relative to time spent immobile, which has been interpreted as a sign of behavioural despair or passivity¹². Here we compared mice with VTA dopamine neurons expressing eNpHR3.0 to eYFP-expressing controls, and observed a significant and reversible reduction in escape-related behaviour upon illumination (Fig. 1c). We investigated whether this reduction in struggling was related to a gross locomotor effect, rather than a more selective decrease in motivation to escape, by evaluating inhibition of VTA dopamine neurons in these same animals during exploration of an open-field-test (OFT) arena. There was no significant difference in locomotion between groups (Fig. 1d and Supplementary Figs 3 and 4). Although no difference was detected, any trend towards subtly decreased locomotion in the eNpHR3.0 group upon illumination in the OFT would still be consistent with a depression-related phenotype, given that related motor changes are clinically observed as psychomotor retardation and/or reduced motivation to explore (Supplementary Information).

We next developed a temporally precise version of an assay for anhedonia, the sucrose-preference test^{13,14}. We quantified (by automated detection) the number of licks on spouts delivering either water or 1% sucrose during a 90-min session consisting of a baseline 30-min light-off epoch, followed by a 30-min light-on epoch, and ending with another 30-min light-off epoch (Fig. 1e and Supplementary Fig. 5a). Notably, we observed a significant reduction in sucrose preference during illumination in eNpHR3.0 mice but not eYFP control mice (Fig. 1e), and no significant group-by-epoch interaction (two-way analysis of variance (ANOVA)) in total licks (Supplementary Fig. 5a). Therefore, optogenetic inhibition of VTA dopamine neurons defined a phenotype that could be immediately induced and reversed, and that was consistent with multiple depression-symptom categories of behavioural despair and anhedonia¹².

To test for a causal link to existing depression-like states, we also probed the ability of dopamine-neuron activation to correct independent depression-like phenotypes induced by stress⁴. As clinical depression can be linked to stressors operating over months, we used the time-intensive chronic mild stress (CMS) paradigm in which unpredictable mild stressors are delivered twice daily for 8 to 12 weeks to induce a depressive-like state¹³. CMS has been shown to produce decreases in motivation, assayed by reduction in escape-related

¹Picower Institute for Learning and Memory, Brain and Cognitive Sciences, Massachusetts Institute of Technology, Cambridge, Massachusetts 02139, USA. ²Department of Bioengineering, Stanford University, Stanford, California 94305, USA. ³Neurosciences Program, Stanford University, Stanford California 94305, USA. ⁴Department of Psychiatry and Behavioral Sciences, Stanford University, Stanford, California 94305, USA. ⁵Howard Hughes Medical Institute, Stanford University, Stanford California 94305, USA. ⁶CNC Program, Stanford University, Stanford, California 94305, USA.

*These authors contributed equally to this work.

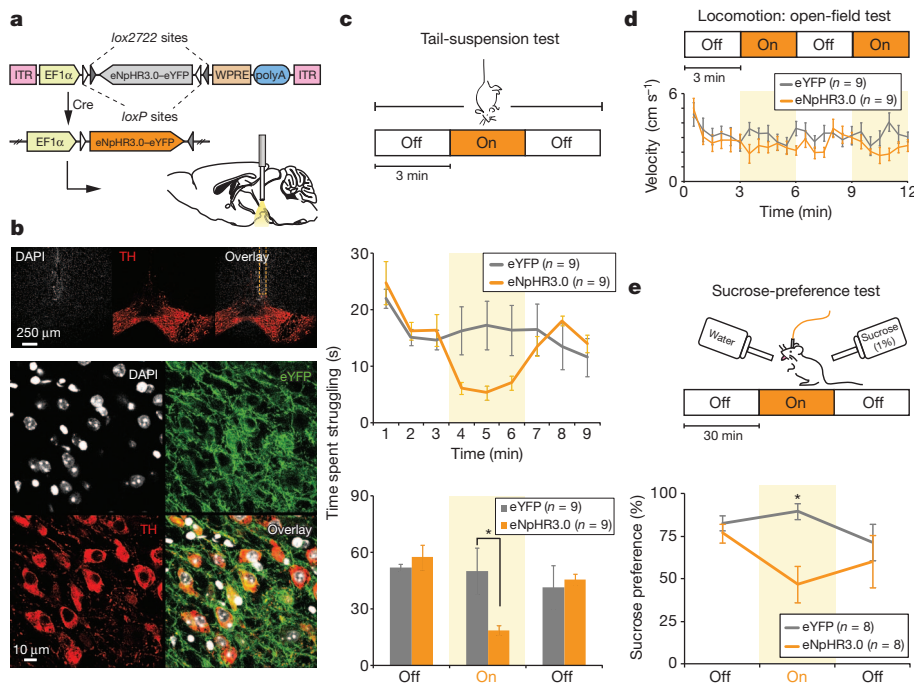


Figure 1 | Selective inhibition of VTA dopamine neurons induces a depression-like phenotype.

a, Cre-dependent AAV. **b**, Confocal images of midbrain dopamine neurons. Orange dotted lines, location of fibre optic. Bottom, images of VTA neurons directly below fibre track. **c**, Photoinhibition of VTA dopamine neurons acutely reduces escape-related behaviour. Two-way ANOVA demonstrates the group-by-light epoch interaction (interaction of the experimental-group factor and light-condition factor in the test), $F_{4,38} = 3.95$, $P = 0.00089$; Bonferroni post-hoc test shows reduced struggling in the eNpHR3.0 group relative to the eYFP group, $*P < 0.05$. Error bars, s.e.m. **d**, Inhibition of VTA dopamine neurons does not produce a significant difference in open-field locomotion; two-way ANOVA did not demonstrate a significant group-by-light epoch interaction, $F_{3,48} = 1.76$, $P = 0.17$. Error bars, s.e.m. **e**, Schematic and results of the 90-min sucrose-preference test. Photoinhibition of VTA dopamine neurons acutely reduces sucrose preference; two-way ANOVA revealed that opsin expression has a significant effect, $F_{1,42} = 6.31$, $P = 0.016$; Bonferroni post-hoc test revealed significant differences between groups only in the light-on epoch, $*P < 0.05$. Error bars, s.e.m. Off, light off; On, light on; WPRE, woodchuck hepatitis virus post-transcriptional regulatory element.

behaviour in the face of inescapable stressors, as well as anhedonia, as measured by reduced sucrose preference^{12–14}.

To phasically activate VTA dopamine neurons, we selectively expressed channelrhodopsin-2 (ChR2) in these cells to achieve temporally precise excitation with light. We included four groups of mice (Fig. 2a and Supplementary Fig. 6): mice with ChR2-transduced VTA dopamine neurons and exposed to CMS; mice with eYFP-transduced VTA dopamine neurons and exposed to CMS; mice with ChR2-transduced VTA dopamine neurons and housed in a low-stress environment (non-CMS); and mice with eYFP-transduced VTA dopamine neurons and non-CMS.

We examined animals during baseline (light-off), phasic illumination (light-on) and post-illumination (light-off) epochs (Fig. 2b) during multiple behavioural assessments. To produce phasic firing in VTA dopamine neurons, we used a physiological, sparse bursting illumination pattern (Fig. 2b; 8 pulses at 30 Hz, 5-ms pulse width, every 5 s) similar to patterns known to elicit phasic spiking and dopamine transients⁶ during illumination epochs. To assess behavioural motivation we exposed all four groups of animals to the TST. At baseline, consistent with previous studies¹⁵, we observed (Fig. 2c) that CMS markedly reduced the amount of escape-related behaviour relative to non-CMS controls by approximately 50%; moreover, upon illumination, the ChR2-CMS group showed a robust increase in escape-related behaviour, relative to the eYFP-CMS group ($P < 0.001$). Thus, phasic illumination of VTA dopamine neurons in ChR2 CMS mice, but not eYFP CMS mice, reversed the CMS-induced depression-like phenotype back to non-CMS levels, with timing on the order of seconds (Fig. 2c).

As dopamine neurons in some systems are linked to locomotion⁹, we examined locomotion in the OFT chamber (of the same mice included in the TST assay) during two 3-min light-on epochs, interleaved with two 3-min light-off epochs using the same phasic illumination parameters described above (Fig. 2d). On the timescale corresponding to TST effects, only statistically non-significant interactions with altered OFT velocity were observed in ChR2 groups upon illumination.

Next, we tested whether phasic activation of VTA dopamine neurons could also reverse CMS-induced decreases in sucrose preference (Fig. 2e). Consistent with previous studies, baseline measurements showed that eYFP and ChR2 CMS mice expressed significantly lower sucrose preference than eYFP and ChR2 non-CMS mice before

illumination on the lickometer assay (Bonferroni post-hoc tests, $P < 0.05$ and $P < 0.01$, respectively). However, phasic activation of VTA dopamine neurons acutely reversed the CMS-induced anhedonic effect in ChR2 CMS, but not eYFP CMS, animals (Fig. 2e) without altering the total number of licks across groups (Supplementary Fig. 5b).

Together these results show bidirectional effects of VTA dopamine neuron activity on rapidly inducing and ameliorating diverse depression-related behaviours. We next considered how chronic mild stress itself might influence VTA neuronal activity. To investigate this, we recorded from the VTA of CMS ($n = 93$ neurons) or non-CMS ($n = 71$ neurons) animals to probe neuronal firing properties (Supplementary Figs 8–10). The mean spike rate was maintained between groups, but out of the total spikes recorded, VTA neurons in non-CMS rats had a significantly greater proportion of spikes occurring within bursts, had longer-duration bursts, and had more spikes in each burst compared to VTA neurons in CMS rats (Supplementary Fig. 9), indicating that CMS alters normal bursting activity.

As VTA dopamine neurons project to multiple regions throughout the brain¹⁶, it is not clear which downstream targets may be contributing to the changes in depression-related behaviours, although it is perhaps relevant that clinical deep brain stimulation in the NAc (among other targets) has been proposed to modulate depression-related symptoms¹⁷. Since the NAc does receive (among many other inputs) dopaminergic innervation *in vivo* that can guide certain motivated behaviours⁵ and glutamatergic innervation involved in reward-related conditioning, we next tested whether glutamate or dopamine transmission in the NAc could mediate the light-induced rescue of the depression-like phenotype, using mice that were implanted with bilateral guide cannulae in the NAc in the setting of viral ChR2 transduction of VTA dopamine neurons and chronic implantation of a fibre-optic cable targeted at the VTA (Supplementary Figs 11 and 12), before undergoing 8 to 12 weeks of CMS.

We carried out within-subject comparisons counter-balanced for order, and infused either saline, or glutamate-receptor antagonists, into the NAc before the TST. Glutamate-receptor antagonism did not attenuate the light-induced reversal of reduced struggling following CMS seen, but instead increased overall struggling (Supplementary Fig. 11a). As the NAc receives glutamatergic innervation from many regions, we speculate that the net effect of these inputs may suppress struggling in the TST, perhaps consistent with acute clinical anti-depressant effects

Because even a lightweight electrophysiological recording headstage impeded normal escape-related behaviours in mice, this experiment required TH::Cre rats³, which were able to express escape-related behaviours while bearing an electrophysiological recording headstage in the FST without mechanical noise (Fig. 3a–c). We used a novel high-speed method of magnetic induction-based assessment of depression-related behaviour, placing a magnetic coil surrounding the forced-swim tank and a small magnet attached to the hind-paw to measure swimming kicks or escape-related behaviour. We validated that illumination of ChR2-expressing VTA dopamine neurons in TH::Cre rats rapidly and reversibly increased escape-related behaviour (Fig. 3 and Supplementary Fig. 13) but did not alter locomotion in the OFT (Fig. 3d and Supplementary Fig. 14).

We carried out *in vivo* electrophysiological recordings in the NAc of TH::Cre rats³ during baseline activity in the home cage, during exploration in the OFT, and during the FST (Fig. 3a and Supplementary Fig. 15) while illuminating ChR2-expressing VTA dopamine neurons following CMS (Fig. 3b, c). We observed a robust increase in kick frequency during light-on epochs relative to light-off epochs, but did not observe time-locked kicking to light pulses on the order of seconds (Fig. 3c–e), suggesting that this behaviour may be modulated by dopaminergic tone rather than individual dopamine transients. We also found that the more NAc neurons showing phasic responses to VTA dopamine activation in an animal, the greater the relative increase in escape-related behaviour, but not OFT locomotion (Supplementary Fig. 16 and Fig. 3f).

We examined the proportion of NAc neurons ($n = 123$) showing phasic responses to light pulses in VTA or phasic responses associated with FST kicks (Supplementary Figs 17 and 18). Many NAc neurons (45 out of 123 (37%); Fig. 4a) showed phasic responses to VTA light (see Supplementary Materials for statistical methods). Of these 45 neurons, 6 showed phasic inhibition to light, whereas the dominant population (39 out of 45) showed phasic excitation. Separate from phasic responses, we also observed that upon FST exposure, more NAc neurons showed decreases than increases in mean epoch firing rate compared with home-cage firing (Supplementary Fig. 19). Furthermore, 49 out of 123 NAc neurons (40%; Fig. 4a) encoded escape-related behaviour, as seen by phasic responses associated with kick events; 14 of these 49 (29%) showed phasic inhibition with kick, and the dominant population (35 out of 49; 71%) showed phasic excitation with kick. Of the 123 neurons, 24 encoded both light pulses and kick events (Fig. 4a and Supplementary Fig. 18; all summary data can be found in Supplementary Fig. 19).

As we found robust phasic electrophysiological responses to escape-related behaviours in the NAc, and observed that VTA dopamine action was causally involved in depression-related behaviour (Figs 1 and 2) and that dopamine signalling in the NAc was required for mediating escape-related behaviours (Supplementary Fig. 11b), we examined relevant circuit responses by determining whether VTA dopamine neurons modulated the neural representation of escape behaviour in the NAc. We began by distinguishing kick events occurring during light-on (VTA dopamine neuron activation) epochs from those occurring during light-off epochs. Of the 123 neurons, 14 (11%) showed phasic responses to kicks that occurred during both light-on and light-off epochs; 13 of these 14 cells similarly represented kick in both epochs (Fig. 4b; Example cell 6), and only 1 of these 14 cells differentially represented kick in the light-on epoch relative to the light-off epoch (Fig. 4b; Example cell 5). Next, we found that light activation of VTA dopamine neurons powerfully altered the encoding of kick events in two substantial populations of NAc neurons (Fig. 4b). Of the 123 neurons, 13 (11%) selectively encoded escape-related behaviour but only during the light-on (VTA dopamine neuron activation) epoch, and 16 out of 123 neurons (13%) selectively encoded escape-related behaviour but only during the light-off (baseline) epoch (Fig. 4b). Optogenetic recruitment of VTA dopamine neurons, which gives rise to antidepressant-like escape behaviour, therefore appeared to recruit a novel representation of the escape action in the NAc of freely moving rodents (Fig. 4).

Here, we have shown that selective inhibition of VTA dopamine neurons acutely induces multiple distinct depression-like behaviours, that chronic mild stress induces a lasting depression-like phenotype with multiple symptoms reversed by phasic activation of VTA dopamine neurons, that NAc dopamine (but not glutamate) receptors are required for the action of these neurons in depression-related escape behaviour, and that NAc neurons encode phasic activation of VTA dopamine neurons as well as depression-related escape behaviour. Furthermore, we have shown that the NAc representation of this depression-related behavioural action is in fact fundamentally altered by VTA dopamine neuron activation. These findings may together provide circuit-level insight into the causal dynamics of depression-related behaviour.

Certain earlier VTA recordings in depression models have shown reduced bursting that was restored after treatment with antidepressant¹⁹, consistent with our results and the finding that attenuation of the mesocortical dopaminergic pathway may be linked to social-defeat susceptibility²⁰. Conversely, other studies have instead shown increased bursting

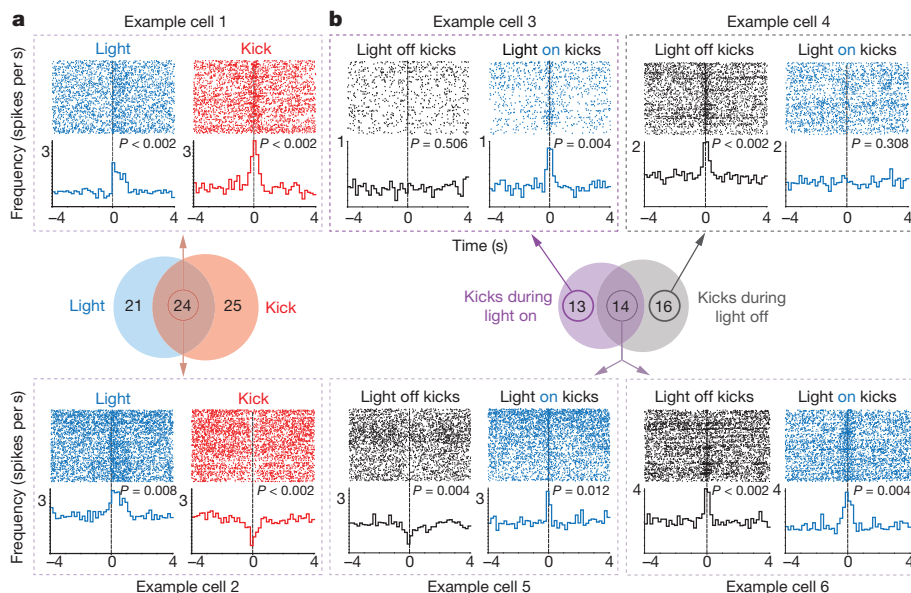


Figure 4 | Phasic activation of VTA dopamine neurons modulates NAc encoding of escape-related behaviour. Recording of 123 NAc neurons from 5 CMS TH::Cre rats expressing ChR2 in VTA dopamine neurons. **a**, Peri-event raster histograms for representative neurons showing phasic excitation associated with both light pulses and kick events (Example cell 1; 15 out of 24 cells) or for representative neurons showing different phasic responses with light pulses versus kick events (Example cell 2; 9 out of 24 cells). **b**, Peri-event raster histograms for representative neurons that selectively encoded kick events during either the light-on epoch (Example cell 3; 13 cells) or the light-off epoch (Example cell 4; 16 cells), or encoded kick events in both light-on and light-off epochs differentially (Example cell 5; 1 out of 14 cells) or similarly (Example cell 6; 13 out of 14 cells).

in mice susceptible to a 10-day social defeat^{21,22}. Differences might stem from the models used, as chronic mild stressors could reduce dopamine neuron firing, whereas more severe stressors analogous to those employed in social defeat models could increase dopamine neuron firing²³. Our results on depression-related behaviours are consistent with models of dopamine-mediated responses in reward-related behaviour^{7,24}, with VTA dopamine firing underlying anticipation or receipt of reward^{2,3,6,25}, with VTA GABA-neuron firing underlying aversion or anhedonia^{26,27}, with chemical and electrical VTA-stimulation effects on feeding, and with antidepressant effects achieved by deep brain stimulation in the NAC^{17,24}. It is important to emphasize in this context that the effects of stress on the mesolimbic dopamine system are highly complex²⁸, as different stressors can cause opposite responses from VTA neurons depending on pre-exposure and severity²³.

Depression and its treatment are likewise exceedingly complex; for example, serotonergic pathways and agents exert antidepressant effects, and antidepressant effects of deep brain stimulation are seen in the subgenual cingulate cortex distinct from the classical mesolimbic dopamine system²⁹. These results underscore the fact that psychiatric diseases defined by a constellation of different classes of symptoms can be influenced by multiple neural circuit processes. The heterogeneity of mood disorders further complicates the pinpointing of precise circuit dysfunctions mediating symptoms of depression³⁰. In animal models, tests such as sucrose consumption (when depressed patients can experience either increased or decreased appetite) and the FST (which may involve transitions between active and passive coping strategies) must be interpreted with caution. However, studying targeted circuits that are well-conserved between rodents and humans, and that (as we have found) specifically cause, correct and encode diverse symptom classes of depression, will likely continue to advance our understanding of the biological underpinnings of depression and related behaviours.

METHODS SUMMARY

Cre-dependent AAVs were packaged as AAV₅; maps and clones are available at <http://www.optogenetics.org>. The VTA in TH::Cre-driver rats or mice was virally transduced and an optical fibre surgically implanted. To confirm opsin expression and fibre targeting, coronal brain slices were prepared for immunohistochemistry and optical microscopy; stained brain sections were imaged with confocal microscopy.

Behavioural and electrophysiological data were analysed in Matlab and Neuroexplorer with custom-written software. For rat tetrode recordings under FST, before the start of recordings rats were anaesthetized for 10 min to facilitate water-proofing of the headstage and electrodes, and were subsequently allowed to recover for at least 1 h.

Full Methods and any associated references are available in the online version of the paper.

Received 2 May; accepted 31 October 2012.

Published online 12 December 2012.

- Kessler, R. C., Chiu, W. T., Demler, O. & Walters, E. E. Prevalence, severity, and comorbidity of 12-month DSM-IV disorders in the national comorbidity survey replication. *Arch. Gen. Psychiatry* **62**, 617–627 (2005); erratum **62**, 709 (2005).
- Schultz, W., Dayan, P. & Montague, P. R. A neural substrate of prediction and reward. *Science* **275**, 1593–1599 (1997).
- Witten, I. B. *et al.* Recombinase-driver rat lines: tools, techniques, and optogenetic application to dopamine-mediated reinforcement. *Neuron* **72**, 721–733 (2011).
- Willner, P., Muscat, R., Papp, M., Stamford, J. & Kruk, Z. Dopaminergic mechanisms in an animal model of anhedonia. *Eur. Neuropsychopharmacol.* **1**, 295–296 (1991).
- Roitman, M. F., Wheeler, R. A., Wightman, R. M. & Carelli, R. M. Real-time chemical responses in the nucleus accumbens differentiate rewarding and aversive stimuli. *Nature Neurosci.* **11**, 1376–1377 (2008).
- Tsai, H.-C. *et al.* Phasic firing in dopaminergic neurons is sufficient for behavioral conditioning. *Science* **324**, 1080–1084 (2009).
- Wise, R. A. Dopamine, learning and motivation. *Nature Rev. Neurosci.* **5**, 483–494 (2004).
- Koob, G. Hedonic valence, dopamine and motivation. *Mol. Psychiatry* **1**, 186 (1996).

- Ikemoto, S. & Panksepp, J. The role of nucleus accumbens dopamine in motivated behavior: a unifying interpretation with special reference to reward-seeking. *Brain Res. Brain Res. Rev.* **31**, 6–41 (1999).
- Nestler, E. J. & Carlezon, W. A., Jr. The mesolimbic dopamine reward circuit in depression. *Biol. Psychiatry* **59**, 1151–1159 (2006).
- Lammel, S. *et al.* Input-specific control of reward and aversion in the ventral tegmental area. *Nature* (2012).
- Porsolt, R. D., Le Pichon, M. & Jalfre, M. Depression: a new animal model sensitive to antidepressant treatments. *Nature* **266**, 730–732 (1977).
- Willner, P., Muscat, R. & Papp, M. Chronic mild stress-induced anhedonia: a realistic animal model of depression. *Neurosci. Biobehav. Rev.* **16**, 525–534 (1992).
- Strelakova, T., Spanagel, R., Bartsch, D., Henn, F. A. & Gass, P. Stress-induced anhedonia in mice is associated with deficits in forced swimming and exploration. *Neuropsychopharmacology* **29**, 2007–2017 (2004).
- Cryan, J. F., Mombereau, C. & Vassout, A. The tail suspension test as a model for assessing antidepressant activity: Review of pharmacological and genetic studies in mice. *Neurosci. Biobehav. Rev.* **29**, 571–625 (2005).
- Fields, H. L., Hjelmstad, G. O., Margolis, E. B. & Nicola, S. M. Ventral tegmental area neurons in learned appetitive behavior and positive reinforcement. *Annu. Rev. Neurosci.* **30**, 289–316 (2007).
- Bewernick, B. H. *et al.* Nucleus accumbens deep brain stimulation decreases ratings of depression and anxiety in treatment-resistant depression. *Biol. Psychiatry* **67**, 110–116 (2010).
- Berman, R. M. *et al.* Antidepressant effects of ketamine in depressed patients. *Biol. Psychiatry* **47**, 351–354 (2000).
- Friedman, A., Friedman, Y., Dremencov, E. & Yadid, G. VTA dopamine neuron bursting is altered in an animal model of depression and corrected by desipramine. *J. Mol. Neurosci.* **34**, 201–209 (2008).
- Tanaka, K. *et al.* Prostaglandin E2-mediated attenuation of mesocortical dopaminergic pathway is critical for susceptibility to repeated social defeat stress in mice. *J. Neurosci.* **32**, 4319–4329 (2012).
- Cao, J.-L. *et al.* Mesolimbic dopamine neurons in the brain reward circuit mediate susceptibility to social defeat and antidepressant action. *J. Neurosci.* **30**, 16453–16458 (2010).
- Krishnan, V. *et al.* Molecular adaptations underlying susceptibility and resistance to social defeat in brain reward regions. *Cell* **131**, 391–404 (2007).
- Valenti, O., Gill, K. M. & Grace, A. A. Different stressors produce excitation or inhibition of mesolimbic dopamine neuron activity: response alteration by stress pre-exposure. *Eur. J. Neurosci.* **35**, 1312–1321 (2012).
- Ikemoto, S. & Wise, R. A. Mapping of chemical trigger zones for reward. *Neuropharmacology* **47** (Suppl. 1), 190–201 (2004).
- Cohen, J. Y., Haesler, S., Vogt, L., Lowell, B. B. & Uchida, N. Neuron-type-specific signals for reward and punishment in the ventral tegmental area. *Nature* **482**, 85–88 (2012).
- Tan, K. R. *et al.* GABA neurons of the VTA drive conditioned place aversion. *Neuron* **73**, 1173–1183 (2012).
- van Zessen, R., Phillips, J. L., Budygin, E. A. & Stuber, G. D. Activation of VTA GABA neurons disrupts reward consumption. *Neuron* **73**, 1184–1194 (2012).
- Lemos, J. C. *et al.* Severe stress switches CRF action in the nucleus accumbens from appetitive to aversive. *Nature* <http://dx.doi.org/10.1038/nature11436> (19 September 2012).
- Mayberg, H. S. *et al.* Deep brain stimulation for treatment-resistant depression. *Neuron* **45**, 651–660 (2005).
- Tye, K. M. & Deisseroth, K. Optogenetic investigation of neural circuits underlying brain disease in animal models. *Nature Rev. Neurosci.* **13**, 251–266 (2012).

Supplementary Information is available in the online version of the paper.

Acknowledgements We thank T. Davidson, S. Pak, C. Ramakrishnan, L. Grosenick, Z. Chen and the members of the Deisseroth Laboratory for support. I.B.W. was supported by the Helen Hay Whitney Foundation; K.M.T. was supported by NARS fellowship F32 MH880102 and the JPB Foundation; K.R.T., M.R.W. and K.D. are NARSAD grant awardees. K.D. was supported by the Wieggers Family Fund and by the NIMH, the NIDA, the DARPA REPAIR Program, the Keck Foundation, the McKnight Foundation, the Gatsby Charitable Foundation, the Snyder Foundation, the Woo Foundation and the Albert Yu and Mary Bechman Foundation. All tools and methods described are distributed and supported freely (<http://www.optogenetics.org>).

Author Contributions K.M.T., J.J.M., M.R.W., H.-C.T. and K.D. contributed to study design. K.M.T., J.J.M., M.R.W., H.-C.T., J.F., S.-Y.K., E.A.F., A.A., K.R.T., L.A.G., I.B.W. and K.D. contributed to data collection or interpretation. K.M.T. coordinated all experiments, M.R.W. led development of the induction-coil FST and the FST electrophysiology; K.M.T., J.J.M., M.R.W. and A.S.A. contributed to data analysis, and K.D. supervised the project. K.M.T. and K.D. wrote the paper.

Author Information Reprints and permissions information is available at www.nature.com/reprints. The authors declare competing financial interests: details are available in the online version of the paper. Readers are welcome to comment on the online version of the paper. Correspondence and requests for materials should be addressed to K.M.T. (kaytye@mit.edu) and K.D. (deissero@stanford.edu).

METHODS

Subjects. TH::IRES-Cre homozygous male mice (Figs 1 and 2) obtained from the European Mouse Mutant Archive (mouse line EM:00254) were bred with wild-type C57BL/7 females to produce subjects. Only heterozygous TH::IRES-Cre male offspring that had been back-crossed for at least five generations were used for experiments. Animals were age matched, underwent surgery and were divided into two groups: the chronic mild stress (CMS) group and the control non-CMS group. Non-CMS animals were housed in a quiet room with a reverse 12 h light–dark cycle and given food and water *ad libitum*. CMS animals were housed separately and were subjected to standard CMS protocols; two stressors per day for 8 to 12 weeks before behavioural testing. Mice in this group experienced one stressor during the day and a different stressor during the night. Well-validated and approved standard stressors were randomly chosen from the following list so as to be unpredictable for subjects: cage tilt on a 45° angle for 1 to 16 h; food deprivation for 12 to 16 h; white noise (<http://www.simplynoise.com>) for 1 to 16 h; strobe light illumination for 1 to 16 h; crowded housing (4 to 5 mice in a 10 cm × 13 cm × 13 cm plastic box with air holes) for 1 to 3 h; individual housing (separating cage-mates into single-housing cages) for 1 to 16 h; light cycle (continuous illumination) for 24 to 36 h; dark cycle (continuous darkness) for 24 to 36 h; water deprivation for 12 to 16 h; damp bedding (200 ml water poured into sawdust bedding) for 12 to 16 h.

When not undergoing crowded housing, food deprivation or water deprivation stressors, water and food were available *ad libitum*. Experimental protocols were approved by Stanford University Institutional Animal Care and Use Committee (IACUC) and meet guidelines of the National Institutes of Health guide for the Care and Use of Laboratory Animals.

TH::Cre BAC transgenic rats (Fig. 4) were bred by mating Cre-positive founders to wild-type rats to produce TH::Cre heterozygous transgenic rats on a Long-Evans background. Only male rats aged 5 to 7 months were used for experiments. All rats underwent a 5- to 7-week chronic mild stress paradigm before behavioural testing and electrophysiological recording. Animals were subjected to the same twice-daily stressors on the same time course, except crowded housing and individual housing were both replaced with a standard restraint tube stressor in which the animal is immobilized in a cylindrical plastic tube (Baintree Scientific) for 30 to 45 min. All rats were singly housed with a 12 h standard light–dark cycle and when not undergoing water deprivation, food deprivation or restraint stress, water and food were available *ad libitum*. Experimental protocols were approved by Stanford University IACUC and meet guidelines of the NIH guide for the Care and Use of Laboratory Animals.

Virus preparation. Virus preparation was as described previously⁶ with Chr2-eYFP (mice), Chr2(H134R)-eYFP (rats only), eNpHR3.0-eYFP (mice) or the eYFP alone (all) inserted between incompatible *loxP* and *lox2722* sites in reverse orientation. In all cases, the cassette was cloned into a pAAV2-MCS vector carrying the EF-1 α promoter, and the woodchuck hepatitis virus post-transcriptional regulatory element (WPRE) to enhance expression. All Cre-inducible recombinant AAV vectors were packaged with AAV5 coat proteins at the University of North Carolina Vector Core. The final viral concentration was 3×10^{12} particles per ml for Chr2 virus and 1.5×10^{12} particles per ml for the eNpHR3.0 virus.

Stereotactic injection into VTA, and cannula and fibre implantation. Mice in Figs 1 and 2 were aged 2 to 4 months. These mice were deeply anaesthetized with isoflurane and placed into a stereotactic apparatus. The head was levelled using Bregma and Lambda reference points and a craniotomy was preformed. Virus was injected at 2 sites in the VTA of the right hemisphere using a 33-gauge metal needle and a 10- μ l syringe controlled by an injection pump at $0.1 \mu\text{l min}^{-1}$ for 2 μl : (1 μl at anterior–posterior, -3.3 ; lateral–medial, 0.5 ; dorsal–ventral, -4.1 ; and 1 μl at dorsal–ventral, -4.6). The needle was left in place after injection for 10 min before slowly being withdrawn. For all mice, an implantable fibre-optic light guide (IFL), consisting of a metal ferrule, 2.5 mm in diameter with a 200-mm thick, 5-mm long cleaved bare optic fibre (Doric Lenses) was implanted at anterior–posterior, -3.3 ; lateral–medial, $+0.5$; and dorsal–ventral, -3.9 . In addition to this implant, mice used for pharmacological manipulations were also implanted with a bilateral guide cannula with a 1 mm centre to centre distance for guides at coordinates (anterior–posterior, $+1.2$; lateral–medial, $+0.5$; lateral–medial, -0.5 ; dorsal–ventral, -3.25), 0.5 mm above the NAc. Instant adhesive was placed between the base of the cannula and the skull, and skull fixture adhesive was used to cement the cannula to the skull.

Blue and yellow light delivery and protocols. A 200- μ m patch cord was connected to the external portion of the chronically implantable optical fibre with a zirconia sleeve. Optic fibres were attached through an FC/PC adaptor to a 473-nm blue laser diode (no. BCL-473-050-M), and light pulses were generated through a stimulator (no. 33220A). For rats and mice expressing Chr2 and their eYFP controls, the light paradigm was 8 light pulses at 30 Hz every 5 s. Light-on epochs were 3 min for all assays (TST, OFT and FST) other than for anhedonia, for which the light epoch was 30 min. Optical-fibre light power from the patch cord was

measured using a light sensor (S130A) and intensity calculated using a model based on empirical measurements from mammalian brain tissue for predicting irradiance values (<http://www.stanford.edu/group/dlab/cgi-bin/graph/chart.php>). For Chr2-transduced mice and controls, estimated light intensity at 0.5 mm from fibre tip ranged from 22.7 to 26.2 mW mm⁻². For yellow light stimulation in eNpHR3.0 animals and eYFP controls, a 593-nm yellow laser was used; light intensity was calculated to be from 1.9 to 4.9 mW mm⁻², and illumination was constant in light-on epochs. For rats, 300- μ m patch cords and FC/PC cables were used with 0.37 NA fibre, and light intensity ranged from 17.0 to 23.8 mW mm⁻².

Pharmacological infusion of glutamate and dopamine receptor antagonists. For pharmacological experiments, drug or saline were infused in a volume of 0.4 μl through a 26-gauge stainless steel double internal cannula (PlasticsOne) that was 0.5 mm longer than the guide cannula. Each graph in Fig. 3 depicts a within-subjects matched comparison, counter-balanced for treatment order. The internal cannula was connected to a microsyringe pump by a PE20 tube. Solutions were administered at a constant rate of 100 nl min⁻¹, and the injection cannula was removed 2 min after the termination of the injection; TST was performed 10 min post infusion. For dopamine receptor antagonist experiments, 800 ng of SCH23390 per 0.4 μl per side at a concentration of 6.16 mM SCH23390 was infused for antagonism of D1-like receptors and 400 ng per 0.4 μl per side at a concentration of 2.89 mM raclopride was infused for D2-like receptor antagonism. For glutamate receptor antagonism, 3 μg per 0.4 μl per side, at a concentration of 22.3 mM for NBQX and 3 μg per 0.4 μl per side at a concentration of 38.04 mM for AP5 was used to antagonize AMPA (α -amino-3-hydroxy-5-methyl-4-isoxazole propionic acid) and NMDA (N-methyl-D-aspartate) receptors, respectively. Each animal was experimentally tested using the TST, once post drug infusion and once post saline infusion, with order counterbalanced; the two tests were carried out in different contexts on different days.

Immunohistochemistry. To determine the specificity of eNpHR3.0-eYFP expression in dopamine neurons, TH::IRES-Cre mice transduced with the double-floxed AAV encoding eNpHR3.0-eYFP were anaesthetized and transcardially perfused with PBS followed by 4% paraformaldehyde (PFA) dissolved in PBS. Brains were removed and post-fixed in PBS containing 4% PFA overnight at 4 °C, and subsequently immersed in a cryoprotectant consisting of PBS containing 30% sucrose until settling (~ 48 h at 4 °C). Coronal brain sections (40 μm) were collected and washed in PBS; blocking solution, primary and secondary solutions contained 0.3% Triton X-100 (PBST) and 3% normal donkey serum dissolved in PBS. Localization of dopamine cell bodies and fibres was confirmed by labelling with chicken anti-tyrosine hydroxylase antibody (1:300). Cell bodies were identified using the 4',6-diamidino-2-phenylindole (DAPI) stain (1:50,000). Transduction efficiency was quantified using a confocal microscope by comparing the eYFP cells with TH-immunoreactive cells.

Behavioural testing. For animals undergoing CMS, behavioural testing occurred after 8 to 12 weeks of CMS for mice (or 8 to 12 weeks of no CMS for non-CMS controls) or 4 to 6 weeks of CMS for rats. For NpHR animals and eYFP controls, behavioural testing occurred at least 1 month post surgery. All behaviour was conducted during the dark cycle (07:00 to 19:00).

Open field test. The open-field test was conducted in an open plastic chamber (50 cm long, 50 cm wide and 40 cm deep). Mice were plugged into a patch cord connecting to the external portion of the chronically implanted optical fibre, individually placed in the centre of the chamber and allowed to freely explore for 12 min. Velocity of the animal in the field was measured using an automated video-tracking system (Viewer II, BiObserver). Measurement began immediately after placement in the chamber. Light stimulation occurred for minutes 3 to 6 and 9 to 12 only. Although no difference was detected, any trend towards subtly decreased locomotion in the eNpHR3.0 group after illumination in the OFT would still be consistent with a depression-related phenotype, as related motor changes are clinically observed as psychomotor retardation and/or reduced motivation to explore³¹.

Tail-suspension test. Mice were plugged into a patch cord and the tail was placed between two strips of autoclave labelling tape. The end of one strip of tape was then secured to a horizontal bar 40 cm from the ground, ensuring that the animal could not make other contact or climb during the assay. Video recording was started 90 s from the time that the animal was inverted and taped; light stimulation was between minutes 3 to 6 of the assay. Time spent struggling was measured by blind scoring each minute of video material after the testing was completed, and was reported in seconds for each minute of the assay.

Sucrose-preference test. TH::Cre males transduced with Chr2-eYFP or eNpHR3.0-eYFP were tested alternately with their respective eYFP-only controls. Animals were water-restricted overnight before exposure to the lickometer. A Med Associates operant chamber was used to count every tongue contact made ('licks') with either the 1% sucrose in water solution or the water alone. Bottle side and animal group tested were counterbalanced among chambers. In the 90-min test, the first 30 min of the assay were used to collect a baseline sucrose preference. Over

the next 30 min of the session (minutes 30–60), light delivery occurred through a jacketed patch cord, with blue light for Chr2 animals and eYFP controls (CMS and non-CMS groups) at 8 pulses at 30 Hz every 5 s, or constant yellow light for the eNpHR3.0 animals and their eYFP controls at the same light intensities used for TST assays. The last 60 to 90 min of the test was again a no-light post light delivery measure of sucrose preference. To ensure that all animals had consumed liquid from both spouts, identified the location of the sucrose and water spouts (counter-balanced across animals), and familiarized themselves with the placement of the bottles, light delivery between 30 and 60 min only occurred if both spouts had been used in the first 30-min baseline epoch. If the animal failed to lick at either spout during the first epoch (indicating that the mouse did not discover the spout and identify the solution within), the test was aborted at 30 min, the animal did not receive any light and the test was repeated on a different day.

In vivo NAc electrophysiology. TH::Cre rats received AAV5-EF1a-DIO-ChR2-eYFP to enable expression before CMS. Two small craniotomies were drilled unilaterally over the VTA at the following coordinates: anterior–posterior, -5.4 and -6.2 ; lateral–medial, ± 0.7 . A bevelled 33-gauge needle was used to deliver $1.0 \mu\text{l}$ of virus at 2 depths in each hole (dorsal–ventral, -8.2 and -7.0 ; all coordinates from skull surface) for a total of $4.0 \mu\text{l}$ per animal. Each $1.0 \mu\text{l}$ of virus was infused at a speed of 100 nl min^{-1} using a syringe pump; the virus infuser was left in place for an additional 10 min after each injection before being removed slowly. After the CMS protocol described above, these animals had a 24-wire fixed electrode array implanted into the medial shell of the NAc (anterior–posterior, 1.6 ; lateral–medial, 1.3 ; dorsal–ventral, -7.5). A third burr hole was drilled (anterior–posterior, -5.8 ; lateral–medial, ± 0.7 ; dorsal–ventral -7.5) for the insertion of an implantable optical fibre targeted just dorsal to the VTA. Ground wires were implanted at a depth of approximately 2 mm lateral to the optical fibre. After behavioural and recording experiments, electrolytic lesions were created just before sacrifice to allow histological identification of electrode-tip location.

Forced swim test. On day 1, a 15-min pre-test swim was conducted for each animal, and on day 2 rats were plugged into a patch cord and a HS-27 pre-amplifier head stage with 24 electrode channels and 3 reference channels. The patchcord and HS-27 tether were waterproofed with a latex tube before being connection. Immediately after a 5-min recording in the home cage and a 12-min OFT, the rat was placed into a cylindrical tank of water (25 to 26°C), in which the animal could not touch the bottom of the tank. Minutes 6 to 51 were used for analysis of neural data. Light stimulation occurred during minutes 12 to 15, 21 to 24, 30 to 33, 39 to 42 and 48 to 51, to create an alternating 6 min off, 3 min on light-stimulation paradigm. Magnetic induction was used to provide a high temporal-resolution readout; swimming activity (referred to as ‘kicks’ or ‘kick events’) was timed and quantified with a coil and a hind-paw magnet to give a continuous analogue signal. This continuous signal was then thresholded at 3 standard deviations from the mean for all rats through both light-on and light-off epochs in the FST.

Analysis of in vivo awake-behaving NAc electrophysiological recordings. To test the relevance of phasic-firing-rate changes for individual neurons in relation to either light-pulse onsets or kick-signal threshold crossings (Fig. 4), two time windows relative to the event time were used. For the statistical analyses of neural responses to the first light pulse in each 8-pulse train and kick signals (all trials were included unless otherwise stated), a baseline window was compared to a response window for each reference event. For the reference event referred to as ‘light’, the event was the onset of the first light pulse in each 8-pulse train occurring every 5 s; we selected a baseline window from $t = -3 \text{ s}$ to -2 s , and selected the response window that initiated after first light-pulse onset and spanned from

$t = 0 \text{ s}$ to 1 s . For kick events (animal-initiated rather than experimenter-initiated), we used a baseline window further from the event onset given the variable inter-event interval latency; -4 s to -2 s was used as a measure of baseline firing rate for all kick events, and a response window from -0.5 s to 0.5 s was used as a measure of the response. Bin size for rate calculations was 200 ms . For all phasic responses discussed in this study, the fractional change in the average firing rate between the baseline and response window was computed across all event occurrences (for events, the number of events ranged from 1,971 to 4,718 events), and the significance of this change was determined by its percentile within a non-parametric bootstrap distribution estimated using 500 random circular permutations of spike times relative to events times, in which P values of less than 0.05 were considered significant responses. For all classes of reference events, the number of significantly modulated neurons statistically exceeded the expected number of false positives given multiple comparisons (95% confidence interval of 2 to 11 false positives occurring, binomial test, $n = 123$, $\alpha = 0.05$). Mean firing-rate changes are indicated in Supplementary Fig. 17 and described in the main text.

Extended, counterbalanced open-field test. For data shown in Supplementary Fig. 3, the open-field test was conducted in an open plastic chamber (50 cm long, 50 cm wide and 40 cm deep). Mice were plugged into a patch cord connecting to the external portion of the chronically implanted optical fibre, individually placed in the centre of the chamber and allowed to freely explore for 30 min. Velocity and distance travelled were measured using an automated video-tracking system (Viewer II, BiObserver). Measurements began immediately after animals were placed in the chamber. For one-half of each group, light stimulation occurred for minutes 0 to 10 and 20 to 30, and for the remaining half, light stimulation occurred from minutes 10 to 20.

In vivo VTA electrophysiology. Adult ($>300\text{-g}$) male Long Evans rats underwent either the rat CMS ($n = 5$) protocol described above or spent equal time in a quiet, low-traffic animal housing facility with water and food *ad libitum* (non-CMS; $n = 4$). In the last week of the treatment, animals were deeply anaesthetized and implanted with a 12- or 24-wire array into the VTA (anterior–posterior, -5.8 ; lateral–medial, ± 0.7 ; dorsal–ventral, -8.2) as described with NAc recording subjects. After recovery and before recording, subjects were connected to an HS-27 (Neuralynx), returned to the home cage and given 45 min to habituate to the tether. After these 45 min, approximately 60-min recordings were carried out in the home cage for each animal. After recording experiments, electrolytic lesions were created just before animals were euthanized to enable histological identification of electrode-tip location (Supplementary Fig. 10).

Burst-firing analysis. Bursts were defined as beginning when 2 spikes occurred with an inter-spike interval of less than 80 ms and as ending when the inter-spike interval was greater than 135 ms , as described by previously³² (see also refs 33, 34). Spike sorting was performed using the Offline Sorter (Plexon) and burst analyses were calculated using NeuroExplorer (Plexon), with the parameters specified above, and the minimum number of spikes in a burst was set at two.

31. Lemke, M. R., Wendorff, T., Mieth, B., Buhl, K. & Linnemann, M. Spatiotemporal gait patterns during over ground locomotion in major depression compared with healthy controls. *J. Psychiatr. Res.* **34**, 277–283 (2000).
32. Ungless, M. A., Magill, P. J. & Bolam, J. P. Uniform inhibition of dopamine neurons in the ventral tegmental area by aversive stimuli. *Science* **303**, 2040–2042 (2004).
33. Grace, A. A. & Bunney, B. S. The control of firing pattern in nigral dopamine neurons: burst firing. *J. Neurosci.* **4**, 2877–2890 (1984).
34. Freeman, A. S. & Bunney, B. S. Activity of A9 and A10 dopaminergic neurons in unrestrained rats: further characterization and effects of apomorphine and cholecystokinin. *Brain Res.* **405**, 46–55 (1987).

Serine starvation induces stress and p53-dependent metabolic remodelling in cancer cells

Oliver D. K. Maddocks¹, Celia R. Berkers¹, Susan M. Mason¹, Liang Zheng¹, Karen Blyth¹, Eyal Gottlieb¹ & Karen H. Vousden¹

Cancer cells acquire distinct metabolic adaptations to survive stress associated with tumour growth and to satisfy the anabolic demands of proliferation. The tumour suppressor protein p53 (also known as TP53) influences a range of cellular metabolic processes, including glycolysis^{1,2}, oxidative phosphorylation³, glutaminolysis^{4,5} and anti-oxidant response⁶. In contrast to its role in promoting apoptosis during DNA-damaging stress, p53 can promote cell survival during metabolic stress⁷, a function that may contribute not only to tumour suppression but also to non-cancer-associated functions of p53⁸. Here we show that human cancer cells rapidly use exogenous serine and that serine deprivation triggered activation of the serine synthesis pathway and rapidly suppressed aerobic glycolysis, resulting in an increased flux to the tricarboxylic acid cycle. Transient p53-p21 (also known as CDKN1A) activation and cell-cycle arrest promoted cell survival by efficiently channeling depleted serine stores to glutathione synthesis, thus preserving cellular anti-oxidant capacity. Cells lacking p53 failed to complete the response to serine depletion, resulting in oxidative stress, reduced viability and severely impaired proliferation. The role of p53 in supporting cancer cell proliferation under serine starvation was translated to an *in vivo* model, indicating that serine depletion has a potential role in the treatment of p53-deficient tumours.

As p53 contributes to the survival of cells deprived of glucose⁹, we investigated whether removal of other nutrients found in normal medium induced a differential response in p53^{+/+} and p53^{-/-} HCT116 cells. Whereas removal of the non-essential amino acids serine and glycine impaired proliferation of p53^{+/+} cells, p53^{-/-} cells showed a more marked loss of proliferation (Fig. 1a) and substantial loss of viability (Fig. 1b, c). The contribution of p53 to growth and survival during serine and glycine depletion was also seen in RKO cells (Supplementary Fig. 2a–c) and primary mouse embryonic fibroblasts (MEFs; Supplementary Fig. 2d). By removing serine or glycine individually, we established that serine depletion was the major contributor to the starvation phenotype (Fig. 1a–c), as removal of glycine alone had no detrimental effect. Whereas serine and glycine may be inter-converted by serine hydroxymethyltransferase (SHMT), serine to glycine conversion supports proliferation via methyl-tetrahydrofolate (THF) production (Supplementary Fig. 1). The reverse reaction (glycine to serine) depletes methyl-THF, which is presumably why excess glycine has been shown to inhibit proliferation^{9,10}. As expected, removal of lysine (an essential amino acid) did not cause a differential response, being equally incompatible with proliferation in p53^{+/+} and p53^{-/-} cells (Supplementary Fig. 2e).

Analysis of cell culture medium by liquid chromatography–mass spectrometry (LC–MS) revealed rapid serine consumption by p53^{+/+} and p53^{-/-} cells (Fig. 1d), whereas glycine uptake was low (Supplementary Fig. 2f). A recent screen of NCI-60 cancer cell lines showed that elevated SHMT expression and glycine uptake were correlated with rapid proliferation¹¹. Notably, all 60 lines consumed more serine than glycine, including seven lines with the shortest doubling times (<22 h), which on average consumed 7.7-fold more serine than glycine¹¹. Furthermore, cells with the shortest doubling times and highest glycine

uptake also consumed most of the available serine¹¹, raising the possibility that these highly proliferative cells switch to glycine consumption because they have exhausted the available serine. Overall this demonstrates that cancer cells avidly consume serine, which may, through high SHMT expression, be used to generate glycine and methyl-THF.

Unlike essential amino acids, the chronic depletion of non-essential amino acids can be tolerated *in vivo*. Mice tolerated diets lacking serine and glycine well (Supplementary Fig. 3a), and LC–MS confirmed a significant drop in serum levels of serine and glycine, but not other amino acids (Supplementary Fig. 3b). HCT116 cells rapidly formed tumours in animals fed control diet, without a significant difference in volume between p53^{+/+} and p53^{-/-} tumours (Fig. 1e). However, animals fed matched diet lacking serine and glycine displayed significant reduction in the volume of tumours of both genotypes, and survived significantly longer before tumour size or ulceration end-points (Fig. 1e, f). As with our *in vitro* studies, serine and glycine starvation had a more dramatic effect on p53^{-/-} xenografts, which had significantly reduced volume compared to p53^{+/+} tumours in serine- and glycine-deprived animals (Fig. 1e).

Mammalian cells synthesize serine *de novo* by channelling the glycolytic intermediate 3-phosphoglycerate into the ‘phosphorylated pathway’ of serine synthesis¹² (Supplementary Fig. 1). Flux through this biosynthetic pathway is controlled primarily by the demand for serine, rather than the availability of substrate 3-phosphoglycerate¹³. The serine synthesis pathway (SSP) supports anabolism by providing precursors for biosynthesis of proteins, nucleotides, creatine, porphyrins, phospholipids and glutathione, and SSP upregulation occurs in some breast cancers^{14–16}. A recent study demonstrated that serine starvation activates the SSP¹⁷; we found that serine starvation induced strong p53-independent upregulation of PHGDH and PSAT1, with a modest increase in PSPH (Fig. 1g and Supplementary Fig. 4a, b). The failure of p53^{-/-} cells to proliferate during serine starvation could not therefore be attributed to a deficiency in SSP enzyme expression. p53 has been shown to downregulate PGAM¹⁸—potentially allowing 3-phosphoglycerate to be channelled to the SSP. However, PGAM expression did not vary greatly during serine starvation (Supplementary Fig. 4a, b). Consistent with their ability to activate the SSP, both p53^{+/+} and p53^{-/-} cells achieved *de novo* serine synthesis, as detected using [U-¹³C]glucose labelling (Fig. 1h). However, p53^{-/-} cells had lower serine levels, indicating some defect in the ability of these cells to adapt to *de novo* serine synthesis. We therefore sought to explore the mechanisms through which cells adapt to serine starvation.

The mTOR pathway senses amino acid availability, and whereas mTORC1 activity was lowered by serine starvation, it was maintained at very similar levels in p53^{+/+} and p53^{-/-} cells (Supplementary Fig. 5). This demonstrated that the effect of serine starvation on mTORC1 was p53-independent and therefore unlikely to contribute to the enhanced sensitivity of p53^{-/-} cells. A similar maintenance of mTORC1 activity in serine-starved cells has recently been shown, and is promoted by PKM2 expression¹⁷. Serine activates PKM2¹⁹ and decreased PKM2 activity following serine starvation causes an accumulation of upstream glycolytic intermediates for diversion to the SSP²⁰. To balance lower

¹The Beatson Institute for Cancer Research, Switchback Road, Glasgow G61 1BD, UK.

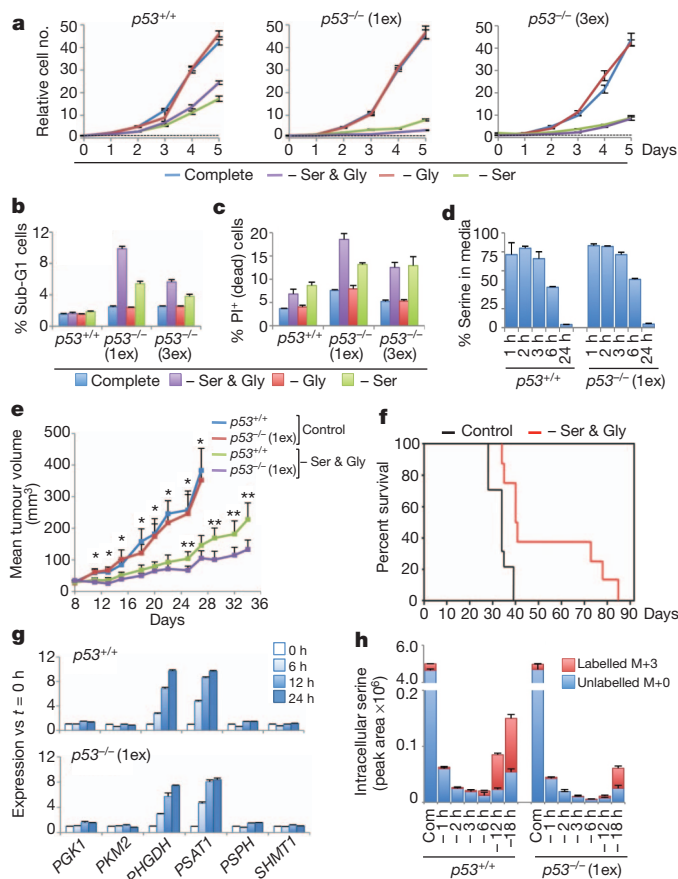


Figure 1 | p53 promotes cell survival and proliferation during serine starvation *in vitro* and *in vivo*. **a**, HCT116 cells were grown in complete medium (containing serine and glycine) or equivalent medium lacking these amino-acids (averages of triplicate wells). $p53^{-/-}$ (1ex), deletion of p53 exon 2; $p53^{-/-}$ (3ex), deletion of p53 exons 2, 3 and 4. **b**, **c**, Viability of HCT116 cells was assessed by analysing sub-G1 DNA content (**b**, $n = 3$) and propidium iodide (PI) exclusion (**c**, $n = 3$). **d**, LC-MS was used to determine the relative consumption of serine by HCT116 cells fed complete medium (averages of triplicate wells versus fresh medium). **e**, Nude mice were subcutaneously injected with HCT116 cells ($p53^{+/+}$ right flank, $p53^{-/-}$ left flank), and fed diet with or without serine and glycine. Tumour volume is plotted until the first animal in each group reached the experimental end-point (* $P < 0.05$ control diet group versus -Ser & Gly group; ** $P < 0.05$ for $p53^{+/+}$ versus $p53^{-/-}$ within -Ser & Gly group). **f**, Kaplan-Meier plot of survival until experimental end-point for diet groups (mean survival; control = 33.3 days ($n = 10$), -Ser & Gly = 53.2 days ($n = 8$), log rank $P = 0.001$, Wilcoxon $P = 0.003$). **g**, Expression of glycolytic and SSP genes (averages of triplicate quantitative PCR). **h**, Intracellular serine levels in HCT116 cells fed medium containing [U - ^{13}C]glucose were measured by LC-MS (averages of triplicate wells). Labelled serine (M+3, mass isotopomer with 3 ^{13}C incorporated) and unlabelled serine (M+0, mass isotopomer with 0 ^{13}C incorporated) is shown in cells grown in complete (Com) or serine- and glycine-deficient (-) medium for the indicated times. All error bars are s.e.m.

glycolysis following PKM2 inhibition, cells increase flux of pyruvate to the tricarboxylic acid (TCA) cycle, requiring cells depleted of PKM2 to display increased O_2 consumption to support elevated oxidative phosphorylation²⁰. Both $p53^{+/+}$ and $p53^{-/-}$ cells displayed elevated phosphoenolpyruvate (PEP) levels and decreased pyruvate and lactate levels, evidence of low PKM2 activity following serine starvation (Fig. 2a). The importance of oxidative phosphorylation during serine starvation was demonstrated by treatment with the mitochondrial ATP synthase inhibitor Oligomycin (Fig. 2b), which completely inhibited the growth of serine-deprived $p53^{+/+}$ cells. As p53 supports oxidative phosphorylation^{3,21,22}, we considered the possibility that $p53^{-/-}$ cells would be unable to upregulate oxidative phosphorylation in response to serine starvation.

As expected, $p53^{-/-}$ cells showed lower O_2 consumption than $p53^{+/+}$ cells under fed conditions. Surprisingly, $p53^{-/-}$ cells responded to serine starvation with increased O_2 consumption, whereas $p53^{+/+}$ cells showed lower O_2 consumption (Fig. 2c). Closer analysis of metabolic flux into the TCA cycle revealed that whereas both $p53^{+/+}$ and $p53^{-/-}$ cells showed an increase in glycolytic TCA cycle flux in the immediate response to serine starvation, this response was reversed over time in $p53^{+/+}$ cells, but sustained in the $p53^{-/-}$ cells (Fig. 2d, e). This correlated with the changes in O_2 consumption observed during serine starvation, indicating that the initial response of $p53^{+/+}$ and $p53^{-/-}$ to serine depletion is similar, but $p53^{-/-}$ cells sustain a metabolic profile indicative of low PKM2 activity, including elevated O_2 consumption.

We predicted that the disruption to glycolysis in the immediate response to serine starvation would impede ATP production, indeed ATP levels dropped in both $p53^{+/+}$ and $p53^{-/-}$ cells (Fig. 2f). We considered that as glycolytic flux to pyruvate is lowered by serine starvation, increasing pyruvate levels (by adding exogenous pyruvate) would potentially alleviate the ATP shortage by further enhancing flux to the TCA cycle. We observed a significant recovery in proliferation of $p53^{-/-}$ cells after adding pyruvate (Fig. 2g). LC-MS analysis of

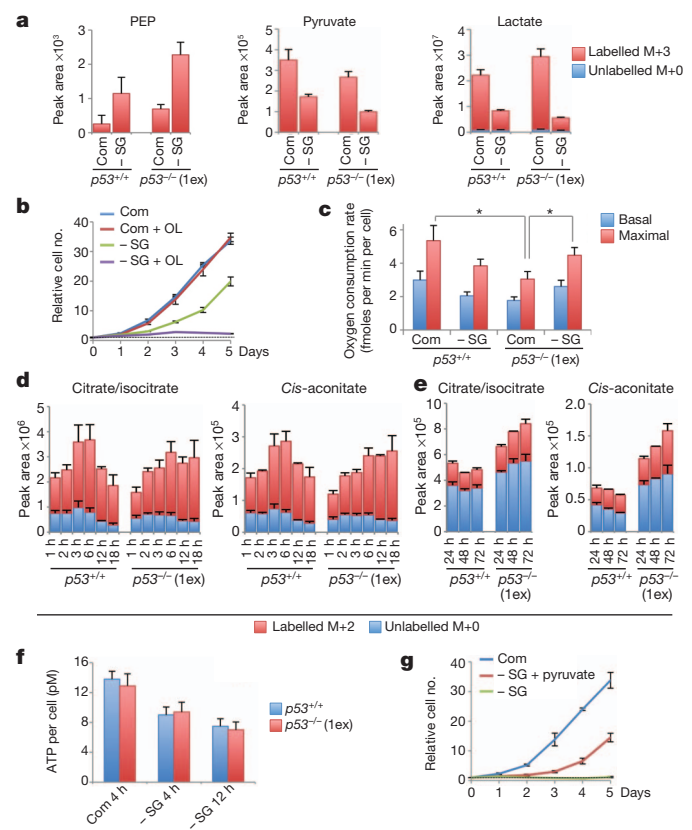


Figure 2 | Serine starvation differentially changes energy metabolism in $p53^{+/+}$ and $p53^{-/-}$ cells. **a**, HCT116 cells were fed complete (Com) or serine- and glycine-deficient (-SG) medium for 24 h, in the presence of [U - ^{13}C]glucose for the final 2 h. LC-MS was used to detect relative intracellular quantities of glycolytic intermediates (averages of triplicate wells). **b**, HCT116 cells were grown with or without serine, glycine and oligomycin (OL) 1 ng ml $^{-1}$ (averages of triplicate wells). **c**, Oxygen consumption rate of HCT116 cells was measured after 48 h of serine and glycine starvation ($n = 3$, * $P < 0.05$). **d**, **e**, Relative intracellular levels of TCA cycle intermediates in HCT116 cells deprived of serine and glycine (in the constant presence of [U - ^{13}C]glucose) were analysed by LC-MS (averages of triplicate wells) (**d**) and, after long-term starvation, with [U - ^{13}C]glucose added for the final hour (averages of triplicate wells) (**e**). **f**, ATP levels were measured in HCT116 cells ($n = 3$). **g**, HCT116 $p53^{-/-}$ (1ex) cells were grown in complete medium or medium lacking serine and glycine with or without pyruvate 5 mM (averages of triplicate wells). All error bars are s.e.m.

serine-starved $p53^{-/-}$ cells fed unlabelled pyruvate (in the presence of [$U^{13}C$]glucose) confirmed increased TCA cycle flux (Supplementary Fig. 6). However, this enhanced TCA cycle flux was not sufficient to fully restore proliferation (Fig. 2g). Importantly, although it has recently been shown that serine can be synthesised from pyruvate (reviewed in ref. 30), we detected only labelled serine in the cells fed unlabelled pyruvate (Supplementary Fig. 6), demonstrating that the serine in these cells was derived from glucose.

Serine contributes to the synthesis of purines via glycine, which is incorporated into GMP and AMP via inosine monophosphate (IMP). Serine starvation resulted in lower GMP and AMP levels in $p53^{+/+}$ and $p53^{-/-}$ cells (Fig. 3a). Previous studies show that GMP depletion can activate p53-dependent G1 arrest^{23,24}. Consistently, we found that serine starvation led to a small elevation in p53 expression, accompanied by more marked, but transient, elevation of the p53 target protein p21 (Fig. 3b). Treatment of $p53^{+/+}$ cells with low doses of mycophenolic acid (an inhibitor of GMP synthesis) replicated this subtle p53-p21 response (Supplementary Fig. 7a, b). Recruitment of p53 to the *p21* promoter during serine starvation was

confirmed by chromatin-immunoprecipitation (Fig. 3c). As only a modest increase in p53 expression was observed, we speculate that p53 was activated via post-translational modification, rather than MDM2 inhibition. Although our data are consistent with p53 activation in response to nucleotide depletion, activation of AMPK (Supplementary Fig. 7c) due to lower ATP levels could also contribute to the p53 response⁷.

As expected following p53 activation, $p53^{+/+}$ cells starved of serine and glycine initially showed an accumulation of cells in G1 and reduced S-phase, correlating with the increased expression of p21 (Fig. 3d). By 48 h, these cells resumed a normal cell cycle. By comparison, $p53^{-/-}$ cells failed to establish a strong G1 arrest, showing a more gradual decrease in S-phase (corresponding to an increase in sub-G1 cells, Fig. 1b) and did not recover normal cell cycle (Fig. 3d). Because p21 is a major mediator of p53-induced G1 arrest²⁵, we examined the effect of p21 loss in $p53^{+/+}$ cells. $p21^{-/-}$ (*CDNK1A*^{-/-}) cells showed a similar cell-cycle response as $p53^{-/-}$ cells (Fig. 3d), indicating that induction of p21 may be critical for adaptation to serine starvation. Indeed, $p53^{+/+}$ cells depleted of p21 by siRNA were unable to increase in number without serine (similar to $p53^{-/-}$ cells, Fig. 3e), a response even more notable in cells genetically deleted of *p21* (Fig. 3f).

We next considered whether $p53^{+/+}$ and $p53^{-/-}$ cells use the low levels of intracellular serine available under conditions of starvation differently. Specifically, we analysed the balance between purine-nucleotide and glutathione synthesis, both of which require serine/glycine. LC-MS showed that after 24 h, $p53^{-/-}$ cells retained flux of *de novo* serine/glycine into IMP (M+7), but this was inhibited in $p53^{+/+}$ cells (Fig. 4a). Re-feeding serine-starved cells with [$U^{13}C$, ^{15}N]L-serine confirmed sustained serine flux into IMP, GMP and AMP in $p53^{+/+}$ cells (Supplementary Fig. 8a). However, in serine-starved $p53^{+/+}$ cells, flux of the replenished labelled serine to nucleotides was blocked, despite plentiful intracellular serine. This demonstrated that a feature of p53-p21-induced cell-cycle arrest in response to serine starvation is inhibition of nucleotide synthesis, a known function of p21^{26,27}. Reduced glutathione (GSH) is the principal cellular anti-oxidant, and we found that levels of GSH dropped significantly in $p53^{+/+}$ and $p53^{-/-}$ serine-starved cells (Fig. 4b). However, in contrast to nucleotides, $p53^{+/+}$ cells maintained and, over time, enhanced flux to GSH synthesis during starvation. Notably, this maintenance of flux to glutathione was not seen in $p53^{-/-}$ and $p21^{-/-}$ cells (Fig. 4b and Supplementary Fig. 8b). Consequently, total GSH levels showed recovery in $p53^{+/+}$ but not $p53^{-/-}$ or $p21^{-/-}$ cells (Fig. 4c and Supplementary Fig. 8c).

The failure of $p53^{-/-}$ cells to recover GSH levels combined with their elevated oxygen consumption suggested that these cells would accumulate increased intracellular reactive oxygen species (ROS) levels. p53 has well-established anti-oxidant functions^{1,6}, but hydrogen peroxide treatment demonstrated that $p53^{-/-}$ cells were only slightly more susceptible than $p53^{+/+}$ to oxidative stress under normal conditions (Fig. 4d). Although serine and glycine starvation increased the sensitivity of both genotypes to peroxide treatment, this effect was more marked in $p53^{-/-}$ cells (Fig. 4d), and rescued by adding GSH (Fig. 4e). Staining with an oxidation-activated fluorescent dye confirmed increased intracellular ROS in $p53^{-/-}$ cells during serine starvation (Fig. 4f and Supplementary Fig. 9a). To assess the importance of ROS in limiting proliferation, we tested the effect exogenous GSH or N-acetyl cysteine. Whereas anti-oxidant treatment alone modestly improved proliferation of serine-starved $p53^{-/-}$ cells, either of the ROS-limiting treatments almost completely rescued the proliferation of serine-starved $p53^{-/-}$ cells in combination with pyruvate (Fig. 4g). We confirmed that the exogenous GSH did not lead to accumulation of intracellular glycine or serine, demonstrating that rescue was achieved by increasing the intracellular GSH pool (Supplementary Fig. 9b). Adding GSH to serine-starved $p53^{+/+}$ cells did not greatly enhance proliferation, supporting the theory that $p53^{+/+}$ cells are able to maintain GSH pools independently (Supplementary Fig. 9c).

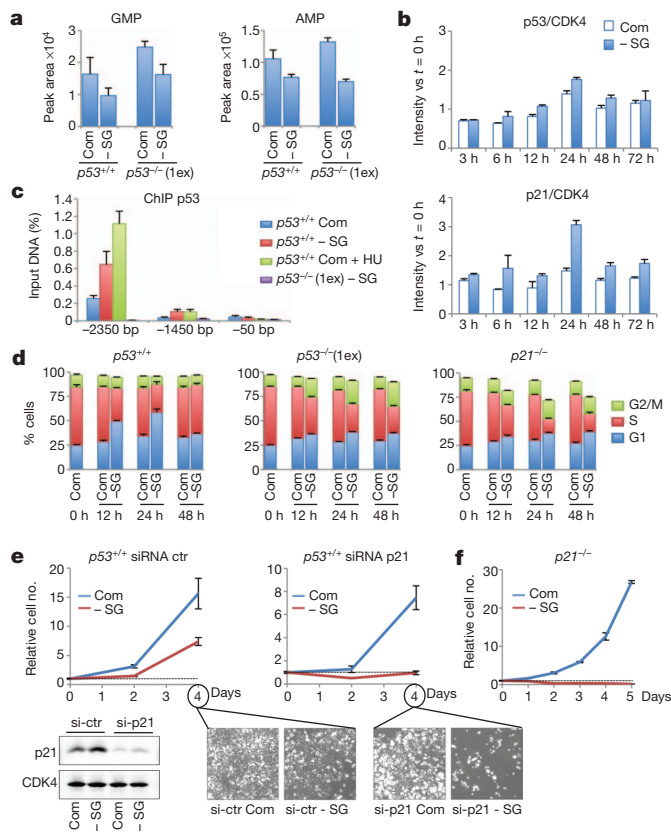


Figure 3 | Serine starvation causes recruitment of p53 to the p21 promoter and activation of a transient p21-dependent G1 arrest. **a**, LC-MS was used to quantify total relative amounts of intracellular purine nucleotides GMP and AMP in serine and glycine fed (Com) and starved (-SG) HCT116 cells (averages of triplicate wells). **b**, p53 and p21 protein expression was quantified in $p53^{+/+}$ HCT116 cells via western blot and detection with infrared-conjugated secondary antibodies ($n = 3$). CDK4 expression was used as a control for normalisation. **c**, Chromatin-immunoprecipitation (ChIP) was performed for p53 with quantitative PCR for two p53-response elements (-2350 bp and -1450 bp) and the transcription initiation region (+50 bp) of the *p21* promoter ($n = 3$). HU, hydroxyurea. **d**, BrdU labelling and PI staining followed by flow cytometry were used to assess cell cycle ($n = 3$). **e**, p21 was transiently knocked down in $p53^{+/+}$ HCT116 cells using short interfering RNA (siRNA, averages of triplicate wells). **f**, $p21^{-/-}$ HCT116 cells (retaining wild-type p53) were grown in medium with or without serine and glycine (averages of triplicate wells). All error bars are s.e.m.

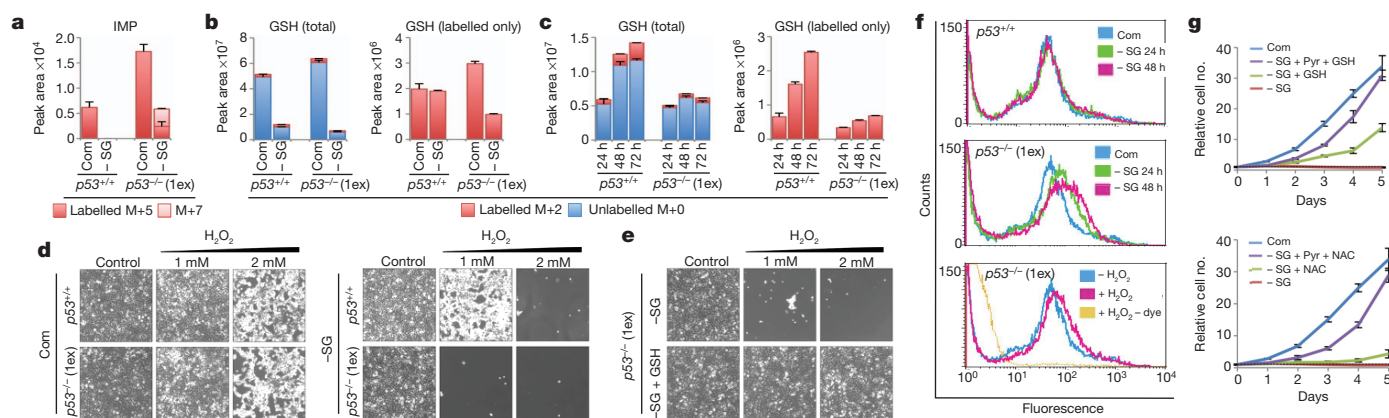


Figure 4 | **p53-p21 activation allows serine-deprived cells to synthesize GSH in preference to nucleotides.** a–c, LC-MS was used to detect relative intracellular quantities of IMP (a) and GSH (b) in HCT116 cells fed complete medium (Com) or medium lacking serine and glycine (–SG) for 24 h, in the presence of [U - ^{13}C]glucose for the final 2 h, and in HCT116 cells fed –SG medium for the indicated times in the presence of [U - ^{13}C]glucose for the final hour (averages of triplicate wells) (c). d, e, HCT116 cells were grown with or

without serine and glycine (d) or medium lacking serine and glycine with 5 mM glutathione (GSH) (e) for 48 h in the presence of hydrogen peroxide (H_2O_2) for the final 24 h. f, HCT116 cells were treated with an oxidation-activated fluorescent dye and analysed by flow cytometry. g, HCT116 $p53^{-/-}$ (1ex) cells were grown with or without serine, glycine, pyruvate 5 mM (Pyr) and/or GSH 5 mM, or N-acetyl cysteine 0.2 mM (NAC) (averages of triplicate wells). All error bars are s.e.m.

Our data therefore show that the sensitivity of $p53^{-/-}$ cells to serine depletion is due to a combination of impaired glycolysis and elevated ROS. Whereas the initial response of cells with or without p53 to serine depletion was similar, $p53^{+/+}$ cells underwent p21-dependent G1 arrest, allowing the limited levels of *de novo* serine to be channelled to GSH production to counter oxidative stress. Depletion of p21 (while retaining p53) caused severe sensitivity to serine depletion (Fig. 3e, f), indicating that activation of other arms of the p53 response may contribute to the death of these cells. Our data also demonstrate that the ability of p53-deficient cells to engage higher rates of oxidative phosphorylation is not entirely defective, but that oxidative phosphorylation in these cells is probably limited by a requirement to prevent ROS generation. This observation ties in with the suggestion that cancer cells adopt aerobic glycolysis (the Warburg effect) to avoid generation of metabolic ROS²⁸. It has recently been shown that increased ROS levels inhibit PKM2²⁹, providing an explanation for why $p53^{-/-}$ cells show evidence of sustained PKM2 inhibition during serine starvation.

In conclusion, our study underlines the importance of p53 in coordinating metabolic remodelling in response to metabolic stress. We demonstrate that serine uptake supports the Warburg effect, indicating that many cancer cells may show some sensitivity to serine depletion, particularly those lacking p53. However, it is likely that other genetic alterations (such as *PHGDH* amplification^{14–16}) may circumvent serine-dependence in other cancer cells. Taken together, our work suggests the therapeutic utility of serine depletion—either by removal from the diet, enzymatic depletion *in vivo*, or other means—is worthy of further investigation.

METHODS SUMMARY

HCT116 $p53^{+/+}/p21^{+/+}$ (parental), $p53^{-/-}$ (1ex) (deletion of p53 exon 2), $p53^{-/-}$ (3ex) (deletion of p53 exons 2, 3 and 4), $p21^{-/-}$ and RKO $p53^{+/+}$ and $p53^{-/-}$ cells were a gift of B. Vogelstein. Litter-matched $p53^{+/+}$ and $p53^{-/-}$ MEFs were prepared from embryonic day 14.5 (E14.5) embryos derived from mating $p53^{+/+}$ mice. For starvation, cells were initially grown in DMEM (which contains serine 0.4 mM and glycine 0.4 mM); complete medium (Com) was formulated by supplementing MEM with additional nutrients to closely match the nutrient content of DMEM. Serine- and glycine-deficient medium (–SG) was formulated in the same way as complete medium, without addition of serine and glycine. Bilateral subcutaneous injections of HCT116 cells were carried out on CD-1-Foxn1^{nu} female mice (Charles River); $p53^{+/+}$ on right flank and $p53^{-/-}$ (1ex) on the left. Following injection, mice were placed either on control diet (containing serine and glycine as part of the amino-acid mix) or diet deficient in serine and glycine (TestDiet, International Product Supplies). The diets had equal caloric value and equal total amino acid content. Animals were housed in sterile IVC cages,

monitored thrice weekly and killed humanely when tumours reached clinical endpoint of predetermined size (volume = (length \times width²)/2) or ulceration. All animal work was undertaken in line with the UK Animals (Scientific Procedures) Act of 1986 and the EU directive 2010. Cell-cycle analysis was performed by labelling with 5-bromo-2'-deoxyuridine (BrdU) and propidium iodide (PI) staining followed by flow cytometry. Oxygen consumption rates were measured with an XF-24 extracellular flux analyser (SeaHorse Bioscience). ROS levels were detected with CellROX deep red reagent (Invitrogen). ATP levels were assayed with a luciferase-based kit. The relative quantities of intracellular metabolites after labelling with [U - ^{13}C]glucose or [U - ^{13}C , ^{15}N]L-serine were analysed by LC-MS and plotted as the peak area for each metabolite.

Full Methods and any associated references are available in the online version of the paper.

Received 29 May; accepted 31 October 2012.

Published online 16 December 2012.

- Bensaad, K. *et al.* TIGAR, a p53-inducible regulator of glycolysis and apoptosis. *Cell* **126**, 107–120 (2006).
- Jiang, P. *et al.* p53 regulates biosynthesis through direct inactivation of glucose-6-phosphate dehydrogenase. *Nature Cell Biol.* **13**, 310–320 (2011).
- Matoba, S. *et al.* p53 regulates mitochondrial respiration. *Science* **312**, 1650–1653 (2006).
- Suzuki, S. *et al.* Phosphate-activated glutaminase (GLS2), a p53-inducible regulator of glutamine metabolism and reactive oxygen species. *Proc. Natl Acad. Sci. USA* **107**, 7461–7466 (2010).
- Hu, W. *et al.* Glutamine 2, a novel p53 target gene regulating energy metabolism and antioxidant function. *Proc. Natl Acad. Sci. USA* **107**, 7455–7460 (2010).
- Budanov, A. V. *et al.* Regeneration of peroxiredoxins by p53-regulated sestrins, homologs of bacterial AhpD. *Science* **304**, 596–600 (2004).
- Jones, R. G. *et al.* AMP-activated protein kinase induces a p53-dependent metabolic checkpoint. *Mol. Cell* **18**, 283–293 (2005).
- Maddocks, O. D. K. & Vousden, K. H. Metabolic regulation by p53. *J. Mol. Med.* **89**, 237–245 (2011).
- Rose, M. L. *et al.* Dietary glycine prevents the development of liver tumors caused by the peroxisome proliferator WY-14,643. *Carcinogenesis* **20**, 2075–2081 (1999).
- Rose, M. L., Madren, J., Bunzendorf, H. & Thurman, R. G. Dietary glycine inhibits the growth of B16 melanoma tumors in mice. *Carcinogenesis* **20**, 793–798 (1999).
- Jain, M. *et al.* Metabolite profiling identifies a key role for glycine in rapid cancer cell proliferation. *Science* **336**, 1040–1044 (2012).
- Snell, K. The duality of pathways for serine biosynthesis is a fallacy. *Trends Biochem. Sci.* **11**, 241–243 (1986).
- Snell, K. & Fell, D. A. Metabolic control analysis of mammalian serine metabolism. *Adv. Enzyme Regul.* **30**, 13–32 (1990).
- Pollari, S. *et al.* Enhanced serine production by bone metastatic breast cancer cells stimulates osteoclastogenesis. *Breast Cancer Res. Treat.* **125**, 421–430 (2011).
- Possemato, R. *et al.* Functional genomics reveal that the serine synthesis pathway is essential in breast cancer. *Nature* **476**, 346–350 (2011).
- Locasale, J. W. & Cantley, L. C. Genetic selection for enhanced serine metabolism in cancer development. *Cell Cycle* **10**, 3812–3813 (2011).

17. Ye, J. *et al.* Pyruvate kinase M2 promotes de novo serine synthesis to sustain mTORC1 activity and cell proliferation. *Proc. Natl Acad. Sci. USA* **109**, 6904–6909 (2012).
18. Kondoh, H. *et al.* Glycolytic enzymes can modulate cellular life span. *Cancer Res.* **65**, 177–185 (2005).
19. Mazurek, S. Pyruvate kinase type M2: a key regulator of the metabolic budget system in tumor cells. *Int. J. Biochem. Cell Biol.* **43**, 969–980 (2011).
20. Chaneton, B. *et al.* Serine is a natural ligand and allosteric activator of pyruvate kinase. *Nature* **491**, 458–462 (2012).
21. Okamura, S. *et al.* Identification of seven genes regulated by wild-type p53 in a colon cancer cell line carrying a well-controlled wild-type p53 expression system. *Oncol. Res.* **11**, 281–285 (1999).
22. Stambolsky, P. *et al.* Regulation of AIF expression by p53. *Cell Death Differ.* **13**, 2140–2149 (2006).
23. Linke, S. P. *et al.* A reversible, p53-dependent G0/G1 cell cycle arrest induced by ribonucleotide depletion in the absence of detectable DNA damage. *Genes Dev.* **10**, 934–947 (1996).
24. Messina, E. *et al.* Guanine nucleotide depletion triggers cell cycle arrest and apoptosis in human neuroblastoma cell lines. *Int. J. Cancer* **108**, 812–817 (2004).
25. Deng, C. *et al.* Mice lacking p21^{CIP1/WAF1} undergo normal development, but are defective in G1 checkpoint control. *Cell* **82**, 675–684 (1995).
26. Almasan, A. *et al.* Deficiency of retinoblastoma protein leads to inappropriate S-phase entry, activation of E2F-responsive genes, and apoptosis. *Proc. Natl Acad. Sci. USA* **92**, 5436–5440 (1995).
27. Dimri, G. P. *et al.* Inhibition of E2F activity by the cyclin-dependent protein kinase inhibitor p21 in cells expressing or lacking a functional retinoblastoma protein. *Mol. Cell. Biol.* **16**, 2987–2997 (1996).
28. Grüning, N.-M. & Ralser, M. Cancer: sacrifice for survival. *Nature* **480**, 190–191 (2011).
29. Anastasiou, D. *et al.* Inhibition of pyruvate kinase M2 by reactive oxygen species contributes to cellular antioxidant responses. *Science* **334**, 1278–1283 (2011).
30. Kalhan, S. C. & Hanson, R. W. Resurgence of serine: an often neglected but indispensable amino acid. *J. Biol. Chem.* **287**, 19786–19791 (2012).

Supplementary Information is available in the online version of the paper.

Acknowledgements This work was funded by Cancer Research UK. C.R.B. is a recipient of a Rubicon Fellowship from the Netherlands Organisation for Scientific Research. The authors thank A. Vigneron, B. Chaneton, M. O'Prey, E. Cheung, D. Athineos, G. Kalna, G. Mackay and B. Ludwig for advice and technical assistance.

Author Contributions K.H.V. and O.D.K.M. conceived the project and wrote the manuscript with C.R.B.'s help. C.R.B. and L.Z. performed and optimized LC–MS, C.R.B. and O.D.K.M. analysed LC–MS raw data. E.G. contributed to the design and interpretation of LC–MS experiments. K.B. and S.M.M. carried out the xenograft experiment, from which K.B. and O.D.K.M. analysed the data. O.D.K.M. performed all other experiments and data analysis. All the authors discussed the results and commented on the manuscript.

Author Information Reprints and permissions information is available at www.nature.com/reprints. The authors declare no competing financial interests. Readers are welcome to comment on the online version of the paper. Correspondence and requests for materials should be addressed to K.H.V. (k.vousden@beatson.gla.ac.uk).

METHODS

Cell culture. Unless otherwise stated, chemicals were obtained from Sigma-Aldrich, and cell culture reagents from Gibco (Invitrogen). HCT116 $p53^{+/+}$ ($p21^{+/+}$ (parental), $p53^{-/-}$ (1ex) (deletion of p53 exon 2), $p53^{-/-}$ (3ex) (deletion of p53 exons 2, 3 and 4), $p21^{-/-}$ and RKO $p53^{+/+}$ and $p53^{-/-}$ cells were a gift of B. Vogelstein³¹. Litter-matched wild-type and $p53^{-/-}$ MEFs (passage < 4) were prepared from E14.5 embryos derived from mating $p53^{+/+}$ mice³² (C57Bl6/J background, >20 gen). Cells were kept at 37 °C in humidified 5% CO₂ in air, stock HCT116 and RKO cells were maintained in McCoy's 5A medium (26600) containing 2 mM L-glutamine and 10% FBS (PAA Laboratories). For experiments cells were seeded in DMEM (21969) with 10% FBS and 2 mM L-glutamine. Complete (Com) medium was formulated to closely match the nutrient composition of DMEM (which contains 0.4 mM serine and 0.4 mM glycine); complete medium consisted of MEM (21090) supplemented with additional 1× MEM vitamins (11120), 10% dialysed-FBS (Hyclone, Thermo Scientific), L-glutamine 2 mM, additional D-glucose (to 25 mM), serine 0.4 mM and glycine 0.4 mM. For starvation experiments cells were fed the same medium formulation without serine and glycine (–SG medium).

Proliferation assays. HCT116 and RKO cells were seeded in 24-well plates (8×10^4 cells per well), MEFs in 12-well plates ($p53^{+/+}$ 2×10^4 cells per well, $p53^{-/-}$ 1×10^4 cells per well) in DMEM and allowed to grow for 16–24 h. Cells were then washed with PBS and received complete or –SG medium supplemented with the stated nutrients and/or drugs. To maintain constant nutrient levels and remove nutrients liberated from dead cells, medium was replaced every 24 h. Cell counts were performed with a CASY TT cell counter (Innovatis, Roche Applied Science). siRNA for p21 (sc-29427, Santa Cruz Biotechnology, UGUCAGAACCGGUGGGGA and UCCCCAGCCGGUUCUGACA) or non-targeting control (si-ctr, ON-TARGETplus, Dharmacon D-001810-10-20, UGGUUUACAUGUCGACUAA, UGGUUUACAUGUUGUGUGA, UGGUUUACAUGUUUUCUGA and UGGUUUACAUGUUUCCUA) was transfected with Metafectene SI (Biontex) in DMEM for 24 h before washing and adding complete or –SG medium.

Xenografts. Bilateral subcutaneous injections of 3×10^6 HCT116 cells were carried out on 8 week CD-1-Foxn1^{nu} female mice (Charles River); $p53^{+/+}$ on right flank and $p53^{-/-}$ (1ex) on the left. Immediately following injection mice were placed either on control diet ($n = 10$) (containing serine and glycine as part of the amino acid mix) or diet deficient in serine and glycine ($n = 10$) (TestDiet, International Product Supplies), formulations as follows. Control diet ingredients: sucrose (25.9%), corn starch (41.8%), corn oil (5.0%), Baker amino acid vitamin mix (0.2%), Baker amino acid mineral mix (10.0%), sodium bicarbonate (1.0%), DL-alpha tocopheryl acetate (0.004%), ethoxyquin (preservative, 0.019%), choline chloride (0.1%), amino acid premix (16.0%). Amino acid pre-mix: L-arginine-HCL (1.60%), L-cystine (0.64%), L-glutamine (1.60%), glycine (1.33%), L-histidine-HCL (0.80%), L-isoleucine (1.07%), L-leucine (1.60%), L-lysine-HCL (1.87%), L-methionine (0.80%), L-phenylalanine (1.07%), L-serine (1.33%), L-threonine (1.07%), L-tryptophan (0.27%), L-tyrosine (0.53%), L-valine (1.07%). The serine- and glycine-free diet has the same basic formulation as the control diet, but the amino acid mix lacks serine and glycine. Serine- and glycine-free diet ingredients: sucrose (25.9%), corn starch (41.8%), corn oil (5.0%), Baker amino acid vitamin mix (0.2%), Baker amino acid mineral mix (10.0%), sodium bicarbonate (1.0%), DL-alpha tocopheryl acetate (0.004%), ethoxyquin (preservative, 0.019%), choline chloride (0.1%), amino acid premix (16.0%). Amino acid pre-mix: L-arginine-HCL (1.60%), L-cystine (0.64%), L-glutamine (1.60%), L-histidine-HCL (0.96%), L-isoleucine (1.28%), L-leucine (1.92%), L-lysine-HCL (2.24%), L-methionine (0.96%), L-phenylalanine (1.28%), L-serine, L-threonine (1.28%), L-tryptophan (0.32%), L-tyrosine (0.64%), L-valine (1.28%).

The diets had equal caloric value and equal total amino acid content. Animals were housed in sterile IVC cages, monitored thrice weekly and killed humanely when tumours reached clinical endpoint of predetermined size (volume = (length \times width²)/2) or ulceration. All animal work was approved by the Ethical Review Process (University of Glasgow) and undertaken in line with the UK Animals (Scientific Procedures) Act of 1986 (PPL 60/4181) and the EU directive 2010.

Western blot. Cells were seeded in 6-well plates and grown in DMEM for ~40 h. Cells were washed with PBS then received complete or –SG medium. Cell numbers were titrated at the time of seeding to be ~90% confluent at protein isolation. Cell lysates were prepared in RIPA buffer with complete protease inhibitors (Roche), resolved via PAGE and transferred to nitrocellulose. Primary antibodies: phospho-p70S6K (9206) and total-p70S6K (2708), phospho-S6 (2215) and total-S6 (2217), AMPK- α (2532) and phospho-AMPK- α (2535) all from Cell Signaling Technology, PHGDH (Sigma Life Science, HPA021241), PSAT1 (Novus Biologicals, 21020002), PSPH (sc-98683), CDK4 (sc-260), p53 DO-1 (sc-126), p21 (sc-397) and PGAM1 (sc-130334) all from Santa Cruz Biotechnology. Secondary antibodies were IRDye800CW- or IRDye680LT-conjugated (LiCor

Biosciences), and were detected using an Odyssey infrared scanner (LiCor Biosciences) and quantified with Odyssey software.

Oxygen consumption rates (OCR). An XF24 Extracellular Flux Analyser (SeaHorse Bioscience) recorded OCR. HCT116 cells were grown in XF-plates for 48 h in complete or –SG medium (90–100% confluent at measurement). OCR was recorded after equilibration and after CCCP (0.5 μ M) and antimycin (1.5 μ M) treatments, these values were used to calculate basal and maximal OCR. All OCR measurements were normalized with well-by-well haemocytometer cell counts.

Peroxide sensitivity assay. HCT116 cells were seeded in 24-well plates in DMEM. After 16–20 h cells were washed with PBS and received complete or serine- and glycine-deficient medium. After 24 h the medium was replaced with matching medium containing the stated concentrations of hydrogen peroxide, after a further 24 h cells were washed and images captured using a light microscope. We noted that cell number had a large impact on peroxide sensitivity; therefore cell seeding was carefully titrated so that cell number was equal across the different experimental conditions at the time of peroxide addition.

Reactive oxygen species detection. CellROX deep red reagent (Invitrogen) was added to cell culture medium for 30 min. For flow cytometry, cells were detached by washing with PBS-EDTA followed by treatment with PBS-EDTA with trypsin (0.025%) and analysed on a FACSCalibur cytometer (BD Bioscience). For confocal microscopy, live cells were imaged using an inverted confocal fluorescence microscope (Fluoview FV1000, Olympus).

Liquid chromatography-mass spectrometry (LC-MS). HCT116 cells ($0.5\text{--}1.5 \times 10^6$) were seeded in triplicate wells of 6-well plates in DMEM, duplicate plates were seeded for cell counts. After 16–24 h cells were washed with PBS and received complete or –SG medium for the stated times. For glucose flux experiments, medium was replaced with HEPES-buffered Krebs–Ringer solution with 25 mM [$U\text{-}^{13}C$]D-glucose (Cambridge Isotopes), 10% dialysed FBS, 1× MEM amino acids (11130), 2× MEM vitamins and 2 mM L-glutamine. For serine flux experiments, medium was replaced with complete medium, with serine substituted for 0.4 mM [$U\text{-}^{13}C,^{15}N$]L-serine (Cambridge Isotopes). Cells were washed with PBS and metabolites extracted using methanol/acetonitrile/dH₂O (5:3:2) ($2\text{--}4 \times 10^6$ cells per ml). Samples were snap frozen, thawed at 4 °C, spun at 16,000g for 15 min and supernatants collected and filtered through 0.45 μ m PTFE membranes (Millipore). Serum samples were collected at time of killing. 20 μ l of serum was added to 980 μ l of extraction buffer and prepared as above. LC-MS analyses were performed on an Orbitrap Exactive (Thermo Scientific) in line with an Accela autosampler and an Accela 600 pump (Thermo Scientific). The Exactive operated in the polarity-switching mode with positive voltage 4.5 kV and negative voltage 3.5 kV. Column hardware consisted of a Sequent ZIC-PHILIC column (2.1×150 mm, 5 μ m) coupled to a Sequent ZIC-PHILIC guard column (2.1×20 mm, 5 μ m) (Merck). Flow rate was 100 μ l min^{–1}, buffers consisted of acetonitrile (ACN) for A, and 20 mM (NH₄)₂CO₃, 0.1% NH₄OH in H₂O for B. Gradient ran from 80% to 40% ACN in 20 min, followed by a wash at 20% ACN and re-equilibration at 80% ACN. Metabolites were identified and quantified using LCquan software (Thermo Scientific). Metabolites were positively identified on the basis of exact mass within 5 p.p.m., further validated by concordance with standard retention times and plotted as the peak area for each metabolite.

Quantitative PCR. Primers: *PGK1* forward: CTGTGGCTTCTGGCATACCT, *PGK1* reverse: CGAGTGACAGCCTACGAT; *PHGDH* forward: ATCTCTCA CGGGGGTTGTG, *PHGDH* reverse: AGGCTCGCATCAGTGTCC, *PSAT1* forward: CGGTCTCTGGAATACAAGGTG, *PSAT1* reverse: AACCAAGCCCATG ACGTAGA, *PSPH* forward: GAGCGGACTCCCTTTTAAGC, *PSPH* reverse: CAGGGAGGTGAGCTGTGC, *SHMT1* forward: CCCTCCCCATTGTAACACT, *SHMT1* reverse: GGGATCCACACTTTTCACTCC, *PKM2* forward: CTCGGG CTGAAGGCAGT, *PKM2* reverse: AATTGCAAGTGAGTAGTGCA, actin forward: TCCATCATGAAGTGTGACG, actin reverse: TACTCCTGCTTGCTGA TCCAC. Reactions used SYBR Green master-mix on a 7500 Fast Real-Time PCR System (both Applied Biosystems).

Chromatin-immunoprecipitation. Assays were performed as described previously³³. Cells ($6\text{--}8 \times 10^5$) were seeded in 6-well plates in DMEM, allowed to grow for ~40 h, then washed with PBS and received complete or –SG medium for 15 h, hydroxyurea (HU, 0.4 mM) was added as a positive control.

Cell-cycle analysis. For sub-G1 analysis, cells were grown and detached from plates as described above, then fixed and stained with propidium iodide (PI, 50 μ g ml^{–1}) for 30 min. For cell-cycle analysis BrdU (Invitrogen) was added to live cells for 100 min and detected as described previously³³. Flow cytometry was performed on a FACSCalibur cytometer.

PI exclusion. PI was added to cell culture medium (1 μ g ml^{–1}) for 5 min. Non-adherent and adherent cells were collected and analysed by Flow cytometry on a FACSCalibur cytometer.

ATP assay. Aliquots of cell suspension were added to TE buffer (pH 7.75) heated to 99 °C and assayed with an ATP determination kit (Invitrogen) on a Veritas Microplate luminometer (Turner Biosystems). Cell suspensions were counted to normalize for cell number.

Statistics. Survival was assessed by non-parametric distribution analysis (right censoring), using log-rank and Wilcoxon tests calculated on Minitab 16 (Minitab Ltd). The following *t*-test comparisons were performed with Microsoft Excel (v12.3.4): tumour volume between diet groups; unpaired, one tail. Tumour volume within diet groups; paired, one tail. Serum amino acids

between diet groups; unpaired, one tail. Oxygen consumption rate within genotype; paired, one tail. Oxygen consumption rate between genotypes; unpaired, one tail.

31. Bunz, F. *et al.* Requirement for p53 and p21 to sustain G2 arrest after DNA damage. *Science* **282**, 1497–1501 (1998).
32. Donehower, L. A. *et al.* Mice deficient for p53 are developmentally normal but susceptible to spontaneous tumours. *Nature* **356**, 215–221 (1992).
33. Vigneron, A. M., Ludwig, R. L. & Vousden, K. H. Cytoplasmic ASPP1 inhibits apoptosis through the control of YAP. *Genes Dev.* **24**, 2430–2439 (2010).

Apoptotic cell clearance by bronchial epithelial cells critically influences airway inflammation

Ignacio J. Juncadella^{1,2,3}, Alexandra Kadl⁴, Ashish K. Sharma⁵, Yun M. Shim⁴, Amelia Hochreiter-Hufford^{1,2,3}, Larry Borish^{1,4,6} & Kodi S. Ravichandran^{1,2,3}

Lung epithelial cells can influence immune responses to airway allergens^{1,2}. Airway epithelial cells also undergo apoptosis after encountering environmental allergens³; yet, relatively little is known about how these are cleared, and their effect on airway inflammation. Here we show that airway epithelial cells efficiently engulf apoptotic epithelial cells and secrete anti-inflammatory cytokines, dependent upon intracellular signalling by the small GTPase Rac1. Inducible deletion of *Rac1* expression specifically in airway epithelial cells in a mouse model resulted in defective engulfment by epithelial cells and aberrant anti-inflammatory cytokine production. Intranasal priming and challenge of these mice with house dust mite extract or ovalbumin as allergens led to exacerbated inflammation, augmented Th2 cytokines and airway hyper-responsiveness, with decreased interleukin (IL)-10 in bronchial lavages. *Rac1*-deficient epithelial cells produced much higher IL-33 upon allergen or apoptotic cell encounter, with increased numbers of neutrophil-like cells^{4,5}. Administration of exogenous IL-10 'rescued' the airway inflammation phenotype in *Rac1*-deficient mice, with decreased IL-33. Collectively, these genetic and functional studies suggest a new role for *Rac1*-dependent engulfment by airway epithelial cells and in establishing the anti-inflammatory environment, and that defects in cell clearance in the airways could contribute to inflammatory responses towards common allergens.

Exposure to environmental pollutants, allergens and pathogens can induce apoptosis of airway epithelial cells^{3,6,7}. In fact, clusters of uncleared epithelial cells referred to as 'Creola bodies' in the sputum have been seen in patients with asthma for decades^{8,9}. Although the lung contains professional phagocytes such as macrophages and dendritic cells, many so-called 'non-professional phagocytes' can engulf apoptotic cells^{10,11}. Because the bronchial epithelial cells come in contact with allergens first, and greatly outnumber the professional phagocytes *in situ*, we asked whether epithelial cells might contribute to cell clearance in the airways.

We tested phagocytosis by primary murine airway epithelial cells, the human bronchial epithelial cell line BEAS-2B and the murine alveolar epithelial cell line MLE-12. To score internalization, we labelled the apoptotic epithelial cells with a pH-dependent dye (CypHer5), whose fluorescence increased within acidic phagolysosomes^{12,13} (Fig. 1a, b). BEAS-2B, MLE-12 and the primary murine airway epithelial cells (CD45⁻ EpCAM⁺) engulfed apoptotic targets; this was dependent on phosphatidylserine (PtdSer) recognition on the apoptotic cells (inhibitable by annexin V) (Fig. 1b). Apoptotic cell recognition by professional phagocytes is known to elicit anti-inflammatory mediators that dampen inflammation in the local tissue environment^{14,15}. Airway epithelial cells also produced active transforming growth factor (TGF)- β and PGE₂ after apoptotic cell recognition, and dependent on phosphatidylserine and Rac1 (Fig. 1c, d and Supplementary Fig. 1a, b). This suggests that airway epithelial cells can engulf apoptotic targets and produce anti-inflammatory mediators.

To test the importance of cell clearance by airway epithelial cells *in vivo*, we wished to delete engulfment genes specifically within epithelial cells and assess airway inflammation. Because phagocytes often express several engulfment receptors, and the relative importance of particular engulfment receptors on the epithelial cells is not fully characterized, we targeted the small GTPase Rac1, which functions downstream of several engulfment signalling pathways^{15,16}. Deletion of *Rac1* in the airway epithelial cells was achieved by crossing *Rac1*^{fl/fl} mice with clara cell secretory protein (CCSP)-^{rtTA/tetO}-Cre transgenic mice, which express Cre under tissue-specific and temporal control (Fig. 1e and Supplementary Fig. 2a)^{16,17}. Doxycycline (Dox) given through drinking water induced Cre expression in the epithelial cells of the trachea, bronchi and bronchioles under the promoter for the Clara cell-specific secretory protein (CCSP)¹⁸ (Supplementary Fig. 2b). Dox administration to CCSP-Cre/*Rac1*^{fl/fl} mice led to *Rac1* deletion specifically in the epithelial cells (Fig. 1f, g), but not in other cells in the bronchial tissue, or in CD45⁺ haematopoietic cells (Fig. 1f). *Rac1* expression in CCSP-Cre/*Rac1*^{fl/fl} mice was unaffected before doxycycline treatment, and Dox treatment of *Rac1*^{wt/wt} mice did not affect *Rac1* or *Rac2* expression.

The doxycycline-inducible system allowed the airways to develop normally, until *Rac1* deletion at 8 weeks. However, because *Rac1* is a key cytoskeletal regulator in many cell types, we were concerned about potential unintended effects. Several independent lines of evidence alleviated this concern. First, the architecture and epithelial cell morphology of the airways were comparable at steady state in control and *Rac1* deleted mice (Supplementary Fig. 2b). Second, numbers of yellow fluorescent protein (YFP⁺)-expressing epithelial cells in CCSP-Cre/*Rac1*^{fl/fl} mice crossed to Rosa26^{STOP-YFP} reporter mice were comparable to controls (Fig. 1f); importantly, *Rac1* expression was deleted in the YFP⁺ epithelial cells but not CD45⁺ YFP⁻ haematopoietic cells (Fig. 1f and Supplementary Fig. 3c). Third, primary epithelial cell cultures yielded similar total numbers of cells positive for nitroterrazolium blue from control and CCSP-Cre/*Rac1*^{fl/fl} mice (Supplementary Fig. 4a). Fourth, the epithelial cell integrity and tight junction formation was unaffected after *Rac1* deletion, on the basis of staining for the tight-junction protein occludin (Supplementary Fig. 4c, d) and transmission electron microscopy (Supplementary Fig. 5a). Fifth, integrity of the alveolar-capillary membrane in CCSP-Cre/*Rac1*^{fl/fl} was intact on the basis of intravenous injection of Evan's blue and tracking the dye in the lung (Supplementary Fig. 4b). Sixth, the uptake of intranasally administered fluorescently labelled antigens by epithelial cells, dendritic cells, and alveolar macrophages was similar between control and *Rac1*-deficient mice (Supplementary Fig. 5b, c). Collectively, Dox-induced deletion of *Rac1* in the airway epithelial cells in the CCSP-Cre/*Rac1*^{fl/fl} mice did not affect the integrity of the epithelial cells.

Airway epithelial cells from CCSP-Cre/*Rac1*^{fl/fl} mice showed significant reduction in phagocytosis of apoptotic cells *in vitro* (Fig. 1h), and after intranasal administration of apoptotic cells *in vivo*

¹Carter Immunology Center, University of Virginia, Charlottesville, Virginia 22908, USA. ²Department of Microbiology, University of Virginia, Charlottesville, Virginia 22908, USA. ³The Center for Cell Clearance, University of Virginia, Charlottesville, Virginia 22908, USA. ⁴Department of Medicine, University of Virginia, Charlottesville, Virginia 22908, USA. ⁵Department of Surgery, University of Virginia, Charlottesville, Virginia 22908, USA. ⁶Center for Asthma and Allergic Diseases, University of Virginia, Charlottesville, Virginia 22908, USA.

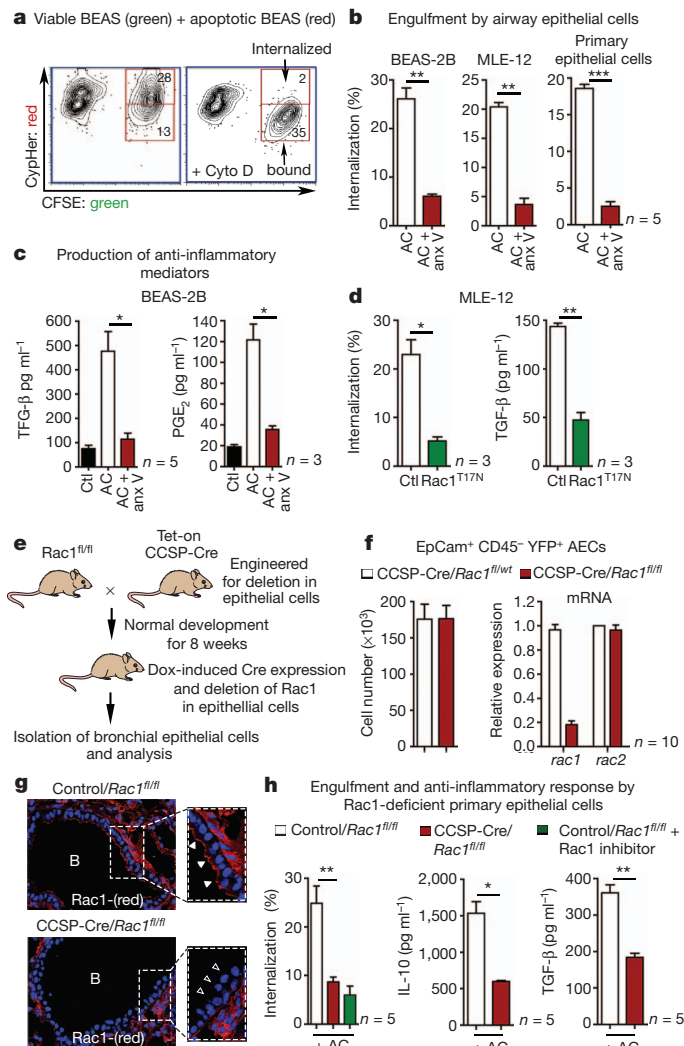


Figure 1 | Rac1-dependent engulfment and anti-inflammatory cytokine production by airway epithelial cells. **a**, Uptake of CypHer5-labelled apoptotic epithelial cells by viable epithelial cells (CFSE). **b**, Internalization is blocked by annexin (anx) V ($n = 5$). AC, airway epithelial cells. **c**, TGF- β ($n = 5$) and PGE₂ ($n = 3$) production by BEAS-2B epithelial cells. **d**, Phagocytosis and TGF- β production in MLE-12 epithelial cells transfected with Rac1^{T17N} ($n = 3$). **e**, Schematic for generating CCSP-Cre/*Rac1*^{fl/fl} mice and Dox-induced ('Tet-On') Rac1 deletion in airway epithelial cells. **f**, Left, YFP⁺ epithelial cells from control and Rac1-deficient mice. Right, Rac1 mRNA expression in epithelial cells ($n = 10$). **g**, Loss of Rac1 in the airways of Dox-treated CCSP-Cre/*Rac1*^{fl/fl} mice (open arrowheads). **h**, Left, engulfment by airway epithelial cells from control and Rac1-deficient mice ($n = 5$). $^{*}P < 0.01$, representative of three experiments. Middle and right, IL-10 and TGF- β in BAL fluid of control and Rac1-deficient mice after intranasal administration of apoptotic cells (**f**, **h**, $n = 5$ –10 mice from three experiments). $^{*}P < 0.05$, $^{**}P < 0.01$, unpaired Student's *t*-test with Welch's correction (**b**, **c**, **d**, **h**), Mann-Whitney test (**h**). Error bars, s.e.m.

(Supplementary Fig. 6a); in contrast, alveolar macrophages from these mice showed no phagocytic defect (Supplementary Fig. 6b). Intranasal administration of apoptotic cells resulted in significantly decreased amounts of anti-inflammatory cytokines IL-10 and TGF- β in the CCSP-Cre/*Rac1*^{fl/fl} mice (Fig. 1h). Because the CCSP-Cre/*Rac1*^{fl/fl} mice have normal Rac1 in CD45⁺ cells (such as macrophages), the epithelial cells clearly influenced cytokine production in the bronchial spaces in response to apoptotic cells. Furthermore, in *Rac1*^{fl/fl} mice crossed with LysM-Cre mice (Cre expression targeted to the myeloid lineage)¹⁹, intranasal administration of apoptotic cells did not show a decrease in IL-10 or TGF- β in the bronchoalveolar lavage (BAL) fluid

(Supplementary Fig. 8b). Thus, mice lacking Rac1 in the airway epithelial cells showed defective ability to engulf apoptotic cells and altered inflammatory response *in vivo*.

We next tested these mice in airway inflammation models. One common approach to induce airway inflammation is to prime with antigen intraperitoneally and subsequently challenge with the same antigen by the intranasal route. We tested the development of allergic inflammation in CCSP-Cre/*Rac1*^{fl/fl} mice to low-endotoxin house dust mite (HDM) extract, a common airway allergen. The control mice showed T-cell and eosinophil infiltration, along with immunoglobulin-E (IgE) response and Th2 cytokines IL-4, IL-5 and IL-13, but all these parameters were heightened in the CCSP-Cre/*Rac1*^{fl/fl} mice (Supplementary Fig. 7), suggesting that losing Rac1 expression in airway epithelial cells exacerbates inflammation.

Because humans encounter environmental antigens through the airways before developing symptoms of airway inflammation, we established a system where both the primary allergen encounter and secondary challenge were through the intranasal route (Fig. 2a). After Dox-induced Rac1 deletion followed by intranasal priming and challenge with HDM, the CCSP-Cre/*Rac1*^{fl/fl} mice showed a strong airway inflammation phenotype with significant accumulation of mucus (Fig. 2b). In contrast, controls showed minimal or undetectable airway inflammation after intranasal priming and challenge. These control conditions included Dox-treated, saline injected CCSP-Cre/*Rac1*^{fl/fl} mice, Dox-treated *Rac1*^{fl/fl} mice without Cre, CCSP-Cre/*Rac1*^{fl/wt} mice and CCSP-Cre/*Rac1*^{fl/fl} mice that did not receive doxycycline. Although we often observed more uncleared apoptotic nuclei in allergen challenged airways of CCSP-Cre/*Rac1*^{fl/fl} mice (by TdT-mediated dUTP nick end labelling and cleaved caspase 3 staining), the staining was variable between samples, probably because of mucus and other secretions in inflamed tissues (data not shown).

Allergic airway inflammation involves Th2 responses in the lungs^{5,20,21}. The CCSP-Cre/*Rac1*^{fl/fl} mice showed high concentrations of Th2 cytokines IL-4, IL-5, IL-13, eosinophil and T-cell infiltration in BAL fluid (Fig. 2c). IL-10 was significantly reduced in the Rac1-deficient mice (Fig. 2c), correlating with low IL-10 seen in airways of asthmatic patients²². When re-stimulated with HDM *ex vivo*, CD4⁺ T cells from the mediastinal lymph nodes of CCSP-Cre/*Rac1*^{fl/fl} mice produced much higher amounts of IL-4, IL-5 and IL-13 than control mice (Fig. 2d). When Rac1 deletion in the airway epithelial cells was controlled (by Dox administration) at either the priming (sensitization) or challenge phases, keeping Rac1 expression normal at the priming phase and deleting at the challenge phase showed minimal airway inflammation to HDM (Supplementary Fig. 9). These data suggest that Rac1 expression in airway epithelial cells plays a critical role in preventing sensitization to common airway allergens encountered by the intranasal route.

When we analysed lung function parameters, HDM-sensitized CCSP-Cre/*Rac1*^{fl/fl} mice showed physiological changes consistent with asthma including much greater airway resistance, decreased compliance and higher pulmonary arterial pressure (Fig. 2e). Loss of Rac1 led to a twofold increase in methacholine-induced airway hyper-responsiveness compared with wild-type littermates (Supplementary Fig. 10). Thus, Rac1 expression in airway epithelial cells critically controls allergen-induced airway inflammation and the physiological changes of asthma. Interestingly, intranasal priming and challenge of the LysM-Cre/*Rac1*^{fl/fl} mice with HDM did not show enhanced airway inflammation (Supplementary Fig. 8c, d).

We next asked whether exogenous IL-10 could reverse the inflammatory phenotype in CCSP-Cre/*Rac1*^{fl/fl} mice. Recombinant mouse IL-10 (rIL-10) given at priming and challenge phases with HDM resulted in markedly reduced airway inflammation, manifested by reduced production of mucus (Fig. 3a, b), and lower Th2 cytokines IL-4, IL-5 and IL-13 in the airways. The mediastinal lymph nodes were substantially smaller in the rIL-10-treated CCSP-Cre/*Rac1*^{fl/fl} mice, with a significant decrease in the HDM-induced production of Th2

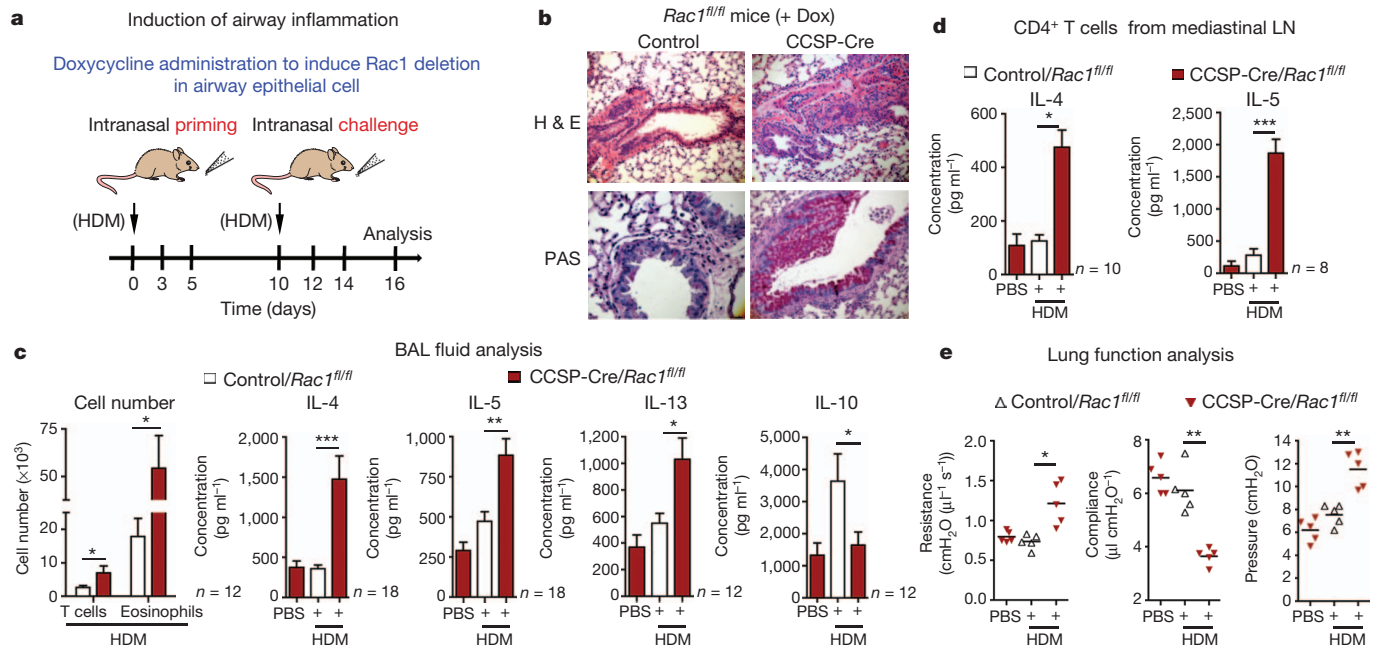


Figure 2 | Mice lacking *Rac1* in airway epithelial cells show increased allergic inflammation. **a**, Protocol for inducing airway inflammation. **b**, Representative haematoxylin and eosin (H&E) and periodic acid Schiff (PAS) staining of lung sections from control or CCSP-Cre/*Rac1*^{fl/fl} mice. **c**, Infiltrating CD4⁺ T cells, eosinophils and Th2-type cytokines in BAL fluid of control or *Rac1*-deficient mice ($n = 12$ –18 mice per group from more than four

experiments). **d**, Cytokine production by mediastinal lymph node (LN) cells re-stimulated *in vitro* for 5 days with HDM ($n = 8$ –10 mice per group from three experiments). **e**, Airway resistance, compliance and pleural pressure in control or in *Rac1*-deficient mice ($n = 5$ mice from two experiments). * $P < 0.05$, ** $P < 0.01$, *** $P < 0.001$, unpaired Student's *t*-test with Welch's correction (c–e).

cytokines (Fig. 3c–e). rIL-10-treated mice also showed improved pulmonary function (Fig. 3f). This suggests that *Rac1* expression in epithelial cells and IL-10 amounts in the airways are complementary factors regulating airway inflammation.

Preparations of HDM are enriched in the type-2-group allergen Der p2, an LPS-binding protein^{23,24}. To test whether mice lacking *Rac1* in the airway epithelial cells are inherently sensitive to allergen exposure in the absence of adjuvant activity, we first primed CCSP-Cre/*Rac1*^{fl/fl}

mice with recombinant Der p1, which showed augmented IgE and IgG1 antibody response and increased inflammation (Supplementary Fig. 7e, f). Second, although intranasal administration of chicken ovalbumin (Ova) without LPS often leads to tolerance induction²⁵, in CCSP-Cre/*Rac1*^{fl/fl} mice intranasal priming/challenge with Ova led to airway inflammation (Fig. 4a–d). Control mice showed minimal inflammation. Mediastinal lymph node cells from *Rac1*-deficient mice also produced higher IL-4, IL-5 and IL-13 (Fig. 4e). We confirmed that control mice primed with (Ova plus alum) by the intraperitoneal route and challenged with Ova by the intranasal route showed airway inflammation (Supplementary Fig. 11). In CCSP-Cre/*Rac1*^{fl/fl} mice, the amounts of IL-10 in the BAL fluid were lower after Ova priming and challenge, and administering rIL-10 significantly reduced this inflammation (Fig. 4f–h). Thus, *Rac1* loss in the bronchial epithelial cells and reduced IL-10 creates a state that is prone to inflammation in response to normally innocuous inhaled allergens.

Thymic stromal lymphopoietin (TSLP) and IL-33 represent two cytokines linked to promoting airway inflammation^{1,26,27}. Although TSLP did increase in the BAL fluid after HDM challenge, this was comparable between control and CCSP-Cre/*Rac1*^{fl/fl} mice. However, IL-33 was significantly higher in the CCSP-Cre/*Rac1*^{fl/fl} mice after allergen challenge (although basal IL-33 without HDM challenge was not increased) (Fig. 5a). Treatment with rIL-10 diminished the IL-33

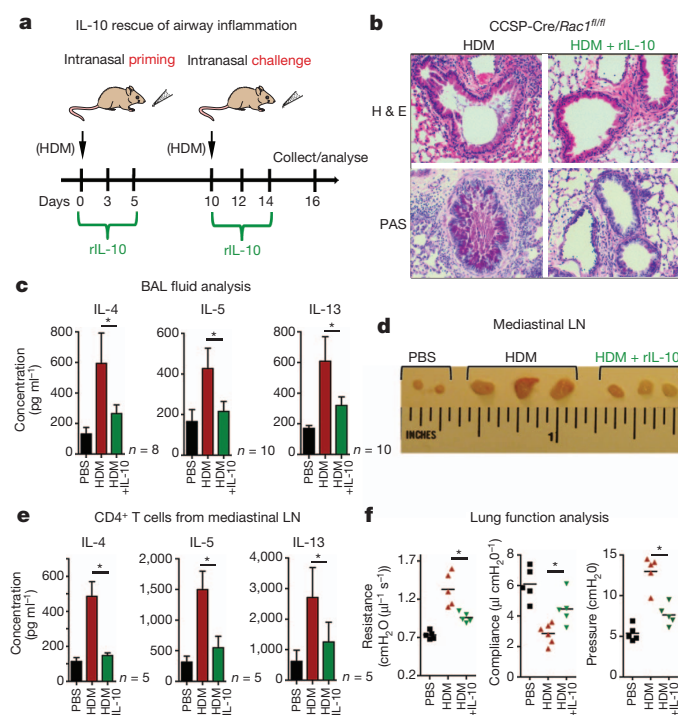


Figure 3 | Allergic airway inflammation in *Rac1*-deficient mice is rescued by rIL-10. **a**, Schematic of inducing airway inflammation and IL-10 treatment. **b**, H&E and PAS staining of lung sections from CCSP-Cre/*Rac1*^{fl/fl} mice treated with or without rIL-10 (1 μg), representative of several experiments. **c**, BAL fluid analysis showing IL-4, IL-5 and IL-13 production by *Rac1*-deficient mice treated with or without rIL-10 ($n = 8$ –10 mice per group, from three experiments). **d**, Image of mediastinal lymph nodes ($n = 3$ mice per group). **e**, Cytokine production by lymph node cells re-stimulated *in vitro* for 5 days with HDM ($n = 5$ mice per group). **f**, Airway resistance, compliance and pleural pressure in *Rac1*-deficient mice treated with or without rIL-10 ($n = 5$) (d–f, representative of three experiments). * $P < 0.05$, unpaired Student's *t*-test with Welch's correction (c, e, f).

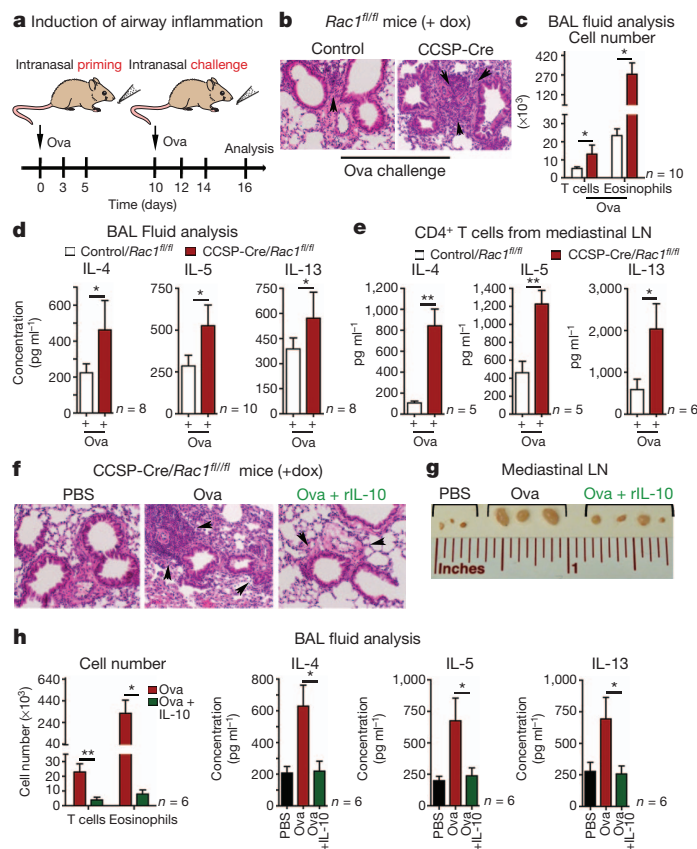


Figure 4 | Airway inflammation with Ova after Rac1 deletion. **a**, Schematic of intranasal priming and challenge with Ova. **b**, H&E staining of lung sections from Dox-treated control and CCSP-Cre/Rac1^{fl/fl} mice ($\times 20$ magnification). **c**, Infiltrating CD4⁺ T cells and eosinophils in BAL fluid of indicated mice. **d**, Th2-cytokines in the BAL fluid. (**c**, **d**, $n = 10$ mice per group). **e**, Cytokine production by mediastinal lymph node T cells re-stimulated *in vitro* for 5 days with Ova ($n = 6$ mice per group). (**c**–**e**, Representative of three experiments). **f**–**h**, Rac1-deficient mice primed and challenged with Ova with IL-10. **f**, H&E staining of lung sections. Arrowheads indicate leukocyte infiltration ($\times 20$ magnification). **g**, Image of mediastinal lymph nodes (**f**, **g**, representative of three experiments). **h**, BAL fluid analysis of infiltrating T-cells, eosinophils and Th2 cytokines ($n = 6$ mice combined from two experiments). * $P < 0.05$, ** $P < 0.01$, unpaired Student's *t*-test with Welch's correction.

contained significantly higher IL-5-expressing cell populations resembling nuocytes (lineage⁺, T1/ST2⁺ CD44⁺, Sca-1⁺, ICOS⁺) (Fig. 5b). Interestingly, after HDM priming of CCSP-Cre/Rac1^{fl/fl} mice (less than 6 days), the lung nuocytes (but not CD4⁺ T cells) were positive for IL-5 (Supplementary Fig. 12a, b), suggesting inducible nuocyte activation. A neutralizing IL-33 antibody reduced the inflammation in the CCSP-Cre/Rac1^{fl/fl} mice, with reduction in lymph node cellularity, infiltrating eosinophils and activated CD4⁺ T cells (Supplementary Fig. 12c, d). Although the function of this lung nuocyte-like population needs further testing, these data suggest a link between enhanced IL-33 production in the CCSP-Cre/Rac1^{fl/fl} mice after allergen challenge, the expansion of an IL-5 producing nuocyte-like population and airway inflammation.

Because epithelial cells are a main source of IL-33, we asked how Rac1 affects IL-33 expression. When MLE-12 epithelial cells were stimulated with HDM or apoptotic cells, IL-33 messenger RNA (mRNA) was upregulated; drug-mediated inhibition of Rac1 (ref. 30) or short interfering RNA (siRNA) knockdown of Rac1 led to a three- to sixfold increase in IL-33 (Supplementary Fig. 13 and Fig. 5c). This IL-33 mRNA upregulation due to Rac inhibition was not a generic effect, as the inhibitor greatly diminished Rac1-dependent TGF- β expression (Supplementary Fig. 13b).

To test whether Rac1 deletion affects IL-33 expression in primary airway epithelial cells during allergen challenge, we used the CCSP-Cre/Rac1^{fl/fl} mice crossed to the Rosa26^{STOP-EYFP} reporter mice.

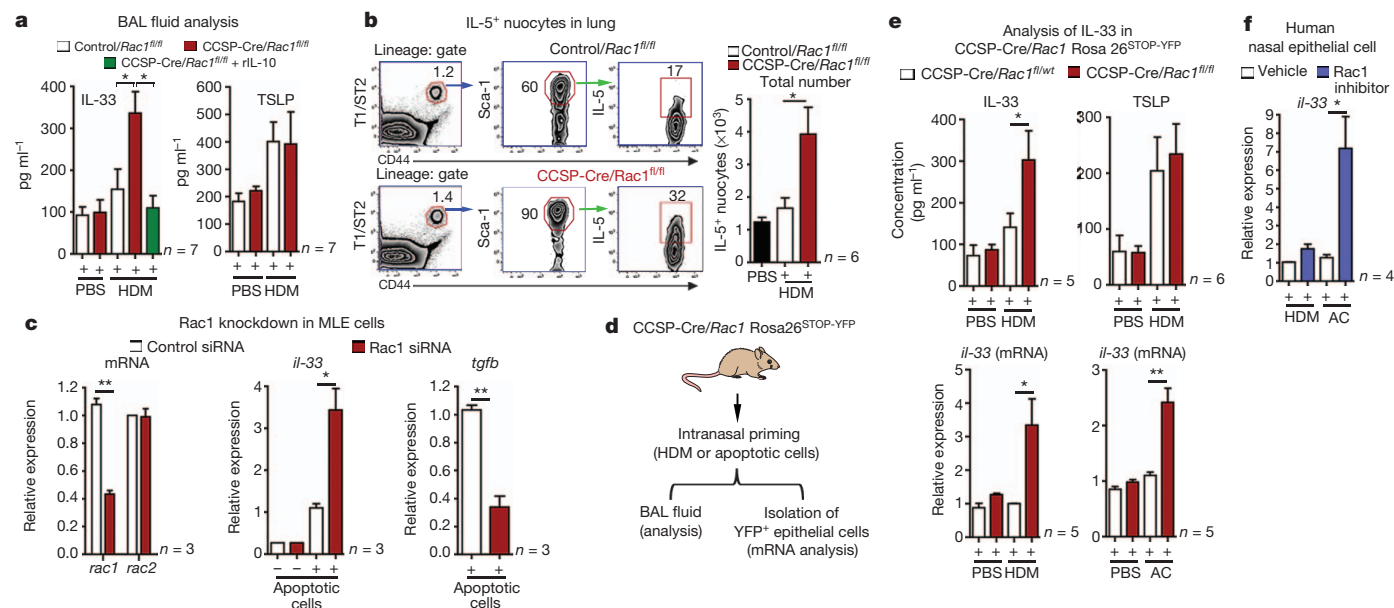


Figure 5 | IL-33 upregulation in Rac1-deficient epithelial cells correlates with airway inflammation. **a**, IL-33 and TSLP in BAL fluid of control or Rac1-deficient mice. **b**, Strategy for gating nuocyte-like cells and their numbers in lungs after HDM priming (**a**, **b**, $n = 6$ or 7 mice from two experiments). **c**, IL-33 or TGF- β expression in Rac1-siRNA-treated MLE-12 cells with apoptotic cells ($n = 3$) (**c**, representative of three experiments). **d**, **e**, *In vivo* IL-33 induction

after intranasal HDM or apoptotic cells in CCSP-Cre/Rosa26^{YFP} mice (**d**), or in purified YFP⁺ EpCam⁺ epithelial cells ($n = 5$ or 6 mice, from three experiments) (**e**). **f**, IL-33 mRNA in human nasal epithelial cells stimulated with HDM or apoptotic cells ($n = 3$); * $P < 0.05$, ** $P < 0.01$, unpaired Student's *t*-test with Welch's correction. Error bars, s.e.m.

Although the YFP⁺ EpCAM⁺ airway epithelial cells from control and CCSP-Cre/Rac1^{fl/fl} mice had comparable amounts of basal IL-33 message, this was significantly increased after HDM stimulation. Second, in the BAL fluid of Rac1-deficient mice, IL-33 cytokine was increased three- to fivefold after intranasal priming with HDM, whereas the TSLP amounts were comparable (Fig. 5d, e). Third, after intranasal injection of apoptotic epithelial cells, purified YFP⁺ EpCAM⁺ epithelial cells from Rac1-deficient mice had much higher IL-33 mRNA (Fig. 5e). This link between Rac1 and *il-33* expression was also seen in human nasal epithelial cells, as production of IL-33 by HDM or apoptotic cells was strongly enhanced by Rac inhibition (Fig. 5f). Collectively, these data suggest a critical role for Rac1 expression in epithelial cells in regulating IL-33 expression and, in turn, the sensitization to inhaled allergens.

Although airway epithelial cells are the first to come in contact with the allergens, their contribution to tolerance towards common airway allergens has been less clear. The data presented here suggest that airway epithelial cells can be phagocytic, and that their ability to secrete/modulate cytokines can critically influence tolerance to common airway allergens. Thus, apart from a physical barrier, phagocytosis in the airways may be part of an extra line of immune protection against innocuous antigens. These data also identify a new Rac-1 dependent IL-33:IL-10 axis in controlling airway inflammation. The amounts of the pro-inflammatory cytokine IL-33 and the anti-inflammatory cytokine IL-10 seem linked, with Rac1 expression in airway epithelial cells controlling both steps. Although asthmatic patients have deficits in IL-10 (ref. 22), the contribution of IL-10 to allergen sensitization and its potential therapeutic use remains unexplored. Our studies suggest IL-10 as a critical regulator of airway inflammation, and IL-10 might prove a new therapeutic approach to limiting airway inflammation. Lastly, although cell clearance and anti-inflammatory cytokine production by professional phagocytes have long been studied, the relative importance of cell clearance by non-professional phagocytes under physiological settings is still limited. These data suggest that airway epithelial cells can be both phagocytic and modulate the cytokine milieu to limit airway inflammation.

METHODS SUMMARY

Mice. Rac1^{fl/fl} mice were crossed with CCSP-rtTA/tetO-Cre mice¹⁸ and Rac1 deletion induced by doxycycline (1 mg ml⁻¹) in drinking water. To track the Rac1-deleted airway epithelial cells specifically, the CCSP-Cre/Rac1^{fl/fl} were crossed with the Rosa26^{STOP-EYFP} reporter mice (JaxMice).

Induction of airway inflammation. Mice were primed intranasally with low-endotoxin HDM extract (10 µg in 50 µl volume, Indoor Biotechnologies), or chicken Ova (20 µg) on days 0, 3, 5. Control mice received saline during the priming and challenge phases. Mice were challenged intranasally on days 10, 12 and 14, and analysed for Th2 cell-dependent airway inflammation on day16. Control or CCSP-Cre/Rac1^{fl/fl} mice were treated intranasally for 24 h with 10 µg of HDM or 5 million to 10 million apoptotic ultraviolet-treated Jurkat cells or etoposide-treated (100 µM) BEAS-2B cells. BAL fluid was collected (24 h) and cytokine production analysed by enzyme-linked immunosorbent assay (ELISA).

In vitro engulfment assay. MLE-12, BEAS-2B cells or primary airway epithelial cell cultures were plated at a density of 3 × 10⁵ in a 12-well plate and incubated with 3 × 10⁶ CypHer5 or TAMRA-labelled apoptotic Jurkat T-cells or etoposide (100 µM)-treated apoptotic BEAS-2B for 4 h.

Full Methods and any associated references are available in the online version of the paper.

Received 16 May; accepted 25 October 2012.

Published online 12 December 2012.

1. Fahy, J. V. & Locksley, R. M. The airway epithelium as a regulator of Th2 responses in asthma. *Am. J. Respir. Crit. Care Med.* **184**, 390–392 (2011).
2. Lambrecht, B. N. & Hammad, H. The airway epithelium in asthma. *Nature Med.* **18**, 684–692 (2012).
3. Jyonouchi, H. Airway epithelium and apoptosis. *Apoptosis* **4**, 407–417 (1999).

4. Locksley, R. M. Asthma and allergic inflammation. *Cell* **140**, 777–783 (2010).
5. Hammad, H. *et al.* House dust mite allergen induces asthma via Toll-like receptor 4 triggering of airway structural cells. *Nature Med.* **15**, 410–416 (2009).
6. White, S. R. Apoptosis and the airway epithelium. *J. Allergy* **2011**, 948406 (2011).
7. Daidoji, T. *et al.* H5N1 avian influenza virus induces apoptotic cell death in mammalian airway epithelial cells. *J. Virol.* **82**, 11294–11307 (2008).
8. Naylor, B. The shedding of the mucosa of the bronchial tree in asthma. *Thorax* **17**, 69–72 (1962).
9. Yamada, Y., Yoshihara, S. & Arisaka, O. Creola bodies in wheezing infants predict the development of asthma. *Pediatr. Allergy Immunol.* **15**, 159–162 (2004).
10. Monks, J. *et al.* Epithelial cells as phagocytes: apoptotic epithelial cells are engulfed by mammary alveolar epithelial cells and repress inflammatory mediator release. *Cell Death Differ.* **12**, 107–114 (2005).
11. Kirsch, T. *et al.* Engulfment of apoptotic cells by microvascular endothelial cells induces proinflammatory responses. *Blood* **109**, 2854–2862 (2007).
12. Park, D. *et al.* Continued clearance of apoptotic cells critically depends on the phagocyte Ucp2 protein. *Nature* **477**, 220–224 (2011).
13. Park, D., Hochreiter-Hufford, A. & Ravichandran, K. S. The phosphatidylserine receptor TIM-4 does not mediate direct signaling. *Curr. Biol.* **19**, 346–351 (2009).
14. Fadok, V. A. *et al.* Macrophages that have ingested apoptotic cells *in vitro* inhibit proinflammatory cytokine production through autocrine/paracrine mechanisms involving TGF-β, PGE2, and PAF. *J. Clin. Invest.* **101**, 890–898 (1998).
15. Ravichandran, K. S. & Lorenz, U. Engulfment of apoptotic cells: signals for a good meal. *Nature Rev. Immunol.* **7**, 964–974 (2007).
16. Ravichandran, K. S. Beginnings of a good apoptotic meal: the find-me and eat-me signaling pathways. *Immunity* **35**, 445–455 (2011).
17. Elliott, M. R. & Ravichandran, K. S. ELMO1 signaling in apoptotic germ cell clearance and spermatogenesis. *Ann. NY Acad. Sci.* **1209**, 30–36 (2010).
18. Perl, A. K., Tichelaar, J. W. & Whitsett, J. A. Conditional gene expression in the respiratory epithelium of the mouse. *Transgenic Res.* **11**, 21–29 (2002).
19. Glogauer, M. *et al.* Rac1 deletion in mouse neutrophils has selective effects on neutrophil functions. *J. Immunol.* **170**, 5652–5657 (2003).
20. Cates, E. C. *et al.* Intranasal exposure of mice to house dust mite elicits allergic airway inflammation via a GM-CSF-mediated mechanism. *J. Immunol.* **173**, 6384–6392 (2004).
21. Thomas, W. R., Hales, B. J. & Smith, W. A. House dust mite allergens in asthma and allergy. *Trends Mol. Med.* **16**, 321–328 (2010).
22. Borish, L. *et al.* Interleukin-10 regulation in normal subjects and patients with asthma. *J. Allergy Clin. Immunol.* **97**, 1288–1296 (1996).
23. Thomas, W. R. Molecular mimicry as the key to the dominance of the house dust mite allergen Der p 2. *Expert Rev. Clin. Immunol.* **5**, 233–237 (2009).
24. Trompette, A. *et al.* Allergenicity resulting from functional mimicry of a Toll-like receptor complex protein. *Nature* **457**, 585–588 (2009).
25. Eisenbarth, S. C. *et al.* Lipopolysaccharide-enhanced, toll-like receptor 4-dependent T helper cell type 2 responses to inhaled antigen. *J. Exp. Med.* **196**, 1645–1651 (2002).
26. Soumelis, V. *et al.* Human epithelial cells trigger dendritic cell mediated allergic inflammation by producing TSLP. *Nature Immunol.* **3**, 673–680 (2002).
27. Lloyd, C. M. IL-33 family members and asthma – bridging innate and adaptive immune responses. *Curr. Opin. Immunol.* **22**, 800–806 (2010).
28. Liew, F. Y., Pitman, N. I. & McInnes, I. B. Disease-associated functions of IL-33: the new kid in the IL-1 family. *Nature Rev. Immunol.* **10**, 103–110 (2010).
29. Barlow, J. L. *et al.* Innate IL-13-producing nuocytes arise during allergic lung inflammation and contribute to airways hyperreactivity. *J. Allergy Clin. Immunol.* **129**, 191–198 (2012).
30. Shutes, A. *et al.* Specificity and mechanism of action of EHT 1864, a novel small molecule inhibitor of Rac family small GTPases. *J. Biol. Chem.* **282**, 35666–35678 (2007).

Supplementary Information is available in the online version of the paper.

Acknowledgements We thank the members of the Ravichandran laboratory for their suggestions, especially J. Kinchen and P. Trampont. We thank J. Whitsett for the rtTA-CCSP/Cre mice, X. Liu for the TGF-β responsive cell line PE25, and J. Steinke and J. Kennedy for providing human nasal epithelial cells. This work was supported by an Immunology Training Grant (I.J.J.), a F32 postdoctoral fellowship from the NHLBI (I.J.J.), and grants from the American Asthma Foundation and the National Institutes of Health (K.S.R.). K.S.R. has been a William Benter Senior Fellow of the American Asthma Foundation.

Author Contributions I.J.J. designed, performed and analysed most of the experiments in this study with input from K.S.R. A.K. optimized and performed the isolations and *ex vivo* cultures of primary epithelial cells and the nitroretroazole staining. A.K.S. performed the lung function analysis. Y.M.S. performed the airway hyper-responsiveness experiments to determine the degree of airway resistance. L.B. provided intellectual input on specific experiments and helped with the human tissue studies. I.J.J. and K.S.R. wrote the manuscript with comments from co-authors.

Author Information Reprints and permissions information is available at www.nature.com/reprints. The authors declare no competing financial interests. Readers are welcome to comment on the online version of the paper. Correspondence and requests for materials should be addressed to K.S.R. (Ravi@virginia.edu).

METHODS

Mice. Mice carrying floxed alleles for *rac1* were crossed with mice carrying the Cre recombinase driven by the rat CCSP promoter (CCSP-*rtTA/tetO-Cre*)¹⁸. *Rac1* deletion in CCSP-Cre/*Rac1*^{fl/fl} mice was achieved by administering doxycycline (1 mg ml⁻¹) in drinking water containing 0.4% sucrose. The various control mice included CCSP-Cre/*Rac1*^{fl/fl} mice that received no doxycycline, *Rac1*^{fl/fl} mice (no Cre) that received doxycycline, doxycycline-treated CCSP-Cre/*Rac1*^{fl/wt} heterozygous mice or CCSP-Cre/*Rac1*^{wt/wt} mice. To facilitate flow cytometric isolation of those airway epithelial cells with *Rac1* deletion, the CCSP-Cre/*Rac1*^{fl/fl} were further crossed with the Rosa26^{STOP-EYFP} reporter mice (The Jackson Laboratory). The Cre/*Rac1*^{fl/fl} mice were also crossed with either LysM-Cre strain to achieve deletion of *Rac1* in the myeloid lineage, or the CD11c-Cre mice to achieve deletion in the dendritic cell lineage. The University of Virginia Animal Care and Use Committee approved all animal experiments.

Induction of airway inflammation. Mice were primed intranasally with 50 µl of low-endotoxin preparation of the HDM extract (10 µg, Indoor Biotechnologies) or with chicken Ova (20 µg, Sigma-Aldrich) on days 0, 3, 5. Control mice received saline during the priming and challenge phases. Mice were then challenged intranasally on days 10, 12 and 14. On day 16, the mice were analysed for Th2 cell-dependent eosinophilic airway inflammation. Alternatively, mice were primed with HDM, Der p1 or Ova by intraperitoneal injection with Alum (2.25 mg, Pierce) on days 0, 3, 5, followed by intranasal challenge on days 10, 12 and 14 and analysed for inflammation.

Collection of BAL fluid and total cell numbers. BAL was performed by injecting 1 ml of phosphate-buffered saline (PBS) containing 0.01 mM EDTA through a cannula, flushing twice and collecting 500–700 µl. The BAL fluid was centrifuged and the cells were washed with PBS containing 1% FBS. The cells were stained for monocytes/macrophages, neutrophils, T cells, alveolar macrophages and eosinophils using the following antibodies: anti-mouse Ly6G, Ly6C, F4/80, CD11b (for macrophages and neutrophils), CD4, CD25, CD44, CD69 (for T cells), CD11c (for dendritic cells) and Siglec F (BD Biosciences) (for eosinophils and alveolar macrophages). The absolute cell numbers of cells were determined by adding reference particles (Spherotec) during flow cytometry (Supplementary Fig. 14). Data were collected on FACS Canto (Becton Dickinson) and analysed with FlowJo software (Treestar). The BAL fluid was stored at -80 °C and further used in analysis of cytokines.

Cytokine analysis. IL-4, IL-5, IL-13, IL-10, IL-33 and TSLP were measured by ELISA (using antibodies from R&D Systems) in the BAL fluid by ELISA 48 h after the last challenge. HDM-specific IgE and IgG1 were measured in the sera and BAL fluid of mice sensitized and challenged with HDM by ELISA (antibodies from BD Biosciences). HDM or Ova-specific CD4⁺ T-cell responses were measured by re-stimulating 5 × 10⁶ cells from mediastinal lymph nodes for 5 days with 10 µg of HDM or Ova in the presence of 5 × 10⁶ mitomycin C-treated splenocytes.

Microscopy and histology. The expression of CCSP, *Rac1* and the Cre recombinase was determined by immunofluorescence staining. An optimal cutting temperature compound (O.C.T., Sakura Finetek) was injected into the lungs through a tracheal cannula. The lungs were excised and 'snap frozen' with liquid nitrogen and stored in -80 °C. Frozen sections (0.8 µm) were cut and stained with primary antibody to CCSP (1:50, Santa Cruz Biotechnology), *Rac1* (1:20, Cytoskeleton) and Cre, using a FITC- (fluorescein isothiocyanate) labelled antibody (1:500, BioLegend) for 30 min at room temperature. The sections were washed three times with PBS and stained for 30 min at room temperature with anti-goat Alexa Fluor® 647 and anti-rabbit Alexa Fluor® 594 secondary antibodies (1:500, Invitrogen). The nuclei were counterstained with DAPI (4',6-diamidino-2-phenylindole) (Invitrogen). The samples were analysed using a Zeiss AxioImager Z2 equipped with Apotome for optical sectioning (Zeiss).

To assess the amount of inflammation and mucus secretion, lung sections were paraffin-embedded, fixed in 10% neutral buffered-formalin and 0.8 µm sections were stained with H&E and PAS, respectively. All staining procedures were performed by the histology core facility at the University of Virginia.

Airway epithelial cell isolation and culture. For primary airway epithelial cell purification and culture, lungs were perfused through the right ventricle with buffered saline and carefully excised. Two millilitres of dispase (BD Bioscience) were instilled into the lungs, followed by 1% low-melting agarose (Invitrogen) and incubated for 1 h at 37 °C. After incubation, the lungs were minced and mechanically disrupted by passing them through 100 and 70 µm nylon strainers. Single-cell suspensions were washed with PBS containing 1% FBS and 100 units of DNaseI and treated with red blood lysis buffer (Sigma-Aldrich) for 5 min. The cells were then washed, centrifuged, and CD45⁺ cells were depleted from the single-cell suspensions by incubating with anti-CD45 microbeads and passed through a MACS® Cell Separation Column (Miltenyi Biotech). The cells were re-suspended in DMEM/F-12 media containing 10% FBS and plated in a 10 cm culture dish at 37 °C for 2 h. After incubation, the non-adherent cells were

collected, centrifuged and seeded on a 10 cm culture plate coated with calfskin collagen type I (Sigma-Aldrich).

Lung function analysis. Lung function was measured using an *in situ* buffer-perfused mouse lung system. Animals were anaesthetized and positive-pressure (2 cmH₂O) ventilation (120 breaths per minute, tidal volume) was initiated. The lungs were perfused with Krebs-Henseleit buffer, containing 2% albumin, 0.1% glucose and 0.3% HEPES. The lungs were allowed to equilibrate for 5 min and pulmonary compliance, resistance and pulmonary arterial pressure were measured and recorded using Pulmodyn data-acquisition software (Hugo Sachs Elektronik).

Airway hyper-responsiveness. Airway hyper-responsiveness was measured by exposing mice to increasing doses of aerosolized methacholine (0–10 mg ml⁻¹). A tracheotomy tube was inserted and then connected to the inspiratory and expiratory ports of a volume-cycled ventilator (flexiVent; SCIREQ Scientific). The data from normal ventilation were collected to establish the baseline values for each animal. The change in airway resistance (ΔR) from baseline was calculated after each dose.

Transmission electron microscopy. Lungs from wild-type or *Rac1*-deficient mice were perfused with buffered saline and fixed in 4% paraformaldehyde solution containing 2% glutaraldehyde for 24 h. Lung sections were prepared and analysed by the University of Virginia advance microscopy facility.

In vitro engulfment assay. MLE-12, BEAS-2B cells or primary airway epithelial cell cultures were plated at a density of 3 × 10⁵ in a 12-well plate and incubated with 3 × 10⁶ CypHer5 or TAMRA-labelled apoptotic Jurkat T-cells or etoposide- (100 µM) treated apoptotic BEAS-2B for 4 h. In some experiments, viable BEAS-2B cells were stained with CFSE (2.5 µM) before incubation with apoptotic cells. Phagocytosis was analysed using a BD FACS Canto (Becton Dickinson). To block phagocytosis, 1 µM of cytochalasin D (Sigma-Aldrich) or 10 µg ml⁻¹ of purified human annexin-V (Enzo Life Sciences) were used. In some experiments the specific *Rac1* inhibitor EHT1864 (30 µM, Sigma-Aldrich) was used.

In vivo engulfment assay. CCSP-Cre/*Rac1*^{fl/fl} mice and control/*Rac1*^{fl/fl} mice crossed with Rosa26^{STOP-EYFP} reporter mice (and therefore having Cre-marked airway epithelial cells) were injected intranasally with 10 × 10⁶ CypHer-labelled apoptotic thymocytes for 3 h. The lungs were then minced, digested with collagenase type II (183 U ml⁻¹) for 1 h and passed through a 70 µm strainer. Single-cell suspensions were gated on YFP^{hi} cells and engulfment of apoptotic cells was analysed. Alveolar macrophages were collected from BAL fluid and stained with anti-CD11b, anti-F4/80 antibodies and analysed for uptake of CypHer-labelled apoptotic cells.

In vivo treatment with HDM or apoptotic cells. Control or CCSP-Cre/*Rac1*^{fl/fl} mice were treated intranasally for 24 h with 10 µg of HDM or 5 million to 10 million apoptotic ultraviolet-treated Jurkat or etoposide-treated (100 µM) BEAS-2B. After 24 h, BAL fluid was collected and the cytokine production was analysed by ELISA.

Vascular permeability. Vascular permeability in the lungs was determined using the Evans blue dye extravasation method. Evans blue (20 mg kg⁻¹, Sigma-Aldrich) was injected intravenously for 1 h before the mice were killed. The mice were then perfused with 10 ml PBS to remove intravascular dye. The lungs were then homogenized in PBS to extract the dye and centrifuged. The absorption of Evans blue was measured in the supernatants at 620 nm, and corrected for the presence of haem pigments as follows: $A_{620}(\text{corrected}) = A_{620} - (1.426A_{740} + 0.030)$.

Antigen uptake assay. Uptake of soluble antigen by dendritic cells, alveolar macrophages, or epithelial cells, 10 µg of fluorescently labelled HDM or Ova (Alexa Fluor® 594) was injected intranasally for 1 h. Total lungs were minced and treated with collagenase or dispase, single-cell suspensions were prepared and stained for dendritic cells, alveolar macrophages and epithelial cells, and analysed for the percentage of antigen uptake.

Identification of nuocyte-like cells in the lung. Total lung suspensions were prepared and gated on lineage-negative populations by staining with the following cocktail of antibodies: mouse anti-CD3, CD4, CD8, B220, CD11c, CD11b, CD49b, Ly6C/Ly6G. These cells were further gated on the basis of T1/ST2 expression (mouse biotin-conjugated anti-T1/ST2 antibody (clone DJ8 1:50 dilution), BioLegend), CD44 and Sca-1 (1:100 dilution, eBioscience). These nuocyte-like cells were further confirmed by ICOS surface expression (anti-ICOS antibody, eBioscience). Intracellular IL-5 expression was analysed by intracellular staining using anti-mouse IL-5 antibody (eBioscience).

Treatment with anti-IL-33 neutralizing antibody. CCSP-Cre/*Rac1*^{fl/fl} or control mice were intranasally primed and challenged with HDM (10 µg) in the presence of anti-IgG (isotype control, 6 µg per dose) or anti-IL-33 (6 µg per dose) antibody (R&D Systems). After the last challenge, the mediastinal lymph nodes were excised and total cellularity was analysed. BAL fluid was collected and stained for activated T cells and eosinophils.

Transfection with siRNA. MLE-12 cells were transfected with a nucleofector, with 250 nM of siRNA targeting Rac1 or a control non-targeting SMARTpool (Thermo Scientific, catalogue number L-041170-00-0005), using the recommended protocol for primary mammalian epithelial cells (Lonza).

Quantitative PCR analysis. Total RNA was extracted from epithelial cells using the Qiagen Qias shredder and RNeasy kit, and cDNA was synthesized using SuperScript III kit (Invitrogen). Quantitative PCR for Rac1, Rac2, TGF- β and

IL-33 was performed using the TagMan Gene Expression Assay (Applied Biosystems), and were run on a STEP One plus instrument (ABI). It is noteworthy that the higher IL-33 measured was not derived from the apoptotic cells as species-specific primers were used (Supplementary Fig. 13b).

Statistical analysis. Statistical significance for individual data points was determined by an unpaired Student's two-tailed *t*-test, unless noted otherwise. A *P* value less than 0.05 was considered statistically significant.

Functional and evolutionary insight from the crystal structure of rubella virus protein E1

Rebecca M. DuBois¹, Marie-Christine Vaney¹, M. Alejandra Tortorici¹, Rana Al Kurdi¹, Giovanna Barba-Spaeth¹, Thomas Krey¹ & Félix A. Rey¹

Little is known about the three-dimensional organization of rubella virus, which causes a relatively mild measles-like disease in children but leads to serious congenital health problems when contracted *in utero*¹. Although rubella virus belongs to the same family as the mosquito-borne alphaviruses, in many respects it is more similar to other aerosol-transmitted human viruses such as the agents of measles and mumps. Although the use of the triple MMR (measles, mumps and rubella) live vaccine has limited its incidence in western countries, congenital rubella syndrome remains an important health problem in the developing world. Here we report the 1.8 Å resolution crystal structure of envelope glycoprotein E1, the main antigen and sole target of neutralizing antibodies against rubella virus. E1 is the main player during entry into target cells owing to its receptor-binding and membrane-fusion functions. The structure reveals the epitope and the neutralization mechanism of an important category of protecting antibodies against rubella infection. It also shows that rubella virus E1 is a class II fusion protein, which had hitherto only been structurally characterized for the arthropod-borne alphaviruses and flaviviruses. In addition, rubella virus E1 has an extensive membrane-fusion surface that includes a metal site, reminiscent of the T-cell immunoglobulin and mucin family of cellular proteins that bind phosphatidylserine lipids at the plasma membrane of cells undergoing apoptosis. Such features have not been seen in any fusion protein crystallized so far. Structural comparisons show that the class II fusion proteins from alphaviruses and flaviviruses, despite belonging to different virus families, are closer to each other than they are to rubella virus E1. This suggests that the constraints on arboviruses imposed by alternating cycles between vertebrates and arthropods resulted in more conservative evolution. By contrast, in the absence of this constraint, the strictly human rubella virus seems to have drifted considerably into a unique niche as sole member of the *Rubivirus* genus.

The human pathogenic rubella virus is the cause of German measles, a highly contagious childhood airborne disease that is endemic throughout the world. The virus efficiently crosses the placental barrier when it infects pregnant women, causing miscarriage or serious congenital disease in newborns. Rubella belongs to the *Togaviridae* family of positive-strand RNA viruses¹. Although it has the same genome organization as the alphaviruses (the only other genus in this family), the corresponding structural proteins show no detectable sequence similarity. Rubella virus has two envelope glycoproteins, E1 and E2 (481 and 282 amino acids long, respectively), which are anchored in the viral membrane by a carboxy-terminal transmembrane segment. E1 carries the principal antigenic determinants² and is responsible for receptor recognition³ and low-pH-triggered membrane fusion upon internalization through receptor-mediated endocytosis^{4–6}. E1 was shown to bind myelin oligodendrocyte glycoprotein to gain entry into certain cells³, which may account for the serious demyelinating symptoms observed in some patients with congenital rubella syndrome.

For structural studies we produced the rubella virus E1 ectodomain (termed E1e, Supplementary Fig. 1) in *Drosophila* S2 cells, as described in Methods. Secreted E1e forms trimers that bind to liposomes (Fig. 1), on which they form hexagonal arrays similar to those formed by their alphavirus and flavivirus counterparts in the post-fusion form^{7–9}, suggesting that recombinant E1e is in the post-fusion conformation. The crystal structure (Fig. 2 and Supplementary Table 1) indeed revealed clear structural homology to viral class II fusion proteins (Supplementary Fig. 2 and Table 1), featuring three β -sheet-rich domains termed I, II and III (Fig. 2). The E1e subunits of the trimer adopt the typical post-fusion hairpin conformation.

Comparisons with the alphavirus and flavivirus class II fusion protein structures (Supplementary Figs 2 and 3a), together with electron micrographs of E1e on liposomes (Fig. 1b, c), unambiguously define the membrane-facing ('top') side and the membrane-distal ('bottom')

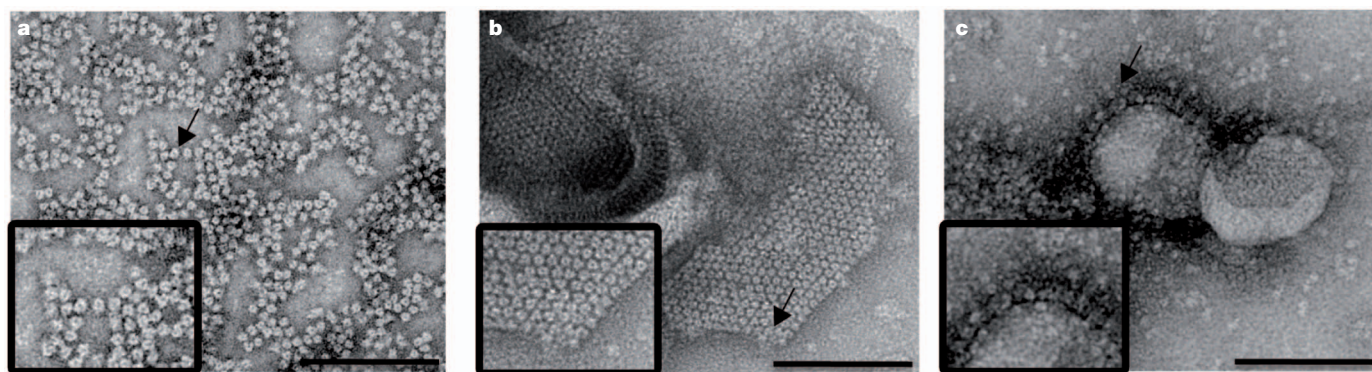
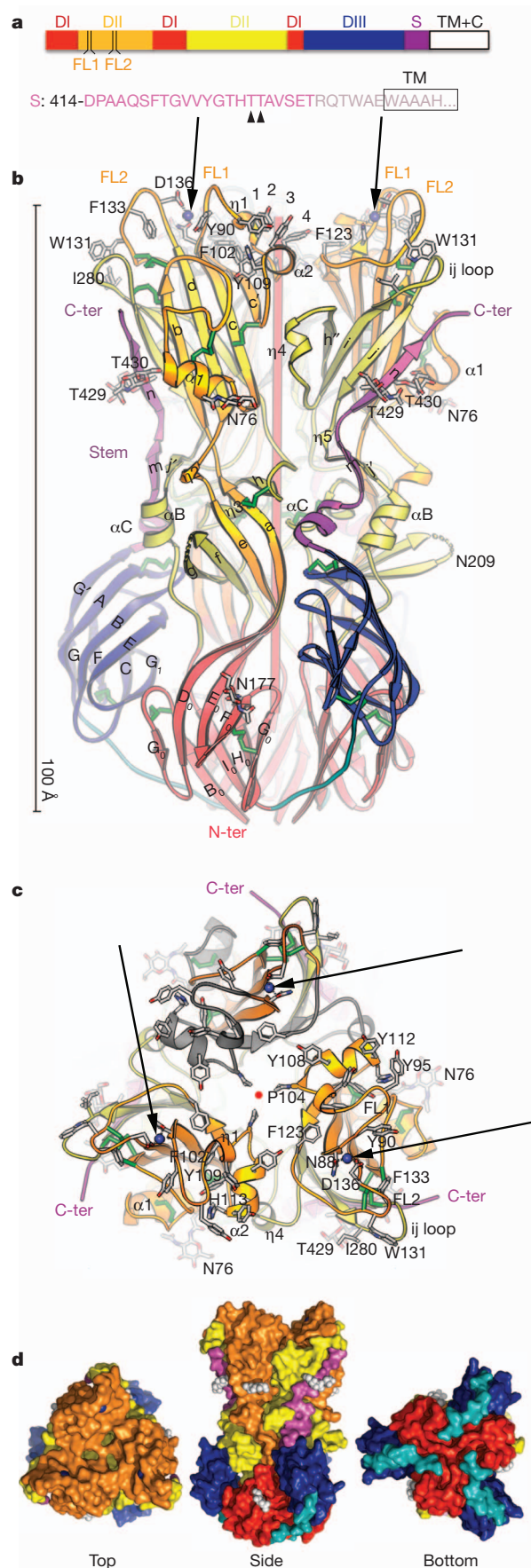


Figure 1 | Negative-stain electron microscopy observations of E1e trimers in isolation and bound to liposomes. **a**, Isolated E1e trimers tend to line up at the air–water interface in the electron microscope grid, with their three-fold axes perpendicular to the plane of the paper. **b**, **c**, Rubella virus E1e covers the

liposome surface forming an ordered hexagonal lattice, viewed from the top (**b**) and from the side (**c**). Note the clear three-fold symmetry of the lattice building blocks. Scale bars, 100 nm. Arrows mark regions that are magnified in insets.

¹Institut Pasteur, Département de Virologie, Unité de Virologie Structurale and CNRS URA 3015, F-75724 Paris Cedex 15, France.



end of trimeric E1e. Domain III is swapped¹⁰ in the E1e trimer, occupying the space taken up by domain III from the neighbouring subunit in the alphavirus and flavivirus class II post-fusion trimers (Supplementary Fig. 2). The 'stem', which connects domain III to the transmembrane anchor, is clearly visible until six residues before the transmembrane segment, ending next to the fusion loops in a region that would be in the lipid-head-contact area in the full-length transmembrane protein (Fig. 2, Supplementary Fig. 2 and Supplementary Video 1). The conformation of the stem had not been observed before, because this segment was absent in the structures of the alphavirus and flavivirus fusion proteins.

Using the Dali server¹¹, comparisons with other protein structures revealed that rubella virus E1 appears equally distant from its alphavirus and flavivirus counterparts (Table 1), which are structurally closer to each other despite belonging to different virus families. The main differences are concentrated in the fusion-loop-containing domain II. In rubella virus E1, domain II is larger because of the presence of three important insertions in its membrane-proximal half, a region termed 'tip' (Fig. 2 and Supplementary Figs 2 and 3). The overall effect is that E1e displays a considerably larger surface for interaction with lipids, as highlighted in Supplementary Fig. 2b. Instead of a fusion loop, which in the alphavirus and flavivirus fusion proteins maps to the connection between strands c and d (the cd loop), rubella virus E1 has an insertion of almost 40 residues in between these two strands ('Insert 2', Supplementary Fig. 3). These extra residues make up a 'fusion surface', so named by analogy to the fusion loop (see Supplementary Video 1), which in the context of the trimer displays a continuous area of about 8,000 Å² (Supplementary Fig. 2b). The short amphipathic helix α 2 is positioned such that it projects a tyrosine side chain per turn towards the membrane (Tyr 108 and Tyr 112), and the 3_{10} helical turn η 1 projects Tyr 101 (Fig. 2b, c; see also Supplementary Fig. 4 for secondary structure nomenclature). In total, the fusion surface projects out 15 aromatic side chains (mainly tyrosines), also including Tyr 95 and Phe 123 from each subunit, clustered around the three-fold molecular axis. The ij loop also reaches the membrane-contact region, exposing the side chain of Ile 280 at the top (Fig. 2b, c). At the centre, the fusion surface is sealed by Pro 104 of the three subunits interacting with each other at the three-fold axis (Fig. 2c). In line with the stabilizing role of this 'proline seal', the P104G mutation was shown to result in 1-log reduction in rubella virus infectivity¹².

The polypeptide segment forming most of the fusion surface is framed at its amino- and carboxy-terminal ends by two loops, termed fusion loops 1 and 2 (FL1 and FL2, residues 88–93 and 131–137, respectively; see Supplementary Fig. 4), which project towards the membrane (Supplementary Fig. 2). The aromatic residues Tyr 90 in FL1 and Trp 131 and Phe 133 in FL2 are at the very top of the molecule, but the side chains are oriented towards the protein with the main-chain amino and carbonyl groups exposed at the very top, together with the side-chain hydroxyl groups of Ser 91, Ser 92 and Thr 135 (Fig. 2b, c). These loops may adopt a different conformation to expose

Figure 2 | Crystal structure of rubella virus E1e. **a–c**, Linear (**a**) and three-dimensional (**b**, **c**) diagrams of E1e colour-coded by domain, with disulphide bonds in green. DI–DIII denote domains I to III (see Supplementary Information for a description of class II domains), with the stem (**S**; sequence displayed in **a**) in magenta and the DI–DIII linker in cyan. FL1 and FL2 denote fusion loops 1 and 2. In **a**, the transmembrane (TM) and cytoplasmic (C) segments are indicated in white. Grey fonts in the stem sequence mark residues absent from the structure. Framed section denotes the beginning of the transmembrane segment. Black triangles denote O-linked glycan sites. Arrows point to the metal sites (blue spheres). Aromatic residues at the membrane-contact area are shown as ball-and-stick; the 1, 2, 3, 4 arc denotes tyrosine residues 95, 101, 112 and 108 in one subunit. The trimer axis is shown in red in **b** (side view) and **c** (top view, red dot). Domain II insertions in rubella virus E1 (see Supplementary Fig. 3) are coloured grey in one subunit in **c**, **d**. Surface representations viewed from top, side and bottom, coloured as above. Glycan atoms are shown as silver spheres.

Table 1 | Dali scores comparing class II viral fusion proteins

| | 1 | 2 | 3 | 4 |
|-------------------|--|--|--|--|
| | Rubella virus E1* | Alphavirus E1 | Flavivirus E | Class III viral fusion proteins |
| A Rubella | A:B† Z n/n_t σ % 49.5 421/ 424 Ca²⁺ 48.7 424/ 431 | SFV Z n/n_t σ % 9.4 278/ 391 7.2 10 | TBEV Z n/n_t σ % 9.4 268/ 387 7.1 10 DEN2 8.9 264/ 380 7.3 9 DEN1 8.6 266/ 379 7.6 10 | VSVG Z n/n_t σ % 1.9 74/ 409 3.5 9 HSV1gB 1.2 43/ 581 3.3 9 |
| | See A2 | A:B† Z n/n_t σ % 49.3 389/ 391 0.7 100 SFV: 37.7 376/ CHV‡ 390 3.0 62 | TBEV Z n/n_t σ % 14.2 325/ 382 4.7 8 DEN2 13.3 320/ 380 5.1 8 DEN1 13.7 324/ 379 5.2 10 TBEV: CHV‡ 11.9 311/ 395 7.1 9 | VSVG Z n/n_t σ % 0.1 102/ 409 5.9 10 HSV1gB 0.5 39/ 576 6.9 3 |
| C Flaviviruses | See A3 | See B3 | TBEV A: Z n/n_t σ % 50.2 387/ B† 388 0.8 100 DEN1: 41.1 372/ DEN2 379 1.0 68 TBEV: 35.3 369/ DEN2 380 2.0 40 TBEV: 34.4 369/ DEN1 379 1.9 38 | HSV1gB Z n/n_t σ % 0.3 35/ 379 4.3 0 |
| D Class III | See A4 | See B4 | See C4 | VSVG A: Z n/n_t σ % 46.0 409/ B† 410 1.0 100 HSV1: 27.4 474/ EBVgB 576 4.3 28 HSV1gB: 5.7 107/ gp64 418 4.5 14 VZVG: 5.3 211/ gp64 409 9.5 4 |

Each row and column includes viruses from the same genus, except for row D and column 4, which include class III protein controls from viruses of different families or subfamilies. The table also gives the variation range: Z scores under 2 are meaningless, whereas Z = 50 corresponds to the same protein in different crystalline environments. n/n_t indicates the number (n) of aligned residues compared to the total residues in the alignment (n_t). σ indicates the root mean square deviation (in angstroms) between backbone α-carbon atoms. % indicates the percentage amino acid identity after structural alignment of the proteins (See 'Evolutionary pace' in Supplementary Information). Unless otherwise specified, the comparisons in rows B and C involve the post-fusion form of SFV E1 (row B) and the post-fusion forms of the flavivirus E proteins (row C). The data to the left and the right of the diagonal are identical.

*All comparisons using rubella virus E1e were done with coordinates in which domain III was manually 'unswapped' to make a trimer organized in the same way as alphavirus E1 or flavivirus E (Supplementary Fig. 2). Without this operation, the Dali score was based on fewer residues and the Z-score value was poorer.

†A:B denotes chain A over chain B within the same trimer, in cases where the chains are in different crystalline environments. Ca²⁺ indicates a comparison between Ca²⁺-bound and Na⁺-bound E1e.

‡This comparison is between pre-fusion forms: SFV:CHV refers to pre-fusion E1 from SFV²¹ compared to pre-fusion E1 from CHV²². TBEV:CHV denotes a comparison between the TBEV E protein^{23,24} and the CHV E1 protein, both in pre-fusion form.

CHV, chikungunya virus; DENn, dengue virus serotype n^{25,26}; EBVgB, Epstein-Barr virus glycoprotein B²⁹; gp64, baculovirus glycoprotein 64 (ref. 30); HSV1gB, herpes simplex virus type 1 glycoprotein B²⁸; SFV, Semliki forest virus; TBEV, tick-borne encephalitis virus; VSVG, vesicular stomatitis virus glycoprotein²⁷.

the aromatic side chains during interactions with the membrane. We indeed identified some degree of conformational flexibility in FL2 in the various crystal forms analysed (see below). The functional importance of this region is also highlighted by the G93D mutation in FL1, which resulted in a 3-fold reduction in virus infectivity¹².

A metal ion is coordinated by Asn 88 in FL1 and Asp 136 in FL2, through main- and side-chain atoms (Figs 2 and 3). The metal site is a unique feature of rubella virus E1, as there is no metal in the other class II fusion proteins, nor in the fusion peptide/loop of any other viral fusion protein reported to date. It is reminiscent of the metal-ion-dependent ligand-binding site of the T-cell immunoglobulin and mucin (TIM) family proteins¹³ shown in Supplementary Fig. 5. TIM proteins specifically bind phosphatidylserine lipids on membranes. As described in Supplementary Information, the E1e metal site can bind Na⁺ or Ca²⁺ ions, the latter with higher affinity. We found that the conformation of FL2 depends on the metal bound (Fig. 3, Supplementary Fig. 5 and Supplementary Video 2). Also, liposome flotation assays showed that in the presence of Ca²⁺ E1e binds membranes at both acidic and neutral pH, whereas in its absence it only binds at acidic pH (Fig. 3). Given that the extracellular environment is in general at neutral pH with Ca²⁺ concentrations in the millimolar range¹⁴, this *in vitro* behaviour may have biological relevance, suggesting that Ca²⁺-bound rubella virus E1 could serve for virion attachment directly

to the cell membrane. A role for E1 binding to lipids at neutral pH would be in line with reports indicating that certain lipids inhibit rubella virus infection¹⁵. As discussed in Supplementary Information, the electrostatic potential at the membrane-fusion surface switches from neutral to basic at the centre at low pH (Supplementary Fig. 6). This feature is independent of the nature of the metal bound, and may also be related to the type of membrane interactions of E1 in internal acidic compartments of the cell, some of which display negatively charged lipids on the luminal side (for instance, late endosomes¹⁶).

An important neutralizing epitope has been mapped to amino acids 223–239 of rubella virus E1 (ref. 17), a segment that includes disulphide bond 8 (DB8; see Supplementary Fig. 4). Antibodies binding to this epitope are abundant in rubella-virus-positive individuals, and their presence is used as a correlate for protection against viral disease. Serum from congenital rubella syndrome patients who are persistently infected despite having high levels of rubella-virus-specific antibodies have little or no reactive antibodies against the DB8 epitope¹⁸. Although the epitope is clearly accessible on infectious virions, the structure shows that it is completely buried at the centre of the E1 trimer (Supplementary Fig. 7), so that it becomes inaccessible upon E1 trimerization for fusion. The structure therefore predicts that antibodies bound to this site would block E1 trimerization for entry, thereby revealing the neutralization mechanism, although we cannot

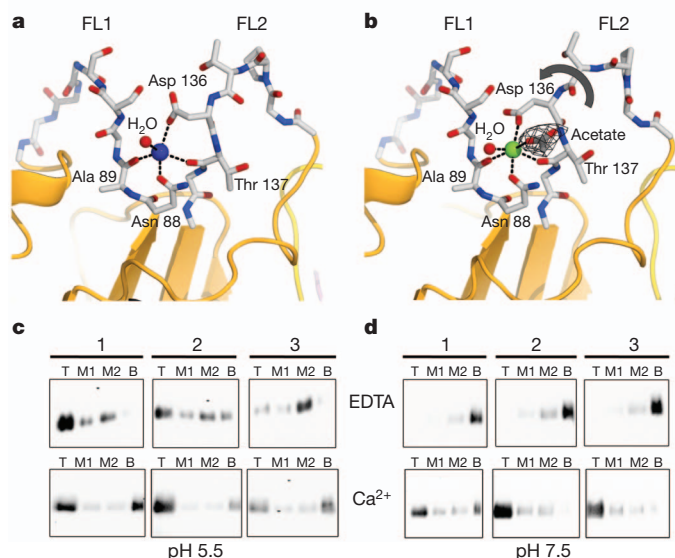


Figure 3 | Metal and pH dependence of liposome binding. **a, b**, Close-up of the metal site occupied by Na^+ (blue sphere; **a**) or Ca^{2+} (green sphere; **b**) ions, coordinated between FL1 and FL2, as seen in our structures at pH 8.0. Note the change in Asp 136 (grey arrow; see Supplementary Video 2) and the bound acetate ion in **b, c, d**. Liposome binding at pH 5.5 (**c**) or 7.5 (**d**) as determined by co-floitation in sucrose gradients. Numbers 1, 2 and 3 correspond to different lipid compositions (see Methods) in the absence (EDTA) or presence (Ca^{2+}) of calcium ions. Top (T), middle (M1, M2) and bottom (B) fractions were analysed by western blot.

rule out an additional block by the antibodies at a stage before endosomal uptake. As discussed in Supplementary Information, the location of this exposed epitope on E1 also provides clues about the way the molecule may be presented at the surface of infectious virions (Supplementary Fig. 8). In particular, it suggests that, unlike alphaviruses and flaviviruses, mature rubella virions may not display a rigid glycoprotein shell covering the viral membrane, in line with very recent electron cryo-tomographic studies on mature rubella virions¹⁹.

The structural comparisons in Table 1 show that the fusion glycoproteins encoded by viruses of the two genera (*Alphavirus* and *Rubivirus*) present in the *Togaviridae* family are much more distant to each other structurally than are their counterparts from different subfamilies in the *Herpesviridae* family, for example. Also, despite belonging to different viral families, the alphavirus and flavivirus envelope proteins seem to have undergone a more conservative evolution (Table 1), perhaps because of stronger constraints exerted on viruses alternating between arthropod and vertebrate hosts. Infecting only humans, rubella virus thus seems to have evolved further to occupy a distant niche. A similar process may have occurred with the strictly human hepatitis C virus in the *Flaviviridae* family²⁰.

In summary, the structure of rubella virus E1 revealed a class II fusion protein that has evolved a number of specific features, placing it apart from the class II fusion proteins of known structure. In particular, its unique fusion surface (Supplementary Video 1) has not been described for any other viral fusion protein. The ability of E1e to form two-dimensional crystalline arrays on membranes (Fig. 1) now offers the opportunity to study the membrane-bound conformation of the fusion surface by electron crystallography. Comparative structural studies such as this one, revealing both specific elements in each virus and functional parallels across families, may help to identify common essential features that could constitute potential Achilles heels against which to direct antiviral strategies.

METHODS SUMMARY

Rubella virus E1e was cloned and produced as a secreted protein from *Drosophila melanogaster* S2 cells as explained in Methods. Purified E1e, alone or co-floating

with liposomes in a sucrose gradient, was analysed by staining with 2% (w/v) uranyl acetate with a Phillips CM12 microscope operated at 120 kV. Images were recorded in low-dose mode at a nominal magnification of $\times 42,000$ in a KeenView Soft Imaging System.

E1e crystals grew overnight in 1–3% polyethylene glycol 4000, 0.1 M HEPES buffer, pH 7.5–8.0, and 30% glycerol. Heavy-atom derivative crystals were obtained by soaking crystals overnight in 8% polyethylene glycol 4000, 0.1 M HEPES, pH 7.5, 30% glycerol and 10 mM potassium hexachlororhenate. Diffraction data were collected at 100 K at synchrotron sources to 1.78 and 3.40 Å resolution for native and rhenium derivative crystals, respectively. The structure was determined and refined as described in Methods. All data collection and refinement statistics are listed in Supplementary Table 1, and the lipid-head-groups tested in co-crystallization trials are listed in Supplementary Table 2.

Full Methods and any associated references are available in the online version of the paper.

Received 18 June; accepted 31 October 2012.

Published online 6 January 2013.

- Hobman, T. C. & Chantler, J. K. in *Fields Virology* Vol. 1 (ed. D. M. Knipe) 1069–1100 (Lippincott Williams & Wilkins, 2007).
- Katow, S. & Sugiura, A. Antibody response to individual rubella virus proteins in congenital and other rubella virus infections. *J. Clin. Microbiol.* **21**, 449–451 (1985).
- Cong, H., Jiang, Y. & Tien, P. Identification of the myelin oligodendrocyte glycoprotein as a cellular receptor for rubella virus. *J. Virol.* **85**, 11038–11047 (2011).
- Katow, S. & Sugiura, A. Low pH-induced conformational change of rubella virus envelope proteins. *J. Gen. Virol.* **69**, 2797–2807 (1988).
- Kee, S. H. *et al.* Effects of endocytosis inhibitory drugs on rubella virus entry into VeroE6 cells. *Microbiol. Immunol.* **48**, 823–829 (2004).
- Petruzzello, R. *et al.* Pathway of rubella virus infectious entry into Vero cells. *J. Gen. Virol.* **77**, 303–308 (1996).
- Gibbons, D. L. *et al.* Visualization of the target-membrane-inserted fusion protein of Semliki Forest virus by combined electron microscopy and crystallography. *Cell* **114**, 573–583 (2003).
- Stiasny, K., Allison, S. L., Schlich, J. & Heinz, F. X. Membrane interactions of the tick-borne encephalitis virus fusion protein E at low pH. *J. Virol.* **76**, 3784–3790 (2002).
- Stiasny, K., Bressanelli, S., Lepault, J., Rey, F. A. & Heinz, F. X. Characterization of a membrane-associated trimeric low-pH-induced form of the class II viral fusion protein E from tick-borne encephalitis virus and its crystallization. *J. Virol.* **78**, 3178–3183 (2004).
- Bennett, M. J., Schlunegger, M. P. & Eisenberg, D. 3D domain swapping: a mechanism for oligomer assembly. *Protein Sci.* **4**, 2455–2468 (1995).
- Holm, L. & Rosenstrom, P. Dali server: conservation mapping in 3D. *Nucleic Acids Res.* **38**, W545–W549 (2010).
- Qiu, Z., Yao, J., Cao, H. & Gillam, S. Mutations in the E1 hydrophobic domain of rubella virus impair virus infectivity but not virus assembly. *J. Virol.* **74**, 6637–6642 (2000).
- Santiago, C. *et al.* Structures of T cell immunoglobulin mucin receptors 1 and 2 reveal mechanisms for regulation of immune responses by the TIM receptor family. *Immunity* **26**, 299–310 (2007).
- Goldstein, D. A. in *Clinical Methods: The History, Physical, and Laboratory Examinations* Ch 143 (eds H. K. Walker, W. D. Hall, & J. W. Hurst) 677–679 (1990).
- Mastromarino, P., Cioe, L., Rieti, S. & Orsi, N. Role of membrane phospholipids and glycolipids in the Vero cell surface receptor for rubella virus. *Med. Microbiol. Immunol.* **179**, 105–114 (1990).
- Kobayashi, T. *et al.* Separation and characterization of late endosomal membrane domains. *J. Biol. Chem.* **277**, 32157–32164 (2002).
- Wolinsky, J. S. *et al.* An antibody- and synthetic peptide-defined rubella virus E1 glycoprotein neutralization domain. *J. Virol.* **67**, 961–968 (1993).
- Mitchell, L. A. *et al.* Characterization of rubella virus-specific antibody responses by using a new synthetic peptide-based enzyme-linked immunosorbent assay. *J. Clin. Microbiol.* **30**, 1841–1847 (1992).
- Battisti, A. J. *et al.* Cryo-electron tomography of rubella virus. *J. Virol.* **86**, 11078–11085 (2012).
- Krey, T. *et al.* The disulfide bonds in glycoprotein E2 of hepatitis C virus reveal the tertiary organization of the molecule. *PLoS Pathog.* **6**, e1000762 (2010).
- Roussel, A., Lescar, J., Vaney, M. C., Wengler, G. & Rey, F. A. Structure and interactions at the viral surface of the envelope protein E1 of Semliki Forest virus. *Structure* **14**, 75–86 (2006).
- Voss, J. E. *et al.* Glycoprotein organization of Chikungunya virus particles revealed by X-ray crystallography. *Nature* **468**, 709–712 (2010).
- Bressanelli, S. *et al.* Structure of a flavivirus envelope glycoprotein in its low-pH-induced membrane fusion conformation. *EMBO J.* **23**, 728–738 (2004).
- Rey, F. A., Heinz, F. X., Mandl, C., Kunz, C. & Harrison, S. C. The envelope glycoprotein from tick-borne encephalitis virus at 2 Å resolution. *Nature* **375**, 291–298 (1995).
- Modis, Y., Ogata, S., Clements, D. & Harrison, S. C. Structure of the dengue virus envelope protein after membrane fusion. *Nature* **427**, 313–319 (2004).
- Nayak, V. *et al.* Crystal structure of dengue virus type 1 envelope protein in the postfusion conformation and its implications for membrane fusion. *J. Virol.* **83**, 4338–4344 (2009).

27. Roche, S., Bressanelli, S., Rey, F. A. & Gaudin, Y. Crystal structure of the low-pH form of the vesicular stomatitis virus glycoprotein G. *Science* **313**, 187–191 (2006).
28. Heldwein, E. E. *et al.* Crystal structure of glycoprotein B from herpes simplex virus 1. *Science* **313**, 217–220 (2006).
29. Backovic, M., Longnecker, R. & Jardetzky, T. S. Structure of a trimeric variant of the Epstein–Barr virus glycoprotein B. *Proc. Natl Acad. Sci. USA* **106**, 2880–2885 (2009).
30. Kadlec, J., Loureiro, S., Abrescia, N. G., Stuart, D. I. & Jones, I. M. The postfusion structure of baculovirus gp64 supports a unified view of viral fusion machines. *Nature Struct. Mol. Biol.* **15**, 1024–1030 (2008).

Supplementary Information is available in the online version of the paper.

Acknowledgements We thank A. Haouz of Institut Pasteur and the PXI beam line staff at the Swiss Light Source and PROXIMA 1 beam line at SOLEIL synchrotron facilities for assistance; C. Vornrhein at Global Phasing for expertise in phase determination; G. Bricogne for input, G. Dupras and J. M. Mallet at École Normale Supérieure in Paris for the synthesis of galactose-3-sulphate used in co-crystallization trials; and J. Casasnovas, L. Chernomordik, Y. Gaudin, S. Harrison, F. Heinz, M. Kielian and J. Lepault for discussion. R.M.D. was supported by a ‘Pasteur–Howard’ fellowship. This work was mainly funded by grant ANR-05-MIIM-012-02-Dentry to F.A.R., who also

acknowledges support from Merck-Serono from the French Government’s Investissements d’Avenir program: Laboratoire d’Excellence ‘Integrative Biology of Emerging Infectious Diseases’ (grant no. ANR-10-LABX-62-IBED).

Author Contributions R.M.D. produced and crystallized E1e. R.M.D. and M.-C.V. solved the E1e structure (with initial help from C. Vornrhein) and participated in manuscript preparation. M.A.T. performed liposome flotation assays and crystallized E1e with calcium acetate. R.A.-K. performed liposome flotation assays and electron microscopy studies. G.B.-S. characterized E1e produced in mammalian cells. T.K. constructed the modified pMT plasmid used for E1e expression. F.A.R. conceived the experiments and wrote the manuscript with R.M.D. and M.C.V.

Author Information The atomic coordinates and structure factors have been deposited in the Protein Data Bank under accession numbers 4ADI, 4ADG, 4ADJ and 4B3V. They correspond to the atomic models of Na⁺-bound E1e, Ca²⁺-bound E1e (from the galactose-3-sulphate headgroup soak (see Supplementary Table 2)), and to E1e crystallized in the presence of calcium acetate at 1 and 20 mM, respectively. Reprints and permissions information is available at www.nature.com/reprints. The authors declare no competing financial interests. Readers are welcome to comment on the online version of the paper. Correspondence and requests for materials should be addressed to F.A.R. (rey@pasteur.fr).

METHODS

E1e production. Codon-optimized synthetic cDNA corresponding to rubella virus envelope glycoproteins E2 and E1 was cloned into a modified pMT plasmid engineered for production of secreted protein from *Drosophila melanogaster* S2 cells. E2 is believed to chaperone the correct folding of E1. The amino-acid sequence corresponds to strain M33 (Swiss-Prot accession number P08563) from position 301 (the N terminus of E2) to position 1018 (that is, before the E1 transmembrane segment) of the polyprotein precursor (Supplementary Fig. 1a). The pMT plasmid was modified to add C-terminal residues: FEDDDDKAG WSHPQFEKGGGSGGGSGGWSHPQFEK (an enterokinase cleavage site is underlined and two Strep-tactin purification tags are in italics). The plasmid contains a metallothionein promoter for induction of gene expression. For translocation into the endoplasmic reticulum lumen, the plasmid encodes the signal peptide of the *Drosophila* endoplasmic reticulum-resident binding immunoglobulin protein immediately upstream of E2.

The resulting E1e expression plasmid along with a hygromycin resistance plasmid (pCoHygro) was used to obtain stably transfected S2 cells. Cells were grown to $\sim 1 \times 10^7$ cells ml^{-1} in Insect-XPRESS medium and expression was induced with 500 μM CuSO_4 . After 3 days, 100-fold concentrated S2 media supernatant was supplemented with 10 $\mu\text{g ml}^{-1}$ avidin and 0.1 M Tris buffer, pH 8.0, and E1e was purified on a Strep-tactin affinity column. E1e was further purified by Superdex 200 16/60 size-exclusion column in 10 mM Tris, pH 8.0, and 150 mM NaCl. Trimeric E1e was dialysed overnight into 10 mM Tris, pH 8.0, with no NaCl and concentrated to 2.0 mg ml^{-1} .

E1e structure determination. Crystals were grown overnight in 1–3% polyethylene glycol (PEG) 4000, 0.1 M HEPES buffer, pH 7.5, and 30% glycerol. Heavy-atom derivative crystals were obtained by soaking overnight in 8% PEG 4000, 0.1 M HEPES, pH 7.5, 30% glycerol and 10 mM K_2ReCl_6 . Crystals were plunged directly into liquid nitrogen. Diffraction data were collected at the Swiss Light Source and at SOLEIL synchrotrons. Because of clear damage at some disulphide bonds, the final data for refinement was collected with low beam intensity at cryogenic temperature on the Pilatus detector at the PX I beam line of the Swiss Light Source synchrotron and were processed with XDS³¹. Two single-wavelength anomalous dispersion (SAD) data sets were collected from derivative crystal Re-1 and one SAD data set was collected from derivative crystal Re-2 using the inverse beam method at the peak of the rhenium absorption edge (1.762 Å). SCALA combined the three SAD data sets and showed anomalous signal to 4.6 Å resolution. Location of eight rhenium sites was performed using SHELXC/D³² within autoSHARP³³. Eight additional sites were found with SHARP³⁴. The figure of merit was 0.21 for initial phases calculated from a total of 12 rhenium sites. Solvent flattening with SOLOMON³⁵ gave initial SAD phases. PROFESS identified nine rhenium sites (out of the 12 found) with three-fold symmetry and LSQKAB located the three-fold non-crystallographic axis. Density modification was performed with 1.78 Å native data using DM³⁶ and the figure of merit increased to 0.80. An initial model was built with ARP-wARP³⁷ and refinement and rebuilding was carried out with BUSTER³⁸ and Coot³⁹, respectively. In BUSTER, the local structural similarity restraints² and the autonc method were applied. Refinement was monitored following the R_{free} value calculated for a random subset (10%) of

reflections omitted from refinement. Data collection and refinement statistics are listed in Supplementary Table 1. The programs SCALA, PROFESS, LSQKAB and DM are part of the CCP4 programs suite⁴⁰. Supplementary Fig. 4c shows the final electron density in one of the regions of poorest quality, the linker between domains I and III.

Metal site analysis. On the basis of several structural validation criteria and further crystallization studies described in Supplementary Information, we identified that the Na^+ had been replaced by Ca^{2+} .

Liposome flotation experiments. Liposomes were freshly prepared by the freeze-thaw and extrusion method⁴¹. DOPS (1,2-dioleoyl-*sn*-glycero-3-phospho-L-serine), DOPE (1,2-dioleoyl-*sn*-glycero-3-phosphoethanolamine), DOPC (1,2-dioleoyl-*sn*-glycero-3-phosphocholine), cholesterol and sphingomyelin were purchased from Avanti Polar Lipids. Type 1, 2 and 3 liposomes were formed by molar ratios of 1/1/2 of DOPE/DOPS/DOPC, 1/1/2/2 of DOPE/DOPS/DOPC/cholesterol, and 1/1/2/2/2 of DOPE/DOPS/DOPC/cholesterol/sphingomyelin. E1e (1 mM) and liposomes (1 mM) were incubated overnight at 30 °C in the absence (1 mM EDTA) or presence (10 mM $\text{Ca}(\text{CH}_3\text{COO})_2$) of calcium ion at pH 5.5 (10 mM sodium phosphate buffer) and pH 7.5 (10 mM Tris-Cl) in 100 μl . To keep the amount of sodium ions constant at each pH, 10 mM NaCl was added to the samples with Tris. Samples were then mixed with an equal volume of 40% sucrose, loaded into a 5–40% sucrose gradient (at pH 5.5 or 7.5) and centrifuged overnight at 40,000 r.p.m. at 4 °C in a SW 55 Ti rotor. Fractions from top, middle and bottom regions of the gradient were analysed by western blot using an anti-Strep-tag antibody.

Electron microscopy. Samples were negatively stained with 2% (w/v) uranyl acetate and screened in a Phillips CM12 microscope operating at an accelerating voltage of 120 kV. Images were recorded in low-dose mode at a nominal magnification of $\times 42,000$ in a KeenView Soft Imaging System.

31. Kabsch, W. XDS. *Acta Crystallogr. D* **66**, 125–132 (2010).
32. Schneider, T. R. & Sheldrick, G. M. Substructure solution with SHELXD. *Acta Crystallogr. D* **58**, 1772–1779 (2002).
33. Vonrhein, C., Blanc, E., Roversi, P. & Bricogne, G. Automated structure solution with autoSHARP. *Methods Mol. Biol.* **364**, 215–230 (2007).
34. Bricogne, G., Vonrhein, C., Flensburg, C., Schiltz, M. & Paciorek, W. Generation, representation and flow of phase information in structure determination: recent developments in and around SHARP 2.0. *Acta Crystallogr. D* **59**, 2023–2030 (2003).
35. Abrahams, J. P. & Leslie, A. G. Methods used in the structure determination of bovine mitochondrial F1 ATPase. *Acta Crystallogr. D* **52**, 30–42 (1996).
36. Cowtan, K. dm: an automated procedure for phase improvement by density modification. *Joint CCP4 and ESF-EACBM Newsletter on Protein Crystallography* **31**, 34–38 (1994).
37. Langer, G., Cohen, S. X., Lamzin, V. S. & Perrakis, A. Automated macromolecular model building for X-ray crystallography using ARP/wARP version 7. *Nature Protocols* **3**, 1171–1179 (2008).
38. Bricogne, G. et al. BUSTER, version 2.8.0 (Global Phasing, 2009).
39. Emsley, P. & Cowtan, K. Coot: model-building tools for molecular graphics. *Acta Crystallogr. D* **60**, 2126–2132 (2004).
40. Collaborative Computational Project, Number 4. The CCP4 suite: programs for protein crystallography. *Acta Crystallogr. D* **50**, 760–763 (1994).
41. Castile, J. D. & Taylor, K. M. Factors affecting the size distribution of liposomes produced by freeze-thaw extrusion. *Int. J. Pharm.* **188**, 87–95 (1999).

RNAi triggered by specialized machinery silences developmental genes and retrotransposons

Soichiro Yamanaka¹, Sameet Mehta¹, Francisca E. Reyes-Turcu¹, Fanglei Zhuang², Ryan T. Fuchs², Yikang Rong¹, Gregory B. Robb² & Shiv I. S. Grewal¹

RNA interference (RNAi) is a conserved mechanism in which small interfering RNAs (siRNAs) guide the degradation of cognate RNAs, but also promote heterochromatin assembly at repetitive DNA elements such as centromeric repeats^{1,2}. However, the full extent of RNAi functions and its endogenous targets have not been explored. Here we show that, in the fission yeast *Schizosaccharomyces pombe*, RNAi and heterochromatin factors cooperate to silence diverse loci, including sexual differentiation genes, genes encoding transmembrane proteins, and retrotransposons that are also targeted by the exosome RNA degradation machinery. In the absence of the exosome, transcripts are processed preferentially by the RNAi machinery, revealing siRNA clusters and a corresponding increase in heterochromatin modifications across large domains containing genes and retrotransposons. We show that the generation of siRNAs and heterochromatin assembly by RNAi is triggered by a mechanism involving the canonical poly(A) polymerase Pla1 and an associated RNA surveillance factor Red1, which also activate the exosome. Notably, siRNA production and heterochromatin modifications at these target loci are regulated by environmental growth conditions, and by developmental signals that induce gene expression during sexual differentiation. Our analyses uncover an interaction between RNAi and the exosome that is conserved in *Drosophila*, and show that differentiation signals modulate RNAi silencing to regulate developmental genes.

In *S. pombe*, centromeric transcripts are processed by RNAi factors including the Argonaute (Ago1)-containing RNA-induced transcriptional silencing (RITS) complex, the RNA-dependent RNA polymerase (Rdp1) and Dicer (Dcr1)². Processing of transcripts into siRNAs is coupled to loading of Clr4, a homologue of mammalian SUV39H, required for histone H3 lysine 9 methylation (H3K9me)^{3,4}. Whereas most siRNAs correspond to centromeric repeats^{5,6}, siRNAs that match other repetitive structures such as *Tf2* retrotransposons have not previously been detected.

The 3′–5′ exonuclease activity of the exosome that also processes heterochromatic transcripts^{7–9} acts in an overlapping manner to RNAi to silence centromeric transcripts¹⁰, suggesting that RNAi and the exosome share targets. Recent studies have revealed widespread transcription of the genome^{7,11,12}, producing transcripts that are regulated by the exosome⁷. Under specific growth or developmental conditions, some of these transcripts may also feed into the RNAi pathway to generate siRNAs for heterochromatin assembly. Such RNAi targets might be detected in an exosome mutant, in which transcripts would be processed preferentially by RNAi machinery.

We performed high-throughput sequencing of small RNAs in cells lacking the exosome subunit Rrp6 to identify RNAi targets throughout the genome. We observed small RNA clusters mapping to various genomic locations. Equal densities of small RNA reads match forward and reverse strands of specific loci, and are abolished in RNAi mutants (Supplementary Table 1 and Figs 1 and 2). Overlapping transcription at convergent genes could induce RNAi¹³, but siRNA clusters are also observed at non-convergent loci, indicating an alternative mechanism.

Previously unknown RNAi targets include loci in subtelomeric regions as well as protein-coding genes, and siRNA clusters correlate with H3K9me enrichment (Supplementary Fig. 1 and Supplementary Table 1). H3K9me peaks are dependent on RNAi (Figs 1 and 2), and are distinct from heterochromatin islands that can be assembled without RNAi¹⁴. Closer examination of heterochromatin domains (HOODs) formed by RNAi shows that H3K9me and siRNA clusters are preferentially targeted to genes upregulated during sexual differentiation, as well as genes encoding transmembrane domain proteins (Supplementary Table 1). Several siRNA clusters overlap non-coding

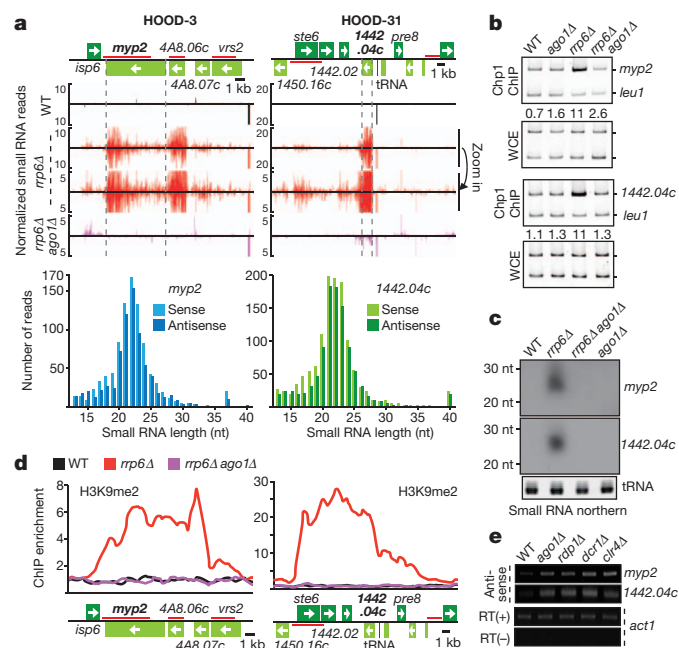


Figure 1 | siRNA clusters and RNAi-dependent assembly of heterochromatin at gene-containing regions. **a**, The normalized number of small RNA reads are plotted. The signals above and below the line represent small RNAs that map to the top and bottom DNA strands, respectively. siRNA mapping to *myo2* and *SPCC1442.04c* (1442.04c) and their length profiles are shown. nt, nucleotides. **b**, Chromatin immunoprecipitation (ChIP) showing ChIP enrichment at the indicated loci. The intensities of bands representing each locus and the *leu1* control in ChIP and whole-cell crude extract (WCE) lanes were used to calculate the relative fold enrichments shown. **c**, Northern blot with probes specific to *myo2* or *SPCC1442.04c* was used to detect siRNAs. Transfer RNA serves as a loading control. **d**, The H3K9me2 was mapped by ChIP-chip. siRNA clusters and H3K9me map to the open reading frames of multiple genes, but their distribution decreases sharply, in some cases coinciding with transcription factor TFIIC-binding sites, such as *tRNAs*, that are known to serve as heterochromatin boundaries. **e**, Detection of antisense transcripts generated from *myo2* or *SPCC1442.04c* loci was performed using PCR with reverse transcription (RT-PCR). The *act1* transcript level was used as a control. RT(+) and RT(–), reverse transcriptase present or absent, respectively.

¹Laboratory of Biochemistry and Molecular Biology, National Cancer Institute, National Institutes of Health, Bethesda, Maryland 20892, USA. ²New England Biolabs, Ipswich, Massachusetts 01938, USA.

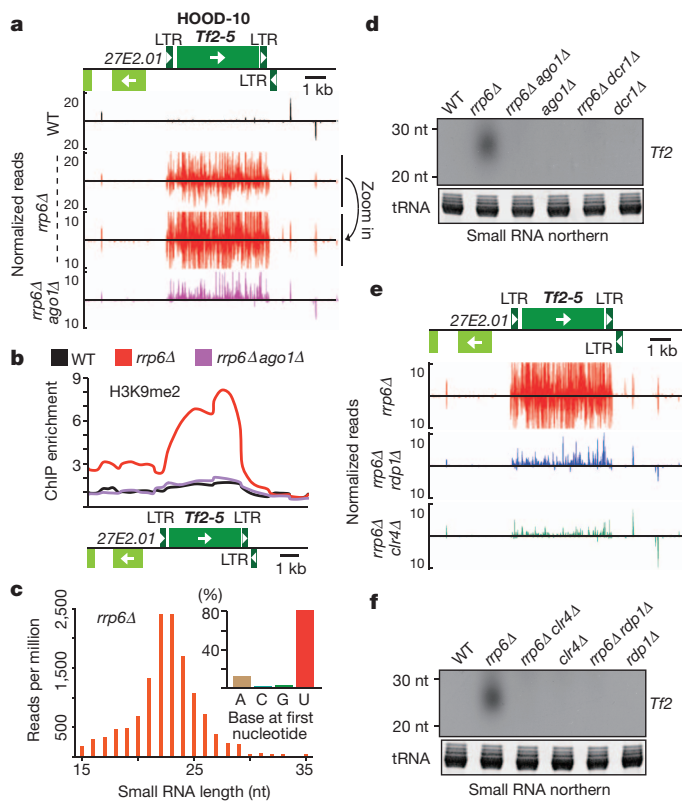


Figure 2 | *Tf2* retrotransposons produce siRNAs and show RNAi-dependent heterochromatin formation. **a**, The small RNA reads that map to the region containing *Tf2-5* in the indicated strains are plotted. **b**, The H3K9me2 distribution was determined by ChIP-chip. **c**, The length profile of small RNAs mapping to the antisense strand of *Tf2* is shown. The inset graph shows the frequency of the base at the 5' end of reads that map to *Tf2*. **d**, Northern blot with probes specific for *Tf2* was used to detect siRNAs. tRNA serves as a loading control. **e**, Effects of Clr4 and Rdp1 on siRNAs mapping to *Tf2*. The small reads mapping to *Tf2-5* in the indicated strains are plotted. **f**, Analysis of Clr4 and Rdp1 requirement for production of *Tf2* siRNAs. Results of the northern blot analysis using the indicated strains are shown.

RNA (ncRNA; Supplementary Table 1)¹⁵, which could potentially trigger RNAi¹⁶.

Small RNAs that map to genes are predominantly 20–24 nucleotides long (Fig. 1a), consistent with RITS-associated siRNAs⁵. Indeed, RITS subunit Chp1 localized to these loci (Fig. 1b). Small RNA production also requires Ago1 (Fig. 1a). The remaining reads in *ago1Δ rrp6Δ* display a broad length distribution consistent with degradation products (Supplementary Fig. 2). Ago1-dependent production of siRNA from *myp2* and *SPCC1442.04c* was confirmed by northern blot (Fig. 1c), and is required for H3K9me at these loci (Fig. 1d and Supplementary Fig. 3a). In *rrp6*⁺ cells, loss of Ago1, Dcr1, Rdp1 or Clr4 stabilized antisense transcripts from *myp2* and *SPCC1442.04c* (Fig. 1e), implicating RNAi and Clr4 in the regulation of these loci in wild-type cells.

Retrotransposons are silenced by several mechanisms to ensure genome stability¹⁷. In *S. pombe*, centromere protein CENP-B homologues and chromatin modifiers silence *Tf2* retrotransposons and their remnants^{18,19}. RNAi mutants show mild *Tf2* derepression and siRNAs mapping to these loci have not been detected^{20,21}. We observed siRNA clusters and H3K9me in *rrp6Δ* at *Tf2* (Fig. 2a, b and Supplementary Fig. 3b). Small RNAs that map to the antisense strand show a preference for uridine at the 5' end and a length profile of 20–24 nucleotides, whereas a portion of those mapping to the sense strand are probably degradation products (Fig. 2c). H3K9me is restricted to the *Tf2* open reading frame except for *Tf2* retrotransposons located in close proximity where H3K9me could be detected at intervening

regions (Supplementary Fig. 4a). siRNA generation and H3K9me at *Tf2* requires Ago1 and Dcr1 (Fig. 2a, b, d and Supplementary Fig. 4a). RNAi is also required for H3K9me and siRNA clusters at other repetitive elements, including a membrane transporter gene duplicated in tandem and flanked by long terminal repeats (LTRs; Supplementary Fig. 4b).

We next asked whether Clr4 is required for generation of siRNAs in a manner similar to its role at centromeres². Small RNA profiling of *rrp6Δ clr4Δ* revealed that Clr4 is essential for siRNA production at *Tf2* (Fig. 2e, f), genes (Supplementary Fig. 5 and Supplementary Table 1) and regions with little or no H3K9me (Supplementary Fig. 6a, b). Loss of Rdp1, which requires Clr4 for chromatin association², also abolished siRNA clusters (Fig. 2e, f and Supplementary Fig. 5). Thus, heterochromatin and RNAi factors cooperate to generate siRNA clusters.

We also explored assembly of HOODs in wild-type *S. pombe* cells cultured under varied growth conditions experienced in the natural environment. HOODs were observed in cells grown in carbon-limiting conditions or at low temperature (Supplementary Fig. 7). In low glucose, cells showed elevated levels of H3K9me at several HOODs including *Tf2*, *SPBC2D10.04* and the meiotic *mcp5* gene (Supplementary Fig. 7a, 8). Importantly, generation of siRNAs and HOOD formation at these loci were impaired in *ago1Δ* (Supplementary Fig. 8). Thus, assembly of HOODs is regulated by growth conditions in wild-type cells.

We investigated the functional significance of RNAi and heterochromatin factors in silencing target loci. Cells lacking Clr4 or RNAi in combination with *rrp6Δ* showed severe defects in silencing of *Tf2* and sexual differentiation genes (for example, *mug5*, *mcp3*, *mek1* and *SPCC1442.04c*), in contrast to mild or no defects in single mutants (Fig. 3 and Supplementary Fig. 6c). Transcript levels were higher when *rrp6Δ* was combined with RNAi mutants than when combined with *clr4Δ* (Fig. 3a). These data clearly show that both RNAi and the exosome are important to fully silence these target loci.

Targeting of centromeric repeats by RNAi confers epigenetic repression on surrounding loci^{22,23}. We found that both RNAi and the exosome coordinate the silencing of multiple loci within HOODs (Fig. 3b–d). Importantly, deletion of *man1* caused loss of H3K9me and defective silencing of surrounding genes (Fig. 3c, d). This finding reveals that nucleation of heterochromatin at genes via RNAi can modulate expression of other genes in *cis*.

Several siRNA clusters map to known targets of the RNA surveillance factor Red1, which silences sexual differentiation genes, genes encoding transmembrane proteins and *Tf2* (ref. 24). Red1 interacts with the poly(A) polymerase Pla1 and degrades transcripts via a mechanism involving the poly(A)-binding protein Pab2 and the exosome^{24–26}. Combining *rrp6Δ* with *red1Δ*, *pab2Δ* or *pla1-37* caused a reduction in siRNAs and H3K9me at *Tf2* and most genes (Fig. 4a, b and Supplementary Figs 1, 9–11 and Supplementary Table 2). By contrast, loss of the RNA-binding protein Mmi1 that directs the exosome and RNAi to certain meiotic loci²⁷ had no effect on siRNAs and H3K9me at most HOODs, except for a few loci including *man1* (Supplementary Figs 5 and 10 and Supplementary Table 2). Interestingly, defects in Pla1 or Pab2 caused a reduction of H3K9me and siRNA clusters at *SPCC1442.04c* and *ste6*, whereas *red1Δ* had little effect (Fig. 4c). Therefore, Pla1 and Pab2 may represent core machinery that cooperates with other factors, as dictated by genomic contexts, to direct H3K9me by RNAi.

We asked whether Pla1 channels transcripts into the exosome and RNAi pathways. Our analysis revealed increased stabilization of *Tf2* and gene transcripts in *pla1-37 rrp6Δ*, similar to *ago1Δ rrp6Δ* or *dcr1Δ rrp6Δ* (Fig. 4d). Together with previous findings^{24,26}, these results indicate that Pla1 and associated factors such as Red1 process RNAs that feed into the exosome and RNAi machinery. Indeed, loss of both Rrp6 and Ago1 was required to abolish H3K9me at *mcp5*, whereas *red1Δ* single deletion eliminated heterochromatin modification at this locus (Supplementary Fig. 12).

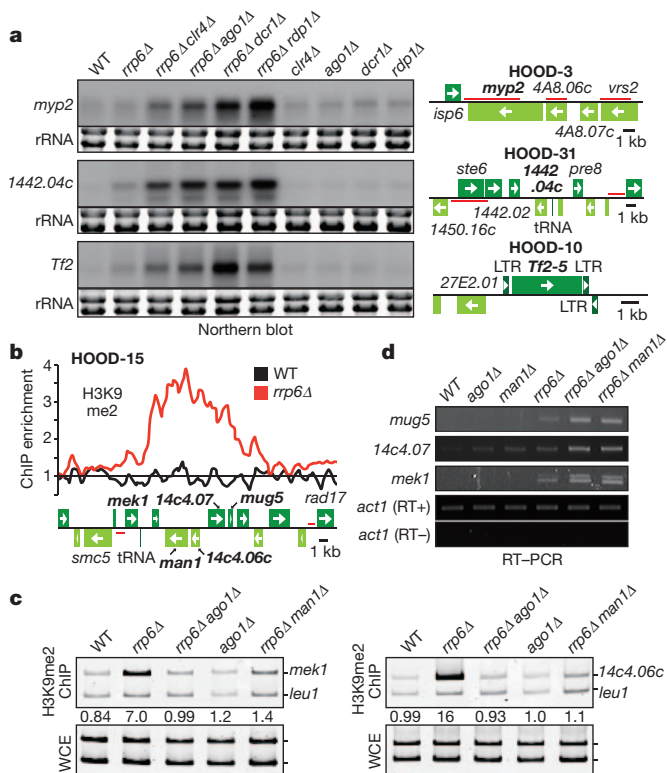


Figure 3 | RNAi and heterochromatin factors act in an overlapping manner with the exosome to silence genes located in HOODs. **a**, The role of Ctr4 and RNAi in silencing *myp2*, *SPCC1442.04c* and *Tf2* was analysed by northern blot analysis with a strand-specific probe to detect sense transcript. rRNA, ribosomal RNA. **b**, The H3K9me distribution across HOOD-15 as determined by ChIP-chip analysis of wild-type and *rrp6Δ* cells is shown. **c**, The effect of deleting the HOOD-15 *man1* gene, which contains a major siRNA cluster, on H3K9me at the nearby *mek1* and *SPAC14c4.06c* loci was determined by ChIP. **d**, The effect of *man1Δ* on silencing of other genes in HOOD-15 was determined by strand-specific RT-PCR.

Because many of the RNAi targets are developmentally regulated, we asked whether assembly of HOODs might be regulated in a similar manner. We induced sexual differentiation in nitrogen-starved *M* (*mat1-M*) cells through ectopic expression of *mat1-Pc*. Whereas nitrogen starvation alone had no effect, *mat1-Pc* expression caused the loss of siRNAs and H3K9me at *myp2* and *SPCC1442.04c* (Fig. 4e). siRNAs that map to *Tf2* were still detected (Fig. 4f), indicating that developmental signals selectively target HOODs that contain genes activated during sexual differentiation.

Finally, we explored the connection between RNAi and the exosome in higher eukaryotes. Small-RNA profiling of *Drosophila rrp6*^{-/-} revealed an increase in reads that map to repeat elements, as compared with control *rrp6*^{+/-} larvae (Supplementary Fig. 13a, b). These small RNAs are predominantly 25–28 nucleotides and frequently begin with uracil, similar to Piwi-interacting RNA (piRNAs; Supplementary Fig. 13c, d)¹⁷. The sense and antisense transcripts of retroelements are upregulated in *rrp6*^{-/-} larvae (Supplementary Fig. 13e). An increase in small RNAs that correspond to piRNA clusters (such as 42AB) was also observed (Supplementary Fig. 14), indicating that RNAi processes repeat transcripts in the absence of the exosome.

Our analyses indicate that RNAi collaborates with heterochromatin factors to silence developmentally regulated loci and retrotransposons, which are also targeted by the exosome. Although not all loci displaying siRNA clusters in *rrp6Δ* might be bona fide targets, RNAi regulates several of these loci in response to physiological conditions in wild-type cells. The exosome may modulate the level of transcripts and/or siRNAs that trigger RNAi in response to developmental and environmental signals. In this regard, RNAi serves as an adaptive response

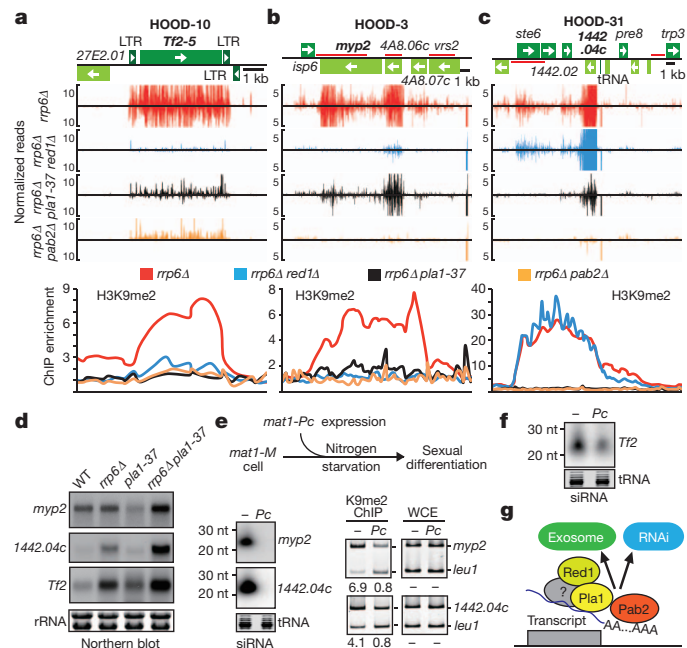


Figure 4 | Specialized machinery triggers RNAi to regulate developmental genes and silence retroelements. **a–c**, Small RNA reads in the indicated strains are plotted along the genomic region of HOOD-10 (**a**), HOOD-3 (**b**) and HOOD-31 (**c**). Because *pla1* is essential, a partial loss-of-function *pla1-37* allele was used. H3K9me distribution was determined by ChIP-chip. **d**, Northern blot analysis of sense transcripts produced from *myp2*, *SPCC1442.04c* and *Tf2* loci in the indicated strains. **e**, Induction of sexual differentiation by ectopic expression of *mat1-Pc* (*Pc*) in *M* (*mat1-M*) cells under nitrogen starvation conditions was used to assay siRNA and H3K9me at the *myp2* and *SPCC1442.04c* loci. **f**, Detection of siRNAs mapping to *Tf2* under conditions that induce sexual differentiation. **g**, Schematic representation of the current model. Transcripts from sexual differentiation genes, genes containing transmembrane domains and retroelements are recognized by a mechanism involving Pla1, Red1 and Pab2, which promotes degradation of RNAs by RNAi and/or the exosome.

mechanism that reprograms the genome under specific growth conditions. RNAi is triggered at developmentally regulated loci by specialized machinery that includes Red1 and Pla1 (Fig. 4g). These factors redistribute during sexual differentiation²⁴, and may be targets of a signalling cascade that regulates siRNA production. Other poly(A) polymerases, including Mlo3-TRAMP (Trf4–Air2–Mtr4 polyadenylation, note that Trf4 and Air2 are known as Cid14 and Air1, respectively, in *S. pombe*) that also activates both the exosome and RNAi⁷, may share targets with Pla1 and Red1. Indeed, Mlo3 and TRAMP are required for silencing *Tf2* and duplicated genes⁷. Future studies may reveal interaction between RNA processing activities required for gene silencing during development and for genome stability in *S. pombe* and higher eukaryotes.

METHODS SUMMARY

ChIPs were performed using an anti-H3K9me antibody (Abcam) as described previously⁵. The preparation of small RNA libraries is described in the Methods. For detection of small RNAs by northern blot, 10 μg of small RNAs, purified using a mirVana miRNA isolation kit (Ambion), were resolved on a 15% denaturing gel, crosslinked to neutral nylon membranes (Amersham/Pharmacia) and detected using a ~50-nucleotide ³²P-labelled single-stranded RNA probe.

Full Methods and any associated references are available in the online version of the paper.

Received 2 April; accepted 26 October 2012.

Published online 14 November 2012.

- Matzke, M. A. & Birchler, J. A. RNAi-mediated pathways in the nucleus. *Nature Rev. Genet.* **6**, 24–35 (2005).

2. Reyes-Turcu, F. E. & Grewal, S. I. S. Different means, same end-heterochromatin formation by RNAi and RNAi-independent RNA processing factors in fission yeast. *Curr. Opin. Genet. Dev.* **22**, 156–163 (2012).
3. Bayne, E. H. *et al.* Stc1: a critical link between RNAi and chromatin modification required for heterochromatin integrity. *Cell* **140**, 666–677 (2010).
4. Zhang, K., Mosch, K., Fischle, W. & Grewal, S. I. S. Roles of the Ctr4 methyltransferase complex in nucleation, spreading and maintenance of heterochromatin. *Nature Struct. Mol. Biol.* **15**, 381–388 (2008).
5. Cam, H. P. *et al.* Comprehensive analysis of heterochromatin- and RNAi-mediated epigenetic control of the fission yeast genome. *Nature Genet.* **37**, 809–819 (2005).
6. Djupedal, I. *et al.* Analysis of small RNA in fission yeast; centromeric siRNAs are potentially generated through a structured RNA. *EMBO J.* **28**, 3832–3844 (2009).
7. Zhang, K. *et al.* Ctr4/Suv39 and RNA quality control factors cooperate to trigger RNAi and suppress antisense RNA. *Science* **331**, 1624–1627 (2011).
8. Murakami, H. *et al.* Ribonuclease activity of Dis3 is required for mitotic progression and provides a possible link between heterochromatin and kinetochore function. *PLoS ONE* **2**, e317 (2007).
9. Bühler, M., Haas, W., Gygi, S. P. & Moazed, D. RNAi-dependent and -independent RNA turnover mechanisms contribute to heterochromatic gene silencing. *Cell* **129**, 707–721 (2007).
10. Reyes-Turcu, F. E., Zhang, K., Zofall, M., Chen, E. & Grewal, S. I. S. Defects in RNA quality control factors reveal RNAi-independent nucleation of heterochromatin. *Nature Struct. Mol. Biol.* **18**, 1132–1138 (2011).
11. Dutrow, N. *et al.* Dynamic transcriptome of *Schizosaccharomyces pombe* shown by RNA-DNA hybrid mapping. *Nature Genet.* **40**, 977–986 (2008).
12. Wilhelm, B. T. *et al.* Dynamic repertoire of a eukaryotic transcriptome surveyed at single-nucleotide resolution. *Nature* **453**, 1239–1243 (2008).
13. Gullerova, M. & Proudfoot, N. J. Cohesin complex promotes transcriptional termination between convergent genes in *S. pombe*. *Cell* **132**, 983–995 (2008).
14. Zofall, M. *et al.* RNA elimination machinery targeting meiotic mRNAs promotes facultative heterochromatin formation. *Science* **335**, 96–100 (2012).
15. Rhind, N. *et al.* Comparative functional genomics of the fission yeasts. *Science* **332**, 930–936 (2011).
16. Bitton, D. A. *et al.* Programmed fluctuations in sense/antisense transcript ratios drive sexual differentiation in *S. pombe*. *Mol. Syst. Biol.* **7**, 559 (2011).
17. Malone, C. D. & Hannon, G. J. Small RNAs as guardians of the genome. *Cell* **136**, 656–668 (2009).
18. Cam, H. P., Noma, K., Ebina, H., Levin, H. L. & Grewal, S. I. S. Host genome surveillance for retrotransposons by transposon-derived proteins. *Nature* **451**, 431–436 (2008).
19. Anderson, H. E. *et al.* The fission yeast HIRA histone chaperone is required for promoter silencing and the suppression of cryptic antisense transcripts. *Mol. Cell. Biol.* **29**, 5158–5167 (2009).
20. Hansen, K. R. *et al.* Global effects on gene expression in fission yeast by silencing and RNA interference machineries. *Mol. Cell. Biol.* **25**, 590–601 (2005).
21. Woolcock, K. J., Gaidatzis, D., Punga, T. & Buhler, M. Dicer associates with chromatin to repress genome activity in *Schizosaccharomyces pombe*. *Nature Struct. Mol. Biol.* **18**, 94–99 (2011).
22. Hall, I. M. *et al.* Establishment and maintenance of a heterochromatin domain. *Science* **297**, 2232–2237 (2002).
23. Partridge, J. F., Scott, K. S., Bannister, A. J., Kouzarides, T. & Allshire, R. C. *cis*-acting DNA from fission yeast centromeres mediates histone H3 methylation and recruitment of silencing factors and cohesin to an ectopic site. *Curr. Biol.* **12**, 1652–1660 (2002).
24. Sugiyama, T. & Sugioka-Sugiyama, R. Red1 promotes the elimination of meiosis-specific mRNAs in vegetatively growing fission yeast. *EMBO J.* **30**, 1027–1039 (2011).
25. Lemay, J. F. *et al.* The nuclear poly(A)-binding protein interacts with the exosome to promote synthesis of noncoding small nucleolar RNAs. *Mol. Cell* **37**, 34–45 (2010).
26. Yamanaka, S., Yamashita, A., Harigaya, Y., Iwata, R. & Yamamoto, M. Importance of polyadenylation in the selective elimination of meiotic mRNAs in growing *S. pombe* cells. *EMBO J.* **29**, 2173–2181 (2010).
27. Hiriart, E. *et al.* Mmi1 RNA surveillance machinery directs RNAi complex RITS to specific meiotic genes in fission yeast. *EMBO J.* **31**, 2296–2308 (2012).

Supplementary Information is available in the online version of the paper.

Acknowledgements We thank M. Zofall and K. Zhang for contributions, J. Barrowman for editing the manuscript, M. Yamamoto for the *pla1-37* strain, E. Lei for the *Drosophila rrp6* mutant, B. Walker and M. Pineda for their help in sequencing, and Grewal laboratory members for discussions. This study used the Helix Systems and the Biowulf Linux cluster at the National Institutes of Health. This work was supported by the Intramural Research Program of the National Institutes of Health, National Cancer Institute.

Author Contributions S.Y. and S.I.S.G. designed the experiments. F.Z., R.T.F., S.Y. and G.B.R. prepared the library of small RNA for deep sequencing. S.M. processed the deep-sequencing data. S.Y., S.M. and S.I.S.G. analysed the data. F.E.R.-T. and S.Y. carried out ChIP-chip. Y.R. performed the *Drosophila* genetic crosses. S.Y. performed all other experiments, if not stated. S.I.S.G. wrote the paper with input from all of the authors.

Author Information Microarray and sequencing data are available at the NCBI Gene Expression Omnibus (GEO) repository under the accession number GSE41643. Reprints and permissions information is available at www.nature.com/reprints. The authors declare no competing financial interests. Readers are welcome to comment on the online version of the paper. Correspondence and requests for materials should be addressed to S.I.S.G. (grewals@mail.nih.gov).

METHODS

Strains and media. Standard protocols were used for cell culture, sporulation and tetrad analysis. Deletion of endogenous *man1* was performed by PCR-based gene targeting with clonNAT resistant genes as selection markers. Because the *pla1* gene is essential for growth, a partial loss-of-function mutant allele of *pla1* (*pla1-37*) (a gift from M. Yamamoto's laboratory) was used. Wild-type and mutant cells were grown at 30 °C or 32 °C in either rich (YEA) or minimal (EMM) media. For nitrogen starvation, cells were cultured in EMM medium lacking nitrogen source. Strains and oligonucleotides used in this study are listed in Supplementary Tables 3 and 4, respectively.

Small RNA library construction. Small RNA fractions <40 nucleotides were prepared by gel purification from denaturing acrylamide gels, or by using flashPAGE fractionation (Life Technologies) according to the manufacturer's recommendation²⁸. Small RNAs were treated with calf intestinal alkaline phosphatase (CIP) for 1 h at 37 °C at a ratio of 1 unit of CIP (New England Biolabs (NEB)) per pmol of RNA to remove mono-, di- and triphosphates. After phenol/chloroform/isoamyl alcohol extraction and ethanol precipitation, 3'-adapters (5'-AppTCGTATGCGTCTTCTGCTTGT-NH₂-3', App denotes phosphorylated adenosine) were ligated overnight at 16 °C under conditions that are insensitive to 2'-O-methylation of the terminal nucleotide²⁸ (50 mM Tris pH 7.5, 10 mM MgCl₂, 1 mM DTT, 12.5% PEG.) Typical ligations contained ~1–3 pmol (~10–30 ng) of small RNA. Adapters were in molar excess of RNA, and reactions contained 200 units of T4 Rnl2 truncated enzyme and 20 units of murine RNase inhibitor in a total volume of 20 µl. Ten microlitres of the 3'-ligated RNA was phosphorylated by adding 3 µl of water, 0.5 µl of T4 Rnl1 buffer and 0.5 µl (20 U) of murine RNase inhibitor, and 1 µl (10 units) of T4 PNK (NEB) followed by incubation at 37 °C for 30 min. Final buffer composition for this reaction was 50 mM Tris pH 7.5, 10 mM MgCl₂, 1 mM DTT, 8.25% PEG, 0.33 mM ATP in a 15 µl reaction volume. The kinase was inactivated and the reverse transcription primer was annealed by adding a twofold molar excess (compared to 3'-linker) of reverse transcription primer and water in a volume of 5 µl. The 20 µl mixture was heated to 75 °C for 10 min, incubated at 37 °C for 10 min, and then cooled to 25 °C. 22.5 pmol of 5'-adapters (5'-rGrUrUrCrArGrArGrUrUrCrArGrUrCrCrGrArCrGrArUrC-3'), 20 units of murine RNase inhibitor and 20 units of T4 RNA ligase 1 were added directly to the 3'-ligations and annealed to small RNA in a total reaction volume of 24 µl. Ligation reactions were incubated at 25 °C for 1 h. Half (12 µl) of the doubly ligated small RNA was reverse transcribed using avian myeloblastosis virus reverse transcriptase following the manufacturer's instructions (NEB) for 30 min at 42 °C. One-third of the cDNA was PCR amplified for 6–12 cycles using the primers 5'-CAAGCAGAAGACGGCATACG-s-A-3', and 5'-AATGATACGGCGACCACCGACAGGTTCTAGAGTCTACAGTCCG-s-A-3' (where -s- denotes phosphorothioate linkage) using 2× LongAmp Taq Mastermix (NEB). PCR reactions were separated by native 6% PAGE. Amplified DNA was visualized by ultraviolet transillumination using SybrGold nucleic acid stain (Life Technologies), and regions of the gel corresponding to RNA insert sizes of 18–40 nucleotides were excised, crushed and eluted from the gel in TE pH 8 for >2 h at 25 °C. Libraries were concentrated using QiaQuick columns (Qiagen) and analysed using DNA1000 chips and reagents on an Agilent 2100 BioAnalyzer (Agilent).

ChIP analysis. ChIP and ChIP-chip analyses were performed as described previously with antibodies against dimethylated H3K9 (Abcam)⁵. In brief, exponentially growing cells (5 × 10⁸) were fixed in 3% paraformaldehyde and chromatin. For ChIP of Chp1, cells were subsequently crosslinked by treatment with 10 mM dimethyl adipimidate. Cells were washed with PBS, resuspended in lysis buffer (50 mM HEPES/KOH, pH 7.5, 140 mM NaCl, 1 mM EDTA, 1% Triton X-100, 0.1% deoxycholate) and homogenized with glass beads. Chromatin was sheared by sonication to fragments of 500–1,000 base pairs, precleared with protein A slurry and immunoprecipitated with 2–4 µg of antibody. Immunoprecipitated chromatin was recovered by incubation with protein A or protein G slurry, washed extensively and reverse crosslinked by incubation at 65 °C.

Immunoprecipitated DNA and DNA isolated from WCE were analysed by multiplex PCR or subjected to microarray-based ChIP-chip analysis.

Northern blot analysis. Northern blot analysis was performed as described previously²⁹. Total RNA was isolated from cells with MasterPure yeast RNA purification kit (Epicentre). 10 µg total RNA was loaded into each lane. Total RNA was transferred from gels to a positively charged nylon membrane (BrightStar-Plus, Ambion) using a specific transfer buffer (NorthernMax transfer buffer, Ambion). The ³²P-labelled single-stranded RNA probes were hybridized overnight to the membrane in ULTRAhyb buffer (Ambion).

Detection of small RNAs by northern blot. For small RNA detection, short RNAs (<200 nucleotides) were purified with the mirVana miRNA isolation kit (Ambion). 10 µg of small RNA was resolved on a 15% denaturing acrylamide gel, followed by transfer to a neutral nylon membrane (Amersham/Pharmacia). Chemical cross-linking was performed as previously described³⁰. Cross-linked membrane was probed with ³²P-labelled single stranded RNA probes (~50 nucleotides) corresponding to *Tf2*, *myo2* or *SPCC1442.04c*.

RT-PCR. Strand-specific RT-PCR was carried out as previously described³¹. DNase-treated total RNA (100 ng), isolated with MasterPure yeast RNA purification kit (Epicentre), was reverse-transcribed using the One-step RT-PCR kit (Qiagen).

Drosophila melanogaster genetics. The *rrp6* alleles used were f007001, which is a piggybac insertion into the *rrp6* coding region and was a gift from E. Lei, and *Df(3R)Exel6172*, which is a chromosomal deletion of the *rrp6* region and was obtained from the Bloomington Stock Center. Homozygous *rrp6* mutants were generated by crossing heterozygous *rrp6* flies that contained a balancer chromosome with an actin-driven green fluorescent protein (GFP) marker gene. Homozygous larvae were identified by the lack of GFP fluorescence throughout the body. Heterozygous siblings were used as controls. Because *rrp6*^{-/-} flies failed to grow beyond the L1 larval stage, we profiled small RNAs from the L1 larvae of *rrp6*^{-/-} and *rrp6*^{+/-} flies.

Small RNA-seq analysis. Small RNA was sequenced using Illumina sequencing platform. Analysis of deep-sequencing data was performed using the commercial program Novalign (<http://www.novocraft.com>). Novalign was used to strip the adaptor sequences from the reads, and align them with the reference genome assembly of either *S. pombe* (September 2007 release) or *D. melanogaster* (NCBI release 5_30, 30 May 2011). The output parameters were set to report all valid alignments for each read, and only mapped reads were used in further analysis. Python and R scripts were used to further analyse the aligned read data. Python scripts were used to compile information about genome mapping coverage that included the length and the genomic coordinates of each read, and to generate a count of the number of times each position in the genome was represented in the data set. The coverage count (the number of times a read in the data set was mapped to a given location in the genome) was normalized to per million mapped reads. For the analysis of repetitive regions in *D. melanogaster*, the mapped reads were processed through the open source program, RepeatMasker³². RepeatMasker revealed the identity and abundance of repeats in the small RNA data set, which were plotted using R.

28. Munafó, D. B. & Robb, G. B. Optimization of enzymatic reaction conditions for generating representative pools of cDNA from small RNA. *RNA* **16**, 2537–2552 (2010).
29. Zofall, M. *et al.* Histone H2A.Z cooperates with RNAi and heterochromatin factors to suppress antisense RNAs. *Nature* **461**, 419–422 (2009).
30. Pall, G. S. & Hamilton, A. J. Improved northern blot method for enhanced detection of small RNA. *Nature Protocols* **3**, 1077–1084 (2008).
31. Volpe, T. A. *et al.* Regulation of heterochromatic silencing and histone H3 lysine-9 methylation by RNAi. *Science* **297**, 1833–1837 (2002).
32. Tarailo-Graovac, M. & Chen, N. Using RepeatMasker to identify repetitive elements in genomic sequences. *Curr. Protoc. Bioinformatics* **25**, 4.10.1–4.10.14 (2009).

TET2 promotes histone O-GlcNAcylation during gene transcription

Qiang Chen¹, Yibin Chen¹, Chunjing Bian¹, Ryoji Fujiki^{2,3} & Xiaochun Yu¹

Ten eleven translocation (TET) enzymes, including TET1, TET2 and TET3, convert 5-methylcytosine to 5-hydroxymethylcytosine¹ and regulate gene transcription^{2–5}. However, the molecular mechanism by which TET family enzymes regulate gene transcription remains elusive^{5,6}. Using protein affinity purification, here we search for functional partners of TET proteins, and find that TET2 and TET3 associate with O-linked β -N-acetylglucosamine (O-GlcNAc) transferase (OGT), an enzyme that by itself catalyses the addition of O-GlcNAc onto serine and threonine residues (O-GlcNAcylation) *in vivo*^{7,8}. TET2 directly interacts with OGT, which is important for the chromatin association of OGT *in vivo*. Although this specific interaction does not regulate the enzymatic activity of TET2, it facilitates OGT-dependent histone O-GlcNAcylation. Moreover, OGT associates with TET2 at transcription start sites. Down-regulation of TET2 reduces the amount of histone 2B Ser112 GlcNAc marks *in vivo*, which are associated with gene transcription regulation. Taken together, these results reveal a TET2-dependent O-GlcNAcylation of chromatin. The double epigenetic modifications on both DNA and histones by TET2 and OGT coordinate together for the regulation of gene transcription.

Using protein affinity purification, we sought functional partners to the TET family enzymes. Mass spectrometry analysis showed that both TET2 and TET3 associate with OGT, an enzyme that catalyses O-GlcNAcylation^{7,8} (Fig. 1a, Supplementary Table 1 and Supplementary Fig. 1a, b). To confirm this interaction, we performed a co-immunoprecipitation assay with overexpressed TET1, TET2, TET3 and OGT. TET2 and TET3, but not TET1, associated with OGT (Fig. 1b and Supplementary Fig. 2a). To study the endogenous interaction, we used mouse embryonic stem (ES) cells in which TET2, but not TET3, was expressed^{1,6,9}. Again, TET2 associated with OGT endogenously in ES cells (Fig. 1c and Supplementary Fig. 2d). To map the regions of interaction between TET2 and OGT, we generated a series of TET2-deletion mutants, and found that the carboxy-terminal catalytic double-strand β -helix (DSBH) domain of TET2 interacts with OGT (Fig. 1d and Supplementary Fig. 2b). The tertiary structure of OGT has been examined^{10–12}. There are two major functional domains in OGT. One is the amino-terminal regulatory domain that is composed of 13.5 tetratricopeptide repeats (TPR); the other is the C-terminal catalytic domain that transfers GlcNAc from UDP-GlcNAc to Ser/Thr residues of the substrate. Using the internal-deletion mutants, we found that TPR5 and TPR6 of OGT are required for the interaction with TET2 (Fig. 1e and Supplementary Fig. 2c, e, f). We also generated baculoviruses encoding either TET2 catalytic domain (TET2CD) or OGT. After co-infecting Sf9 cells with these two types of baculovirus, the recombinant proteins of streptavidin-binding peptide (SBP)-tagged TET2CD and glutathione S-transferase (GST)-tagged OGT could be co-purified at 1:1 stoichiometry from cell lysates, suggesting TET2 tightly binds OGT (Fig. 1f). Moreover, the internal-deletion mutants D4 (which lacks TPR9 and TPR10) and D5 (which lacks TPR11 and TPR12) of OGT slightly reduced the interaction with TET2, indicating that other TPR repeats may also regulate

the interaction between OGT and TET2 (Fig. 1e and Supplementary Fig. 2f). In addition, recombinant TET3 catalytic domain also directly binds OGT (Supplementary Fig. 2g). Taken together, these results demonstrate that TET2 and TET3 form a complex with OGT both *in vitro* and *in vivo*.

TET enzymes were originally identified as homologues of JBP1 and JBP2 in *Trypanosoma brucei*; these two thymidine hydroxylases are involved in the synthesis of the modified DNA base β -D-glucosyl-hydroxymethyluracil (also known as base J)¹. Synthesis of base J consists of two steps in which it is directly converted from thymidine bases incorporated in DNA strands. In the first step, JBP1 and JBP2 catalyse the oxidation of thymidine to hydroxymethyluracil. During the second step, a yet unknown enzyme transfers a glucose residue onto the hydroxyl group of hydroxymethyluracil to form base J¹³. We wondered whether OGT could catalyse the glycosylation on hydroxyl groups of 5-hydroxymethylcytosine (5hmC). To test this hypothesis, 5-methylcytosine (5mC) was incubated with recombinant TET2 and OGT *in vitro*. However, OGT failed to convert 5hmC into any new base *in vitro* (Supplementary Fig. 3a, b). Co-expression of OGT with TET2 in cells did not alter the TET2-dependent 5hmC synthesis (Supplementary Figs 3c and 4). Furthermore, we could not detect glycosylated 5hmC *in vivo* using mass spectrometry (Supplementary Figs 3d, e and 5). These results suggested that OGT does not affect TET2-dependent 5hmC synthesis.

Next, we asked whether TET2 regulates the function of OGT. We fractionated ES cell lysates using different salt concentrations and pH levels. A subset of TET2 and OGT could only be eluted from the chromatin using 300 mM NaCl or 0.2 M HCl, indicating that these TET2 and OGT species are tightly associated with the chromatin (Supplementary Fig. 6a). Interestingly, knockdown of TET2 by short hairpin RNA (shRNA) in ES cells abolished the chromatin-associated OGT, suggesting that TET2 may target OGT to chromatin (Supplementary Fig. 6a). To verify this phenomenon, we used 293T cells stably expressing TET2. Because the exogenous TET2 level was much higher than the endogenous level (Supplementary Fig. 7), the chromatin-bound OGT was markedly increased in 293T cells stably expressing TET2 (Supplementary Fig. 6b). Moreover, because the D2 mutant of OGT abolished the interaction with TET2, only wild-type OGT but not the D2 mutant existed in the chromatin fraction, suggesting that the interaction with TET2 is important for the chromatin localization of OGT (Supplementary Fig. 6c). In addition, knockdown of OGT by shRNA did not significantly affect the chromatin retention of TET2 (Supplementary Fig. 6d). Collectively, these results suggest that TET2 recruits OGT to chromatin.

Recently, it has been shown that histones can be modified by OGT at different sites^{14–17}. In particular, OGT regulates O-GlcNAcylation of histone 2B (H2B) at Ser112 *in vivo*¹⁵. Because TET2 targets OGT to chromatin, we wondered whether TET2 regulates OGT-dependent H2B O-GlcNAcylation. With a specific antibody for H2B Ser112 GlcNAc, we found that H2B Ser112 GlcNAc was significantly reduced in TET2-depleted ES cells (Fig. 2a). Moreover, TET2 also regulates

¹Division of Molecular Medicine and Genetics, Department of Internal Medicine, University of Michigan Medical School, 1150 West Medical Center Drive, 5560A MSRBII, Ann Arbor, Michigan 48109, USA.

²Institute of Molecular and Cellular Biosciences, University of Tokyo, 1-1-1 Yayoi, Bunkyo-ku, Tokyo 113-0032, Japan. ³JST, PRESTO, 4-1-8 Honcho Kawaguchi, Saitama 332-0012, Japan.

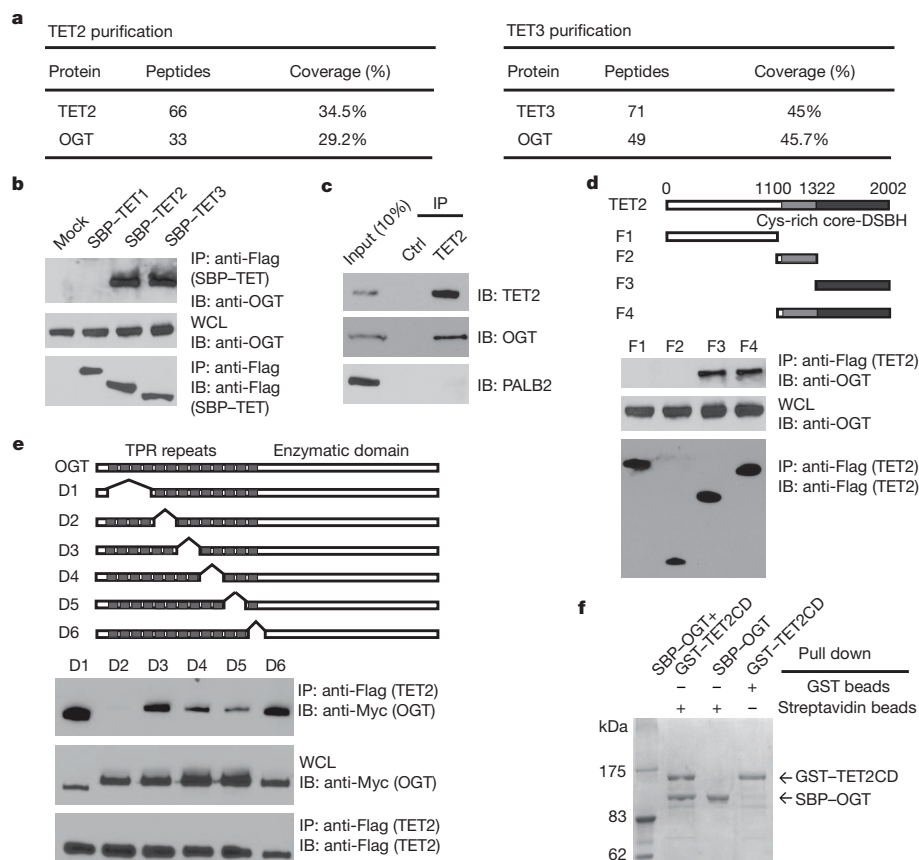


Figure 1 | TET2 forms a complex with OGT. **a**, Purification of TET2- and TET3-associated proteins. TET2- and TET3-associated proteins were analysed by mass spectrometry and are shown in the Supplementary Fig. 1a. **b**, OGT interacts with TET2 and TET3 but not with TET1. SBP-tagged TET1–3 proteins were expressed and examined with indicated antibodies. Whole cell lysate (WCL) was used as the input. **c**, OGT interacts with TET2 endogenously in ES cells. Irrelevant IgG was used as the immunoprecipitation control (ctrl); PALB2 was used as the negative control. **d**, The DSBH domain of TET2

interacts with OGT. Deletion mutants of TET2 mutants were expressed. The F3 mutant containing the core-DSBH domain (catalytic domain) interacts with OGT. **e**, TPR5 and TPR6 of OGT interact with TET2. The D2 mutant of OGT, which lacks TPR5 and TPR6, abolished the interaction with TET2. **f**, OGT directly binds TET2. Sf9 cells were infected with baculoviruses encoding SBP-OGT and/or GST-TET2CD. The protein complex was purified by streptavidin beads or GST beads and examined by Coomassie blue staining.

O-GlcNAcylation of other histones (Supplementary Fig. 8). Concurrent with TET2 overexpression inducing OGT association with chromatin, H2B Ser 112 O-GlcNAcylation was increased (Fig. 2b). Interestingly, the TET2 enzymatic-dead mutant (His1382Tyr/Asp1384Ala) that still interacted with OGT also increased H2B Ser 112 O-GlcNAcylation, suggesting that the enzymatic activity of TET2 is not required for the regulation of H2B O-GlcNAcylation (Fig. 2b and Supplementary Fig. 9). Moreover, only wild-type OGT but not the enzymatic-dead mutant of OGT (Gly482Ser) nor the D2 mutant lacking the interaction with TET2 could induce H2B S112 O-GlcNAcylation *in vivo* (Fig. 2c). These data therefore suggest that the interaction between TET2 and OGT is important for OGT-dependent histone glycosylation *in vivo*. To examine the mechanism by which TET2 boosts the enzymatic activity of OGT, we performed an *in vitro* glycosylation assay using wild-type OGT and its D2 mutant. Using histone octamers as the substrate, both wild-type OGT and the D2 mutant only weakly glycosylated histones. The enzymatic activity of wild-type OGT was indistinguishable from that of the D2 mutant as both proteins can auto-glycosylate themselves (Supplementary Fig. 10). Moreover, supplementation of TET2 did not affect the enzymatic activity of either wild-type OGT or the D2 mutant (Fig. 2d). However, when mono-nucleosomes were used as the substrates, supplementation of recombinant TET2 markedly increased the enzymatic activity of wild-type OGT but not the D2 mutant (Fig. 2d and Supplementary Fig. 11), suggesting that the interaction with TET2 facilitates OGT recognition of the substrate. Although histones H3

and H4 were glycosylated *in vivo*, only GlcNAcylation of H2A and H2B could be clearly detected in this *in vitro* glycosylation assay (Supplementary Fig. 11). One possibility is that glycosylated H2A and H2B suppresses H3 and H4 glycosylation by OGT. Alternatively, the glycosylation sites on H3 and H4 either in the histone octamer or as mono-nucleosomes are not well exposed to the enzyme. In contrast to many other enzymes, OGT only efficiently glycosylates the substrates that it associates with^{18–21}. Thus, it is likely that TET2 recognizes the chromatin and recruits OGT to the chromatin, and the chromatin-associated OGT glycosylates nucleosomal histones at its vicinity. Consistently, only TET2 but not OGT recognizes double-stranded DNA or mono-nucleosome with 5mC (Supplementary Fig. 12).

To examine the distribution of OGT and TET2 on the chromatin of ES cells, we performed genome-wide chromatin immunoprecipitation (ChIP) sequencing analysis (ChIP-seq) using anti-OGT, anti-H2B Ser 112 GlcNAc and anti-mouse TET2 antibodies. We validated our ChIP-seq results using ChIP-quantitative PCR (qPCR) to examine 45 different loci that represent a broad range of ChIP-seq fragment counts (Supplementary Fig. 13). Next, we compared the TET2 target genes with a published hmeDIP database³, and found that 47% of 5hmC-positive genes are bound by TET2 (Supplementary Fig. 14a). Most of the TET2 target genes are associated with high- and intermediate-density CpG promoters (Supplementary Fig. 14b, c), which are also positive for the trimethylated form of histone H3 at lysine 4 (H3K4me3)²² (Supplementary Fig. 14d). Gene Ontology analysis showed that OGT, H2B Ser 112 GlcNAc and TET2 are involved in a

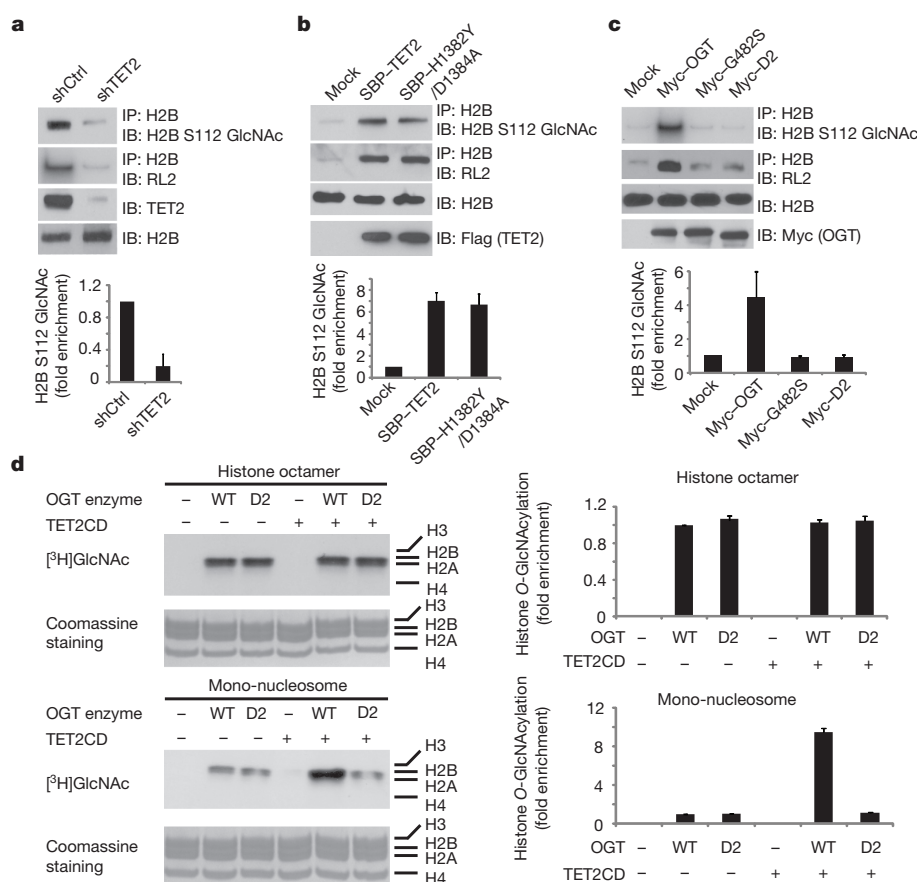


Figure 2 | TET2 enhances histone glycosylation. **a**, Downregulation of TET2 impairs H2B O-GlcNAcylation in ES cells. H2B O-GlcNAcylation was examined by immunoprecipitation with an anti-H2B antibody and western blot with an anti-GlcNAc antibody (RL2) or anti-H2B Ser 112 GlcNAc antibody. Histogram shows the relative level of H2B Ser 112 GlcNAc in TET2-downregulated cells (shTET2) compared to that in control-shRNA-treated cells (shCtrl). **b**, Upregulation of wild-type TET2 or TET2 enzymatic-dead mutant (His1382Tyr/Asp1384Ala) induced H2B Ser 112 O-GlcNAcylation in 293 cells.

c, The interaction between OGT and TET2 is important for H2B O-GlcNAcylation and H2B Ser 112G O-GlcNAcylation. Wild-type OGT, the enzymatic-dead mutant of OGT (Gly482Ser) and the D2 mutant were expressed in 293T cells. H2B O-GlcNAcylation and H2B Ser 112 O-GlcNAcylation were examined. **d**, TET2 facilitated OGT-dependent histone glycosylation in mono-nucleosomes but not in recombinant core histones. Tritium-labelled GlcNAc was incorporated into the histones in the *in vitro* O-GlcNAcylation assay. All error bars denote s.d., $n = 3$.

variety of basic cellular processes (Supplementary Fig. 15). The analysis showed that OGT and H2B Ser 112 GlcNAc display a considerable overlap of target genes with TET2 (Fig. 3a), and similar binding profiles to TET2 at transcriptional start sites (TSS) (Fig. 3b, c). Moreover, the binding sites of OGT, H2B Ser 112 GlcNAc and TET2 have the highest density around TSS (Fig. 3c). Knockdown of TET2 markedly suppressed the recruitment of OGT to tested target genes and reduced the level of H2B Ser 112 GlcNAc at those loci (Fig. 3d). By contrast, knockdown of OGT had little effect on TET2 at these loci, suggesting that OGT does not contribute to the recruitment of TET2 to these loci (Fig. 3d). Next, we asked whether there was a correlation between TET2-mediated OGT targeting and the targeted gene transcription levels. In wild-type ES cells, we found that genes that were occupied by OGT and TET2 and enriched with H2B Ser 112 GlcNAc were associated with high levels of transcription in ES cells (Fig. 3e and Supplementary Fig. 16). Moreover, we examined alterations to the gene transcription profile in TET2 knockdown ES cells. The percentage of downregulated genes that were occupied by OGT, H2B Ser 112 GlcNAc and TET2 was significantly higher than that of genes not occupied by OGT, H2B Ser 112 GlcNAc and TET2 (Supplementary Fig. 17). To validate these results, we performed qPCR to confirm the downregulation of a number of OGT, H2B Ser 112 GlcNAc and TET2 target genes (Fig. 3f and Supplementary Fig. 18). In addition, we reconstituted TET2-depleted ES cells with the His1382Tyr/Asp1384Ala mutant that abolishes the enzymatic activity of TET2. The His1382Tyr/Asp1384Ala mutant could not restore 5hmC at

the TSS of a set of the TET2 and OGT common target genes. However, the His1382Tyr/Asp1384Ala mutant restored H2B Ser 112 GlcNAc and partially rescued the TET2 and OGT target gene expression (Supplementary Fig. 19). These results indicate that OGT-dependent histone O-GlcNAcylation contributes to TET2-dependent gene transcription.

Taken together, here we have shown that TET2 and OGT form a complex, which might regulate gene transcription (Supplementary Fig. 20). Besides TET2, TET3 also interacts with OGT. Like TET2, TET3 might also target OGT to chromatin for gene transcription regulation. Owing to the different tissue distribution^{9,23–25}, it is TET2 that targets OGT to the chromatin and regulates H2B O-GlcNAcylation in ES cells. Recently, it has been reported that H2B O-GlcNAcylation is associated with active TSS and positively regulates transcription¹⁵. However, 5hmC-enriched regions are associated with both transcriptional activation and repression^{2–4,26}. Because TET1 is associated with the transcriptional repression complex Sin3A, it is likely that TET1-dependent 5hmC is associated with transcriptional repression²⁷. By contrast, TET2 exists in a totally different complex with OGT but not Sin3A. Thus, the TET2–OGT complex might be involved in transcriptional activation in ES cells. Further analysis on each individual 5hmC-enriched locus could distinguish the identity of 5hmC in transcription regulation. Moreover, OGT also affects other histone modifications during mitosis²⁸. It is possible that chromatin remodelling regulated by histone GlycNAcylation could be a general phenomenon in other biological processes. In addition to the transcription activation,

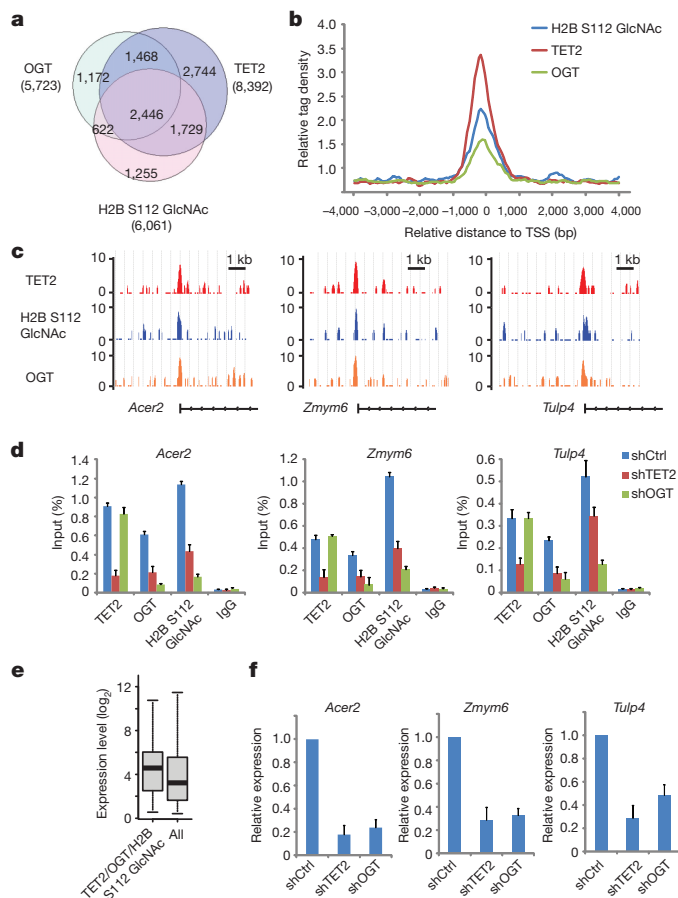


Figure 3 | TET2 regulates H2B Ser 112 GlcNAc and gene transcription. **a**, Venn diagram shows a considerable overlap between OGT, H2B Ser 112 GlcNAc and TET2 target genes. **b**, Mean distribution of tags at gene TSS (± 4 kilobases (kb)). bp, base pairs. **c**, Examples of OGT, H2B Ser 112 GlcNAc and TET2 ChIP-seq results in mouse ES cells. **d**, ChIP-qPCR was performed to examine TET2, OGT and H2B Ser 112 GlcNAc in control, TET2-knockdown or OGT-knockdown cells (using shCtrl, shTET2 or shOGT, respectively). **e**, The expression of TET2 and OGT common target genes is higher than average gene expression in ES cells. Data analysis is explained in the Methods. Box plots show median, twenty-fifth and seventy-fifth percentile expression levels in ES cells. $P < 0.00001$. **f**, Loss of TET2 or OGT is associated with the reduced expression of their common target genes. All error bars denote s.d., $n = 3$.

OGT is also involved in transcription repression^{19,29,30}. Thus, TET2 is only one of the functional partners of OGT. OGT in other complexes may have an important role in gene silencing^{19,29,30}.

METHODS SUMMARY

Details of cell cultures, plasmids, RNA interference and antibodies used, as well as descriptions of methods for purification of TET enzymes associated proteins, western blotting, immunoprecipitation, mass spectrometry analysis, *in vitro* 5hmC assay, dot blotting assay, silver staining, *in vitro* O-GlcNAcylation assay, histone fraction, electrophoretic mobility shift assay, chromatin immunoprecipitation assay, DNA immunoprecipitation assay, ChIP sequencing, messenger RNA analysis and statistical analyses are provided in Methods.

Full Methods and any associated references are available in the online version of the paper.

Received 20 January; accepted 31 October 2012.

Published online 9 December 2012; corrected online 23 January 2013 (see full-text HTML version for details).

1. Tahliliani, M. *et al.* Conversion of 5-methylcytosine to 5-hydroxymethylcytosine in mammalian DNA by MLL partner TET1. *Science* **324**, 930–935 (2009).

2. Ficiz, G. *et al.* Dynamic regulation of 5-hydroxymethylcytosine in mouse ES cells and during differentiation. *Nature* **473**, 398–402 (2011).
3. Pastor, W. A. *et al.* Genome-wide mapping of 5-hydroxymethylcytosine in embryonic stem cells. *Nature* **473**, 394–397 (2011).
4. Xu, Y. *et al.* Genome-wide regulation of 5hmC, 5mC, and gene expression by Tet1 hydroxylase in mouse embryonic stem cells. *Mol. Cell* **42**, 451–464 (2011).
5. Wu, H. *et al.* Dual functions of Tet1 in transcriptional regulation in mouse embryonic stem cells. *Nature* **473**, 389–393 (2011).
6. Ito, S. *et al.* Role of Tet proteins in 5mC to 5hmC conversion, ES-cell self-renewal and inner cell mass specification. *Nature* **466**, 1129–1133 (2010).
7. Vosseller, K., Sakabe, K., Wells, L. & Hart, G. W. Diverse regulation of protein function by O-GlcNAc: a nuclear and cytoplasmic carbohydrate post-translational modification. *Curr. Opin. Chem. Biol.* **6**, 851–857 (2002).
8. Kreppel, L. K., Blomberg, M. A. & Hart, G. W. Dynamic glycosylation of nuclear and cytosolic proteins. Cloning and characterization of a unique O-GlcNAc transferase with multiple tetratricopeptide repeats. *J. Biol. Chem.* **272**, 9308–9315 (1997).
9. Gu, T. P. *et al.* The role of Tet3 DNA dioxygenase in epigenetic reprogramming by oocytes. *Nature* **477**, 606–610 (2011).
10. Clarke, A. J. *et al.* Structural insights into mechanism and specificity of O-GlcNAc transferase. *EMBO J.* **27**, 2780–2788 (2008).
11. Martinez-Fleites, C. *et al.* Structure of an O-GlcNAc transferase homolog provides insight into intracellular glycosylation. *Nature Struct. Mol. Biol.* **15**, 764–765 (2008).
12. Lazarus, M. B., Nam, Y., Jiang, J., Sliz, P. & Walker, S. Structure of human O-GlcNAc transferase and its complex with a peptide substrate. *Nature* **469**, 564–567 (2011).
13. Borst, P. & Sabatini, R. Base J: discovery, biosynthesis, and possible functions. *Annu. Rev. Microbiol.* **62**, 235–251 (2008).
14. Zhang, S., Roche, K., Nasheuer, H. P. & Lowndes, N. F. Modification of histones by sugar β -N-acetylglucosamine (GlcNAc) occurs on multiple residues, including histone H3 serine 10, and is cell cycle-regulated. *J. Biol. Chem.* **286**, 37483–37495 (2011).
15. Fujiki, R. *et al.* O-GlcNAcylation of histone H2B facilitates its monoubiquitination. *Nature* **480**, 557–560 (2011).
16. Sakabe, K., Wang, Z. & Hart, G. W. β -N-acetylglucosamine (O-GlcNAc) is part of the histone code. *Proc. Natl Acad. Sci. USA* **107**, 19915–19920 (2010).
17. Fong, J. J. *et al.* β -N-Acetylglucosamine (O-GlcNAc) is a novel regulator of mitosis-specific phosphorylations on histone H3. *J. Biol. Chem.* **287**, 12195–12203 (2012).
18. Capotosti, F. *et al.* O-GlcNAc transferase catalyzes site-specific proteolysis of HCF-1. *Cell* **144**, 376–388 (2011).
19. Yang, X., Zhang, F. & Kudlow, J. E. Recruitment of O-GlcNAc transferase to promoters by corepressor mSin3A: coupling protein O-GlcNAcylation to transcriptional repression. *Cell* **110**, 69–80 (2002).
20. Kreppel, L. K. & Hart, G. W. Regulation of a cytosolic and nuclear O-GlcNAc transferase. Role of the tetratricopeptide repeats. *J. Biol. Chem.* **274**, 32015–32022 (1999).
21. Iyer, S. P., Akimoto, Y. & Hart, G. W. Identification and cloning of a novel family of coiled-coil domain proteins that interact with O-GlcNAc transferase. *J. Biol. Chem.* **278**, 5399–5409 (2003).
22. Mikkelsen, T. S. *et al.* Genome-wide maps of chromatin state in pluripotent and lineage-committed cells. *Nature* **448**, 553–560 (2007).
23. Branco, M. R., Ficiz, G. & Reik, W. Uncovering the role of 5-hydroxymethylcytosine in the epigenome. *Nature Rev. Genet.* **13**, 7–13 (2012).
24. Iqbal, K., Jin, S. G., Pfeifer, G. P. & Szabo, P. E. Reprogramming of the paternal genome upon fertilization involves genome-wide oxidation of 5-methylcytosine. *Proc. Natl Acad. Sci. USA* **108**, 3642–3647 (2011).
25. Inoue, A. & Zhang, Y. Replication-dependent loss of 5-hydroxymethylcytosine in mouse preimplantation embryos. *Science* **334**, 194 (2011).
26. Wu, H. *et al.* Genome-wide analysis of 5-hydroxymethylcytosine distribution reveals its dual function in transcriptional regulation in mouse embryonic stem cells. *Genes Dev.* **25**, 679–684 (2011).
27. Williams, K. *et al.* Tet1 and hydroxymethylcytosine in transcription and DNA methylation fidelity. *Nature* **473**, 343–348 (2011).
28. Sakabe, K. & Hart, G. W. O-GlcNAc transferase regulates mitotic chromatin dynamics. *J. Biol. Chem.* **285**, 34460–34468 (2010).
29. Gambetta, M. C., Oktaba, K. & Muller, J. Essential role of the glycosyltransferase *sxc*/Ogt in polycomb repression. *Science* **325**, 93–96 (2009).
30. Sinclair, D. A. *et al.* *Drosophila* O-GlcNAc transferase (OGT) is encoded by the *Polycomb* group (*PcG*) gene, *super sex combs* (*sxc*). *Proc. Natl Acad. Sci. USA* **106**, 13427–13432 (2009).

Supplementary Information is available in the online version of the paper.

Acknowledgements We thank H. Kuang for proofreading the manuscript and J. Hutchins for research support. This work was supported by the National Institutes of Health (CA132755 and CA130899 to X.Y.), the University of Michigan Cancer Center and GI Peptide Research Center. X.Y. is a recipient of the Era of Hope Scholar Award from the Department of Defense.

Author Contributions X.Y. conceived the project and designed the experiments; Q.C. performed the experiments with Y.C., C.B. and R.F.; Q.C. and X.Y. analysed the data and wrote the manuscript.

Author Information The ChIP-seq and microarray data have been deposited in the Gene Expression Omnibus under accession number GSE41720. Reprints and permissions information is available at www.nature.com/reprints. The authors declare no competing financial interests. Readers are welcome to comment on the online version of the paper. Correspondence and requests for materials should be addressed to X.Y. (xiayu@med.umich.edu).

METHODS

Plasmids and antibodies. For protein affinity purification and other analyses, full-length complementary DNAs of human *TET1*, *TET2* and *TET3* were cloned into the pS-Flag-SBP (SBP) vector. For generating internal-deletion mutants, *OGT* cDNA fragments were PCR amplified and cloned into pCMV-Myc. For generating truncation mutants, *TET2* cDNA was PCR amplified and cloned into the SBP vector. *TET2CD* (amino acids 916–1921) was cloned into the SBP vector and pFast-Bac vector. Internal-deletion mutants of *OGT*, enzymatic-dead mutant (Gly482Ser) of *OGT* and enzymatic-dead mutant (His1382Tyr/Asp1384Ala) of *TET2* were generated using the QuikChange site-directed mutagenesis kit (Stratagene).

Rabbit anti-mouse *TET2* antibody was raised against amino acids 1–200 of mouse *TET2*. Rabbit anti-mouse *TET1* antibody was raised against the C terminus (amino acids 1500–2008) of mouse *TET1*. Anti-*OGT* antibody was purchased from Novus. Anti-Flag, anti-Myc and anti- β -actin antibodies were purchased from Sigma. Anti-5hmC polyclonal antibody was purchased from Zymo Research. Antibodies against histone H2A, H2B, H3, H4, H3K4me3, H3K27me3 and H3 acetylated at Lys 14 (H3K14Ac) were purchased from Millipore. RL2 monoclonal antibody against O-GlcNAc was purchased from Abcam. CTD110.6 monoclonal antibody against O-GlcNAc was purchased from Covance. Monoclonal antibody against H2B Ser 112 GlcNAc was generated as described previously¹⁵.

Purification of TET-associated proteins. To search for binding partners of *TET2* and *TET3*, we collected 11293T cells stably expressing SBP–*TET2* and SBP–*TET3*, respectively, and washed the cell pellets with PBS. Cells were lysed with 30 ml ice-cold NETN300 buffer (50 mM Tris-HCl, pH 7.4, 2 mM EDTA and 300 mM NaCl). The soluble fraction was incubated with 0.5 ml streptavidin-conjugated agarose beads. The beads were washed with NETN100 buffer (50 mM Tris-HCl, pH 7.4, 2 mM EDTA and 100 mM NaCl) three times. Associated proteins were eluted with 2 mM biotin (Sigma) in PBS, and further incubated with 50 μ l S-protein-agarose beads (Novagen). The bound proteins were eluted with SDS sample buffer (20% glycerol, 120 mM Tris-HCl, pH 6.8, 4% SDS, 0.02% bromophenol blue and 2.5% β -mercaptoethanol), and analysed by 10% SDS-PAGE and mass spectrometry. Cells expressing empty vector were used as purification controls.

Silver staining. Purified materials were load onto 8% SDS-PAGE for electrophoresis. The gel was fixed with 50% methanol, 10% acetic acid for 15 min, and followed by further fixation with 10% ethanol, 5% acetic acid for 6 min. For staining, the gel was agitated in 50 ml 20 mg l⁻¹ Na₂S₂O₄ for 30 min, then stained in 50 ml AgNO₃ solution (100 mg AgNO₃ in 0.1% formaldehyde) for 30 min. After washed with ddH₂O, the gel was treated with 50 ml image developer (3% Na₂CO₃, 50 μ l 37% formaldehyde and 250 μ l 0.2% sodium thiosulphate). The reaction was stopped using stop solution (12.5 ml acetic acid and 25 g Tris in 500 ml ddH₂O) when clear bands were observed.

Recombinant proteins. Recombinant proteins were purified from Sf9 insect cells. For generating baculovirus, DNA fragments containing full-length *OGT*, and deletion mutants of *OGT*, *TET2CD* and *TET3CD* were subcloned into the pFastBac vector with a GST or SBP tag. Baculoviruses were generated according to manufacturer's instructions (Invitrogen). After Sf9 cells were infected with baculoviruses for 48 h, the cells were collected, washed with PBS and lysed with ice-cold NETN100 buffer. The soluble fraction was incubated with glutathione-sepharose beads (for GST-tag proteins) or streptavidin-conjugated beads (for SBP-tag proteins) and eluted with glutathione or biotin, respectively. To purify protein complex, Sf9 cells were co-infected with baculoviruses encoding GST–*TET2CD* and SBP–*OGT* for 48 h. The cells were then lysed and the soluble fraction was incubated with glutathione-sepharose beads or streptavidin-conjugated beads as indicated.

Cell lysis, immunoprecipitation and western blotting. For immunoprecipitation, cells were lysed with ice-cold NETN300 buffer containing 10 mM NaF and 50 mM β -glycerophosphate. Supernatants were incubated with indicated antibodies and protein-G-conjugated sepharose beads (Amersham Pharmacia). Precipitates were washed five times with NETN100, subjected to SDS-PAGE and western blotting with indicated antibodies.

To examine the localization of *OGT* (Supplementary Fig. 6), cell pellets were lysed with 400 μ l NETN100 buffer. After centrifugation, the supernatants were named as 100 mM NaCl samples. The insoluble pellets were collected, washed with ice-cold PBS, and incubated with 400 μ l NETN300 buffer on ice. After centrifugation, the supernatants were named as 300 mM NaCl samples. The remaining pellets were washed twice with ice-cold PBS and then treated with 200 μ l 0.2 N HCl. The supernatants were neutralized with 200 μ l Tris-HCl, pH 8.8, and named as 0.2 N HCl fractions. Twenty microlitres of each sample was loaded onto 7.5% SDS-PAGE gels and immunoblotted by indicated antibodies. The total amount of *OGT* was calculated by adding *OGT* from these three different fractions in each sample. The percentage of *OGT* in each fraction was presented.

Histone fraction. To examine histone glycosylation by immunoprecipitation and western blot, we followed a protocol from ref. 16. In brief, cells were lysed in 20 mM Tris-HCl, pH 8.0, 600 mM NaCl, 0.5% NP-40, 0.5% SDS, 0.5% deoxycholate, 1 mM EDTA and 2 μ M of the OGA inhibitor PUGNAc (Sigma). The cells were sonicated and clarified by centrifugation. The lysate was then diluted by NETN100 and histones were immunoprecipitated with the indicated antibodies.

To examine histone glycosylation by western blot, cells were lysed by NETN300 buffer with 2 μ M PUGNAc. The pellets were washed twice with NETN300 and treated with 0.2 N HCl. After centrifugation, the supernatants were neutralized by the same volume of Tris-HCl, pH 8.8. Samples were examined by 10–20% gradient SDS-PAGE or 15% triton-acidic acid-urea (TAU) gel electrophoresis.

TAU gel electrophoresis. Fifteen per cent TAU gel was prepared as reported³¹. In brief, the gel contained 15% acryl:bisacrylamide 60:0.4, 6 M urea, 5% acetic acid and 0.37% Triton X-100. Acid-extracted histones, histone octamers or mono-nucleosomes were dissolved in 2 \times loading buffer (8 M urea, 10% glycerol and 2.5% acetic acid) and loaded onto the gel. The gel was run in 5% acetic acid at 200 V for 140 min. For Coomassie blue staining, the gel was stained with Coomassie blue 250. For autoradiography, the gel was treated with EN3HANCE (PerkinElmer) before exposure to X-ray film. For western blot, the gel was washed twice in 300 ml of 50 mM acetic acid and 0.5% SDS for 30 min each time, and twice in 300 ml of transfer buffer (25 mM Tris, 192 mM glycine, 20% (v/v) methanol and 0.1% SDS) for 30 min each time. The electrotransfer reaction was carried out at a constant current of 400 mA for 2 h at room temperature.

RNA interference. shRNA sequences targeting human *OGT* (5'-GCACATAG CAATCTGGCTTCC-3' (ref. 32) or 5'-CCAACTTTCTGGATGCTTAT-3'), mouse *Ogt* (5'-GCACACAGCAATCTGGCTTCC-3' or 5'-AGGGAACCTAGAT AACATGCTT-3' (ref. 33)) and mouse *Tet2* (5'-CACTACTAAGTCCACCC TAAA-3' (ref. 34) or 5'-GCTCTGAACAGTATTCAAAGC-3' (ref. 6)) were inserted into the pMSCV-puro-pSilencer vector. Generating retrovirus was carried out as previously described³⁵. pMSCV-puro-shmock, pMSCV-puro-shOGT or pMSCV-puro-shTET2 vectors were used to transfect packaging cell line 293T with two other helper packaging plasmids pMD-MLV-OGP (*gag-pol*) and pVSV-G (*env*). Tissue culture supernatants from 293T packaging cells transfected with the above plasmids were collected. Viral particles were concentrated by centrifugation at 50,000g for 3 h and then added to the culture media of ES cells. The viral-infected cells were selected by puromycin for 72 h and then used in the following experiments. Similar results were obtained from shRNA treatment with different sequences.

In vitro O-GlcNAcylation assay. Recombinant SBP–*OGT* protein (0.5 μ g) was incubated with 2 μ g substrates (histone octamers, mono-nucleosomes or 210-bp 5hmC-containing oligonucleotides with sequence listed in Supplementary Table 7) and 0.5 mM (0.5 μ Ci) UDP-[³H]GlcNAc (from ARC) in 25 μ l reaction buffer (50 mM Tris-HCl, pH 7.5, 12.5 mM MgCl₂ and 1 mM dithiothreitol (DTT)) for 1 h at 37 °C. The reaction was stopped by 10 mM EDTA. To detect potential DNA glycosylation, DNA was pulled down by streptavidin beads. The beads were subjected to scintillation counter measurement. β -glucosyltransferase (Zymo Research) was used as a positive control to produce GlcNAcylated-5hmC (5ghmC) following the protocol of Zymo Research, with UDP-[³H]GlcNAc as the donor. For histone glycosylation analyses, the reaction was resolved with SDS-PAGE, and then subjected to autoradiography after incubation with EN3HANCE (from PerkinElmer). Nucleosome packaging was performed as described below with recombinant core histones purified from bacteria.

Electrophoretic mobility shift assay. The 157-bp DNA oligonucleotide (Supplementary Table 7) containing 5mC was produced by PCR using dATP, dGTP, dCTP and dTTP. The oligonucleotide was [³²P]-labelled at the 5' end by T4 DNA kinase and purified using a G50 spin column (Pharmacia Biotech). The labelled oligonucleotide (0.1 pmol) was incubated with GST (0.4 μ g), GST–*OGT* (0.4 μ g) and/or GST–*TET2CD* (0.1, 0.2 or 0.4 μ g), in reaction buffer (50 mM HEPES, pH 7.9, 10 mM MgCl₂, 50 mM NaCl, 75 μ M Fe(NH₄)₂ and 0.1 mg ml⁻¹ bovine serum albumin (BSA)) for 30 min at room temperature. The samples were loaded onto 6% native polyacrylamide gel and run at 150 V in 0.5 \times Tris-borate-EDTA (TBE) buffer. The gels were then fixed with 30% methanol and 10% acetic acid and exposed to X-ray film.

For electrophoretic mobility shift assays using mono-nucleosomes, we generated oligonucleotides containing cytosine or 5mC by PCR. PCR products were end-labelled with ³²P and purified by gel electrophoresis. To generate mono-nucleosomes, labelled DNA oligonucleotides were incubated with core histones at a 1:1 molar ratio in a buffer containing 2 M NaCl and 1 mM DTT to a total volume of 30 μ l. Mixtures were then serially dialysed against 2 M, 0.85 M, 0.65 M and 0.2 M NaCl in 10 mM Tris-HCl, pH 7.5, 1 mM EDTA and 1 mM DTT for 4–10 h at each step. Mono-nucleosomes were separated from free DNA by ultracentrifugation in 5–30% linear glycerol gradients. After centrifugation at 150,000g in a SW50.1 rotor for 18 h at 4 °C, gradient fractions were collected. Fractions

containing mono-nucleosomes were pooled, and dialysed against 10 mM Tris-HCl, pH 8.0, and 1 mM DTT. For nucleosome-binding reactions, GST-OGT (0.2 µg) and GST-TET2CD (0.05, 0.1 or 0.2 µg) were incubated with 20 nM mono-nucleosomes in 20 µl, with final buffer conditions of 50 mM HEPES, pH 7.9, 10 mM MgCl₂, 75 µM Fe(NH₄)₂, 50 mM NaCl, 1 mM DTT, 1% glycerol and 1 mg ml⁻¹ BSA. The reactions were incubated at room temperature for 1 h. Binding reactions were loaded onto 4% native polyacrylamide gels at 150 V in 0.5× TBE buffer. After electrophoresis, gels were dried and examined by autoradiography.

ChIP assay and DNA immunoprecipitation assay. ChIP assays were performed according to the protocol described by Upstate. ES cell DNA was sonicated to an average size between 300 and 600 bp. Solubilized chromatin was immunoprecipitated with antibodies against TET2, OGT, H2B Ser 112 GlcNAc, H3K4me3 and H3K27me3. Antibody–chromatin complexes were pulled-down using protein A–sepharose, washed and then eluted. After cross-link reversal and proteinase K treatment, immunoprecipitated DNA was extracted with phenol–chloroform, ethanol precipitated and treated with RNase. ChIP DNA was quantified using PicoGreen.

For hydroxymethylated DNA immunoprecipitation assay, genomic DNA was extracted using the Qiagen QIAamp DNA mini kit. The purified genomic DNA was sonicated using Diagenode Bioruptor 200. The DNA fragment size was determined by 2% agarose gel, and should be 200–800 bp. The samples were heat-denatured and mixed with 1 µg 5hmC antibody. The mixtures were incubated overnight at 4 °C and then pulled down by protein A–sepharose beads. The beads were extensively washed and digested by proteinase K. DNA was further purified by phenol–chloroform extraction and ethanol precipitation. 5hmC immunoprecipitated DNA was quantified using PicoGreen.

ChIP sequencing. DNA fragments isolated from ChIP were repaired to blunt ends by T4 DNA polymerase and phosphorylated with T4 polynucleotide kinase using the END-IT kit (Epicentre). A single 'A' base was added to the 3' end with Klenow. Double-stranded adaptors (75 bp with a 'T' overhang) were ligated to the fragments with DNA ligase. Ligation products between 200 and 600 bp were gel-purified to remove unligated adaptors and subjected to 20 PCR cycles. Completed libraries were quantified with PicoGreen. For ChIP-seq analyses, the DNA libraries were analysed by Solexa/Illumina high-throughput sequencing. The read quality of each sample was determined by FastQC software. After prefiltering the raw data by removing sequence adapters and low-quality reads, the tags were mapped to the mouse genome (assembly mm9) by Bowtie software. Parameter settings were listed as follows: -v, 3 (reported alignments with at most three mismatches), -5, 3 and -3, 3 (trim 3 bases from 5' and 3' end to remove low-quality bases). Peak detection was performed using MACS software from Galaxy browser (<http://www.galaxy.psu.edu>). Parameters settings were as follows: IgG ChIP-seq aligned reads were used as control file, tag size with 25 bp, band width with 300 bp. Venn diagram analysis was performed with Galaxy browser. The peaks obtained from ChIP sequencing were matched to the annotated reference genome (mouse mm9) using Cisgenome 2.0. To view the peak density and position, Cisgenome 2.0 was used. The relative accumulations of tags around the TSS were performed using SEQMINER software. The TSS position of each gene was downloaded from the UCSC genome browser. Gene Ontology analysis was performed using Panther. All the statistics and plottings were obtained using the statistical program R. To compare TET2 and 5hmC, hmeDIP database was downloaded from NCBI³. A set of 30 PCR primer pairs (Supplementary Table 5) was designed to amplify 100–140-bp fragments from genomic regions showing a wide range of signals for TET2, OGT and H2B Ser 112 GlcNAc by ChIP-seq. ChIP-qPCR values reflect two independent ChIP assays; each was evaluated in duplicate by qPCR.

Messenger RNA analysis. To examine gene expression, total RNA was purified from mouse ES cells using RNeasy (Qiagen). The RNA was reverse transcribed using TaqMan reverse transcription reagents from ABI. qPCR was carried out in 20 µl aliquots using SYBR green master mix (NEB) containing 10 nM 6-carboxyfluorescein (Sigma) as a reference dye, 50 to 100 ng of cDNA and 2 µM primers. The reactions were performed on a Bio-Rad iCycler and quantified using

the iCycler iQ software. The relative quantities of each mRNA were determined for each sample based on the threshold cycle (*C_T*) value normalized to the corresponding values for mouse *Gapdh*. Oligonucleotide sequences of the primers for qPCR assays are listed in the Supplementary Table 6. All reactions were performed in triplicates.

RNA expression data for shCtrl and shTET2 ES cells were generated from polyA RNA using GeneChip Mouse Genome 430 arrays (Affymetrix) following Affymetrix procedures and analysis. The results were shown in Supplementary Table 3. The expression value of each transcript was showed in log₂ scale. The data analysis was performed using Cluster 3.0 and Java Treeview.

In vitro 5hmC assay. To examine enzymatic activity of TET2 *in vitro*, 0.4 µg double-stranded DNA oligonucleotides (listed in Supplementary Table 7) that contain C, 5mC or 5hmC were incubated with 1 µg TET2CD or 1 µg TET2CD, together with 1 µg OGT proteins in the presence of 50 mM HEPES, pH 7.9, 100 mM NaCl, 75 µM Fe(NH₄)₂, 2 mM ascorbate and 1 mM α-ketoglutarate at 37 °C for 40 min. The DNA substrates were then purified by ethanol precipitation and digested with TapI. After the treatment with calf intestinal alkaline phosphatase, the DNA substrates were labelled with [γ-³²P]ATP by T4 polynucleotide kinase, purified by ethanol precipitation and digested with 10 µg DNase I and 10 µg phosphodiesterase I. The samples were separated by thin layer chromatography (TLC) on PERcellulose TLC plates (Merck) using isobutyric acid:NH₄OH:H₂O at 66:2:20. After air drying, the TLC plates were exposed to X-ray film.

Dot blotting assay. Genomic DNA isolated from 293T cells expressing TET2, OGT or both was denatured by 0.2 N NaOH and dotted on Hybond-N⁺ nitrocellulose membrane (Amersham Pharmacia Biotech). After ultraviolet cross-linking, membranes were blocked overnight with 10% non-fat milk and 1% BSA in TBST (150 mM NaCl, 10 mM Tris, pH 8.0, and 0.1% Tween20) at 4 °C followed by 1 h incubation with either anti-5mC or anti-5hmC antibodies at room temperature. Membranes were washed four times with TBST, incubated with horseradish peroxidase (HRP)-conjugated goat anti-mouse or anti-rabbit antibodies (GE Healthcare), washed with TBST and developed using the ECL+ detection system (GE Healthcare).

Mass spectrometry analysis. For 5ghmC standard, β-glucosyltransferase was used to produce 5ghmC following the protocol of Zymo Research using UDP-GlcNAc as the donor. The DNA was digested with DNA degradase plus (Zymo Research). The samples were subjected to liquid chromatography tandem mass spectrometry (LC-MS/MS). Liquid chromatography was performed using a 2.1 × 50 mm HSS T3 1.8 µm column (Waters), with gradient elution at a flow rate of 500 µl min⁻¹ using 0.02% acetic acid in water as mobile phase A and methanol as mobile phase B. The gradient was (96% A + 4% B) to (70% A + 30 B) in 4.7 min. The elutes were directed to the mass spectrometer that was running in the product scan mode (60–500 *m/z*) selecting 461 as precursor ion (5ghmC). The collision energy used was 30 V.

For detecting 5ghmC or glucosylated-5hmC, genomic DNA from 293T cells expressing TET2 and OGT was digested as above and subjected to LC-MS/MS analysis using the same column and conditions as above. The mass spectrometer was running in multiple reaction monitoring mode, monitoring the transition of *m/z* 242.0 to 126.0 (5mC), *m/z* 258.0 to 142.0 (5hmC), 461.0 to 345.0 (5ghmC) and *m/z* 420.0 to 304.0 (glucosylated-5hmC), with the collision energy as 15 V.

- Shechter, D., Dormann, H. L., Allis, C. D. & Hake, S. B. Extraction, purification and analysis of histones. *Nature Protocols* **2**, 1445–1457 (2007).
- Fujiki, R. *et al.* GlcNAcylation of a histone methyltransferase in retinoic-acid-induced granulopoiesis. *Nature* **459**, 455–459 (2009).
- Robinson, K. A., Ball, L. E. & Buse, M. G. Reduction of O-GlcNAc protein modification does not prevent insulin resistance in 3T3-L1 adipocytes. *Am. J. Physiol. Endocrinol. Metab.* **292**, E884–E890 (2007).
- Ko, M. *et al.* Impaired hydroxylation of 5-methylcytosine in myeloid cancers with mutant TET2. *Nature* **468**, 839–843 (2010).
- Yang, Z. *et al.* MicroRNA hsa-miR-138 inhibits adipogenic differentiation of human adipose tissue-derived mesenchymal stem cells through adenovirus EID-1. *Stem Cells Dev.* **20**, 259–267 (2011).

CAREERS

FUNDING US National Science Foundation expands application requirements **p.567**

TENURE University librarians seek recognition and faculty status **p.567**

NATUREJOBS For the latest career listings and advice www.naturejobs.com

LUCIANO LOZANO/IKON/CORBIS



BY KELLY RAE CHI

Before Edward Chu entered his fourth year at Icahn School of Medicine at Mount Sinai in New York, he took a 12-month sabbatical to launch his first clinical trial. He wanted to evaluate whether patients using an anti-blood-clotting drug, usually to prevent heart attacks, should stop before general surgery. He thought that if he dedicated himself to the project for 12 months, he could wrap up any loose ends before he graduated in 2013. That was optimistic, to say the least.

Chu admits that his goal — to recruit 200 patients, half of whom would continue taking the drug before surgery while the other half discontinued it — was ambitious for a year-long project. His adviser offered guidance throughout, but the day-to-day logistics were up to Chu.

Even with an encouraging adviser, financial support from a Doris Duke Clinical Research Fellowship and access to hundreds of potential participants, planning the trial was far more time-consuming than Chu had expected. All investigators need help from specialists and other partners to embark on a clinical trial, but especially first-timers. Although leading a trial often falls to senior researchers, junior investigators training as physicians or undertaking PhDs can have a major role — especially if they are hoping to make clinical studies a big part of their career. Chu needed assistance at almost every step — from his adviser, support staff such as nurses and research coordinators, biostatisticians, members of regulatory review boards, surgeons and cardiologists. In the end, he had to scale the work back into a pilot study, but the experience taught him a great deal about what it takes to make a trial happen.

FIRST STEPS

Initiating and sponsoring a clinical trial to generate safety and efficacy data for a drug, diagnostic test, device or therapy protocol is an all-consuming team project. The planning stages, which involve transforming an idea into a detailed protocol, assessing and procuring resources and getting approval to do the study, are almost always more complicated and time consuming than a junior investigator expects. They involve multiple reviews from regulatory agencies, and a sometimes gruelling effort to motivate busy clinicians — who often have little stake in the outcome — and their staff, key collaborators who help to provide access to a pool of patients. All these moving parts require careful orchestration. For a new ►

CLINICAL RESEARCH

Conducting a trial

Beginners hoping to initiate and complete a clinical trial must understand the complexities of the process.

► investigator, each step of a clinical trial represents an important learning experience, says Karen Zier, associate dean for medical-student research at Mount Sinai, who helped to pair Chu with his adviser. These are not lessons that trainees can learn solely from a textbook.

A clinical trial starts with a scientific question. But before designing the trial, researchers must have an idea of whether it is feasible: they must transform the idea into a testable hypothesis; consider the target patient population; and determine the appropriate time frame in which to get results, says Edward Kim, chair of solid-tumour oncology and investigational therapeutics at Levine Cancer Institute in Charlotte, North Carolina. Feasibility analysis is often handled by clinical-research coordinators or other experts at the investigator's home institution, who can help the investigator to decide, from a financial and operational standpoint, whether the study goal is realistic. "There are many cases when you can have a great scientific idea, but it's not practical [to do a clinical trial]," says Kim. Failure is likely, he says, if a trial has too many rigid requirements for patient inclusion, or is too complex to attract or treat enough patients. Junior investigators should talk to mentors and experienced clinical researchers in their field to help them to decide whether an idea is realistic.

Just calculating the appropriate number of participants can be a challenge, says Norma Terrin, director of the Research Design Center and the Biostatistics Research Center at Tufts Medical Center in Boston, Massachusetts. A biostatistician or epidemiologist can help. Other concerns include whether to do a blinded study (in which the participants, researchers or both are unaware of which treatment is being administered), a randomized one (in which participants are assigned to a treatment group by chance) or both; whether there are any potential sources of bias; how researchers will analyse the data; why data might be missing (reasons include patients dropping out of the study or not complying with protocols); and how researchers will deal with missing data points. With due consideration, the study can be designed to minimize data loss, says Terrin.

FINANCIAL STRUGGLE

Trials can be expensive: they range from tens of thousands of dollars for small studies to several hundred million for large, multicentre trials, according to a 2010 report from the Institute of Medicine in Washington DC (Forum on Drug Discovery, Development, and Translation *Transforming Clinical Research in the United States* National Academies Press, 2010). Costs vary from nation to nation owing in part to differing regulatory standards and patient-recruitment practices. Even within a single country, institutions bill in different ways for insurance, lab tests and supplies, staffing and other study costs. This combination of factors makes financing a major hurdle.

Early-career investigators might be able to get their own institutions or foundations to provide small start-up grants — typically ranging from US\$20,000 to \$50,000 — to fund collection of preliminary data. At the MD Anderson Cancer Center in Houston, Texas, for example, the Duncan Family Institute Seed Funding Research Program awards \$50,000 per year for two years to support preliminary research on cancer prevention and risk, with the goal of improving the success of proposals submitted for larger grants. And some of the 60 institutions supported by US National Institutes of Health Clinical and Translational Science Awards (CTSAs) provide money for pilot studies. For example, the Institute for Clinical and Translational Science at the University of Iowa in Iowa City offers up to \$50,000 for a preliminary study lasting no longer than one year. There is a wide range of CTA start-up grants, from a small amount to screen an assay to larger amounts to get projects off the ground, says Bobbi Gardner, a spokeswoman for the National Center for Advancing Translational Sciences in Bethesda, Maryland, which administers the CTSAs.

The figures are similar in other countries. Cancer Research UK, for example, offers feasibility-study grants of around £25,000 (US\$40,000) a year for two years. In rare cases, it might provide as much as £80,000.

Many institutions, including those with CTSAs, fund shared clinical-trial resources in the form of, for example, a biostatistics department, a study facilitator or coordinator, or specific programmes. Foundations run by patient advocates — who are often impatient with the slow pace of clinical research — not only fund clinical trials but also support them by, for example, helping to recruit participants. If a trainee's institution has no track record in clinical research, there is the possibility of collaborating with a researcher at one that does.

Then there are industry partnerships: companies will often fund clinical trials of their own drugs or devices. Junior investigators should keep in mind, however, that involving industry can mean that it takes longer to sort out reimbursement, data sharing, intellectual-property issues and any extra reviews required legally or by the company itself.

Before putting together a team or enrolling patients, clinical-trial investigators must

secure regulatory approval for their study plan. The specifics of the approval process vary by country and even within countries, but the basic goal is the same: to protect the safety of research participants. Protocols should be written according to the local version of Good Clinical Practice, an international standard for designing and carrying out clinical trials, provided by International Conference on Harmonisation in Geneva, Switzerland.

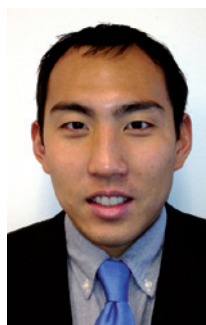
In some countries, including the United States, Australia, Japan, New Zealand and South Africa, the protocol is usually examined by an institutional review board (IRB) affiliated with the investigator's hospital or medical centre. IRBs uphold federal, state and local regulations and university policies. Each board interprets regulations differently, so multisite studies involving more than one board are often complicated. As a general rule, researchers should make their protocols extremely easy to understand — members of review-board panels will not necessarily be familiar with the subject area.

Researchers must be prepared to justify every aspect of a protocol; for example, if it calls for four biopsies, the investigator must be able to explain the reason for each. If the IRB thinks that the risks of any of the steps outweigh the potential benefits, it will ask for changes. This back-and-forth can take months, and it doesn't end there: IRBs often ask for update reports at regular intervals during the trial.

Researchers in the United States may also need to allow an extra one or two months to file an application for an investigational new drug or investigational new device to the Food and Drug Administration (FDA), which will do a safety review. This step doesn't just apply to new pharmaceutical compounds: it may also be necessary if, for example, an investigator is using a nutritional supplement to treat a disease; in that case, the supplement is technically a new drug and requires an FDA review, notes Harvey Arbit, a regulatory-affairs consultant who lectures at the University of Minnesota in Minneapolis. Complicating matters, the wording of the protocol may influence whether filing is necessary: if the filer states that the supplement is "normalizing physiological functions" rather than "treating", the decision becomes more difficult. There is no foolproof way to decide, says Arbit — when in doubt, it is safer to file. Even if the investigator does this but ends up receiving a letter from the FDA stating that filing was unnecessary, it is good to have the documentation.

THE RIGHT PEOPLE

Chu's goal of enrolling at least 200 patients in his study meant that he had to work with multiple clinical specialists. But he found it daunting, especially as a newcomer, to approach cardiologists and surgeons individually to sell his study. Specialists tend to be sceptical of studies and protective of their patients — and Chu's study had associated risks. But after



"A study can fall by the wayside unless someone is there to push the protocol and research agenda."

Edward Chu

E CHU

approaching many physicians, he was eventually able to get about a dozen on his team.

Clinicians help to identify patients eligible for the study. Crucially, they can boost recruitment by mentioning that they are excited about the project, says Jeff Burns, director of the Clinical and Translational Science Unit at the University of Kansas Medical Center in Kansas City. But the next steps of enrolment — pre-screening the patients by reviewing medical histories, approaching them to gauge interest, discussing protocols and informed consent, and setting up in-person screening visits — require a huge amount of work. A common mistake is for novice investigators to rely too much on the clinician's office to sign up patients. Clinicians and their staff focus on treating patients, not research; as a result, a study can fall by the wayside “unless someone is there to push the protocol and research agenda”, says Chu. Enrolment should be monitored at each step by a team member fully invested in the study — perhaps the principal investigator, a trainee physician doing a medical residency or a medical student. Researchers with sufficient funds can hire a dedicated recruitment coordinator to screen prospective participants for any reasons they should be disqualified from the study, as well as to explain the study and its risks and send out consent forms.

RECRUITMENT DRIVE

It took Chu six months to design his study, get IRB approval and assemble a research team. Only then could he begin recruiting patients and collecting data. A few months into data collection, he ran a preliminary analysis that revealed that he would in fact need several hundred participants in each study group to provide a significant result. By the end of his fellowship year, he had enrolled only 50.

One problem was that a potential participant's cardiologist and surgeon often disagreed about whether they should discontinue or continue the anti-platelet medication, so Chu could not invite that person to participate in the study. Furthermore, potential participants' medical histories were often more complex than anticipated, making it difficult to determine who was suitable for the trial.

Enrolment challenges are not unusual. A 2011 study found that nearly one-third of clinical studies terminated at Oregon Health and Science University (OHSU) in Portland between 2006 and 2009 were under-enrolled for various reasons; such terminations cost OHSU at least \$1 million in 2009 alone (D R. Kitterman *et al. Acad. Med.* 86, 1360–1366; 2011). Low recruitment is a big problem in the United States and elsewhere, says William Balke, a programme director of clinical-research services at the University of California, San Francisco (UCSF). “If we don't do

a better job [at recruitment], we're wasting the public's money and we're not advancing science,” he adds. One reason for the problem is a lack of thorough feasibility analysis to determine, for example, whether there are enough patients to do the desired study.

Some institutions run formal recruitment programmes; for example, UCSF has a Recruitment and Implementation Core, which serves the university and affiliated investigators. Investigators can also turn to online participant registries and tools such as ResearchMatch.org — a free online service that connects volunteers with researchers — or even use less conventional communication routes, such as social media. “We have been extraordinarily, surprisingly successful recruiting patients through Craigslist and keeping in touch with them through e-mail, text messages and Twitter,” says Balke.

But researchers need to exercise caution when reaching out to patients through social media. Rahlyn Gossen, founder of Rebar Interactive, a digital-marketing company based in New Orleans, Louisiana, which recruits and retains study subjects, says that researchers' messages to potential participants need to be approved by the local IRB, regardless of whether they are online. Regulations on patient recruitment were not



“If we don't do a better job at recruitment, we're wasting the public's money.”

William Balke

to be completed while Chu finishes medical school. Still, he feels that he accomplished a lot in one year — and he learned a lot about the complexities of the clinical-trial process. Now in his fourth year of medical school, Chu is still enrolling patients and collecting data, and is looking forward to launching a new clinical trial in the future. “It's a learning experience,” he says. With the understanding he has gained, Chu expects his next trial to be “easier to manage”. ■

Kelly Rae Chi is a freelance writer based in Cary, North Carolina.

FUNDING

NSF grant changes

The US National Science Foundation (NSF) has changed some of its grant-submission requirements, effective from 14 January. The project-summary section of the submission now asks applicants to use separate text boxes for their proposal overview, their description of the project's intellectual merit and their explanation of its broader impacts. Submitting these sections as one document will cause the application to be rejected. NSF spokeswoman Maria Zacharias says that reviewers were spending too long teasing out the merits and impacts of proposals. Applicants may also now list research products such as patents, data sets or software in addition to publications — a boon for junior investigators, says Zacharias. The changes stem from a review by the NSF's oversight board, and a federal directive that the agency recognize the broader impact of research it supports.

TENURE

Respect for librarians

Many more US university librarians should be tenured faculty members, argue groups representing universities and colleges, academic libraries and professors. A statement released on 10 January and spearheaded by the American Association of University Professors in Washington DC notes that librarians support research needs, contribute to intellectual and academic freedom, perform outreach and should have a right to contribute to university policy. “There's a lack of recognition as to what librarians actually do,” says Deanna Wood, an associate professor and reference librarian at the University of New Hampshire in Durham and part of the Joint Committee on College Library Problems, which drafted the statement.

SALARIES

Academic pay lagging

Early-career scientists with full-time jobs in US academia earn an average of US\$58,000 annually, less than those in industry, non-profit or government, says a report from the US National Science Foundation (NSF). Industry pays the most: \$100,000 per year in early career, and \$130,000 for those 10 years past their PhDs. Academics who got a doctorate a decade ago or more earn \$93,000 a year on average. Daniel Foley, a statistician for the NSF in Arlington, Virginia, says that the data underscore the need to train researchers for work outside academia.

THE SHORTLIST

Time management.

BY ADAM KUCHARSKI

“Top work everyone. Seriously, this is outstanding,” Hugo Vriers leafed through the stack of papers. “Two dogs and a monkey, extraordinary.”

“Chimp,” Professor Reed muttered.

Vriers squinted at the page. “Quite. And how is he doing, Janet?”

Dr Cranmer leant forward in her chair. “He’s pretty sprightly, all things considered.”

Vriers turned to Professor Garcia, who was busy jabbing his phone with an elderly finger. “Pablo, did everything stay within the limits this time?”

Garcia nodded. “All was smooth. No repeats of the second test.”

“What happened in the second test?” Reed asked.

“Knocked out the power in half of London,” Vriers said.

“Which half?”

“South.”

Reed chuckled. “Ah well, these things happen.”

“Tell that to the Mayor,” Vriers pushed the papers to one side. “Now, there’s a few things we need to discuss. I’ve had a chat with the board, and we’ve decided to draw up a shortlist of objectives.”

Garcia shook his phone as if it were a sandy shoe. “Objectives?”

“Yes. We need a proper plan for this technology. It’s all very well sending a beagle to the Renaissance or a chimp to the jazz age, but human time travel... well, the possibilities are endless. Literally.”

“What’s on your shortlist?” Reed asked.

Vriers flipped open a notebook. “Number one: ‘Get rid of post tyrants.’” He paused. “Past. I think that should say ‘past.’”

“Which ones?” asked Cranmer.

“We haven’t decided yet. All of them perhaps? Top ten?” He tapped his pen against the pad. “Hitler seems like an obvious place to start.”

Garcia frowned. “Time is a delicate tapestry. We should not naively pull at her threads.”

Vriers looked at Cranmer, who shrugged, then turned back to Garcia. “I have a feeling you’re not so keen, Pablo?”

Garcia sighed, shaking his head. “You talk of changing history as if it were a grocery list. We cannot just decide to —”

“Okay,” Vriers said, “how about I just put Hitler for now? With

maybe a little question mark in brackets. We can always add more later. Right, number two: mysteries. There’s a few things we ought to get to the bottom of.”

“Can we find out what happened to Kit Marlowe?” Cranmer asked.

Vriers’ pen hovered over the page. “Shakespeare’s friend? See, I’m not sure the board will go for that. How about Roswell, or JFK?”

“Or the Amber Room,” Reed said.

“What’s that?” Cranmer asked.

“Big room. Made of amber. Someone pinched it from the Russians in the ’40s.”

Cranmer raised her eyebrows. “Worth much?”

“Probably.”

“Actually, is dosh on your list, Hugo?” she asked.

“Dosh?” Vriers said.

“With our machine, we could get the lottery numbers.”

Vriers winced. “Isn’t that a little...?”

“A little?”

“Unethical? I imagine the committee would get annoyed.”

“What committee?”

“I don’t know. I just assumed you lot had a committee for that sort of thing.”

Cranmer removed her glasses. “Even if we do, there isn’t much in the kitty anymore.”

Reed nodded. “And school fees don’t pay themselves.”

“I see,” Vriers said, scribbling on his pad. “Right, how about this? ‘Win lottery... but only a bit.’”

“Need five year’s boarding at least,” Reed said.

“Very well,” Vriers turned the page. “Next we have ‘Inspiration’. The directors were hoping we could get some new ideas from somewhere. Or somewhere, rather. Any suggestions?”

“I’d love to meet Newton,” Cranmer said. “That would certainly inspire me.”

“And Monroe,” Reed added.

“Can we try and focus on —”

“I think she was best in 1955,” Reed said, leaning back in his chair. “*The Seven Year Itch*, what a —”

“The future!” Vriers groaned. “Please, concentrate on the future. What can we bring back? What technology do we need?”

“Do we not risk a paradox?” Garcia said. “I am concerned that —”

“It’s fine,” Vriers said. “Our logic team are on it.”

“Logic team?” Reed asked.

“The laddies in the basement,” Cranmer said, pointing downwards, “the ones with toy DeLoreans on their desks.”

Reed laughed. “I thought they were someone’s kids.”

“It is not so simple,” Garcia said. “No one can truly see how —”

“They know what they’re doing,” Vriers said. “Trust me, we’re fine on the paradox front.”

“As long as nobody gets someone pregnant,” Cranmer said.

“What?”

“You know, like in *The Terminator*. Time babies.”

“Look, nobody is having any, um, time...”

“Babies.”

“... time babies. Now, let’s focus on business. There are nine more objectives to get through.”

Vriers glanced at his phone, sat atop one of the piles of papers. “It’s almost three o’clock, and I’ve got a meeting at four. So let’s get on with it.”

As he picked up his pen, the phone started to ring. He answered it and a draught sent the documents billowing across the room.

“Are you serious?” Vriers asked, surrounded by the dancing sheets. He waved them away, the colour draining from his face. “When did this happen? Who left it turned on? Okay, I’ll be right down.”

“What’s the problem?” Cranmer said.

Vriers stood up. “The chimp’s stolen the machine.”

“Sorry, what?”

“The chimp. He’s vanished with the machine.”

The room fell silent.

“Come on,” Vriers said, slamming his palms against the table. “Don’t just sit there! We need to get it back! Think, what are we going to do?”

Garcia smiled. “Put it on your list?” ■

Adam Kucharski is based in London, where he researches the cocktail of influences behind disease outbreaks.



JACEY

➔ NATURE.COM

Follow Futures:

@NatureFutures

go.nature.com/mtoodm